
Towards bottom-up reconstitution of a functional FtsZ-based cell division machinery

Adrián Merino Salomón



2023

Towards bottom-up reconstitution of a functional FtsZ-based cell division machinery

Adrián Merino Salomón

Dissertation
an der Fakultät für Biologie
der Ludwig-Maximilians-Universität
München

vorgelegt von
Adrián Merino Salomón
aus Fuenlabrada, Madrid; Spain

München, den 6th March 2023

Erstgutachter: Prof. Dr. Thorben Cordes

Zweitgutachter: Prof. Dr. Petra Schwille

Tag der Abgabe: 6th März 2023

Tag der mündlichen Prüfung: 11th Oktober 2023

A mi familia
Jamás lo hubiera logrado sin vosotros

Eidesstattliche Erklärung

Hiermit versichere ich an Eides statt, dass die vorliegende Dissertation von mir selbstständig und ohne unerlaubte Hilfe angefertigt wurde. Des Weiteren erkläre ich, dass ich nicht anderweitig ohne Erfolg versucht habe, eine Dissertation einzureichen oder mich der Doktorprüfung zu unterziehen. Die Dissertation liegt weder ganz, noch in wesentlichen Teilen einer anderen Prüfungskommission vor.

München, 6. März 2023

Adrián Merino Salomón

Table of contents

Eidesstattliche Erklärung	VII
List of Figures	XI
Abstract	XIII
List of Publications	XV
Contributions	XVII
1 Introduction	1
1.1 Bottom-up synthetic biology	1
1.1.1 The top-down approach	1
1.1.2 The bottom-up approach	3
1.1.3 <i>In vitro</i> reconstitution of molecular systems	4
1.1.4 Cellular membranes	5
1.1.5 Macromolecular crowding and microenvironments	5
1.1.6 Vesicles as synthetic cellular models	8
1.1.7 The prospect of building a minimal synthetic cell	12
1.2 The bacterial cell division machinery	17
1.2.1 FtsZ, the central protein of division	21
1.2.2 Membrane attachment of the FtsZ-ring	25
1.2.3 Spatiotemporal localization of the FtsZ-ring by the MinCDE system	29
1.2.4 FtsZ-ring stabilization and assembly	32
1.2.5 FtsZ-ring structure and function	34
2 Objectives	41
3 Publications	43
3.1 Publication P1.	
Self-organized protein patterns: the MinCDE and ParABS systems	43
	IX

3.2	Publication P2.	
	FtsZ reorganization facilitates deformation of giant vesicles in microfluidic traps	55
	- Supplement to publication P2	63
3.3	Publication P3.	
	FtsZ induces membrane deformations via torsional stress upon GTP hydrolysis	85
	- Supplement to publication P3	99
3.4	Publication P4.	
	<i>In vitro</i> assembly, positioning and contraction of a division ring in minimal cells	107
	- Supplement to publication P4	123
3.5	Publication P5.	
	Crosslinking by ZapD drives the assembly of short, discontinuous FtsZ filaments into ring-like structures in solution	167
	- Supplement to publication P5	199
4	Discussion and perspectives	219
5	Bibliography	231
	List of abbreviations	267
	Acknowledgements	269
	Curriculum Vitae	273

List of Figures

1.1	The bottom-up and top-down approaches in synthetic biology.	2
1.2	The crowded and complex internal cellular environment.	6
1.3	Lipid vesicles and methods for vesicle production.	9
1.4	Essential modules of an ideal synthetic cell from the bottom-up.	13
1.5	Overview of the cell division process in <i>E. coli</i>	19
1.6	FtsZ is the central protein of bacterial division.	22
1.7	FtsZ filaments follow a GTP-driven treadmilling mechanism.	24
1.8	FtsZ-ring attachment to the membrane.	26
1.9	The MinCDE system.	30
1.10	Stabilization of the FtsZ-ring and filament crosslinking.	33
1.11	Structure of the FtsZ-ring.	35
1.12	Function of the FtsZ-ring.	37

Abstract

Synthetic biology aims at the understanding of living organisms through an engineering perspective, with the goal of improving or creating new biological systems. The prospect of building a synthetic cell focuses on producing life from basic elements by combining synthetic and/or organic cellular components in a bottom-up manner. To create a synthetic cell, the minimal functions of life are required and cell-free synthetic biology offers a suitable framework for understanding biological processes outside the inherently noisy environment of cells. A synthetic cell is expected to exhibit characteristics of a living cell, such as fundamental metabolism, proliferation, and communication. The bottom-up approach utilizes a wide range of *in vitro* tools/technologies such as biomimetic membranes, protein reconstitution, cell-free expression reactions, and microfluidics. As tools, they enable the thorough characterization of functional modules such as metabolism, replication, and cell division. The ultimate goal is to integrate these modules to construct a predictable, customizable, and controllable entity.

Among the functional modules of living organisms, cell division stands out as a hallmark feature. The machinery of division has evolved into a highly organized set of proteins with the aim of accurately splitting a mother cell into two daughter cells, while preserving the genetic information and cellular integrity. In the case of bacteria, and more concretely *Escherichia coli*, cell division is mediated by the divisome, a contractile ring consisting of a multiprotein complex that precisely assembles at midcell. At the center of this machinery is the essential FtsZ protein, which is able to polymerize and form the FtsZ-ring. This ring is key to the process, serving as a scaffold for the divisome and driving the division process. However, the molecular details of how the ring is functionally assembled, stabilized, and positioned are still not well understood. Therefore, the aim of this thesis is to develop and expand the knowledge about the molecular mechanism of the FtsZ-ring assembly and its function as a potential primary component in the minimal division machinery of synthetic cells.

To this end, and following a bottom-up approach, we conducted assays based on the *in vitro* reconstitution of FtsZ in cellular mimic environments using lipid vesicles. This allows the characterization of FtsZ's behavior and functionalities in environments that are similar to a potential synthetic cell. Firstly, we designed a microfluidic device to deform lipid vesicles into bacterial rod-shaped compartments to analyze the effect of different geometries and membrane tension on FtsZ. We found that FtsZ filaments align with the shorter axis of the rod-shaped vesicles and reorganize into cone-like structures when the membrane tension is lowered, causing membrane deformations. This suggests that there is a geometry and tension-dependent mechanism in the assembly of FtsZ structures on membranes. Secondly, we designed an *in vitro* reconstitution assay based on soft lipid tubes pulled from FtsZ-decorated vesicles using optical tweezers. We observed the transformation of lipid tubes into 3D spring-like structures, where the GTPase activity of FtsZ drives spring compression likely through torsional stress. This allowed us to gain mechanistic insights into the molecular dynamics behind the force generated by FtsZ filaments. Thirdly, we studied the spatiotemporal localization of the division ring by co-reconstituting FtsZ inside lipid vesicles with the MinCDE system, which is involved in positioning the divisome *in vivo*, and FtsA, the natural tether of FtsZ to the membrane. We achieved the assembly, placement, and onset of constriction of a minimal division ring inside lipid vesicles using two different approaches: purified components or cell-free expression of the MinCDE, FtsA, and FtsZ proteins. This represents a significant advance towards the *in vitro* reconstitution of functional modules in a synthetic cell and expands our understanding of the molecular mechanism underlying the spatiotemporal organization of the FtsZ-ring. Lastly, we employed biochemical studies combined with cryo-ET visualization to characterize the stabilization of the division ring and the crosslinking of FtsZ filaments by ZapD, a protein known as one of the stabilizers of the divisome. We observed the formation of toroidal structures in solution that are assembled by short FtsZ filaments connected by ZapD and have bacterial size. Their characterization in 3D brings valuable structural information about the FtsZ-ring and its functional stabilization, which is important for its further reconstitution in minimal systems.

In conclusion, this thesis provides important insights into the molecular dynamics of the central protein of division in *E. coli* and most bacteria, addressing its activity on the membrane, mechanism of force constriction, spatiotemporal localization and stabilization of the FtsZ-ring. Furthermore, we demonstrate significant advancements towards the implementation of FtsZ-based division systems in minimal synthetic cells using a bottom-up approach.

List of publications

- P1 **Merino-Salomón, A.***, Babl, L.* and Schwille, P. (2021). Self-organized protein patterns: The MinCDE and ParABS systems. *Current Opinion in Cell Biology*, 72:106-115. DOI: 10.1016/j.ceb.2021.07.001 (*Review*)
- P2 Ganzinger K.*, **Merino-Salomón, A.***, García-Soriano, D., Butterfield, N. A., Litschel, T., Siedler, F. and Schwille, P. (2020). FtsZ Reorganization Facilitates Deformation of Giant Vesicles in Microfluidic Traps. *Angew. Chem. Int. Ed.* 2020, 59, 21372-21376. DOI: 10.1002/anie.202001928
- P3 Ramirez-Diaz, D. A., **Merino-Salomón, A.**, Meyer, F., Heymann, M., Rivas, G., Bramkamp, M. and Schwille, P. (2021). FtsZ induces membrane deformations via torsional stress upon GTP hydrolysis. *Nature Communications* 12, 3310. DOI:10.1038/s41467-021-23387-3
- P4 Kohyama, S.*, **Merino-Salomón, A.*** and Schwille, P. (2022). *In vitro* assembly, positioning and contraction of a division ring in minimal cells. *Nature Communications* 13:6098. DOI: 10.1038/s41467-022-33679-x
- P5 **Merino-Salomón, A.**, Schneider, J., Babl, L., Krohn, J-H., Sobrinos-Sanguino, M., Schäfer, T., Luque-Ortega, J.R., Alfonso, C., Jiménez, M., Jasnin, M., Rivas, G., Schwille, P. (2023). Crosslinking by ZapD drives the assembly of short, discontinuous FtsZ filaments into ring-like structures in solution. *BioRxiv* 2023.01.12.523557 DOI: 10.1101/2023.01.12.523557 (*Submitted*)

Contributions

P1 Self-organized protein patterns: The MinCDE and ParABS systems.

Co-first author (review).

A.M.-S. and L.B. wrote the parts concerning the MinCDE system and ParABS system, respectively. A.M.-S., L.B., and P.S. integrated the introduction and discussion; revised and edited the manuscript. Therefore, the contributions of A.M.-S. and L.B. are estimated to be shared equally.

P2 FtsZ Reorganization Facilitates Deformation of Giant Vesicles in Microfluidic Traps.

Co-first author

K.G. and P.S. conceived the study. K.G. and A.M.-S. designed and performed the experiments, analyzed the data and made the figures. All authors participated in the optimization and testing of the microfluidic device. K.G. and A.M.-S. wrote the original draft. All authors discussed the results, revised, and edited the manuscript. The contributions of K.G. and A. M.-S. are estimated to be shared equally.

P3 FtsZ induces membrane deformations via torsional stress upon GTP hydrolysis.

Second author

D.A.R.-D. and P.S. conceived this study and wrote the manuscript with the support of M.B. for the *in vivo* spheroplasts section. D.A.R.-D. designed, performed, and analyzed all experiments with FtsZ-YFP-mts and FtsZ-YFP-mts*[T108A]. A.M.-S. designed, performed, and analyzed experiments with ZipA + FtsZ using proteins provided by G.R. M.H. manufactured wafer for microstructures and provided PMDS microstructures. M.B. and F.M. designed, performed, and analyzed *in vivo* spheroplasts experiments. MATLAB custom scripts for data acquisition and analysis were coded by D.A.R.-D. All authors discussed, interpreted results and revised the manuscript.

P4 *In vitro* assembly, positioning and contraction of a division ring in minimal cells.

Co-first author

S.K., A.M.-S., and P.S. conceived the study and wrote the manuscript. S.K. designed, performed, and analyzed all experiments with cell-free expression. S.K. made the custom ImageJ macro script for the analysis and kymograph visualization. A.M.-S. designed, performed, and analyzed all experiments with purified proteins within vesicles and SLBs. S.K. designed plasmids for cell-free expression and purification of Min proteins and FtsZ-G55-Venus-Q56. A.M.-S. purified FtsZ-YFP-mts and purified and fluorescently labelled FtsZ-wt. A.M.-S. also characterized FtsZ-G55-Venus-Q56

and FtsZ-wt by performing a GTPase assay. The contributions of A. M.-S. and S.K. are estimated to be shared equally.

P5 Crosslinking by ZapD drives the assembly of short discontinuous FtsZ filaments into ring-like structures in solution.

First author

A.M.-S., M. Jiménez and G.R. conceived the study. A.M.-S. purified and fluorescently labelled ZapD and FtsZ. M.S.-S. performed FtsZ GTPase assays. A.M.-S. and J.-H.K. designed, performed and analyzed FCS and fluorescence anisotropy experiments. A.M.-S. and M. Jiménez designed and performed light scattering assays. M. Jiménez, C.A. and J.R.L.-O. designed, performed and analyzed the AUC data. A.M.-S., J.S., T.S. and M. Jasnin designed, performed, and analyzed the cryo-EM and cryo-ET experiments. L.B. designed the plasmid and purified mZapD. A.M.-S. performed the encapsulation in lipid vesicles. A.M.-S. wrote the original draft. A.M.-S., L.B., M. Jiménez, M. Jasnin, G.R. and P.S. revised the manuscript and figures. All authors discussed the results and revised the manuscript.

We hereby confirm the contributions to the above-mentioned publications.

Leon Babl [P1]

Adrián Merino Salomón

Kristina Ganzinger [P2]

Thorben Cordes

Shunshi Kohyama [P4]

Petra Schwille

Introduction

1.1 Bottom-up synthetic biology

Synthetic biology is an interdisciplinary research field focused on engineering artificial biological systems that mimic selected cellular functions and processes or build completely new functionalities not found in nature [1, 2, 3]. This novel research field was born after the combination of classical biological and chemical approaches were complemented with an engineering view of modularity, modification and construction (**Figure 1.1a**). Synthetic biology could be broadly categorized into two groups: (1) the top-down approach consisting of the manipulation of existing natural systems or (2) the bottom-up approach assembling artificial functional systems from their fundamental biological components such as DNA, proteins and lipids (**Figure 1.1b**). Among many different purposes, both approaches share the same goal of creating fully functional synthetic cells with desired functionalities. Reviewed in [4, 2, 5, 6, 7, 8, 9, 10, 11].

1.1.1 The top-down approach

The top-down strategy exploits the huge diversity of existing natural parts found in living systems to engineer them with predictable and controllable functions that are potentially beneficial for a wide range of human activities [12, 13]. For instance, the creation of artificial compositions of new genetic, metabolic, or signalling networks enables the exploitation of cellular metabolic processes aiming at the creation of living factories that produce drugs, biofuels, biomaterials, or fine chemicals. The top-down approach has experienced a great improvement in recent years thanks to the new tools to synthesize, recombine, engineer and sequence DNA, allowing the simplification, modification or addition of functional modules to living systems [14, 15, 16].

The top-down approach has proven its potential in research answering questions about the fundamental understanding of life. The most representative success of the top-down

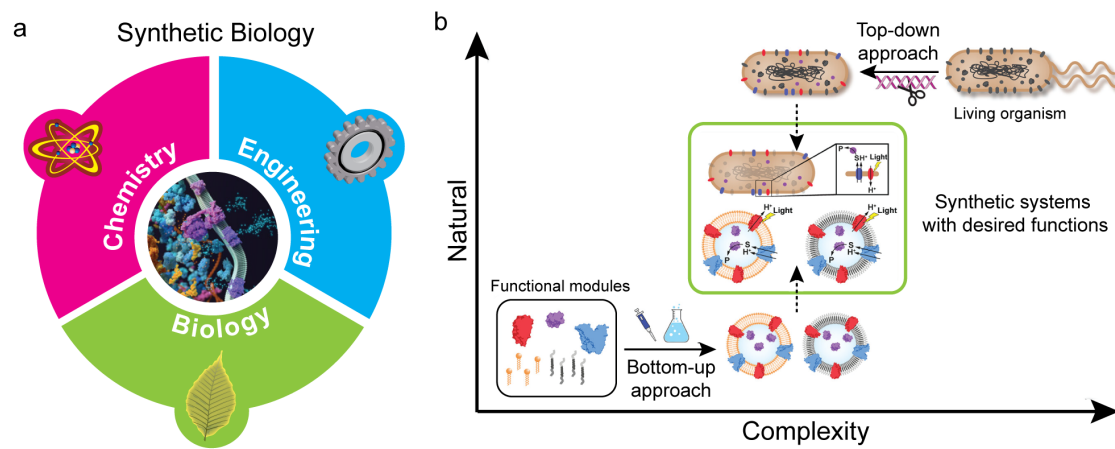


Figure 1.1: The bottom-up and top-down approaches in synthetic biology.

a) Synthetic biology is a multidisciplinary field of science that focuses on living entities and combines biology and chemistry with engineering principles to develop new biological parts, devices, and systems or to redesign existing systems found in nature. **b)** Representation of the bottom-up and top-down approaches in synthetic biology. a and b have been adapted with permission from [2]. Copyright 2022 American Chemical Society.

approach pursuing the aim of the synthetic cell is the synthesis of the minimal bacterial genome achieved by Craig Venter and coworkers. They genetically reduced the genome of *Mycoplasma mycoides* to only the essential genes for life. This minimal genome was chemically synthesized and it supported cell growth when transplanted into cytoplasm creating the JCV-syn1.0 [17, 18, 19]. After years of research, characterization and optimization, they created the genetic minimal bacterium JCV-syn3.0A with only 493 genes in a 543kbp DNA [20, 21]. Curiously, out of 452 protein-coding genes, approximately 90 remain without known function. Ongoing efforts are being carried out to understand the participation of each gene in the cell cycle as an essential factor for the development and survival of JCVI-syn3 [20]. This knowledge may help to understand basic cellular processes by identifying the fundamental components essential for life with the limitation from the inherent complexity of living cells themselves [22, 23].

In addition, the top-down approach aims for the controllable generation of application-driven modified synthetic organisms to achieve certain functions or products that are absent in nature. From the synthesis of products of interest to the use of desirable properties in the field of biomedicine, biotechnology, or bioremediation among others, this approach offers exciting perspectives for the future [24, 2, 13, 23].

1.1.2 The bottom-up approach

In contrast to the top-down, the bottom-up approach pursues the construction of cell-free systems designed from scratch to perform cellular processes, in order to understand their molecular mechanisms and ultimately allow for customizable designs of life-systems with adapted or repurposed functions [25, 8, 26]. This multidisciplinary field requires a combination of many biological disciplines such as biochemistry, molecular and cell biology, biophysics; and bioengineering disciplines, including micro-fabrication and microfluidics. The bottom-up approach is based on studying isolated components and minimal biological systems reconstituted in a controllable fashion and capable of performing basic biological phenomena, such as self-organization, self-replication, and self-sustainability [27, 2].

This approach employs the engineering principles in a much more efficient way than the top-down, as it provides unprecedented control over the independent functional modules due to the defined and simplified experimental setups [28, 29]. In these synthetic systems, every component can be defined and located in a quantitative manner, along with specified interactions between molecules. In addition, if there is sufficient biological information available regarding the function, behavior, and biochemical properties of each part, mathematical modelling is more precise, which is helpful for the design of synthetic systems.

The bottom-up approach strongly relies on the fundamental understanding of the different modules of life to be able to reconstitute, engineer and reshape them to fulfil their biological function or acquire new ones [30]. To achieve this in the long term, it is essential to study independent cellular processes on appropriate cellular-like platforms, eventually combining them into functional modules. Full reconstitution of proteins has revealed insights not accessible by cell biological approaches, such as detailed molecular characterization, self-assembly dynamics, or hidden functions.

Thus, by following a bottom-up approach and employing *in vitro* cell-like platforms, complex biological processes can be broken down into simpler modular parts defined at the molecular level. The characterization of each independent component within those modules will enable the understanding of their functionality and therefore confer further control of those molecules by design, which will open a new range of applications [31, 32]. Therefore, a bottom-up approach has been chosen in this thesis to gain insights into the molecular dynamics of a complex cellular system, such as bacterial cell division, aiming for the understanding of its minimal pieces and further reconstitution *in vitro*.

1.1.3 *In vitro* reconstitution of molecular systems

The ability to express and purify proteins has allowed an impressive improvement in our understanding of life on the molecular scale, making it possible to characterize the physical and biochemical features of isolated macromolecules. Their analysis in simplified experimental environments in a test tube has provided the base and essential insights into the current knowledge of most of the biological processes in life [33, 34]. However, the study of purified protein systems in aqueous buffers can fail in revealing their function, as many proteins require the presence of certain geometries, co-factors, biochemical environments or platforms to resemble their biological functionality, especially the ones that emerge their complex behaviors upon protein-lipid interactions [35, 36, 37]. For this reason, the study of macromolecules in conditions that mimic the cellular environment is often required for their functional reconstitution and eventually the understanding of biological processes. It is therefore of special interest to understand how molecules are linked and coordinated to generate remarkably robust cellular processes, which usually involve the creation of large structures in the order of dozens of micrometers over timescales of seconds to hours.

In vitro reconstitution can identify the properties of individual cellular components, understanding their interaction and coordination with other elements in a controlled manner. Therefore, they can complement *in vivo* studies and help to refine and improve molecular models of biological processes, facilitating their interpretation and providing information on how new ones could be engineered from scratch. Unexpected dynamics, hidden functions, or secondary mechanisms can arise in simplified reconstitutions, which might yield new insights into biological organization. However, the reconstitution of more complex cellular processes such as cell division, motility, or chromosome segregation involves the combination and self-organization of multiple components, including compartmentalization, signalling, energy or mechanical force [27]. This challenging task requires the study and characterization of every component at the molecular level, reconstituting them in cell-mimicking environments as similar as possible to their native state. This can only be achieved by using cellular-like platforms suitable to be used *in vitro*, including key components that can affect the behavior and dynamics of biological molecules.

1.1.4 Cellular membranes

Among all the cellular components found in living organisms, the cellular membrane stands up as one of the most important elements of the cell (**Figure 1.2a**). The cellular membrane is a semipermeable bilayer made of lipids [38, 39], containing a variety of proteins and sugars inside and on its surface, whose composition is highly heterogeneous and related to the specific function of the cell or organelle [40, 39]. Membranes are the base of the exchange of substrates and information, mediated by either a passive transport of small solutes or the protein-mediated exchange of components. In addition to its role as boundary and protection for cells and organelles, membranes provide the core and reaction platform for multiple cellular processes [41], such as signalling, generation of energy (respiration or photosynthesis), motility, adhesion or cellular division among others [42].

The role of the cell membrane in such a high number of cellular processes in both eukaryotic and prokaryotic organisms, together with its physical properties and biological importance, makes it a good target for research and a perfect candidate to be used as a reaction platform to reconstitute molecular systems in cell-mimic environments [43, 29, 44]. In addition, the physicochemical properties of the lipid molecules allow the generation of simplified artificial membranes *in vitro*. These artificial membranes mimic most of the biophysical and biochemical features found inside the cell, without having the uncontrollable heterogeneity of sugars and other molecules [45, 46, 47]. For this reason, the use of artificial lipid-based platforms is a popular approach to understand cellular processes *in vitro*. Some of the most used strategies are supported lipid bilayers (SLBs), free-standing membranes, lipid-coated beads [48, 49, 50, 51, 52], or liposomes and lipid droplets, providing tridimensional confinement [44, 53, 39]. Multiple examples of systems that have been successfully reconstituted into lipid-based platforms can be found in the literature, such as membrane proteins, cytoskeletal systems or enzymatic reactions [54, 44, 55, 39].

1.1.5 Macromolecular crowding and microenvironments

Another important aspect when comes to the *in vitro* reconstitution using cell-like systems is to mimic the properties of the cellular environments in which the biological processes take place (**Figure 1.2a**). The cellular interior is constituted by a highly heterogeneous mix of biomolecules of different natures, which crowds the available space and can therefore create unique microenvironments that typically are not found *in vitro*. It is estimated that about 30 % of the cytoplasm is occupied by polysaccharides, proteins, and nucleic acids, whose concentration is calculated to reach 300–400 g/L in the cytoplasm [57] or even 500 g/L in cellular organelles [58]. This crowded setting can considerably influence the behavior, diffusion, reactivity and distribution of the macromolecules participating in biochemical processes, which can eventually impact the enzymatic reactions and modulate

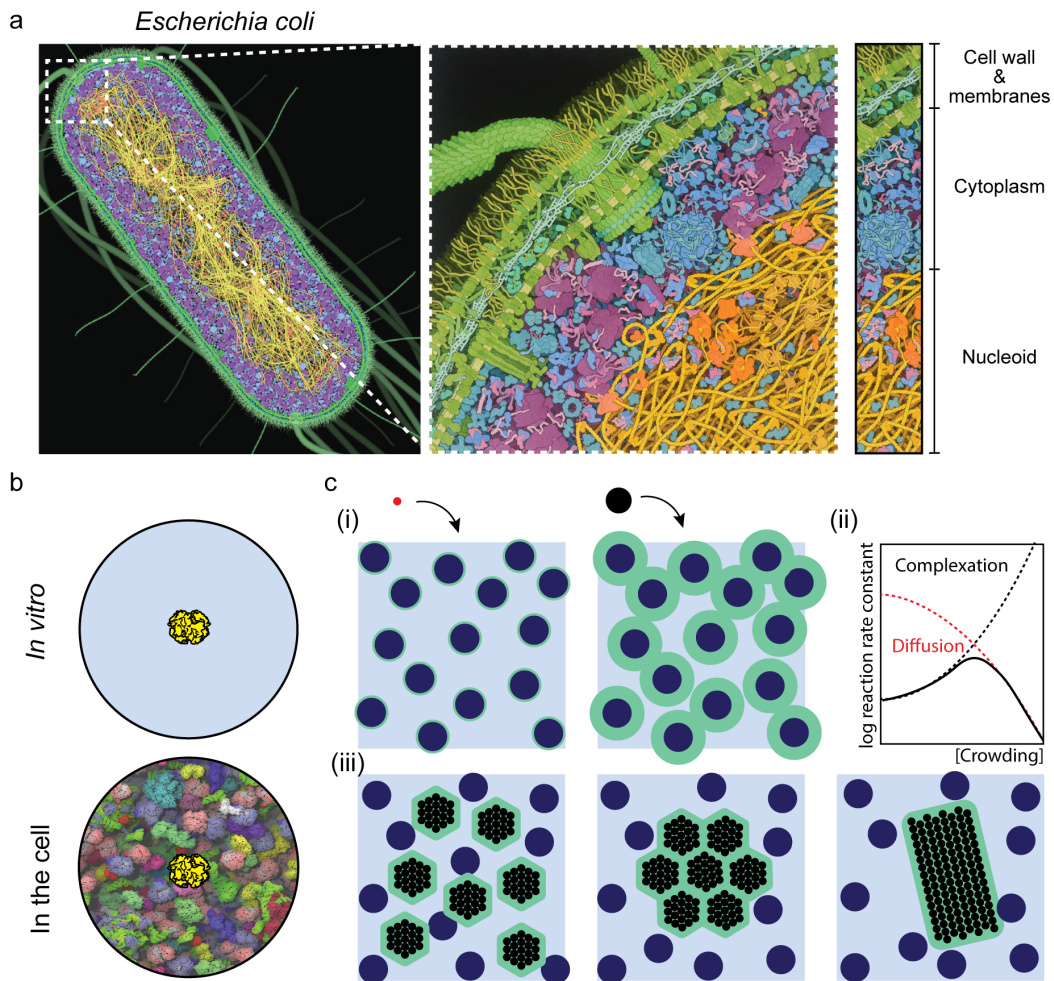


Figure 1.2: The crowded and complex internal cellular environment.

a) Representation of a cross-section through an *E. coli* cell. A closer view of the bacterial cell features, such as cell-wall, membranes, cytoplasm, and nucleoid shows the highly crowded internal environment of the bacterial cell. Cartoons adapted from David S. Goodsell gallery <https://pdb101.rcsb.org/sci-art/goodsell-gallery>. **b)** Schematic representation of common *in vitro* experiments in aqueous buffers and the environment *in vivo*, which is complex and fully crowded with a heterogeneous mixture of molecules. **c)** (i) The crowding-induced volume exclusion effect results in a smaller available space for a large particle (black sphere) compared to a small particle (red). The free space for the particle is represented in blue. (ii) In many biochemical processes and reactions, an optimal level of crowding exists at which the complexation rate (blue curve) is maximized and the diffusivity (red curve) is decreased due to the enhanced excluded volume effect. (iii) Depletion forces play a role in decreasing the overall excluded volume by bringing molecules together. Adapted from [56].

protein-protein interactions [59, 60]. Weak, nonspecific interactions might have little contribution to independent systems, while in physiological environments, these interactions could collectively modulate the kinetics and/or equilibria of a variety of biochemically

important reactions [61].

A crowded cytoplasm has more similar properties to gels than solutions, which can lead to the formation of liquid-liquid phase separation (LLPS) and eventually membrane-free compartments [62]. In the context of the cytoplasm, these membrane-less organelles ensure orderly biochemical reactions, by creating microenvironments to modulate cellular processes [63, 64, 65, 66]. The crowded environment can also cause a reduction in the diffusion coefficients of molecules by a volume exclusion effect [67, 68]. Furthermore, it can increase the equilibrium constants of macromolecules [69] and might enhance the association of proteins, facilitating the folding of proteins or protein aggregations. All these effects are important parameters in biological systems that need to be considered [56] (**Figure 1.2b and c**).

The reconstitution of the crowded environment in cell-like systems is then crucial to understand the dynamics of protein systems and their real behavior within the cell. In confined systems, the addition of inert crowding agents, such as polyethylene glycol (PEG), dextran, and ficoll can mimic the crowded cellular interior to some extent [70]. Following this strategy, the effects derived from crowded environments can be studied and quantified [61]. *In vitro* experiments supported by theoretical studies have shown the potential influence of these effects on the states of proteins association and their functions in the cell [71, 72, 73, 74].

Importantly, volume exclusion effects on soluble proteins enhance the adsorption of proteins on the membrane surface and their self- and hetero-association into fibers or aggregates [75]. Therefore, it is an important aspect to take into consideration in membrane-based experiments, where the nucleation and assembly of protein systems on the membrane are key to understand their functionality. For instance, the volume exclusion effect from macromolecular crowding promotes FtsZ bundling in solution when it is forming filaments [76] or drives the assembly of condensates when the protein is depolymerized [77]. These set of indirect effects as a result of the cellular environment can significantly modulate complex biological processes. Their understanding is required to design, control and engineer them and therefore of special interest in the context of a bottom-up approach.

1.1.6 Vesicles as synthetic cellular models

The compartmentalization of cellular components inside lipid vessels is an essential principle that all living organisms use to isolate their minimal parts as independent units, namely “cells”. At the same time, cells compartmentalize biochemical reactions and cellular processes from each other and from external environments. This essential requirement of life enables multiple pathways or reactions to proceed independently with individually optimized environmental conditions and without the risk of unwanted crosstalk among them [26, 67, 78]. Compartmentalization is therefore not only a fundamental principle of living systems, but also a desired approach for the bottom-up reconstitution of cellular processes, as it adds another controllable layer to optimize the features of synthetic biological systems [27].

Artificial lipid vesicles provide a perfect biomimetic membrane model of simple protocells [79, 80]. They are thus a highly valuable model system to study the function of isolated cellular processes and the interaction of their components in controllable environments, providing important advances in the understanding of macromolecular systems [29, 24, 45, 44, 79, 81]. They have been useful for a broad range of studies, including the analysis of isolated proteins, membrane-protein interaction, complex enzymatic reactions, membrane transporters, the origin of life, and membrane biophysics [82, 83, 84, 85, 86]. In addition, lipid vesicles have also gained attention in recent years as suitable biomimetic platforms not only for basic research but also for biotechnological and biomedical applications. Vesicular platforms have been useful for the discovery of new drugs targeting membrane receptors [87, 88, 89, 90], as biosensors, or as pharmaceutical devices for the delivery of drugs [91, 12, 92, 93, 88, 2, 94, 95, 32, 96].

The biological membranes are mimicked by synthetic lipids in the form of vesicular compartments or liposomes of various sizes depending on the method used for their preparation. Principally, they are usually divided into small, large, or giant unilamellar vesicles (SUVs, LUVs, or GUVs, respectively) ranging from 20 to 100 nm in diameter for the SUVs, from 100 - 1000 nm for LUVs, and more than 1 μm for GUVs (**Figure 1.3a**) [79]. Lipid bilayers are usually around 3-5 nm thick and their composition determines their physical properties which, in turn, regulates their ability to encapsulate, release cargo, or incorporate membrane proteins or other molecules.

Lipids can be broadly defined as hydrophobic or amphiphilic small molecules and they can be categorized depending on their hydrophilic head group (positive, negative or zwitterionic), the length of their fatty acids or the saturation of the chain [98]. The choice of the lipidic composition can be adapted to the purpose of study, determining the properties of the vesicles including the size, membrane fluidity, permeability of small soluble molecules through the membrane, mechanical stability, surface charge density, hydrodynamic prop-

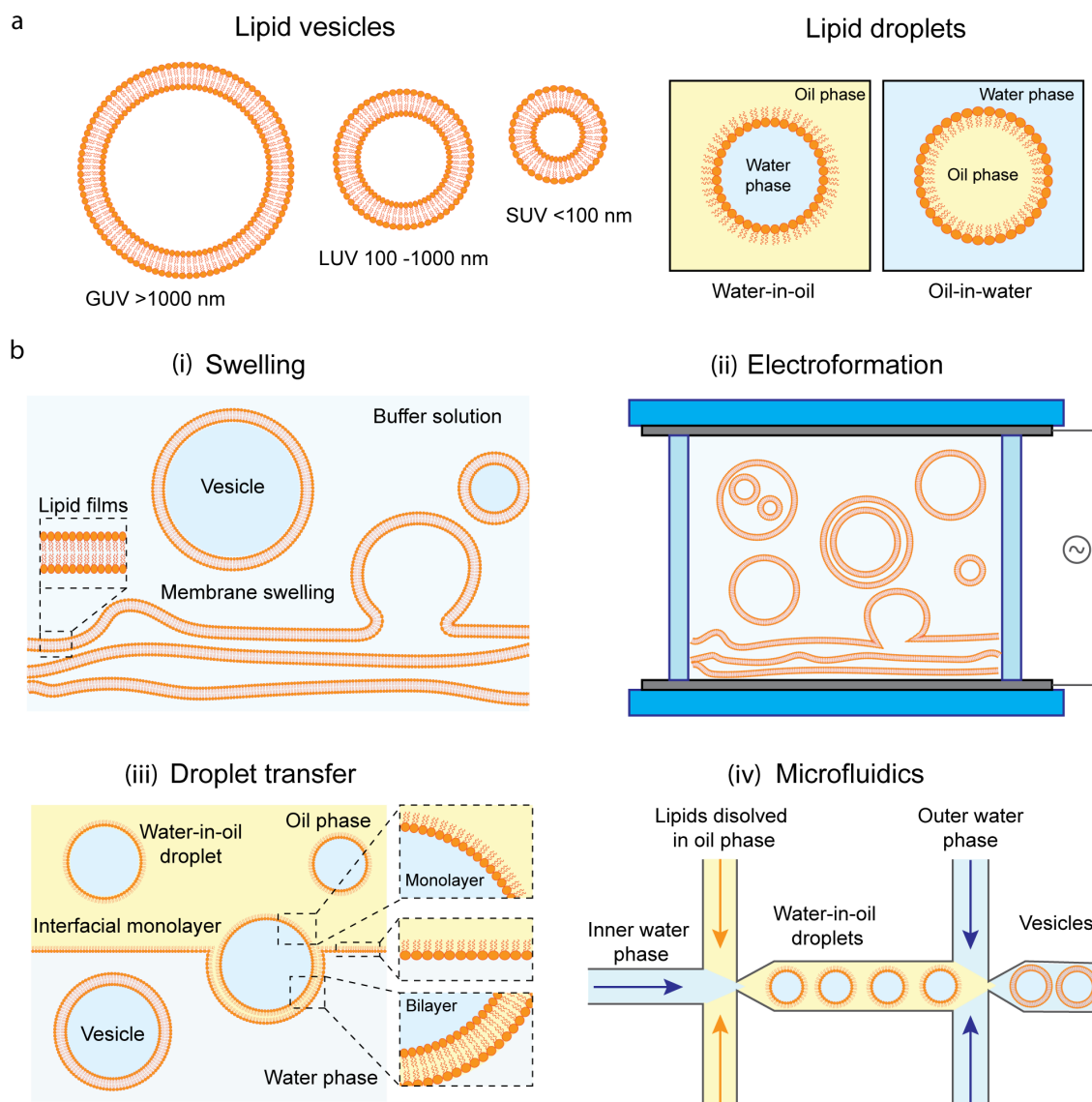


Figure 1.3: Lipid vesicles and methods for vesicle production.

a) Lipid vesicles are classified by their size in GUVs, LUVs and SUVs. Lipid droplets can also be categorized as water-in-oil or oil-in-water. **b)** Methods for vesicle production. (i) Swelling or gentle hydration methods. (ii) Electro-formation of vesicles using dry lipid films and applying an electric field. Dry lipid films can be deposited on one or both ITO slides. (iii) Droplet phase transfer methods, where lipid vesicles are generated by water-in-oil droplets transfer to the aqueous phase through a lipid-stabilized oil–water interface. (iv) Formation of lipid vesicles by the microfluidic generation of w/o/w double emulsions and subsequent oil extraction. Other microfluidic methods can use different strategies to generate lipid vesicles. Schemes adapted from [97].

erties, the efficiency of encapsulation of the cargo, and compatibility with the encapsulated system [86, 99].

Other alternatives to lipid vesicles have been explored to expand the range of available tools for *in vitro* reconstitution. Some examples are block copolymers-based polymersomes [79, 100], hybrid systems composed by polymers and lipids, as well as other artificial systems like proteinosomes [101] dendrimersomes [102], nanocompartments or encapsulines [103]. In the case of polymers, they usually have a larger molecular weight than lipids and polymersome membranes are therefore thicker than lipid membranes, which results in differences in elasticity and viscosity of the membrane. These differences lead to lower leakage and permeability, lower lateral mobility, higher stability, and chemical versatility of polymersomes compared to liposomes [86]. Thus, those alternative vesicle systems will show different properties depending on the target molecular system, offering the potential of being combined and tailored to specific applications. Indeed, some examples have been already shown using different biological systems [97, 104, 39, 105].

One of the challenges of bottom-up reconstitution is the encapsulation of protein modules and other biomolecules into artificial vesicles. The encapsulation of cellular components involves certain challenges intrinsic to its methodology [83, 44, 85]. Most of the methods to generate lipid vesicles are not suitable for the encapsulation of protein systems since they involve apolar solvents, high heat, long incubation time and/or incompatibilities [91, 83]. However, several methodologies for the encapsulation of molecules inside lipid vesicles have been developed and broadly tested in diverse systems. The strategies of encapsulation and formation of vesicles could be categorized into three major methodological groups: Lipid film hydration, inverted emulsion transfer or microfluidic techniques (**Figure 1.3b**) [106].

Lipid film hydration, also called swelling, is the most conventional and used method for the formation of vesicles as cellular models (**Figure 1.3b (i)**) [107]. Briefly, a lipid film is hydrated in an aqueous solution, which induces the penetration of aqueous media into the lipid film and thus spontaneous formation of vesicles. This type of vesicle formation has been widely used as the simplest method for vesicle production, however, it has certain restrictions regarding lipid compositions and salt conditions [108]. In addition, the encapsulation of molecules into the vesicles is difficult, as they need to penetrate through the lipid film while the vesicles are being formed, rendering low encapsulation efficiency [109]. A variation of this method is electroformation, where the lipids are usually deposited in a conductive surface and the swelling is assisted by an externally applied electric field [110, 111, 112] (**Figure 1.3b (ii)**). Although the process of vesicle formation in this method follows the same principle as simple hydration, it often benefits from faster formation and higher yields of homogeneous vesicles compared to the hydration method. However, this method also has several limitations regarding charged molecules and rele-

vant buffer conditions for protein function [113]. To overcome them, further improvements in this methodology have been developed through the years to allow a broader range of buffer conditions [114, 115] and charged lipids [116], although it is still problematic for the encapsulation of proteins or molecules. Nevertheless, electroformation is still the most used methodology for vesicle production and protein reconstitution on the outer leaflet of the membrane.

On the other hand, inverted transfer methods have become the most efficient way to encapsulate molecules into lipid vesicles for the last 20 years, thanks to various contributions and methodological developments [117] (**Figure 1.3b (iii)**). This method can be adapted to almost every type of protein system and has been also successful in the encapsulation of cell-free expression systems, membrane proteins or membrane transport systems, among others [118, 44, 119]. In this strategy, the ability of lipid molecules to assemble into monolayers when exposed to water-oil interfaces is used to eventually form lipid vesicles. To achieve this, first, a lipid monolayer is formed on the oil-water interface of an aqueous solution. Then, water-in-oil droplets are transferred to the aqueous phase through this second lipid-stabilized oil-water interface previously generated, so that the monolayer of the interface wraps the droplets to produce vesicles. Centrifugation is often used to promote this process and improve the phase transfer efficiency [117, 85, 120]. Modification and improvements of the methodology can be done depending on the experimental setup, involving the use of differential lipid composition, oils, density gradient and/or centrifugation. Recent modifications of the emulsion transfer principle have used microfluidic components to improve certain aspects of the encapsulation and vesicle formation [121, 122] as the cDICE (continuous droplet interface crossing encapsulation) [123, 124, 125] or the one-pot synthesis [126]. The customization and optimization of the encapsulation method for each individual application are critical to achieve a faithful reconstitution of the target biological system.

Finally, also based on the double emulsion principle, microfluidic-based methodologies have recently emerged to improve the efficiency of the process and the encapsulation yield [127, 128, 129, 130] (**Figure 1.3b (iv)**). Microfluidic technology not only offers an improvement on the encapsulation of biological systems, but also enables the handling and manipulation of picoliter volumes of fluids via highly customizable PDMS-based microchannels [28]. This technology allows the integration of multiple functions as modules at different scales into one microfabricated chip, which significantly improves the reproducibility, accuracy and data analysis speed. A stable water-oil-water emulsion is directly formed in the microfluidic device, and the intermediate oil phase solvent is extracted by evaporation. This concentrates the lipids into bilayers generating unilamellar vesicles. Various designs have been developed to form vesicles and optimize their yield, size or protein incorporation [131, 132, 133, 134]. These systems have multiple advantages such as the production of

larger number of vesicles, higher encapsulation rates or more homogeneous sizes facilitating high-throughput analysis [135, 132]. Microfluidic approaches are attractive alternatives to control and manipulate the reconstituted systems, becoming one of the best options to achieve the bottom-up construction of a minimal synthetic cell [28, 10].

In summary, hydration methods are still the standard for protein reconstitution experiments, when only addition from the outside and further reconstitution on the outer leaflet are required. However, they fail in the encapsulation of complex systems, where the emulsion transfer methodologies become more efficient. The methodological strategy of choice needs to be adapted to each particular system [106].

In the last years, the reconstitution of proteins has gained interest and many biological systems have been successfully reconstituted inside lipid vesicles, putting this method forward as great model systems to study the functionality of proteins in membrane environments. Cytoskeletal, soluble or membrane proteins and enzymes have been tested over recent years, gaining insights into their functionality [44, 97]. Among lipid vesicles, GUVs are considered the best candidates to reconstitute biological systems and eventually reassemble a synthetic cell, enabling essential cellular functions such as metabolism, growth or autonomous self-replication etc. Recent developments in the production and encapsulation of lipid vesicles have enabled their extensive use and supported further improvements of GUVs as a reaction platform towards building a functional synthetic cell and the reconstitution of complex biological processes.

1.1.7 The prospect of building a minimal synthetic cell

As has been described above, one of the major goals of synthetic biology is the reconstruction of a fully-functional synthetic cell from a bottom-up approach. In order to reach this goal, it is necessary to ensure complete autonomy and sustainability, including all the required features found in biological cells [136], such as (1) compartmentalization, (2) source of energy, (3) protein production, (4) specific transport across the compartment, (5) metabolism, (6) replication of the genetic information, and (7) machinery of division (**Figure 1.4**). All of these crucial cell processes are being currently explored independently by isolating their components to study them and be eventually implemented as functional modules in a fully synthetic bottom-up system [54, 27, 2, 137, 5, 138, 136]. These functional modules could be further summarized into four essential features of life: metabolism, energy supplement, proliferation, and communication [136]. Metabolism encompasses all the biochemical reactions that provide the material base for life. Most of these reactions and life activities are energy-dissipative, thus requiring sufficient energy input to support their functions. Finally, the ability of proliferation allows growth, self-replication of the genetic material, and eventually division. Considering these minimal requirements, the

most effective strategy to reconstitute a synthetic cell from the bottom-up approach is to rebuild natural functional networks by combining different modules as building blocks [27].

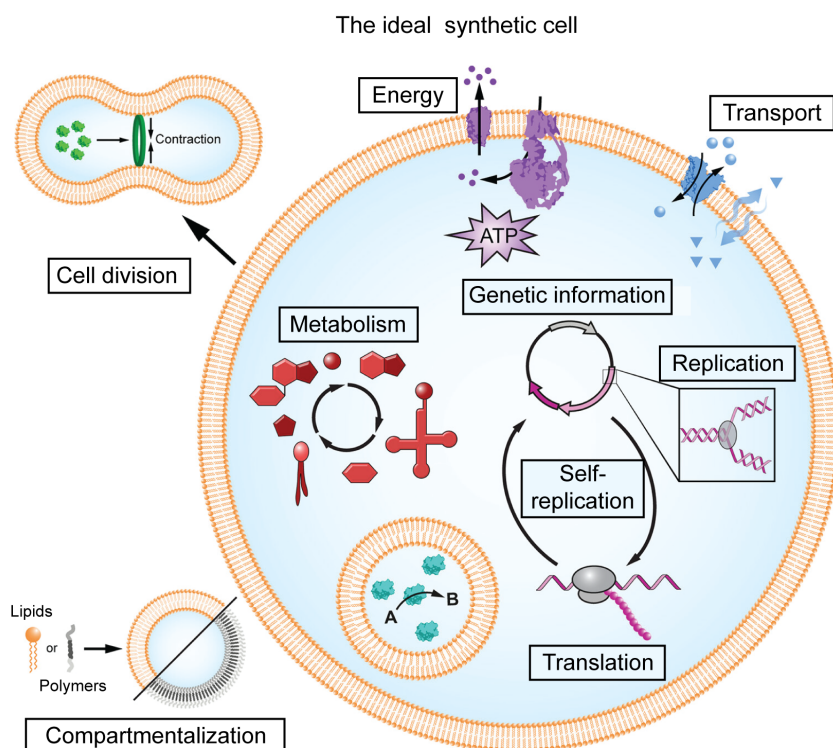


Figure 1.4: Essential modules of an ideal synthetic cell from the bottom-up.

The creation of a synthetic cell is the result of assembling and synchronizing isolated biological and chemical components in a modular way to achieve desired traits and functions. The synthetic cell consists of at least one main compartment and optional sub-compartments (vesicles) enclosed by a membrane made of either lipids (brown) or polymers (gray). Sub-compartments can contain individual processes and biochemical reactions, as exemplified by a compartmentalized enzymatic reaction (cyan). To ensure that the artificial cell functions properly, energizing modules provide energy for energy-dependent processes; transport modules supply building blocks, nutrients and dispose of waste products; while a minimal metabolism (red) replenishes essential components. Replication, transcription, and translation (enzymes in gray) of genetic information enable continuous and autonomous function. The artificial cell's ability to divide ensures sustainable growth and proliferation (illustrated by the component of a minimal divisome in green). The synchronization of all these independent processes and modules is fundamental to sustain the synthetic cell's function. Reprinted with permission from [2]. Copyright 2022 American Chemical Society.

Among all the individual modules needed for the synthetic cell, self-replication of the genetic material and division of cell-like compartments are some of the most important and challenging tasks to overcome [137, 139, 138]. Despite all the essential modules for life are interdependent, self-replication and further division of the compartment are especially important, as they ensure the expansion of unicellular organisms and the development of

advanced species. A robust and steady division system is the foundation of life, although the detailed processes involved in the replication of the genetic material and division of cells have not yet been fully revealed in most organisms.

Replication and division cannot be fulfilled only by nucleic acids themselves plus their replicative and segregation machinery, energy supply, transcription and translation machineries, but also requires a precisely coordinated nucleus/cell division machinery to physically divide the reaction compartment. The orchestration and coordination of all these components is a challenging milestone towards the reconstruction of a functional synthetic cell, due to the intrinsic complexity of these processes and the high number of components involved. In this regard, many studies have already approached different protein modules from a bottom-up perspective *in vitro*, succeeding to reproduce, at least partially, their biological function [54, 2, 39].

The production of proteins inside cell-like systems is another key step to construct a self-replicative synthetic cell [140, 141, 142, 143]. The most common strategy to achieve the production of proteins *in vitro* is the use of cell-free expression systems. Essentially, cell-free expression can be achieved by using either cell extracts containing all transcription-translational machinery in cells or recombinant protein systems composed of purified components involved in protein synthesis [144, 31]. These approaches have experienced a huge development in the last decade by improving the yield and efficiency of protein synthesis as well as their integration inside cell-like containers [145, 146, 142, 141]. Recent studies have addressed the implementation of protein expression systems to supply synthetic cells with essential proteins and other cellular components such as DNA replication and transcription [138, 147], energy generation [148], lipid synthesis [149], and cell division components [150, 151, 152]. A combination of different strategies and further developments of the cell-free expression systems should allow the autonomous self-replication and survivance of the synthetic cell, mimicking living cellular systems. Despite being far from the construction of essential functionalities for life to some extent, these studies set up the basis for the reconstitution of functional modules in synthetic cells.

Among the designed recombinant systems, the PURE system is one of the most common platforms to express proteins *in vitro* [153, 154]. The PURE system contains all enzymes involved in transcription and translation, together with purified 70S ribosomes and all other essential components such as an energy regeneration system, nucleotides, tRNA, and salts. In contrast to cell extracts-based systems, PURE or other reconstituted expression systems lack proteases, ribonucleases, and non-essential molecules for protein synthesis found in the cell and carried along in cell extracts. In addition, recombinant systems offer a higher controllability of the components and enzymatic reactions involved in the process, as all of them are pre-defined and therefore exchangeable, which is more suitable for a

bottom-up approach.

On the other hand, the autonomous self-replication of genetic information also requires the physical division of its compartment, which is still a mostly unexplored ground due to its complexity. The physical separation of the replicated genetic material such as genomic DNA is needed to ensure the continuation of the division process, allowing symmetric segregation before the physical separation in different compartments [137, 155]. To complete this process, the division of a synthetic cell involves the previous segregation of its components, deformation of the membrane and finally scission, dividing the mother cell into daughter cells. The most plausible mechanism to divide an artificial lipid compartment involves the isolation and reconstitution of division machineries found in nature, such as the bacterial divisome or the mitotic spindle [54, 156]. Recent efforts have been made focusing on the bacterial division system based on FtsZ, which stands up as one of the most promising candidates to achieve controllable division in synthetic cells due to the extensive research using *in vitro* systems. The bacterial division offers advantages in reconstitution studies compared to eukaryotic systems, as it is a simpler and faster process. Concretely, division in *E. coli* consists of the assembly of a presumably contractile FtsZ ring that splits the cell into two equal daughter cells. In addition, the *in vitro* reconstitution of FtsZ has proven its ability to form ring-like structures and to constrict synthetic membranes [157, 158, 159]. FtsZ's role as a center protein in the bacterial division process facilitates its combination with other division proteins involved in chromosome segregation, cell wall and lipid synthesis, or cytokinesis. From a bottom-up approach, FtsZ can be a great tool to construct a minimal division machinery. All these aspects are further addressed in the section below.

Other division systems have also been explored, as membrane deformations and blebbing could be observed in GUVs containing actin and myosin [160, 161] or full membrane scission when some components of the eukaryotic endosomal sorting complexes for transport (ESCRT) were reconstituted inside GUVs [162, 163]. Other mechanisms have been proposed as alternatives to the symmetric segregation, such as random partitioning in systems containing multiple copies of a small genome [164], entropy-driven segregation [165], mechanical division [166] or DNA origami-based structures to promote scission of the membrane [167]. All of these systems have great potential, although they are still far from being functional and further developments have to come [54].

The division process also requires the synthesis of new membrane components to maintain the continuous growth of the daughter cells after division. These additional membrane components could be externally added by fusing lipidic SUVs from the extravesicular environment [168, 169] or synthesized inside the compartment. The synthesis of phospholipids has been already demonstrated using nonenzymatic [170, 171] or enzymatic reactions

[149, 172, 173], eventually achieving a membrane synthesis machinery which is able to synthesize lipids of different nature at desired ratios by cell-free expressed enzymes inside vesicular compartments [149].

The achievement of a full division of the cell-like system is a milestone that the bottom-up reconstitution has to achieve. The improvements done to date and the raising number of studies approaching these aspects are good indicators that we are on a good track to accomplish such reconstitution of controllable division machinery inside cell-like systems in a near future.

As addressed in this chapter, the bottom-up assembly of functional modules has experienced significant advances in mimicking cellular functions *in vitro*, providing not only a fundamental understanding of the molecular dynamics of the components but also tools for applications in bioremediation, biomedicine, biosensing and biotechnology. However, the combination of these fundamental modules to assemble a minimal synthetic cell still needs to tackle a number of issues. Among them, the lack of autonomy and self-regulation is a limiting feature that makes them dependent on external control, while the lack of self-replication modules restricts their function to short lifetimes. Many individual cellular processes have been already isolated and successfully reconstituted inside vesicular compartments, but their coordination and combination into a fully-functional system still is one of the greatest challenges for present and future studies. For these reasons, it is important to study natural processes such as bacterial cell division in model systems like *E. coli*, in order to comprehend the coordination of the essential parts driving the process and eventually their implementation in a synthetic cell.

1.2 The bacterial cell division machinery

The mechanisms underlying the capacity of a cell to self-replicate and proliferate are primordial for life. These mechanisms are known to be highly conserved throughout evolution, even though bacterial cells have evolved into very efficient proliferative systems independently of the other domains over billions of years. As single-cell organisms, they typically proliferate by binary fission, duplicating the population exponentially even under severe stress conditions and allowing their successful expansion and adaptation to extremely diverse environments found on Earth. Throughout evolution, they have developed a robust and efficient cell cycle, tightly regulated by a complex cellular organization, which is vital for the proper coordination of all cellular processes [174, 175]: from the assembly of the nucleoid to protein patterning across the cytoplasm and the cellular membrane to ensure the progression of the cell cycle. Concretely, the coordination of cell growth, the replication of the genetic material, and the division of the cell are essential for bacterial proliferation. The regulation of these critical processes together with their functionality itself has caught the eye of the scientific community since their discovery, reaching important advances in how they are controlled and coordinated at the molecular level by the host organism. However, they are still far from being fully understood and more research has to come.

The study and characterization of the bacterial cell division process from a bottom-up reconstitution approach offers great benefits for the understanding of the system and also for its implementation as a functional module within a synthetic cell. In a more general view, we can gain insights into how complex spatiotemporally controlled processes work *in vivo* and *in vitro*, how to employ them in synthetic cell-like settings, and eventually how to engineer them to design new functionalities.

In all organisms, the end of cell division must be tightly coupled to the cell cycle to faithfully ensure that each daughter cell receives a complete copy of the genome to proliferate [176, 177, 178, 179, 180]. In the case of *E. coli*, the division process could be split into different stages: the determination of the division site, the recruitment and assembly of the division machinery, the activation of the cell-wall synthesis, and, eventually, the cytokinesis dividing the cell (**Figure 1.5**). The whole process is organized by the divisome, a multiprotein complex constituted by more than 30 proteins participating in the process [181, 182, 178, 183]. Although most of the components of the complex are known in *E. coli*, their coordination, activation and assembly into the divisome are still under investigation [184, 185, 186]. Despite the intrinsic complexity involved in the division process, the machinery responsible for the binary division in bacteria is far simpler than in eukaryotic systems, which makes it a particularly interesting target to understand the coordination of complex systems in cells. Concretely, focusing on *E. coli* as a model system for bacterial division is beneficial due to the broad knowledge of its cell cycle and the shared mechanisms

of division among bacteria, even considering the variability of the bacterial kingdom [187].

The first step in the cell division process in *E. coli* is the assembly of the FtsZ-ring at the division site [189]. FtsZ is the first component to localize at the future division site and the central protein of division, polymerizing upon GTP hydrolysis forming filaments [190]. These FtsZ filaments are attached to the membrane via its interaction with the bitopic membrane protein ZipA or the amphitropic protein FtsA [191], allowing the reversible attachment of the FtsZ filaments into the inner membrane of the cell forming the FtsZ-ring [192, 183]. This FtsZ-ring is then condensed and stabilized by the Zap proteins (ZapA, ZapB, ZapC and ZapD), which crosslink the FtsZ filaments laterally allowing their stabilization [193, 194] and further recruitment of division proteins [177, 188]. The localization and placement of the FtsZ-ring are tightly regulated to ensure its preferential assembling at midcell, placing the divisome machinery in between the segregated chromosomes and avoiding aberrant septation [195]. The mechanisms of spatial regulation include negative and positive modulators. They vary among diverse bacteria and their absence often leads to altered morphology due to misplacement of the division site [195, 196, 197]. In addition, these regulatory systems often have redundant roles to enhance the robustness of the spatial localization of the system, ensuring proper placement of the division machinery. In *E. coli* cells, the main negative regulators of the placement of the division ring are the MinCDE and the Nucleoid Occlusion (NO) systems, while only the Ter-linkage has been identified as a positive regulator.

The MinCDE proteins oscillate between the cell poles creating a MinC protein gradient on the membrane with its maxima at the poles and minima at the center of the cell. As a result of this gradient, MinC disrupts the assembly of the FtsZ-ring at the cell poles, allowing its formation only at midcell [198, 199, 200]. In addition, the NO system supports the Min function by preventing the formation of the ring over the nucleoid and therefore the loss of genetic information in daughter cells. The NO is mediated by SlmA, a protein that interacts with FtsZ upon binding to a specific region of the chromosomal DNA containing a SlmA binding site (SBS) [201, 202], disrupting the stabilization of FtsZ polymers on the membrane. Thus, SlmA remains bound along the chromosome preventing the assembly of the FtsZ-ring until it is transported away from the cellular center by segregation of the nucleoid, creating a void at midcell which allows the FtsZ filaments to persist at the membrane [203, 204]. On the other hand, the Ter-linkage represents the only positive regulator of the positioning of the ring [205, 206]. It is mediated by ZapA, ZapB and MatP, which interact one to another in sequential order, constituting a complex that anchors the Ter region of the *E. coli* chromosome and the FtsZ-ring [207, 208, 209]. This Ter region is located at the cell center when the chromosomes are completely replicated [209], promoting the formation of the FtsZ-ring at the midcell. The coordination of nucleoid segregation and FtsZ-ring formation by the Ter-linkage allows the progression of division without

1.2 The bacterial cell division machinery

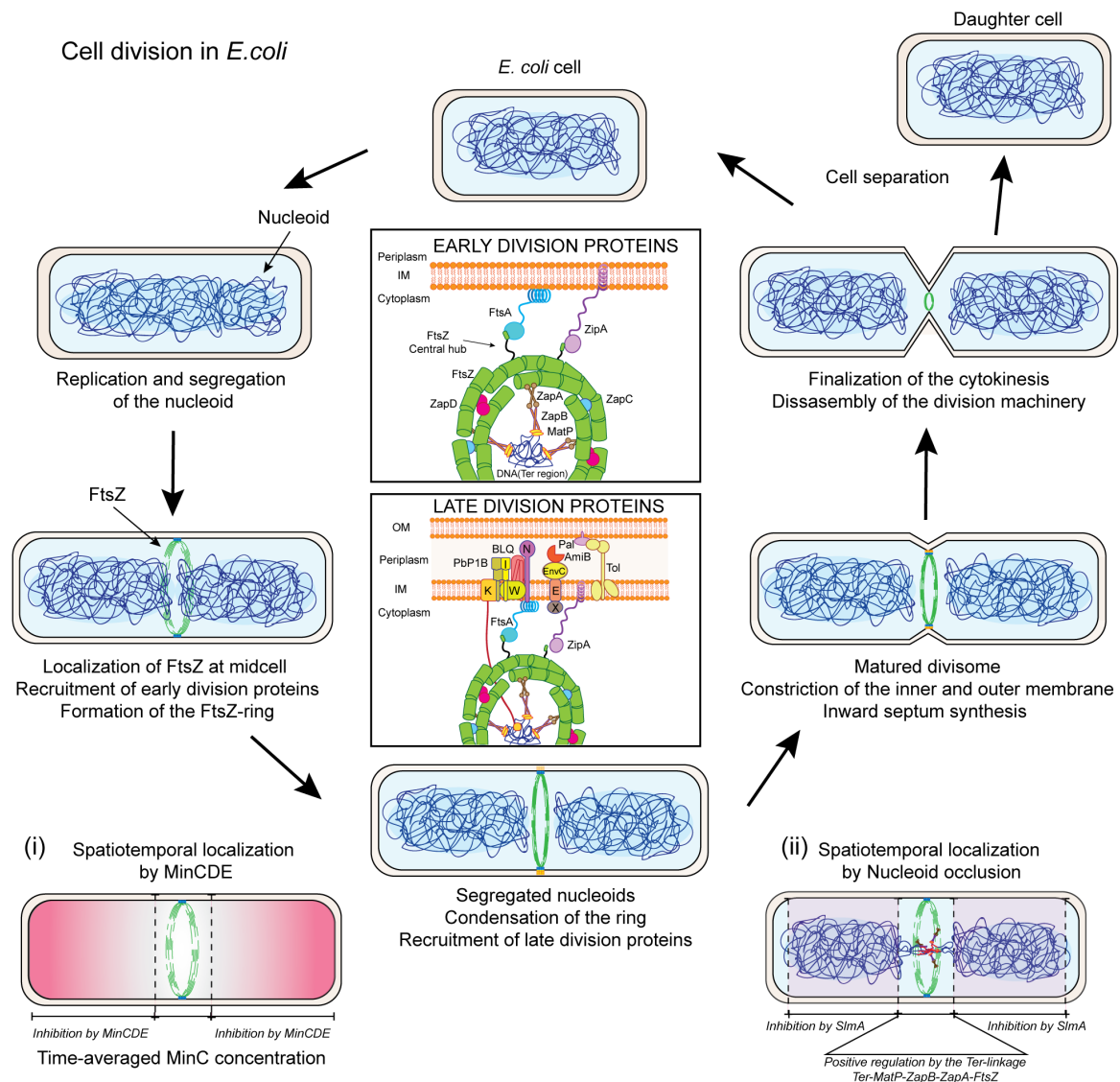


Figure 1.5: Overview of the cell division process in *E. coli*. a) Schematic depicting the proposed mechanism of cell division in *E. coli*. After the *E. coli* cell replicates and segregates its chromosome, FtsZ is concentrated at mid-cell and tethered to the membrane by FtsA and ZipA, forming the essential FtsZ-ring. FtsZ filaments recruit the early division proteins, mainly involved in the stabilization of the ring (ZapA-D). Following a continuous process, the FtsZ-ring is stabilized and recruits the late-division proteins, resulting in the formation of a mature divisome. Most of these proteins participate in the synthesis of the cell wall and cytokinesis. Some of them are FtsK, FtsW, FtsI, FtsQLB, FtsN, FtsEX, EnvC, Tol-Pal system and AmiB among others. After triggering the cytokinesis process, the divisome coordinates the constriction of the inner and outer membranes, ultimately leading to the separation of the bacterial cell. Scheme based on [188]. The spatiotemporal localization of the division machinery is determined by the MinCDE system (i), nucleoid occlusion (NO) and Ter-linkage (ii). (i) The MinCDE system inhibits the assembly of the FtsZ-ring by creating a dynamic protein concentration gradient of MinC. (ii) The NO is mediated by SlmA, which prevents the assembly of the FtsZ-ring over the nucleoid location.

chromosome disruption. Eventually, the DNase translocator FtsK participates in the spatial segregation of the chromosome relative to the division system and the recruitment of downstream proteins [210, 211, 196].

Once the FtsZ-ring is correctly positioned and stabilized at midcell, it functions as a scaffold to recruit the late division components in a hierarchical order. This process could be considered the maturation or development of the division machinery, eventually forming the divisome that leads the process of cytokinesis [184, 188, 212]. The downstream proteins recruited in this phase are mainly involved in carrying out the septal peptidoglycan (PG) synthesis, the activation of the contraction and the outer membrane invagination (Tol-Pal) [213, 214]. In *E. coli*, the PG layer is located between the inner and outer cellular membranes, maintaining the shape of the cell and protecting it from the mechanical stress that results from high intracellular turgor [215, 216, 217]. PG is the main component of the bacterial cell wall and its synthesis is one of the essential cellular functions [218]. Its biosynthesis is carried out by a macromolecular complex formed by downstream proteins, such as FtsK, FtsW, FtsI, FtsQLB, FtsN and FtsEX among others [184, 185, 218, 219].

The molecular mechanisms of how the proteins involved in PG synthesis are recruited into the FtsZ-ring scaffold, assembled and activated as well as their whole functionality are still an active area of investigation [184]. The late division components are recruited and assembled in a highly coordinated and hierarchical manner to form the (PG) synthase (PBP1b-FtsW-FtsI complex) [220], which is linked to the FtsZ-ring by the FtsQLB sub-complex [221, 222, 223]. Subsequent recruitment of FtsN at the division site is thought to finalize the divisome assembly by triggering the septal PG synthesis [224, 225]. FtsN then binds to the FtsQLB complex and relieves the inhibition of the PG synthase, starting the process of PG synthesis [226, 227, 228]. When the PG synthesis is completed, the trans-membrane FtsEX complex recruits EnvC to activate specific amidases (AmiA, B and C) that hydrolyze the septal PG when the cell wall needs to split into two daughter cells [229, 230, 231].

Intriguingly, one of the biggest questions that remain open in the process of cell division is the molecular mechanism of the constrictive force generation that completes cell constriction and division. Despite several hypotheses have been discussed for many years, an agreement has not yet been reached. Essentially, as a result of a large number of components and their regulatory dynamics, it is not known yet whether the main source of the force generation to split the bacterial cell comes from the contractile FtsZ-ring or the cell-wall synthesis machinery [184, 232, 185, 233, 217].

Finally, the precise divisome disassembly is still hardly understood, although it is thought to occur in a coordinated sequential order [234]. It is initiated by FtsZ, which seems to disassemble from the division septum before the full closure of the cell envelope [235],

however, recent data defined FtsZ as an essential player in the late stages of constriction [236]. After the fusion of the inner membrane, ZipA and FtsA disassemble, followed by the components of the PG synthesis machinery and a subpopulation of FtsN. Lastly, the remaining FtsN molecules also disassemble and the two daughter cells separate. This sequence of events follows an order of disassembly similar to that of the assembly process, indicating that disassembly might follow a first-in, first-out principle [237, 234].

As introduced, each stage of the division process requires coordinated regulation and spatial control, tightly synchronized with the previous and subsequent processes to ensure their collective function. The molecular mechanism underlying the control and functionality of bacterial cell division inside the cell is still far from being understood and many years of research lie ahead. What seems to be clear by now is that a combination of *in vivo* approaches and classical biochemistry, together with bottom-up reconstitution in cellular-mimic environments are going to be required to fully understand the intriguing coordination of this essential module of life. The use of the *E. coli* cell division components as a functional module to build a minimal division machinery from scratch raises a hope to eventually be able to divide the synthetic compartments in a controllable manner. In addition, a detailed understanding of this process can help us to comprehend the function of complex division systems and eventually enable us to construct functional synthetic cells.

1.2.1 FtsZ, the central protein of division

FtsZ is the central cytoskeletal protein that organizes the formation of the divisome and orchestrates the division process [238, 193, 179]. It is a soluble 40.3 kDa GTPase protein [239] that is essential in the cell, widely conserved in bacterial and archaeal species and considered the ancestral homologue of Tubulin (**Figure 1.6a and b**) [240, 241, 242, 243, 244]. Since its first description in the early 90s [189, 239, 245], many studies have focused on understanding its molecular dynamics both *in vivo* and *in vitro*. However, due to its dynamic nature and the small size of the bacterial cell, a full characterization and understanding of its molecular interactions are still not achieved.

The structure of FtsZ was determined in 1998 [242] and the atomic structure of FtsZ monomers or dimers from different bacterial species are currently available [250, 251, 252, 253, 254]. FtsZ contains five different domains: (1) a short and unstructured N-terminal peptide (NTP), (2) a highly conserved globular core that includes the GTP-binding domain, (3) a variable C-terminal linker (CTL), (4) a conserved and short C-terminal tail (CTT) and (5) a C-terminal variable region (CTV) (**Figure 1.6c**). Importantly, the C-terminal region, consisting of the CTT and CTV domains, acts as a central hub for many of the interactions with other division components [255]. Proteins like FtsA, ZipA,

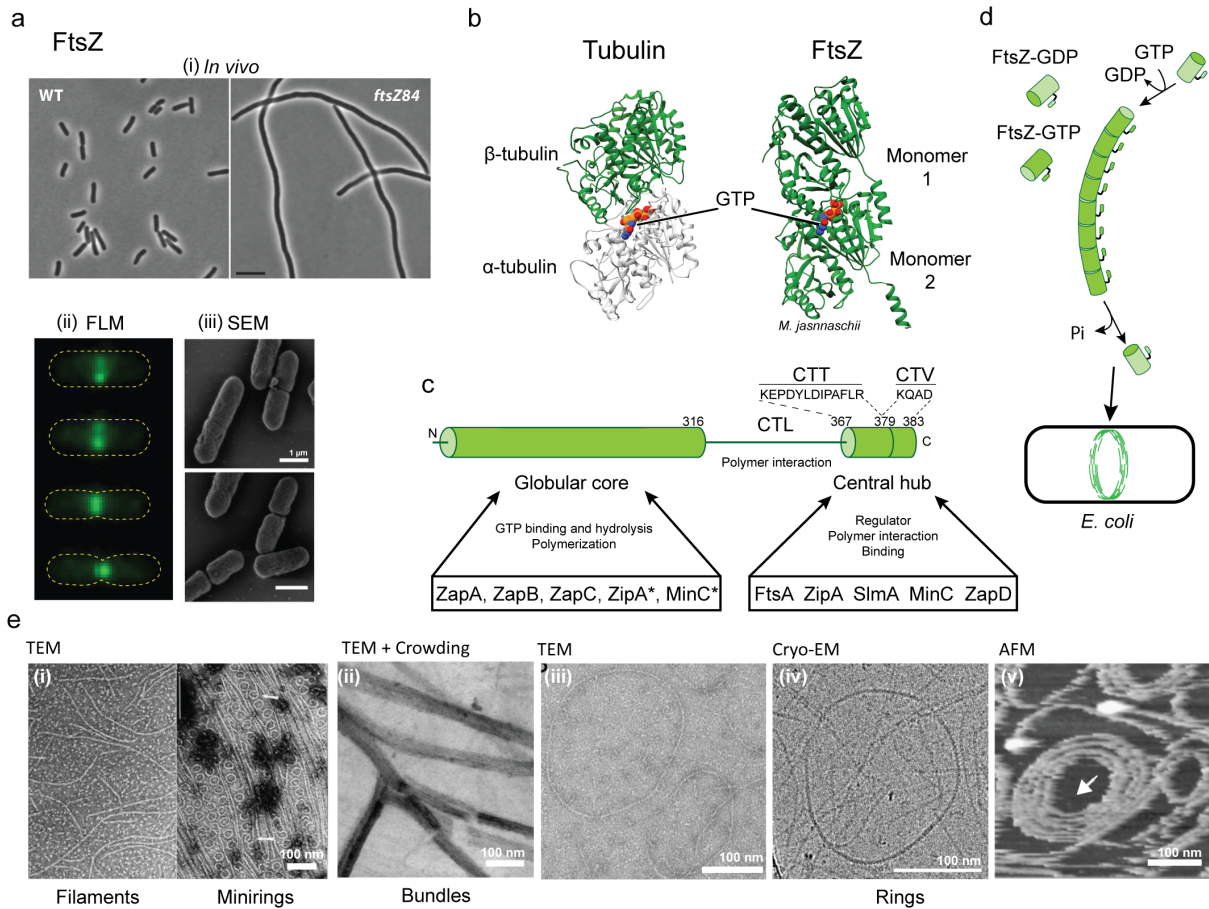


Figure 1.6: FtsZ is the central protein of bacterial division. **a**) (i) Phase images of wild-type *E. coli* and *ftsZ84* (*Ts*) mutant cells under permissive and restrictive growth temperatures, respectively. Scale bar is 5 mm. (ii) Fluorescence images of FtsZ-GFP in *E. coli* cells during the division process. Images from a and b reprinted from [185]. (iii) SEM images of *E. coli* cells during division [246]. **b**) Representation of the structures of Tubulin and FtsZ: heterodimer of tubulin (left) and a homodimer of *M. jannaschii* FtsZ (right). The C-terminal linker (CTL) and C-terminal tail (CTT) domains are not present in the structure. Sandwiched between the dimeric units of each protein is a space-filled model of GTP. **c**) Schematic domain architecture of FtsZ. The globular core contains the motif responsible for binding GTP and GTP hydrolysis. This globular domain is linked to the CTT by the CTL. The CTT contains a variable region (CTV) and is known as the central hub of FtsZ, which binds various FtsZ binding proteins listed in the figure. **c**) FtsZ self-assembles into single-stranded filaments upon binding and hydrolysis of GTP. These polymers will eventually form the FtsZ-ring in bacterial cells, driving the division of the cell. **e**) Visualization of FtsZ filaments *in vitro* using TEM, TEM and AFM. (i) Straight and curved FtsZ filaments are absorbed into a cationic membrane and visualized by TEM. FtsZ mini rings of approximately 24 nm diameter, probably stabilized with GDP-FtsZ. (ii) TEM micrograph of FtsZ forming straight bundles with 220 g/l ficoll. FtsZ filaments forming single-stranded rings in TEM (iii) or in cryo-EM (iv). (v) AFM image of FtsZ ring-like structures on surfaces. Images reprinted from (i) [247], (ii) [76], (iii) [248], and (v) [249].

SlmA, ZapD or MinC modulate the behavior of FtsZ by interaction through the central hub [256, 257, 258, 259, 260, 261], which is then essential for its functionality. At the same time, the flexible C-terminal linker participates in the assembly of FtsZ, enabling weak lateral interactions between filaments, and also providing extra flexibility to the interactions through the central hub for the proper division of the cell [262, 263, 255, 264, 265, 266, 267, 268].

FtsZ homopolymerizes upon GTP consumption, forming polymers both *in vivo* and *in vitro* [192, 269, 270]. Structural studies have determined the formation of two FtsZ isoforms of the monomer due to its flexible structure [271, 272, 273, 274], resulting in a tense and relaxed form for FtsZ-GDP and GTP bound monomers, respectively [275] (**Figure 1.6d**). The conformational change of the monomers from relaxed to tense upon GTP hydrolysis generates a twist of around 30 degrees in the polymers, providing their intrinsic curvature. [276, 277, 278]. FtsZ filaments are dynamic due to a continuous exchange of monomers coupled to GTP hydrolysis, polymerizing and depolymerizing directionally [279, 280]. The FtsZ filaments can adopt multiple conformations into straight, curved, or circular single-stranded filaments. They can further assemble into multistranded sheets, bundles, helices or rings depending on environmental conditions such as ionic strength, metal ions, pH, and molecular crowding agents among others [281, 247, 76, 193, 180, 282, 283] (**Figure 1.6e**). This high level of polymorphism and adaptability is likely the reason why the study of FtsZ has been challenging by crystallographic or electron microscopic studies. In addition, FtsZ filaments themselves possess an intrinsic curvature and bending rigidity optimized to align curvatures of around 1000 nm in radius [284], although ring-like structures ranging from 24-1000 nm have been also observed by transmission electron microscopy (TEM) [285, 286]. Thus, FtsZ assembles into soft flexible and polymorphic filaments that can adopt a large range of conformations, which are easily modulable through the modification of the environmental conditions, but also by other FtsZ-associated proteins (ZipA, FtsA, MinC, ZapA-D, MatP, SlmA). However, the understanding of how such dynamic and plastic filaments are responsible for the organization, coordination, and maintenance of the divisome structure at the membrane are still some of the most attractive questions in the field.

The association of FtsZ with the membrane is essential for its function, assembling the FtsZ-ring tethered to the cellular membrane. The attachment of FtsZ to the membrane is mediated by the interaction of the adaptor proteins FtsA and ZipA [289, 290], although chimeric FtsZ fused to a membrane targeting sequence (mts) region has also shown to be functional *in vivo* and *in vitro* [291, 287]. The membrane attachment regulates the filament dynamics, likely affected by the distance and strength of the attachment [292, 55, 293]. For this reason, *in vitro* studies have focused on the reconstitution of FtsZ on lipid-based platforms to understand its behavior and polymerization dynamics, especially under the spatial confinement of the lipid membrane to reassemble the features of the cell. It has been

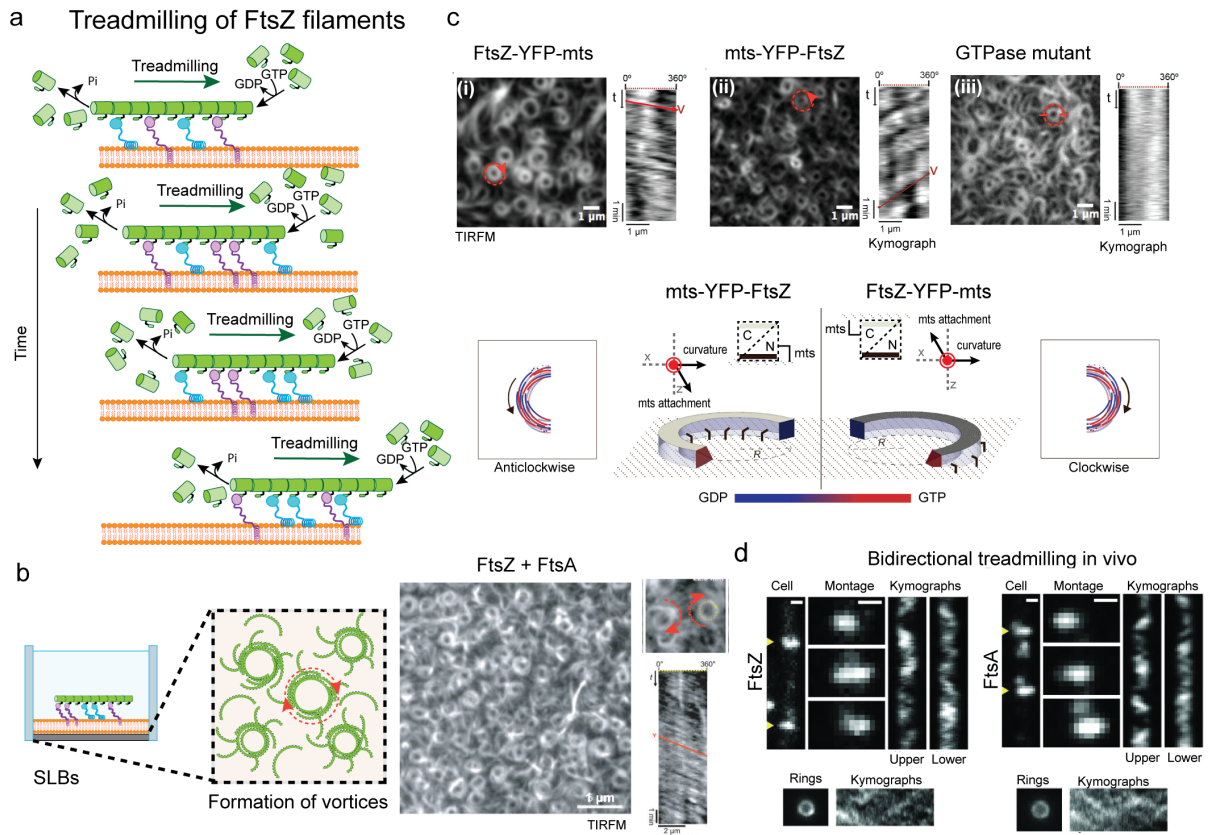


Figure 1.7: FtsZ filaments follow a GTP-driven treadmilling mechanism.

a) Schematic depicting the treadmilling behavior of FtsZ filaments on membranes. The FtsZ filaments treadmill by growing at the front of the polymer concurrently with depolymerizing at the opposite end, maintaining the same filament length. Thus, when FtsZ filaments (green) are bound to the membrane through FtsA (blue) and ZipA (purple), the treadmilling of filaments emerges as an apparent directional movement of the filament by continuous polymerization/depolymerization, although individual monomers remain stationary. **b)** Reconstitution of FtsZ filaments on supported lipid bilayers (SLBs) shows the assembly of FtsZ vortices. (right) TIRFM images of FtsZ tethered to the membrane by FtsA demonstrated a clockwise treadmilling. Kymographs of the image reveal the directionality of the filaments over time. Image adapted from [55]. **c)** Reconstitution of the FtsZ-YFP-mts (i) shows the self-assembly into vortices that treadmill in a clockwise direction, while a mts-YFP-FtsZ mutant follows an anticlockwise directionality (ii). They contain the membrane attachment at the C- or N-domain (Scheme below). The localization of the attachment modifies the apparent directionality of the treadmilling. Additionally, a FtsZ-YFP-mts GTPase defective mutant shows successful filament assembly but lacks directional treadmilling (iii). Figure adapted from [287]. **d)** Treadmilling of FtsZ filaments has been demonstrated *in vivo*. *Bacillus subtilis* cells were immobilized and imaged over time. Montages from time-lapse imaging of cells labelling FtsZ (left) and FtsA (right). Kymographs of the division ring demonstrated bidirectional treadmilling in both cases. (below) Vertically immobilized cells show multiple, independent filaments moving in both directions around the division site. Cropped rings and radial kymographs are shown in the image. Scale bar is 500 nm. Images adapted from [288]

proven that surface confinement can dramatically modulate the filament dynamics [294, 295, 296], such as preferential curvature, lateral interactions and twist between monomers [297, 298, 299, 300]. The interaction of FtsZ with other division proteins can also impact the behavior of the filaments on the membrane, such as the enhancement of FtsZ assembly in presence of Zap proteins (ZapA) [301] or the detachment and disassembling of the filaments via interaction with MinC [302, 303] and SlmA [304].

On the other hand, *in vitro* studies on supported lipid membranes (SLBs) have also demonstrated critical aspects of FtsZ dynamics at the molecular level. For instance, FtsZ filaments follow a directional cooperative behavior upon GTP hydrolysis following a GTP-driven treadmilling fashion, forming bacterial size vortices of around 1 μm independently of the nature of the attachment (FtsA, ZipA or -mts) [55, 287], resembling some of the dynamics observed *in vivo* (**Figure 1.7 a - c**). Treadmilling is the apparent directional movement of a filament by the continuous polymerization at the front of the polymer concurrent with depolymerization at the opposite end, although individual monomers remain stationary [274] (**Figure 1.7a**). The treadmilling of filaments has been also confirmed *in vivo* and it is tightly coupled to FtsZ's GTPase activity [288, 305, 306, 246] (**Figure 1.7d**), although its role in the cell and the molecular mechanism are still not fully understood [307, 306]. Nevertheless, two main functions are hypothesized to be related to it: the spatial distribution of the cell-wall synthesis enzymes and force generation.

In vitro reconstitution of FtsZ on lipid platforms has been successful in recent years, advancing substantially the knowledge of its functionality, and providing important mechanistic insights into its molecular details [186]. However, many questions remain open regarding its functionality and implication in the cytokinesis process or its assembly *in vivo*. Further analysis involving the co-reconstitution of FtsZ filaments and other division proteins can reveal the dynamic molecular mechanisms behind the assembly of the division machinery.

1.2.2 Membrane attachment of the FtsZ-ring

The recruitment of FtsZ and the formation of the FtsZ-ring at the midcell region is the first step of division. One of the critical steps of this event is the attachment of the FtsZ filaments to the plasma membrane. The correct attachment and formation of the FtsZ-ring at midcell are essential to achieve proper cytokinesis and division of the cell. In *E. coli*, the attachment of FtsZ to the membrane is mediated by two proteins: ZipA and FtsA. Both proteins have overlapping functions in the recruitment of FtsZ to the membrane, although their nature is completely different. The main properties and differences of those proteins will be briefly described below, as well as for the autonomous membrane-binding FtsZ chimera, the FtsZ-YFP-mts (**Figure 1.8**).

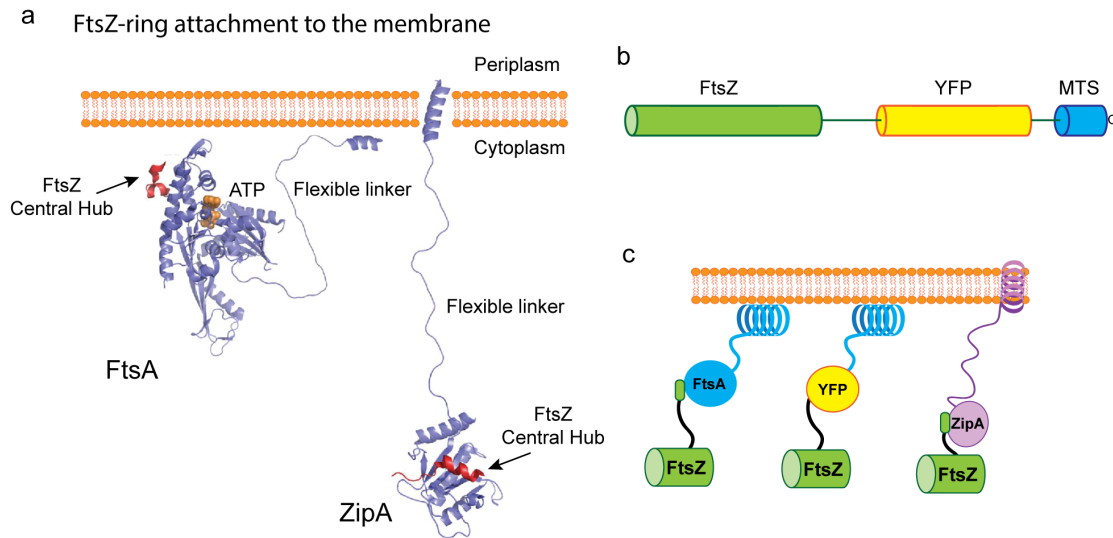


Figure 1.8: FtsZ-ring attachment to the membrane.

a) Crystal structures of *T. maritima* FtsA and *E. coli* ZipA. The FtsA molecule includes the ATP and the central hub of FtsZ, while ZipA only includes the FtsZ central hub. Both linkers are depicted as unstructured peptides and the amphipathic helix (FtsA) and alpha helix (ZipA) bind each protein to the membrane. Images adapted from [194]. **b)** FtsZ-YFP-mts is an FtsZ chimera that contains the amphipathic helix from MinD to attach the membrane independently to the interaction with FtsA or ZipA. The schematic domain structure of this chimera is shown in the picture, including the globular core of FtsZ, a YFP “Venus” protein and the mts attachment. **c)** Schematic representation of FtsZ bound to the membrane through FtsA (left) or by the mts domain in the case of FtsZ-YFP-mts (right). Scheme adapted from [308].

1.2.2.1 FtsA

FtsA is an actin-like protein that contains a conserved C-terminal amphipathic helix able to bind the bacterial membrane [309] (**Figure 1.8a**). Although the function of FtsA overlaps with ZipA in recruiting FtsZ filaments to the membrane, FtsA is conserved among bacteria and is an essential protein for division [310]. Membrane binding is a fundamental function of FtsA, although the sequence of the membrane binding domain does not play a direct interaction with FtsZ. It has been reported that FtsA can oligomerize and form filaments upon ATP consumption [260]. Moreover, FtsA can also assemble into mini-ring structures that inhibit FtsZ bundling and ring formation [311, 312]. The conformational change of the FtsA protein can affect the formation of the FtsZ-ring and the process of bacterial division, as it may cause membrane deformation that might eventually lead to the contraction of the membrane [313]. Nevertheless, the role of FtsA’s ATPase activity and polymerization are still not clear and further studies are needed to clarify the physiological role of this ability to form energy-dissipative high-order structures.

On the other hand, FtsA not only tethers FtsZ filaments to the membrane but participates in the recruitment of downstream division proteins to the FtsZ ring [184, 314, 227]. FtsA recruits FtsK and FtsQLB and also interacts with FtsN, which are essential proteins of the septal PG synthesis machinery [315, 226, 312, 316, 317]. A recent *in vitro* study together with previous observations suggest a mechanism of divisome maturation and cell constriction that depends on the switch of FtsA from inactive polymers to an active monomeric form [318, 226]. The binding of FtsN and other divisome proteins would depolymerize FtsA and activate the division machinery through FtsN. However, another study challenges this model by demonstrating FtsA polymerization and alignment of filaments when FtsN is present, suggesting that the conformational switch from mini-rings to filaments is important for FtsA function [312]. Thus, FtsN and FtsA's role in the recruitment and activation of the PG synthesis machinery is still to be disclosed [184].

1.2.2.2 ZipA

ZipA is bitopic protein that integrates into the membrane through its N-terminal transmembrane domain [290, 310], (**Figure 1.8a**). ZipA connects FtsZ to the bacterial membrane through an interaction of a flexible, unstructured linker region of ZipA with the central hub of FtsZ [259], although a secondary binding site in the globular domain has been recently found [319]. ZipA is only present in Gram-negative gammaproteobacteria such as *E. coli*, and its function is essential for cell division [193, 320]. However, a gain of function form of FtsA* can bypass the need for ZipA in cells [314]. In *E. coli*, ZipA functionally overlaps with FtsA in the attachment of FtsZ to the membrane [310], but their combination provides a stronger attachment of the filaments to the membrane [183], probably enhancing the FtsZ-ring stability [314, 321].

FtsA and ZipA directly interact with each other [322] and ZipA prevents FtsA polymerization, although the effect on division is still not clear [323, 324]. The *in vitro* reconstitution of ZipA in lipid membranes has been challenging due to its transmembrane region, which hinders its purification and subsequent use. Thus, a His-tagged soluble variant of ZipA (siZipA) lacking the transmembrane domain was made to facilitate its purification and further use through DGS-NTA derivative lipids as membrane attachment [325, 50, 53, 326]. Reconstitution studies have proposed that ZipA can recruit FtsZ monomers to the membrane while FtsA only recruits FtsZ polymers [292, 55]. Furthermore, *in vitro* experiments using GUVs also described the interaction between ZipA and FtsZ, promoting the membrane constriction upon GTP consumption [325, 150].

1.2.2.3 FtsZ-YFP-mts

As mentioned above, FtsZ does not bind the membrane by itself but it requires the natural anchors FtsA or ZipA to interact with the lipidic membrane. However, the addition of these two membrane proteins to the *in vitro* experiments challenges the reconstitution of FtsZ on synthetic lipid membranes, limiting the bottom-up studies. Therefore, to bypass these natural anchors and provide autonomous membrane attachment, a chimeric membrane-targeted FtsZ protein (FtsZ-YFP-mts) was constructed substituting the central hub by inserting a YFP-Venus fluorescent protein and a membrane targeting sequence (mts) to its C-terminal region, allowing a direct reversible binding to the membrane [291] (**Figure 1.8b and c**). This mts region corresponds to the amphipathic helix from *E. coli* MinD, one of the elements of the MinCDE system able to bind the inner membrane. This membrane targeting sequence is a 15 amino acids sequence, containing hydrophobic and positively charged residues that promote the binding of MinD with anionic phospholipids [327]. The use of this mutant form facilitates the reconstitution of FtsZ *in vitro*, which is a major advantage to reveal its function.

Using GUVs, Erickson and coworkers demonstrated that FtsZ-YFP-mts cells are viable *in vivo* and FtsZ-YFP-mts can bind membranes *in vitro*, assembling stable ring-like structures and inducing membrane deformation and tubulation upon GTP addition [291, 158, 159]. *In vitro* reconstitution using SLBs demonstrated that FtsZ-YFP-mts behaves similarly to FtsZ, showing a fast exchange of monomers with a half-life of 10 s [198], similar to the rate found *in vivo* [328] and single filaments in solution [192]. Further studies achieved the reconstitution of bacterial size vortices on SLBs, demonstrating a directional treadmilling behavior [287] (**Figure 1.7c**). The directionality of the treadmilling depends on the localization of the -mts at the N-terminal or C-terminal domain of FtsZ, while the velocity of subunit-exchange is greatly affected by the membrane affinity of the -mts region, slowing down the treadmilling for higher affinities [329]. The use of this membrane-bound FtsZ greatly facilitates the *in vitro* studies with FtsZ, not only to understand the dynamics and interactions of FtsZ with other division proteins [303], but also its use in studies of protein printing [330] or as a platform to test effects of Halogenation [331, 332].

However, it is noteworthy that the attachment of FtsZ to membranes via either autonomous FtsZ attachment or anchoring through ZipA or FtsA, may have a significant impact on the structural organization of the filaments. The most significant difference among them is related to the spatial distance to the membrane. Cryo-EM images of FtsA and FtsZ on lipid membranes showed filaments with a 6-9 nm spacing [285, 333], while the negative stain images of FtsZ-YFP-mts showed a spacing of around 5 nm [334]. A larger separation of FtsZ with the membrane can provide different filament dynamics that could eventually play a role in the recruitment of downstream proteins or in the assembly of the FtsZ-ring.

Nevertheless, the use of FtsZ-YFP-*mts* has permitted a great advance and development in the *in vitro* reconstitution of FtsZ and it is a great tool to characterize the molecular dynamics of division systems.

1.2.3 Spatiotemporal localization of the FtsZ-ring by the MinCDE system

The MinCDE system is responsible for the spatiotemporal positioning of the FtsZ-ring and division machinery, defining the cellular midcell and preventing septal aberrations [335]. The Min system is constituted by three proteins called MinD, MinE and MinC that self-organize into reproducible and stable pole-to-pole oscillations inside the bacterial cell [336] (**Figure 1.9a**).

MinD and MinE induce spatiotemporal heterogeneity of their concentrations on the membrane following a biological pattern formation system, the so-called reaction-diffusion mechanism, that generates a concentration gradient of MinC with the maximum at cell poles and the minimum at midcell (**Figure 1.9b**). As MinC inhibits the polymerization of FtsZ on the membrane, the MinCDE oscillations inhibit the formation of the division ring at the cell poles, limiting it only at the midcell [336, 199]. The apparent simplistic mechanism behind the MinCDE oscillations has been subjected to extensive *in silico*, *in vivo* and *in vitro* studies, reaching a detailed knowledge of the molecular mechanism of the system [337, 338, 335]. Interestingly, the *E. coli* MinCDE system shares similar structures and functions with the ParABS system found in many bacteria. The ParABS system also follows a reaction-diffusion mechanism and it is involved in the segregation of the newly synthesized genetic material [339]. Despite their functional differences, Min and Par systems share remarkably similar molecular components, mechanisms, and strategies. A comparison of these two reaction-diffusion systems, as well as an introduction to the MinCDE system, is addressed in **Publication 1**.

MinD is an ATPase that contains an amphipathic helix at the C-terminal end of the protein, which functions as a membrane targeting sequence (*mts*). MinD dimerizes upon the exchange of ADP to ATP, allowing its binding to the membrane [342, 343, 344]. Once on the membrane, MinD dimers interact laterally with each other, increasing their residence time and stability on the membrane [345, 346, 344]. On the other hand, MinE is a small dimeric protein that acts as an ATPase-activating protein of MinD [347, 348]. Similar to MinD, MinE also possesses a *mts* domain, although its membrane affinity is low before binding to MinD [349, 350]. MinE interacts with membrane-bound MinD, which induces a conformational change that enhances its membrane-binding affinity and allows the formation of an asymmetric MinDE complex [351]. This interaction then stimulates MinD's ATPase activity [349, 352] and triggers the monomerization and further detachment

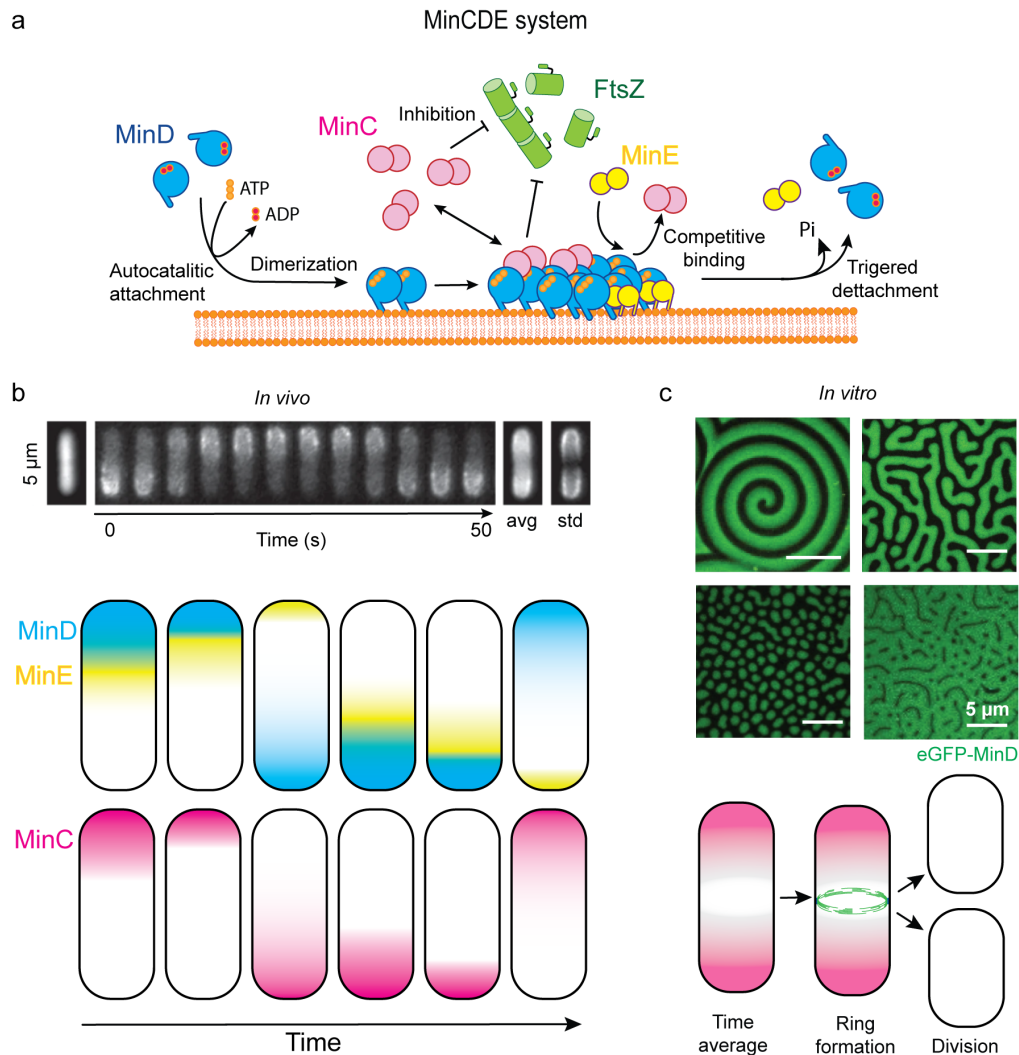


Figure 1.9: The MinCDE system.

a) Schematic depicting the molecular mechanism of the MinCDE system and the interaction with FtsZ. MinD (blue) binds ATP, dimerizes and attaches the membrane in a cooperative fashion. On the membrane, MinD can either recruit MinC dimers (magenta), forming a MinCD complex and inhibiting FtsZ-ring formation (green); or bind MinE (yellow), which competes with MinC for the binding site and enhances the ATPase activity of MinD, promoting its detachment to the membrane. **b)** Min oscillations *in vivo*. (Top) trapped *E. coli* cells show Min pole-to-pole oscillations over time. The average intensity is shown on the right. Images adapted from [340]. (Middle, bottom) Schematic representation of the Min protein gradients during the oscillatory mechanism in the cell. Via the reaction-diffusion mechanism shown in (a), the MinDE proteins emerge pole-to-pole oscillations along the bacterial membrane. MinC is transported along the membrane with MinD, creating a protein gradient that allows the assembly of the FtsZ-ring only at midcell. **c)** Confocal images of the Min system reconstituted on SLBs show a high variety of patterns. Images reprinted from [341]

of MinD from the membrane [351]. This molecular interaction between MinE and MinD is responsible for generating reaction-diffusion patterns on the membrane, by creating an oscillatory cycle of ATP-driven exchange of those proteins between membrane and cytoplasm that results in pole-to-pole oscillations.

The third participant of the Min system is the effector protein MinC, which is an inhibitor of FtsZ polymerization. MinC is a dimeric protein [353, 354] that is recruited to the cell membrane by MinD, competing with MinE for the MinD's binding site [355, 356, 357]. This competition allows MinE to displace MinC from membrane-bound MinD, which enhances MinD's ATPase activity and further detachment from the membrane [358, 342]. Thus, MinC undergoes the oscillatory behavior together with MinD and the antagonistic protein MinE, providing the ability of the MinCDE system to position the FtsZ-ring. MinC can interact with the FtsZ's central hub, disrupting the assembly of FtsZ on the membrane by shortening the length of FtsZ filaments, although the molecular mechanism behind the inhibition is still not fully understood [359, 360].

Although the MinCDE system forms pole-to-pole oscillations *in vivo* [336, 361], *in vitro* studies have demonstrated that they can self-organize generating a large range of dynamic patterns on planar membranes, even resembling Turing-like patterns [362] (**Figure 1.9c**). The first observation of Min oscillations *in vitro* was done by Loose et al. [363] showing the formation of “travelling waves” on SLBs. Since then, a large number of *in vitro* studies have employed the Min system not only to understand the molecular dynamics of Min proteins but also other biological reaction-diffusion systems [337]. As a result of all these efforts in recent years, the understanding of the molecular details of the Min system has advanced significantly, defining the detailed functionality of the Min proteins and their interaction in synthetic environments [335].

Importantly, the extensive knowledge of the Min system both *in vivo* and especially *in vitro*, makes it interesting to reconstitute the cell division machinery inside synthetic cell models in combination with FtsZ. Previous studies have demonstrated a successful reconstitution of the MinDE oscillations inside GUVs [364] even observing a geometrical response of the membrane compartment arising from the interaction with the Min proteins. Moreover, further developments have enabled the emergence of Min oscillations by “*de novo*” proteins expressed using PURE cell-free expression systems on SLBs or inside lipid droplets and GUVs [151, 152], determining the effect of protein ratios (MinD/MinE) [365] or the effect of macromolecular crowders [366] on the emergence of waves. On SLBs, deep characterization of the Min system has significantly advanced the understanding of their functionality. Importantly, a recent study demonstrated the ability of Min proteins to displace any molecule bound to the membrane by a friction-driven diffusiophoresis mechanism [341], a desirable feature for the *in vitro* reconstitution of synthetic systems.

In addition, the co-reconstitution of FtsZ and the Min system demonstrated a displacement of FtsZ antagonizing the MinCDE waves on SLBs [302, 303, 367], reassembling their biological function *in vitro*. This displacement can be further enhanced by the presence of macromolecular crowders [302]. On the other hand, the co-reconstitution of FtsZ-YFP-*mts* and Min system inside open rod-shape chambers allowed the emergence of Min pole-to-pole oscillations and localization of FtsZ filaments only at the middle of the chamber [367]. However, MinDE was proven to also displace FtsZ by a diffusiophoresis mechanism, although the presence of MinC sharpens the inhibition of the FtsZ polymerization [368, 303]. The combination of cell-free expressed MinDE proteins and purified FtsZ achieved the emergence of Min travelling waves on SLBs without showing a clear formation of a FtsZ structure stabilized at the MinC minima [151]. Although the bottom-up reconstitution of MinCDE and FtsZ has experienced great development in recent years, a clear localization of the FtsZ filaments in membrane-based platforms has not been achieved so far. The complexity involved in both FtsZ polymerization and MinCDE self-organization makes their co-reconstitution far more challenging than individual reconstitution. However, the spatiotemporal localization of the FtsZ filaments driven by the Min system at the equatorial plane of a synthetic cell raises a hope to establish systems which can potentially accomplish a controllable minimal division system *in vitro*.

1.2.4 FtsZ-ring stabilization and assembly

The condensation and stabilization of the FtsZ filaments in the midcell region of the bacterial cell is a process yet to be fully understood mediated directly by both, the positive and negative regulators of division. The FtsZ filaments are arranged on the membrane and the FtsZ-ring is then assembled and condensed, creating a tight structure once the division is initiated [369, 370, 371]. One of the features already described is that the FtsZ-associated Zap proteins (ZapA, ZapB, ZapC and ZapD) are responsible for the stabilization of the FtsZ-ring, interacting at an early stage of the ring assembly and colocalizing with it.

The biological function of the Zap proteins is the crosslinking of FtsZ filaments, promoting lateral interactions to assemble and stabilize the FtsZ-ring structure (**Figure 1.10**). Deletion of either of the Zap genes alone does not affect dramatically the cell viability, but deletion of more than two genes leads to filamentation, which suggests that Zap proteins have overlapping functions in the cell [207, 372, 257, 373, 374]. ZapA is highly conserved, whereas ZapB, ZapC and ZapD are only found in *gammaproteobacteria* [257, 375, 376]. ZapA is a dimeric protein that tetramerizes at high concentration [377] and simultaneously binds to the globular domain of two FtsZ filaments, promoting bundling [376, 377, 378]. ZapC is a monomeric protein that crosslinks FtsZ filaments by binding the FtsZ globular domain [373, 379]. ZapD is a dimeric protein that interacts with the central hub of FtsZ, connecting filaments into bundles [257, 380, 381]. Curiously, ZapB is a dimeric coiled-coil

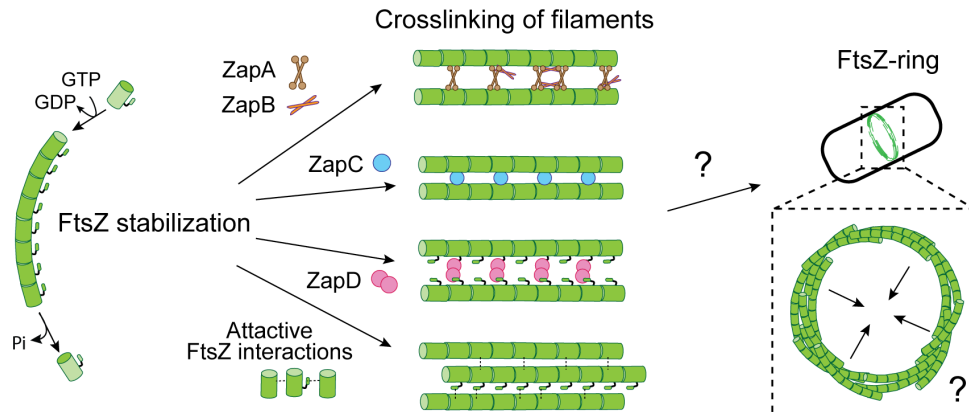


Figure 1.10: Stabilization of the FtsZ-ring and filament crosslinking.

Schematic depicting the stabilization of FtsZ filaments into an FtsZ ring. The Zap proteins (ZapA, ZapB, ZapC and ZapD) crosslink FtsZ filaments laterally, although their mechanisms of interaction are not entirely clear. Here, a simplified representation of filament crosslinking by every Zap protein is shown. Additionally, lateral attractive forces can occur between filaments, either between globular cores or with the central hub mediating the lateral interactions. Nevertheless, the mechanism of functional stabilization of a constrictive FtsZ-ring by Zap proteins is still unknown. Scheme based on [194]

protein that binds FtsZ through ZapA [382, 375], also interacting with MatP, a DNA-binding protein involved in the chromosome condensation and segregation [372, 209]. The complex formed by ZapA, ZapB and MatP is designated as the Ter-linkage, which ensures the correct segregation of the chromosome. Thus, ZapB links MatP to the FtsZ-ring through ZapA, functioning as a continuous link between the Ter region of the chromosome and the divisome machinery, coordinating them during the division process [372, 208, 383].

Despite the Zap proteins have been proven to be functionally redundant, they do not share common sequences and their structure and molecular mechanism of filament crosslinking are clearly differentiated. These differences provide an extra layer of complexity and plasticity to form the FtsZ-ring through different mechanisms. Their biological function is key in the division process, although the molecular mechanism of their interaction with FtsZ and the crosslinking of filaments is still far from being understood.

It is known that even without those crosslinking factors, FtsZ can form bundles in the presence of macromolecular crowders and divalent cations *in vitro* [384, 193, 385]. Formation of filament assemblies is likely mediated by weak attractive forces via the C-terminal linker of FtsZ, which can modulate FtsZ bundling *in vitro* [263, 255, 386, 285, 266, 267]. This suggests that non-protein mediated lateral interactions between filaments might also play a role in the FtsZ functionality in the cellular environment. However, the presence of bundles *in vivo* is doubted [387], and the FtsZ's ability to form bundles is highly variable,

differing substantially between species [255, 193]. *In vivo* studies have not clarified the role of bundling in the FtsZ-ring assembly, confirming that lateral interaction defective FtsZ mutants are lethal in cells [268, 188, 388, 324], despite it is not fully clear whether they are defective to form the FtsZ-ring or in any of the subsequent steps. Experiments using cryo-electron tomography (cryo-ET) of the FtsZ-ring determined that the spacing between individual filaments is too distant for lateral interactions, although their coexistence could not be discarded [285, 389, 333] (**Figure 1.11**). Therefore, lateral connections via weak FtsZ-FtsZ interactions might collaborate in the assembly of the FtsZ-ring, despite the crosslinking of filaments via Zap proteins is the main mechanism of the divisome stabilization.

Importantly, among the Zap proteins, ZapD is the only one that binds FtsZ through the C-terminal domain [380, 381]. This can provide an extra degree of freedom in the spacing and crosslinking of filaments, enabling longer distances between filaments and higher flexibility in the interaction. In addition, the presence of ZapD will compete with other division proteins for the FtsZ's binding site such as negative regulators (MinC or SlmA) or membrane tethers (FtsA or ZipA). This competition may be important to modulate the condensation of the FtsZ-ring in the cell. A combination of different crosslinking strategies together with lateral interactions of filaments may also have interesting mechanistic implications that can be translated into higher forces on the membrane, different filament curvatures or local densities within the FtsZ-ring structure.

Thus, the stabilization of the division ring is a critical step that determines its ability to complete its biological function of positioning at midcell, recruit further division components and even drive or trigger the constriction of the cell. A better understanding of the mechanism behind the assembly and stabilization of the FtsZ-ring can shed light on the whole process of division, a step ahead in our comprehension of an essential biological function.

1.2.5 FtsZ-ring structure and function

As introduced above, the divisome stands by the orchestration of a large number of components, which we are only starting to understand. It is broadly accepted that the FtsZ-ring serves as the scaffold and main coordination of the division site, recruiting the division components and leading them to complete the entire division event. However, the internal architecture of the FtsZ-ring and its participation as a force generator during cytokinesis are controversial and no agreement has yet been reached.

Both the structure of the FtsZ-ring and its function are strongly related to each other, and many studies have revealed interesting insights regarding this interrelation. The understanding of the FtsZ-ring structure has experienced a substantial improvement in re-

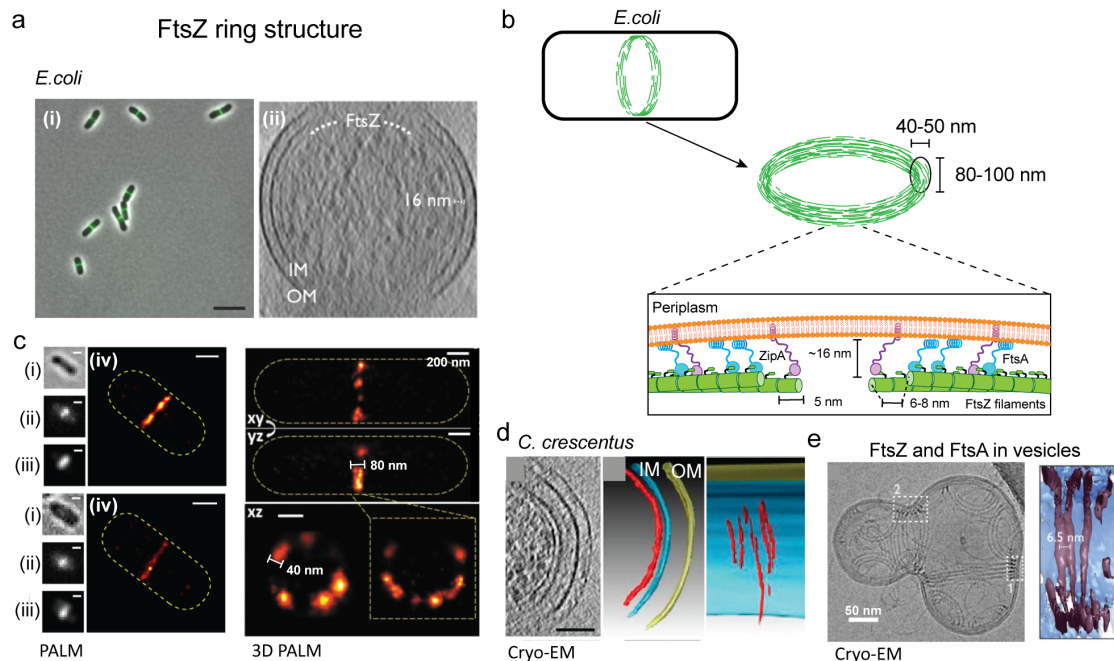


Figure 1.11: Structure of the FtsZ-ring.

a) (i) Conventional fluorescence images of FtsZ-ring at midcell in wild-type *E. coli* cells. Scale bar is 5 μm. (ii) Cryo-ET micrograph of the cross-section of an *E. coli* division site shows that FtsZ filaments are located around 16 nm underneath the inner membrane (IM). Image adapted from [333]. **b)** Schematic depicting the current FtsZ-ring model. It consists of a toroidal area of discontinuous filaments, probably connected laterally by crosslinkers and attached to the membrane via FtsA and ZipA. The FtsZ-ring is located around 16 nm underneath the membrane. **c)** Images of photoactivated localization microscopy (PALM) of the division ring. They show that the FtsZ-ring is a discontinuous arrangement of filament nodes. Images of cells expressing FtsZ-mEos2 in the order of bright-field (i), green fluorescence (ii), regenerated fluorescence image (iii), and PALM images (iv). Scale bar is 500 nm. Approximate cell outlines are depicted by yellow dashed lines. Images adapted from [390]. (Right) 3D PALM images of two-dimensional projections of alive *E. coli*. In the top panel, the corresponding division rings are outlined in dashed boxes in the panel below. Xy, yz panel of the *E. coli* cell and below the xz of the cross-section of the ring. x is the short axis and y is the long axis of the cell parallel to the imaging plane, while z is the axis of the cell perpendicular to the imaging plane. Scale bar, 200 nm. Images adapted from [391] **d)** Cryo-ET of *Caulobacter crescentus* cells showing the cross-section of a division ring. The segmentation of these cells shows spacing between filaments. Scale bar is 200 nm. Images adapted from [389]. **e)** Cryo-EM images of a lipid vesicle containing *T. maritima* FtsZ and FtsA. Dashed white lines highlight the junction points of the rings with the membrane. Cryo-ET and further segmentation of the rings assembled on these vesicles also showed space between filaments (right). Images adapted from [333].

cent years, mostly due to the advances in high-resolution imaging [177, 185, 186] (**Figure 1.11**). The FtsZ-ring is most certainly constituted by a collection of single-stranded FtsZ filaments, which could be laterally associated with each other. However, the arrangement or architecture of the FtsZ filaments in the FtsZ-ring *in vivo* remains elusive. Studies using

conventional fluorescence microscopy described a structure of a condensed ring at midcell [392, 393, 189, 190] (**Figure 1.6a and Figure 1.11a**). Further studies using advanced super-resolution imaging and (cryo-ET) supported a discontinuous and heterogeneous arrangement of filaments, overlapping and condensed into nodes of higher density in a belt-like array [390, 391, 190, 394, 333] (**Figure 1.11a, c, d and e**). The current model based on these studies supports a dynamic molecular system of FtsZ filaments loosely associated with each other via protein factors such as Zaps or weak lateral attractive forces between FtsZ filaments [268, 193, 389, 249, 333] (**Figure 1.11b**). These associations might allow the alignment and sliding of adjacent filaments while maintaining their juxtaposed organization [186, 395, 333]. The FtsZ filaments are condensed on the membrane, in a toroidal area of around 80–100 nm in width located around 13–16 nm underneath the inner membrane [207, 396, 390, 397, 391]. The dependence of this condensation on the GTPase activity of FtsZ is not clear, as FtsZ mutants with low GTPase activity are also able to form condensed FtsZ-rings. [390, 391]. The mechanistic implications behind this phenomenon are still to be studied.

In addition, *in vivo* studies have proven that only around 30% of cellular FtsZ is participating in the FtsZ-ring structure at a given time, due to the rapid exchange of FtsZ molecules with the cytoplasmic pool, which has a lifetime of around 8 s [328, 192]. Single-molecule tracking indicated that individual FtsZ molecules within the ring are immobile, consistent with a GTP-driven treadmilling behavior [288, 246]. Furthermore, FtsZ treadmilling polymers are oriented in both directions around the division plane, which can contribute to the uniform distribution of the PG synthesis machinery [288, 398, 246] and perhaps the contraction of the ring, in good agreement with the current model of the FtsZ-ring [186](**Figure 1.11a and b**). *In vivo*, tracking of single molecules of PG synthases has revealed a directional movement at the division plane, affecting the spatial distribution, but not the rate of PG synthesis (**Figure 1.7d**). Likewise, FtsZ GTPase mutants retain the ability to form the septum *in vivo*, although their formation is aberrant [392, 246], suggesting that the GTPase activity of FtsZ could be dispensable for the generation of forces in cytokinesis [399, 396, 239, 206, 391, 400, 401, 246]. However, a recent study confirmed that FtsZ was still required in the late stages of constriction, pointing towards a role of FtsZ in the contraction of the membrane [236].

The functions of the FtsZ-ring as the scaffold of the divisome and division coordinator of the system are clear, although its role as a force generator to drive the cytokinesis process has been discussed for the last years [402, 232, 384, 233, 298, 395, 186, 403] (**Figure 1.12a**). Basically, it is argued whether the mechanism and source of force generation to split the bacterial cell comes from the cell-wall synthesis machinery or the contractile FtsZ-ring. Experimental evidence has been collected supporting both hypotheses both *in vitro* and in *E. coli* cells. Despite the cell-wall synthesis machinery seems to be the leading force of

1.2 The bacterial cell division machinery

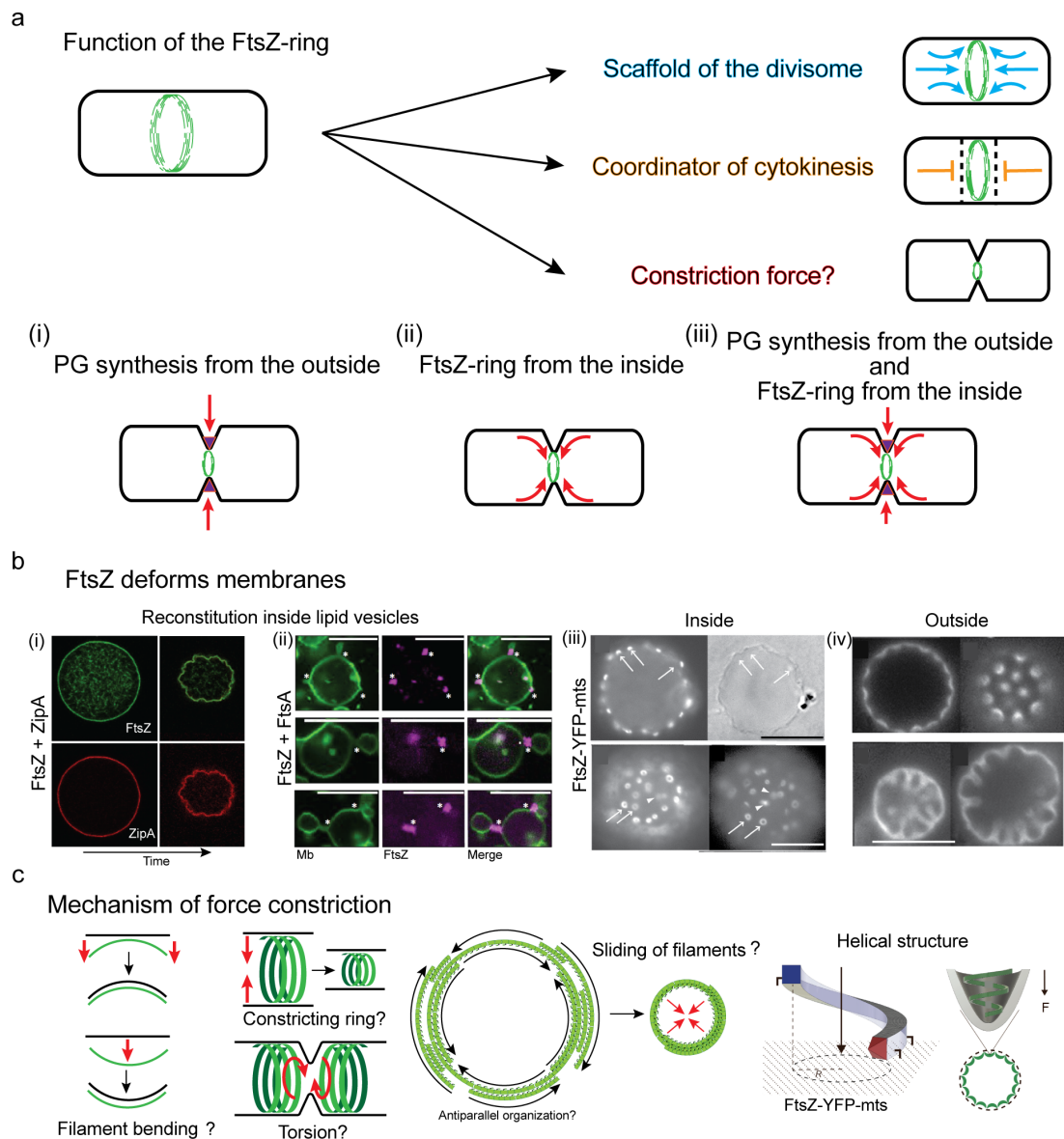


Figure 1.12: Function of the FtsZ-ring. **a)** Schematics depicting the known functions of the FtsZ-ring *in vivo*. FtsZ-ring serves as a scaffold to recruit all division proteins and functions as a coordinator of cytokinesis. However, its participation as a constriction force is debated. The constriction force can either come from the PG synthesis machinery, pushing from the outside (i); from the FtsZ ring, constricting from the inside (ii); or a combination of both (iii). **b)** Confocal images of GUVs containing FtsZ with siZipA (i) or FtsZ and FtsA (ii) demonstrated membrane deformation. Confocal images of FtsZ-YFP-mts reconstituted on the inside (iii) or the outside (iv) show outwards and inwards membrane deformations, respectively. Images adapted from [325, 157, 159]. Scale bars are 10 μm . **c)** Scheme of the force mechanisms of the FtsZ filaments. Some of them are the bending of filaments, torsional stress from the treadmilling forces, the sliding of filaments and constriction, or drilling forces from the helical structure of FtsZ.

constriction, as the PG synthesis is the rate-limiting factor for division [396], the participation of the ring as a contractile force is still not clear. The continuous rearrangement of FtsZ on the membrane could provide force to drive membrane constriction, as observed *in vitro*. However, it is doubted that this force would be strong enough to overcome the turgor pressure and membrane stiffness [217]. Instead, some authors proposed the FtsZ-ring as the spatiotemporal coordinator of the bacterial septal machinery, simply guiding it to the correct position without exerting substantial force [288, 404, 215]. A coordinated effort of both systems has been also proposed with FtsZ pulling from the inside and the septal machinery pushing from the outside [396, 217], although further experimental evidence has not been provided yet.

It has been demonstrated that FtsZ filaments can exert forces on lipid bilayers *in vitro*, but their implication *in vivo* and their relation with the cytokinesis are not clear yet (**Figure 1.12b**). Three basic properties of FtsZ filaments are proposed as the main mechanisms in play to exert forces [186]: (1) the persistent length of FtsZ filaments and their intrinsic bending rigidity, (2) the GTP hydrolysis-induced filament conformational change, and (3) the treadmilling result of FtsZ polymerization dynamics [232, 247, 405, 406, 407]. Alternative and more complex mechanisms have been proposed from the combination of the basic three [408, 409, 395, 300, 410], some of which involve the condensation of FtsZ filaments caused by lateral affinity [411] or the antiparallel sliding of FtsZ filaments within the FtsZ-ring [333] (**Figure 1.12c**).

Considering the persistence length of FtsZ in given conditions [412], FtsZ polymers would be able to deform any membrane softer than the filament itself. This was proven using liposomes *in vitro*, which show membrane constrictions on GUVs [291, 158, 159]. It was also proposed that the C-terminal linker plays an important role in driving the bending of FtsZ away from the membrane, generating bending forces [262, 263, 386]. In addition, attachment of the FtsZ filaments through the C-terminal or N-terminal region of FtsZ causes inward or outward forces respectively, [294, 287] (**Figure 1.7c** and **Figure 1.12b**). The continuous bidirectional treadmilling of the filaments on the membrane may involve constrictive forces, which combined with lateral sliding of antiparallel filaments can also generate torsional forces [333, 288, 395]. Likewise, recent computational simulations suggest that a rigid linker connecting to the membrane and lateral associations could also favor the constrictive forces [395]. On the other hand, the conformational change suffered upon GTP hydrolysis has been experimentally observed *in vivo* [389, 413, 275] and *in vitro* by cryo-EM and cryo-ET studies, confirming the presence of curved and straight filaments [285, 414, 407]. The curved conformation has been also described in the GDP-bound *Mycobacterium tuberculosis* FtsZ, in contrast to the straight conformation in other bacterial species [415, 250, 273, 253]. This conformational change driven by GTP binding can create forces on the membrane.

The understanding of the structure and architecture of the FtsZ-ring as well as how the ring is assembled and stabilized is essential to comprehend its role. Unfortunately, technical limitations in either *in vivo* or *in vitro* studies have restricted further knowledge of the dynamics of FtsZ and its natural division partners within the divisome. Many questions remain open, and the ability of FtsZ filaments to generate forces is accepted but still unclear, as well as their implication inside the cell. The softness of the FtsZ filaments in comparison with similar proteins like tubulin or actin suggests that the forces that can be achieved by the FtsZ filaments are more limited. However, most of the studies have only taken into consideration the structure or mechanism of individual filaments, whereas the structure of the FtsZ-ring as a whole could play a bigger role in the molecular mechanics of constriction [384, 233]. It has been proven that factors such as the membrane attachment, presence of cations or lateral interactions between the filaments affect dramatically the dynamics of the filaments and likely their ability to bend or deform membranes.

Considering the current model of the FtsZ-ring, the organization of the filaments could be antiparallel, connected through lateral interactions of different natures that might allow and enhance the sliding of filaments and the treadmilling in both directions. This complex organization might enhance the constriction force exerted on the membrane, although it has not been experimentally addressed yet. *In vitro* experiments following a bottom-up approach and including model membranes and cellular environments could shed light on this important question, making significant progress in the understanding of the bacterial cell division process and its reconstitution in synthetic compartments.

Objectives

FtsZ has been in the spotlight within the field of bacterial cell division due to its importance in the bacterial cell cycle as the central protein of the division process. Its dynamic behavior to homopolymerize, and its function of integrating and coordinating other division components have been of great interest to the community. While previous *in vivo* studies have visualized the positioning and hypothesized the structure of the FtsZ-ring, *in vitro* approaches have determined the structure of the filament and the mechanism of polymerization, defining its great plasticity. Despite all these new mechanistic insights into its functionality, many aspects remain elusive in its biological function, such as the spatial organization and coordination of the division process, assembly of the FtsZ-ring at midcell, the recruitment of division components to form the divisome, and FtsZ's role in cytokinesis and force generation.

The intrinsic complexity of the FtsZ system has its origin in the interaction of FtsZ with multiple division components, which are necessary to regulate and stabilize the FtsZ-ring in the early stages of division. Several division partners are required to anchor FtsZ to the membrane (FtsA or ZipA), position the FtsZ-ring at midcell (MinCDE), or stabilize the FtsZ filaments on the FtsZ-ring (Zap proteins). All of these components are essential for division, which implies that FtsZ functionality strongly depends on its interactions with the environment and other division components. Therefore, it is necessary to assess them together with FtsZ to understand the molecular dynamics underlying the division process.

Due to the high complexity involved in the assembly of the FtsZ-ring and the process of division, bottom-up reconstitution approaches are one of the best strategies to study the interaction and molecular dynamics of such complex systems, as we can dissect the numerous modules. In addition, the use of membranous cell-like model systems allows for deep characterization of protein systems, mimicking important cellular processes. For bacterial cell division, nearly every element in the cellular environment, such as the plasma membrane, the nucleoid, confinement, microenvironments, or the geometry of the reaction compartment, plays a critical role in the division process. This is particularly interesting for the case of FtsZ, due to its structural plasticity and multiple interactions with other division

proteins. Therefore, the improvement and development of bottom-up tools that allow the incorporation of cellular aspects is a relevant and highly sought objective to clarify and understand biological functions, complementing classical *in vivo* and *in vitro* approaches, while opening up new and exciting perspectives about previously studied systems.

The autonomous division is a milestone for fully-functional synthetic cellular systems, requiring the spatiotemporal reorganization of the division machinery to coordinate, deform, and split the synthetic compartment. A minimal division system based on FtsZ and other bacterial components could be an attractive option, as reconstitution of FtsZ in cell-like systems has proved the feasibility of the formation of ring-like structures able to deform synthetic membranes. At the same time, the co-reconstitution of FtsZ with other division components demonstrated their ability to modulate FtsZ's behavior and resemble, at least partially, their native cellular function *in vitro*. This opens up the avenue of reconstituting the entire bacterial cell division machinery *in vitro*. However, we are still far from a comprehensive understanding of the molecular mechanism behind the complex cellular division process in simplified environments. Therefore, bottom-up reconstitution of FtsZ with other division components in cell-like environments can not only provide insights into their functionality but also shed light on their application as a functional module for constructing a fully-functional synthetic cell.

Thus, I set out to investigate and expand our knowledge on the assembly and force constriction of the FtsZ-ring in membranous cell-like environments, with the final aim of reconstituting a functional minimal division system. Based on the above goals, the objectives of my thesis can be listed below:

- To explore the effects of the membrane boundary and geometry of the reaction compartment on FtsZ dynamics.
- To understand the role of FtsZ in the process of force generation during cytokinesis, assessing whether the FtsZ ring participates in or leads to the constriction of the bacterial cell by deforming the plasma membrane.
- To reconstitute a minimal division machinery *in vitro*, consisting of the FtsZ-FtsA and the MinCDE system to position and form a minimal FtsZ-ring structure inside lipid vesicles.
- To study the effects of macromolecular crowding on the behavior of FtsZ and other division components in cell-like environments.
- To investigate the mechanism of assembly, stabilization, and organization of the FtsZ-ring by characterizing the interaction of FtsZ with ZapD, one of the ring stabilizers.

Publications

3.1 Publication P1

Self-organized protein patterns: The MinCDE and ParABS systems

Summary:

The review article explores recent advances in the understanding of two prokaryotic pattern-forming systems, the MinCDE system and the ParABS system, that play important roles in biological decision-making processes such as cell division and DNA segregation. Both systems have similar molecular components, mechanisms, and strategies to achieve biological robustness despite functional differences.

Reprinted with permission from:

Merino-Salomón, A.*, Babl, L.* and Schwille, P. (2021). Self-organized protein patterns: The MinCDE and ParABS systems. *Current Opinion in Cell Biology*, 72:106-115. (*Review*)

Source online: <https://doi.org/10.1016/j.ceb.2021.07.001>



Self-organized protein patterns: The MinCDE and ParABS systems

Adrián Merino-Salomón^a, Leon Babi^a and Petra Schwille

Abstract

Self-organized protein patterns are of tremendous importance for biological decision-making processes. Protein patterns have been shown to identify the site of future cell division, establish cell polarity, and organize faithful DNA segregation. Intriguingly, several key concepts of pattern formation and regulation apply to a variety of different protein systems. Herein, we explore recent advances in the understanding of two prokaryotic pattern-forming systems: the MinCDE system, positioning the FtsZ ring precisely at the midcell, and the ParABS system, distributing newly synthesized DNA along with the cell. Despite differences in biological functionality, these two systems have remarkably similar molecular components, mechanisms, and strategies to achieve biological robustness.

Addresses

Dept. Cellular and Molecular Biophysics, Max Planck Institute of Biochemistry, Am Klopferspitz 18, Martinsried, 82152, Germany

Corresponding author: Schwille, Petra (schwill@biochem.mpg.de)

^a These authors contributed equally to this work.

Current Opinion in Cell Biology 2021, 72:106–115

This review comes from a themed issue on Cell Dynamics

Edited by Danijela Vignjevic and Robert Insall

For a complete overview see the Issue and the Editorial

<https://doi.org/10.1016/j.ccb.2021.07.001>

0955-0674/© 2021 Elsevier Ltd. All rights reserved.

Introduction

Living entities depend on the continuous formation and maintenance of structures and gradients. The spatio-temporal symmetry breaks that these can be achieved based on various levels, ranging from the formation of concentration gradients in single cells up to multicellular or organismic organization [1,2]. Protein gradients, in particular, show interesting properties, pointing to essential requirements for life-like systems. Several well-studied examples of pattern-forming protein systems can be found in various model organisms. In yeast, the Rho family GTPase Cdc42 plays a key role in polarity induction and cytoskeletal organization [3], while the organization and division of *C. elegans* are driven by the PAR proteins [4]. Cell division, in particular, is often

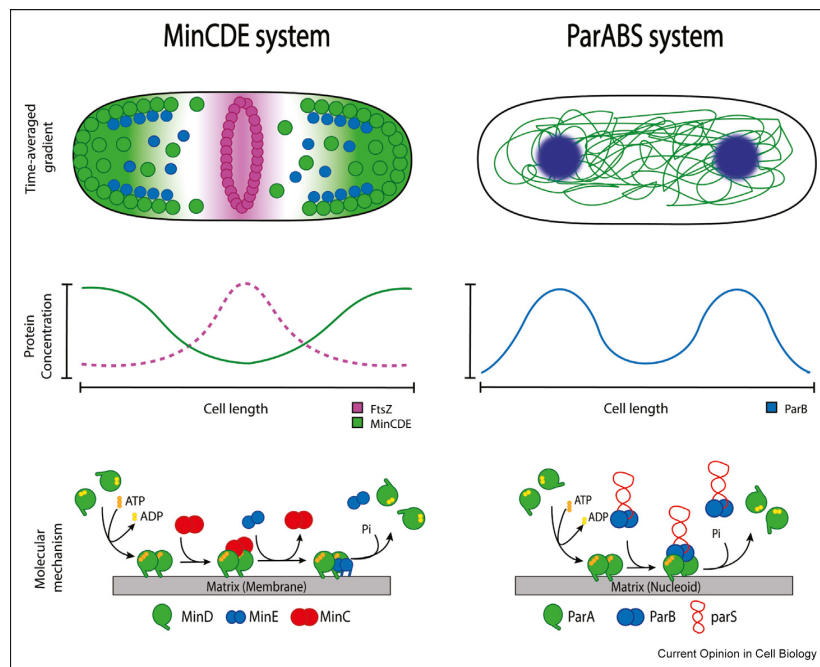
guided by specifically oriented morphogenetic cues that are, in fact, concentration gradients of proteins reflecting on the cell's spatial features. Similarly, prokaryotes use protein patterns and gradients to achieve the positioning of large-scale structures. Extensive research on the *Escherichia coli* Min system has shown a dynamic gradient on the cell membrane which achieves the precise positioning of the division machinery to midcell [5,6]. In a similar manner, the ParABS system forms patterns on the nucleoid and thereby achieves faithful segregation of genetic material [7]. A large number of quantitative biology and theoretical biological physics approaches have been accompanying the experimental investigations of pattern and gradient formation throughout the history of modern cell biology, with increasing success and predictive power [1,8–12]. However, elucidating the fundamental molecular features supporting the emergence of self-organized patterns generated by protein reaction-diffusion, actively regulated by the cell through energy dissipation to maintain its out-of-equilibrium state is still a formidable goal in biology.

The prokaryotic Min system has been extensively studied, and the mechanisms of pattern formation and regulation are thought to be well understood [5]. However, recent advances have revealed not only new surprising discoveries on pattern formation, linking the biochemical reaction-diffusion mechanisms to biophysical phenomena, such as active directional transport on membranes induced by MinCDE, but also the role of charge-dependent effects, such as liquid condensate formation, in the ParABS system. Intriguingly, these new insights point toward important differences in the molecular mechanisms of pattern formation, despite several conceptual and molecular similarities of the Min and Par systems. Thus, in this study, we focus particularly on a comparison between pattern-forming mechanisms of these prokaryotic systems, highlighting the general importance of the Min and the Par system as models for understanding biological self-organization mechanistically from first principles (see Figure 1).

The MinCDE system

The Min protein system constitutes a spatiotemporal regulatory mechanism for positioning the division machinery in *E. coli* [13]. Min proteins self-organize after a reaction-diffusion mechanism forming a protein concentration gradient that allows the assembly of the divisome only at midcell (Figure 2A and B).

Figure 1



Comparison of the cellular organization of the two pattern-forming protein systems MinCDE and ParABS. The MinCDE system positions the FtsZ ring (purple) through negative feedback, while the ParABS system localizes cargo DNA through a positive feedback mechanism. The time-averaged gradients of the systems display the differences of negative versus positive feedback. However, the molecular mechanisms of both systems are intriguingly similar.

Briefly, the P-Loop ATPase MinD dimerizes in an ATP-dependent fashion, enhancing its membrane affinity and binding to the plasma membrane in a cooperative manner [14–16]. The MinD ATPase-activating protein MinE is then recruited by a threshold concentration of membrane-bound MinD, forming an asymmetric MinDE complex. MinE stimulates the ATPase activity of MinD, which in turn results in MinD's monomerization and detachment from the membrane (Figure 2A) [14,17–20]. Thereby, MinDE proteins appear to move along the bacterial membrane through a reaction-diffusion mechanism of membrane attachment-detachment that generates pole-to-pole oscillations.

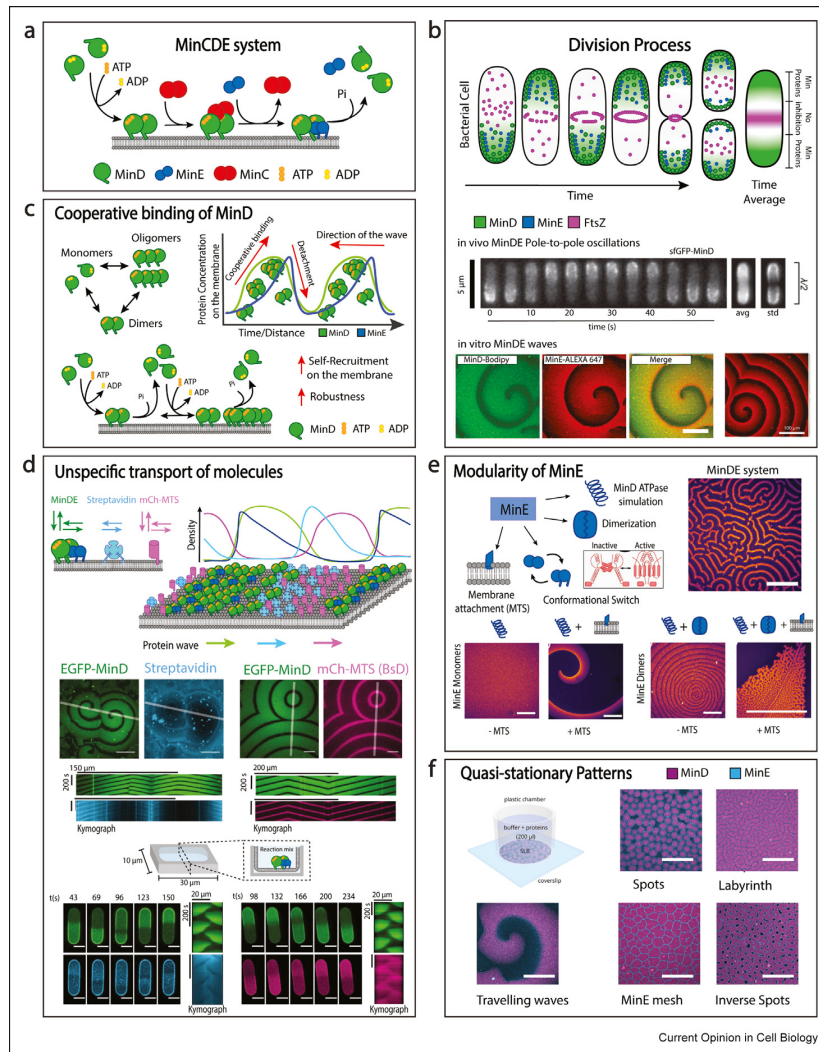
The third component of the Min system is MinC, which is also recruited by membrane-bound MinD and inhibits the assembly of the early division machinery on the membrane [14,17]. MinC does not participate in the reaction-diffusion mechanism, although it is displaced by MinE during the MinDE oscillatory process. As a result, MinC travels with the MinDE movement generating a time-averaged MinC gradient that prevents the assembly of the divisome at the cell poles, driving its formation at the geometric cell center.

Despite its compositional simplicity, the actual interaction mechanisms of MinDE self-organization on the

structural level are still far from being comprehensively understood. However, a key feature underlying the Min dynamics is the dimerization and cooperative self-enhancement of MinD on the membrane after ATP complexation (Figure 2C) [21,22]. Previous studies suggested that membrane-bound MinD dimers recruit further proteins from solution, although the mechanism has long been unknown [21,23]. However, a recent study has determined the presence of MinD–MinD interaction interfaces distinct from the canonical dimerization site, allowing the formation of higher-order oligomers [16]. The presence of multiple transient low-affinity interactions gives rise to a dynamic oligomeric equilibrium that leads to higher robustness needed for the MinDE wave formation and propagation on the membrane [16]. Thus, the classical model of MinD monomeric/dimeric state is now expanded to a dynamic scenario in which MinD exists in a range of oligomeric states.

Interestingly, it has recently been found that Min proteins can also regulate the localization of other peripheral membrane proteins without any specific molecular interactions (Figure 2D) [24]. Cooperative self-recruitment of MinD generates a mobile diffusion barrier able to locally affect the membrane attachment and detachment of proteins by binding site competition

Figure 2



MinCDE system. (a) Scheme of the MinCDE reaction mechanism. (b) Min proteins drive the localization of the division machinery. Pole-to-pole oscillations generate a time average protein gradient that inhibits the formation of the FtsZ ring at cellular poles. Min proteins form pole-to-pole oscillations *in vivo* and dynamic waves (among other patterns) *in vitro*. Scale bar is 50 μm (Images adapted by permission from the study by Loose et al. [15], Wu et al. [37]). (c) MinD shows a cooperative membrane binding forming oligomeric species on the membrane that favor its self-recruitment from the cytoplasm. (d) MinDE proteins can regulate the localization of other membrane proteins without any specific molecular interaction by binding site competition and repulsion. *In vitro* reconstitution of the MinDE system in supported lipid bilayers (SLBs) adding Membrane-bound streptavidin (restricted detachment from the membrane, only lateral movement) and mCherry-mts (Lateral movement, exchange with cytoplasm). (Top) Scheme of the unspecific binding and fluorescence intensity profiles. (middle) Representative time-lapse images and kymographs of MinDE oscillations, streptavidin and mCherry-mts counter-oscillations. Scale bars 50 μm . (below) Reconstitution of those systems in cell-sized PDMS microcompartments, scheme of the experimental setup and representative images of the time-lapse images. Scale bar 10 μm . Images and schemes adapted by permission from the study by Ramm et al. [24]. (e) MinE can be dissected into four functional modules: ATPase stimulation, dimerization, conformational switch and membrane attachment. Representative images of the MinDE system reconstituted in SLBs using minimal MinE modules. Scale bars 300 μm . Images adapted with permission from the study by Glock et al. [29]. (f) Quasi-stationary patterns formed using MinDE proteins reconstituted in SLBs. Representative confocal images of patterns were observed under different MinD-MinE protein ratios. Adapted with permission from the study by Glock et al. [44]. Scale bar 50 μm .

[24,25]. Even more intriguingly, diffusible membrane proteins unable to dissociate will be directionally pushed by the traveling MinDE by repulsive and frictional forces into large-scale gradients, described as diffusiophoresis [26]. This mechanism may function as an unspecific active transport system in bacteria and might disclose new insights of possible additional roles of the Min system inside the cell [27]. In particular, the Min system may play a role in the chromosomal segregation process by directly or indirectly driving the localization of components involved in the process [28]. Even though more research has to be conducted on this phenomenon, the unspecific transport of molecules is an interesting feature that might be found in other self-organizing systems able to generate protein gradients.

The second key molecule of the dynamic Min system, MinE, has been the primary target of bottom-up functionality engineering because of its small size. MinE's structure can be principally dissected into four functional modules: ATPase stimulation of MinD, dimerization, membrane binding and conformational switch between a catalytically active and inactive form [29] (Figure 2E). MinE ATPase stimulation of MinD is mediated by a short peptide [15,30] and its dimerization has been found to be important to generate patterns *in vitro* [31]. While the MinE membrane attachment regulates the Min wave shape and dynamics *in vitro* [32–34], its conformational switch enhances the robustness of the pattern formation over different protein concentrations [35,36]. Curiously, Glock *et al.* have reduced MinE to the minimum function of each module, revealing the structure-function relationship and the minimal requirements to form Min patterns *in vitro* (Figure 2E) [29]. The minimal peptide of MinE required to stimulate MinD ATPase activity is not able to generate patterns, although its combination to either of the two protein motifs for membrane attachment or dimerization results in MinDE patterns with different dynamics [29]. Importantly, these modular features may be replaced by artificial units of similar function. This has recently been demonstrated by fusing the catalytic MinE peptide to minimal dimerizing motifs, such as short complementary nucleic acid strands, the DNA-peptide hybrids resulting in clear pattern formation [31]. The combination of different functional modules enriches the capacity of MinE to modulate the MinDE dynamics, affecting the outcome of the reaction-diffusion system, and highlighting the structural plasticity of MinE.

New insights about the Min system have been possible thanks to a remarkable improvement of its *in vitro* reconstitution in recent years, which have revealed a rich variety of different dynamics [5,8]. Besides traveling waves, several patterns can be found mostly driven by differential protein densities [32]. Interestingly, other factors such as geometry or bulk-to-surface ratio of

the chambers are found critical for the MinDE oscillatory features [37–39]. Min proteins adapt their behavior and pattern formation under different geometries, highlighting the high plasticity of the system [40]. At the same time, 3D confinement into lipid vesicles and other transformable membrane structures revealed the Min proteins' capacity to affect the physical properties of the membrane and actually induce mechanical forces [41–43]. Furthermore, a recent study has observed the formation of quasi-stationary patterns that assemble into a variety of shapes reminiscent of 'Turing patterns' depending on the protein concentration and MinD/MinE ratio [10–12,44] (Figure 2F). In those patterns, Min proteins are in constant exchange with the membrane, although the patterns appear to be arrested in space once they are established [44]. To our knowledge, they represent the first reconstitution of dynamic Turing-like patterns by a biological reaction-diffusion system, an interesting discovery for the self-organized systems [1,9,12].

To sum up, improvements in the understanding of the cooperative membrane binding of MinD and detailed MinE structure-function relationships have shed light on the dynamics of the Min system. Formation of quasi-stationary patterns and new and unexpected Min features and functionalities, such as non-specific active transport of membrane proteins or mechanical membrane transformations, suggest interesting secondary roles of the system in the cellular context that may have been lost or masked in the progress of evolution.

The ParABS system

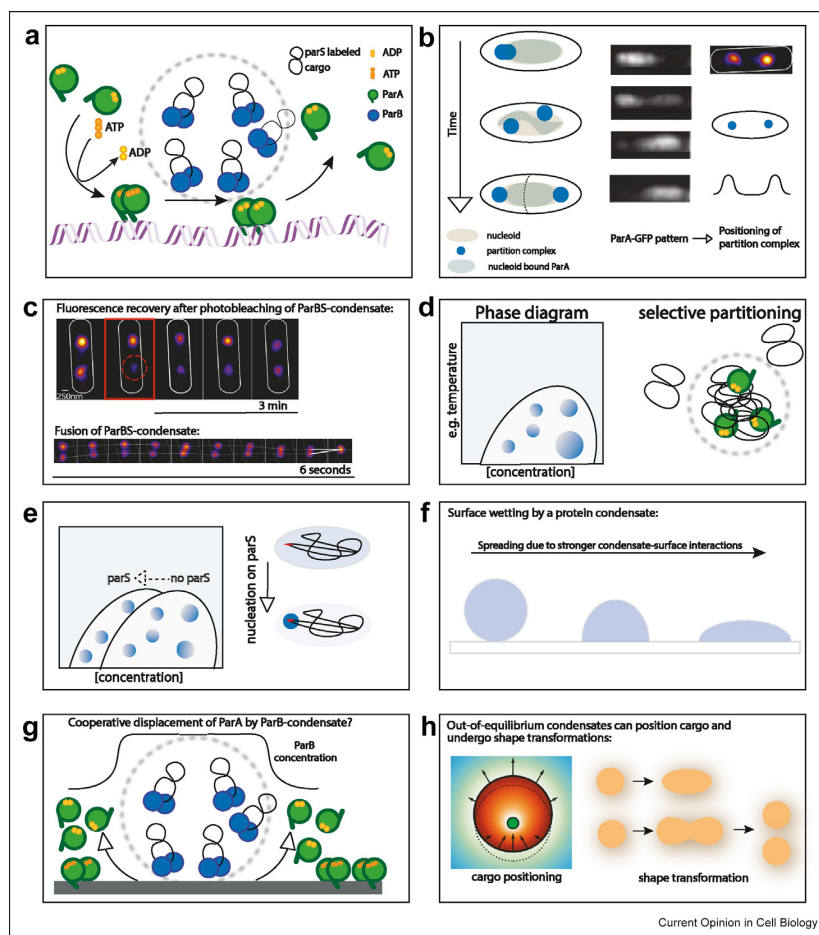
Similar to the positioning of the division site, faithful segregation of genetic material is a fundamental requirement for functional cell division. Many bacteria achieve this complex task using the so-called ParABS system. Like for the Min protein system, the active, that is, energy-dissipating core of the ParABS system is a P-Loop ATPase, ParA. However, unlike the Min system that operates *via* variable membrane affinity, the Par system attaches to DNA as a template, achieving cargo positioning by a DNA-binding protein (ParB) and a DNA sequence (*parS*). But still, the proposed mechanism of DNA segregation shows many parallels to the MinCDE system: The P-Loop ATPase ParA dimerizes in an ATP-dependent manner which increases non-specific template — in this case, DNA-binding affinity, recruiting the ParA dimers to the nucleoid. ParB dimers, bound to *parS* marked cargo, interact with nucleoid-bound ParA and stimulate the ParA-ATP hydrolysis rate. ATP hydrolysis subsequently leads to ParA-DNA dissociation, which generates a ParA-gradient on the nucleoid. This ParA-gradient is thought to cause the ParBS complex to travel along with the formed patterns through a still debated mechanism, separating the newly synthesized DNA or plasmid cargo [45–47] (Figure 3A and B).

The mechanisms of formation and regulation of the ParB Δ S complex are not yet fully understood, and different models have been discussed. These models can be categorized by their different modes of ParB–ParB and ParB–DNA interactions. A one-dimensional (1D) ParB binding to parS and either recruiting more ParB through ParB–ParB interactions [48] or sliding along the DNA until a conformational switch modulates ParB–DNA affinity [49] was used to explain the spreading from parS sites found in ChIP-Seq data. Other models assume a higher-order structure of the ParB Δ S complex. Herein, ParB initially binds parS and then bridges DNA through interactions with non-specific

DNA and other ParB dimers bound to non-specific DNA [50–52]. However, a more detailed structure of the partition complex remains elusive.

An intriguing possible explanation on how the ParB Δ S complex is formed and regulated has been theoretically proposed in the study by Broedersz et al. [50] and was recently experimentally supported *in vivo* by Guilhas et al. [60]. It involves the possibility of liquid condensate formation, at present, very widely discussed phenomenon in the cell biological context [53]. Single-molecule imaging revealed that the ParB Δ S complex is a spherical and ParB-rich structure with lowered

Figure 3



ParABS liquid–liquid phase separation. (a) Mechanism of ParB mediated ParA displacement. (b) In vivo pattern of ParA (images adapted from the study by Ringgaard et al. [71]) and ParBS positioning (Image adapted from the study by Guilhas et al. [60]). (c) FRAP and fusion of ParBS condensate adapted from the study by Guilhas et al. [60]. (d) Phase diagram describes parameter space for demixing of homogenous solution into two distinct liquids. These demixed liquids can have different biochemical and biophysical properties. (e) Potential lowering of ParB phase boundary and dependence of condensate formation on parS. (f) Condensate wetting surfaces. (g) Potential cooperative displacement of ParA by a ParB condensate; (h) Properties of active condensates (adapted from the study by Zwicker et al. [57], Zwicker et al. [64]).

molecular mobility. Fluorescently tagged ParB was able to diffuse between different ParB Δ S clusters, and these clusters were observed to fuse upon contact (Figure 3C). Also, fluorescence recovery after photobleaching indicates a mobile phase rather than a solid-like structure. Taken together, these experiments point toward a formation of the partition complex through liquid–liquid phase separation (LLPS).

LLPS has been shown to organize a wealth of biochemical processes in eukaryotes, from pattern-forming P-granules in *C. elegans* embryos to complex stress responses [54,55]. More recently, a variety of bacterial proteins involved in different biological functions have been shown to undergo LLPS *in vitro* and *in vivo* [56].

LLPS is a highly cooperative molecular process. Upon reaching a saturation concentration, a homogenous solution is separated into two distinct phases. These liquid phases usually differ in composition, dielectric constant, and viscosity and are, therefore, thought to provide a distinct chemical environment for certain biological processes [53] (Figure 3D). They have even been discussed in the context of constituting the first potential compartmentation strategies in the evolution of cells before the emergence of membranes from amphipathic building blocks as defined boundaries [57].

Intriguingly, key properties of the ParB Δ S complex could be explained by liquid–liquid phase separation. Nucleic acids have been shown to organize many LLPS driven processes and alter the biophysical properties of condensates [58,59]. ParB condensate formation depends on the presence of at least one parS site [51,60], and biophysical properties of ParB condensates could be altered by parS as has been observed for other phase separating systems [59]. ParB specifically binds to parS sites, and therefore, local protein concentration at parS sites is significantly enriched when compared to cytoplasmic concentrations. Thus, this would be a plausible mechanism to spatially control the nucleation of ParB Δ S condensates (Figure 3E).

Recently, it was found that different ParB orthologs have enzymatic CTPase activity, which is stimulated upon parS binding [49,61,62]. The ParB CTPase activity was shown to facilitate the reopening of closed ParB dimers to unload ParB from non-specific DNA. Intriguingly, mutations of the CTP binding pocket lead to a more uniform distribution of ParB in cells, pointing toward a regulatory mechanism of the energy dissipation in the potential liquid–liquid phase separation of the ParB Δ S complex [61].

ParB clusters are known to spread to non-parS sites *in vivo*, but until recently *in vitro* reconstitution of this spreading behavior was not possible. In the study by Soh *et al.* [49], 1D spreading *in vitro* is achieved by addition

of CTP, which was shown to facilitate the formation of a ring-like structure of ParB. However, ChIP-Seq data points to more complex behavior *in vivo* with 3-dimensional interactions within the ParB Δ S cluster [52,72]. LLPS of ParB offers an exciting mechanistic explanation for these observations. Interactions of condensates with large surface structures can lead to a wetting behavior, where the liquid phase spreads around the original nucleation point, like a drop of water wets a glass surface. Therefore, a ParB condensate could bridge and condense surrounding non-specific DNA as observed *in vivo* (Figure 3F).

Also, ParB–CTPase activity and its dependence on parS presence could be another physiologically relevant representation of the theoretically predicted ‘out-of-equilibrium’ condensates [64]. The positioning of parS sites within ParB condensates could, in this case, be explained by the theoretical framework of active particle behavior within condensates. Herein, the particle is positioned precisely in the middle of a condensate because of chemical fluxes originating at the particle surface [64]. This theory was successfully applied to eukaryotic centrosome formation through liquid–liquid phase separation [65] and could potentially be transferred to the bacterial ParB Δ S complex, where parS stimulates ParB–CTPase activity. It was recently argued that ParB foci sizes do not scale with cell length, as expected by equilibrium LLPS [66]. However, energy-dissipating condensates can regulate size, shape, and localization through kinetic rates of chemical reactions [67] (Figure 3H).

Interactions of ParB Δ S condensates with ParA could answer some outstanding questions with regard to the ParABS mechanism. All currently discussed diffusion ratchet models assume a lag time after ParA displacement where no rebinding is occurring [45–47]. This could be achieved by partitioning of ParB-displaced ParA monomer into the viscous ParB Δ S condensate (Figure 3D). Also, the ParB Δ S condensate interface constitutes a strong chemical gradient, and its interaction with nucleoid-bound ParA dimers could lead to the highly cooperative displacement of ParA, reminiscent of the traveling wavefront of the MinCDE system as discussed previously, generating higher chemical gradients and larger molecular forces to act on the ParB Δ S condensate (Figure 3G).

Taken together, the recently hypothesized concept of the partition complex as a bacterial condensate offers interesting insights and may help to explain pertinent questions regarding the mechanisms of complex formation, function, and interaction with ParA. The formation of dynamic patterns through liquid–liquid phase separation has been shown for eukaryotic systems, where protein gradients achieve the spatial positioning of phase-separated P granules [54].

		MinCDE		ParABS	
Components		MinD	P-Loop ATPase Protein Dimerization (ATP-dependent) Membrane Attachment (ATP-dependent) Cooperative Binding Interaction with MinE and MinC	ParA	P-Loop ATPase Protein Dimerization (ATP-dependent) DNA Attachment (ATP-dependent) Interaction with ParB
		MinE	Dimeric Protein Membrane attachment Conformational switch MinD ATPase activating protein Unclear mechanism of traveling on the membrane	ParB	Dimeric Protein CTPase activity DNA attachment Conformational switch ParA ATPase-activating protein Unclear mechanism of traveling through the Nucleoid Cooperative LLPS
		MinC	Dimeric Protein Cargo of the system Interaction with MinD Inhibitor of Z-ring	parS	DNA sequence Cargo-tether of the system Interaction with ParB
Matrix			Plasma membrane		DNA from Nucleoid
Cooperativity			Oligomerization		potential LLPS
Function			Positioning of divisome by negative feedback		Chromosomal Segregation by positive feedback
Pattern	<i>In vivo</i>		Pole-to-pole Oscillations		Oscillations on the Nucleoid
Formation	<i>In vitro</i>		High Variety		(?)

Summary and perspectives

MinCDE and ParABS represent two pattern-forming protein systems in bacteria that show remarkable similarities at first glance (Table 1). The purpose of both protein patterns is to provide a spatiotemporal cue for cell division by the generation of a protein gradient on a matrix. Their modular composition and mechanistic details of the pattern-forming systems are remarkably similar. The two systems use ATP-dependent dimerization and subsequent binding to a matrix, that is, dramatic reduction of their diffusional mobility, to generate a uniform layer of protein-covered matrix. The molecular antagonist of the matrix binding protein then stimulates ATP hydrolysis and causes detachment of the matrix-bound protein. Intriguingly, this ATP-operated and thus, energy-dissipating switch of molecular mobility and consequently, diffusional range of an ‘activator’ molecule, additionally classified by cooperative binding to its matrix, is a biologically very straightforward variant of the local self-amplification and long-range inhibition, as originally proposed by Gierer and Meinhard [68]. Herein, the long-range inhibition is simply implemented by dramatically slowing down the activator molecule — with respect to its inhibitor — upon matrix binding. For the MinDE system, it has already been demonstrated that MinD binding to the membrane reduces the diffusion coefficient by at least two orders of magnitude [15,19]. Similar to the change of diffusion by MinD membrane binding, ParA mobility is drastically reduced by three orders of magnitude upon DNA binding [69]. To drive the speculations further,

also the transition of molecules into liquid condensates, with their presumably increased viscosity and thereby reduced diffusion, could be one way of fulfilling the condition early formulated for pattern-forming systems of symmetry breaking in diffusional mobility.

However, despite these conceptual similarities, the detailed modes of assembly and the mechanisms of transport in the two discussed bacterial systems appear to be different. Moreover, while the MinCDE system positions the divisome through negative feedback, the ParABS system achieves positioning through positive feedback. On a molecular scale, this difference is obvious by the inhibition of FtsZ polymerization through MinC on one hand and the direct interaction of ParB with parS on the other hand. Both systems use cooperativity to enhance the stability of the positioning, however, different players show cooperative behavior. MinD forms higher-order oligomers to ensure the robustness of the MinCDE pattern [16], and the ParB liquid–liquid phase separation offers a mechanism to buffer cellular noise through a cooperative process [56,70].

To conclude, even though there seem to be some shared conceptual motifs in the design of the two discussed bacterial pattern-forming protein systems, a remarkably similar composition, and conserved crucial details of the molecular mechanism, their variations are remarkable and intriguing. Both patterns forming systems make use of different strategies to achieve cargo positioning and to

confer robustness. In better understanding these differences, we hope to be able to significantly enrich our conceptual toolkit for the bottom-up design of biological structure and function. With respect to the physiological understanding of the principles that govern self-organized systems, their reconstitution *in vitro* in recent studies has not only helped to shed light on the common mechanisms of protein gradient formation but also revealed functionalities that have neither been observed nor hypothesized in the cellular context so far, such as the ability of the MinDE system to directionally transport membrane-attached molecules of mechanically transform membranes. It seems, therefore, obvious that *in vitro* reconstitution should ideally accompany any mechanistic study in cell biology to enlarge our still far too limited assortment of mechanistic hypotheses for the fundamental functions of life.

Conflict of interest statement

Nothing declared.

Acknowledgements

The authors would like to thank Tamara Heermann for helpful discussions. This work has been supported by the Transregional Collaborative Research Center "Spatiotemporal dynamics of bacterial cells" (TRR 174) and the Max Planck-Bristol Centre for Minimal Biology. A.M is part of IMPRS-LS. L.B. is funded by the Max Planck School "Matter to Life".

References

Papers of particular interest, published within the period of review, have been highlighted as:

- * of special interest
- ** of outstanding interest

1. Schweisguth F, Corson F: **Self-organization in pattern formation.** *Dev Cell* 2019, <https://doi.org/10.1016/j.devcel.2019.05.019>.
2. McCusker D: **Cellular self-organization: generating order from the abyss.** *Mol Biol Cell* 2020, <https://doi.org/10.1091/mbc.E19-04-0207>.
3. Khalili B, Lovelace HD, Rutkowski DM, Holz D, Vavylonis D: **Fission yeast polarization: modeling Cdc42 oscillations, symmetry breaking, and zones of activation and inhibition.** *Cells* 2020, <https://doi.org/10.3390/cells9081769>.
4. Lang CF, Munro E: **The PAR proteins: from molecular circuits to dynamic self-stabilizing cell polarity.** *Development* 2017, <https://doi.org/10.1242/dev.139063>.
5. Ramm B, Heermann T, Schwille P: **The E. coli MinCDE system in the regulation of protein patterns and gradients.** *Cell Mol Life Sci* 2019, <https://doi.org/10.1007/s00018-019-03218-x>.
Excellent review summarizing all previous studies using the MinCDE system.
6. Raskin DM, de Boer PAJ: **MinDE-dependent Pole-to-Pole oscillation of division inhibitor MinC in Escherichia coli.** *J Bacteriol* 1999, <https://doi.org/10.1128/jb.181.20.6419-6424.1999>.
7. Jindal L, Emberly E: **DNA segregation under Par protein control.** *PLoS One* 2019, <https://doi.org/10.1371/journal.pone.0218520>.
8. Vendel KJA, Tschirpke S, Shamsi F, Dogterom M, Laan L: **Minimal *in vitro* systems shed light on cell polarity.** *J Cell Sci* 2019, <https://doi.org/10.1242/jcs.217554>.
9. Landge AN, Jordan BM, Diego X, Müller P: **Pattern formation mechanisms of self-organizing reaction-diffusion systems.** *Dev Biol* 2020, <https://doi.org/10.1016/j.ydbio.2019.10.031>.
10. Halatek J, Frey E: **Rethinking pattern formation in reaction-diffusion systems.** *Nat Phys* 2018, <https://doi.org/10.1038/s41567-017-0040-5>.
Highly recommended theoretical study to better understand the role of protein gradients and how they drive the formation of functional patterns.
11. Frey E, Halatek J, Kretschmer S, Schwille P: **Protein pattern formation.** In *Physics of biological membranes*; 2018.
12. Kondo S, Miura T: **Reaction-diffusion model as a framework for understanding biological pattern formation.** *Science* 2010, <https://doi.org/10.1126/science.1179047> (80-).
13. De Boer PAJ, Crossley RE, Hand AR, Rothfield LI: **The MinD protein is a membrane ATPase required for the correct placement of the Escherichia coli division site.** *EMBO J* 1991, <https://doi.org/10.1002/j.1460-2075.1991.tb05015.x>.
14. Lackner LL, Raskin DM, De Boer PAJ: **ATP-dependent interactions between Escherichia coli Min proteins and the phospholipid membrane *in vitro*.** *J Bacteriol* 2003, <https://doi.org/10.1128/JB.185.3.735-749.2003>.
15. Loose M, Fischer-Friedrich E, Ries J, Kruse K, Schwille P: **Spatial regulators for bacterial cell division self-organize into surface waves *in vitro*.** *Science* 2008, <https://doi.org/10.1126/science.1154413> (80-).
16. Heermann T, Ramm B, Glaser S, Schwille P: **Local self-enhancement of MinD membrane binding in min protein pattern formation.** *J Mol Biol* 2020, <https://doi.org/10.1016/j.jmb.2020.03.012>.
This study aims to elucidate the molecular origin of cooperative membrane binding, supposed to be of key importance for pattern formation in the MinDE system. MinD mutants arrested in monomeric or dimeric state revealed self-interaction apart from the canonical dimerization site to efficiently form oligomers on the membrane.
17. Hu Z, Saez C, Lutkenhaus J: **Recruitment of MinC, an inhibitor of Z-ring formation, to the membrane in Escherichia coli: role of minD and minE.** *J Bacteriol* 2003, <https://doi.org/10.1128/JB.185.1.196-203.2003>.
18. Park KT, Wu W, Lovell S, Lutkenhaus J: **Mechanism of the asymmetric activation of the MinD ATPase by MinE.** *Mol Microbiol* 2012, <https://doi.org/10.1111/j.1365-2958.2012.08110.x>.
19. Loose M, Fischer-Friedrich E, Herold C, Kruse K, Schwille P: **Min protein patterns emerge from rapid rebinding and membrane interaction of MinE.** *Nat Struct Mol Biol* 2011, <https://doi.org/10.1038/nsmb.2037>.
20. Ayed SH, Cloutier AD, McLeod LJ, Foo ACY, Damry AM, Goto NK: **Dissecting the role of conformational change and membrane binding by the bacterial cell division regulator MinE in the stimulation of MinD ATPase activity.** *J Biol Chem* 2017, <https://doi.org/10.1074/jbc.M117.805945>.
21. Miyagi A, Ramm B, Schwille P, Scheuring S: **High-speed atomic force microscopy reveals the inner workings of the MinDE protein oscillator.** *Nano Lett* 2018, <https://doi.org/10.1021/acs.nanolett.7b04128>.
22. Mileykovskaya E, Fishov I, Fu X, Corbin BD, Margolin W, Downan W: **Effects of phospholipid composition on MinD-membrane interactions *in vitro* and *in vivo*.** *J Biol Chem* 2003, <https://doi.org/10.1074/jbc.M302603200>.
23. Wettmann L, Kruse K: **The min-protein oscillations in Escherichia coli: an example of self-organized cellular protein waves.** *Philos Trans R Soc B Biol Sci* 2018, <https://doi.org/10.1098/rstb.2017.0111>.
24. Ramm B, Glock P, Mücksch J, Blumhardt P, García-Soriano DA, Heymann M, Schwille P: **The MinDE system is a generic spatial cue for membrane protein distribution *in vitro*.** *Nat Commun* 2018, <https://doi.org/10.1038/s41467-018-06310-1>.
First report of a new unexpected feature of the Min system by which membrane-attached molecules of no functional connection can be directionally transported through MinDE self-organization and made to form large-scale gradients on the membrane.

25. Shih YL, Huang LT, Tu YM, Lee BF, Bau YC, Hong CY, Lee H lin, Shih YP, Hsu MF, Lu ZX, *et al.*: **Active transport of membrane components by self-organization of the min proteins.** *Biophys J* 2019, <https://doi.org/10.1016/j.bpj.2019.03.011>.
26. Ramm B, Goychuk A, Khmelinskaia A, Blumhardt P, Eto H, Ganzinger KA, Frey E, Schwille P: **A diffusio-phoretic mechanism for ATP-driven transport without motor proteins.** *Nat Phys* 2021, 17:850–858, <https://doi.org/10.1038/s41567-021-01213-3>.
27. Taviti AC, Beuria TK: **Bacterial Min proteins beyond the cell division.** *Crit Rev Microbiol* 2019, <https://doi.org/10.1080/1040841X.2018.1538932>.
28. Shen JP, Chang YR, Chou CF: **Frequency modulation of the Min-protein oscillary by nucleoid-associated factors in Escherichia coli.** *Biochem Biophys Res Commun* 2020, <https://doi.org/10.1016/j.bbrc.2020.02.161>.
29. Glock P, Brauns F, Halatek J, Frey E, Schwille P: **Design of biochemical pattern forming systems from minimal motifs.** *Elife* 2019, <https://doi.org/10.7554/eLife.48646>.
This paper describes a modular deconstruction approach of a pattern-forming protein in the true spirit of bottom-up synthetic biology. Herein, MinE of the Min system is dissected into four structural modules associated with different functions. It could be shown that the core functional unit responsible for ATPase stimulation may be complemented by a single additional function (dimerization or membrane binding) to become effective for self-organization.
30. Glock P, Broichhagen J, Kretschmer S, Blumhardt P, Mücksch J, Trauner D, Schwille P: **Optical control of a biological reaction–diffusion system.** *Angew Chem Int Ed* 2018, <https://doi.org/10.1002/anie.201712002>.
31. Heermann T, Franquelim HG, Glock P, Harrington L, Schwille P: **Probing biomolecular interactions by a pattern-forming peptide–conjugate sensor.** *Bioconjug Chem* 2020, <https://doi.org/10.1021/acs.bioconjugchem.0c00596>.
32. Vecchiarelli AG, Li M, Mizuuchi M, Hwang LC, Seol Y, Neuman KC, Mizuuchi K: **Membrane-bound MinDE complex acts as a toggle switch that drives Min oscillation coupled to cytoplasmic depletion of MinD.** *Proc Natl Acad Sci U S A* 2016, <https://doi.org/10.1073/pnas.1600644113>.
33. Kretschmer S, Zieske K, Schwille P: **Large-scale modulation of reconstituted Min protein patterns and gradients by defined mutations in MinE's membrane targeting sequence.** *PLoS One* 2017, <https://doi.org/10.1371/journal.pone.0179582>.
34. Kretschmer S, Harrington L, Schwille P: **Reverse and forward engineering of protein pattern formation.** *Philos Trans R Soc B Biol Sci* 2018, <https://doi.org/10.1098/rstb.2017.0104>.
35. Denk J, Kretschmer S, Halatek J, Hartl C, Schwille P, Frey E: **MinE conformational switching confers robustness on self-organized Min protein patterns.** *Proc Natl Acad Sci U S A* 2018, <https://doi.org/10.1073/pnas.1719801115>.
36. Kohyama S, Fujiwara K, Yoshinaga N, Doi N: **Conformational equilibrium of MinE regulates the allowable concentration ranges of a protein wave for cell division.** *Nanoscale* 2020, <https://doi.org/10.1039/d0nr00242a>.
37. Wu F, Van Schie BGC, Keymer JE, Dekker C: **Symmetry and scale orient Min protein patterns in shaped bacterial sculptures.** *Nat Nanotechnol* 2015, <https://doi.org/10.1038/nnano.2015.126>.
38. Zieske K, Schwille P: **Reconstituting geometry-modulated protein patterns in membrane compartments.** *Methods Cell Biol* 2015, <https://doi.org/10.1016/bs.mcb.2015.02.006>.
39. Brauns F, Pawlik G, Halatek J, Kerssemakers J, Frey E, Dekker C: **Bulk-surface coupling reconciles Min-protein pattern formation in vitro and in vivo.** *bioRxiv* 2020, <https://doi.org/10.1101/2020.03.01.971952>.
40. Schweizer J, Loose M, Bonny M, Kruse K, Morich I, Schwille P: **Geometry sensing by self-organized protein patterns.** *Proc Natl Acad Sci U S A* 2012, <https://doi.org/10.1073/pnas.1206953109>.
41. Godino E, López JN, Foschepoth D, Cleij C, Doerr A, Castellà CF, Danelon C: **De novo synthesized Min proteins drive oscillatory liposome deformation and regulate FtsA-FtsZ cytoskeletal patterns.** *Nat Commun* 2019, <https://doi.org/10.1038/s41467-019-12932-w>.
First comprehensive demonstration of cell-free produced MinDE proteins that self-organize in SLBs and inside liposomes. Global shape transformations and local membrane undulations can result from dynamic redistribution of the in synthesized Min proteins inside vesicles.
42. Litschel T, Ramm B, Maas R, Heymann M, Schwille P: **Beating vesicles: encapsulated protein oscillations cause dynamic membrane deformations.** *Angew Chem Int Ed* 2018, <https://doi.org/10.1002/anie.201808750>.
43. Mazor S, Regev T, Mileykovskaya E, Margolin W, Dowhan W, Fishov I: **Mutual effects of MinD-membrane interaction: I. Changes in the membrane properties induced by MinD binding.** *Biochim Biophys Acta Biomembr* 2008, <https://doi.org/10.1016/j.bbame.2008.08.003>.
44. Glock P, Ramm B, Heermann T, Kretschmer S, Schweizer J, Mücksch J, Alagöz G, Schwille P: **Stationary patterns in a two-protein reaction-diffusion system.** *ACS Synth Biol* 2019, <https://doi.org/10.1021/acssynbio.8b00415>.
45. Lim HC, Surovtsev IV, Beltran BG, Huang F, Bewersdorf J, Jacobs-Wagner C: **Evidence for a DNA-relay mechanism in ParABS-mediated chromosome segregation.** *Elife* 2014, <https://doi.org/10.7554/eLife.02758>.
46. Vecchiarelli AG, Neuman KC, Mizuuchi K: **A propagating ATPase gradient drives transport of surface-confined cellular cargo.** *Proc Natl Acad Sci U S A* 2014, <https://doi.org/10.1073/pnas.1401025111>.
47. Le Gall A, Cattoni DI, Guilhas B, Mathieu-Demazière C, Oudjedi L, Fiche JB, Rech J, Abrahamsson S, Murray H, Bouet JY, *et al.*: **Bacterial partition complexes segregate within the volume of the nucleoid.** *Nat Commun* 2016, <https://doi.org/10.1038/ncomms12107>.
48. Rodionov O, ŁObocka M, Yarmolinsky M: **Silencing of genes flanking the P1 plasmid centromere.** *Science* 1999, <https://doi.org/10.1126/science.283.5401.546> (80-).
49. Soh YM, Davidson IF, Zamuner S, Basquin J, Bock FP, Taschner M, Veening JW, de Los Rios P, Peters JM, Gruber S: **Self-organization of parS centromeres by the ParB CTP hydrolase.** *Science* 2019, <https://doi.org/10.1126/science.aay3965> (80-).
Biochemical and structural description of ParB CTPase activity showing N-engagement. The authors use crosslinking studies beside other biochemical methods to identify changes in ParB structure upon CTP binding. Together with (Osorio *et al.*, 2019), this work is the first demonstration of CTPase activity.
50. Broedersz CP, Wang X, Meir Y, Loparo JJ, Rudner DZ, Wingreen NS: **Condensation and localization of the partitioning protein ParB on the bacterial chromosome.** *Proc Natl Acad Sci U S A* 2014, <https://doi.org/10.1073/pnas.1402529111>.
51. Graham TGW, Wang X, Song D, Etsen CM, van Oijen AM, Rudner DZ, Loparo JJ: **ParB spreading requires DNA bridging.** *Genes Dev* 2014, <https://doi.org/10.1101/gad.242206.114>.
52. Debaugny RE, Sanchez A, Rech J, Labourdette D, Dorignac J, Geniet F, Palmeri J, Parmeggiani A, Boudsocq F, Anton Leberre V, *et al.*: **A conserved mechanism drives partition complex assembly on bacterial chromosomes and plasmids.** *Mol Syst Biol* 2018, <https://doi.org/10.15252/msb.20188516>.
53. Hyman AA, Weber CA, Jülicher F: **Liquid-liquid phase separation in biology.** *Annu Rev Cell Dev Biol* 2014, <https://doi.org/10.1146/annurev-cellbio-100913-013325>.
54. Brangwynne CP, Eckmann CR, Courson DS, Rybarska A, Hoege C, Gharakhani J, Jülicher F, Hyman AA: **Germline P granules are liquid droplets that localize by controlled dissolution/condensation.** *Science* 2009, <https://doi.org/10.1126/science.1172046> (80-).
55. Protter DSW, Parker R: **Principles and properties of stress granules.** *Trends Cell Biol* 2016, <https://doi.org/10.1016/j.tcb.2016.05.004>.

56. Azaldegui CA, Vecchiarelli AG, Biteen JS: **The emergence of phase separation as an organizing principle in bacteria.** *Biophys J* 2020, <https://doi.org/10.1016/j.bpj.2020.09.023>.
A detailed review of currently known bacterial condensates and methods that can be used to study these *in vivo*.
57. Zwicker D, Seyboldt R, Weber CA, Hyman AA, Jülicher F: **Growth and division of active droplets provides a model for protocells.** *Nat Phys* 2017, <https://doi.org/10.1038/nphys3984>.
A landmark theoretical framework discussing physical properties of energy-dissipating condensates. First predictions of shape transformations in active condensates suggesting a potential role of co-acervates as protocells.
58. Langdon EM, Qiu Y, Niaki AG, McLaughlin GA, Weidmann CA, Gerbich TM, Smith JA, Crutchley JM, Termini CM, Weeks KM, *et al.*: **mRNA structure determines specificity of a polyQ-driven phase separation.** *Science* 2018, <https://doi.org/10.1126/science.aar7432> (80-).
59. Elbaum-Garfinkle S, Kim Y, Szczepaniak K, Chen CCH, Eckmann CR, Myong S, Brangwynne CP: **The disordered P granule protein LAF-1 drives phase separation into droplets with tunable viscosity and dynamics.** *Proc Natl Acad Sci U S A* 2015, <https://doi.org/10.1073/pnas.1504822112>.
60. Guilhas B, Walter JC, Rech J, David G, Walliser NO, Palmeri J, Mathieu-Demaziere C, Parmeggiani A, Bouet JY, Le Gall A, *et al.*: **ATP-driven separation of liquid phase condensates in bacteria.** *Mol Cell* 2020, <https://doi.org/10.1016/j.molcel.2020.06.034>.
Super resolution microscopy and single molecule tracking showing liquid condensate like structure and material properties for *E. coli* partition complex. The authors show that there are two ParB populations with highly different diffusion dynamics.
61. Osorio-Valeriano M, Altegoer F, Steinchen W, Urban S, Liu Y, Bange G, Thanbichler M: **ParB-type DNA segregation proteins are CTP-dependent molecular switches.** *Cell* 2019, <https://doi.org/10.1016/j.cell.2019.11.015>.
In vitro and *in vivo* study identifying ParB's CTPase activity and demonstrating necessity of ParB-CTP interaction in DNA segregation and partition complex assembly.
62. Jalal AS, Tran NT, Le TB: **ParB spreading on DNA requires cytidine triphosphate in vitro.** *Elife* 2020, <https://doi.org/10.7554/eLife.53515>.
The authors characterize ParB spreading on open and closed DNA substrates, characterizing ParB-parS interactions in presence and absence of CTP for a variety of ParBs.
64. Zwicker D, Baumgart J, Redemann S, Müller-Reichert T, Hyman AA, Jülicher F: **Positioning of particles in active droplets.** *Phys Rev Lett* 2018, <https://doi.org/10.1103/PhysRevLett.121.158102>.
65. Zwicker D, Decker M, Jaensch S, Hyman AA, Jülicher F: **Centrosomes are autocatalytic droplets of pericentriolar material organized by centrioles.** *Proc Natl Acad Sci U S A* 2014, <https://doi.org/10.1073/pnas.1404855111>.
66. Biedzinski S, Parmar B, Weber SC: **Beyond equilibrium phase diagrams: enzymatic activity shakes up bacterial condensates.** *Mol Cell* 2020, <https://doi.org/10.1016/j.molcel.2020.06.035>.
67. Söding J, Zwicker D, Sohrabi-Jahromi S, Boehning M, Kirschbaum J: **Mechanisms for active regulation of biomolecular condensates.** *Trends Cell Biol* 2020, <https://doi.org/10.1016/j.tcb.2019.10.006>.
68. Gierer A, Meinhardt H: **A theory of biological pattern formation.** *Kybernetik* 1972, <https://doi.org/10.1007/BF00289234>.
69. Surovtsev IV, Lim HC, Jacobs-Wagner C: **The slow mobility of the ParA partitioning protein underlies its steady-state patterning in Caulobacter.** *Biophys J* 2016, <https://doi.org/10.1016/j.bpj.2016.05.014>.
70. Klosin A, Oltch F, Harmon T, Honigmann A, Jülicher F, Hyman AA, Zechner C: **Phase separation provides a mechanism to reduce noise in cells.** *Science* 2020, <https://doi.org/10.1126/science.aav6691> (80-).
71. Ringgaard S, Van Zon J, Howard M, Gerdes K: **Movement and equi-positioning of plasmids by ParA filament disassembly.** *Proc Natl Acad Sci U S A* 2009, <https://doi.org/10.1073/pnas.0908347106>.
72. Walter J-C, Rech J, Walliser N-O, Dorignac J, Geniet F, Palmeri J, Parmeggiani A, Bouet J-Y: **Physical modeling of a sliding clamp mechanism for the spreading of ParB at short genomic distance from bacterial centromere sites.** *Iscience* 2020, **23**: 101861, <https://doi.org/10.1016/j.isci.2020.101861>.

3.2 Publication P2

FtsZ reorganization facilitates deformation of giant vesicles in microfluidic traps

Summary:

In this manuscript, we introduce a microfluidic device to trap and reversibly deform GUVs into bacterial rod-shape. Non-geometrical vesicles are particularly desirable for reconstituting membrane shape- or curvature-dependent protein systems that request elongated geometries. Using this microfluidic tool, we studied membrane-bound FtsZ, defining a tension-dependent reorganization on the membrane, from filaments perpendicularly aligned with the short GUV axis into dynamic rings that stabilize membrane protrusions after the release from the device.

Reprinted with permission from:

Ganzinger K.*, **Merino-Salomón, A.***, García-Soriano, D., Butterfield, N. A., Litschel, T., Siedler, F. and Schwille, P. (2021). FtsZ Reorganization Facilitates Deformation of Giant Vesicles in Microfluidic Traps. *Angew. Chem. Int. Ed.* 2020, 59, 21372-21376.

Source online: <https://doi.org/10.1002/anie.202001928>

Synthetic Biology
How to cite: *Angew. Chem. Int. Ed.* **2020**, *59*, 21372–21376

International Edition: doi.org/10.1002/anie.202001928

German Edition: doi.org/10.1002/ange.202001928

FtsZ Reorganization Facilitates Deformation of Giant Vesicles in Microfluidic Traps**

Kristina A. Ganzinger^{†,*}, Adrián Merino-Salomón[†], Daniela A. García-Soriano,
A. Nelson Butterfield, Thomas Litschel, Frank Siedler, and Petra Schwille^{*}

Abstract: The geometry of reaction compartments can affect the local outcome of interface-restricted reactions. Giant unilamellar vesicles (GUVs) are commonly used to generate cell-sized, membrane-bound reaction compartments, which are, however, always spherical. Herein, we report the development of a microfluidic chip to trap and reversibly deform GUVs into cigar-like shapes. When trapping and elongating GUVs that contain the primary protein of the bacterial Z ring, FtsZ, we find that membrane-bound FtsZ filaments align preferentially with the short GUV axis. When GUVs are released from this confinement and membrane tension is relaxed, FtsZ reorganizes reversibly from filaments into dynamic rings that stabilize membrane protrusions; a process that allows reversible GUV deformation. We conclude that microfluidic traps are useful for manipulating both geometry and tension of GUVs, and for investigating how both affect the outcome of spatially-sensitive reactions inside them, such as that of protein self-organization.

One hallmark of living entities is their ability to self-organize into complex architectures, both on the level of cells and tissues, with molecular gradients controlling cell polarity, division, and the spatial dynamics of signaling.^[1,2] Interestingly, cell geometry itself can induce the required spatial symmetry breaks in signaling activity.^[3] In eukaryotes, cell shape is controlled by both plasma membrane properties and components of the membrane-proximal cytoskeleton, most importantly the actin network.^[4] Recently, bottom-up syn-

thetic biology has been increasingly able to reconstitute these cellular phenomena in vitro, including spatially organized processes such as cell division.^[5,6]

Reconstituting cell division in vitro represents a desirable, albeit ambitious, goal towards the bottom-up construction of an artificial cell.^[7–9] Cell division involves the segregation of chromosomes and other intracellular components, concluding with cytokinesis, the physical splitting of the cell envelope. In bacteria, cytokinesis requires constriction and fission of the cell membrane as well as the peptidoglycan layer.^[10] Cell division in many bacteria involves the GTPase protein and tubulin homologue FtsZ.^[10] FtsZ polymerizes into a dynamic ring-like structure at the division site (“Z-ring”), where it is anchored to the membrane by adaptor proteins FtsA and ZipA.^[11–13] The Z-ring serves then as a platform to recruit further divisome proteins.^[7] The process of FtsZ assembly has been reconstituted in vitro at supported lipid bilayers.^[14] On these, FtsZ spontaneously assembles into dynamic ring structures, in which individual FtsZ filaments undergo treadmilling to drive chiral ring rotations.^[15] Reconstituting FtsZ in spherical aqueous droplets in oil showed dynamic FtsZ bundles, while studying FtsZ behavior inside rod-shaped droplets was also attempted.^[16] FtsZ behavior in membrane-bound compartments (polymersomes or giant unilamellar vesicles (GUVs)) has also been studied.^[8,17] However, bacteria are not spherical, and it is clear that cell shape has a great impact on the boundary conditions of these processes.


In the present study, we therefore introduce a single-layer microfluidic chip based on previous work^[18,19] in which GUVs can be reversibly deformed into cigar-like shapes by capturing them between narrowing PDMS posts. After several iterations (Figures S1–4), we found that the design shown in Figure 1 was optimal for GUV capture and deformation (Figure S1, design FS814): adjacent columns of traps (in 2 channels with 280 traps each) are vertically offset to maximize GUV capture, and post spacing is step-wise reduced towards the chip outlet, such that differently-sized GUVs are efficiently captured. Since we were interested in reconstituting elements of a synthetic cell division machinery in these elongated GUVs, we also designed the traps to mimic the “neck” of the division site (Figure 1 a). Each trap has multiple indentations for stable GUV trapping, and a “stopper” to prevent GUVs from escaping if they slip through the posts. Since the constriction features are small with a high aspect ratio (2 × 2 × 13 μm), we imaged both wafer using laser scanning based profilometry (Figure S5) and PMDS mold using scanning electron microscopy (SEM) for quality control (Figure 1 b). To test how encapsulated FtsZ filaments respond to compartment geometry, we made GUVs containing


[*] Dr. K. A. Ganzinger,^[‡] A. Merino-Salomón,^[‡] Dr. D. A. García-Soriano, A. N. Butterfield, T. Litschel, Dr. F. Siedler, Prof. Dr. P. Schwille
Department of Cellular and Molecular Biophysics,
Max Planck Institute of Biochemistry
Am Klopferspitz 18, 82152 Martinsried (Germany)
E-mail: schwille@biochem.mpg.de

Dr. K. A. Ganzinger^[‡]
Living Matter, AMOLF
P.O. Box 41883-1009 DB Amsterdam (The Netherlands)
E-mail: k.ganzinger@amolf.nl

[†] These authors contributed equally to this work.

[**] A previous version of this manuscript has been deposited on a preprint server (<https://doi.org/10.1101/791459>).

 Supporting information and the ORCID identification number(s) for the author(s) of this article can be found under:
<https://doi.org/10.1002/anie.202001928>.

 © 2020 The Authors. Published by Wiley-VCH GmbH. This is an open access article under the terms of the Creative Commons Attribution License, which permits use, distribution and reproduction in any medium, provided the original work is properly cited.

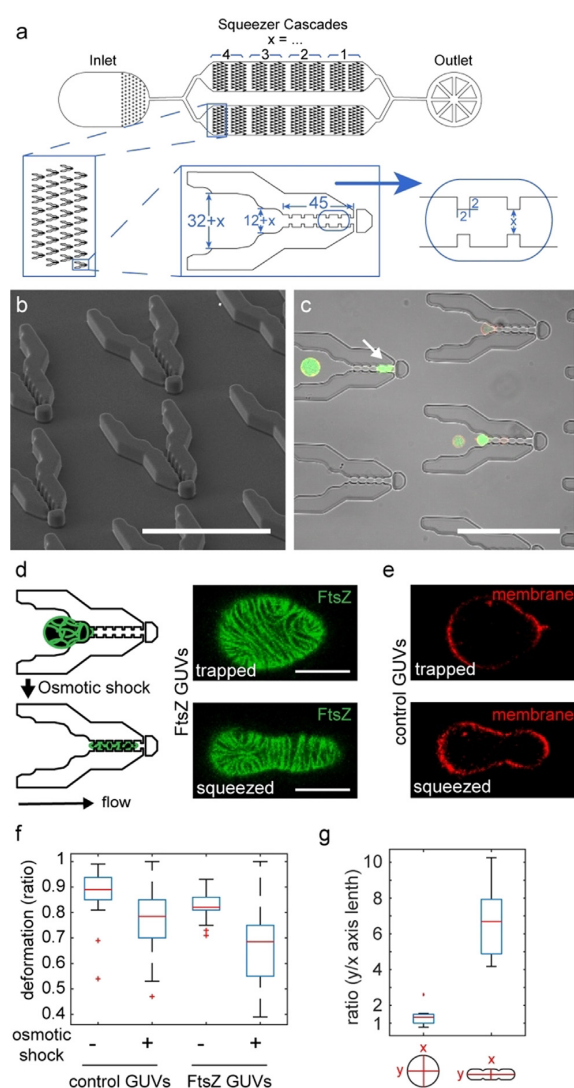


Figure 1. Design of microfluidic GUV traps. a) Schematic depiction of chip design, zooming in on the trap features. All dimensions in μm . b) SEM image of PDMS mold as a quality control step showing clean trap features. c) Brightfield and fluorescent microscopy composite image showing traps and trapped GUVs (containing FtsZ-YFP-mts, green and DOPE-ATTO655 in the membrane, red). Scale bars for (b,c) are $100\ \mu\text{m}$. d) Schematic depiction and confocal images of trapped (top) and deformed (bottom) FtsZ-GUVs (GUVs containing FtsZ-YFP-mts, green) and e) GUVs containing FtsZ buffer (control, DOPE-ATTO655 in membrane, red). Scale bars are $10\ \mu\text{m}$. f) Maximum deformation of FtsZ- or control GUVs before and after osmotic deflation. g) GUV aspect ratios before and after squeezing. Box plots in (f,g) denote median in red, interquartile range as blue box, the 2.7σ (99.3%) confidence interval as whiskers and outliers with a red cross. $n(\text{GUVs}) > 10$ from > 4 independent experiments.

purified FtsZ-YFP-mts (henceforth referred to as FtsZ) in polymerizing conditions. The membrane targeting sequence (mts) included in the protein's C-terminal domain circumvents the need for ZipA or FtsA by directly attaching FtsZ to

the membrane, and YFP allows direct visualization of FtsZ polymerization.^[15,20–22] Importantly, this construct has also been shown to form functional Z-rings *in vivo*.^[22] Using a syringe pump to apply negative pressure from the outlet to suck FtsZ-containing GUVs (FtsZ-GUVs) into the chip, we were able to capture and trap GUVs for minutes (flow rates $5\text{--}10\ \mu\text{L h}^{-1}$, Figure 1c). Some GUVs deformed from a spherical to an elongated shape (Figure 1c, white arrow), but most trapped GUVs remained spherical. Using up to 50 times higher flow rates, we succeeded in “squeezing” GUVs fully into the trap funnels (Figure 1d,e, bottom images). Interestingly, compared to GUVs only containing FtsZ buffer (control GUVs), FtsZ-GUVs deformed strongly and at lower flow rates, but only if FtsZ was membrane-bound and GTP was present (Figure 1f, Figure S6a). This suggests that FtsZ filament attachment and treadmilling at membranes may affect spontaneous membrane curvature and hence extent of vesicle deformation obtained under forces. When we applied a mild osmotic deflation (14–23% increase in buffer osmolarity), GUV deformation was greatly facilitated, even more so in the presence of FtsZ (Figure 1f). GUVs assumed non-spherical shapes likely more readily as osmotic deflation likely increased the membrane area-to-volume ratio, although we could not reliably quantify GUV volumes by confocal microscopy (see SI methods for further discussion). After the initial deformation flow rates of $5\ \mu\text{L h}^{-1}$ were sufficient to keep GUVs stable in rod-like shapes and the mean aspect ratio from ≈ 1 for spherical GUVs changed to 6.7 ± 1.9 (Figure 1g). We were thus able to create GUVs with a height of $13\ \mu\text{m}$ and width of $7\ \mu\text{m}$ (or $5\ \mu\text{m}$ at the constriction sites), corresponding to the trap dimensions, and lengths up to $\approx 50\ \mu\text{m}$ depending on initial GUV size (Figure S6b).

In elongated FtsZ-GUVs, FtsZ filaments aligned preferentially perpendicular to the GUVs' long axis (Figure S7), particularly at GUVs' necks (Figure 2a,b). Releasing GUVs from the traps by reversing flow direction, they reassumed spherical shapes within a minute (Figure 2c,d, S8a). Strikingly, this shape change was accompanied by FtsZ filament reorganization: elongated FtsZ filaments re-polymerized into ring-like structures (Figure 2d, i-ii). Although our image resolution is insufficient to discern filament organization, the dimensions make it likely that these structures correspond to the dynamic rings previously described (see Figure S9 for experiments under identical conditions to^[23]). These ring-like filaments formed in short cone-like membrane protrusions at GUV surfaces, as soon as the mechanical membrane tension was decreased upon isosmotic GUV release from the traps (σ_{mec} (shape change) = $-70 \pm 10\ \text{mN m}^{-1}$; $n(\text{GUV}) = 10$, Figure 2e–f, Figure S8b; see SI for details on calculation of σ_{mec} from Figure S6 data). The change from filaments to rings was also apparent from a shorter mean filament length (Figure 2g). Interestingly, we observed that osmotic deflation instead of FtsZ-GUV trapping and elongation also induced FtsZ-stabilized membrane protrusions (Figure S10a–c). Taken together, these results suggest that lowering elastic membrane tension, either by releasing external forces (GUV release from traps) or by osmotic deflation, both lead to FtsZ reorganization and FtsZ-driven membrane shape changes.

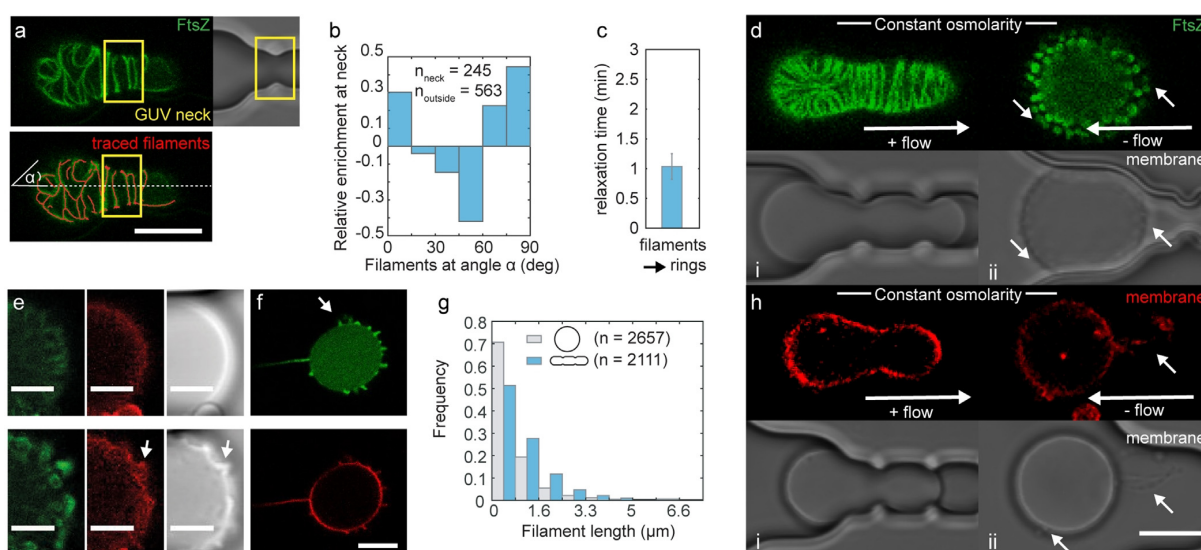


Figure 2. GUV deformation affects FtsZ filament alignment and filaments reorganize as constraints on GUV shape are released. a) Confocal images of trapped FtsZ-GUVs (FtsZ in green, top), the same image overlaid with automatically traced filaments (red, bottom) and DIC image (right). Neck region marked with yellow box (manually defined from brightfield image). Scale bar is 10 μm . b) Relative enrichment of filaments at angles α with the GUV axis at GUV necks; $n(\text{filaments}) > 245$. c) Mean relaxation times for FtsZ reorganization. Error bars are s.d. d, h) Confocal images of the equatorial plane of a trapped and reversibly elongated FtsZ-GUV (d, i-ii, top) or a control GUV (h, i-ii, top, membrane labelled with DOPE-ATTO655) and corresponding DIC images (d, h, bottom). The scale bar is 10 μm . e) Close-up images of FtsZ reorganization, from left to right: confocal images of FtsZ-GUVs (FtsZ, green; DOPE-ATTO655, red) and corresponding DIC images. Elongated GUV (top) and the same GUV after isotonic release from the trap, having reassumed a spherical shape (bottom). Scale bars are 5 μm . f) Membrane protrusions are filled with FtsZ. (FtsZ, green; DOPE-ATTO655, red) Scale bar is 10 μm . g) Distribution of filament lengths in FtsZ-GUVs. n is the number of filaments analyzed. For all experiments, $n(\text{GUVs}) > 12$ from > 4 independent experiments.

Importantly, higher solute concentrations alone, as expected for osmotically deflated GUVs, did not result in increased FtsZ-stabilized membrane protrusions, but even at higher solute concentrations, FtsZ-protrusions could still be reliably induced by osmotic deflation (Figure S10d).^[23] We also note that elastic membrane tension only affects membrane-bound FtsZ, as for GUVs containing FtsZ without a membrane targeting sequence (FtsZ wt) FtsZ organization was unaffected by osmotic deflation (Figure S11a). In contrast to the short cone-like protrusions observed for FtsZ-GUVs, we observed that in control GUVs, the excess membrane area upon reobtaining spherical shapes was stored by the formation of longer and percolated membrane tubules, as previously described (Figure 2h, white arrows). Similar tubules were also observed when relaxing mechanically-tensioned GUVs containing FtsZ wt, confirming that FtsZ needs to be membrane-bound to affect GUV membrane shapes (Figure S11b). In summary, our data suggest that FtsZ filaments reorganize on low-tension membranes into ring-like structures at membrane regions of higher curvature (“cones”), possibly driven by an intrinsic preference of membrane-bound FtsZ for higher membrane curvature.

With membrane area being “stored” in membrane protrusions (cones), we tested whether these structures could act as membrane area reservoirs to facilitate deformation of GUVs into aspherical shapes, analogously to applying an osmotic shock before deforming GUVs. When we pushed FtsZ-GUVs with membrane protrusions back into the traps

after a first (osmotically facilitated) deformation cycle, we observed that deformation was now indeed fully reversible under isotonic conditions, merely by changing flow direction (Figure 3a, S12). Again, GUV shape changes were accompanied by FtsZ filament reorganization: in a few minutes, rings gave way to elongated filaments as protrusions were re-incorporated into the membranes of elongated GUVs (Figure 3a, i-iii, S8, Movie 1). While almost all FtsZ-GUVs repeatedly deformed, the majority of control GUVs did not (success rate of individual attempt $\approx 90\%$ for FtsZ-GUVs versus $< 50\%$ for all controls, Figure 3b). In addition, more deformation cycles could be achieved, on average, for FtsZ-GUVs (up to 5, mean of 2.5 versus < 2 for all controls, Figure S13a). Even when control GUVs could be successfully deformed, higher flow rates were required for shorter vesicle deformation compared to FtsZ-GUVs (Figure 3c, S13b). Taken together, our data suggest that membrane-bound FtsZ filament reorganization facilitates GUV membrane shape changes. This facilitation required FtsZ to cycle between different polymerization states (rings and filaments) in an energy-dependent (i.e. GTP-dependent) process depending on overall membrane tension, allowing to reversibly store excess membrane area (Figure 3d).

In summary, we have designed microfluidic traps for deforming GUVs with constriction sites mimicking the indentation of a division furrow and at mean aspect ratios close to that of rod-like bacterial shapes. Fanalista et al. have also developed microfluidic traps to deform water-in-oil

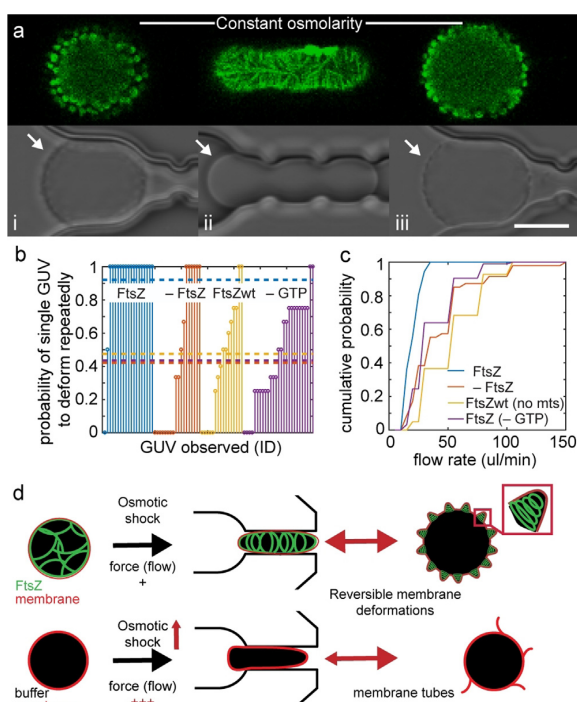


Figure 3. Reversible transitions between FtsZ filaments and rings allow reversible deformation of FtsZ-GUVs. **a**) Confocal images of a trapped and elongated GUV containing FtsZ filaments (i-iii, FtsZ shown in green, top) and corresponding DIC images (bottom). White arrows point to membrane topography changes. Scale bar is 10 μm . **b**) Probability that an individual GUV could be deformed five times for FtsZ-GUVs or control GUVs without FtsZ (red), with FtsZ-wt without membrane targeting sequence (-mts, purple) and with FtsZ without GTP in the buffer (no dynamic FtsZ polymerization, yellow). The value for the mean deformation probability for each experimental condition is plotted as a horizontal line (color-coded). **c**) Cumulative probability of flow rate required to deform FtsZ- or control GUVs (controls as in (b)). **d**) Schematic depiction of model: FtsZ structural reorganization from filaments to rings stores membrane reversibly in protrusions, facilitating transitions between GUV shapes. $n(\text{GUVs}) = 17\text{--}35$ (controls) and 19 (FtsZ) from >10 independent experiments.

droplets to spheroid-like shapes.^[24] In contrast to our observations, they reported FtsZ alignment along the long axis of deformed droplets.^[24] In their experiments, however, FtsZ is not membrane-anchored which likely explains the discrepancy. In principle, our microfluidic chip can deform many GUVs in parallel. In practice, we studied single GUVs at a time to resolve the GUVs' responses at maximal temporal resolution. However, the large number of traps was still advantageous to select specific GUVs (e.g. those encapsulating FtsZ) from a heterogeneous population.

Using these traps to deform FtsZ-GUVs, we show that imposing a rod-like geometry with a central membrane neck is sufficient to align FtsZ filaments along the short axis, preferentially at the neck location, mimicking FtsZ assembly into the Z-ring at the division site in live bacteria. This is in agreement with previous results for elongated lipid-bilayer coated containers or liposomes.^[14,25,26] When rod-shaped

GUVs were released from the traps, GUVs relaxed back into a spherical shape with a lower surface/volume ratio. As expected, the concomitant excess of membrane area led to the formation of membrane tubules in absence of FtsZ. However, FtsZ-GUVs showed highly-curved membranes in form of cone-like, FtsZ-filled membrane protrusions as filaments reorganized into ring-like structures, independently of GUV size. Low membrane tension has been shown to play an important role for FtsZ filaments to induce membrane shape changes:^[27] FtsZ reorganization similar to that observed by us has also been shown on deflated vesicles decorated with FtsZ on the outside.^[23]

Interestingly, changes in membrane and filament organization were fully reversible: repeated GUV trapping and release cycled FtsZ-GUVs between (1) a state of tense GUV membranes, with elongated FtsZ filaments and macroscopically smooth membrane surfaces, and (2) a state of relaxed GUV membranes, with GUV membranes showing protrusions stabilized by ring-like FtsZ filaments (see Movie 2 and 3).^[23] In contrast, shape changes in control GUVs required increasingly higher forces and/or repeated osmotic deflation. Therefore, we conclude that FtsZ on its own is able to not only actively influence membrane shapes, but also facilitates externally-induced changes by conserving and releasing excess membrane area (in an energy-dependent process). Our results suggest that FtsZ organization into ring-like filaments and FtsZ-driven membrane deformation may only occur as membrane tension is decreased during the division process (e.g. by de novo membrane synthesis), and that this could contribute to controlling the timing of cell division machinery assembly and thus cytokinesis. Reorganized FtsZ filaments may then also constrict lipid membranes, generating forces by GTP-fueled treadmilling.^[28,29]

Overall, we present this microfluidic device as a platform for studying the effect of compartment geometry and membrane tension on processes reconstituted in and on the membrane of GUV-based minimal cells. In future experiments, these membrane tension changes could be measured quantitatively using tension-sensitive dyes or by quantifying the hydrodynamic forces in our microfluidic devices.^[30] Beyond GUVs, our traps could also be used to deform vesicle-like membranes derived from cells, such as spheroblasts^[31] and giant plasma membrane-derived vesicles.^[32,33] Likewise, it will be interesting to study compartment geometry effects on other processes, such as MreB, the Min reaction-diffusion system, or the cell-polarity inducing Cdc42 system.^[34,35] With the increasing capacity to create artificial, minimal cells, for example, by encapsulation of cell-free expression systems,^[36] a device such as the one presented herein will be useful for studying how compartment geometry affects the behavior of increasingly complex molecular networks.

Acknowledgements

The authors are grateful to Germán Rivas (CSIC, Madrid, ES) and Lennard van Buren (TU Delft, NL) for helpful discussions and providing FtsZ wt protein (G.R.). We

acknowledge the MPIB Biochemistry Core Facility for assistance in protein purification. K.A.G. has received funding from the European Union's Horizon 2020 research and innovation program under the Marie Skłodowska-Curie grant agreement No. 703132. D.A.G.-S. and P.S. acknowledge financial support from the DFG through the Graduate School of Quantitative Biosciences Munich (QBM). This work is part of the MaxSynBio consortium, which is jointly funded by the Federal Ministry of Education and Research of Germany (BMBF) and the Max Planck Society (MPG). Open access funding enabled and organized by Projekt DEAL.

Conflict of interest

The authors declare no conflict of interest.

Keywords: cell division · membranes · microfluidics · protocells · vesicles

- [1] P. Niethammer, *Science* **2004**, *303*, 1862–1866.
- [2] M. Schmick, P. I. H. Bastiaens, *Cell* **2014**, *156*, 1132–1138.
- [3] D. Thalmeier, J. Halatek, E. Frey, *Proc. Natl. Acad. Sci. USA* **2016**, *113*, 548–553.
- [4] A. Haupt, N. Minc, *J. Cell Sci.* **2018**, *131*, jcs214015.
- [5] K. A. Ganzinger, P. Schwille, *J. Cell Sci.* **2019**, *132*, jcs227488.
- [6] M. D. Vahey, D. A. Fletcher, *Curr. Opin. Cell Biol.* **2014**, *26*, 60–68.
- [7] A. Martos, M. Jiménez, G. Rivas, P. Schwille, *Trends Cell Biol.* **2012**, *22*, 634–643.
- [8] P. Schwille, J. Spatz, K. Landfester, E. Bodenschatz, S. Herminghaus, V. Sourjik, T. J. Erb, P. Bastiaens, R. Lipowsky, A. Hyman, P. Dabrock, J.-C. Baret, T. Vidakovic-Koch, P. Bieling, R. Dimova, H. Mutschler, T. Robinson, T.-Y. D. Tang, S. Wegner, K. Sundmacher, *Angew. Chem. Int. Ed.* **2018**, *57*, 13382–13392; *Angew. Chem.* **2018**, *130*, 13566–13577.
- [9] S. Kretschmer, K. A. Ganzinger, H. G. Franquelim, P. Schwille, *BMC Biol.* **2019**, *17*, 43.
- [10] J. Xiao, E. D. Goley, *Curr. Opin. Microbiol.* **2016**, *34*, 90–96.
- [11] E. Bi, J. Lutkenhaus, *Nature* **1991**, *354*, 161–164.
- [12] C. A. Hale, P. A. de Boer, *Cell* **1997**, *88*, 175–185.
- [13] S. Pichoff, J. Lutkenhaus, *Mol. Microbiol.* **2005**, *55*, 1722–1734.
- [14] S. Arumugam, Z. Petrásek, P. Schwille, *Proc. Natl. Acad. Sci. USA* **2014**, *111*, E1192–E1200.
- [15] D. A. Ramirez-Diaz, D. A. García-Soriano, A. Raso, J. Mücksch, M. Feingold, G. Rivas, P. Schwille, *PLoS Biol.* **2018**, *16*, e2004845.
- [16] S. Mellouli, B. Monterroso, H. R. Vutukuri, E. te Brinke, V. Chokkalingam, G. Rivas, W. T. S. Huck, *Soft Matter* **2013**, *9*, 10493.
- [17] T. J. Lagny, P. Bassereau, *Interface Focus* **2015**, *5*, 20150038.
- [18] T. Robinson, P. Kuhn, K. Eyer, P. S. Dittrich, *Biomicrofluidics* **2013**, *7*, 044105.
- [19] Q. Wang, M. Taschner, K. A. Ganzinger, C. Kelley, A. Villaseñor, M. Heymann, P. Schwille, E. Lorentzen, N. Mizuno, *Nat. Commun.* **2018**, *9*, 4684.
- [20] S. Pautot, B. J. Frisken, D. Weitz, *Langmuir* **2003**, *19*, 2870–2879.
- [21] E. J. Cabré, A. Sánchez-Gorostiaga, P. Carrara, N. Roperio, M. Casanova, P. Palacios, P. Stano, M. Jiménez, G. Rivas, M. Vicente, *J. Biol. Chem.* **2013**, *288*, 26625–26634.
- [22] M. Osawa, D. E. Anderson, H. P. Erickson, *Science* **2008**, *320*, 792–794.
- [23] D. A. Ramirez-Diaz, A. Merino-Salomon, F. Meyer, M. Heymann, G. Rivas, M. Bramkamp, P. Schwille, *bioRxiv* **2020**, <https://doi.org/10.1101/587790>.
- [24] F. Fanalista, A. Birnie, R. Maan, F. Burla, K. Charles, G. Pawlik, S. Deshpande, G. H. Koenderink, M. Dogterom, C. Dekker, *ACS Nano* **2019**, *13*, 5439–5450.
- [25] K. Zieske, P. Schwille, *eLife* **2014**, *3*, e03949.
- [26] M. Osawa, H. P. Erickson, *Mol. Microbiol.* **2011**, *81*, 571–579.
- [27] S. Arumugam, E. P. Petrov, P. Schwille, *Biophys. J.* **2015**, *108*, 1104–1113.
- [28] E. Godino, J. N. López, I. Zarguit, A. Doerr, M. Jimenez, G. Rivas, C. Danelon, *bioRxiv* **2020**, <https://doi.org/10.1101/2020.03.29.009639>.
- [29] L. T. Nguyen, C. M. Oikonomou, G. J. Jensen, *bioRxiv* **2019**, <https://doi.org/10.1101/737189>.
- [30] A. Goujon, A. Colom, K. Straková, V. Mercier, D. Mahecic, S. Manley, N. Sakai, A. Roux, S. Matile, *J. Am. Chem. Soc.* **2019**, *141*, 3380–3384.
- [31] T. G. Chew, J. Huang, S. Palani, R. Sommesse, A. Kamnev, T. Hatano, Y. Gu, S. Oliferenko, S. Sivaramakrishnan, M. K. Balasubramanian, *J. Cell Biol.* **2017**, *216*, 2657–2667.
- [32] H. Pick, A. C. Alves, H. Vogel, *Chem. Rev.* **2018**, *118*, 8598–8654.
- [33] E. Sezgin, H.-J. Kaiser, T. Baumgart, P. Schwille, K. Simons, I. Levental, *Nat. Protoc.* **2012**, *7*, 1042–1051.
- [34] K. J. A. Vendel, S. Tschirpke, F. Shamsi, M. Dogterom, L. Laan, *J. Cell Sci.* **2019**, *132*, jcs217554.
- [35] H. Shi, B. P. Bratton, Z. Gitai, K. C. Huang, *Cell* **2018**, *172*, 1294–1305.
- [36] D. Garenne, V. Noireaux, *Curr. Opin. Biotechnol.* **2019**, *58*, 19–27.

Manuscript received: February 6, 2020

Revised manuscript received: July 27, 2020

Accepted manuscript online: July 31, 2020

Version of record online: September 17, 2020

Supplement to publication P2

Reprinted with permission from:

Ganzinger K.*, **Merino-Salomón, A.***, García-Soriano, D., Butterfield, N. A., Litschel, T., Siedler, F. and Schwille, P. (2021). FtsZ Reorganization Facilitates Deformation of Giant Vesicles in Microfluidic Traps. *Angew. Chem. Int. Ed.* 2020, 59, 21372-21376.

Source online: <https://doi.org/10.1002/anie.202001928>

Supporting Information

FtsZ Reorganization Facilitates Deformation of Giant Vesicles in Microfluidic Traps**

Kristina A. Ganzinger^{+,} Adrián Merino-Salomón^{+,} Daniela A. García-Soriano, A. Nelson Butterfield, Thomas Litschel, Frank Siedler, and Petra Schwille^{*}*

anie_202001928_sm_miscellaneous_information.pdf

anie_202001928_sm_Movie1.mp4

anie_202001928_sm_Movie2.mp4

anie_202001928_sm_Movie3.mp4

Material and Methods

Chemicals

All reagents used in this work were from Sigma-Aldrich. Lipid compositions were prepared with DOPG (1,2-Dioleoyl-sn-glycero-3 phosphoglycerol, Avanti Polar Lipids, Inc.), EggPC (L- α -phosphatidylcholine (Egg, Chicken), Avanti Polar Lipids, Inc.), DOPC (1,2-Dioleoyl-sn-glycero-3-phosphocholine, Avanti Polar Lipids, Inc.) and DOPE-ATTO655 (ATTO-tec).

Microfluidic device fabrication

The microfluidic vesicle trap squeezer devices were fabricated from PDMS using rapid prototyping and standard soft lithography techniques. The geometry was inspired by the traps we used in a previous study¹, but here extended the trapping structure along the flow axis with a narrow squeezing channel containing evenly spaced indentations, and added a larger entrance funnel to increase GUV capture efficiency (Figure S1). We found it advantageous to design device channels with a high density of traps, which have progressively narrower funnels and squeezing channels towards the outlet.

Wafer fabrication and coating. Master moulds of 13 μ m height were produced on a 4-inch silicon wafer (University Wafer) using SU-8 3010 (Microchem corp.) according to the manufacturer's data sheet and developed in PGMEA (process parameters were optimized by direct laser writing (uPG101, Heidelberg Instruments, Germany) as described in Figure S2 to S4). Due to the small size of the PDMS features to be released from the mould, fluorophilic coating with Cytop was used routinely prior to the hard-baking step. In brief, 250 μ L of a 1:10 dilution of Cytop CTL-809M in CTSOLV180 (Asahi Glass Co. Ltd., Japan) was dispensed on the SU-8 features and excess removed by spinning at 4000rpm for 1min. The coated wafer was then hard-baked for 30min at 180°C on a hot-plate and then allowed to cool down to room temperature slowly by turning off the heating. Quality control of the final SU-8 molds was done by laser profilometry (VKX1100, Keyence, Japan; Figure S5).

PDMS moulding. A 10:1 mixture of PDMS base and curing agent (Sylgard 184, Dow Corning) was homogenized and degassed simultaneously for 2min using a Thinky Planetary Vacuum Mixer (ARV-310, Thinky Corp., Japan) and subsequently poured to about 4mm height onto the master in a petri-dish. After curing over-night in an oven at 75°C the PDMS was peeled off the wafer and cut to size. Fluid ports were then punched with a 3 mm and 0.75 mm diameter biopsy puncher (World-Precision-Instruments) for the reservoir and outlet, respectively. For quality control, images of PDMS chips were taken by Scanning Electron Microscopy (Mira3, Tescan) using sputter coated samples (1.5nm Pd/Pt, Cressington 208HR). In brief, samples were sputter coated with platinum/palladium on a high-resolution automatic sputter coater (Cressington 208HR) at 20 mA and 0.1mbar Ar for 3x 20s. Thickness of the applied coatings was measured with a build-in thickness controller to be 2.0 nm. Coated surfaces were viewed using a TESCAN MIRA3 FESEM operating at an accelerating voltage of 10 kV in SE mode. The microchannels of chips with well-resolved structures were then sealed by plasma bonding them onto glass cover slips (24 x 32 mm, thickness 1.5, VWR) using oxygen plasma (15 s at 0.3mbar, 50% power, model ZEPTO, Diener electronic, Germany) and baking them for 15–30 min at 75 °C on a hot-plate.

Preparation of FtsZ-containing GUVs

Giant unilamellar vesicles (GUVs) were prepared using a water-in-oil (w/o) emulsion transfer method.^[2] The lipid-oil-suspension was made by first drying lipid films from lipids dissolved in chloroform (Uvasol): L- α -phosphatidylcholine (Egg, Chicken; EggPC) and 1,2-dioleoyl-sn-glycero-3-phospho-(1'-rac-glycerol (DOPG) in a ratio of 80:20 mol % (both Avanti Lipids), adding 0.02 or 0.07 mol % of 1,2-dioleoyl-sn-glycero-3-phosphoethanolamine (DOPE)-ATTO655 (ATTO-TEC) to label the lipid membrane. For this, the chloroform was evaporated from the lipid mixture by placed in a desiccator connected to a vacuum pump for >1h. The phospholipid-oil suspension was prepared by dissolving the lipid film in mineral oil (M5904, Sigma Aldrich) and sonicating the suspension for 30 min, reaching a homogeneous suspension with 0.5 mg/mL as final lipid concentration. GUVs were prepared by adding 15 μ l of inner buffer into 500 μ l phospholipid oil suspension pipetting carefully up and down to create a homogeneous emulsion. This emulsion was deposited over a lipid monolayer previously formed for >1h between 500 μ l of phospholipid-oil suspension and 500 μ l of the outer buffer in 2 ml Eppendorf tubes. The mixture was centrifuged for 10 min at 100 rcf to deposit the GUVs at the bottom of the tube. GUVs were collected and added into the inlet reservoir of the microfluidic chip or into microtitre plates for visualization.

Inner solution of FtsZ samples was prepared by diluting purified FtsZ-YFP-mts^[3] to a final concentration of 2 μ M in its buffer (25 mM Tris-HCl, 125 mM KCl, 6.25mM MgCl₂ pH 7.5) and adding 20% iodixanol (OptiPrep™, Sigma Aldrich) to increase the density of the encapsulated solution, in order to improve the vesicle yield obtained.^[4] FtsZ samples were encapsulated in the polymeric form by adding 2 mM GTP and previously described GTP regeneration system (RS) to prolong the polymerised FtsZ lifetime^[5]. Control FtsZ without GTP was prepared without the presence of the regeneration system. In all experiments, the outer and inner buffer solutions were the same but an additional 180 mM glucose was added to the outer solution to match the osmolarity of the inner solution (~480 mOsm/kg) (measured with Fiske Micro-Osmometer Model 210).

Samples containing FtsZ wt were prepared by diluting FtsZ wt to a final concentration of 2 μ M including 0.8 μ M FtsZ-wt-Alexa 488 as a fluorescent tracer. Both proteins were cordially provided by German Rivas' laboratory, purified and labelled as described.^[5] (We note similar results were obtained using 1.65 μ M, 1.4mM GTP and 2mM MgCl₂ as in reference ^[6](Figure S9). Experiments using GUVs with higher concentrated content were made by proportionally increasing all inner buffer components (including FtsZ, GTP regeneration system and iodixanol) by 20% or 50%. Glucose content of both outer solutions were also increased to match the osmolarities of the inner and outer buffers (620 mOsm/kg and 740 mOsm/kg for 20% and 50% respectively). Control GUVs without FtsZ were prepared using FtsZ buffer adding 160 mM glucose and 20% iodixanol to match the osmolarity of FtsZ-GUVs so the outer buffer was identical in all conditions.

We note that the yield of FtsZ-containing GUVs of desired sizes (10-20 μ m diameter) was variable even under identical experimental conditions, and that not all GUVs showed FtsZ filaments at the GUV membranes, likely due to variations in the final FtsZ concentration inside the vesicles. A high degree of variation in both vesicle content and yield is commonly observed for GUVs made by emulsion transfer. As we trapped many GUVs in our microfluidic device, we could focus our studies on those GUVs that initially showed visible FtsZ filaments when trapped and imaged by confocal microscopy.

Handling of microfluidic device and experimental setup

Microfluidic devices were passivated to prevent vesicle rupture upon contact with the walls by adding 20 μL of pluronic F-127 (Sigma Aldrich) at 10-50 mg/mL in phosphate buffered saline (PBS) in the inlet reservoir and centrifuging at 800 rcf for 10 min. The remaining pluronic was removed and cleaned with outer buffer. After passivation, the microfluidic devices were loaded with approximately 40 μL volume of vesicles in the inlet reservoir. A syringe joined to a pump system (neMESYS base 120 with neMESYS 290N, cetoni, Germany) and filled with 250 μL of ~60% ethanol was connected to the outlet of the device, avoiding any air in between the device and the syringe. Negative flow was applied at a rate of approximately 5-10 $\mu\text{L}/\text{h}$ to draw the vesicle solution and reagents through the fluid channels during the experiments. After 10-20 min, a high number of vesicles were collected in the microfluidic traps. To deform the GUVs, we osmotically deflated them by replacing the buffer solution in the inlet reservoir with fresh buffer with a higher osmolarity. Some buffer exchanges with progressively higher osmolarity were sometimes necessary to induce vesicle deformation. Osmolarity was not increased more than 10-15% at a time to avoid vesicle rupture. Once the vesicles were partially deformed, the flow rate was progressively increased to introduce the GUVs completely into the trap, deforming them slowly. To move the vesicles out of the traps (and back in again, this time keeping osmolarity constant), the flow rate was usually changed within a range of $\pm 15\text{-}20$ $\mu\text{L}/\text{h}$ for FtsZ experiments, although this flow rate range was increased depending on the conditions we tested. Our pump set up does not allow to calculate the forces exerted by the fluid flow on the vesicles inside the chip.

Experiments with FtsZ GUVs in the absence of trapping

FtsZ vesicles were deposited in a microtiter plate for imaging (Greiner Bio-One, 364-well glass bottom SensiPlate™) previously passivated by 1 min of plasma cleaning (air plasma; model MiniFlecto®, Plasma Technology, Germany) and followed by a 30 min incubation with 10 mg/mL pluronic F-127 to avoid vesicle rupture. The plate was incubated tilted at $\sim 45^\circ\text{C}$ for 10 min to favour vesicle accumulation in one of the borders improving thus their visualization. Vesicle deflation was then induced by replacing most of the buffer solution with fresh buffer with a higher osmolarity. For experiments with FtsZ GUVs, the osmotic difference varies from ~ 480 mOsm/kg in its initial buffer to ~ 560 mOsm/kg in the higher osmotic buffer, while for higher concentrated FtsZ vesicles, the osmolarity varies from ~ 620 to ~ 740 mOsm/kg in vesicles with 20% increased content and from ~ 740 to ~ 840 mOsm/kg for vesicles with 50% higher concentrated content. “Undetermined” category shown in Figure S9 includes vesicles with no protein in the membrane (depolymerized) and GUVs with no obvious filament or ring structures but showing protein binding to the membranes (likely meaning that the protein is polymerized in filaments smaller than the resolution of our confocal imaging ($< 1\mu\text{m}$)).

Microscopy setup

All the experimental data were recorded with an LSM 780 confocal microscope (Carl Zeiss, Germany) equipped with a C-Apochromat, 40x/1.2 W objective. Fluorescence emission was detected by using laser excitation at 488 nm for YFP (FtsZ experiments) and Alexa 488 (FtsZ-wt

experiments), while 633 nm was used for Atto655. All the experiments were conducted at room temperature.

Image analysis

All image data was manually prepared for visualisation using ImageJ^[7]. Image data was further analysed using ImageJ^[7], either manually or using ImageJ plugins, or by MATLAB scripts as described in the following section.

Vesicle deformation (Figures 1f,g; 3b,c; S6; S12) was quantified using ImageJ by fitting an ellipse to the vesicle through the ATTO 655 laser channel. Aspect ratios in deformed or partially deformed vesicles were analysed by using the major and minor axis of the ellipses fitted in vesicles under different osmotic conditions and flow rates. Excel and MATLAB (2014/18b, The MathWorks; Statistics Toolbox) were used for plotting and descriptive statistics. For Figures 3b,c and S12a, the threshold for counting a GUV as successfully deformed was a deformation ratio of 0.7, which corresponds the mean value achieved for FtsZ-GUVs after an initial osmotic deflation.

Quantification of the volume change before and after osmotic shock was attempted but measurement scatter was very large, due to GUVs movement during z-stack acquisition, and as volume change was small this error was too large to allow us to discriminate volumes size before and after osmotic shock with confocal microscopy.

For Figure 2, filament angles were calculated using first the RidgeDetection plug-in from ImageJ (<https://zenodo.org/badge/latestdoi/18649/thorstenwagner/ij-ridgedetection>) that is based on the ridge / line detection algorithm by Steger.^[8] The settings used were: line width '1.5', high Contrast '300', low contrast '100' and method for overlap resolution: 'slope'. The coordinates for the traced filaments were then exported to MATLAB via the ImageJ ROI tool for further automated analysis. We (1) calculated filament angles with respect to the GUV axis (Figure S7) and assigned whether they were positioned in the 'neck' region of the elongated GUV or not (Figure 2b; this region was manually defined around trap feature using the bright field image) and (2) analysed filament lengths and plotted the distribution of filament lengths for trapped (elongated) and released (spherical) vesicles (Figure 2g). Calculation of relaxation times (Figure 2c; S8a) was done manually by counting frames between trapping/releasing GUVs and complete resolution of FtsZ filaments or rings/protrusions.

Filament and ring detection in experiments with non-trapped vesicles (Figure S9) was done by collecting Z-stacks images from different positions selected in a tile image of the whole sample well. Z-stack spacing 2 μm was selected to optimize the vesicle visualization. The same procedure is repeated after the addition of the higher osmolarity fresh buffer to deflate the vesicles. Addition of new buffer involves a vesicle movement that makes difficult to track single vesicle state before and after the osmotic change. Filament and Ring detection was done manually using ImageJ. Further data analysis was done using MATLAB and Excel.

Estimate of mechanical membrane tension upon iso-osmotic GUV release from geometric confinement (microfluidic traps) from microscopy data

To infer the change in membrane tension that a GUV experiences as it is iso-osmotically released from the traps, we determine the GUV shape transformation upon trapping from our microscopy data and hence extrapolate the new GUV's surface area for elongated GUVs. In the absence of external forces or constraints (*i.e.* after release from the traps), a GUV membrane aims to attain

a new optimal area A_{opt} for its now spherical shape, which corresponds to the optimal packing of its molecules. The membrane thus experiences a mechanical tension, σ_{mec} , when its original area A deviates from this new optimal area A_{opt} . This mechanical tension can be expressed as^[9]

$$\sigma_{mec}(A) = K_A \frac{A - A_{opt}}{A_{opt}} \text{ with } K_A \text{ being on the order of } 200 \frac{\text{mN}}{\text{m}} \text{ for lipid bilayers.}^{[10]}$$

Measuring the length and height of the deformed vesicles (Figure S6) and assuming a cylindrical shape, we obtain A_C and V_C of the cylinder. Then we can calculate the surface area A_S upon reassuming a spherical shape (at constant volume $V_C = V_S$). With $\frac{A - A_{opt}}{A_{opt}} = \frac{A_S - A_C}{A_C}$:

$$\sigma_{mec}(A_S) = -70 \pm 10 \frac{\text{mN}}{\text{m}}; n(GUV) = 10$$

References

- [1] Q. Wang, M. Taschner, K. A. Ganzinger, C. Kelley, A. Villasenor, M. Heymann, P. Schwille, E. Lorentzen, N. Mizuno, *Nat. Commun.* **2018**, *9*, 4684.
- [2] L. L. Pontani, J. van der Gucht, G. Salbreux, J. Heuvingh, J. F. Joanny, C. Sykes, *Biophys J* **2009**, *96*, 192–198.
- [3] M. Osawa, D. E. Anderson, H. P. Erickson, *Science (80-.)*. **2008**, *320*, 792–794.
- [4] T. Litschel, B. Ramm, R. Maas, M. Heymann, P. Schwille, *Angew. Chemie Int. Ed.* **2018**, *57*, 16286–16290.
- [5] J. M. González, M. Jiménez, M. Vélez, J. Mingorance, J. M. Andreu, M. Vicente, G. Rivas, *J. Biol. Chem.* **2003**, DOI 10.1074/jbc.M305230200.
- [6] D. A. Ramirez-Diaz, A. Merino-Salomon, F. Meyer, M. Heymann, G. Rivas, M. Bramkamp, P. Schwille, *bioRxiv* **2020**, 587790.
- [7] C. T. Rueden, J. Schindelin, M. C. Hiner, B. E. DeZonia, A. E. Walter, E. T. Arena, K. W. Eliceiri, *BMC Bioinformatics* **2017**, *18*, 529.
- [8] C. Steger, *IEEE Trans. Pattern Anal. Mach. Intell.* **1998**, *20*, 113–125.
- [9] R. Lipowsky, *Adv. Colloid Interface Sci.* **2014**, *208*, 14–24.
- [10] E. Evans, D. Needham, *J. Phys. Chem.* **1987**, *91*, 4219–4228.

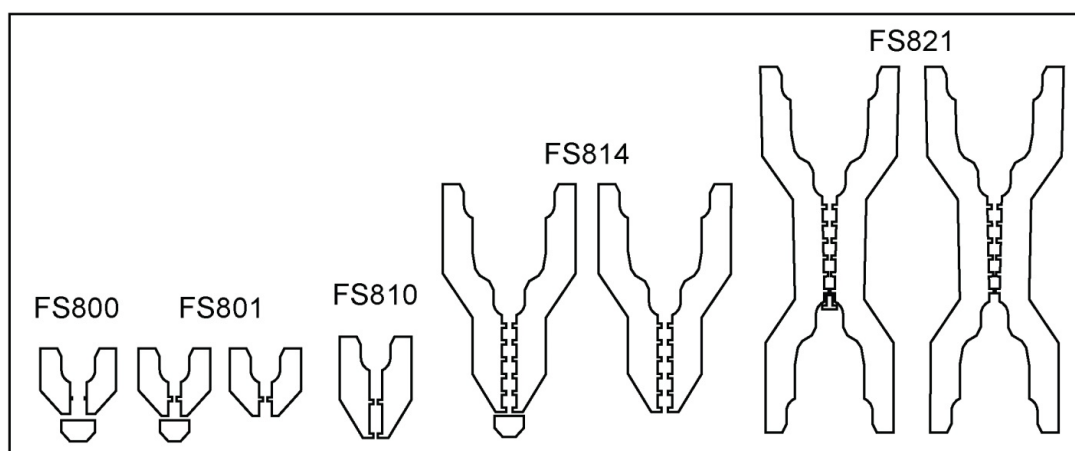


Figure S1. Evolution of microfluidic designs. To trap and squeeze GUVs in a microfluidic environment funnel like structures with various features were designed and tested. Structures are named by Experiment-ID. The central idea in the beginning was to capture GUVs in a funnel and then, by carefully rising the flow, to squeeze them past the subsequent neck. Indentations were intended to mimic the naturally occurring constriction site that is a part of cell division. Finally, the addition of stoppers was tested to prevent GUVs from escaping the traps too early.

In FS800 indentations were too small to be reproduced sufficiently precise and they did not induce a clear indentation of membranes of trapped GUVs. With FS801, a stopper was found to be necessary but the overall design showed already a reliable performance, and therefore all necessary exposure optimizations were done with this design. For some bigger GUVs, however, the relatively short neck section was a problem. Our preferred design was finally found with FS814, which was used in combination with a stopper for all experiments reported in this work. The prototype FS821 with a double funnel to facilitate back and forth shifting of GUVs and a slight narrowing of the central channel was not found to show any advantages.

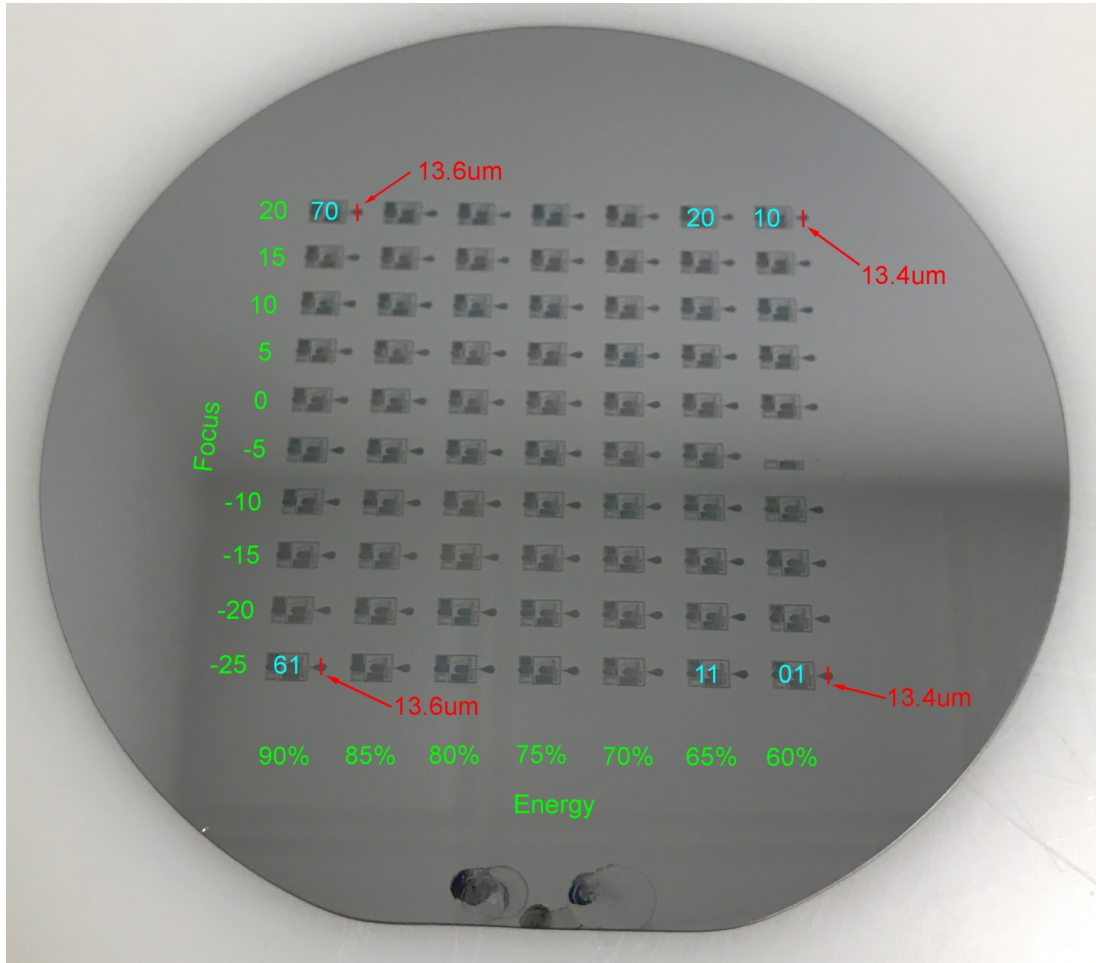


Figure S2. Optimization of Exposure Parameters. To find the best set of parameters for rapid prototyping via direct laser writing, a 7x10 array of test structures comprising the most delicate structural features was exposed on a 4 inch silicon wafer. Parameters varied were focus setting (y-direction; arbitrary units) and energy attenuation (x-direction; % of 10mW). For unique identification positions in the array are numbered from bottom to top and right to left as indicated by cyan numbers. Results of height measurements by laser profilometry are indicated in red.

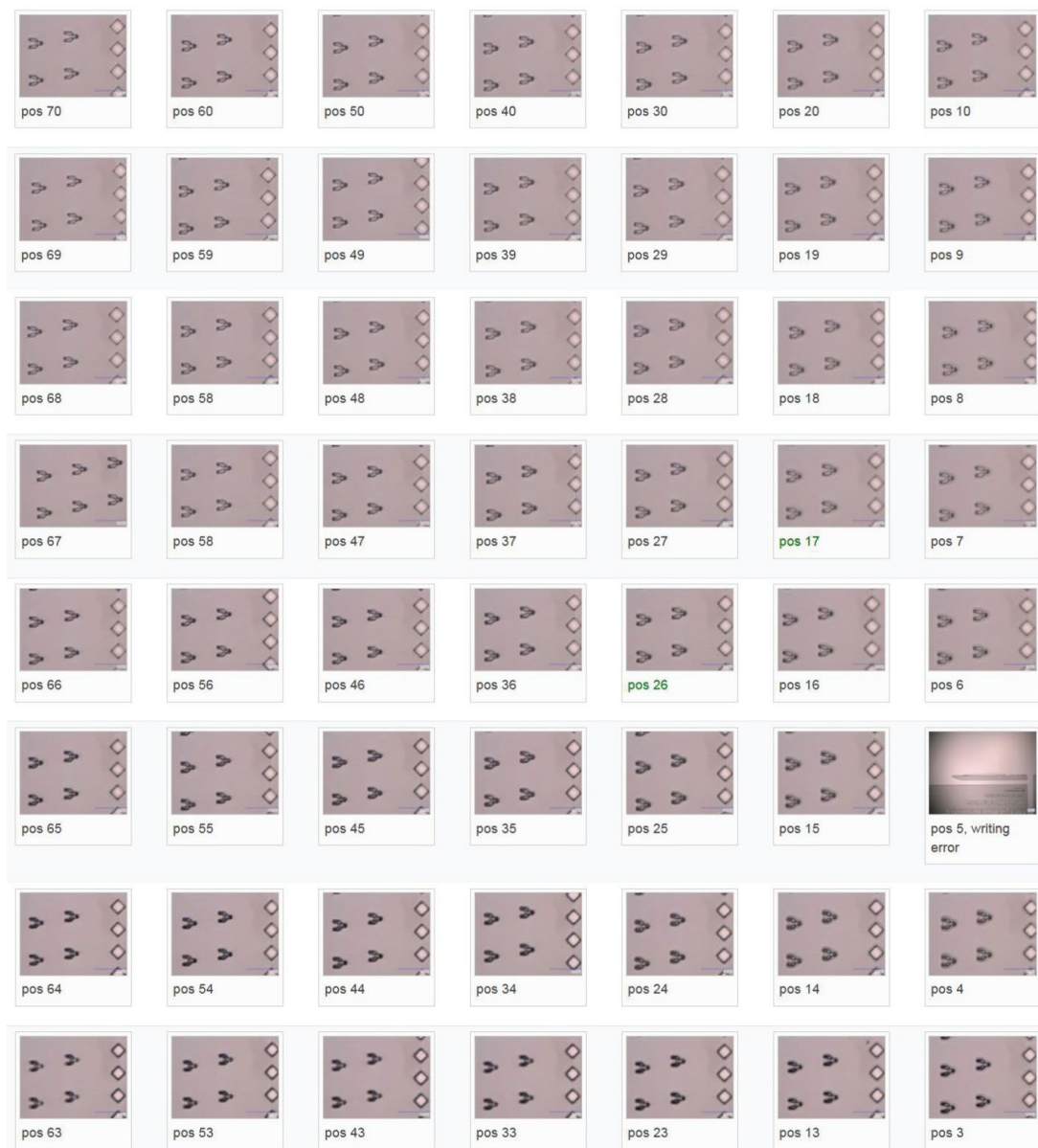


Figure S3. Light-microscopic inspection of the test array from Fig.S2. For all positions, images were taken from the same part of the test structure at constant microscopic settings. This overview is best suited to narrow down the parameter space to useful values. Close-ups indicating the subsequent decision making process are shown in Fig.S4

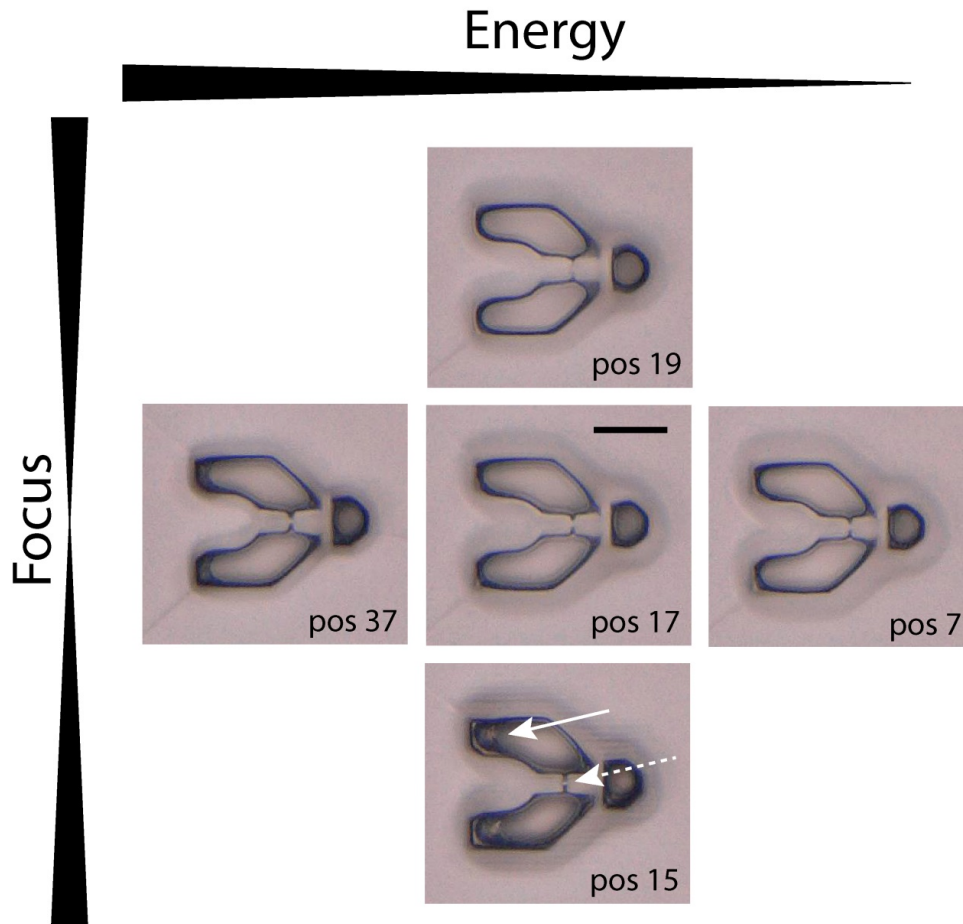


Figure S4. Optical inspection of the test structures from the array (Fig. S3) by light microscopy. In the course of the experiment, exposure energy and focus correction were varied as indicated on the top and left. Position numbers correspond to the ones given in the overview (Fig.S3). Areas important for quality judgement are marked by white arrows. Changing focus correction from negative values to zero (pos15 -> pos17) reduces unwanted reflections on the wafer surface (solid arrow) at the expense of sharpness (dashed arrow). Shifting focus correction even further to the positive (pos19) shows clearly a blurring of the structure.

A similar effect can be observed for the energy setting: Too high energy settings lead to reflections at the bottom and therefore cure resist in unwanted regions (pos37), whereas too low energy settings produce too soft and therefore undefined structures (pos7). In both directions, the best compromise appeared to be in pos17. Starting from these settings, the best parameter set for production could be estimated and tested (resist: SU8-3010, 13um height; laser writer: Heidelberg Instruments uPG101, 2mm writing head, energy 67% of 10mW, defoc +2). Scale bar 20µm.

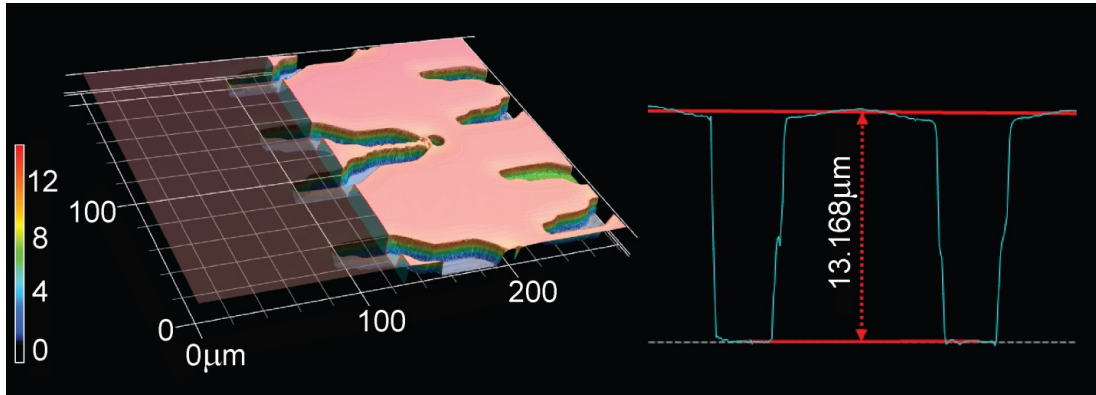


Figure S5. Quality control of final SU8 mold. The exact 3D structure of the final mold (FS814) was determined using laser profilometry (Keyence VKX1100). In the landscape representation (left), the smooth surface on the top and the intended steepness of the shoulders is visible. Height measurements on the 3D dataset can be done at any location (right).

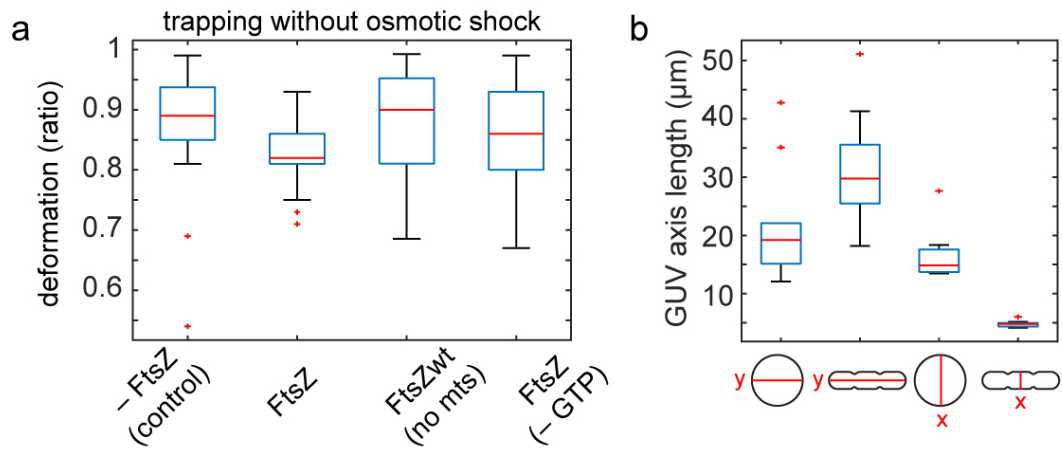


Figure S6 Maximum deformation of FtsZ- or control GUVs before osmotic deflation and determination of GUV aspect ratios after trapping and osmotic shock. a) Deformation of FtsZ- or control GUVs before osmotic deflation. Additional controls for Fig. 1f; data for GUVs with FtsZ-*mts* and without FtsZ is plotted again for comparison and identical to that of Fig. 1f. Additional controls are FtsZ-wt without membrane targeting sequence (*mts*) and with FtsZ without GTP in the buffer (no dynamic FtsZ polymerisation). b) The aspect ratio of trapped GUVs was manually determined in ImageJ at GUV mid plane; *x* and *y* axis length (input for the *y/x* ratio plotted in Fig. 1F). Box plot denotes median in red, interquartile range as blue box, the 2.7σ (99.3%) confidence interval as whiskers and outliers as red dots. $n(\text{GUVs}) = 10$.

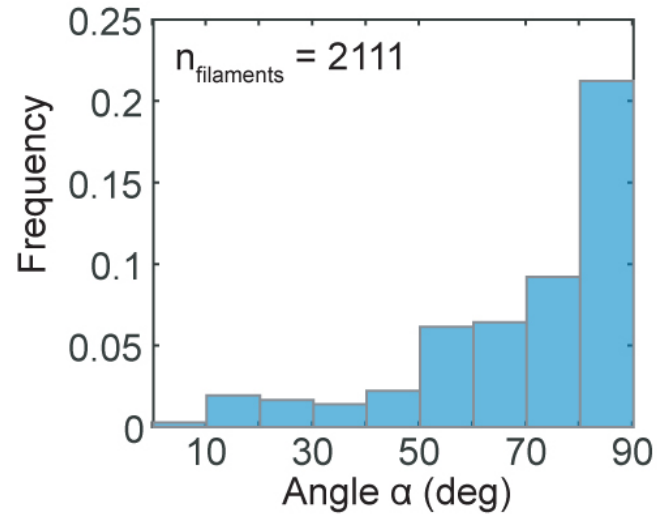


Figure S7 Orthogonal FtsZ filament alignment to the long axis in elongated GUVs. Elongation and indentation of GUVs containing FtsZ filaments leads to filament alignment orthogonal to the long axis at the GUV neck. Distribution of filament angles α for all filaments observed in maximum intensity projections of elongated GUVs. Angles were calculated as described in the methods section.

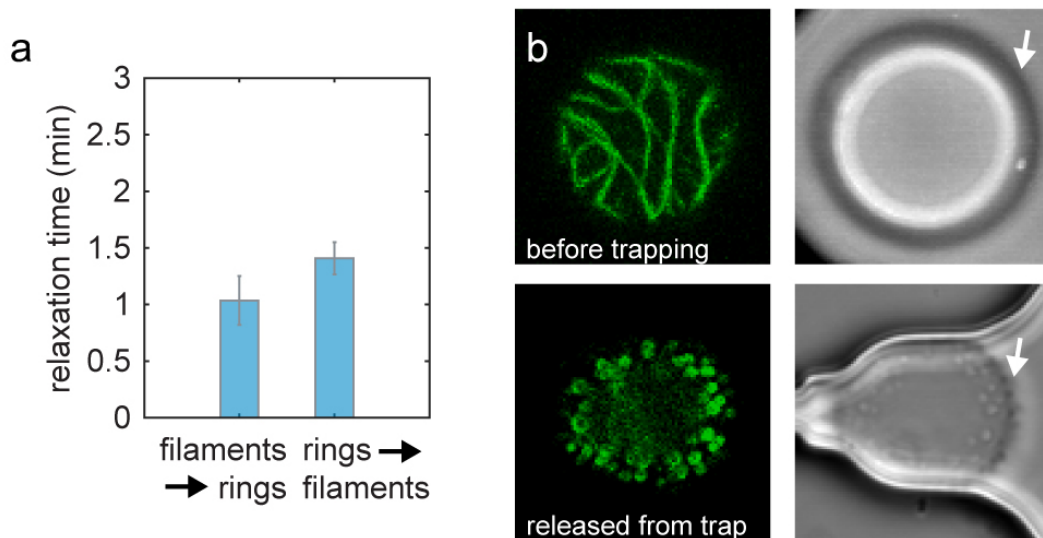


Figure S8 Upon membrane deflation (release from geometric confinement to spherical shape), FtsZ reorganises into dynamic rings that result in membrane protrusions. a) relaxation times for filament to ring transitions as observed by confocal microscopy of GUVs that were pushed out (filament \rightarrow rings) or into (rings \rightarrow filaments) traps. b) Confocal and corresponding bright field microscopy images of GUVs containing membrane-bound FtsZ filaments (green); example for elongated filaments observed in an untrapped GUV and ring-like filaments observed in a GUV after release from the trap, having assumed a spherical shape again. Note that the membrane shows protrusions after FtsZ filaments have rearranged into dynamic rings (bottom DIC image, white arrow) that are absent in the presence of long filaments (top DIC image, white arrow). Osmolarity was not changed in this experiment.

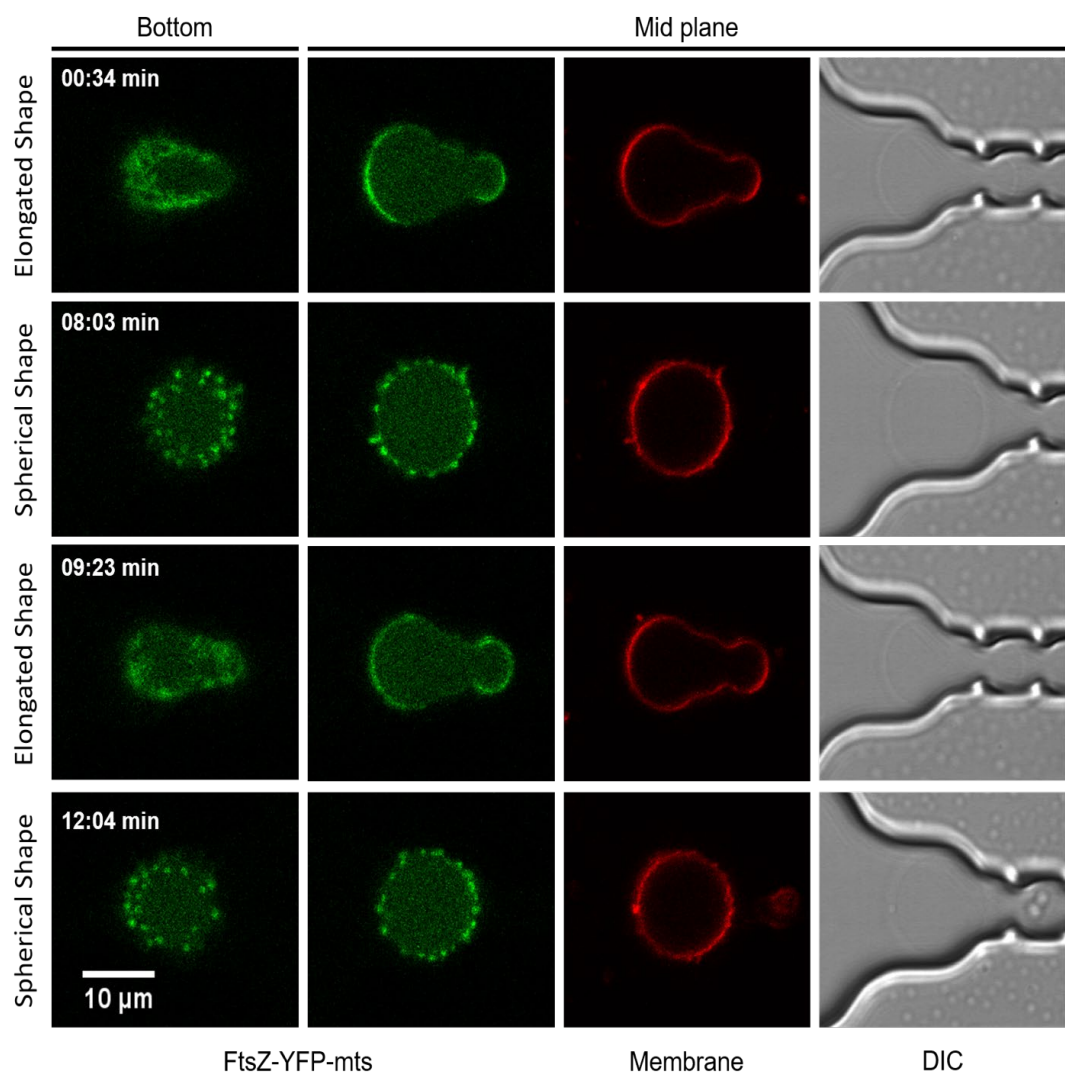
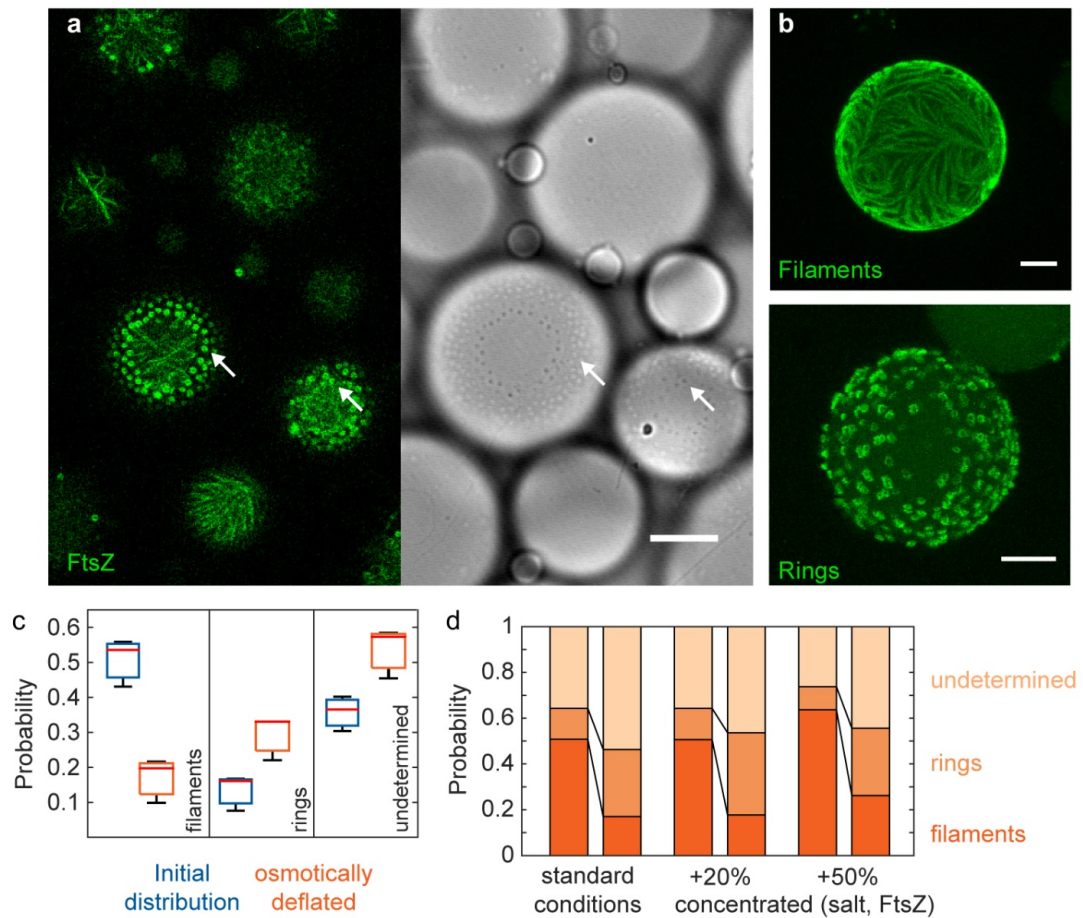


Figure S9 Different buffer conditions does not affect the behaviour of FtsZ. Slightly different buffer and protein conditions previously used in reference [6] were tested, showing that FtsZ is able to form membrane protrusions and filaments under this condition (1.65 μM FtsZ-YFP-mts and 1.4 mM GTP in buffer 125 mM KCl, 25 mM Tris-HCl, 2 mM MgCl_2), in agreement with results in our working buffer. Confocal images of a trapped and elongated FtsZ GUV into our microfluidic device. Images of FtsZ-YFP-mts (Green) at the bottom (left), and equatorial plane of the lipid vesicle.



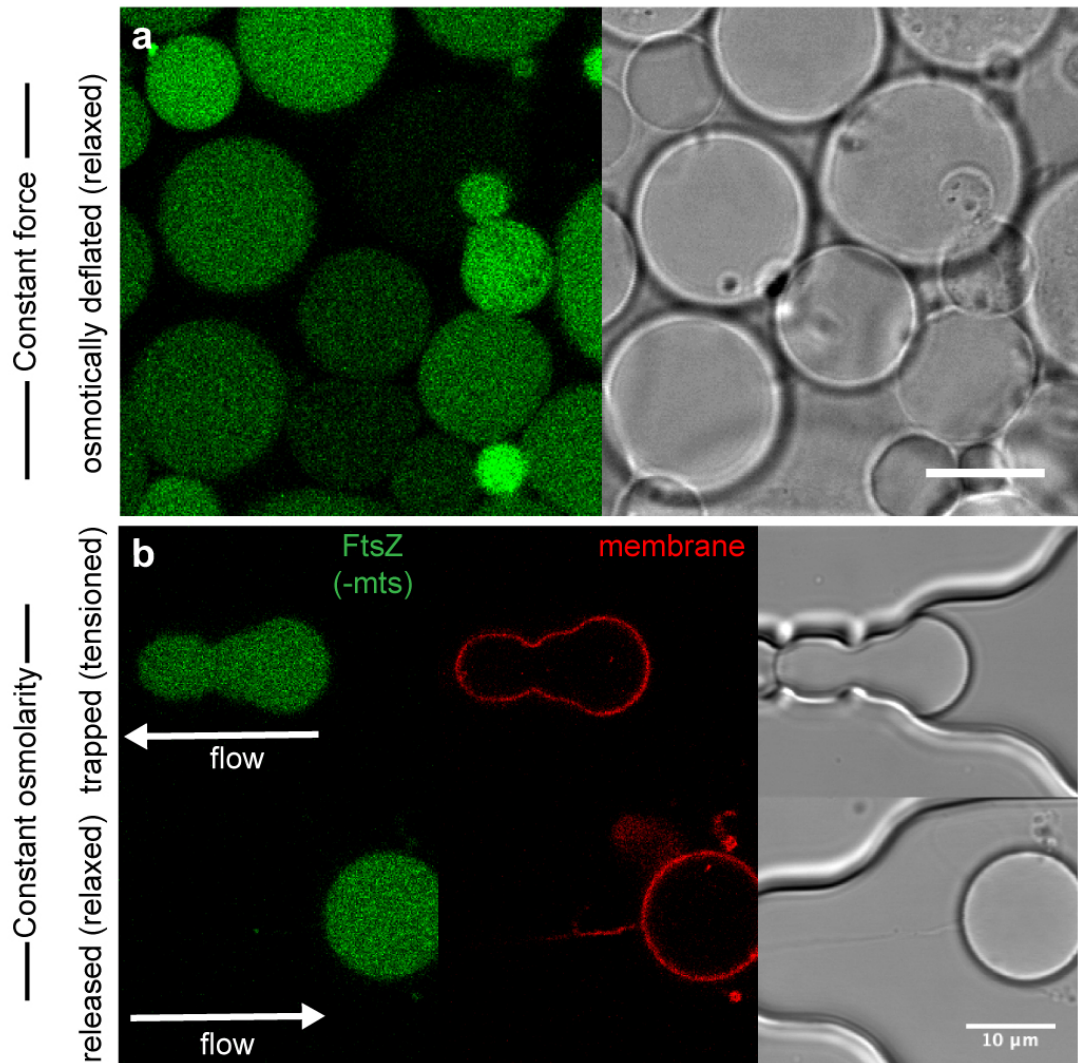


Figure S11 Membrane attachment of FtsZ is required to shape GUV membranes (into cone-like membrane spikes) upon relaxation from mechanically tensioned shapes or upon osmotic deflation. a) confocal and corresponding bright field microscopy images of non-trapped GUVs in a microtitre plate after an osmotic shock, GUVs with FtsZ-wt without membrane targeting sequence (mts) show no FtsZ-stabilised membrane protrusions after osmotic deflation b) Confocal images of the equatorial plane of an elongated (trapped) GUV (top row) and the same GUV after isosmotic release from the trap (bottom row), having reassumed a spherical shape. GUV contains FtsZ-wt without membrane targeting sequence (left, FtsZ wt-Alexa 488, green; middle, membrane labelled with DOPE-ATTO655; right, corresponding DIC images). Scale bar are 10 μm. Data is representative of GUVs from 12 independent experiments.

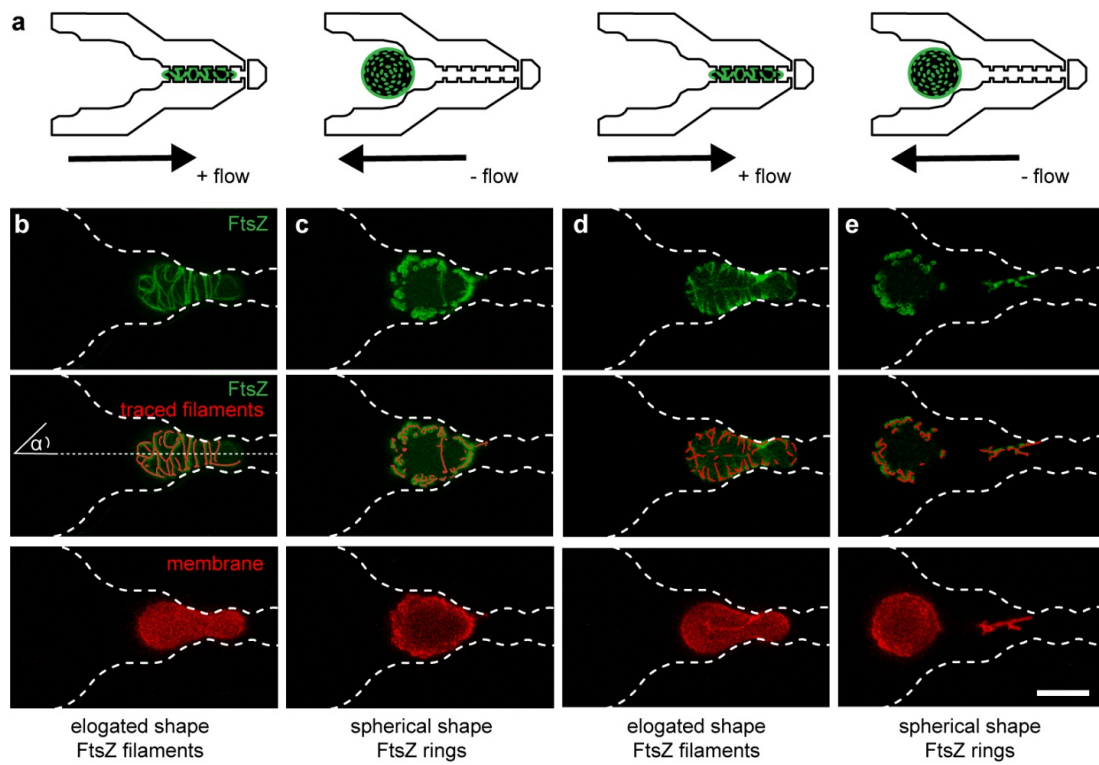


Figure S12 Reversible elongation and relaxation of FtsZ GUVs leads to transitions between FtsZ rings and long filaments. a) Schematic depiction of experiment. FtsZ forms elongated filaments in rod-shaped (tense) vesicles while FtsZ rings are formed when the vesicle is relaxed back to its spherical shape; b) confocal images of the equatorial plane of a trapped and elongated GUV showing FtsZ filaments (top), traced filaments (middle) and GUV membrane (bottom); FtsZ is shown in green. Trap outline is marked (white dotted line). c,d,e) transition of the same GUV between spherical c) and e) and elongated d) shapes purely by manipulation of flow rates and direction. Flow range was -15 to +10 $\mu\text{l/h}$ and osmolarity was kept constant. Data is representative of GUVs from 12 independent experiments. The scale bar is 10 μm

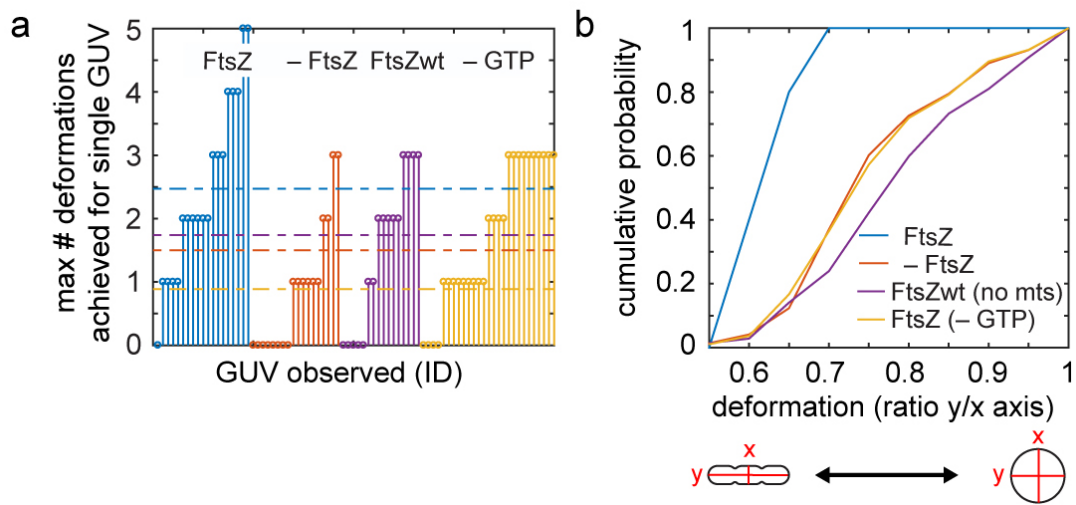


Figure S13 GUVs with a membrane-bound, dynamically polymerising FtsZ cytoskeleton can be deformed more often and more strongly under the same conditions (osmolarities, flow rates). a) Maximum number of deformations achieved for individual GUVs by repeated trapping for GUVs containing FtsZ or control GUVs without FtsZ (red), with FtsZ-wt without membrane targeting sequence (- mts, purple) and with FtsZ without GTP in the buffer (no dynamic FtsZ polymerisation, yellow). Stem plot shows # of deformations achieved for a single GUV; the value for the mean # deformations for each experimental condition is plotted as a horizontal line (colour coded). b) Cumulative probability of GUV deformation ratio achieved by trapping FtsZ or control GUVs without FtsZ (red), with FtsZ-wt without membrane targeting sequence (- mts, purple) and with FtsZ without GTP in the buffer (no dynamic FtsZ polymerisation, yellow). All osmolarities >480 mOsm/kg (internal osmolarity).

Movie legends

Movie 1 FtsZ-GUV can be reversibly elongated and relaxed into spherical shape. The movie shows the filament/ring transitions and formation of membrane protrusions generated by FtsZ rings. Osmolarity of the surrounding buffer remains unchanged. Green and red channel correspond to FtsZ-YFP-mts and lipid membrane (DOPE-ATTO 655), respectively. For the video, several confocal movies (played back at 80x) were stitched together. Therefore, time intervals are not constant throughout the entire videos as we do not know the precise time interval between individual videos.

Movie 2 FtsZ-GUV can be deformed into rod- or cigar- shapes using the microfluidic devices. The movie shows reversible squeezing and elongation of a FtsZ-GUV by controlling the flow rate in the device microchannels. Osmolarity of the surrounding buffer remains unchanged. Green channel corresponds to FtsZ-YFP-mts while red channel corresponds to lipid membrane (DOPE-ATTO 655). For the video, several confocal movies (played back at 70x) were stitched together. Therefore, time intervals are not constant throughout the entire videos as we do not know the precise time interval between individual videos.

Movie 3 Continuous time-lapse of reversible FtsZ-GUV deformations in microfluidic devices. The flow rate used in this video varies from $-20 \mu\text{l/h}$ to $+5 \mu\text{l/h}$ to push in and out the vesicle. Reversible transition between FtsZ filaments and rings can be observed. Green and red channel correspond to FtsZ-YFP-mts and lipid membrane (DOPE-ATTO 655), respectively. Two first digits of the time counter represent minutes while the last two correspond to seconds (the movie is played back at 150x).

3.3 Publication P3

FtsZ induces membrane deformations via torsional stress upon GTP hydrolysis

Summary:

In this manuscript, we investigate the mechanism behind FtsZ's force constriction in bacterial cell division. FtsZ forms the FtsZ ring and has two known features: self-organizing into treadmilling vortices and shape deformation of flexible liposomes. We employed an assay using soft lipid tubes pulled from FtsZ-decorated giant lipid vesicles and we observe that FtsZ filaments actively compress the tubes into spring-like structures. We could estimate the directional forces exerted by FtsZ to be in the pN range, sufficient to induce membrane budding and constriction on lipid vesicles and wall-less *E. coli* cells. The forces are believed to result from torsional stress in a GTPase-dependent manner.

Reprinted with permission from:

Ramirez-Diaz, D. A., **Merino-Salomón, A.**, Meyer, F., Heymann, M., Rivas, G., Bramkamp, M. and Schwille, P. (2021). FtsZ induces membrane deformations via torsional stress upon GTP hydrolysis. *Nature Communications* 12, 3310.

Source online: <https://doi.org/10.1038/s41467-021-23387-3>

ARTICLE



<https://doi.org/10.1038/s41467-021-23387-3>

OPEN

FtsZ induces membrane deformations via torsional stress upon GTP hydrolysis

Diego A. Ramirez-Diaz^{1,2}, Adrián Merino-Salomón^{1,3}, Fabian Meyer⁴, Michael Heymann^{1,5}, Germán Rivas⁶, Marc Bramkamp⁴ & Petra Schwille¹✉

FtsZ is a key component in bacterial cell division, being the primary protein of the presumably contractile Z ring. In vivo and in vitro, it shows two distinctive features that could so far, however, not be mechanistically linked: self-organization into directionally treadmilling vortices on solid supported membranes, and shape deformation of flexible liposomes. In cells, circumferential treadmilling of FtsZ was shown to recruit septum-building enzymes, but an active force production remains elusive. To gain mechanistic understanding of FtsZ dependent membrane deformations and constriction, we design an in vitro assay based on soft lipid tubes pulled from FtsZ decorated giant lipid vesicles (GUVs) by optical tweezers. FtsZ filaments actively transform these tubes into spring-like structures, where GTPase activity promotes spring compression. Operating the optical tweezers in lateral vibration mode and assigning spring constants to FtsZ coated tubes, the directional forces that FtsZ-YFP-mts rings exert upon GTP hydrolysis can be estimated to be in the pN range. They are sufficient to induce membrane budding with constricting necks on both, giant vesicles and *E.coli* cells devoid of their cell walls. We hypothesize that these forces result from torsional stress in a GTPase activity dependent manner.

¹Department of Cellular and Molecular Biophysics, Max Planck Institute of Biochemistry, Martinsried, Germany. ²Graduate School for Quantitative Biosciences (QBM), Ludwig-Maximilians-University, Munich, Germany. ³International Max Planck Research School for Molecular Life Sciences (IMPRS-LS), Munich, Germany. ⁴Institute of General Microbiology, Christian-Albrechts-University, Kiel, Germany. ⁵Institute of Biomaterials and Biomolecular Systems, University of Stuttgart, Stuttgart, Germany. ⁶Centro de Investigaciones Biológicas Margarita Salas, Consejo Superior de Investigaciones Científicas (CSIC), Madrid, Spain. ✉email: schwille@biochem.mpg.de

In biology, fundamental mechanical processes, such as cell division, require an intricate space-time coordination of respective functional elements. However, how these elements, mostly proteins, can self-organize to exert forces driving large-scale transformations is poorly understood. In several organisms, ring-like cytoskeletal elements appear upon cytokinesis; for instance, the FtsZ-based contractile Z ring in bacteria. Ring-like FtsZ structures have previously been shown to deform liposome membranes^{1,2}. When reconstituted on flat membranes, FtsZ self-assembles into treadmill vortices with conserved direction^{3,4}. In vivo, FtsZ shows circumferential but bidirectional treadmill that is assumed to serve as a pacemaker guiding peptidoglycan synthesis around the septum^{5,6}. In vivo^{5,6} and in vitro³ experiments have suggested that the emergence of FtsZ treadmill phenomenon is intimately related to its GTPase activity.

Despite of these exciting findings, it is not clear how exactly FtsZ treadmill filaments may at all contribute to the physical process of constriction^{7,8}. The challenge is twofold: (i) to determine the forces that are actually required to divide a bacterial cell with its much more complex architecture than a membrane shell, and (ii) to formulate the exact mechanism by which forces on membranes could at all be exerted by FtsZ treadmill filaments. For instance, considering the mechanical bearing related to internal turgor pressure (~MPa), models have suggested that FtsZ forces in the range of 8–80 pN would be required for constriction⁹. In contrast, it has been proposed that turgor pressure need not be considered, due to the possibility of same

osmolarity between periplasm and cytoplasm¹⁰. For this case, very low FtsZ forces in the range of 0.35–2.45 pN could exert membrane deformations leading to constriction¹⁰. In conclusion, in vivo and in vitro experimental approaches addressing those two major questions are needed to gain deeper understanding in cell division in bacteria. While (i) can only be addressed by extensive in vivo studies and may remain a notorious challenge in bacterial cell biology for many years, (ii) is more readily accessible by state-of-the-art biophysics on in vitro reconstituted systems, aiming at elucidating the mechanistic features of FtsZ as a membrane-deforming polymer.

Regardless of whether or not FtsZ is the major force contributor in cell division, it remains a fundamental question whether forces can be associated to GTP consumption and whether there is a structural connection to the emergence of treadmill. And if so, how this force could be transmitted to constrict the membrane. To approach these questions, we introduced an experimental strategy to produce cylindrical membrane geometries mimicking rod-like bacterial shapes, by pulling soft lipid tubes from deflated giant unilamellar vesicles (GUVs) using optical tweezers. Our aim is to quantitatively elucidate the physical principles underlying membrane deformations induced by dynamic FtsZ rings and the scale of delivered forces. These particular principles are key to understand the nature of FtsZ membrane deformations in vitro and in vivo.

Results and discussion

Based on our recent study³, we externally added FtsZ-YFP-*mts* to GUVs made of *E. coli* lipid extract. Conditions to obtain ring-like structures were determined by tuning GTP and Mg²⁺ (Fig. 1a). Since no clear deformations were observed for tensed vesicles (Fig. 1a), we designed a two-side open chamber allowing for slow water evaporation to obtain deflated and deformable GUVs. After 20–30 min, we evidenced that rings were inducing inwards cone structures emerging from the membrane surface, indicative of drilling-like inward forces (Fig. 1b). Motivated by this specific geometry, we designed PDMS microstructures mimicking such inward cones (Figs. 1c and S1A). After coating these with supported lipid bilayer (SLB) and triggering protein polymerization, we observed individual filaments/bundles to wrap the cone in a dynamic fashion resembling a vortex (Fig. 1d) (Supplementary Movie S1). We noticed that the dynamic vortices rotate both clockwise and anticlockwise (Fig. 1e), indicating that preferential directionality observed on flat SLBs is absent in conical geometry. Rotational velocities were estimated around 43 nm/s, showing relatively good agreement with our previous results on flat surfaces (34 nm/s)³.

To quantitatively characterize the impact of FtsZ on soft tubular geometries, we developed a method based on optical tweezers. Contrary to prior approaches using micropipettes¹¹, we pulled soft tubules from weakly surface-attached GUVs (Fig. 2a) by moving the GUVs relative to an optically trapped bead. Lipid tubes with mean diameter of ca. 0.47 μm (Fig. S2A) were now pulled from deflated GUVs decorated with ring-like FtsZ structures and inward-conical deformations (Supplementary Movie S2). Given the mobility of FtsZ rings and filaments over the GUV surface, protein from the vesicle started entering the tube immediately after pulling. After 175 s, helical tube shapes were clearly observed (Fig. 2b), indicative of dynamic coiling (Supplementary Movie S3). As more protein entered the tube, the spring-like structure became compressed (Fig. 2b, 500 s). These helical tube deformations can be rationalized by twisting of an elastic rod subjected to constant tensile force (Fig. 3f). Similar to the experiment in Fig. 1d, filaments grew toward (clockwise) and away from (counterclockwise) the tip of the tube. If filament

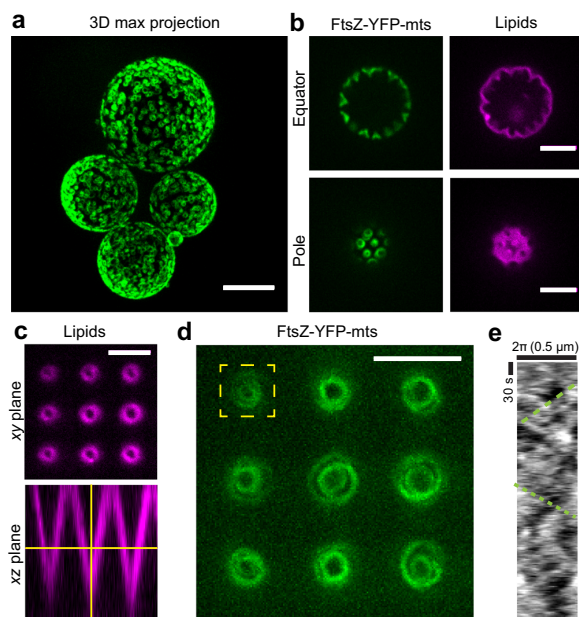


Fig. 1 Bidirectional FtsZ treadmill rings yield directional screw-like lipid membrane deformations. **a** FtsZ-YFP-*mts* ring structures externally decorating GUVs (scale bar = 10 μm). **b** After GUV deflation, inwards conical deformations emerged from FtsZ rings (GUVs: $N > 20$) (scale bar = 5 μm). **c** Inspired by deformations in **(b)**, we designed a PDMS microstructure with inwards conical geometry covered with a supported lipid bilayer (SLB). The imaging plane was chosen to have a cross-section of 1–2-μm diameter (scale bar = 5 μm). **d** Inside cones, FtsZ-YFP-*mts* self-assembled into dynamic vortices (Supplementary Movie S1) (scale bar = 5 μm). **e** A representative kymograph ($N > 3$) showed negative and positive slopes indicating the presence of clockwise and anticlockwise directions.

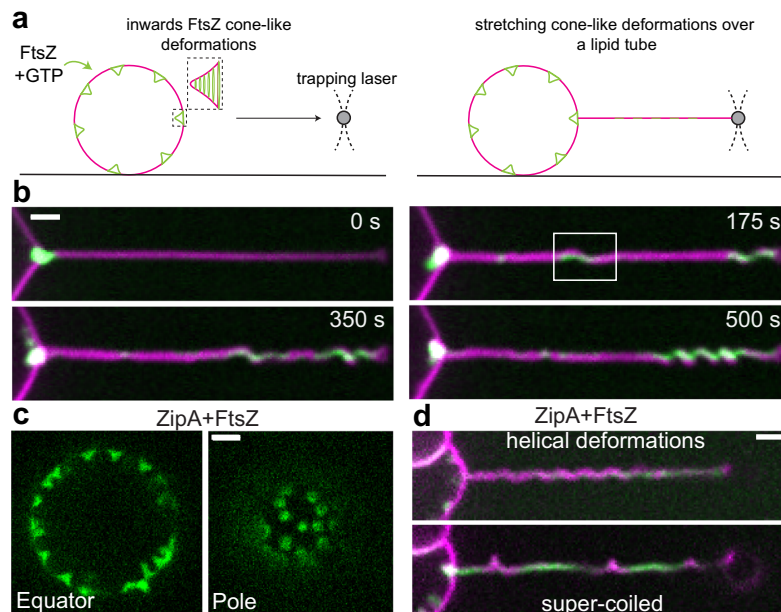


Fig. 2 Inwards FtsZ-induced conical deformations are geometrically equivalent to spring-like deformations on a tubular surface. **a** To characterize the protein structures forming the cone-like deformations, we stretched the deformed vesicle membrane into a tubular geometry. Large and soft lipid tubes were pulled from weakly surface-attached GUVs by moving the GUVs relative to an optically trapped bead. **b** A representative time acquisition shows that FtsZ-YFP-mts entered the tube promoting coiling as a function of time ($N = 12$). Clustering of protein toward the tip correlates with a spring-like shape. Green and magenta corresponds to fluorescence signal of FtsZ-YFP-mts and lipid, respectively. **c** To rule out that artificial attachment of the FtsZ-YFP-mts is responsible of the helical transformation, we reconstituted wild-type FtsZ anchored to the membrane via ZipA. When wild-type FtsZ was added to ZipA-decorated vesicles, rings were self-assembled causing inwards cone-like deformations ($N = 74$) such as in the case of FtsZ-YFP-mts. **d** After pulling lipid tubes, similar helical deformations and supercoiled regions were observed confirming that torsion is related to the FtsZ core of the polymer ($N = 3$ out of 18 pulled tubes). Fluorescence signal of wt-FtsZ-Alexa 488 is shown in green while siZipA remains unlabeled and lipids are shown in magenta. (Scale bar = 2 μm).

growth imposes torsion, the counter-growing filament will generate torsion in the opposite direction. The importance of bidirectional filament growth can be understood using a shoelace analogy: opposite torque should be exerted on both ends of the shoelace to observe a helical deformation. If one end is loose, the opposite end will only rotate accordingly (sliding).

Since spring-like deformations were observed with a FtsZ protein chimera that binds autonomously to membrane (FtsZ-YFP-mts), we attempted to confirm whether this phenomenology is intrinsic to the FtsZ polymer and not due to chimera artifacts, e.g., induced by the membrane targeting sequence. Based on the reconstitution of treadmilling dynamic rings on flat membranes using the *E. coli* FtsZ natural anchor ZipA¹², we aimed to establish appropriate conditions for WT-FtsZ rings externally decorating GUVs using ZipA. First, as a control, ZipA-decorated vesicles were examined under deflation conditions, and none of them showed inwards deformations ($N = 14$, Fig. S2B). In addition, we pulled lipid tubes with only ZipA and none showed any relevant deformation over time ($N = 10$, Fig. S2B). Only after adding wild-type FtsZ, we obtained rings and inward deformations (Fig. 2b). We then pulled tubes from these vesicles and observed helical transformations (Fig. 2c) ($N = 3$ out of 18 pulled tubes), indicating that FtsZ polymer and not its membrane attachment (in this case ZipA) caused this effect. Interestingly, FtsZ+ZipA (as well as FtsZ-YFP-mts) displayed in plectonic/supercoiled regions (Figs. 2c and S1E) as further indicative of torsion over the lipid tube.

After having established that the spring-like membrane transformations do not result from membrane anchors only, we

needed to explore the active role of the GTPase activity. To investigate the role of GTP hydrolysis for the spring-like deformations, we reconstituted FtsZ-YFP-mts*[T108A], a mutant with low GTPase activity³. This mutant self-assembles into rings at similar times (comparable polymerization rates) with respect to FtsZ-YFP-mts but lacks dynamic treadmilling³. Once reconstituted here on soft vesicle surfaces, FtsZ-YFP-mts*[T108A] rings (Fig. S1B) also induce cone-like deformations (Fig. S1C) as well as helical deformations, after 300 s, in lipid tubes (Fig. 3b). The pitch of these helices, however, remained unaffected ($\lambda > 3 \mu\text{m}$) at longer times (900 s, Supplementary Movie S4). In contrast, helices decorated with GTP-active FtsZ-YFP-mts (Fig. 3a) underwent compression to a pitch of $\lambda \sim 1.5 \mu\text{m}$ already before 300 s. By plotting the arclength of the spring against FtsZ density on the tubes in Fig. 3a, b as a function of time (Fig. S2D), we clearly observed a greater membrane-deforming activity for FtsZ-YFP-mts (Fig. 3c). The timescale of deformations likely depends on the amount of protein on the tube. Thus, since the initial amount of protein on the tubes varies among independent experiments, further statistical analysis was performed in steady state.

Since the deflation of individual GUVs could fluctuate, we also tested whether compression could be biased by GUV membrane tension and protein density over the tube. The tube diameter d represented our observable for membrane tension according to the relation $d = \sqrt{\frac{2\kappa}{\sigma}}$, where κ denotes the lipid bending modulus and σ the membrane tension^{11,13}. The lower the membrane tension by deflation, the larger the tube diameter. Therefore, we plotted the mean pitch vs. tube diameter (Fig. 3d), considering

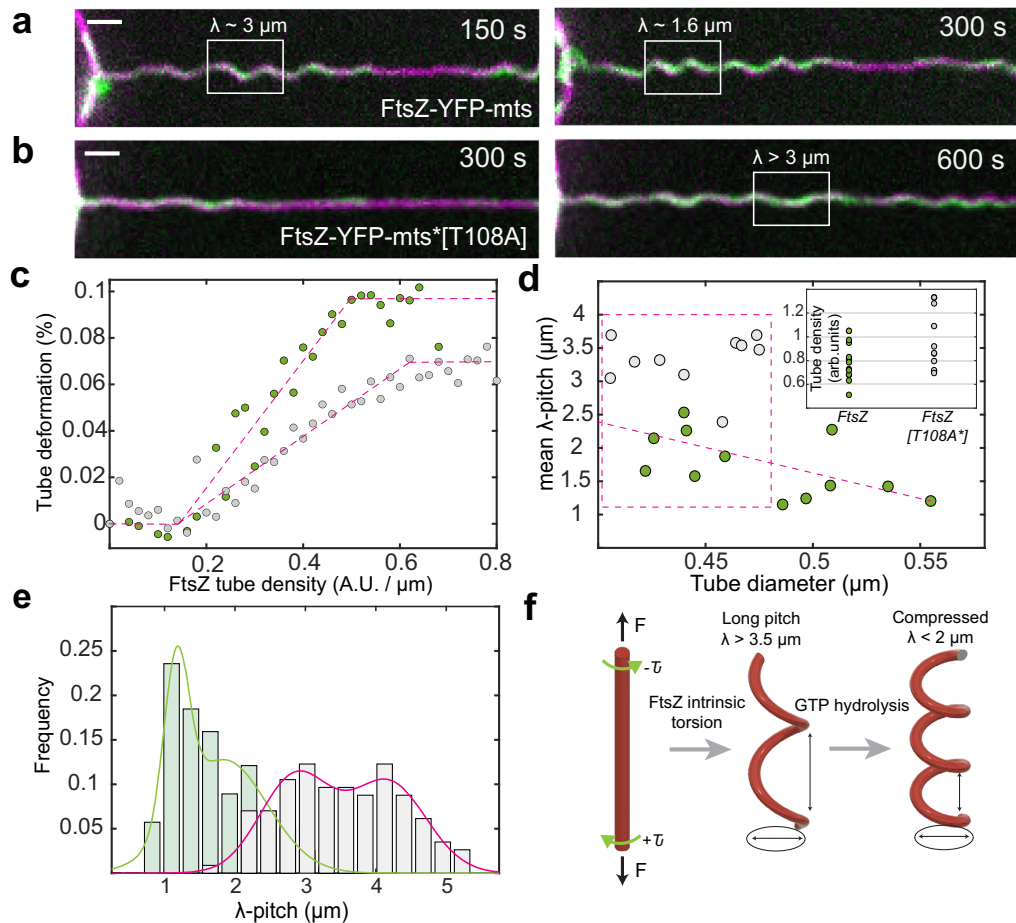


Fig. 3 GTPase activity in FtsZ filaments promotes spring compression and condensation. Time-lapse acquisition of lipid tubes covered by **a** FtsZ-YFP-mts ($N = 12$) and **b** FtsZ-YFP-mts*[T108A] ($N = 10$). Both proteins promote helical deformations with the difference that GTPase activity induces compression ($\lambda \sim 1.6 \mu\text{m}$) of initially longer pitch ($\lambda > 3 \mu\text{m}$). FtsZ-YFP-mts is shown in green while lipids are shown in magenta (scale bar = $2 \mu\text{m}$). **c** Tube deformation (arclength) in **(a, b)** against FtsZ-YFP-mts (green circles) and FtsZ-YFP-mts*[T108A] (gray circles) tube density, as function of time (Fig. 2SD), evidenced that GTPase activity caused greater tube deformation. **d** To rule out that compression was biased by the deflation state, we plotted tube diameter vs. mean pitch for FtsZ-YFP-mts ($N = 12$) (green) and FtsZ-YFP-mts*[T108A] ($N = 10$) (gray) in steady state. Despite of higher tube densities (arbitrary units) for FtsZ-YFP-mts*[T108A] as shown in **(d)**—insert, the mean pitch for no GTPase case is longer at comparable tube diameters. **e** We observed two clear pitch states for FtsZ-YFP-mts (light green bars/green line) and FtsZ-YFP-mts*[T108A] (gray bars/magenta line) with a clear dominance of longer pitch for the mutant without GTPase activity. **f** Helical deformations can be understood by twisting an elastic rod subjected to constant force. We postulate that FtsZ has an intrinsic torsion that is enhanced by GTPase activity, driving further compression. Intrinsic FtsZ torsion rules long-pitch transformations ($\lambda > 3 \mu\text{m}$) while GTP enhances further torsion causing higher pitch states ($\lambda < 2 \mu\text{m}$).

also the amount of protein (Fig. 3d—insert). Although there was a mild correlation between pitch and diameter (Fig. 3d) for FtsZ-YFP-mts ($N = 12$), the mean pitch was consistently longer for ($N = 10$) FtsZ-YFP-mts*[T108A] (Fig. 3d) in the case of tubes with comparable or higher protein density (Fig. 3c—insert). To better visualize the impact of GTPase activity, we plotted the pitch distribution for both proteins: the GTPase activity contributed to a decrease of pitch (Fig. 3e) as clear indicative of spring compression. Interestingly, both distributions can be reasonably considered to be bimodal. We suggest that this might indicate two states of torsion: a structural intrinsic torsion (longer pitch) that is further enhanced (shorter pitch) via GTPase activity (Fig. 3f). Note that FtsZ-YFP-mts*[T108A] exhibits residual GTPase activity, driving some compression and potentially explaining the bimodality of this distribution.

To assess mechanical properties of FtsZ-YFP-mts-induced spring-like structures, we implemented an alternative approach based on the elastic response of the $\text{GUV} + \text{tube}$ system to a specific dynamic input. Using a piezoelectric stage, we induced a lateral oscillation of the GUV position ($A = 3 \mu\text{m}$, $f = 1 \text{ Hz}$) and recorded forces by the optical trap (Supplementary Movie S5). We here measured the resistive force of the material per micrometer (k -spring constant). The stiffer the material, the higher force detected by the optical trap. To calculate the amplitude of the signal at 1 Hz, the signal was Fast Fourier-transformed, as depicted in Fig. 4b, where the magenta line refers to the pure lipid tube and the green line to FtsZ. The pure lipid contribution ($N = 11$) yielded values between 0.15 and 0.59 $\text{pN}/\mu\text{m}$ (Fig. 4d), while values between 0.23 and 1.52 $\text{pN}/\mu\text{m}$ (Fig. 4d) were obtained for FtsZ. Although forces were recorded for tubes fully covered with FtsZ (Fig. 4a); for some vesicles, the lipid

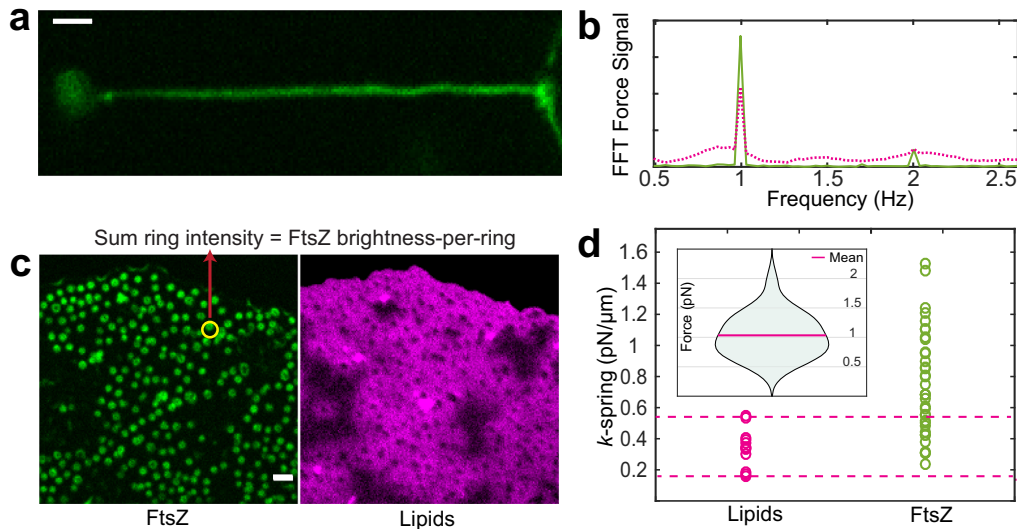


Fig. 4 Dynamic FtsZ-YFP-mts rings exert forces in the pN range. **a** Spring-like structures ($N = 36$) were mechanically assessed by forcing the tube length to oscillate with an amplitude of $3 \mu\text{m}$ and a frequency of 1Hz . To measure a reliable force contribution from the protein, we increased the protein sample concentration (see “Methods”) to guarantee a full/high protein coverage of the tube. **b** To measure forces, we tracked bead-displacement as response of the dynamic input. Then we Fast Fourier-transformed (FFT) the data to calculate the amplitude of the signal. Magenta line: lipid signal and green line: FtsZ. **c** Spontaneous flattening of vesicles over the glass surface permitted to characterize the total brightness of single rings ($N = 412$) with exactly same conditions as lipid tube experiments. **d** By calculating the amplitude of each FFT force signal (**b**), we assessed the spring constant for the case of the only lipid contribution ($N = 11$) and FtsZ ($N = 36$). Dashed magenta lines indicate the range where the lipid dominated over the FtsZ contribution to the spring constant. (**d**—insert) The total FtsZ brightness for each data point in (**d**) was determined to approximate the FtsZ brightness-per-ring in accordance with Fig. S2E. Thus, the distribution of forces/ FtsZ brightness-per-ring was plotted ($N = 23$) showing a mean value around 1pN per ring unit. (Scale bar = $2 \mu\text{m}$).

response still dominated the spring constant measurement, meaning that some FtsZ data points lie in the lipid range (dashed magenta lines, Fig. 4d). This means that for some vesicles, the oscillation amplitude was not sufficient to fully unfold the membrane excess, and then the force induced by FtsZ range falls into the lipid contribution. For others, the membrane is completely unfolded, and in this case, we are able to pick up the resistive contribution from FtsZ itself. Thus, FtsZ data points overlapping the lipid contribution were discarded for further analysis.

Interestingly, in our GUVs in vitro assays (also encapsulated rings, see Fig. 5d), we observed that discernible FtsZ-YFP-mts rings appeared to be of fairly similar size and brightness (Fig. S2E, with $N = 412$ analyzed rings). To estimate the range of forces that these ring units could exert in our particular assays, we took advantage of the fact that some ring-decorated vesicles flattened on the glass surface (Fig. 4b) allowing precise imaging of single rings on the surface using the same conditions as in the FtsZ coated tubes. Although the absolute number of monomers or filaments within the treadmill ring units is unknown, the actuation of these ring-associated filaments shaped the lipid tube into a spring by exerting forces that are proportional to the here measured spring constant. Then, by knowing the spring constant, the oscillation amplitude, and the number of rings, we estimate that each ring unit exerts forces in the range of 1pN (Fig. 4d—insert). In addition, one can estimate the dependence of this force on GTPase activity by using the pitch difference in Fig. 3e ($\Delta\lambda \sim 2 \mu\text{m}$), the average for the k-spring constant ($k_{\text{FtsZ}+\text{lipid}} \sim 0.9 \text{pN}/\mu\text{m}$), and the number of rings-per- μm (~ 1 ring). A force of $\sim 0.9 \text{pN}$ suggests a significant contribution in the total ring-unit force resulting from GTPase activity. Note that these force estimations did not exclude an intrinsic lipid contribution.

The validity of our k-spring measurements can be evaluated by assuming the persistence length of FtsZ filaments. Previously, we

had inferred that FtsZ-YFP-mts rings on SLB are made of filamentous structures of $\sim 0.39 \mu\text{m}$ length in an average³. Assuming a persistence length as $0.39 \mu\text{m}$, FtsZ filaments would exhibit a flexural rigidity $K = 1.59 \times 10^{-27} \text{Nm}^2$ ($K = l_p k_B T$ ¹⁴) that agrees well with previous experimental reports¹⁵. Based on this, we could assess the Young’s modulus of FtsZ filaments: $E_{\text{FtsZ}} = 51.8 \text{MPa}$. ($K = EI$, where $I = \pi r^4/4$, the area moment of inertia, $r = 2.5 \text{nm}$ ¹⁶). On the other hand, the Young’s modulus E of a spring is related to the spring constant through $E = (kl_0)/S$, where k denotes the spring constant, l_0 is the spring initial length, and S the cross-section. By considering two independent hollow cylinders, one made of lipid bilayers (lipid bilayer thickness: $\sim 5 \text{nm}$) and one made of FtsZ-YFP-mts (one FtsZ monomer diameter: $\sim 5 \text{nm}$), the ratio l_0/S was fairly constant in our tube experiments, and therefore the relationship $E_{\text{FtsZ}}/E_l = (k_{\text{FtsZ}}/k_l)$ is reasonably valid. To calculate $\frac{k_{\text{FtsZ}}}{k_l}$, we here considered raw averages for distributions shown in Fig. 4d and subtracted the lipid contribution in the case of FtsZ: $k_l = 0.34 \text{pN}/\mu\text{m}$ and $k_{\text{FtsZ}} = 0.59 \text{pN}/\mu\text{m}$. Then, the ratio $\frac{k_{\text{FtsZ}}}{k_l} = 1.72$ showed good agreement compared to $\frac{E_{\text{FtsZ}}}{E_l} = 2.26$ assuming $E_l = 22.9 \text{MPa}$ (lipids with bending = $20k_B T$)^{17,18}. This confirmed that our force measurements corresponded well with previous flexural rigidity values for FtsZ fibers. In addition, our data provide further evidence that FtsZ filaments are softer than other cytoskeleton proteins such as microtubules ($K \sim 10^{-23}$) or actin ($K \sim 10^{-26}$)^{19,20}.

The helical nature of FtsZ and its torsional dynamics have been experimentally observed^{21,22}; however, its relation to a potential mechanism of actively deforming membranes has not yet been clearly established. According to our observations, the helical membrane transformation caused in this study by FtsZ filaments can best be understood by assuming Darboux torque around the lipid tube. Darboux torques are tangential torques caused by a local mismatch between the plane defined by the filament curvature and

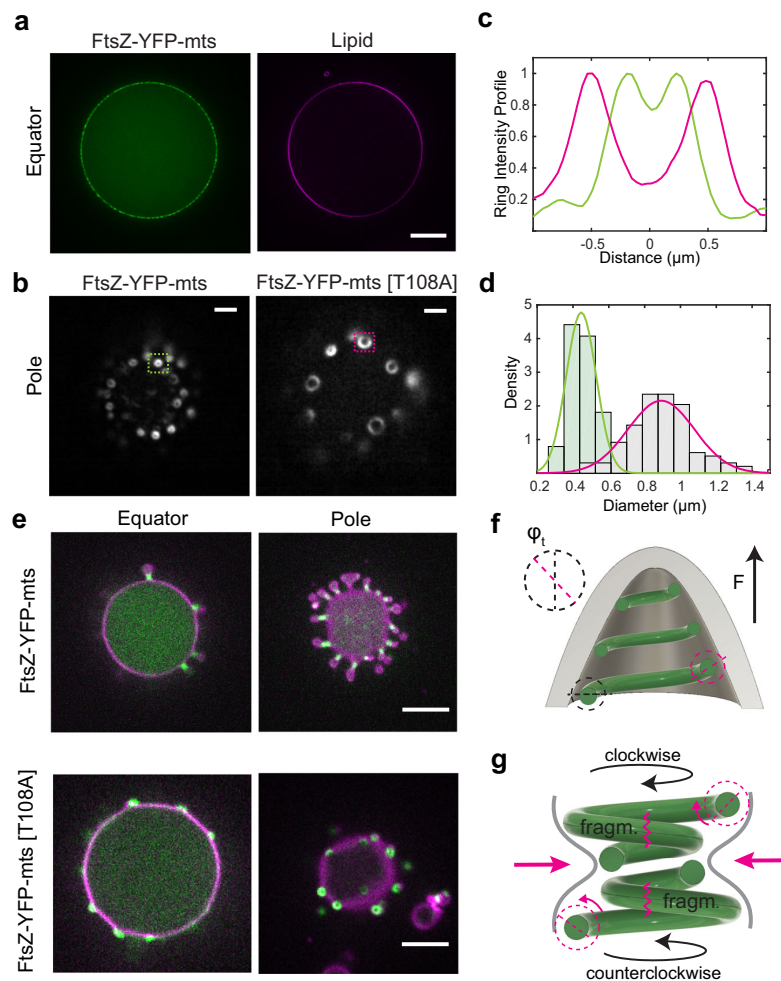


Fig. 5 FtsZ-YFP-mts rings inside deflated GUVs cause membrane deformations that depend on GTPase activity. **a** Representative image of GUVs encapsulating FtsZ ($N > 10$, each condition) (scale bar = $5 \mu\text{m}$). **b** TIRF microscopy imaging of FtsZ-YFP-mts and FtsZ-YFP-mts*[T108A] rings at the bottom-inside GUVs ($N > 10$, each condition) (scale bar = $2 \mu\text{m}$). **c** Intensity profile of structures indicated in **b** showed that FtsZ-YFP-mts (green line) rings exhibit smaller diameter than FtsZ-YFP-mts*[T108A] (magenta line). **d** Size distribution of ($N = 112$) FtsZ-YFP-mts*[T108A] (gray bars and magenta line) and ($N = 102$) FtsZ-YFP-mts showed a drastic reduction in ring diameter due to GTP hydrolysis. **e** After deflation, both mutants yielded outwards deformations. For the case of FtsZ-YFP-mts, $N = 21/26$ (80%) vesicles showed outwards deformations and constriction necks compared to $N = 4/15$ (26%) for FtsZ-YFP-mts*[T108A]. This suggests that GTPase activity promotes constriction and neck formation (scale bar = $5 \mu\text{m}$). **f** We suggest that intrinsic torsion can create out-of-plane forces; however, **g** GTP hydrolysis triggered a super-constricted state favoring higher curvatures. These higher curvatures and membrane deformations cause a mechanical strain on the polymer that promotes fragmentation and then the emergence of clockwise and anticlockwise FtsZ treadmilling filaments.

the membrane attachment direction²³. This twisting angle along the one filament is key to produce torque. A molecular dynamics study showed that dynamin, a helical endocytic constriction protein, required twisting of the “adhesive-stripe” to achieve full membrane hemifusion²³. In the case of FtsZ, molecular dynamics studies have predicted an angle of “twisting” along the c-terminus, where membrane attachment occurs^{24,25}. Also, Fierling et al. have theoretically studied membrane deformations produced by filaments inducing torques²⁶. Strikingly, they found inward vortex-like deformations from flat surfaces and spring-like shapes when filaments wrapped around a tubular geometry²⁶. These predictions agree remarkably well with our observations.

So far, we had investigated an inverse geometry, i.e., FtsZ added from the outside, as compared to the physiological case. Now, we also reconstituted FtsZ-YFP-mts and FtsZ-YFP-mts*[T108A]

inside GUVs (Fig. 5a). Conditions to obtain ring-like structures (Fig. 5b) or filaments wrapping the vesicle (Fig. S1D) were again found by tuning GTP and Mg^{+2} . Interestingly, the diameters of FtsZ-YFP-mts*[T108A] rings were significantly larger ($0.89 \mu\text{m}$) than FtsZ-YFP-mts ($0.44 \mu\text{m}$) (Fig. 5d). This difference was not observed in the case of SLBs³, suggesting that enclosure and deformability of the lipid surface affect the steady state of FtsZ assembly. In addition, the wide size distribution in the low GTPase mutant case (Fig. 5d) might indicate that polymers were more flexible to accommodate a larger variety of curvatures. Strikingly, both FtsZ mutants could create outwards deformations emerging from rings (Fig. 5e). But only in the case of FtsZ-YFP-mts, there was clear evidence of ring constriction (Fig. 5e) in agreement with previous reports¹. Indeed, 80% ($N = 21/26$) vesicles showed outwards deformations and constriction

necks simultaneously; in contrast to 26% for FtsZ-YFP-mts* [T108A].

In view of this data, we suggest that FtsZ ring formation creates outwards out-of-plane forces on deflated GUVs due to filament structure and polarity (Fig. 5f). However, FtsZ filaments only exhibiting structural torsion (low GTPase activity) are unable to stabilize smaller diameters in agreement with long-pitch spring deformations in lipid tubes. In contrast, upon GTP hydrolysis, FtsZ filaments drive constriction and condensation inside deflated GUVs in a similar way to how the same GTPase activity drives spring compression in a tubular geometry when the protein is externally added. This establishes an interesting similarity between FtsZ and dynamin, a motor protein well-known for torsional and contractile features in which GTP hydrolysis triggers a super-constricted state leading to fragmentation and clustering^{27,28}. This similarity let us to hypothesize an alternative explanation for the emergence of FtsZ treadmilling and indicate a possible connection to force generation. While the leading-edge of the filament grows, a significant increase in the torsional stress over the trailing edge of the filament (due to GTP hydrolysis) drastically deforms the membrane, which in turn imposes a mechanical strain on the FtsZ filament. This strain would be highest in the membrane region between two filaments growing against each other (Fig. 5g), promoting fragmentation and bidirectional treadmilling. This also suggests that the physical properties of the membrane (e.g., membrane tension) plays a role in the emergence of FtsZ dynamic-treadmilling patterns.

Although it has been pointed out that these mechanistic studies on FtsZ in controlled membrane environments may not easily be transferred to the situation in vivo, it is tempting to evaluate the ability of FtsZ-YFP-mts construct to deform and actuate lipid membranes in a more physiological setting. Therefore, *E. coli* cells were transformed with a plasmid containing the corresponding gene under control of an inducible promoter. Upon IPTG induction, FtsZ-YFP-mts fluorescence signals in the cells were observed. The FtsZ-YFP-mts construct localizes in several ring-like structures around midcell (Fig. 6a). Multiple Z-ring structures were observed, due to the overexpression of the FtsZ-YFP-mts protein. A 3D-reconstruction reveals that these FtsZ assemblies are indeed ring structures that resemble those formed by native FtsZ rings at the division site (Fig. 6b). Importantly, without addition of inductor, no FtsZ-YFP-mts structures were observed (Fig. 6a). Since FtsZ-driven membrane deformations could not be observed in tensed GUVs (Fig. 5), we reasoned that they were even less likely to appear in walled bacteria with turgor pressure. Therefore, cells were treated with lysozyme to create *E. coli* spheroplasts in osmoprotective media. Cells expressing the FtsZ fusion protein were highly fragile and prone to lysis. We therefore started microscopic analyses before all cells have converted to spheroplasts (Fig. 6a). Importantly, vesicular structures budding out from spheroplasted cells were observed (Fig. 6a, arrows). These vesicular structures were not observed in control cells lacking the FtsZ-YFP-mts expression, indicating that they are a consequence of protein overproduction. However, in the MBL medium, the occurrence of FtsZ-YFP-mts budding was low (Fig. 6a). In contrast, similar lysozyme treatment in sucrose-buffer showed cells with (i) small outwards deformations (irregular surface) that correlate with a regions higher protein density and (ii) swelled cells with clear vesiculation (Fig. 6c and Supplementary Movie S6). A membrane stain confirmed that areas with strong FtsZ fusion protein assemblies displayed lipid membrane budding (Fig. S3) and constriction necks. Although the presence of cells with irregular surfaces (small outwards deformations), single and multiple vesiculation was not exclusive of overexpression, the frequency of such events clearly increased due to FtsZ-YFP-mts (Fig. 6d). Further interesting phenotypes

such as cells connected by lipid tubes or “pearl-necklaces” were observed (Fig. S3). These results agreed remarkably well with our outwards deformations and constriction necks from FtsZ rings inside GUVs. Directional screw-like forces promoting extrusion of lipid material or budding (Figs. 5h and 6b), as well as constriction necks (Figs. 5g and 6c), are both explained in terms of a FtsZ polymer able to exert torsional stress as explained above. Interestingly, this demonstrates the possibility of FtsZ filaments playing an active role in cell division organisms that divide by budding, such as *Acholeplasma laidlawii*²⁹.

In this work, we show that FtsZ filaments can deform lipid membranes via torsional stress due to an intrinsic twist along the FtsZ filament. In addition, we demonstrate that the GTPase activity, which is otherwise responsible for filament treadmilling, enhances this torsional stress promoting further constriction/condensation. As a result of this interaction, FtsZ-YFP-mts rings exert forces in the range of 1 pN upon GTP hydrolysis; directional forces that suffice membrane deformations and constriction/condensation in deflated GUVs as well as wall-less *E. coli* cells. Although this force range might not suffice for the entire process of bacterial cytokinesis of walled rod-like cells, given the temporal relevance of FtsZ dynamics in the coordination of synthesis of new wall material^{5,6}, an initial inwards membrane deformation may be key to trigger cytokinesis in the form of a FtsZ-curvature-trigger. Interestingly, viable FtsZ-GTPase mutants⁶ as well as temperature-sensitive mutants³⁰ exhibit abnormal septum formation or twisted septum. In agreement with our data, GTPase FtsZ-deficient mutants could generate inwards membrane deformations along a helical FtsZ filament. Due to the lack of further twisting/condensation in FtsZ, the synthesis of new wall material would follow a relaxed-helix pattern (twisted septum) rather than a compressed-helix or “ring”. We also hypothesize that if the membrane tension is lowered by incorporation of de novo synthesized lipids¹⁰, the here reported forces range might become relevant for the initiation of cell division.

Methods

Plasmids and primers. Please refer to Supplementary Information (Tables S1 and S2).

Protein purification. FtsZ-YFP-mts*[T108A] mutation was constructed using site-directed mutagenesis. T108A_RV and T108A_FW oligonucleotides were designed using NEBaseChanger-Substitution to replace the Thr in position 108 by an Ala, as described in our previous work³. Briefly, FtsZ-YFP-mts was first amplified using the FW and RV oligonucleotides in different PCR reactions, testing three different temperatures: 54 °C, 58.5 °C, and 65 °C. In a second PCR reaction, the PCR products from the FW and RV oligonucleotides were mixed; also, three different temperatures were tested: 54 °C, 58.5 °C, and 65 °C. After digestion with DpnI, the three PCR products were used to transform CH3-Blue competent cells. Efficient colonies were picked and confirmed by sequencing.

FtsZ-YFP-mts and FtsZ-YFP-mts*[T108A] were purified as described³. Briefly, the protein was expressed from a pET-11b expression vector and transformed into *E. coli* strain BL21. Overexpression was performed at 20 °C for the proteins FtsZ-YFP-mts. Cells were lysed by sonication and separated by centrifugation. Then, protein was precipitated from the supernatant, adding 30% ammonium sulfate and incubating the mixture for 20 min on ice (slow shaking). After centrifugation and resuspension of the pellet, the protein was purified by anion exchange chromatography using a 5 × 5-ml Hi-Trap Q-Sepharose column (GE Healthcare, 17515601). Protein purity was confirmed by SDS-PAGE and mass spectrometry.

Wild-type FtsZ was purified from *E. coli* cells (BL21 strain) using the plasmid pET-28a containing the *E. coli* FtsZ gene as previously described³¹. Briefly, overexpression of wild-type FtsZ was performed at 37 °C for 3 h after induction with IPTG. Cells were lysed, and the soluble fraction was separated by centrifugation. The protein was extracted by two cycles of Ca²⁺-induced precipitation. First, the sample was incubated during 15 min at 30 °C after addition of 1-mM GTP and 20-mM CaCl₂. The sample was centrifuged and resuspended, followed by a second cycle of Ca²⁺-induced precipitation. The protein was then purified by anion exchange chromatography using a 5 × 5-ml Hi-Trap Q-Sepharose column (GE Healthcare, 17515601).

The soluble six-His tags (sZipA) construct of ZipA was produced by elimination of the hydrophobic N-terminal domain (first 25 amino acids) as described previously³². Having the plasmid pET-15ZIP as template DNA, deletion of amino

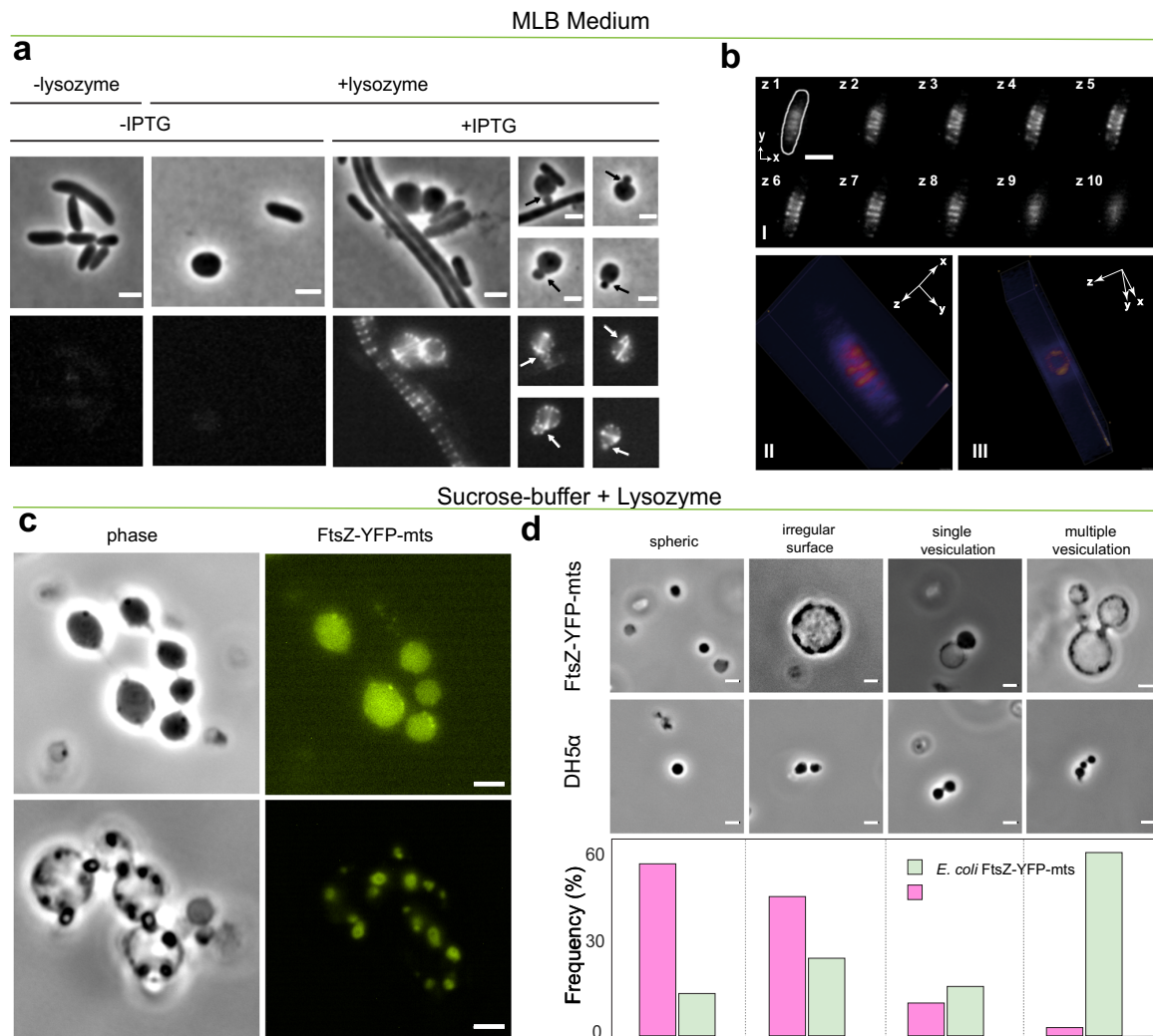


Fig. 6 In wall-less *E. coli* cells, FtsZ-YFP-mts rings exert outward forces causing budding, vesiculation, and constriction necks. **a** *E. coli* DH5α cells expressing FtsZ-YFP-mts show impaired division and a regular fluorescence pattern. Removal of the cell wall by lysozyme treatment leads to spheroplast formation. Occasional membrane vesiculation can be correlated to the localization of FtsZ-YFP-mts (arrows) (scale bar = 2 μm). **b** Upon induction, cells express FtsZ-YFP-mts polymeric structures perpendicular to the cell length, around midcell (bl). 3D rendering reveals ring-like structures (bII–bIII) (scale bar = 2 μm). **c** Attempts to enhance the spheroplasting efficiency (sucrose-buffer) resulted in the emergence of multi vesiculated structures. Points of membrane constriction correlate with presence of FtsZ-YFP-mts. Deformations of the plasma membrane indicate a force generation by FtsZ assemblies that leads to local membrane invaginations and eventually pinching off of vesicles (scale bar = 2 μm). **d** Quantitative morphological classification of induced *E. coli* DH5α *pEKEx2-ftsZ-yfp-mts* cells ($N = 50$ cells) compared to *E. coli* DH5α ($N = 43$ cells), after lysozyme treatment in sucrose-buffer, within the four categories: spheric, irregular surface, single and multiple vesiculation. (Scale bar = 2 μm).

acids was obtained by inverse polymerase chain reaction (PCR) using primers sZipAI and ZipAII. After PCR purification, the product was digested with DpnI, and ligated with T4 DNA ligase. Overexpression of sZipA was induced with IPTG for 3 h at 37 °C in transformed BL21 cells carrying the pET-15ZIP cloning vector. After cell lysis and centrifugation, the soluble fraction was loaded on a 5-mL Ni-NTA resin column (Novagen) and the protein was eluted in buffer containing imidazole. Protein purity was confirmed by SDS-PAGE and mass spectrometry.

Wild-type FtsZ and sZipA were covalently labeled in the amino groups with Alexa Fluor 488 carboxylic acid succinimidyl ester dye (Molecular Probes/Invitrogen) as earlier stated³³.

Imaging chamber for slow evaporation. The imaging chamber (Fig. S4A) was made using—customized size—coverslip glasses (Menzel, Germany) and a PMMA 3-mm height spacer (Fig. 1). The bottom coverslip has 1.5 thickness and 12-mm width. The upper one was 1.0 thickness and 10-mm width. Glued coverslips to the spacer form a two-side-open chamber of ~380-μl volume. Coverslips were cleaned

by immersion in a 50:50 water/ethanol solution followed by 1-min air-plasma cleaning. After this, coverslips were glued to the spacers and passivated for more than 2 h using 5-mg/ml b-casein (Sigma, Germany). Samples are examined for 1 h with a consistent evaporation osmolarity ~50 mOsm per hour under constant humidity and temperature conditions. Examined vesicles were located in the central area of the chamber, fairly distant from the evaporation meniscus.

Confocal spinning disk imaging and optical tweezers setup. Confocal spinning disk imaging was performed using a Yokogawa CSU10-X1 spinning disk system connected to a Nikon Eclipse Ti inverted microscope (Nikon, Japan). A DPSS laser stack with 488, 561, and 640-nm laser lines (3i, Denver, Colorado USA) is used for illumination and an Andor Ixon Ultra 512 × 512 EMCCD camera for fluorescence detection. 3i-Slidebook software controlled lasers, filter selection, microscope, xy stage, and acquisition (3i, Denver, Colorado USA). For simultaneous FtsZ-YFP-mts and ATTO655-DOPE excitation, 488 and 640-nm lasers were rapidly switched by an AOTF. For image detection, the use of an appropriated quad-band filter avoided

mechanical filter switch. Samples were imaged using a CFI Plan Apochromat Lambda 100X oil, NA = 1.45 (Nikon, Japan).

The optical tweezers setup (Fig. S4B) was built according to previous reports^{34,35}. Briefly, a 3W 1064-nm DPSS laser (Cobolt, Sweden) was used as trapping laser. A half-wavelength plate ($\lambda/2$ plate) and a polarizing beam splitter control the laser power entry to the scope. A two-lens telescope expands the laser beam to fill the back aperture of—above mentioned—100 \times objective. In addition, two mirrors adjust the laser-beam xy position. The force detection arm was mounted in the illumination pillar of the microscope, collecting (from above) the light from the laser using a—long working distance—condenser 20X, NA = 0.6 (Edmund optics, USA). A micrometric xyz stage positions the condenser (and the detection arm) in $-z$ to achieve Köhler illumination and $-xy$ - for centering. For alignment, once the proper laser axis has been defined, the position of field diaphragm (having Köhler illumination) is imaged through an auxiliary camera DCC3240M (Thorlabs, USA) on the right port of the microscope. Using camera software options, a drawing masking the field diaphragm was saved in a file. This drawing can be reused in such a way that the drawing overlays the real-time camera acquisition. Therefore, xyz knobs are moved to position the field diaphragm according to the drawing mask.

In the detection arm, a relay lens imaged the back focal plane of the condenser in a quadrant positional detector (QPD) PDQ80A (Thorlabs, USA). The signal voltage of the QPD defined the position of the trapped bead. The force detection module OTKBFM (Thorlabs, USA) was used for data acquisition. This DAQ acquired a voltage signal from the QPD at a maximum rate of 100 kHz. In addition, this module was customized to control a 20×20 - μm range LT2 piezoelectric stage (Piezoelectric, France) using an analog signal (1–10 V). Position calibration and trap-stiffness determination was performed using the OTKBFM software (Thorlabs, USA). To calibrate position, beads were attached to a clean glass coverslip in high salt medium (1-M NaCl). Here, the streptavidin-coated beads have a mean diameter of 1.71 μm (Spherotech, USA). The laser beam is focused over one bead. The xy position of the bead, relative to laser beam, was adjusted using the piezo stage to maximize the signal in QPD. Similarly, the focus $-z$ - position of the laser beam was adjusted to maximize QPD output. Then, the piezo stage was moved 4×4 - μm xy and changes in QPD signal were recorded. From the typical “s-shape” response curve, a straight line was fitted representing the volts to μm conversion. The trap stiffness was determined using the power-spectrum analysis. Using this, the frequency corner of a xy Brownian motion subjected to a trapping potential was fitted from data. The stiffness of the trap was measured over different laser powers to determine the linear range. All experiments are performed at the same laser power of 200 mW (before objective) with a 1.66-V/ μm conversion and a trap stiffness of 74.4 ± 2.5 pN/ μm . Experiment acquisition was performed using a Matlab script controlling the OTKBFM. This Matlab script set (for 60 s) an oscillatory motion for the piezo stage with an amplitude of 3 μm and a frequency of 1 Hz. In parallel, QPD data were acquired at a rate of 10 kHz.

FtsZ rings reconstitution in vesicles

FtsZ externally added to vesicles and tube experiments with force detection. GUVs were produced using electro-swellings. *E. coli* lipid extract was dissolved in chloroform to reach a final concentration of 3 mg/ml. To image lipids in the red channel, 0.05% (mol) of ATTO655-DOPE (ATTO-Tech GmbH, Germany) was added to the lipid mixture. In addition, 0.15% of DSPE-PEG (2000) Biotin (Avanti, AL, United States) was also added to achieve binding between GUVs and streptavidin-coated beads. For experiments with Wt-FtsZ, 0.5% DGS-NTA lipids were also added to enable the attachment of sZipA protein. In our home-made Teflon chambers, three drops (~1 μl) were carefully seeded in Pt wires and rapidly air-dried. After 1-h vacuum of further chloroform drying, GUVs were swelled in 250-mOsm sucrose solution at 10 Hz for 2 h and 2 Hz for 1 additional hour (detachment). Lipid concentration and electroformation times were carefully optimized to guarantee an appropriated GUV yield. Furthermore, to obtain similar GUV-lipid concentrations, two identical chambers underwent same procedure and mixed afterwards.

GUVs were mixed in buffer (120-mM KCl, 20-mM Tris-HCl, and 1.5-mM MgCl₂ pH 7.5) with an osmolarity of 250 mOsm. In details, 4 μl of GUVs were highly diluted in 360 μl of buffer in a reaction tube. FtsZ-YFP-mts and FtsZ-YFP-mts*[T108A] were added to reach a final concentration around 0.07 μM . For experiments with Wt-FtsZ and sZipA, the same procedure was used adding first sZipA at around 0.2 μM followed by addition of FtsZ reaching ~0.8 μM supplemented with ~0.2- μM wt-FtsZ-Alexa 488. In both cases, polymerization is triggered by adding 1.25 mM of GTP (Sigma, Germany). Flaccid vesicles with FtsZ rings and inward deformation were observed after 20 min. On these vesicles, tubes were pulled and imaged for 10 min (1 fps) in two colors: FtsZ-YFP-mts/wt-FtsZ-Alexa 488 and lipid channel. This time was enough to obtain helical deformations and reach a steady state of protein entering the tube, at least for FtsZ-YFP-mts. Right after, force measurements (oscillations) were performed for 60 s. Experiments with pulled tubes longer than 10 min were prone to display contamination on the “force channel” (beads, small vesicles, and protein clusters were attracted to the trapping bead). This made force measurements with FtsZ-YFP-mts*[T108A] difficult since the timescale of deformation was significantly longer. To analyze pitch, $N = 12$ experiments for FtsZ-YFP-mts and $N = 10$ for FtsZ-YFP-mts*[T108A] were analyzed.

To measure forces and estimating spring constants, we used the oscillation mode as described above. Force experiments were carried out in tubes without protein to be contrasted to experiments with FtsZ-YFP-mts and helical deformations. As mentioned above, data were acquired in Matlab (Mathworks, USA) and signal amplitude determined by the amplitude of the FFT (Fast Fourier transformation) at 1 Hz. Then, these values are converted to force using volts/ μm conversion and the trap stiffness and further divided by the oscillation amplitude ($A = 3$ μm). To guarantee high/full protein coverage of the tube in FtsZ force experiments, we increased the protein sample concentration to 0.08–0.09 μM . To characterize single FtsZ ring brightness, we imaged vesicle (outside FtsZ) rings that have flattened over the glass surface. Using same light conditions as used for tube experiments, the brightness of FtsZ rings of $N = 421$ rings was analyzed and plotted (Fig. S2E).

FtsZ encapsulated in lipid vesicles. FtsZ encapsulating vesicles were produced using droplet emulsion transfer³⁶. Lipid composition was EggPC/DOPG 80:20 (Avanti, AL, United States) with 0.05% mol ATTO655-DOPE (ATTO-Tech GmbH, Germany). Briefly, vacuum-dried lipids were dissolved in mineral oil (Sigma, Germany) to reach a final concentration of 0.5 mg/ml. To form lipid vesicles, two interfaces are required: outer and inner interface. In a reaction tube (A), 500 μl of lipid + oil mixture was added to 500 μl of outer buffer (150 KCl 50-mM Tris-HCl pH 7.5). At the oil–water interface, a lipid monolayer was assembled after 30 min. In a second reaction tube, 15 μl of protein master mix was added 500 μl of lipid + oil and vigorously vortexed for 2 min to obtain a homogenous cloudy emulsion. The inner monolayer was rapidly formed (~2 min). This protein master mix was composed of inner buffer (125-mM KCl, 25-mM Tris-HCl, 2-mM MgCl₂ pH 7.5), 20% OptiPrep (Density Gradient Medium, Sigma, Germany), protein and GTP. FtsZ-YFP-mts (or FtsZ-YFP-mts*[T108A]) and GTP final concentrations were 1.65 μM and 1.4 mM, respectively. Therefore, the emulsion was transferred to the reaction tube (A) and centrifuged at 100 g for 7 min. Finally, the oil-based supernatant is discarded and 300- μl final vesicles are 1:2 or 1:3 diluted in fresh outer buffer.

Image analysis. Image analysis and plotting were carried out in MATLAB (MathWorks, USA) and ImageJ (NIH, USA).

To generate kymographs (Fig. 1), a script allows the user to define a circular section by providing two coordinates such as described in reference³. This circular section is automatically fitted to a circle with radius r (in this case, $r = 0.5$ μm). Then, three trajectories corresponding to three concentric circles having radii r , $r + 1$, and $r - 1$ pixels are determined. At this point, the script read the time-series data and calculate a kymograph for each time point and trajectory. The final kymograph corresponds to the average of the three different trajectories³.

To determine tube diameter (Fig. S2A), the intensity over a representative tube section was normalized to be fitted to a Gaussian function. Then, the here reported diameter represented half-width of the Gaussian. To quantify the arclength (helical shapes projection to an 2D image), tubes were binarized and fitted to a function using linear interpolation (Fig. 3). Then, the arclength of the function was calculated. The protein density was calculated by measuring, over the tube, the FtsZ-intensity difference between initial and final acquisition. This difference was divided by the FtsZ intensity on the GUV (in the tube proximity) times the tube length.

To measure the pitch in the spring-like tubes (Fig. 3), a Gaussian filter was applied. The tube red-lipid-intensity profile was integrated and normalized, in a perpendicular direction (to the tube), to find the pixel position where the normalized intensity was “1” and closer to “0.3”. The 1 (maximum) position pixel defined the center of the tube while “0.3” defined the upper and lower limit of the tube. The intensity profile, now in parallel direction to the tube, was plotted for these three locations: up, center, and down. Using this intensity profile, peaks are automatically found and then pitch was calculated. Every experiment is manually inspected to avoid miscalculation.

To measure the size distribution of FtsZ encapsulated rings (Fig. 5), TIRF imaging was used according to our previous work³. The diameter was manually measured using intensity profile in ImageJ (NIH, USA). Diameters were exported and plotted in MATLAB. For both protein mutants, the number of analyzed rings was $N > 100$.

In vivo assays, spheroplasts generation, and imaging. For overexpression of FtsZ-YFP-mts in *E. coli* cells, the respective DNA sequence was amplified by PCR using oligonucleotides SacI-mts and SalI-fsZ, respectively. The pET-11b-fsZ-yfp-mts plasmid served as template DNA. The resulting PCR product was ligated into SacI/SalI opened pEKEx2-vector. The final plasmid pEKEx2-fsZ-YFP-mts was transformed into competent *E. coli* DH5 α cells.

E. coli cells expressing FtsZ-YFP-mts were cultured in osmoprotective MLB-medium (1% peptone, 0.5% yeast extract, 1-mM CaCl₂, 30-mM glucose, 25-mM MOPS (pH 7.2), 340-mM NaCl)³⁷. Plasmid maintenance was ensured by addition of 25- $\mu\text{g/ml}$ kanamycin and cultures were incubated at 37 $^{\circ}\text{C}$ with constant shaking (120 rpm). Expression was induced by adding 100- μM IPTG. The formation of spheroplasts was induced by addition of 0.5-mg/ml lysozyme, followed by an incubation of 30 min at 37 $^{\circ}\text{C}$. For microscopy, a 0.1% agarose-pad in MLB medium was used.

In order to improve spheroplasting efficiency, an adaptation of the method described in ref. ³⁸ was used. Therefore, single colonies were picked and cultivated

overnight in 10-ml LB-medium (10-g/l tryptone, 5-g/l yeast extract, and 10-g/l NaCl), using environmental conditions like described above. The next day 200 μ l of the overnight culture were used to inoculate the respective over day culture. For the mutant, kanamycin (25 μ g/ml) was used in both pre-cultures, induction with IPTG was performed on the over day culture only. After 4 h, 1 ml of exponentially growing cells was harvested at 3000 g for 1 min. The pellet was gently resuspended in 0.8-M sucrose, together with 30- μ l Tris-HCl (pH 8.0), 24- μ l 0.5-mg/ml lysozyme, 6- μ l 5-mg/ml DNaseA and 6- μ l EDTA-NaOH (pH 8.0) and incubated for 5 min at room temperature. One hundred microliter of a STOP solution (10-mM Tris-HCl (pH 8.0), 0.7-M sucrose, and 20-mM MgCl₂) were added to complex-free EDTA. For one replicate, phospholipid membranes were stained for 5 min with 1- μ g/ml Nile red (Invitrogen). For microscopy, 2 μ l of the suspension were directly applied on the sample slide with a cropped pipet-tip and covered with a high-precision coverslip.

Fluorescence and phase contrast imaging for in vivo studies were performed on a Zeiss Axio Imager M1 microscope equipped with an immersion condenser, a 2.5x optovar and an EC Plan Neofluar 100x/1.3 Oil Ph3 objective (Zeiss). YFP fluorescence was imaged using filterset 46 HE shift free (EX BP 500/25, BS FT 515, EM BP 535/30), and Nile red fluorescence was detected with filter 43 HE Cy 3 shift free (EX BP 550/25, BS FT 570, EM BP 605/70). Image acquisition was carried out using the AxioVision software-package (Zeiss). For image analysis, Fiji was used³⁹.

Reporting summary. Further information on research design is available in the Nature Research Reporting Summary linked to this article.

Data availability

All other data and materials supporting this publication are available from the corresponding author upon reasonable request. Source data are provided with this paper.

Code availability

Custom code has been deposited in https://github.com/diegoalejandrord/FtsZ_Torsion_NatComm (<https://doi.org/10.5281/zenodo.4695237>)⁴⁰.

Received: 11 October 2020; Accepted: 27 April 2021;

Published online: 03 June 2021

References

- Osawa, M., Anderson, D. E. & Erickson, H. P. Reconstitution of contractile FtsZ rings in liposomes. *Science* **320**, 792–794 (2008).
- Osawa, M. & Erickson, H. P. Liposome division by a simple bacterial division machinery. *PNAS* **110**, 11000–11004 (2013).
- Ramirez-Diaz, D. A. et al. Treadmilling analysis reveals new insights into dynamic FtsZ ring architecture. *PLoS Biol.* **16**, e2004845 (2018).
- Loose, M. & Mitchison, T. J. The bacterial cell division proteins FtsA and FtsZ self-organize into dynamic cytoskeletal patterns. *Nat. Cell Biol.* **16**, 38–46 (2014).
- Bisson-Filho, A. W. et al. Treadmilling by FtsZ filaments drives peptidoglycan synthesis and bacterial cell division. *Science* **355**, 739–743 (2017).
- Yang, X. et al. GTPase activity-coupled treadmilling of the bacterial tubulin FtsZ organizes septal cell wall synthesis. *Science* **355**, 744–747 (2017).
- Holden, S. Probing the mechanistic principles of bacterial cell division with super-resolution microscopy. *Curr. Opin. Microbiol.* **43**, 84–91 (2018).
- Coltharp, C. & Xiao, J. Beyond force generation: why is a dynamic ring of FtsZ polymers essential for bacterial cytokinesis? *BioEssays* **39**, e201600179 (2017).
- Lan, G., Wolgemuth, C. W. & Sun, S. X. Z-ring force and cell shape during division in rod-like bacteria. *PNAS* **104**, 16110–16115 (2007).
- Osawa, M. & Erickson, H. P. Turgor pressure and possible constriction mechanisms in bacterial division. *Front. Microbiol.* **9**, 111 (2018).
- Roux, A. et al. Membrane curvature controls dynamin polymerization. *PNAS* **107**, 4141–4146 (2010).
- Krupka, M., Sobrinos-Sanguino, M., Jiménez, M., Rivas, G. & Margolin, W. *Escherichia coli* ZipA organizes FtsZ polymers into dynamic ring-like protofilament structures. *mBio* **9**, e01008–e01018 (2018).
- Bassereau, P., Sorre, B. & Lévy, A. Bending lipid membranes: experiments after W. Helfrich's model. *Adv. Colloid Interface Sci.* **208**, 47–57 (2014).
- Broedersz, C. P. & MacKintosh, F. C. Modeling semiflexible polymer networks. *Rev. Mod. Phys.* **86**, 995–1036 (2014).
- Turner, D. J. et al. The mechanics of FtsZ Fibers. *Biophys. J.* **102**, 731–738 (2012).
- Huecas, S. et al. Energetics and geometry of FtsZ polymers: nucleated self-assembly of single protofilaments. *Biophys. J.* **94**, 1796–1806 (2008).
- Picas, L., Rico, F. & Scheuring, S. Direct measurement of the mechanical properties of lipid phases in supported bilayers. *Biophys. J.* **102**, L01–L03 (2012).
- Rawicz, W., Olbrich, K. C., McIntosh, T., Needham, D. & Evans, E. Effect of chain length and unsaturation on elasticity of lipid bilayers. *Biophys. J.* **79**, 328–339 (2000).
- Gittes, F., Mickey, B., Nettleton, J. & Howard, J. Flexural rigidity of microtubules and actin filaments measured from thermal fluctuations in shape. *J. Cell Biol.* **120**, 923–934 (1993).
- van Mameren, J., Vermeulen, K. C., Gittes, F. & Schmidt, C. F. Leveraging single protein polymers to measure flexural rigidity. *J. Phys. Chem. B.* **113**, 3837–3844 (2009).
- Szwedziak, P., Wang, Q., Bharat, T. A. M., Tsim, M. & Löwe, J. Architecture of the ring formed by the tubulin homologue FtsZ in bacterial cell division. *eLife* **3**, e04601 (2015).
- Arumugam, S. et al. Surface topology engineering of membranes for the mechanical investigation of the tubulin homologue FtsZ. *Angew. Chem. Int. Ed.* **51**, 11858–11862 (2012).
- Pannuzzo, M., McDargh, Z. A. & Deserno, M. The role of scaffold reshaping and disassembly in dynamin driven membrane fission. *eLife* **7**, e39441 (2018).
- Salas, P. G. de P. et al. Torsion and curvature of FtsZ filaments. *Soft Matter* **10**, 1977–1986 (2014).
- Hsin, J., Gopinathan, A. & Huang, K. C. Nucleotide-dependent conformations of FtsZ dimers and force generation observed through molecular dynamics simulations. *PNAS* **109**, 9432–9437 (2012).
- Fierling, J., Johner, A., Kulić, I. M., Mohrbach, H. & Müller, M. M. How bio-filaments twist membranes. *Soft Matter* **12**, 5747–5757 (2016).
- Colom, A., Redondo-Morata, L., Chiaruttini, N., Roux, A. & Scheuring, S. Dynamic remodeling of the dynamin helix during membrane constriction. *PNAS* **114**, 5449–5454 (2017).
- Takeda, T. et al. Dynamic clustering of dynamin-amphiphysin helices regulates membrane constriction and fission coupled with GTP hydrolysis. *eLife* **7**, e30246 (2018).
- Gao, Y. *Cell Division in Walled Bacillus Subtilis and Cell Wall-lacking Acholeplasma Laidlawii*. PhD thesis, University of Amsterdam (2019).
- Addinall, S. G. & Lutkenhaus, J. FtsZ-spirals and -arcs determine the shape of the invaginating septa in some mutants of *Escherichia coli*. *Mol. Microbiol.* **22**, 231–237 (1996).
- Rivas, G. et al. Magnesium induced linear self-association of the FtsZ bacterial cell division protein monomer. The primary steps for FtsZ assembly. *J. Biol. Chem.* **275**, 11740–11749 (2000).
- Martos, A. et al. Characterization of self-association and heteroassociation of bacterial cell division proteins FtsZ and ZipA in solution by composition gradient-static light scattering. *Biochemistry* **49**, 10780–10787 (2010).
- González, J. M. et al. Essential cell division protein FtsZ assembles into one monomer-thick ribbons under conditions resembling the crowded intracellular environment*. *J. Biol. Chem.* **278**, 37664–37671 (2003).
- Lee, W. M., Reece, P. J., Marchington, R. F., Metzger, N. K. & Dholakia, K. Construction and calibration of an optical trap on a fluorescence optical microscope. *Nat. Protoc.* **2**, 3226–3238 (2007).
- Neuman, K. C. & Block, S. M. Optical trapping. *Rev. Sci. Instrum.* **75**, 2787–2809 (2004).
- Pautot, S., Frisken, B. J. & Weitz, D. A. Production of unilamellar vesicles using an inverted emulsion. *Langmuir* **19**, 2870–2879 (2003).
- Osawa, M. & Erickson, H. P. Y. L form bacteria growth in low-osmolality medium. *Microbiology* **165**, 842–851 (2019).
- Renner, L. D. & Weibel, D. B. Cardiolipin microdomains localize to negatively curved regions of *Escherichia coli* membranes. *PNAS* **108**, 6264–6269 (2011).
- Schindelin, J. et al. Fiji: an open-source platform for biological-image analysis. *Nat. Methods* **9**, 676–682 (2012).
- Ramirez-Diaz, D. A. FtsZ induces membrane deformations via torsional stress upon GTP hydrolysis. <https://doi.org/10.5281/zenodo.4695237> (2021). [diegoalejandrord/FtsZ_Torsion_NatComm](https://doi.org/10.5281/zenodo.4695237)

Acknowledgements

We acknowledge Sven Vogel, Allen Liu, and Ethan Garner and for very useful discussions in addition to Rudy Mendez and Sophie Dvali for experimental help. We thank to Daniela Garcia, Ana Raso, and the MPIB Core Facility for assistance in FtsZ-YFP-mts protein purification. This work was funded through MaxSynBio (MPG together with Federal Ministry of Education and Research of Germany) Grant Number 031A359A to P.S., and the Transregio CRC 174 by the DFG (Deutsche Forschungsgemeinschaft) to P.S. and M.B. Work at GR Lab was supported by Spanish Government Grants BFU2016-75471-C2-1-P and 2019AEP088.

Author contributions

D.A.R.-D. and P.S. conceived this study and wrote the manuscript with the support of M.B. for the in vivo spheroplasts section. D.A.R.-D. designed, performed, and analyzed all experiments with FtsZ-YFP-mts and FtsZ-YFP-mts*[T108A]. A.M.-S. designed, performed, and analyzed experiments with ZipA + FtsZ using proteins provided by G.R.

M.H. manufactured wafer for microstructures and provided PMDS microstructures. M.B. and F.M. designed, performed, and analyzed in vivo spheroplasts experiments. MATLAB custom scripts for data acquisition and analysis were coded by D.A.R.-D. All authors discussed and interpreted results and revised the manuscript.

Funding

Open Access funding enabled and organized by Projekt DEAL.

Competing interests

The authors declare no competing interests.

Additional information

Supplementary information The online version contains supplementary material available at <https://doi.org/10.1038/s41467-021-23387-3>.

Correspondence and requests for materials should be addressed to P.S.

Peer review information *Nature Communications* thanks the anonymous reviewers for their contribution to the peer review of this work. Peer reviewer reports are available.

Reprints and permission information is available at <http://www.nature.com/reprints>

Publisher's note Springer Nature remains neutral with regard to jurisdictional claims in published maps and institutional affiliations.



Open Access This article is licensed under a Creative Commons Attribution 4.0 International License, which permits use, sharing, adaptation, distribution and reproduction in any medium or format, as long as you give appropriate credit to the original author(s) and the source, provide a link to the Creative Commons license, and indicate if changes were made. The images or other third party material in this article are included in the article's Creative Commons license, unless indicated otherwise in a credit line to the material. If material is not included in the article's Creative Commons license and your intended use is not permitted by statutory regulation or exceeds the permitted use, you will need to obtain permission directly from the copyright holder. To view a copy of this license, visit <http://creativecommons.org/licenses/by/4.0/>.

© The Author(s) 2021

Supplement to publication P3

Reprinted with permission from:

Ramirez-Diaz, D. A., **Merino-Salomón, A.**, Meyer, F., Heymann, M., Rivas, G., Bramkamp, M. and Schwille, P. (2021). FtsZ induces membrane deformations via torsional stress upon GTP hydrolysis. *Nature Communications* 12, 3310.

Source online: <https://doi.org/10.1038/s41467-021-23387-3>

FtsZ induces membrane deformations via torsional stress upon GTP hydrolysis.

Authors: Diego A. Ramirez-Diaz^{1,2}, Adrian Merino-Salomon^{1,3}, Fabian Meyer⁴, Michael Heymann^{1,5}, German Rivas⁶, Marc Bramkamp⁴ & Petra Schwille^{1*}.

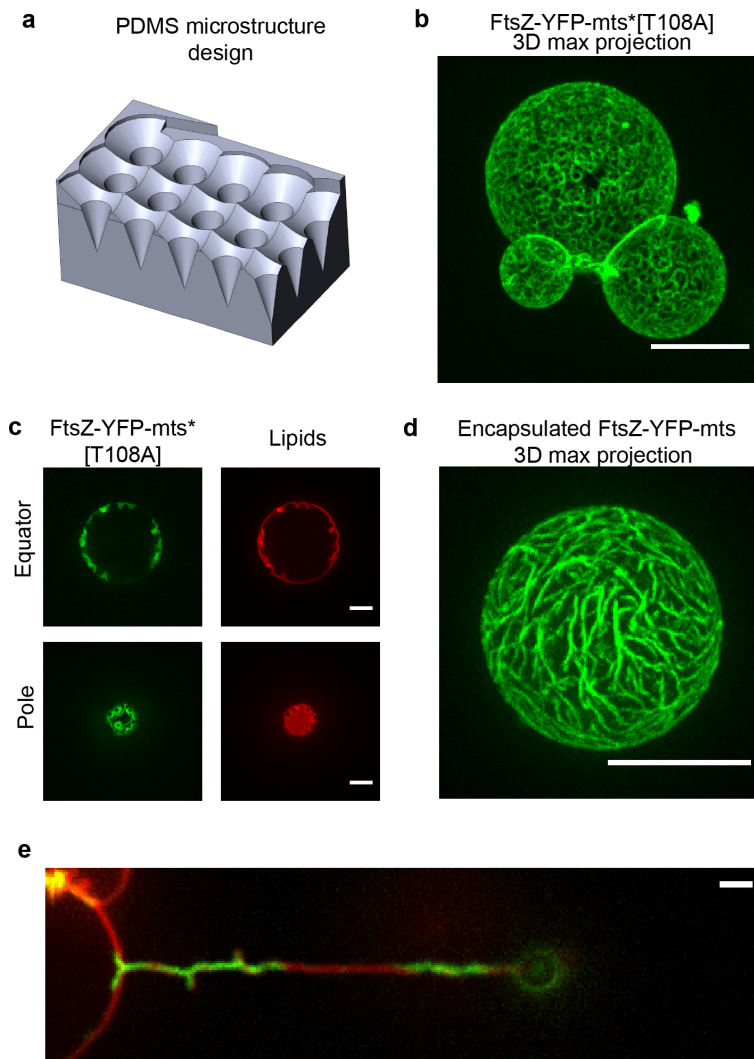
Supplementary Materials

This pdf contains:

Fig. S1 to S4

Supplementary Table 1-2 (Cloning vectors and primers)

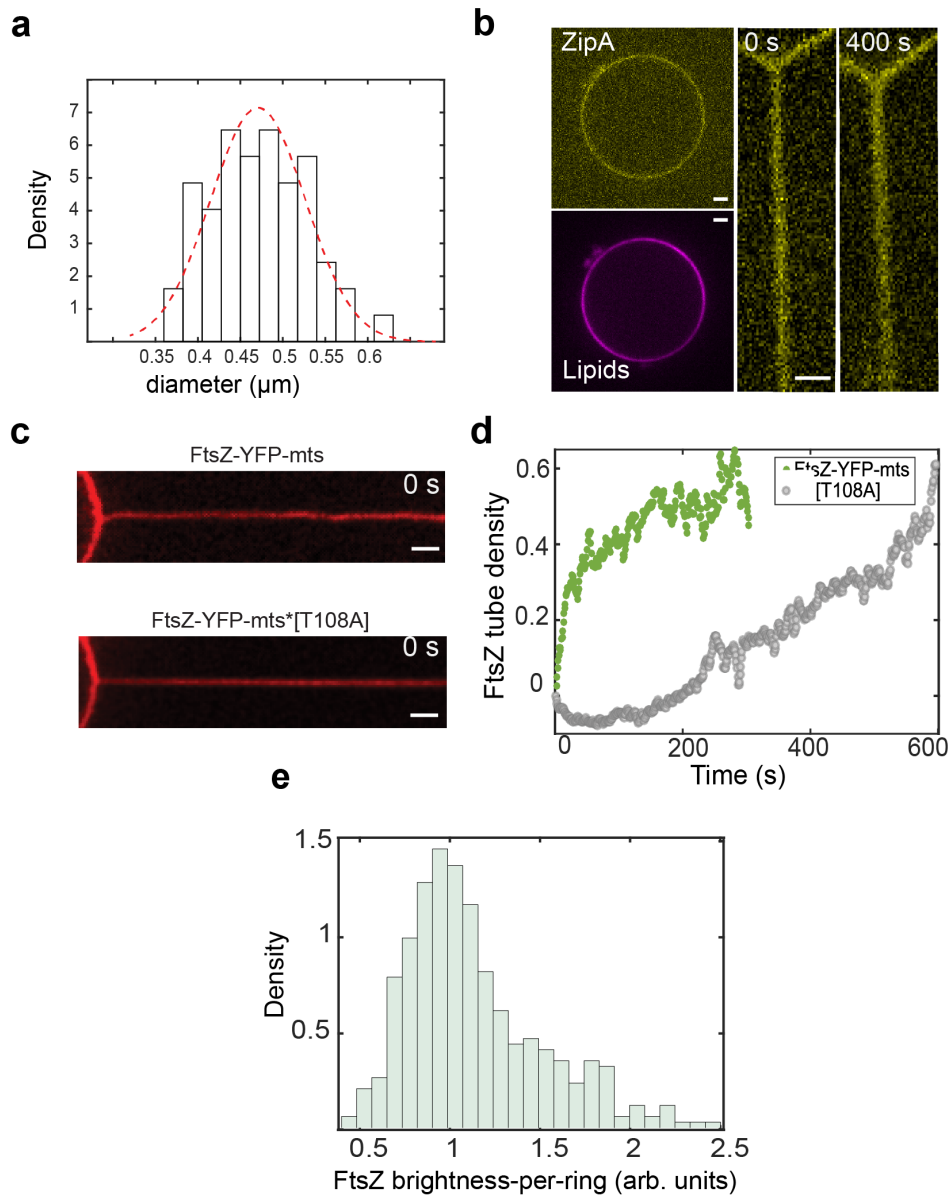
Fig. S1.



Design of microstructure, FtsZ-YFP-mts*[T108A] deformations, high density encapsulated FtsZ-YFP-mts and FtsZ-YFP-mts supercoiling, a) 3D sketch of the PMDS microstructure with inwards cone-like shapes. b) FtsZ-YFP-mts*[T108A] also self-assembled into ring-like structures on GUVs (GUVs:N>20) (Scale bar = 10 μ m). c) After deflation, FtsZ-YFP-mts*[T108A] induced inwards conical deformations emerging from before mentioned rings (GUVs:N>20) (Scale bar = 2 μ m). d) By encapsulating FtsZ-YFP-mts in GUVs, Mg⁺² and GTP content-conditions were fine-tuned to obtain either ring structures (Fig. 5) or nematic phases at a higher membrane protein density (GUVs:N>10) (Scale bar = 10 μ m). e) FtsZ-YFP-

mts torsion over lipid tubes can be found in (less frequent) experiments displaying plectonic/supercoiled regions (N=2). (Scale bar = 2 μm).

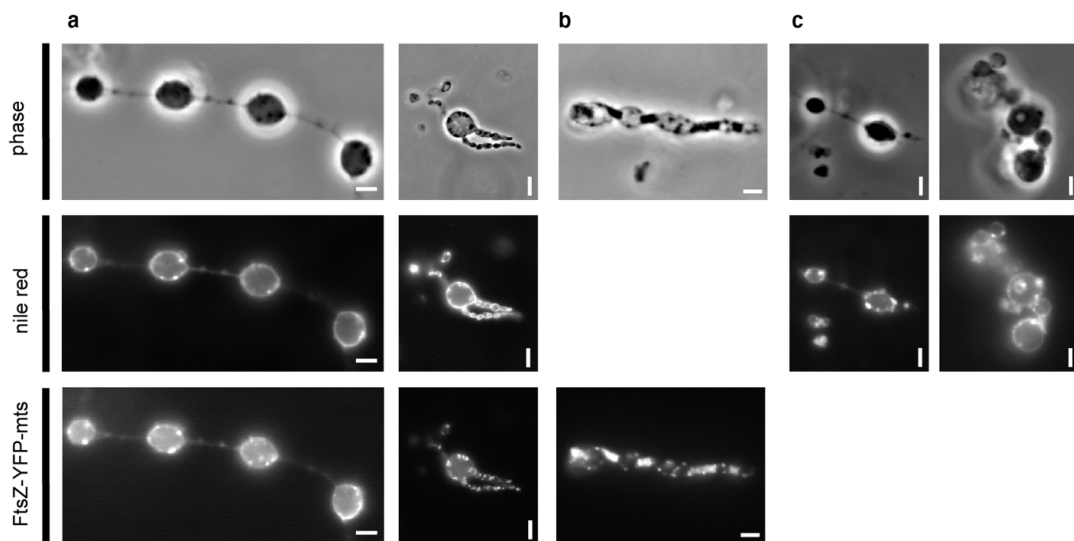
Fig. S2.



Tube diameter distribution, ZipA control experiments and ring-unit-brightness distribution. a) The diameter distribution (N=55) showed a Gaussian distribution with a mean of 0.47 μm . This implied that membrane tensions equivalent to this mean (\pm std) were highly

frequent despite of precise control on the vesicle membrane tension. b) Vesicles decorated with ZipA and imaged under deflation conditions exhibited no deformations (GUVs:N=14). In addition, we examined lipid tubes only coated with siZipA-Alexa 488. No deformations (N=10) were observed in the range of 400-600 seconds. c) Similar initial lipid tube diameter (0.44 μm) for experiments shown in Figure 3 a-b d) For experiments shown in Fig. 3 a-b, FtsZ-YFP-*mts* entered rapidly to the lipid tube while the mutant without GTPase activity (slower). e). Distribution of FtsZ brightness-per-ring (N=412 analyzed rings). The distribution's mode value was chosen as the value for FtsZ brightness-per-ring. (Scale bar = 2 μm).

Fig. S3.



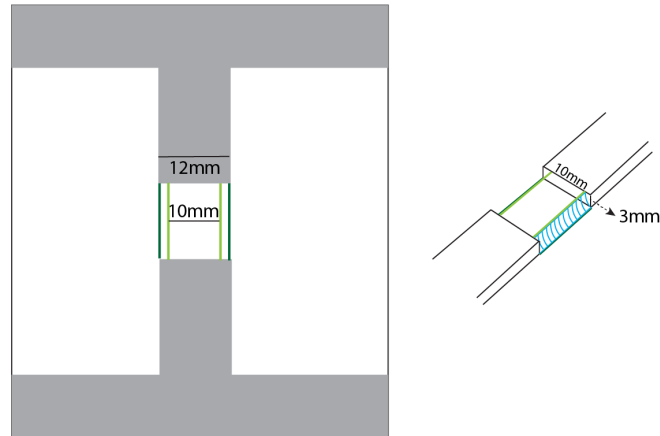
Observed phenotypes of *E. coli ftsZ-YFP-mts* after lysozyme treatment in sucrose-buffer.

The first columns in a, b & b show a pearl necklace like appearance of the cells, while the second column in b might show an earlier stage of this chaining type of vesiculation. Nile red was used to prove that the observed vesicles and tubular connections are actually phospholipid-membranes. As a control unstained cells b) and stained cells c) were also imaged separately in

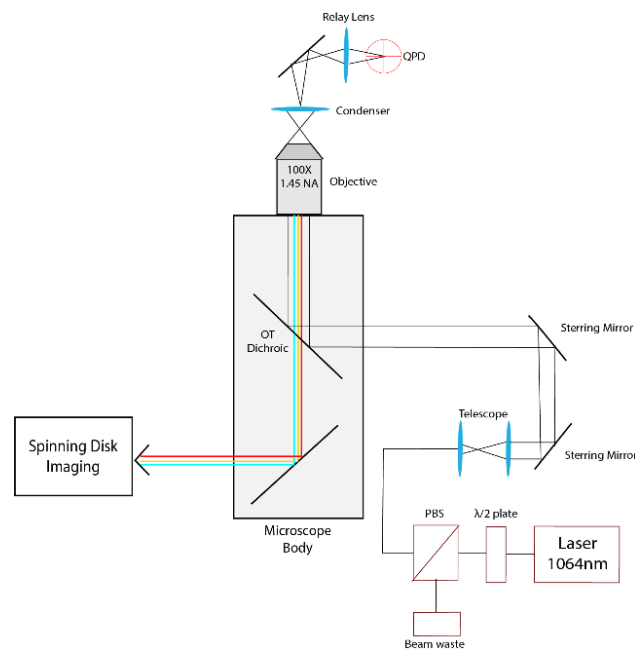
the respective channel. Example micrographs from (N=3) biological replicates. (scale bar = 2 μ m).

Fig. S4

a



b



Drawing for the experiment chamber and optical trapping device a) Sketch of imaging chamber for deflated vesicle preparation. b) Optical tweezers setup layout.

Supplementary Table 1: Cloning Vectors

Vector	Protein	Source/reference
pET-11b	FtsZ-YFP-mts	gifted by Harold Erickson, Ref. 1
pET-11b	FtsZ-YFP-mts*[T108A]	Ref. 3
pET-28a	FtsZ-WT	Ref. 31
pET-15ZIP	sZipA	Ref. 32
pEKEx2	FtsZ-YFP-mts	This publication

Supplementary Table 2: Primers

Name	Sequence 5' – 3'
T108A_RV	GGTGGTGGTGCCGGTACAGGT
T108A_FW	ACCTGTACCGGCACCACCACC
sZipAI	CATATGGCTGCCGCGCG
sZipAII	ACCAGCCGTAAAGAACG
SalI-ftsZ	CATGTCGACATGTTTGAACCAATGGAACCTACC
SacI-mts	CATGAGCTCTTATCCTCCGAACAAGCG

3.4 Publication P4

***In vitro* assembly, positioning and contraction of a division ring in minimal cells**

Summary:

In this publication, we demonstrate the full *in vitro* reconstitution of the *E. coli* MinCDE system within lipid vesicles to construct a machinery for autonomous self-division. The system consists of five proteins (MinCDE, ftsA and FtsZ) and shows the following events in real-time: assembly of an isotropic filamentous FtsZ network, condensation into a ring-like structure, pole-to-pole mode selection leading to equatorial positioning, and onset of ring constriction.

Reprinted with permission from:

Kohyama, S.*, **Merino-Salomón, A.*** and Schwille, P. (2022). *In vitro* assembly, positioning and contraction of a division ring in minimal cells. Nature Communications 13:6098.

Source online: <https://doi.org/10.1038/s41467-022-33679-x>



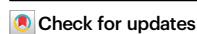
In vitro assembly, positioning and contraction of a division ring in minimal cells

Received: 21 January 2022

Shunshi Kohyama^{1,2}, Adrián Merino-Salomón^{1,2} & Petra Schwille¹✉

Accepted: 27 September 2022

Published online: 15 October 2022



Constructing a minimal machinery for autonomous self-division of synthetic cells is a major goal of bottom-up synthetic biology. One paradigm has been the *E. coli* divisome, with the MinCDE protein system guiding assembly and positioning of a presumably contractile ring based on FtsZ and its membrane adaptor FtsA. Here, we demonstrate the full in vitro reconstitution of this machinery consisting of five proteins within lipid vesicles, allowing to observe the following sequence of events in real time: 1) Assembly of an isotropic filamentous FtsZ network, 2) its condensation into a ring-like structure, along with pole-to-pole mode selection of Min oscillations resulting in equatorial positioning, and 3) onset of ring constriction, deforming the vesicles from spherical shape. Besides demonstrating these essential features, we highlight the importance of decisive experimental factors, such as macromolecular crowding. Our results provide an exceptional showcase of the emergence of cell division in a minimal system, and may represent a step towards developing a synthetic cell.

Constructing a fully synthetic cell from defined biological molecules is one of the great aims of bottom-up synthetic biology^{1–5}. Of the many essential features of cells, such as metabolism, replication, and interaction with the environment, cell division is probably the most tangible goal to be reached with a basic set of functional components, owing to the successful reconstitution and thorough mechanistic understanding of many division-related protein machineries^{6–8}. One of the most advanced systems in this respect is the division machinery of the bacterium *Escherichia coli*^{9,10}. In *E. coli* cells, three Min proteins called MinC, MinD, and MinE constitute a reaction-diffusion system that exhibits temporal oscillations between cell poles, so-called Min waves, generating a protein gradient that forms its maxima at the cell poles and minimum at mid-cell^{11,12}. This protein gradient spatially regulates depolymerization of the division ring protein FtsZ, targeting proto-ring filaments to the middle of the cell by anchoring them to the membrane through FtsA and ZipA proteins, constructing a primary division ring known as FtsZ-ring^{13,14} (Fig. 1a).

Remarkably, the self-organization of the Min gradient patterns and FtsZ polymerization-depolymerization dynamics have been reconstituted in vitro^{15–26} on supported lipid bilayers (SLBs) and inside lipid compartments, such as microdroplets and vesicles,

thereby significantly contributing to a quantitative mechanistic understanding of these systems. FtsZ has been shown to polymerize into dynamic ring-like structures¹⁷ that can deform free-standing membranes^{18–22}, and co-reconstitution of the Min positioning system and membrane-anchored FtsZ on supported membranes has confirmed the spatial regulation of FtsZ polymers by Min patterns^{23–26}. However, the precondition for Min wave-guided assembly of an FtsZ-based ring-like structure with contractile ability is the functional co-reconstitution of the two systems in a closed and deformable membrane compartment such as lipid vesicles. This has so far not been accomplished due to the complexity of controlling the large number of components and environmental factors, as well as their intrinsic complex dynamics^{10,14,27,28}.

To master the multiple-protein system, several studies attempted the generation of Min waves and FtsZ structures via cell-free protein synthesis in vitro^{19,20,26,29}. Although this approach avoids the complications imposed by protein purification, its challenge lies in the expression of multiple functional proteins at the right time and in the right concentration ratios^{30,31} that were shown to be critical for the emergence of self-organization of the MinCDE system in vitro^{29,32–34}, and other divisome proteins in vivo^{10,35,36}. Indeed, cell-free expression

¹Department of Cellular and Molecular Biophysics, Max Planck Institute of Biochemistry, Am Klopferspitz 18, 82152 Martinsried, Germany. ²These authors contributed equally: Shunshi Kohyama, Adrián Merino-Salomón. ✉ e-mail: schwille@biochem.mpg.de

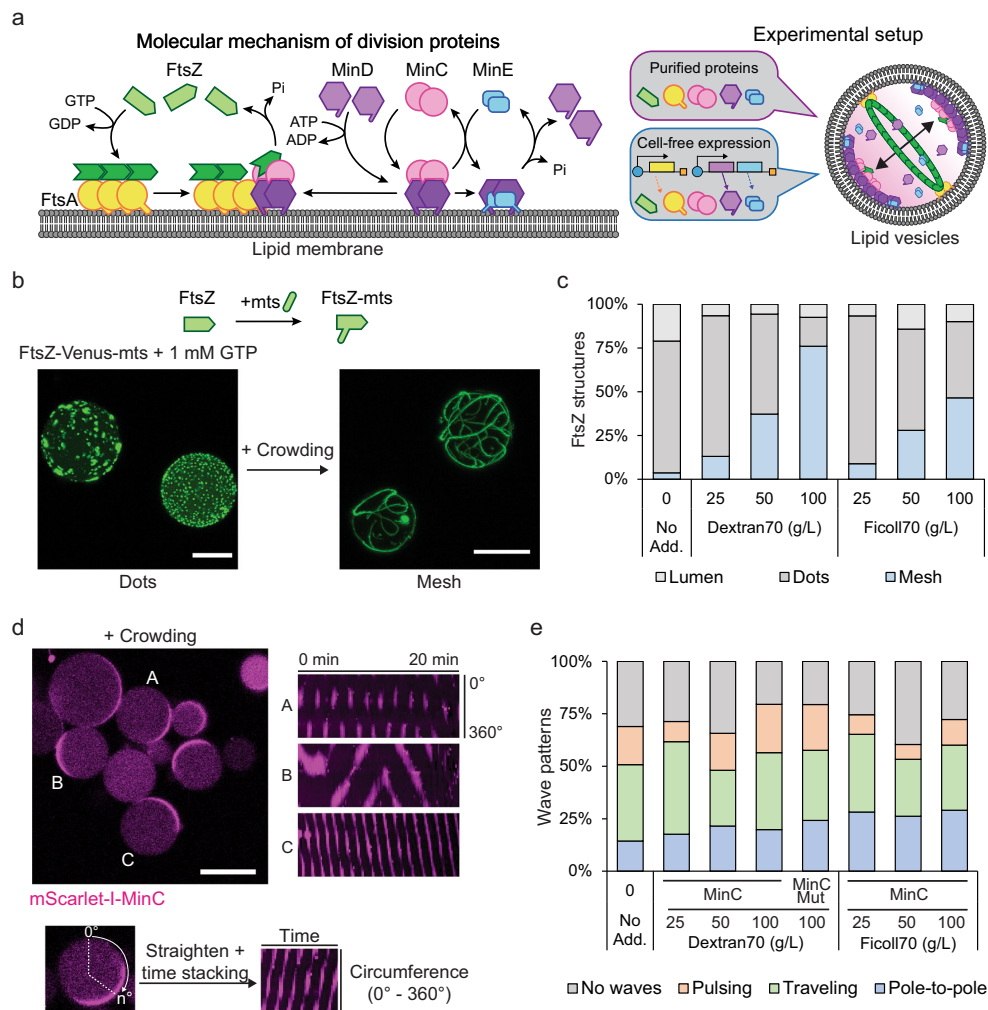


Fig. 1 | Reconstitution of FtsZ or MinCDE systems inside lipid vesicles under macromolecular crowding conditions. **a** Left: Schematic illustration of the molecular mechanism of the minimal bacterial division system. FtsZ polymerizes upon GTP hydrolysis and binds the membrane through FtsA to assemble into the FtsZ-ring. The dynamic MinCDE system self-organizes into oscillatory waves inhibiting FtsZ polymerization at cell poles. Right: Our experimental setup by which the minimal division system is reconstituted inside lipid vesicles using two different approaches: the purified components or the cell-free expression of the system. In both cases, we observe a minimal FtsZ-ring at the equatorial plane of the vesicle. **b** Top: schematic representation of FtsZ-Venus-mts. Bottom: 3D max projection of encapsulated 2 μM of FtsZ-Venus-mts (green) in the absence (left) or presence (right) of macromolecular crowding using 100 g/L Dextran70 and 1 mM GTP. Scale bars: 15 μm. **c** Frequency of FtsZ structures formed inside lipid vesicles. FtsZ structures were differentiated into three categories: Bundles assembling a mesh, FtsZ dots, or luminal localization ($n = 295, 230, 212, 242, 226, 218, 262$ for no additives, 25, 50, 100 g/L Dextran70, 25, 50, 100 g/L Ficoll70, respectively). We could not observe the assembly of FtsZ-rings regardless of crowding conditions. **d** Left: Representative

confocal image of purified MinCDE proteins inside lipid vesicles in the presence of macromolecular crowding (50 g/L Dextran70). Capital alphabet letters correspond to the kymographs on the right side (0.5 μM mScarlet-I-MinC, 3 μM MinD, and 3 μM MinE). Scale bar: 15 μm. Right: Kymographs of different MinCDE wave patterns captured by mScarlet-I-MinC fluorescence. The Kymograph is a 2D representation of a 1D object along with elapsed time. In this case, the fluorescence of mScarlet-I-MinC on the membrane is represented over time. The Y axis represents the signal at the membrane of the circumference (however, circumference was straightened to present the 1D information) while the X axis represents the time. Different intensity patterns observed in the Kymographs can be related with the Min oscillation modes on the membrane. **e** Frequencies of vesicles containing variations on the MinCDE dynamics (absence of waves, pole-to-pole oscillations, traveling waves, or pulsing) at different macromolecular crowding concentrations (0–100 g/L) using Dextran70 or Ficoll70 (0.5 μM mScarlet-I-MinC, 3 μM MinD, and 3 μM MinE) ($n = 374, 227, 181, 161, 297, 181, 298, 303$ for no additives, 25, 50, 100 g/L Dextran70, mScarlet-I-MinC^{G10D} in 100 g/L Dextran70, 25, 50, 100 g/L Ficoll70, respectively). Images were collected after 10 min of vesicle preparation for 1–2 h.

of more than four division-related proteins within a single lipid vesicle has so far not been possible.

Herein, we successfully demonstrate Min wave-assisted FtsZ-ring assembly within lipid vesicles by two alternative approaches: in a fully controlled system with purified proteins, and by employing cell-free protein expression in a specifically tailored assay (Fig. 1a). In both

cases, we were able to follow by time-lapse imaging the origin, condensation, and equatorial placement of a minimal division ring-like FtsZ structure in giant unilamellar vesicles, more than ten times the size of bacterial cells. The more controlled reconstitution using purified proteins, MinCDE and membrane-anchored FtsZ allowed a quantitative assessment of decisive factors and revealed that crowding

environments are essential to form FtsZ-ring structures. As already suspected from our earlier work on MinDE wave-induced diffusiophoresis^{25,37}, we demonstrated that MinC, the main component for spatial regulation of FtsZ, was dispensable for assembly and spatial positioning of FtsZ polymers by MinDE, although the efficiency of ring formation was drastically improved by MinC. Moreover, we observed a positive feedback between the pole-to-pole oscillations of MinCDE and FtsZ-ring formation, in the way that the two processes promoted and spatially stabilized each other. On the other hand, our alternative approach using cell-free protein production within the vesicles supported a time-sensitive sequential expression of all the five components MinCDE, FtsA, and FtsZ. Strikingly, and in contrast to the system with purified proteins, this time-controlled series of events of FtsZ self-assembly and MinCDE oscillation resulted in a noticeable shape transformation of the spherical vesicle along with the Min-induced centric condensation of an originally isotropic FtsZ-FtsA meshwork. Our experiments thus reveal that such progressively condensed FtsZ-ring structures are not only able to constrict the vesicle precisely in the middle, but also induce a clear symmetry breaking of Min oscillations upon deviation from spherical geometry, selecting a single pole-to-pole oscillation mode that intensifies further equatorial FtsZ condensation in a positive feedback mechanism. These exciting findings emphasize how the timing of events may be crucial for unfolding a particular biological activity, and that under the right conditions, complex spatiotemporal biological dynamics can indeed be reconstituted *in vitro*, marking a significant step towards constructing synthetic cells from the bottom-up.

Results

Optimizing FtsZ and MinCDE reconstitution in lipid vesicles under macromolecular crowding conditions

Recent experiments with reconstituted proteins revealed that macromolecular crowding significantly influences the functionality of divisome proteins^{32,38–40}. In particular, it has shown to promote lateral interactions among filaments, thereby enhancing FtsZ polymerization^{39,40} and improving the regulation of FtsZ by Min waves into steeper gradients^{23,41}. It has been suggested that the regulation of FtsZ by MinCDE, as well as FtsZ condensation into pronounced ring structures, is likely to depend critically on excluded volume effects²³. Moreover, previous reports stated that FtsZ can only form bundles inside lipid vesicles under crowding conditions^{18,22,42,43}, which might be essential to achieve the assembly of a FtsZ-ring. On the other hand, much enhanced crowding with non-physiological molecules can easily become artificial and obstructive for the seamless interlocking of more complex biological machineries, in particular under cell-free conditions. Therefore, we first attempted an optimization of environmental conditions with respect to the functionality of the main components, MinCDE and FtsZ. To this end, we adapted an experimental setup and assay that stably generates Min waves via tuning MinE dynamics inside lipid compartments^{29,32,33} and employed Dextran70 and Ficoll70, which are well-known and widely accepted macromolecular crowders *in vitro*^{18,20,38,44,45}. For standardized vesicle production, we used a double-emulsion transfer method^{29,46}.

To simplify our experimental setup and avoid the use of membrane linkers of FtsZ, we employed FtsZ-Venus-*mts*, a commonly used FtsZ mutant containing the YFP variant fluorescent protein Venus and the membrane targeting sequence (*mts*) domain to confer the spontaneous membrane binding ability on FtsZ^{16,18,21,22,47,48} (Fig. 1b and Supplementary Notes). First, we achieved the encapsulation of FtsZ-Venus-*mts* in lipid vesicles, showing a high proportion of FtsZ assembled into bundles, forming an isotropic mesh on the membrane in the presence of crowders (Fig. 1b, c, and Supplementary Fig. 1a). In contrast, the absence of crowders yielded only dot-like structures on the membrane (Fig. 1b, c, and Supplementary Fig. 1b), similar to previous observations²¹. The abundance of vesicles containing FtsZ bundles and

isotropic mesh structures increased considerably at 50 g/L or higher crowding concentrations (Fig. 1c and Supplementary Fig. 1a), which led us to select this concentration regime as optimal for efficient FtsZ bundling.

Next, we investigated the influence of different crowding conditions on Min wave dynamics inside lipid vesicles (Fig. 1d, e), which have been poorly addressed in the different experimental approaches so far^{23,33}. To test this, we first verified the protein concentration dependence of Min wave dynamics *in vitro*, as it has been shown to be highly sensitive to MinD/MinE ratios on SLBs or in microdroplets^{29,32–34}. Following established procedures, we successfully reconstituted Min waves using MinD, MinE, and mScarlet-I-MinC inside lipid vesicles (Supplementary Fig. 2a–d). In agreement with previous studies^{32,33}, we observed an overall higher prevalence of dynamic Min patterns, as compared to stationary localization in the lumen or at the membrane, when the MinDE ratios were roughly balanced (Supplementary Fig. 2b–d and Supplementary Notes). Then, we analyzed the impact of macromolecular crowding on the MinCDE patterns, successfully reproducing the above-described MinCDE dynamics inside lipid vesicles also at high crowding conditions optimal for FtsZ bundling (Fig. 1b, c, and Supplementary Movie 1), without significantly affecting the frequency of Min patterns (Fig. 1e and Supplementary Notes). Therefore, we could verify that both FtsZ and MinCDE systems are functional under macromolecular crowding inside lipid vesicles, a key precondition for their co-reconstitution towards the functional assembly of bacterial division machinery *in vitro*.

Co-reconstitution of MinCDE and FtsZ under crowding conditions yields the assembly of pronounced FtsZ-ring structures

After characterizing the effect of macromolecular crowding over the FtsZ and MinCDE systems independently, we co-reconstituted both systems within vesicles at different crowding conditions (Fig. 2 and Supplementary Fig. 3). Intriguingly, for 50 g/L or higher concentrations of crowders, we observed an efficient condensation of previously isotropic FtsZ bundles into a single ring structure along with an equatorial positioning of this structure in the spherical vesicles, clearly driven by pole-to-pole oscillations of the MinCDE wave (Fig. 2b–e and Supplementary Fig. 3). These FtsZ-rings were slightly fluctuating spatially around the equatorial region of the vesicle as a consequence of Min oscillations. However, the ring structures remained stably positioned in the middle of the vesicles for an extended period of about half an hour, which constitutes a significant accomplishment towards assembling a functional divisome (Fig. 2c, d, and Supplementary Movie 2).

By analyzing the emergence of FtsZ structures inside lipid vesicles, we found that the formation of FtsZ-rings was highly related to the crowding concentration (Fig. 1c and 2f). The occurrence of FtsZ Mesh and FtsZ-rings increased with the concentration of crowders, and especially, it reached around 40% at 100 g/L Dextran70, while we did not find any FtsZ-ring structure in the absence of crowders or MinCDE proteins (Fig. 1c and 2f). In addition, the presence of FtsZ in the equatorial region of the spherical vesicles yielded a significant increase in pole-to-pole Min oscillations, indicating a tendency for mode selection by the presence of the FtsZ-ring structures or FtsZ bundles on the membrane (Fig. 2g). The establishment of Pole-to-pole oscillations under 100 g/L Dextran70 increased up to 43%, in good agreement with the yield of pronounced FtsZ-ring structures found under these conditions (40%) (Fig. 2f, g). Thus, we concluded that Min waves enhance and regulate FtsZ-ring assembly and placement with the help of macromolecular crowding *in vitro*.

MinC is not required for FtsZ ring positioning

Interestingly, we observed that the presence of the FtsZ polymerization inhibitor MinC was not required for the positioning of the FtsZ-ring structure, as clear FtsZ-ring structures were also found in the

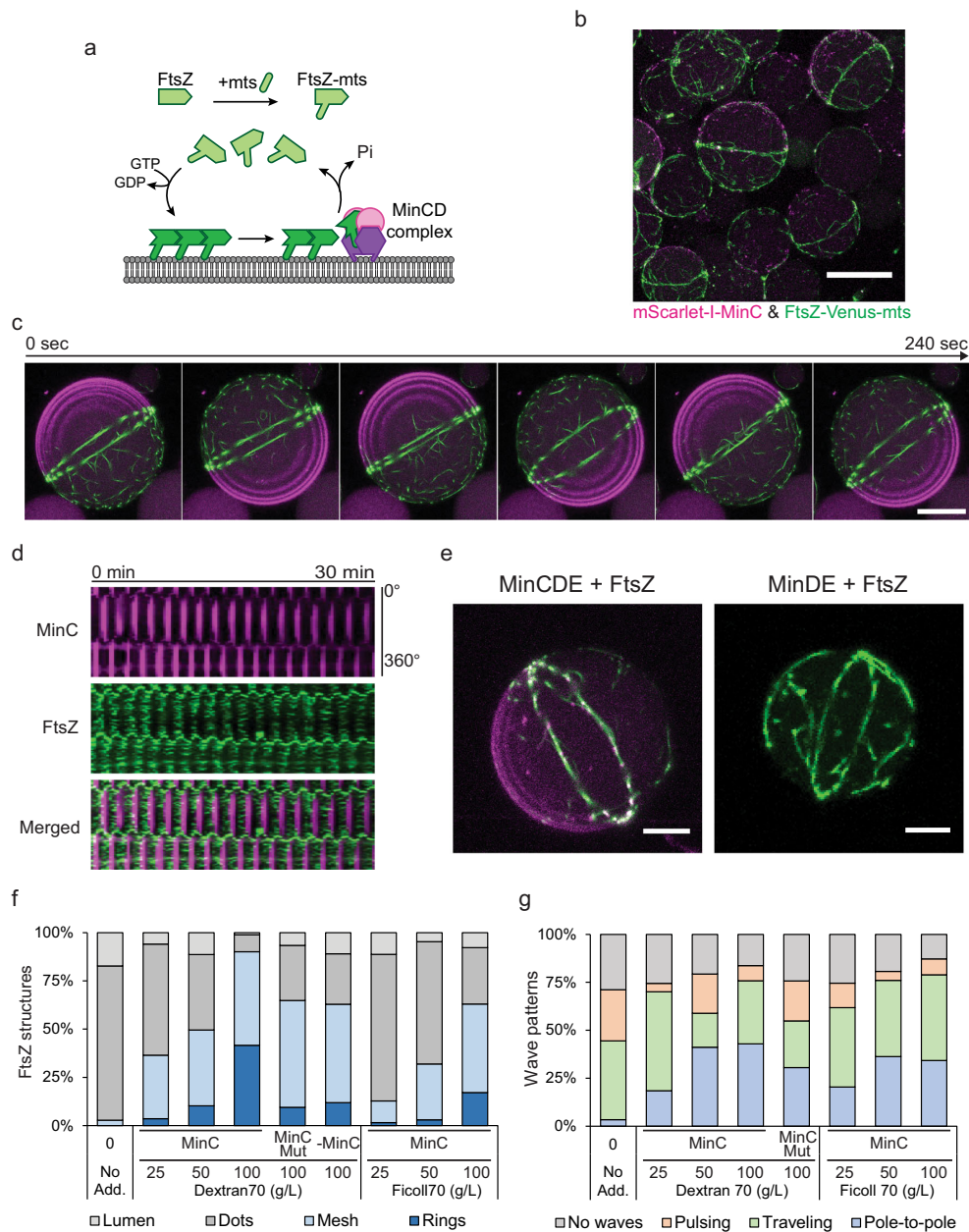


Fig. 2 | FtsZ-ring assembly and positioning inside lipid vesicles. a Schematic illustration of the FtsZ-Venus-mts system interacting with the membrane and the MinCDE system. **b** 3D max projection of a merged confocal image of vesicles containing the MinCDE proteins and FtsZ-Venus-mts in the presence of 100 g/L Dextran70. The Min wave-assisted formation of pronounced FtsZ-rings out of isotropic meshwork can be clearly observed. mScarlet-I-MinC and FtsZ-Venus-mts correspond to green and magenta, respectively (0.5 μ M mScarlet-I-MinC, 3 μ M MinD, 3 μ M MinE, and 2 μ M FtsZ-Venus-mts). Scale bar: 25 μ m. **c** Time-lapse confocal images of the FtsZ-ring structure stabilized by pole-to-pole oscillations of Min waves. 3D max projection of merged images of mScarlet-I-MinC and FtsZ-Venus-mts. Scale bar: 15 μ m. **d** Kymographs of the FtsZ-ring placement shown in Fig. 2c by a pole-to-pole oscillation wave captured by mScarlet-I-MinC (magenta) and FtsZ-Venus-mts (green). **e** (Left) 3D projection of an FtsZ-ring structure positioned by the MinCDE system. (Right) 3D projection of a vesicle containing a FtsZ-ring positioned

by the Min system in the absence of MinC. Min waves are not visible as mScarlet-I-MinC is absent in this case (3 μ M MinD, 3 μ M MinE, and 2 μ M FtsZ-Venus-mts). Scale bars: 5 μ m. **f** Frequency of FtsZ-ring formation in co-reconstituted vesicles. FtsZ structures were differentiated into four categories: rings, mesh, dots, or luminal localization ($n = 180, 252, 615, 473, 1045, 502, 250, 366, 543$ for no additives, 25, 50, 100 g/L Dextran70, 100 g/L Dextran70 with MinC^{100D}, 100 g/L Dextran70 without MinC, 25, 50, 100 g/L Ficoll70, respectively). **g** Frequency of Min wave patterns (pole-to-pole oscillations, traveling waves, pulsing, or absence of waves) inside vesicles containing the MinCDE system co-reconstituted with FtsZ-Venus-mts among the addition of different macromolecular crowding concentrations using Dextran70 or Ficoll70 ($n = 90, 157, 172, 289, 206, 227, 391, 289$ for no additives, 25, 50, 100 g/L Dextran70, 100 g/L Dextran70 with MinC^{100D}, 25, 50, 100 g/L Ficoll70, respectively). Confocal images were recorded after 10 min of the vesicle preparation for a time frame of 1–2 h. Source data are provided as a Source Data file.

absence of MinC at high crowding conditions (Fig. 2e, f). Moreover, similar results were observed using an FtsZ interaction defective MinC mutant (MinC^{G10D})^{41,49} (Fig. 2f). These observations agreed with previous studies that described a diffusio-phoretic mechanism by which the Min proteins can position molecules on the membrane without any specific interaction^{25,37}. Consequently, our results demonstrate that the diffusio-phoretic positioning by the Min waves is preserved even in cell-like models on FtsZ. This calls for a greater future attention to the potential relevance of this mechanism in vivo, where its principle has been demonstrated recently³⁷.

However, it is important to point out that although a non-specific interaction between FtsZ and the Min waves could result in a distinct equatorial FtsZ-ring formation in vesicles, the presence of MinC significantly enhanced the efficiency of this process (Fig. 2e, f), showing FtsZ-ring formation with about four times higher abundance (From -10–12% to -40%), thus emphasizing MinC's role in the regulation of FtsZ polymerization. In contrast, MinC^{G10D} did not increase the pole-to-pole oscillations as much as MinC in our experimental setup (from 25% to 31% for MinC^{G10D}, and from 20% to 43% for MinC) (Fig. 2g). This difference in the yield of pole-to-pole oscillations between MinC and MinC^{G10D} suggests a positive feedback mechanism between Min oscillations and FtsZ positioning inside vesicles, in the way that the formation of the FtsZ-rings promoted by Min pole-to-pole oscillations in turn stabilize the pole-to-pole oscillation mode (Supplementary discussion).

Increasing compositional complexity using PURE cell-free expression

Although the co-reconstitution of purified FtsZ-mts with MinCDE represents a step towards the assembly of a fully controlled minimal division system, this system still lacks a potentially relevant degree of freedom in the regulation of FtsZ membrane attachment, which is in the cellular system conferred by anchoring through FtsA^{17,50,51}. Membrane anchoring through another protein molecule rather than an mts motif on the FtsZ monomers not only decouples the stoichiometries of polymerization and membrane binding, but also confers more structural flexibility to the system. To investigate the potential relevance of this additional regulation feature, we set up the reconstitution of this more complex machinery inside lipid vesicles utilizing the PURE cell-free expression system^{52,53}. Since transcription and translation are the basis of cellular information processing, combining gene expression with a rudimentary division system is an intriguing alternative concept for the bottom-up construction of synthetic cells. Thus, several studies have previously been performed to incorporate cell-free expression into a minimal division system in vitro^{19,20,26,29}. Min waves were reconstituted inside lipid vesicles by de novo expression of MinDE proteins^{26,29}. Also, FtsZ mesh structures and the deformation of lipid vesicles by FtsZ were observed by co-expression of FtsZ and FtsZ-related proteins, such as FtsA, ZipA, and ZapA^{19,20}. However, formation and placement of a distinctive division ring has not yet been accomplished by simultaneous expression of MinCDE, FtsZ, and FtsA. The expression of multiple genes from different, functionally interlocking self-organizing machineries is more challenging, due to the different temporal concentration ramps of expressed proteins.

To conduct cell-free expression within lipid vesicles, we used our standard protocol of vesicle formation and observation. Additionally, we employed a Peltier stage mediated temperature control device to incubate the vesicle-containing chambers for cell-free protein synthesis. After confirming the optimal crowding condition for our cell-free expression setup which allowed us to obtain about 10 μ M of the reporter protein (superfolderGFP) expression (Supplementary Fig. 4 and Supplementary Notes), we first performed cell-free expression of FtsA with purified FtsZ-Alexa488 protein to visualize the integration of the wild-type FtsZ-FtsA cytoskeleton (Supplementary Fig. 5a). In accordance with previous reports^{19,20},

under the Ficoll70 crowding condition FtsZ formed bundles on the membrane, anchored through cell-free expressed FtsA. Moreover, in addition to visualizing the readily formed FtsZ bundles at sufficient expression time (40–60 min), we also captured the process of FtsZ bundle formation on the membrane along with the expression of FtsA over 40 min (Fig. 3b, Supplementary Fig. 5b, c, and Supplementary Movie 3). The time-lapse images show the FtsZ dynamics inside lipid vesicles that gradually formed mesh structures on the membrane, with the bundles branching into even smaller ramifications (Supplementary Fig. 5b). Thus, we conclude that our experimental setup fully supports the transition to cell-free expression of our functional machineries, and that cell-free expressed FtsA enables us to capture the real-time dynamics of the development of an FtsZ-FtsA meshwork inside lipid vesicles.

Direct observation of FtsZ-ring condensation inside vesicles

To test whether the FtsZ-FtsA cytoskeleton system also condenses into discernible FtsZ-ring structures inside vesicles upon spatial regulation by MinCDE waves, we next combined the expression of FtsA and MinDE (Fig. 3a). Since the *minDE* operon structure from the *E. coli* genome successfully resulted in Min patterns through PURE cell-free expression as previously reported²⁹, we constructed the *minDE* operon DNA template as well. Cell-free expression from this operon DNA template supported the MinDE expression system to produce Min patterns inside up to 80% of the vesicles (Supplementary Fig. 6c). We then attempted to express MinDE and FtsA with purified FtsZ-Alexa488 and mCherry-MinC to investigate the FtsZ dynamics under the regulation of Min waves.

Similar to the previous studies that indicate antagonistic membrane localization of FtsZ and MinCDE waves^{23–26,41}, the FtsZ structures dynamically reorganized in a time-dependent manner in response to the emergence of Min wave patterns (Fig. 3c and Supplementary Movie 4). At the beginning of protein expression, neither FtsZ nor Min protein patterns could be observed. Then, FtsZ gradually developed into mesh structures on the membrane, similar to the experiments without MinCDE. Only with a noticeable delay of more than 10 min after FtsZ mesh formation, Min waves emerged predominantly as pole-to-pole oscillations and instantly started to reorganize the FtsZ meshwork, eventually driving FtsZ to condense into a ring-like structure at the middle of the vesicle (Fig. 3c, d, and Supplementary Fig. 5f). Thus, we confirmed that partially cell-free expressed FtsZ-FtsA and MinCDE systems coordinate to assemble and correctly position FtsZ-ring structures inside lipid vesicles. However, the ring structure obtained through this process was not stable for an extended time period beyond 40 min. The Min oscillations eventually degenerated into traveling waves, and FtsZ mesh structures reappeared, however, FtsZ only antagonistically localized against the Min waves, resulting in a continuous spatio-temporal rearrangement of the ftsZ mesh (Fig. 3c and Supplementary Fig. 5f).

These time-dependent pattern changes of Min waves leading to a loss in mode-locked pole-to-pole oscillations were similar to the ones previously reported³². Therein, Min waves inside microdroplets showed pole-to-pole oscillation in the relatively early phase after Min wave emergence, but then deteriorated towards traveling waves due to the change in the MinDE concentration over time²⁹. Indeed, some vesicles showed pole-to-pole oscillation only for less than 5 min and then transitioned to traveling waves (Supplementary Fig. 5f). FtsZ followed this trend and maintained pronounced ring structures only while pole-to-pole oscillations were present (Supplementary Fig. 5f). Together with the previous studies showing the reorganization of FtsZ by Min waves^{23–26,41}, it became obvious that Min waves strictly govern FtsZ patterns, and more importantly, out of the two major dynamic Min patterns, only pole-to-pole oscillations, but not traveling waves, support stable FtsZ-ring formation inside lipid vesicles.

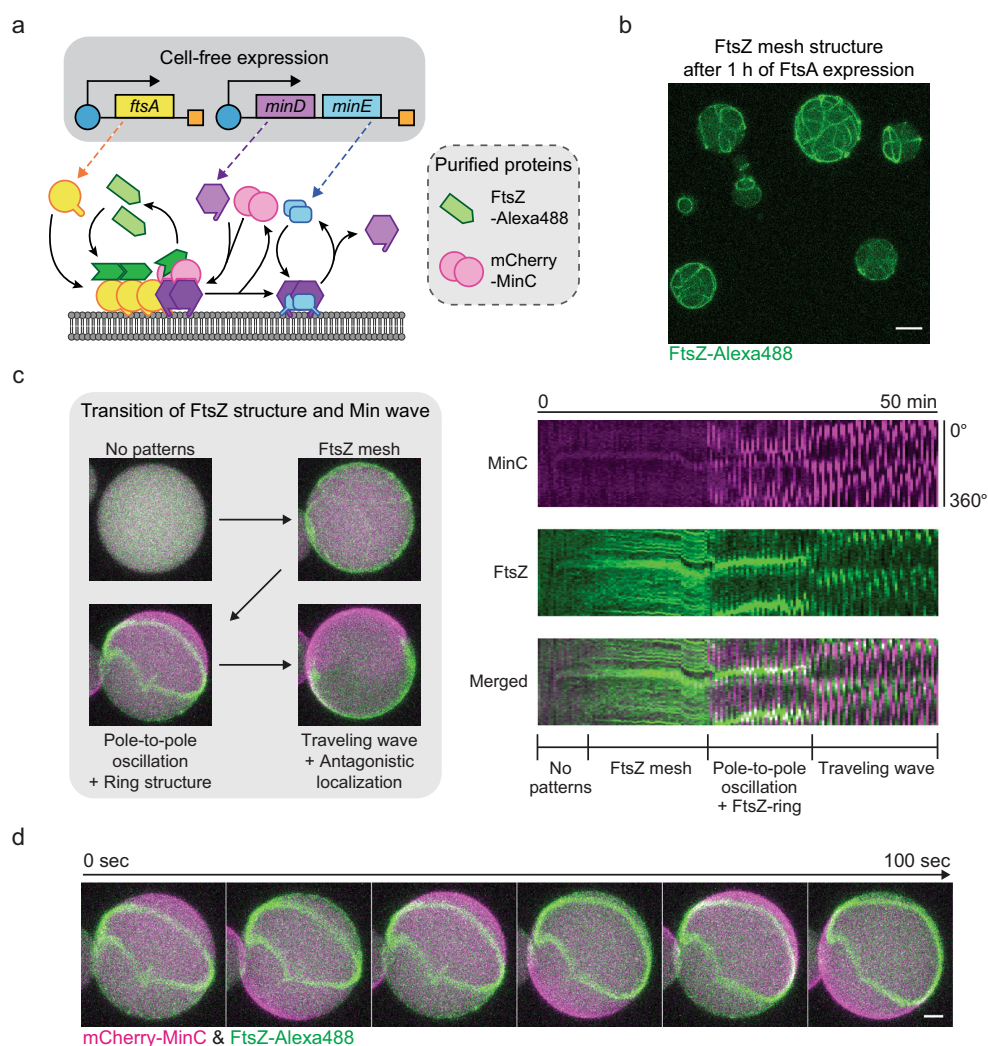


Fig. 3 | Reconstitution of FtsZ-FtsA mesh and Min wave regulated FtsZ-ring structures via cell-free expression. **a** Schematic illustration of PURE cell-free co-expression of FtsA, MinD, and MinE with purified FtsZ-Alexa488 and mCherry-MinC. **b** 3D max projection of FtsZ-Alexa488 mesh structures inside vesicles via FtsA expression (after 1 h of expression with 5 nM of *ftsA* template). Scale bar: 10 μ m. **c** Regulation of FtsZ localization by Min waves. Left: 3D max projection of the transition of FtsZ structures and Min wave patterns by co-expression of FtsA, MinD, and MinE within vesicles (2 nM *ftsA*opt and 2 nM *minDE*operon templates). Starting from no patterns, an FtsZ mesh develops on the

membrane, which is then instantly condensed into an FtsZ-ring structure by the later onset of pole-to-pole oscillations of Min waves, through antagonistic localization of Min and FtsZ proteins. Right: Kymographs of the pattern transition of Min waves and FtsZ structures. Recording started after 5 min of cell-free expression. mCherry-MinC and FtsZ-Alexa488 are indicated in magenta and green, respectively. **d** Time-lapse images of FtsZ-ring like structures induced by pole-to-pole oscillations of Min waves. Experimental condition is the same as Fig. 3c and recording started after 30 min of cell-free expression. Scale bar: 5 μ m.

Ensuring compatibility of fully cell free expressed MinCDE and FtsZ-FtsA systems

After reconstitution of FtsZ-ring structures by partially cell-free expressed proteins, we expanded the system towards building the entire division machinery with genetically encoded proteins. One challenge for this approach is that either one or two proteins must be fused to Fluorescent Proteins (referred as FPs) to monitor their dynamics by fluorescence microscopy. However, *E. coli* FtsZ is known to lose its functionality by fusing tag proteins to the C-terminus^{51,54}. Furthermore, an increase in the molecular weight of FtsZ by conjugating average-size FPs decreases the protein expression yield. On the other hand, since MinDE waves are highly sensitive to the protein

concentration ratio, it needed to be validated that cell-free expressed MinCDE proteins can maintain ideal concentrations to emerge wave dynamics. Thus, we first reconstituted the partial systems (MinCDE vs. FtsZ-FtsA) and verified the self-organization ability of cell-free expressed proteins (Supplementary Fig. 6a).

Since the *minDE* operon DNA template had already been optimized for cell-free expression²⁹, we decided to keep the *minDE* operon structure for the MinDE expression. Therefore, we additionally introduced mCherry-MinC as reporter of the Min wave localization, because it would not be required for self-organization, and is at the same time the regulator for FtsZ localization. As expected, co-expressed MinCDE proteins sustained Min wave emergence inside

vesicles (Supplementary Fig. 6b and Supplementary Movie 5), implying that MinDE concentrations were still within a well-balanced range of co-expression (Supplementary Fig. 6b, c, and Supplementary Notes).

Next, we investigated the assembly of FtsZ-FtsA from fully cell-free synthesized FtsA and FtsZ, which promised to be more complicated than the MinCDE system. To overcome the loss of function in FtsZ-FPs chimeric proteins^{51,54}, we adapted a novel FtsZ mutant according to a previous report⁵⁵, in which FPs are inserted into the G55-G56 position of FtsZ instead of C-terminal conjugation. After the validation of FtsZ and FtsA template concentrations (3 nM for FtsZ and 1 nM for FtsA) to maintain the ideal protein proportions to form FtsZ bundles, we confirmed that co-expressed FtsZ-G55-Venus-Q56 and FtsA generated FtsZ mesh structures on the membrane (Supplementary Fig. 6d, e, and Supplementary Movie 6). Simultaneously, we captured the mesh formation of FtsZ-G55-Venus-Q56 that showed to be similar to the FtsA-only expression with purified FtsZ-Alexa488 (Fig. 3b and Supplementary Fig. 6d), demonstrating a similar correlation of FtsZ intensity on the membrane with vesicle size as observed for purified proteins (Supplementary Fig. 5e, 6h, i, and Supplementary Notes). Together with the reconstitution of the MinCDE system, we concluded that sub-division systems could be faithfully reconstituted from cell-free expressed proteins inside lipid vesicles.

Mid-cell placement and radial constriction of a minimal division ring

Finally, we incorporated the co-expression of MinCDE, FtsZ and FtsA proteins under the established conditions within vesicles (Fig. 4a). We confirmed that upon co-expression of all five proteins, FtsZ-ring structures spatially self-assembled under the regulation of Min waves (Fig. 4b, c, and Supplementary Movie 7). As observed for the partial co-expression described above (Fig. 3c), FtsZ first assembled into isotropic mesh structures, which upon the onset of MinCDE oscillations spatially condensed into an FtsZ-ring structure in the middle of the vesicle (Fig. 4d, Supplementary Fig. 7a, c, d, Supplementary Movie 8, and 9). In turn, as observed for the purified proteins, the formation of the ring structure led to a mode selection of the Min oscillations into a pronounced pole-to-pole dynamics perpendicular to the plane defined by the FtsZ ring structure.

Strikingly, in contrast to all other assays with partly purified proteins, we found that the simultaneous evolution of FtsZ-ring assembly and mode selection into pole-to-pole Min oscillations resulted in a marked deformation of the lipid vesicles away from spherical to a more rod-like shape, reflecting on a radial constriction of up to 19% (Fig. 4f and Supplementary Fig. 8). This vesicle deformation by a central FtsZ-ring structure could also be observed for static bipolar localization of Min proteins but not for traveling waves, implying that the static pattern of Min waves also supports FtsZ-ring assembly and placement (Fig. 4c, Supplementary Fig. 7a, b, and Supplementary Notes).

Evaluation of the vesicle size dependence of FtsZ organization and vesicle deformation revealed more unexpected features of the reconstituted minimal division system. The population of deformed vesicles with pronounced FtsZ-ring structures increased with the vesicle size (22.5% at 12–16 μm , 40% at 16–20 μm , 50% at >20 μm), while relatively small vesicles (~12 μm) remained spherical (Fig. 4e). We also found that the aspect ratio of the deformed vesicles and their original diameters were moderately correlated (r -value = -0.40, Fig. 4f). In several cases such as shown in Fig. 4d, the aspect ratios (diameter/length) of the deformed vesicle approached about 0.75 after 3 h expression. Since we performed all experiments under isosmotic conditions, this suggests that the FtsZ-rings upon spatial condensation generated considerable forces to constrict the vesicles radially by up to 19% (Supplementary Fig. 8). Taken together, these results successfully demonstrate that such a complex biological function as contracting ring-based cell

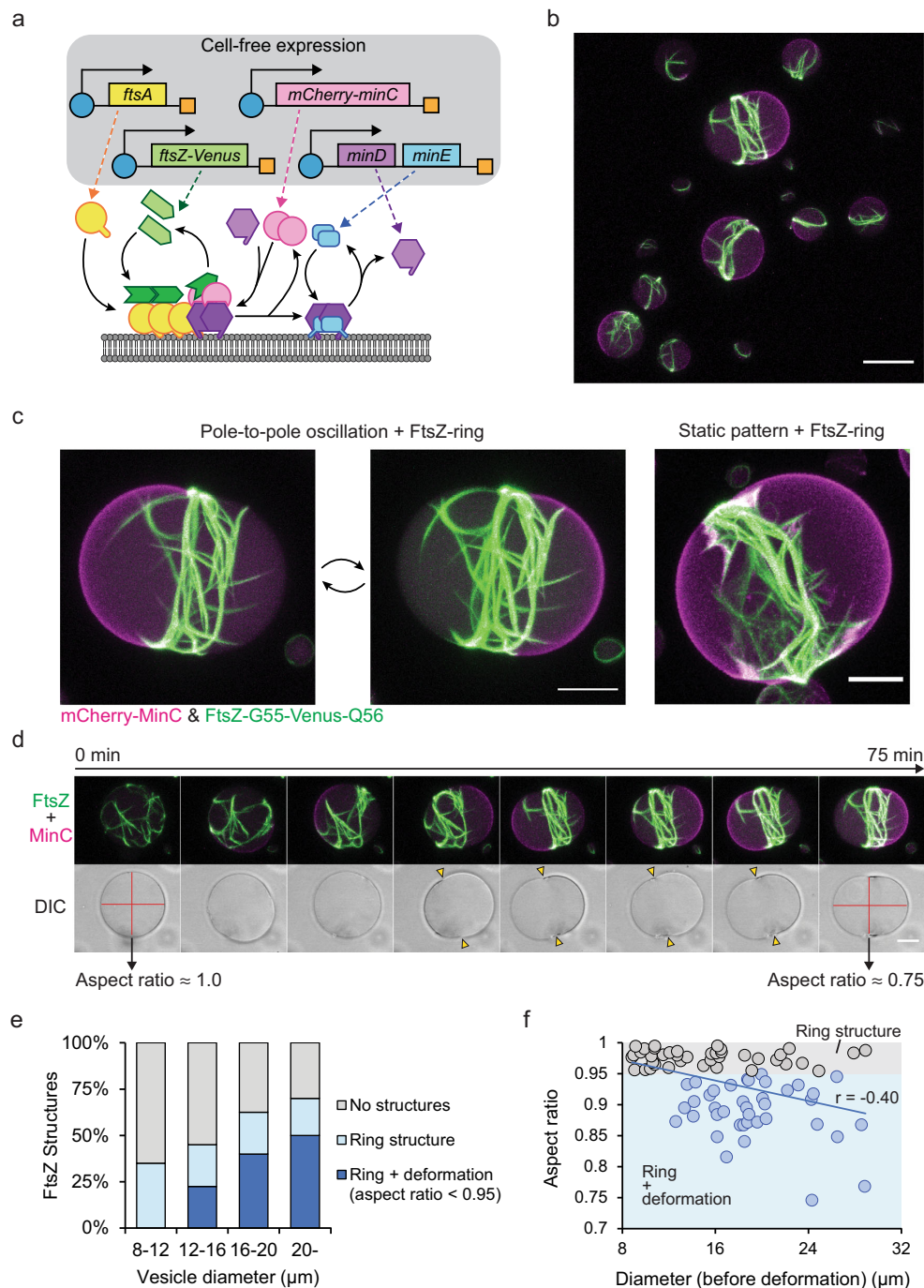
division could indeed originate from a set of well-defined components *in vitro*.

Discussion

In this work, we have reconstituted the bacterial division ring placement system *in vitro* from a minimal set of components, namely, MinC, MinD, MinE, FtsA, and FtsZ by cell-free expression. At the right choice of template ratios, proteins have been orchestrated reliably within giant lipid vesicles to form FtsZ-ring structures, and unexpectedly, even shown to constrict their membrane containers, despite being more than an order of magnitude larger than bacterial cells. In addition to the complete cell-free expressed system, we have quantitatively investigated the assembly and spatial regulation of a FtsZ-ring with MinCDE and FtsZ-Venus-mts in a fully controlled system based on purified proteins, which has allowed us to evaluate the key factors involved in the process, such as optimal Min protein concentrations or macromolecular crowding conditions (Supplementary discussion). Both approaches highlight important features of the bacterial division mechanism *in vitro*, confirming the relevance of the coupled protein systems FtsZ-FtsA and MinCDE as paradigms for minimal cell division in bottom-up synthetic biology.

One of the expected insights gained from our study and in agreement with previous observations⁴¹ is that MinCDE pole-to-pole oscillations indeed seem to be directly responsible for FtsZ-ring formation and placement in the sense that a previously isotropic mesh-like appearance of FtsZ filaments condensed into ring-like structures targeted to the equatorial region of the vesicles (Figs. 2c–e, 3d, and 4c, d). Not directly expected, but nevertheless highly plausible, was our observation that the condensation of FtsZ into ring-like structures, reminiscent of a spatial symmetry breaking, in turn led to a mode selection for oscillatory MinCDE dynamics in the sense that pole-to-pole oscillations perpendicular to the emerging FtsZ ring structures were favored over pulsing or travelling wave modes (Supplementary discussion). By using the FtsZ interaction defective mutant MinC^{G100D} or removing MinC from the system, we also found that the interaction between MinC and FtsZ is not necessary to form and position FtsZ-rings (Fig. 2e, f), although functional MinC significantly enhances the assembly of FtsZ-rings and the emergence of pole-to-pole oscillations. Moreover, Min self-organization dynamics and FtsZ-ring assembly and positioning appear to reinforce each other in a positive feedback mechanism towards division. Indeed, in most cases, FtsZ-ring structures and pole-to-pole oscillations persisted for a long time, supporting this hypothesis (Fig. 2c, d, and Supplementary Movie 2). This positive feedback resulting in spatial symmetry breaking and establishment of a defined axis along which division is particularly remarkable with respect to the originally spherical vesicles, quite distinct from the rod-like shape of *E. coli* bacterial cells. In previous attempts of targeting circumferential actomyosin ring structures with contractile features to spherical membrane vesicles⁵⁶, the lack of a defined division axis resulted in the slipping off from equatorial to polar regions upon ring constriction, in stark contrast of what can be observed in the presence of spatially stabilizing Min oscillations. We can thus conclude that any deviation from spherical symmetry leads to preferential mode selection of pole-to-pole oscillations.

The other highlight of our results was the pronounced vesicle deformation by the interplay of FtsZ-ring assembly and Min wave-induced positioning in the complete set of cell-free expressed proteins on the scale of tens of micrometers. Even though there were previous reports on how FtsZ and related proteins may constrict or deform lipid vesicles^{16,18–22}, our results allowed to visualize the gradual onset of force generation along with the condensation and positioning of a large FtsZ-ring from an isotropic meshwork in a plausible chain of causation (Fig. 2c, 3c, and 4d). Recent studies demonstrated that micron-sized treadmill rings of FtsZ produce weak forces in the 1–2 pN range that can only constrict deflated



vesicles or wall-less *E. coli* cells²¹, much lower than what is estimated for constriction in native cells (8-15 pN)^{57,58}. For the equatorial FtsZ-rings that are more than an order of magnitude larger than any known FtsZ ring-like structure in vitro, we did not observe any deformation of GUVs under isosmotic conditions when FtsZ was directly attached to the membrane (Fig. 2c–e). In contrast, FtsZ-rings anchored to the membrane through FtsA constricted the vesicles (Fig. 4c, d). This suggests that the FtsZ-FtsA system might generate

greater effective forces on membranes, potentially owing to a different mechanism of dynamic membrane attachment, similar to the spatiotemporal imbalance of membrane curvature of lipid vesicles induced by attachment of MinDE proteins through their amphipathic helices^{59,60}, aiding large membrane deformations. In this regard, accumulation of transmembrane proteins that are also part of the bacterial divisome but have been missing in our system so far, such as ZipA, might enhance the local bending of the membrane as

Fig. 4 | Reconstitution of minimal division ring placement system by co-expression of five essential components. **a** Schematic illustration of co-expression systems of FtsA, FtsZ-G55-Venus-Q56, mCherry-MinC, MinD, and MinE. **b** 3D max projection of FtsZ-ring formation and Min protein localization at the pole of the vesicles after 100 min of co-expression at 37 °C (1 nM *ftsAopt*, 3 nM *ftsZopt-G55-Venus-Q56*, 2 nM *mCherry-MinC*, and 1 nM *minDEoperon* templates). mCherry-MinC and FtsZ-G55-Venus-Q56 are indicated in magenta and green, respectively. Scale bar: 20 μm. **c** Enlarged images of FtsZ-structure and Min wave patterns inside lipid vesicles after 3 h of cell-free expression. Pole-to-pole oscillations and static patterns stabilize the FtsZ-ring structures, and in both cases, FtsZ-ring can constrict vesicles. Experimental condition is the same as Fig. 4b. Scale bars: 10 μm. **d** Time-lapse images of the formation of the FtsZ-ring structure and constriction of the vesicle driven by the pole-to-pole oscillations of MinCDE. Top panels: 3D max projection of the merged image of mCherry-MinC (magenta) and FtsZ-G55-Venus-Q56 (green). The isotropic FtsZ mesh is condensed into a ring structure after the emergence of pole-to-pole oscillations, which later constricts the vesicle membrane. Bottom panels: Differential interference contrast (DIC) images of the

equatorial plane of the vesicle. Red lines indicate aspect ratios of the vesicle before and after constriction by FtsZ-ring, yellow triangles indicate necks of the constriction by FtsZ-ring. Experimental condition is the same as Fig. 4b and the recording started after 50 min of cell-free expression. Scale bar: 10 μm.

e Percentage of the ring structure and deformed vesicles among different vesicle sizes after 2–3 h co-expression of 5 essential genes (at the same template ratios as Fig. 4b) at 37 °C. Proportions of both FtsZ-ring structures and deformation of the vesicles increase along vesicle diameter, while deformation never appears under 12 μm in a diameter. $n = 40$ for each diameter range. **f** Scatter plot of the aspect ratios of deformed vesicles against vesicle diameter. The correlation coefficient shows moderate correlation (Pearson's $r = -0.40$), suggesting greater effective force generation by FtsZ-rings within larger vesicles. Gray and blue dots (with respective background colors) indicate non-deformed vesicles (aspect ratio > 0.95) and deformed vesicles (aspect ratio < 0.95), respectively. $n = 79$ from three independent biological replicates. Experimental condition is the same as shown in Fig. 4e. Source data are provided as a Source Data file.

hypothesized previously⁶¹, thus being interesting candidates to improve the reconstitution of bacterial cell division (Supplementary discussion).

In conclusion, although we successfully reconstituted the bacterial division ring placement system in vitro, and could even witness ring-induced shape transformation of the vesicles, further investigations are necessary to develop synthetic cell models that are truly able to autonomously self-divide in an energy-dissipating manner based on their intrinsic biological machinery. Despite the exact sequence of events in bacteria is not fully clear, there is a high plausibility for a major mechanical role of cell wall expansion in vivo, a feature that will be challenging to replace in minimal systems. Further, one of the most promising candidates for additional large-scale force-inducing elements to aid FtsZ-ring constriction is actually the nucleoid, which could exert strong effects on the membrane through its replication and segregation via biochemical, but also biophysical mechanisms, such as wetting and liquid phase separation^{62,63}. Thus, moving from the reconstitution of a minimal division machinery, that has now been accomplished to a large extent, to a more holistic system which also comprises minimal genome replication, appears to be the next exciting goal of bottom-up synthetic biology.

Methods

Plasmid construction

Plasmids for protein purification and cell-free expression were constructed by seamless cloning or blunt end cloning method according to the provider's protocol. All enzymes for cloning were purchased from Thermo Fisher Scientific (Waltham, MA, USA). Briefly, DNA fragments were amplified with overlaps regions between adjacent fragments by PCR using Phusion High-Fidelity DNA Polymerase and origo primers (Sigma-Aldrich, St. Louis, MO, USA). Then, PCR products were treated with DpnI and combined using GeneArt Seamless Cloning and Assembly Enzyme Mix. For deletion of sequences, a DNA fragment amplified from the original plasmid was treated with DpnI, phosphorylated using T4 Phosphokinase, and then ligated with T4 DNA Ligase. All plasmids were propagated in *E. coli* OneShot TOP10 (Thermo Fisher Scientific) and purified from overnight culture using NucleoBond Xtra Midi kit (Macherey-Nagel GmbH, Duren, Germany). Constructed gene sequences were verified using Sanger Sequencing Service (Microsynth AG, Balgach, Switzerland). Detailed construction methods are described in Supplementary Methods, and all primers are listed in Supplementary Table 1.

Protein purification

His-MinD¹⁵, MinE-His¹⁵, FtsA¹⁷, FtsZ-Venus-mts⁴⁷ were purified as previously reported. Wild-type FtsZ was purified by calcium-induced precipitation⁶⁴ and covalently labeled in the amino groups of N-term

amino acid residue with Alexa Fluor 488 carboxylic acid succinimidyl ester dye (Thermo Fisher Scientific) as earlier stated⁴⁰. superfolderGFP (sfGFP), msfGFP-MinC, mCherry-MinC, mScarlet-I-MinC, and mScarlet-I-MinC^{G10D} were purified as described previously^{15,32}. In brief, *E. coli* BL21 (DE3) pLysS cells were transformed with pET28a-His-msfGFP-MinC, pET28a-His-mCherry-MinC, pET28a-His-mScarlet-I-MinC, or pIVEX2.3d-sfGFP-His and incubated in LB medium (with 50 μg/mL Kanamycin or 100 μg/mL Ampicillin) at 37 °C while shaking at 180 rpm. After an optical density at 600 nm reached 0.2–0.3, Isopropyl-β-D-thiogalactopyranoside was added at a final concentration of 1 mM to induce expression of the target protein. Cells were further cultured for 2–4 h and harvested. Consequently, cells were resuspended in Lysis buffer (50 mM Tris-HCl, pH 7.5, 300 mM NaCl, 10 mM Imidazole) and disrupted using a tip sonicator (Branson ultrasonics S-250D, Thermo Fisher Scientific). The crude cell lysate was separated by centrifugation for 30 min at 20,000 × *g* at 4 °C, and the supernatant was mixed with Ni-NTA agarose (QIAGEN, Hilden, Germany). The sample was incubated for 10 min at 4 °C while gently shaking and loaded into an empty column. Ni-NTA agarose was washed with Wash buffer (50 mM Tris-HCl, pH 7.5, 300 mM NaCl, 20 mM Imidazole, 10% Glycerol), and then the target protein was eluted with Elution buffer (50 mM Tris-HCl, pH 7.5, 300 mM NaCl, 250 mM Imidazole, 10% Glycerol). The buffer of the protein solution was exchanged with Storage buffer (50 mM Tris-HCl, pH 7.5, 150 mM GluK, 5 mM GluMg, 10% Glycerol) using Amicon Ultra-0.5 centrifugal filter unit 10 kDa (Merck KGaA, Darmstadt, Germany).

FtsZ-G55-Venus-Q56 was purified using a calcium-induced precipitation method similar as described previously⁶⁴. *E. coli* BL21 (DE3) pLysS cells were transformed with pET11b-FtsZ-G55-Venus-Q56, and the cell culture was prepared using LB medium (with 100 μg/mL Ampicillin) as described above. After collecting cell culture, the pellet was resuspended in PEM buffer (50 mM PIPES-NaOH, pH 6.5, 5 mM MgCl₂, 1 mM EDTA) and disrupted using a tip sonicator. The crude cell lysate was separated by centrifugation for 30 min at 20,000 × *g* at 4 °C, and the supernatant was collected. The supernatant was mixed with 1 mM GTP and 20 mM CaCl₂ and incubated at 30 °C for 15 min to induce FtsZ bundles. Subsequently, the FtsZ bundles were pelleted by centrifugation for 15 min at 20,000 × *g* at 4 °C, and the supernatant was discarded. The pellet was again resuspended in PEM buffer, and the supernatant was collected after a centrifugation for 15 min at 20,000 × *g*, 4 °C. Then, precipitation and resuspension steps were repeated (total two precipitation-resuspension cycles) to purify further. The buffer of the protein solution was exchanged with Storage buffer using Amicon Ultra-0.5 centrifugal filter unit 50 kDa (Merck KGaA).

The concentration of the proteins was measured by Bradford Assay (Bio-Rad, Hercules, CA, USA), and protein solutions were

aliquoted, frozen in liquid nitrogen, and stored at -80°C until further use.

Preparation of crowding solution

Lyophilized BSA (Sigma–Aldrich, catalog number: A6003) was dissolved in Reaction buffer (50 mM Tris-HCl, pH7.5, 150 mM GluK, 5 mM GluMg) at approximately 100 g/L. Then, the buffer was exchanged with Reaction buffer to wash out residual molecules using Amicon Ultra-0.5 centrifugal filter unit 50 kDa. After washing steps, the concentration of BSA was measured by Bradford Assay. Ficoll70 and Dextran70 (Sigma–Aldrich) were dissolved in Reaction buffer, and their concentration was calculated from the weight of crowding agents and total volume of the solution (typically, the final concentration of the solution was 300–500 g/L). Crowding solutions were stored at -20°C until further use.

Preparation of lipid vesicles

1-palmitoyl-2-oleoyl-glycero-3-phosphocholine (POPC) and 1-palmitoyl-2-oleoyl-sn-glycero-3-phospho-(1'-rac-glycerol) (POPG) (Avanti Polar Lipids, Alabaster, AL, USA) were mixed at 7:3 molecular ratio dissolved in chloroform at 25 g/L. In case of visualizing the lipid membrane, 2.5 mg/L of ATTO655 labeled 1,2-dioleoyl-sn-glycero-3-phosphoethanolamine (DOPE) (ATTO-Tech GmbH, Siegen, Germany) was further mixed into the lipid mixture. 50 μL of the lipid mixture was dried by nitrogen gas stream. 10 μL of decane (TCI Deutschland GmbH, Eschborn, Germany) was added to the lipid film, and lipids were resuspended by vortexing shortly, and subsequently, 500 μL of mineral oil (Carl Roth GmbH, Karlsruhe, Germany) was added and vortexed for 1 min to prepare a lipid-oil mixture.

We used the double emulsion transfer method for vesicle production to yield giant unilamellar vesicles^{29,46}. For reconstitution with purified proteins, both inner and outer solutions were prepared in Reaction buffer. For cell-free expression experiments, a homemade PURE solution I based on a previous report³³ was used as the outer solution. The osmolarity of inner and outer was measured using an osmometer (Fiske Micro-Osmometer model120, Fiske Associates, Norwood, MA, USA), and outer buffer was diluted to match the osmolarities between inner and outer solution.

Lipid vesicles containing purified proteins or cell-free expression systems were formed following the same methodology with slight differences. For the case of purified proteins, a 96-Well Flat-Bottom Microplate (SensOPlate, Greiner Bio-One GmbH, Kremsmuenster, Austria) was used for vesicle formation and visualization, while for the cell-free system, vesicles were formed using a 1.5 mL tube. For the encapsulation of purified proteins, emulsion solution was obtained from 2 μL of the inner solution and 100 μL of the lipid-oil mixture mixed in a 1.5 mL tube by tapping. 100 μL of the outer solution was added into a well in a 96 well-plate, and subsequently, 50 μL of the lipid-oil mixture was layered on top of the outer solution. Then, ~ 80 μL of the emulsion solution was further dripped on the multi-layered solution. For the encapsulation of the Cell-free system, emulsion solution was formed by 5 μL of the inner solution and 250 μL of the lipid-oil mixture in a 1.5 mL tube. 500 μL of the outer solution was added to a fresh 1.5 mL tube, and subsequently, 200 μL of the lipid-oil mixture was layered to form a lipid monolayer. 200 μL of the emulsion was added carefully to the multi-layered solution.

After multi-layering, lipid vesicles were obtained by centrifugation for 10 min at room temperature (for purified proteins) or 4°C (for cell-free expression) at appropriate centrifugation force. Applied centrifugation force was varied depending on the density of the inner solution given by crowding agents. Typically, we used $3000 \times g$ for 10 g/L, $500 \times g$ for 60 g/L, and $300 \times g$ for 110 g/L of the density of the inner solution. After centrifugation, the oil phase and the supernatant of the water phase were discarded. The rest of the water phase

(approximately 100 μL) was then gently mixed by pipetting to resuspend lipid vesicles, and 50 μL of the vesicle solution was restored in another fresh tube.

Self-organization assays inside lipid vesicles with purified protein

For reconstitution of the MinCDE system, an inner solution containing different concentrations of MinD and MinE (0.25–3 μM) and 0.5 μM mScarlet-I-MinC, mScarlet-I-MinC^{G10D} were mixed with 10 mg/ml BSA and 2.5 mM ATP in Reaction buffer. For the co-reconstitution of FtsZ and Min system, FtsZ-Venus-mts was added to this mixture at 2 μM in addition to 2 mM GTP to trigger its polymerization. In samples containing crowder, different concentration of either Ficoll70 or Dextran70 was added at 25–100 g/L as the final concentration. Assays using only FtsZ were carried out following the same methodology in the absence of the Min system and ATP. All proteins and crowdres were previously dialyzed or diluted in Reaction buffer. Confocal images were collected after 10 min of vesicle preparation and they were used for up to 1–2 h per sample.

Cell-free expression inside lipid vesicles

Cell-free expression was carried out using PURE^{flex} 2.0 (GeneFrontier, Chiba, Japan) following the supplier's instruction. DNA templates were linearized from corresponding plasmids using PrimeSTAR Max DNA polymerase (Takara Bio, Shiga, Japan) with T7P-F and T7P-R primers (Supplementary Table 1). Linearized templates and original plasmids are listed in Supplementary Table 2. The inner solution consisted of PURE^{flex} 2.0, linearized DNA templates, 10 g/L BSA, and 50 g/L Ficoll70. For expression with purified proteins, 2 μM FtsZ-Alexa488, 0.5 μM mCherry-MinC, or 0.5 μM msfGFP-MinC were additionally supplied to the inner solution. The concentration of DNA templates and ratios were optimized to obtain the Min waves patterns and FtsZ structures. All template conditions are listed in Supplementary Table 3. The crowding agent and its concentration were varied for the estimation of sfGFP expression yield.

A homemade chamber was prepared for incubation with the temperature control stage. Coverslips (Menzel Glasses, # 1.5, 22 mm \times 22 mm, Thermo Fisher Scientific) were washed with 70% EtOH. Then, three imaging spacers (Grace Bio-Labs SecureSeal imaging spacers, 1 well, 9 mm \times 0.12 mm, Sigma–Aldrich) were stacked on a glass slip. 20 μL of 10 g/L BSA solution was added to the chamber to passivate the glass surface and leave for 10 min at room temperature, and subsequently, BSA solution was discarded and then washed with outer buffer. 30 μL of vesicle solution was added to the homemade chamber, and it was enclosed by another coverslip and sealed. Then, the chamber was mounted to the PE120-XY Peltier system (Linkam Scientific Instruments, Surrey, United Kingdom) and placed on Zeiss LSM780 confocal laser scanning microscope (Carl Zeiss AG, Oberkochen, Germany). The temperature was set at 4°C before observation and then kept at 37°C for cell-free expression.

Microscopy and image processing

Images of lipid vesicle samples were taken by a Zeiss LSM780 confocal laser scanning microscope using a Plan-Apochromat 20x/0.80 air objective or C-Apochromat 40x/1.20 water-immersion objective (Carl Zeiss AG). Fluorophores were excited using a 488 nm Argon laser (for Alexa488, sfGFP, msfGFP, and Venus), 561 nm diode-pumped solid-state laser (for mCherry and mScarlet-I), and 633 nm He–Ne laser (for ATTO655). Images were typically acquired with 512×512 pixel resolution, 10–15 Z-stacks with 1–2 μm intervals, and 15–20 s intervals for 10 min to 3 h. All recorded tiff images were processed, visualized, and analyzed using Fiji⁶⁵ (v1.53 f). Z-stacks were visualized in 3D max reconstituted images by the Z projection function. Kymographs were generated using a custom ImageJ macro script. In short, the vesicles

periphery was detected from manually drawn ROIs, and then straightened to obtain time-stacked straight-line images. Subsequently, lines were stacked into an orthogonal direction against the long axis of the images in order of elapsed time (Fig. 1d).

Self-organization assay on SLBs

Preparation of the supported lipid bilayers (SLBs) was described previously²⁵. Briefly, a plastic chamber was attached to a cleaned glass coverslip (Menzel Glasses) using ultraviolet-curable glue (Norland Optical Adhesive 63, Norland Products Inc., Jamesburg, NJ, USA). The slide was cleaned in an oxygen plasma cleaner (model Zepto, Diener electronic, Ebhausen, Germany) for 30 s at 50% power. Small unilamellar vesicles (SUVs) were prepared at a concentration of 4 mg/ml of 1,2-dioleoyl-sn-glycero-3-phosphocholine (DOPC) and 1,2-dioleoyl-sn-glycero-3-phospho-(1'-rac-glycerol) (DOPG) mixture (DOPC:DOPG = 7:3 molar ratio) in a buffer (25 mM Tris-HCl pH 7.5, 150 mM KCl, 5 mM MgCl₂) by sonication in a sonicator bath. To generate the SLBs, SUVs were added to the reaction chamber at a concentration of 0.5 mg/ml and incubated for 3 min on a 37 °C warm heating block. The SLBs were washed 10 times with a total of 2 ml in the same buffer in the absence of magnesium (50 mM Tris-HCl pH 7.5, 150 mM KCl) to remove excess vesicles.

Before self-organization assays, the buffer in the chamber was exchanged with Reaction buffer. Then, FtsA was added to the Reaction buffer at 0.25 μM. After -2 min of incubation, a mixture of either FtsZ-wt and FtsZ-Alexa488 (30%) or FtsZ-G55-Venus-Q56 at 1 μM was added to the chamber. Subsequently, 1 mM ATP and 1 mM GTP were added and mixed carefully. SLBs were incubated for >10 min before visualization. Fluorescence imaging was carried out on an inverted custom-built TIRF microscope⁶⁶ with a UAPON 100x/1.49 oil-immersion objective (Olympus, Tokyo, Japan). Excitation of the sample was made using a 488 nm laser, and the fluorescence signal was detected on a CMOS camera (Zyla 4.2, Andor Technology, Belfast, Northern Ireland).

GTPase assay of FtsZ

GTPase activity of FtsZ was measured by quantifying the inorganic phosphate with a colorimetric phosphate quantification assay (BIOMOL GREEN kit, ENZO life sciences, Lörrach, Germany) for 140 s⁴⁸. Purified FtsZ-wt or FtsZ-G55-Venus-Q56 were used at 3 μM in Reaction buffer, and polymerization was triggered by 1 mM GTP. 13 μL fractions were added to a 96-Well Flat-Bottom Microplate (UV-Star, Greiner Bio-One GmbH) every 20 s after addition of GTP and mixed with 37 μL of Reaction buffer and 100 μL of BIOMOL GREEN reagent, stopping the reaction. After -10 min of incubation at RT, the absorbance at 620 nm was measured in a TECAN plate reader (Tecan Group Ltd., Mannedorf, Switzerland) at room temperature. Phosphate concentrations were calculated from a Na₂HPO₄ standard curve in Reaction buffer, and the GTPase activity reaction rate (V, mol Pi/mol FtsZ/min) was determined from the slope of the linear part of phosphate accumulation curves.

Analysis of the wave patterns and FtsZ structures inside lipid vesicles

Wave patterns of MinCDE proteins inside vesicles were analyzed using a custom ImageJ macro script. Briefly, time-lapse images were used to detect the lipid vesicles and obtain a kymograph from the fluorescence intensity on the peripheral membrane. These Kymographs were classified and checked manually in order to calculate the appearance ratios of each wave mode at each condition. FtsZ structures were visualized and classified manually using the 3D max projection of the lipid vesicles containing FtsZ.

Estimation of the sfGFP expression level within lipid vesicles

First, different concentration series of purified sfGFP (0, 0.1, 0.3, 1, 3, 10, or 30 μM) was encapsulated in vesicles, and the fluorescence

intensity of sfGFP was measured ($n = 30$ individual vesicles) from confocal images for each concentration to obtain the standard curve (Supplementary Fig. 4a). Then, sfGFP was expressed inside lipid vesicles using 2 nM sfGFP template with different macromolecular crowding conditions (no additives, 50 g/L Ficoll70, 100 g/L Ficoll70, 50 g/L Dextran70, or 100 g/L Dextran70), and the fluorescence intensity of sfGFP was measured within 100 individual vesicles for 200 min with 1 min intervals. The box plots were obtained from fluorescence intensities at 200 min (for Supplementary Fig. 4g), and time-development of sfGFP expression level was calculated from fluorescence intensities at each time point (Supplementary Fig. 4b–f).

Analysis of the FtsZ localization inside lipid vesicles along with FtsA expression

Cell-free expression of FtsA was performed with 2 μM FtsZ-Alexa488 (ftsA template was omitted for a negative control) for 60 min with 20 s intervals (total 180 time points, recording started after 20 min incubation at 37 °C). Fluorescence intensity of FtsZ-Alexa488 in the lumen or membrane at the equatorial plane was then measured with a representative vesicle and average intensities at each time point were plotted in Supplementary Fig. 5b or d. The same procedure was repeated to measure the intensity of FtsZ-G55-Venus-Q56 on membrane in the co-expression experiment of FtsA/FtsZ-G55-Venus-Q56 and plotted in Supplementary Fig. 6h. In both cases, average fluorescence intensities of FtsZ on membrane among different vesicles were measured after cell-free expression (total 80 min) and plotted against vesicle diameter in Supplementary Figs. 5e and 6i.

Estimation of the wave occurrence with cell-free expressed Min proteins

Cell-free co-expression of MinD/MinE or mCherry-MinC/MinD/MinE was performed with 0.5 μM purified msfGFP-MinC for 50 min with 20 s intervals (total 150 time points, recording started after 10 min incubation at 37 °C). Then, vesicles were randomly chosen ($n = 116$ and 100 for MinDE and MinCDE expression, respectively.) and the percentage of Min wave patterns inside lipid vesicles were calculated as (sum of the dynamic waves and static patterns)/(vesicle number) at every 3 min time point and plotted in Supplementary Fig. 6c.

Analysis of FtsZ structures and the aspect ratio of deformed vesicles

Before and after 2–3 h of co-expression of FtsA/FtsZ-G55-Venus-Q56/mCherry-MinC/MinD/MinE, Z-stack images of Venus fluorescence were acquired with tile-scan function. Vesicles were classified into four size ranges (8–12, 12–16, 16–20, >20 μm in a diameter, $n = 40$ for each range) from the images before expression. The structures of FtsZ were then detected manually from 3D max projection images, and vesicles with FtsZ-ring structure were further analyzed to determine the aspect ratio. The aspect ratio of the deformed vesicles was calculated as (length of short axis)/(length of long axis). Also, the degree of deformation was calculated as (length of short axis)/(diameter of the vesicle before deformation). The status of the vesicles was classified into three (no ring structure, ring structure, ring structure + deformation (with <0.95 aspect ratio)) and plotted in Fig. 4e. The relation of the aspect ratio of the vesicles with FtsZ-ring and the original vesicle sizes were further plotted in Fig. 4f, and the correlation coefficient was calculated among all vesicles plotted in the figure ($n = 79$).

Surface plot of the FtsZ distribution inside a lipid vesicle

The kymograph of FtsZ distribution at an equatorial plane of the vesicle shown in Supplementary Fig. 7c was obtained using a custom

ImageJ macro. Then, fluorescence intensities of the FtsZ were measured at every 10 min from the kymograph. The intensity profiles were then plotted against relative position on the peripheral of the vesicle (0° – 360°) in Supplementary Fig. 7c.

Statistics and reproducibility

The high number of vesicles per sample and the protein behavior found in them allowed a deep characterization of the phenomenology described in our results in a reliable manner. Wide field images showing multiple vesicles and several micrographs of similar results are shown in the figures to demonstrate and support the high reproducibility of our data together with quantitative analysis. In addition, all the micrographs shown in figures both in the main manuscript and supplementary file correspond to a reproducible result from 3 or more independent biological replicates.

Reporting summary

Further information on research design is available in the Nature Research Reporting Summary linked to this article.

Data availability

The data sets for all experimental conditions, graphs, and oligonucleotide sequences generated in this study are provided in the Supplementary Information/Source Data file. The original image data are available under restricted access for their large file size (>10 GB), access can be obtained by reasonable request from the corresponding author. Source data are provided with this paper.

Code availability

The custom ImageJ macro code for wave pattern analysis and generation of kymographs has been deposited in github [<https://github.com/ShunshiKohyama/Min-wave-analysis-in-GUVs>].

References

- Schwille, P. Bottom-up synthetic biology: Engineering in a tinkerer's world. *Science* **333**, 1252–1254 (2011).
- Schwille, P. et al. MaxSynBio: Avenues towards creating cells from the bottom up. *Angew. Chem. Int. Ed.* **57**, 13382–13392 (2018).
- Rivas, G., Vogel, S. K. & Schwille, P. Reconstitution of cytoskeletal protein assemblies for large-scale membrane transformation. *Curr. Opin. Chem. Biol.* **22**, 18–26 (2014).
- Mulla, Y., Aufderhorst-Roberts, A. & Koenderink, G. H. Shaping up synthetic cells. *Phys. Biol.* **15**, (2018).
- Stano, P. Is research on “Synthetic cells” moving to the next level? *Life* **9**, 3 (2018).
- Rothfield, L., Justice, S. & García-Lara, J. Bacterial cell division. *Annu. Rev. Genet.* **33**, 423–448 (1999).
- Scholey, J. M., Brust-Mascher, I. & Mogilner, A. Cell division. *Nature* **422**, 746–752 (2003).
- Natale, P. & Vicente, M. Bacterial cell division. *eLS* 1–9 (2020).
- Loose, M., Kruse, K. & Schwille, P. Protein self-organization: lessons from the Min system. *Annu. Rev. Biophys.* **40**, 315–336 (2011).
- Ramm, B., Heermann, T. & Schwille, P. The E. coli MinCDE system in the regulation of protein patterns and gradients. *Cell. Mol. Life Sci.* **76**, 4245–4273 (2019).
- Raskin, D. M. & de Boer, P. A. J. Rapid pole-to-pole oscillation of a protein required for directing division to the middle of Escherichia coli. *Proc. Natl Acad. Sci. USA* **96**, 4971–4976 (1999).
- Hu, Z. & Lutkenhaus, J. Topological regulation of cell division in Escherichia coli involves rapid pole to pole oscillation of the division inhibitor MinC under the control of MinD and MinE. *Mol. Microbiol.* **34**, 82–90 (1999).
- Bi, E. & Lutkenhaus, J. FtsZ ring structure associated with division in Escherichia coli. *Nature* **354**, 161–164 (1991).
- McQuillen, R. & Xiao, J. Insights into the structure, function, and dynamics of the bacterial cytokinetic FtsZ-ring. *Annu. Rev. Biophysics* **49**, 309–341 (2020).
- Loose, M., Fischer-Friedrich, E., Ries, J., Kruse, K. & Schwille, P. Spatial regulators for bacterial cell division self-organize into surface waves in vitro. *Science* **320**, 789–792 (2008).
- Osawa, M., Anderson, D. E. & Erickson, H. P. Reconstitution of contractile FtsZ rings in liposomes. *Science* **320**, 792–794 (2008).
- Loose, M. & Mitchison, T. J. The bacterial cell division proteins ftsA and ftsZ self-organize into dynamic cytoskeletal patterns. *Nat. Cell Biol.* **16**, 38–46 (2014).
- Osawa, M. & Erickson, H. P. Liposome division by a simple bacterial division machinery. *Proc. Natl Acad. Sci. USA* **110**, 11000–11004 (2013).
- Furusato, T. et al. De novo synthesis of basal bacterial cell division proteins FtsZ, FtsA, and ZipA inside giant vesicles. *ACS Synth. Biol.* **7**, 953–961 (2018).
- Godino, E. et al. Cell-free biogenesis of bacterial division proto-rings that can constrict liposomes. *Commun. Biol.* **3**, 539 (2020).
- Ramirez-Diaz, D. A. et al. FtsZ induces membrane deformations via torsional stress upon GTP hydrolysis. *Nat. Commun.* **12**, 3310 (2021).
- Ganzinger, K. A. et al. FtsZ reorganization facilitates deformation of giant vesicles in microfluidic traps. *Angew. Chem. Int. Ed.* **132**, 21556–21560 (2020).
- Martos, A. et al. FtsZ polymers tethered to the membrane by ZipA are susceptible to spatial regulation by Min waves. *Biophys. J.* **108**, 2371–2383 (2015).
- Zieske, K., Chwastek, G. & Schwille, P. Protein patterns and oscillations on lipid monolayers and in microdroplets. *Angew. Chem. Int. Ed.* **55**, 13455–13459 (2016).
- Ramm, B. et al. The MinDE system is a generic spatial cue for membrane protein distribution in vitro. *Nat. Commun.* **9**, 3942 (2018).
- Godino, E. et al. De novo synthesized Min proteins drive oscillatory liposome deformation and regulate FtsA-FtsZ cytoskeletal patterns. *Nat. Commun.* **10**, 4969 (2019).
- Litschel, T. & Schwille, P. Protein reconstitution inside giant unilamellar vesicles. *Annu. Rev. Biophysics* **50**, 525–548 (2021).
- Rivas, G., Alfonso, C., Jiménez, M., Monterroso, B. & Zorrilla, S. Macromolecular interactions of the bacterial division FtsZ protein: From quantitative biochemistry and crowding to reconstructing minimal divisomes in the test tube. *Biophys. Rev.* **5**, 63–77 (2013).
- Yoshida, A., Kohyama, S., Fujiwara, K., Nishikawa, S. & Doi, N. Regulation of spatiotemporal patterning in artificial cells by a defined protein expression system. *Chem. Sci.* **10**, 11064–11072 (2019).
- Yue, K., Zhu, Y. & Kai, L. Cell-free protein synthesis: Chassis toward the minimal cell. *Cells* **8**, 315 (2019).
- Garenne, D. et al. Cell-free gene expression. *Nat. Rev. Methods Prim.* **1**, 49 (2021).
- Kohyama, S., Yoshinaga, N., Yanagisawa, M., Fujiwara, K. & Doi, N. Cell-sized confinement controls generation and stability of a protein wave for spatiotemporal regulation in cells. *eLife* **8**, e44591 (2019).
- Kohyama, S., Fujiwara, K., Yoshinaga, N. & Doi, N. Conformational equilibrium of MinE regulates the allowable concentration ranges of a protein wave for cell division. *Nanoscale* **12**, 11960–11970 (2020).
- Glock, P. et al. Stationary patterns in a two-protein reaction-diffusion system. *ACS Synth. Biol.* **8**, 148–157 (2018).
- Rueda, S., Vicente, M. & Mingorance, J. Concentration and assembly of the division ring proteins FtsZ, FtsA, and ZipA during the Escherichia coli cell cycle. *J. Bacteriol.* **185**, 3344–3351 (2003).
- Schmidt, A. et al. The quantitative and condition-dependent Escherichia coli proteome. *Nat. Biotechnol.* **34**, 104–110 (2016).

37. Ramm, B. et al. A diffusio-phoretic mechanism for ATP-driven transport without motor proteins. *Nat. Phys.* **17**, 850–858 (2021).
38. Zhou, H.-X., Rivas, G. & Minton, A. P. Macromolecular crowding and confinement: biochemical, biophysical, and potential physiological consequences. *Annu. Rev. Biophys.* **37**, 375–397 (2008).
39. Robles-Ramos, M. Á. et al. Assembly of bacterial cell division protein FtsZ into dynamic biomolecular condensates. *Biochim. Biophys. Acta - Mol. Cell Res.* **1868**, 118986 (2021).
40. González, J. M. et al. Essential cell division protein FtsZ assembles into one monomer-thick ribbons under conditions resembling the crowded intracellular environment. *J. Biol. Chem.* **278**, 37664–37671 (2003).
41. Zieske, K. & Schwille, P. Reconstitution of self-organizing protein gradients as spatial cues in cell-free systems. *eLife* **3**, e03949 (2014).
42. Groen, J. et al. Associative interactions in crowded solutions of biopolymers counteract depletion effects. *J. Am. Chem. Soc.* **137**, 13041–13048 (2015).
43. Cabré, E. J. et al. Bacterial division proteins FtsZ and ZipA induce vesicle shrinkage and cell membrane invagination. *J. Biol. Chem.* **288**, 26625–26634 (2013).
44. Rivas, G. & Minton, A. P. Macromolecular crowding in vitro, in vivo, and in between. *Trends Biochem. Sci.* **41**, 970–981 (2016).
45. Norred, S. E. et al. Macromolecular crowding induces spatial correlations that control gene expression bursting patterns. *ACS Synth. Biol.* **7**, 1251–1258 (2018).
46. Pautot, S., Frisken, B. J. & Weitz, D. A. Engineering asymmetric vesicles. *Proc. Natl Acad. Sci. USA* **100**, 10718–10721 (2003).
47. Ramirez-Diaz, D. A. et al. Treadmilling analysis reveals new insights into dynamic FtsZ ring architecture. *PLOS Biol.* **16**, e2004845 (2018).
48. Garcia-Soriano, D. A., Heermann, T., Raso, A., Rivas, G. & Schwille, P. The speed of FtsZ treadmilling is tightly regulated by membrane binding. *Sci. Rep.* **10**, 10447 (2020).
49. Hu, Z., Mukherjee, A., Pichoff, S. & Lutkenhaus, J. The MinC component of the division site selection system in *Escherichia coli* interacts with FtsZ to prevent polymerization. *Proc. Nat. Acad. Sci. USA* **96**, 14819–14824 (1999).
50. Addinal, S. G. & Lutkenhaus, J. (1996) FtsA is localized to the septum in an FtsZ-dependent manner. *J. Bacteriol.* **178**, 7167–7172 (1996).
51. Ma, X., Ehrhardt, D. W. & Margolin, W. Colocalization of cell division proteins FtsZ and FtsA to cytoskeletal structures in living *Escherichia coli* cells by using green fluorescent protein. *Proc. Nat. Acad. Sci. USA* **93**, 12998–13003 (1996).
52. Shimizu, Y. et al. Cell-free translation reconstituted with purified components. *Nat. Biotechnol.* **19**, 751–755 (2001).
53. Kuruma, Y. & Ueda, T. The PURE system for the cell-free synthesis of membrane proteins. *Nat. Protoc.* **10**, 1328–1344 (2015).
54. Osawa, M. & Erickson, H. P. Probing the domain structure of FtsZ by random truncation and insertion of GFP. *Microbiology* **151**, 4033–4043 (2005).
55. Moore, D. A., Whatley, Z. N., Joshi, C. P., Osawa, M. & Erickson, H. P. Probing for binding regions of the FtsZ protein surface through site-directed insertions: Discovery of fully functional FtsZ-fluorescent proteins. *J. Bacteriol.* **199**, e00553–16 (2017).
56. Litschel, T. et al. Reconstitution of contractile actomyosin rings in vesicles. *Nat. Commun.* **12**, (2021).
57. Lan, G., Wolgemuth, C. W. & Sun, S. X. Z-ring force and cell shape during division in rod-like bacteria. *Proc. Nat. Acad. Sci. USA* **104**, 16110–16115 (2007).
58. Hénon, S., Lenormand, G., Richert, A. & Gallet, F. A new determination of the shear modulus of the human erythrocyte membrane using optical tweezers. *Biophys. J.* **76**, 1145–1151 (1999).
59. Litschel, T., Ramm, B., Maas, R., Heymann, M. & Schwille, P. Beating vesicles: Encapsulated protein oscillations cause dynamic membrane deformations. *Angew. Chem. Int. Ed.* **57**, 16286–16290 (2018).
60. Christ, S., Litschel, T., Schwille, P. & Lipowsky, R. Active shape oscillations of giant vesicles with cyclic closure and opening of membrane necks. *Soft Matter* **17**, 319–330 (2021).
61. Derganc, J. & Čopič, A. Membrane bending by protein crowding is affected by protein lateral confinement. *Biochim. Biophys. Acta - Biomembr.* **1858**, 1152–1159 (2016).
62. Li, Y., Lipowsky, R. & Dimova, R. Transition from complete to partial wetting within membrane compartments. *J. Am. Chem. Soc.* **130**, 12252–12253 (2008).
63. Andes-Koback, M. & Keating, C. D. Complete budding and asymmetric division of primitive model cells to produce daughter vesicles with different interior and membrane compositions. *J. Am. Chem. Soc.* **133**, 9545–9555 (2011).
64. Rivas, G. et al. Magnesium-induced linear self-association of the FtsZ bacterial cell division protein monomer. The primary steps for FtsZ assembly. *J. Biol. Chem.* **275**, 11740–11749 (2000).
65. Schindelin, J. et al. Fiji: An open-source platform for biological-image analysis. *Nat. Methods* **9**, 676–682 (2012).
66. Stehr, F., Stein, J., Schueder, F., Schwille, P. & Jungmann, R. Flat-top TIRF illumination boosts DNA-PAINT imaging and quantification. *Nat. Commun.* **10**, 1268 (2019).

Acknowledgements

Special thanks to Germán Rivas (CIB Margarita Salas, CSIC, Spain) for providing essential scientific advice on the self-organization with purified proteins under crowding, and his helpful comments and critical reviews on the manuscript. We are grateful to Lei Kai (School of Life Sciences, Jiangsu Normal University, China) for the plasmid pIVEX2.3d-sfGFP-His, Leon Harrington and Tamara Heermann for their help in plasmid construction. We would like to thank MPIIB Core Facility for assistance in protein purification, Michaela Schaper for plasmid cloning, Katharina Nakel for GTPase assay, Sigrid Bauer for lipid preparation, Kerstin Andersson for protein purification, and Michele Russo for assistance with the purification of FtsZ-G55-Venus-Q56. We are also grateful to Jan-Hagen Krohn and Yusuf Qutbuddin for assistance in TIRF microscopy. Further, we thank Leon Babl, Hiromune Eto, Ana Yagüe Relimpio, and Henri Franquelin for helpful discussions. This work has been supported by JSPS Overseas Research Fellowships (S.K.), the Max Planck-Bristol Centre for Minimal Biology (A.M.-S.), and CRC 863 (Forces in Biological Systems) by the Deutsche Forschungsgemeinschaft (P. S.). A.M.-S. is part of IMPRS-LS.

Author contributions

S.K., A.M.-S., and P.S. conceived the study and wrote the manuscript. S.K. designed, performed, and analyzed all experiments with cell-free expression. S.K. made the custom ImageJ macro script for the analysis and kymograph visualization. A.M.-S. designed, performed, and analyzed all experiments with purified proteins within vesicles and SLBs. S.K. designed plasmids for cell-free expression and purification of sfGFP, msfGFP-MinC, mScarlet-I-MinC, mScarlet-I-MinC^{G10D}, mCherry-MinC, FtsZ-Venus, and FtsZ-G55-Venus-Q56. S.K. also purified sfGFP, msfGFP-MinC, mScarlet-I-MinC, mCherry-MinC, and FtsZ-G55-Venus-Q56. A.M.-S. purified and labeled FtsZ-wt. A.M.-S. also characterized FtsZ-G55-Venus-Q56 and FtsZ-wt by performing a GTPase assay.

Funding

Open Access funding enabled and organized by Projekt DEAL.

Competing interests

The authors declare no competing interests.

Additional information

Supplementary information The online version contains supplementary material available at <https://doi.org/10.1038/s41467-022-33679-x>.

Correspondence and requests for materials should be addressed to Petra Schwillle.

Peer review information *Nature Communications* thanks the anonymous reviewer(s) for their contribution to the peer review of this work. Peer reviewer reports are available.

Reprints and permission information is available at <http://www.nature.com/reprints>

Publisher's note Springer Nature remains neutral with regard to jurisdictional claims in published maps and institutional affiliations.

Open Access This article is licensed under a Creative Commons Attribution 4.0 International License, which permits use, sharing, adaptation, distribution and reproduction in any medium or format, as long as you give appropriate credit to the original author(s) and the source, provide a link to the Creative Commons license, and indicate if changes were made. The images or other third party material in this article are included in the article's Creative Commons license, unless indicated otherwise in a credit line to the material. If material is not included in the article's Creative Commons license and your intended use is not permitted by statutory regulation or exceeds the permitted use, you will need to obtain permission directly from the copyright holder. To view a copy of this license, visit <http://creativecommons.org/licenses/by/4.0/>.

© The Author(s) 2022

Supplement to publication P4

Reprinted with permission from:

Kohyama, S.*, **Merino-Salomón, A.*** and Schwille, P. (2022). *In vitro* assembly, positioning and contraction of a division ring in minimal cells. Nature Communications 13:6098.

Source online: <https://doi.org/10.1038/s41467-022-33679-x>

Supplementary Information

***In vitro* assembly, positioning and contraction of a division ring in minimal cells**

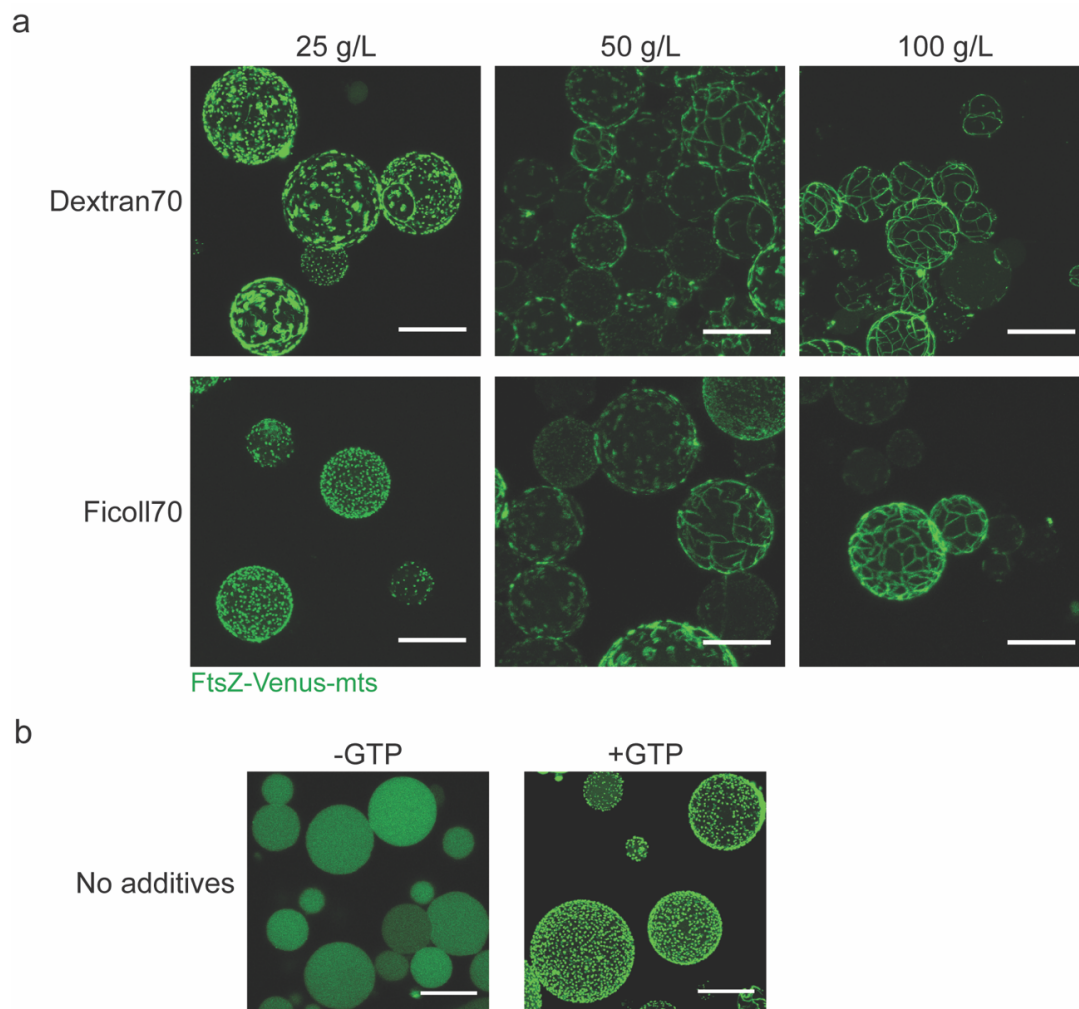
Shunshi Kohyama^{1,§}, Adrián Merino-Salomón^{1,§} and Petra Schwille^{1,*}

[§]These authors contributed equally

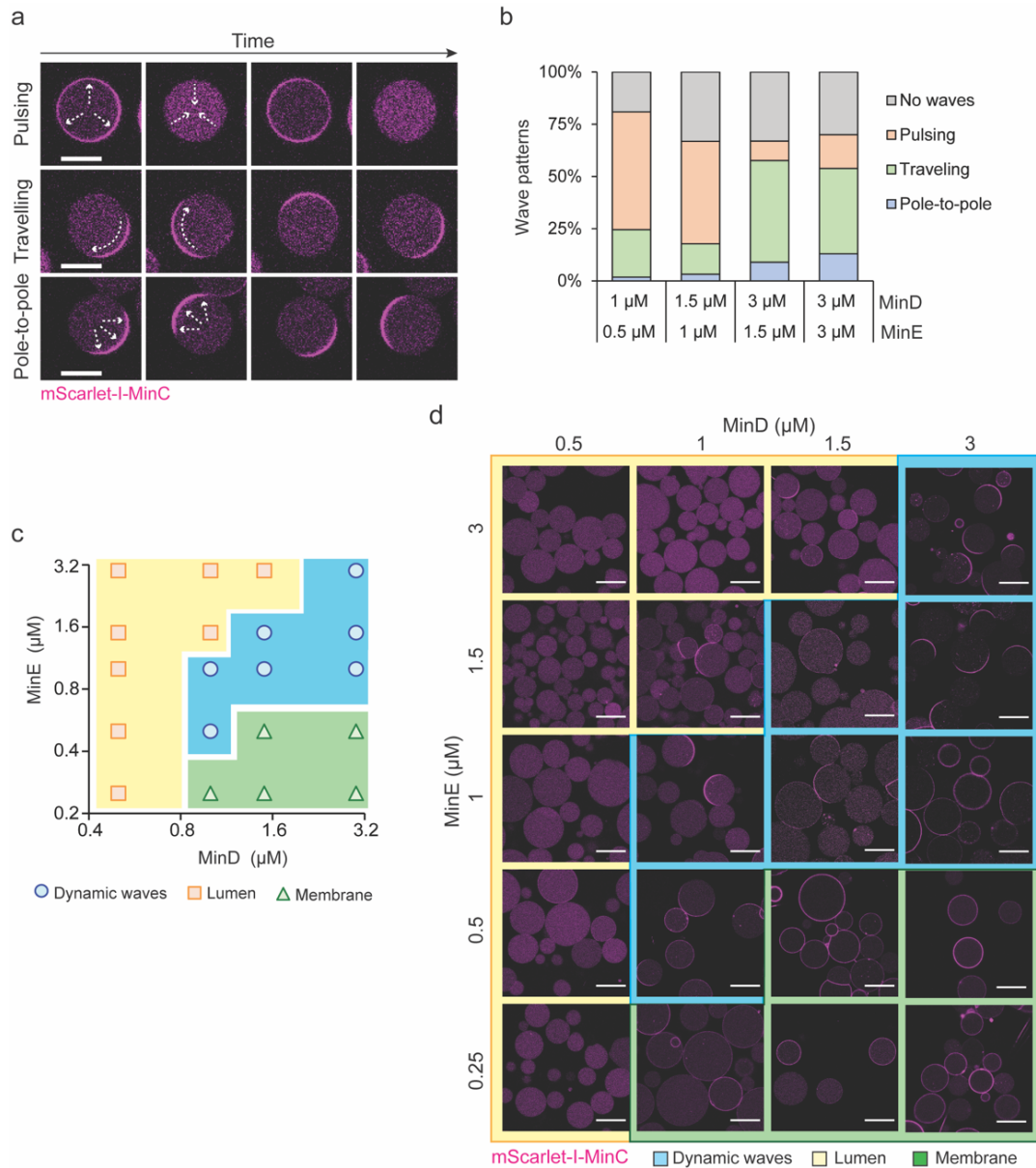
¹Dept. Cellular and Molecular Biophysics, Max Planck Institute of Biochemistry, Am

Klopferspitz 18, 82152 Martinsried, Germany. E-mail: schwille@biochem.mpg.de

Supplementary Figures

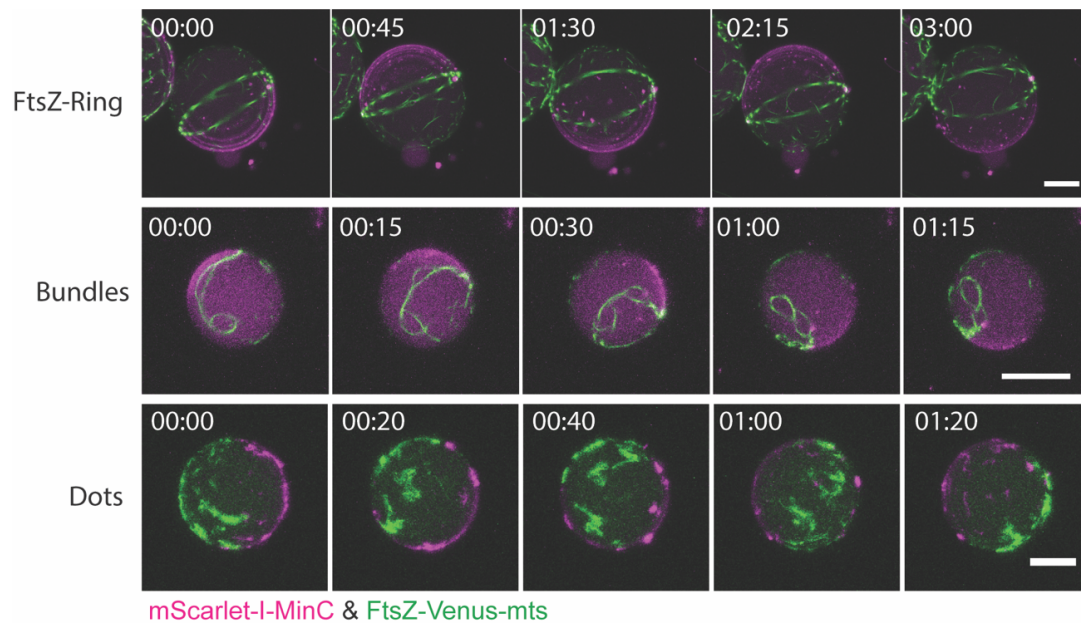


Supplementary Fig. 1 Effect of macromolecular crowding over FtsZ behavior inside lipid vesicles. **a** Representative 3D max projection images of FtsZ-Venus-mts structures inside lipid vesicles under different crowding conditions using Dextran70 and Ficoll70 (2 μ M FtsZ-Venus-mts + 1 mM GTP). Scale bars: 25 μ m. **b** Representative 3D max projection images of FtsZ-Venus-mts (2 μ M) without the addition of crowders with the absence (above) and presence (below) of 1 mM GTP. Scale bars: 25 μ m.

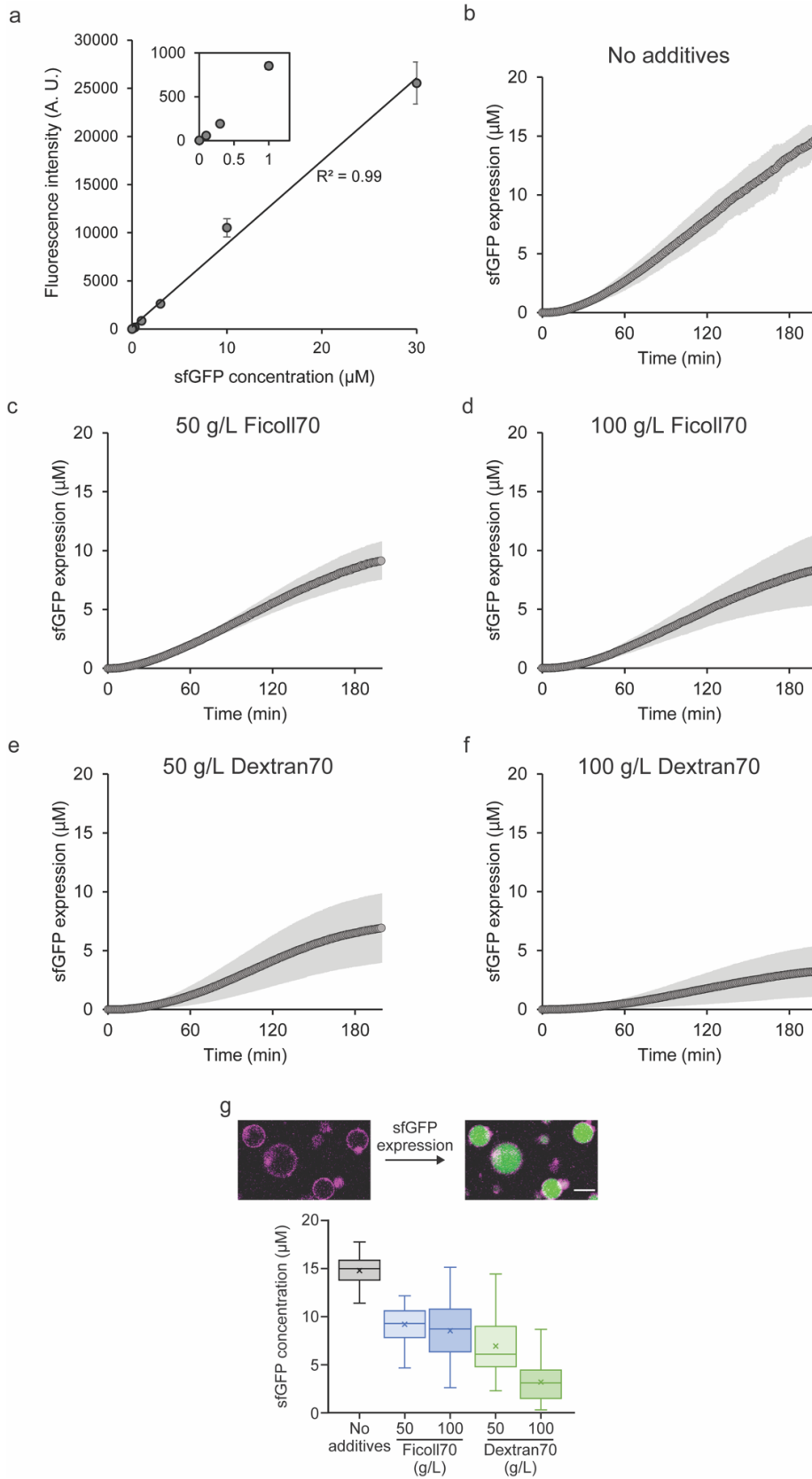


Supplementary Fig. 2 Reconstitution of the MinCDE system inside lipid vesicles. **a** Encapsulation of MinCDE proteins within lipid vesicles result in different Min wave patterns that can be categorized in three main groups depending on their behavior. Pulsing oscillations: MinD oscillates between the lumen of the vesicles and the membrane surface. Travelling or circling: Min proteins continuously revolve on the membrane of the GUV. Pole-to-pole oscillations: Min proteins bind alternately to the membrane of the two hemispheres of the vesicle. White arrows represent the behavior of MinCDE proteins inside vesicles. Scale bars: 15 μm . **b** Frequency of Min wave patterns at different MinDE ratios. Min wave patterns are differentiated into four

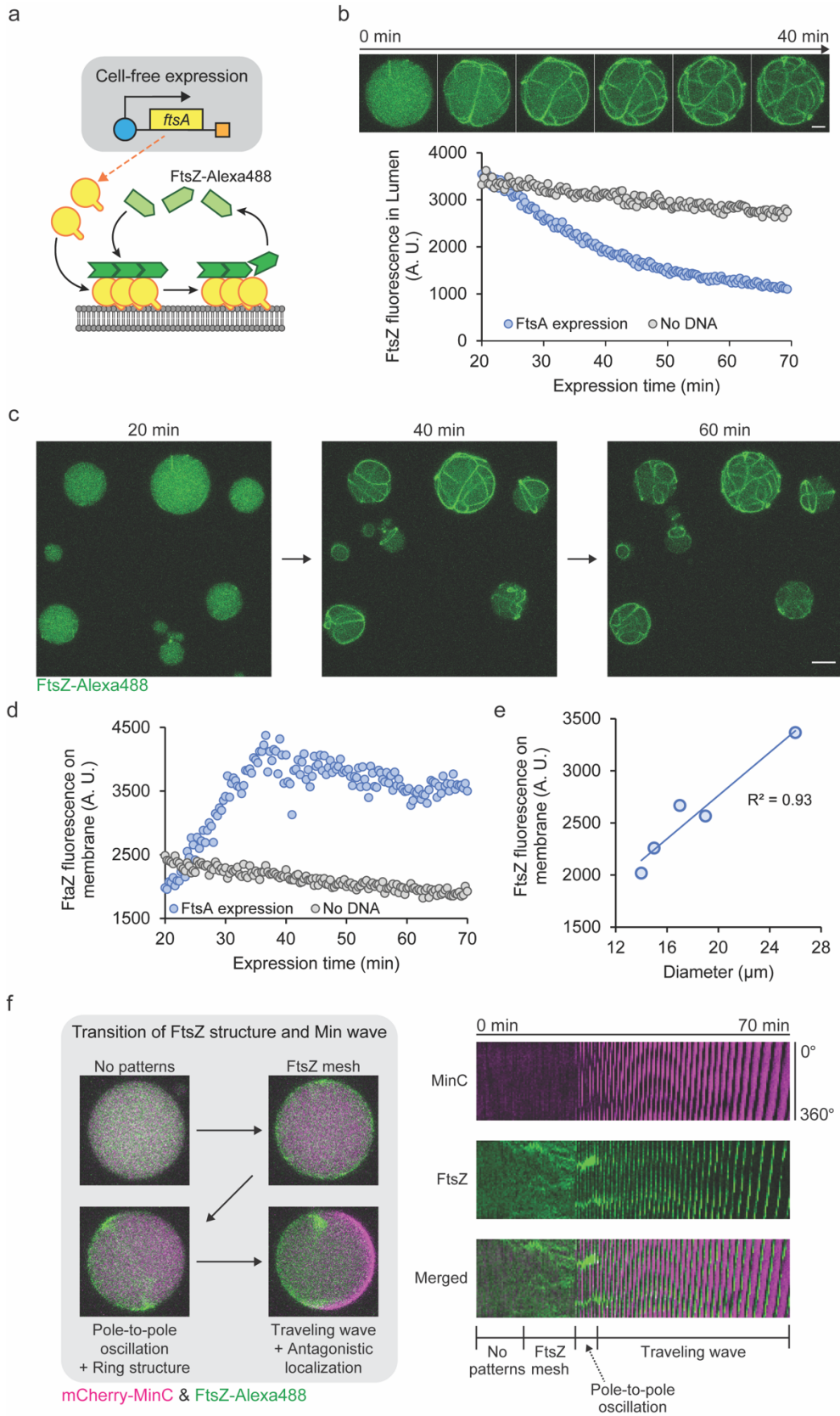
categories: absence of waves, pole-to-pole oscillations, traveling waves, or pulsing inside vesicles at different MinDE ratios ($n = 220$ for each condition). The four MinDE ratios that showed the relatively high percentage ($>65\%$) of dynamic waves were selected for this analysis. **c** Phase diagram of major MinCDE pattern formation inside lipid vesicles without crowding conditions. To facilitate their interpretation, we have grouped the three MinCDE wave patterns (Pulsing, travelling or Pole-to-pole) into the category of “Dynamic” here in contrast with localization in lumen (No significant membrane attachment or protein waves), and localization on membrane (No MinCDE waves). These three categories are represented vs. MinDE concentrations. **d** Representative confocal images of lipid vesicles containing MinCDE proteins at different MinDE ratios. Scale bars: $25\ \mu\text{m}$. Source data are provided as a Source Data file.



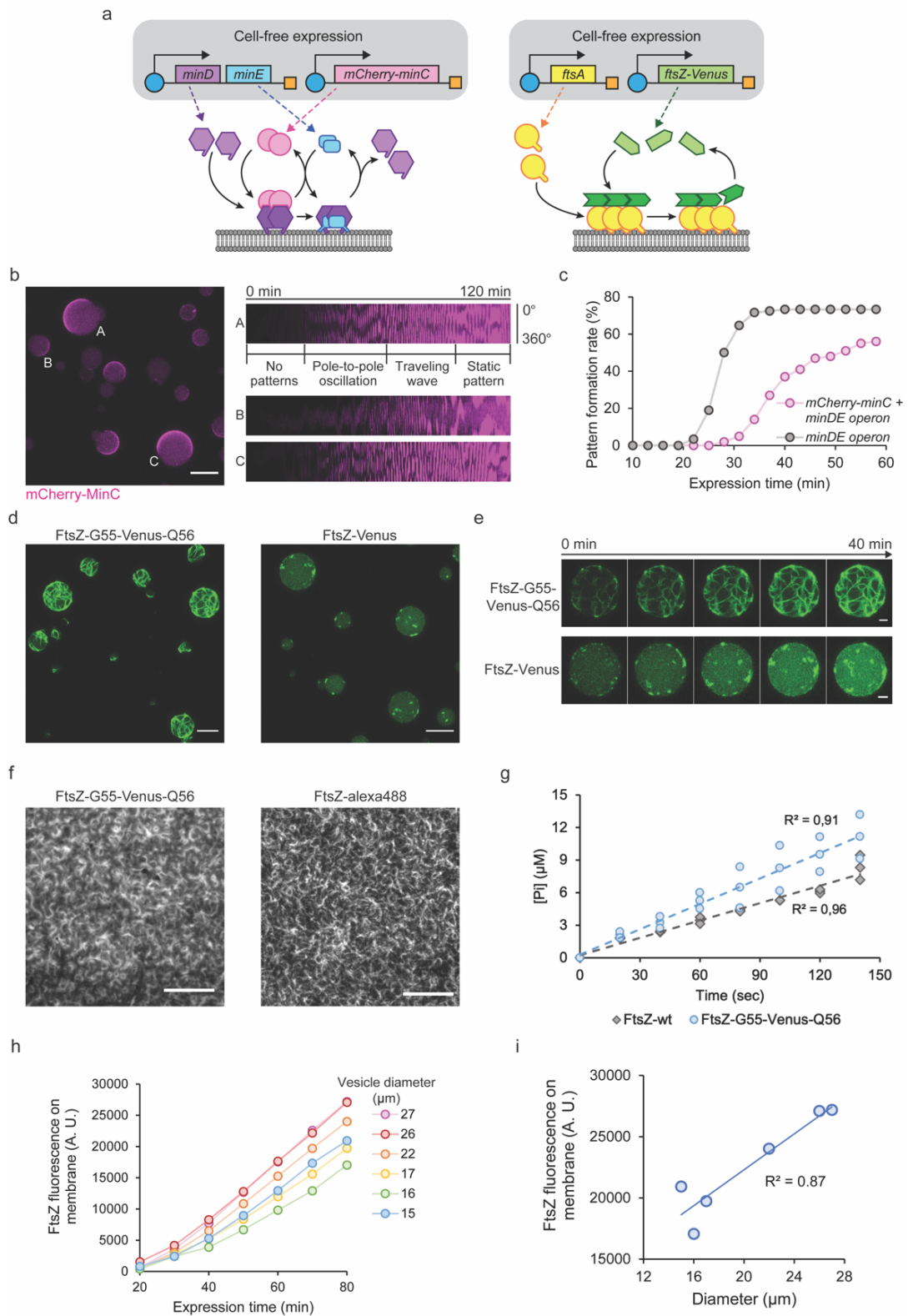
Supplementary Fig. 3 FtsZ structures are reorganized by MinCDE oscillations inside vesicles. Time-lapse confocal images of FtsZ-Venus-mts structures in the presence of MinCDE proteins. FtsZ structures bundles/mesh or dots are reorganized by the MinCDE waves, sometimes forming FtsZ-rings (2 μ M FtsZ-Venus-mts, 3 μ M MinD, 3 μ M MinE, 0.5 μ M mScarlet-I-MinC). Time is represented as mm:ss and Scale bars: 10 μ m. Confocal images were recorded after 10 min of vesicle preparation for 1-2h.



Supplementary Fig. 4 Estimation of cell-free expression level under macromolecular crowding environment within lipid vesicles. **a** Standard curve of sfGFP concentration against fluorescence intensity (Arbitrary Units) within vesicles. 0, 0.1, 0.3, 1, 3, 10, and 30 μM of sfGFP were encapsulated within vesicles, and the mean fluorescence intensities of sfGFP were measured. Plots represent the mean intensity and standard deviation. $n = 30$ for each concentration. **b-f** Time-development of sfGFP expression under macromolecular crowding environments. sfGFP was expressed using 2 nM sfGFP template inside vesicles with no additives (**b**), 50 g/L Ficoll70 (**c**), 100 g/L Ficoll70 (**d**), 50 g/L Dextran70 (**e**), or 100 g/L Dextran70 (**f**). Then, 100 different vesicles were randomly chosen, and the fluorescence intensity of sfGFP in each vesicle was measured every 1 min for 200 min. Plots and bars indicate means and standard deviations, respectively. **g** Cell-free expression of sfGFP within vesicles under different crowding conditions. Top: Expression of sfGFP under 50 g/L of Ficoll7. Images show the same vesicles before incubation and after 200 min incubation at 37 °C. Scale bar: 20 μm . Bottom: Box plot of expression levels of sfGFP inside vesicles after 200 min incubation at 37 °C. Under Ficoll70 crowding, sfGFP expression level reached around 10 μM , while Dextran70 radically impaired expression. Mean is shown as a cross mark, box limits are quartiles 1 and 3, line inside boxes indicate median, and whiskers are the highest or lowest data points. $n = 100$ for each crowding condition. Source data are provided as a Source Data file.



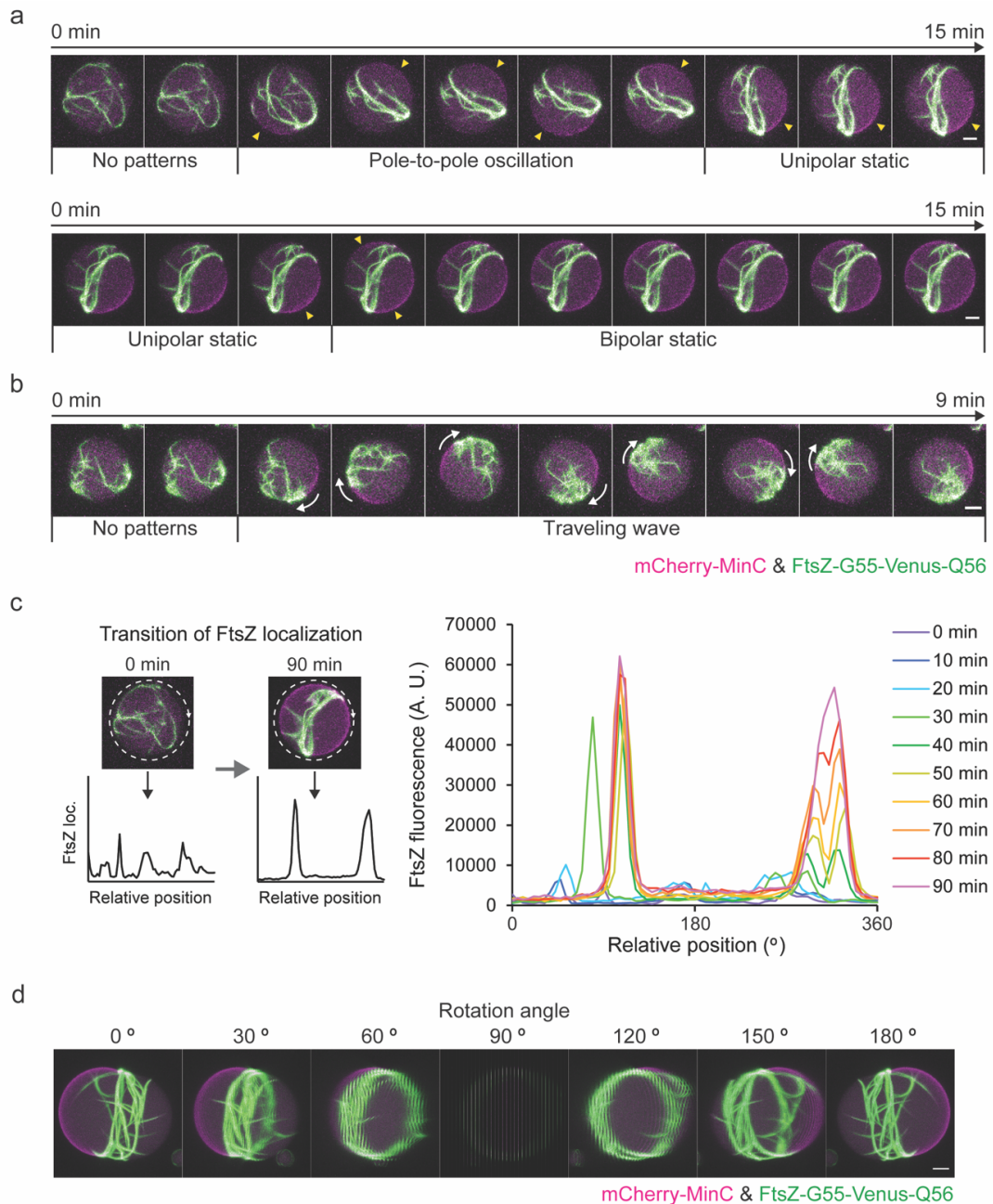
Supplementary Fig. 5 Development of the FtsZ structures within lipid vesicles through cell-free expression of FtsA and MinDE proteins. **a** Schematic illustration of PURE cell-free expression of FtsA with purified FtsZ. **b** FtsZ-FtsA mesh structure inside vesicles via FtsA expression. Top: Time-lapse images of FtsZ mesh structure formation with 3D max projection. FtsZ indicates dynamic assembly into bundles on the membrane inside the vesicle along with FtsA expression using 5 nM of *ftsA* template with 2 μ M purified FtsZ-Alexa488 and 50 g/L Ficoll70. Recording started after 20 min of cell-free expression. Scale bar: 5 μ m. Bottom: localization change of FtsZ-Alexa488 along with FtsA expression in the lumen of the vesicles. FtsZ level (Arbitrary Units) decreases in the lumen by expressing FtsA (5 nM of *ftsA* template), targeting FtsZ to the membrane, while the negative control (no DNA) indicates a slight decrease of fluorescence by photobleaching. **c** Time-lapse images of FtsZ-FtsA mesh development with 3D max projection. FtsA was expressed at 37 °C using 5 nM of *ftsA* template with 2 μ M purified FtsZ-Alexa488 and 50 g/L Ficoll70. FtsZ indicated dynamic assembly into mesh structures on the membrane along with time-lapse. Scale bar: 20 μ m. **d** Localization change of FtsZ-Alexa488 along with FtsA expression on membrane of the vesicles. In contrast to the FtsZ intensity in the lumen (Supplementary Fig. 5b), FtsZ level (Arbitrary Units) increased by expressing FtsA, reaching its maxima between 30-40 min of expression and later slightly decreased the fluorescence probably due to the photobleaching. **e** Size dependency of the FtsZ intensity on lipid membrane among vesicles. After 80 min of cell-free expression of FtsA (with 5 nM of *ftsA* template), fluorescent intensity of FtsZ-Alexa488 (Arbitrary Units) tended to be higher within larger vesicles, suggesting that concentration of FtsZ on membrane become higher in larger vesicles. **f** Regulation of FtsZ localization by stable Min traveling waves via co-expression of FtsA, MinD, and MinE (with 2 nM *ftsAopt* and 2 nM *minDEoperon*). Left: 3D max projections of the transition of Min wave patterns and corresponding FtsZ structures. Right: Kymographs of the pattern transition of Min waves and FtsZ structures. Compared to Fig. 3c, pole-to-pole oscillations of Min waves were unstable and steady at traveling waves. Recording started after 5 min of cell-free expression. mCherry-MinC and FtsZ-Alexa488 are indicated in magenta and green, respectively. Source data are provided as a Source Data file.



Supplementary Fig. 6 Independent reconstitution of MinCDE and FtsZ-FtsA systems

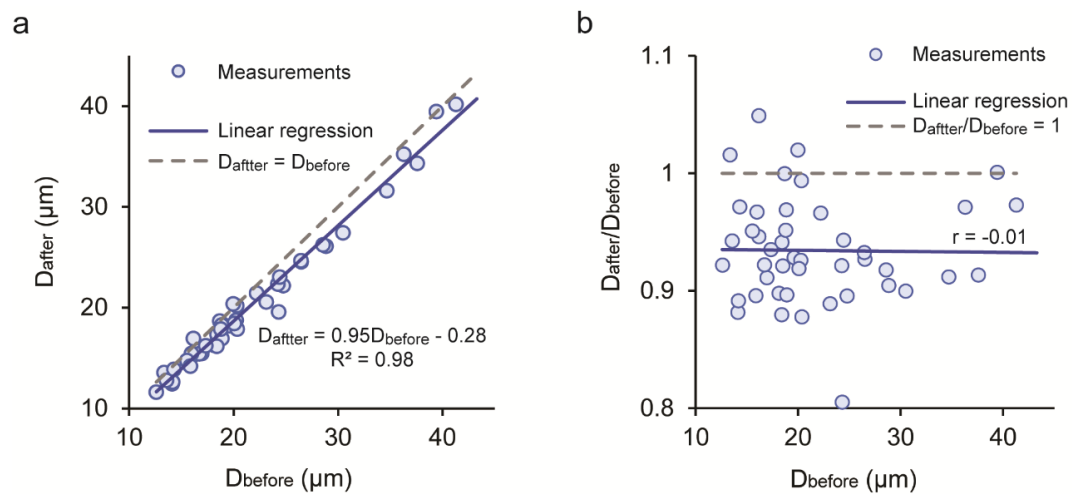
by co-expressing all essential components. **a** Schematic illustrations of co-expression systems. Left: Co-expression of mCherry-MinC, MinD, and MinE. Right: Co-expression of FtsA and FtsZ-Venus mutant. **b** Emergence of Min waves by cell-free expressed mCherry-MinC, MinD, and MinE inside vesicles (with 2 nM *mCherry-MinC* and 1 nM *minDEoperon*). Left: 3D max projection of Min wave pattern formation inside vesicles after 2 h expression of mCherry-MinC, MinD, and MinE at 37 °C. Right: Kymographs of the Min waves inside vesicles correspond to the same letters in the left image captured by mCherry-MinC fluorescence. Wave dynamics were highly sensitive to MinDE concentrations. Scale bar: 20 µm. **c** Time-dependent occurrence of Min wave patterns inside lipid vesicles. Percentage of Min patterns (dynamic waves and static patterns) among vesicles are calculated every 3 min after 10 min incubation. 0.5 nM *minDEoperon* (black points and gray lines) or 1 nM *mCherry-MinC* + 0.5 nM *minDEoperon* (magenta points and pink lines) were used for MinDE or MinCDE co-expression, respectively. n = 116 and 100 for MinDE and MinCDE expression, respectively. **d** 3D max projection of the FtsZ-FtsA mesh structures inside vesicles after 1 h co-expression of either FtsZ-G55-Venus-Q56 or FtsZ-Venus (3 nM *ftsZopt-G55-Venus-Q56* or *ftsZ-Venus*) together with FtsA (1 nM *ftsAopt*) at 37 °C. In contrast to FtsZ-G55-Venus-Q56, FtsZ-Venus mostly localized in the lumen of vesicles and formed several dot structures on the membrane. Scale bars: 20 µm. **e** Comparison of FtsZ mesh formation dynamics for FtsZ-G55-Venus-Q56 and FtsZ-Venus. FtsZ-G55-Venus-Q56 efficiently forms mesh structures on the membrane via co-expression with FtsA, while FtsZ-Venus forms dot-like structures. Experimental conditions were the same as Supplementary Fig. 4d and images were recorded after 20 min incubation at 37 °C. Scale bars: 5 µm. **f** Purified FtsZ bundles on SLBs through FtsA. FtsZ-G55-Venus-Q56 (left) and wild type FtsZ (right) were anchored to the membrane through FtsA and assembled into similar dynamic vortices. Scale bars: 10 µm. **g** Release of Pi as result of GTPase activity of FtsZ-G55-Venus-Q56 and wild type FtsZ. FtsZ-G55-Venus-Q56 has slightly higher GTPase activity (~ 6.2 Pi/FtsZ * min⁻¹) than wild type FtsZ (~ 4.2 Pi/FtsZ * min⁻¹), thus, both proteins are active under our experimental conditions (n=3). Plots represent the mean value of Pi release at each time point. GTPase activity of FtsZ proteins was determined from the slope of the linear phosphate release. **h** FtsZ-G55-Venus-Q56 intensity on the vesicle membrane along with co-expression of FtsA and FtsZ-G55-Venus-Q56 (3 nM *ftsZopt-G55-Venus-Q56* and 1 nM *ftsAopt*) at 37 °C. Similar to the Supplementary Fig. 5b, intensity of the FtsZ (Arbitrary Units) gradually increased with time by binding of FtsZ-G55-Venus-Q56 on the membrane through FtsA. Although similar trends were observed among different vesicle sizes, fluorescence intensities tended to be slightly higher within larger vesicles. **i** Size

dependency of the FtsZ-G55-Venus-Q56 intensity on lipid membrane among vesicles. After 80 min of co-expression of FtsA and FtsZ-G55-Venus-Q56 (with 3 nM *ftsZopt-G55-Venus-Q56* and 1 nM *ftsAopt*), fluorescent intensity of FtsZ (Arbitrary Units) indicated the correlation between vesicle diameter and FtsZ concentration on membrane. Source data are provided as a Source Data file.



Supplementary Fig. 7 FtsZ-ring structures regulated by various Min wave patterns inside lipid vesicles in co-expression system (1 nM *ftsAopt*, 3 nM *ftsZopt-G55-Venus-Q56*, 2 nM *mCherry-MinC*, and 1 nM *minDEoperon* templates). **a** Time-lapse images of the formation of the FtsZ-ring like structure regulated by the pole-to-pole oscillation of Min waves. The static localization of Min waves further stabilized the FtsZ structure. Scale bars: 5 μ m. **b** Time-lapse images of the moving of FtsZ mesh structure driven by Min traveling waves around the membrane. Scale bar: 5 μ m. **c** Surface plot of the FtsZ

distribution regulated by Min waves within a vesicle. Fluorescence intensities of FtsZ-G55-Venus-Q56 (Arbitrary Units) on the equatorial plane of the vesicle were measured along with time. The FtsZ was randomly distributed initially but then formed two peaks that indicate the formation of the FtsZ structure on the membrane by regulation of Min waves. **d** 3D rotational view of a constricted vesicle by the FtsZ-ring. 3D max projected image was rotated along with Y-axis in 30 ° increment between each frame and 7 (0 ° – 180 °) frames were shown. The image was captured started after 3 h of incubation at 37 °C. Scale bar: 5 µm. All images are 3D max projection with the merged color of mCherry-MinC (magenta) and FtsZ-G55-Venus-Q56 (green). Source data are provided as a Source Data file.



Supplementary Fig. 8 Radial constriction of lipid vesicles by FtsZ-ring. Scatter plots of the short axis of the deformed vesicle (D_{after}) (**a**) or the degree of deformation ($D_{\text{after}}/D_{\text{before}}$) (**b**) against diameter of vesicles before deformation (D_{before}). Plots (blue dots) were calculated among deformed vesicles (aspect ratio < 0.95) after 2-3 h co-expression of 5 essential genes at 37 °C. Graphs indicate the diameter of shorter axis of deformed vesicles (D_{after}) was smaller than original vesicle diameters (D_{before}), irrespective of vesicle size, showing that FtsZ-ring radially constricts lipid vesicles. $n = 45$. Source data are provided as a Source Data file.

Supplementary Table 1 List of primers.

Name	Sequence (5' to 3')
KN230	ATGGCACGCATTATTGTTGTTACTT
KN256	GGTATATCTCCTTCTTAAAGTTAAACA
932	AGACCACAACGGTTCCCTCTAGAAATAATTTTGTTTAAC
PG43	TGAAACATGGCAAAGGTAGCGT
933	AAACCGTTGTGGTCTCCCTATAGTGAGTCGTATTAAT
PG44	GCTACCTTTGCCATGTTTCAGAAA
899	TTGCTCACCATGTGATGATGATGATGATGATGCCT
900	CTGTACAAGGGTGCAGCGGGTGAATTCA
227	ATGGTGAGCAAGGGCGAG
641	CTTGTACAGCTCGTCCATGC
885	TTCTTCGCCTTTGCTAACGTGATGATGATGATGATGATGCCTCAT
886	ATGGATGAACTGTATAAAGGTGCAGCGGGTGAATTCAGC
692	GTTAGCAAAGGCGAAGAAC
693	TTTATACAGTTCATCCATACCA
1065	GGTGCAGCGGGTGAATTC
979	GTGATGATGATGATGATGATGCCT
1063	CATCATCACATGGTTTCTAAAGGTGAGGCGGT
1064	CGCTGCACCTTTGTACAGTTCGTCCATACCGC
934	CTAGCATAACCCCTTGGG
510	CATGGTATATCTCCTTCTTAA
945	GATATACCATGATCAAGGCGACGGAC
946	GTTATGCTAGTTAAAACCTTTTTCGCAGCC
947	GAGATATACCATGATTAAGCTACGGACAGAAAA
948	TTTTCTGTCCGTAGCTTTAATCATGGTATATCTC
949	GATTAAAGCTACTGATAGAAAACCTGG
950	CCAGTTTTCTATCAGTAGCTTTAATC

Supplementary Table 1 List of primers (continued).

Name	Sequence (5' to 3')
951	GCTACTGATAGAAAATTAGTAGTAGGAC
952	GTCCTACTACTAATTTTCTATCAGTAGC
KN908	CATGGTATATCTCCTTCTTAAAGTTAAAC
KN170	ATGTTTGAACCAATGGAACTTAC
1051	TCCAACCGCTGTTTTACG
SC46	ATAAAGTTGCAGGACCACTTCTG
1050	CAGACGATTCAAATCGGTAGCG
SC47	CAGAAGTGGTCCTGCAACTTTAT
1052	GCGGTTGGAATGGTGAGCAAGGGCGAG
1053	AATCGTCTGCTTGTACAGCTCGTCCATGC
509	GCACTCGAGCACCACCAC
685	GGTATATCTCCTTCTTAAAGTTAAACAAAA
1021	TAAGAAGGAGATATACCATGAGCAAAGGAGAAGAAGAACTTTTC
1022	TGGTGGTGCTCGAGTGCTCATTTGTAGAGCTCATCCATGCCAT
SC46	ATAAAGTTGCAGGACCACTTCTG
960	CCGCATCATTAGTTAATTCCATTGGTTC
SC47	CAGAAGTGGTCCTGCAACTTTAT
959	GAACCAATGGAATTAATAATGATGCGG
1173	CGAGCTTAAAGACAGTAGCTTCA
1174	TGAAGCTACTGTCTTTAAGCTCG
T7P-F	CCCGCGAAATTAATACGACTCAC
T7P-R	CAAAAACCCCTCAAGACCCGT

Supplementary Table 2 List of DNA templates for cell-free expression.

Linearized template	Original plasmid
<i>sfGFP</i>	pCoofy-sfGFP
<i>ftsA</i>	pET28a-FtsA
<i>ftsAopt</i>	pPT1-FtsAopt
<i>minDEoperon</i>	pPT1-MinD.MinE
<i>mCherry-minC</i>	pET28a-His-mCherry-MinC
<i>ftsZopt-G55-Venus-Q56</i>	pET11b-FtsZopt-G55-Venus-Q56
<i>ftsZ-Venus</i>	pET11b-FtsZ-Venus

Supplementary Table 3 List of DNA templates and concentrations for cell-free expression.

Condition	Templates and concentrations
Estimation of sfGFP expression level (Supplementary Fig. 4)	2 nM <i>sfGFP</i>
FtsA expression with FtsZ-Alexa488 (Fig. 3b, Supplementary Fig. 5b-e, and Supplementary Movie 3)	5 nM <i>ftsA</i>
Co-expression of FtsA, MinD, and MinE (Fig. 3c, d, Supplementary Fig. 5f, and Supplementary Movie 4)	2 nM <i>ftsAopt</i> and 2 nM <i>minDEoperon</i>
Co-expression of mCherry-MinC, MinD, and MinE (Supplementary Fig. 6b and Supplementary Movie 5)	2 nM <i>mCherry-MinC</i> and 1 nM <i>minDEoperon</i>
Estimation of wave emergence (Supplementary Fig. 6c)	0.5 nM <i>minDEoperon</i> with or without 1 nM <i>mCherry-MinC</i>
Co-expression of FtsA and FtsZ variants (Supplementary Fig. 6d, e, h, i, and Supplementary Movie 6)	1 nM <i>ftsAopt</i> and 3 nM <i>ftsZopt-G55-Venus-Q56</i> or <i>ftsZ-Venus</i>
Co-expression of FtsA, FtsZ-G55-Venus-Q56, mCherry-MinC, MinD, and MinE (Fig. 4b-f, Supplementary Fig. 7, 8, Supplementary Movie 7, 8, and 9)	1 nM <i>ftsAopt</i> , 3 nM <i>ftsZopt-G55-Venus-Q56</i> , 2 nM <i>mCherry-MinC</i> , and 1 nM <i>minDEoperon</i>

Supplementary Notes

Validation of MinCDE or FtsZ-mts reconstitution inside lipid vesicles under macromolecular crowding environments

In our experimental setup, we used fluorescently labeled MinC (mScarlet-I-MinC) to avoid any side effects in the Min wave dynamics as result of the fluorescent protein when it is fused to MinD or MinE. When the MinCDE system was encapsulated within lipid vesicles, they self-assembled into different patterns: Dynamic waves at the membrane (further categorized into previously described modes in spherical vesicles: Pole-to-pole oscillations, traveling waves (also referred as circling waves in several literatures¹⁻³, and pulsing) (Supplementary Fig. 2a), stationary localization at the membrane, and stationary localization in the lumen^{3,4}. The emergence of such oscillatory patterns are strongly dependent on the MinDE ratios and concentration⁴. Therefore, spatiotemporal dynamics did not emerge when either MinD or MinE was in excess, resulting in stationary membrane localization at high MinD concentration or in the lumen at high MinE (Supplementary Fig. 2c and d). We further analyzed the relative frequency of different modes among conditions with predominant Min dynamics (>65%). Equimolar concentrations of MinDE at 3 μ M favored the generation of traveling waves and pole-to-pole oscillations (Supplementary Fig. 2b). As pole-to-pole oscillations would be the desired mode for the spatiotemporal regulation of FtsZ at the membrane, we selected this MinDE concentration ratio as our standard condition for further assays.

Moreover, since previous studies stated that macromolecular crowding enhance the FtsZ polymerization⁵⁻⁸ and sharpened the regulation of FtsZ by Min waves into steeper gradients⁹⁻¹¹, we figured that addition of certain macromolecular crowder agents in

solution might improve functional co-reconstitution of both systems. Thus, we encapsulated the Min system in presence of crowding by using Dextran 70 and Ficoll70 and observed that they were also functional. Without crowders, Min proteins had yielded the three dynamic modes; pole-to-pole oscillation, traveling waves, and pulsing, at roughly 15%: 35%: 18% ratios at our standard MinCDE conditions (equimolar concentration of MinDE at 3 μ M and mScarlet-I-MinC at 0.5 μ M). Intriguingly, after adding crowders, we observed a slight increase in the pole-to-pole oscillations, in spite of the unaltered spherical symmetry of the vesicle, which usually precludes mode selection³. Since stable pole-to-pole oscillations are required for correct placement of the FtsZ-ring *in vivo*^{12,13}, any improvement in the prevalence of this wave mode would be highly beneficial for the assembly and placement of a functional division ring. However, the increase in the frequencies was not highly significant at particular crowding conditions, reaching up to 29% of pole-to-pole oscillations at 100 g/L Ficoll70, for instance (Fig. 1e). Therefore, we concluded that macromolecular crowding did not significantly affect the frequency of Min patterns under our experimental conditions. However, we have not analyzed whether other features of Min wave dynamics were affected by crowding in solution such as interaction with the membrane, wavelength, velocity of the Min waves, or protein-protein interactions such as MinD-MinE complex to induce MinD's ATPase activity^{9,14,15}. At the same time, we confirmed that a high percentage of the vesicles (70-80%) showed Min wave dynamics under all crowding conditions, thus supporting the co-reconstitution of Min waves together with FtsZ.

On the other hand, we have also validated the effects of macromolecular crowding environments on FtsZ-Venus-mts, an FtsZ mutant that contains the membrane

attachment sequence from MinD¹⁶. This mutant is able to bind the membrane independently of the interaction with the membrane anchor FtsA, which is challenging to reconstitute, due to their aggregative nature¹⁷. FtsZ-Venus-mts has greatly supported and facilitated the *in vitro* reconstitution and study of FtsZ on membranes without dramatically affecting its assembly dynamics^{9,16,18-20}. Therefore, we have encapsulated FtsZ-Venus-mts in lipid vesicles under our experimental setup, and successfully observed the assembly of different structures upon GTP hydrolysis and addition of macromolecular crowders (Fig. 1b and Supplementary Fig. 1a). The higher amount of FtsZ bundles at higher crowding conditions determined that macromolecular crowding is required to functionally connect the FtsZ and MinCDE system.

Effects of macromolecular crowding on PURE Cell-free expression

Before we started to reconstitute the Min or FtsZ-FtsA system with the cell-free expression system, we first tested the effects of crowding on our experimental setup by expression of sfGFP. Compared to the expression without crowders, we confirmed a relatively lower expression yield of sfGFP under crowding environments, as previously reported²²⁻²⁵ (Supplementary Fig. 4). However, the sfGFP yield reached about 10 μM with Ficoll70 after 200 min of cell-free expression, whereas Dextran70 radically impaired the sfGFP expression level (Supplementary Fig. 4g). Because MinCDE, FtsZ and FtsA proteins would need up to 5 μM of the expression yield, we decided to employ the Ficoll70 as a crowding agent in cell-free expression experiments.

Analysis of reconstituted MinCDE waves via cell-free expression

After we reconstituted MinCDE waves via co-expression of mCherry-MinC, MinD, and

MinE, we further characterized the Min wave dynamics emerged by cell-free expressed proteins. The kymographs revealed that Min wave patterns gradually appeared along with the synthesis of mCherry-MinC (Supplementary Fig. 6b). As for MinDE co-expression (Fig. 4c and Supplementary Fig. 5f), wave patterns dynamically transitioned from pole-to-pole oscillation to traveling waves. Moreover, extended time-lapse observation up to 2.5 h captured that Min waves eventually showed static patterns, which agreed with the emergence of static patterns after 2-4 h of MinDE expression²⁶. Then, we analyzed the time-dependent occurrence of Min wave patterns inside lipid vesicles via cell-free expression system. The efficiency of Min patterns (dynamic waves and static patterns) among vesicles were lower and also slower in full MinCDE co-expression system compared to MinDE expression, (Supplementary Fig. 6c). This impaired efficiency of wave emergence might be due to the conflict of the protein synthesis resources between mCherry-MinC and MinDE templates. However, we confirmed that at least 60% of the vesicles contained Min patterns after 1 h co-expression of MinCDE proteins.

Functional FtsZ-FP for FtsZ-FtsA reconstitution via cell-free expression

In this study, we employed FtsZ-G55-Venus-Q56 to visualize a functional FtsZ using fluorescence microscopy. It is previously known that the C-terminal conjugation with FPs impairs the functionality of FtsZ *in vivo*^{27,28}, because interactions with division proteins occur mainly through the C-terminal domain of FtsZ^{29,30}. At the same time, the considerable gain in molecular weight from the fusion of FPs with wild-type FtsZ (FtsZ-FPs, ~67 kDa) renders it difficult to implement a close-to-physiological concentration of FtsZ (1-6 μ M)³¹⁻³³ using cell-free expression with respect to FtsA (45 kDa, 0.07-0.3

μM)^{32,33}.

To overcome these difficulties, we tested a FtsZ-G55-FP-Q56 mutant, in which a fluorescent protein was inserted in between 55th Gly and 56th Gln FtsZ residues according to a previous report³⁴. As one of those chimeras (FtsZ-G55-mVenus-Q56) was reported as fully functional *in vivo*, it was naturally expected to have similar functionalities as wild-type FtsZ *in vitro*. Together with the validation of template concentration ratio (3 nM for FtsZ-G55-Venus-Q56 and 1 nM for FtsA), we observed the FtsZ mesh structure on the membrane (Supplementary Fig. 6d and e). On the other hand, C-terminally fused FtsZ-Venus did not show preferential membrane localization, verifying that this chimeric FtsZ protein lacks this functionality (Supplementary Fig. 6d and e). Moreover, we checked the activity of purified FtsZ-G55-Venus-Q56 on SLBs and by GTPase assay, confirming that FtsZ-G55-Venus-Q56 is active under our experimental conditions and it is able to form dynamic structures on SLBs (Supplementary Fig. 6f and g).

Intriguingly, we observed a size dependency of FtsZ intensity on the membrane among both FtsA-only and FtsZ-FtsA expression system. In case of FtsA expression with purified FtsZ-Alexa488, the localization of FtsZ molecules in the lumen of the vesicle was gradually decreased by the expression of FtsA (Supplementary Fig. 5b), while an increase of FtsZ intensity was observed on the membrane (Supplementary Fig. 5d). Furthermore, higher FtsZ concentrations on the membrane were observed in larger vesicles, suggesting a correlation between size and membrane coverage of FtsZ (Supplementary Fig. 5e). Since surface-to-volume ratio decreases in larger vesicles, this result suggests that the majority of FtsZ molecules sufficiently bound to the membrane through FtsA expression regardless the vesicle sizes. In parallel, FtsA-FtsZ co-

expression system also indicated gradual increase of the FtsZ intensity on membrane along with cell-free expression (Supplementary Fig. 6h) and relatively higher FtsZ level within larger vesicles (Supplementary Fig. 6h and i). This size dependency also supports the increase of the concentration of FtsZ on the membrane among relatively larger vesicles.

Min wave organized FtsZ structures in co-expression system

After we reconstituted co-expression system of MinCDE and FtsZ-FtsA proteins (Fig. 4), we characterized the time-dependent FtsZ dynamics regulated by Min waves inside lipid vesicles. In some cases, time-lapse images suggested that Min waves first appeared as pole-to-pole oscillations to form the FtsZ-ring, and later transformed into a static bipolar localization depending on MinDE concentrations (Fig. 4c and Supplementary Fig. 7a). Surprisingly, although we suspect that some sort of energy-driven dynamic mechanism is at place in these vesicles, the spatial regulation of the FtsZ-ring like structure to the middle of the vesicles seems to be preserved without pole-to-pole oscillation of Min waves (Fig. 4c and Supplementary Fig. 7a). The circumferential (360°) surface plot of FtsZ intensities revealed that FtsZ was first randomly distributed on the membrane but then formed and reinforced two bands over time, corresponding to a ring-like structure and implying that the Min waves successfully reshaped FtsZ structures and stabilized them (Supplementary Fig. 7c). In addition, also non-deformed vesicles showed FtsZ mesh structures antagonistically localized against Min traveling waves (Supplementary Fig. 7b). The fact that all three wave modes (pole-to-pole oscillation, bipolar static localization, and traveling waves) could be observed after MinCDE expression might reflect differences of MinDE concentrations among vesicles (Supplementary Fig. 6b).

Supplementary Discussion

In this work we have achieved the *in vitro* reconstitution of a minimal division machinery composed by FtsZ-ring located at the equatorial plane of a lipid cell-like container by the dynamic MinCDE system, reassembling their behavior inside the cell. It might represent the first step towards the reconstitution of a functional division machinery able to fulfill division of cell-like systems *in vitro*, one of the major goals of the bottom-up Synthetic biology. Moreover, as mentioned in the main text, the use of two different approaches in this work has allowed us not only the characterization of our experimental setup at higher degree, but also revealing some of the key factors involved in the process (such as protein concentration, protein ratios, crowding conditions and buffer composition). Thus, by using these two approaches, we provided higher robustness to our results and helpful improvements for the *in vitro* reconstitution of protein systems in cell-like platforms.

Although co-reconstitution of the MinCDE system and FtsZ-Venus-*mts* has been performed previously^{1,10,11}, experimental setups used in those studies lack some critical features as a cell model, namely, fully confined spaces and deformable membrane surface, where both features have significant impacts over the FtsZ and MinCDE protein dynamics. For instance, it is known that cell-sized confinement significantly alters the requirements to induce Min waves¹⁴, and also deformable membrane systems play an essential role to study the FtsZ dynamics^{20,21,35,36}. For instance, Zieske and Schille¹⁰ reconstituted the Min pole-to-pole oscillation together with FtsZ-*mts* condensation into the middle of PDMS fabricated chamber in particular, however, this demonstration was far away from the reconstitution of those protein systems inside cell models. Taken together, our observation presented in this study has firstly reported the formation and

assembly of a FtsZ-ring located at the middle of the lipid vesicles regulated by the MinCDE waves.

One of the key features of our work is optimization of macromolecular crowding environments to achieve the assembly of the FtsZ-ring. Macromolecular crowding in solution non-specifically enhances molecular interactions by a volume exclusion effect that have a huge potential to modulate the kinetics and equilibria of a large number of molecular reactions taking place inside the cell^{37,38}. The effect of macromolecular crowding in solution also influence the protein-membrane interactions since they are thermodynamically and kinetically linked. Eventually, any volume exclusion effect over the molecules in solution will affect their equilibria and interaction with the membrane as well. To study these molecular dynamics, synthetic macromolecules like Dextran, Ficoll, or PEG as well as proteins like BSA have been extensively used to mimic the crowded cellular environment *in vitro*³⁹⁻⁴¹. However, a repulsive interaction of PEG with other molecules cannot be fully described quantitatively by an effect of excluded volume alone, involving certain attractive interaction between PEG and the hydrophobic side chains on the protein surface^{37,40,41}. For this reason, we have decided to exclude PEG from our studies.

Previous studies have demonstrated the significant impacts of macromolecular crowding over FtsZ and MinCDE protein functionalities. Briefly, crowding conditions promote FtsZ bundling in solution and inside vesicles, increase oligomerization and promote the assembly of liquid-liquid phase-separated droplets^{5,7,21,22,35,42,43}. On the other hand, macromolecular crowding decreases the wavelength and velocity of MinDE waves^{9,15},

while enhancing the emergence of waves inside lipid microdroplets¹⁴. Thus, we found that macromolecular crowding becomes essential to reconstitute the minimal division system. Even though the emergence of Min pole-to-pole oscillations was only slightly increased under crowding conditions (Fig. 1e), the presence of FtsZ effectively increased the pole-to-pole oscillations for the case of the MinC (from 20% to 40% at 100 g/L Dextran70) in comparison with MinC^{G10D} mutant (From 25% to 31% at 100 g/L Dextran 70) (Fig. 1e and Fig. 2g). In addition, we have also observed a higher increment of FtsZ-ring formation with MinC under 100 g/L Dextran70 crowding condition (~42%), while absence of MinC or MinC^{G10D} mutant could only promote significantly less FtsZ-rings (~10-12%) (Fig. 2f). Since frequency of pole-to-pole oscillations was slightly increased even with MinC^{G10D} mutant, it is plausible to suggest that the FtsZ bundles on the membrane at high crowding conditions is one of the key factors to enhance pole-to-pole oscillation in cellular compartments. However, considering increment of the frequency of both pole-to-pole oscillation and FtsZ-ring formation with wild-type MinC, the formation of FtsZ-ring might have higher impact on enhancement of pole-to-pole oscillations following a mutual positive feedback with the Min waves.

Related to this, the mutual positive feedback between FtsZ-ring formation and pole-to-pole oscillation of Min waves suggested by our data is a new insight that was not expected by the current understanding of the molecular dynamics of those protein systems. However, it is also plausible to assume that this phenomenon is closely related to the geometrical effects on Min waves described previously. Essentially, Min waves can sense geometry and reorganize the wave patterns according to the shape of membrane matrix or physical barriers^{10,15,44}. In this regard, considering the presence of

thick FtsZ bundles on the membrane promoted by crowding, they might behave as a physical barrier, limiting Min proteins to access to the successive membrane area required to emerge traveling waves. Indeed, the presence of FtsZ bundles slightly increased the pole-to-pole oscillations (From 25% to 31%) without effective regulation of Min waves in case of MinC^{G10D} mutant (Fig. 1e and Fig. 2g). Taken together, our observations point to a critical biological relevance of macromolecular crowding in the synergetic dynamics among Min waves, FtsZ bundles, FtsZ-ring structures, and environmental factors such as membrane interaction and confinement. We are only at the beginning of appreciating the mutual relationships of these factors to decipher their roles inside cells.

In order to further improve our experimental setup and eventually achieve the full constriction of the lipid vesicles by the FtsZ-ring together with other division-related proteins, several approaches would be considered in future studies. One of the most intriguing suggestion from our study is the higher deformability observed in bigger vesicles in case of the FtsZ-FtsA system, finding a size dependence of vesicle deformation by FtsZ-rings (Fig. 4f and Supplementary Fig. 7). Since the surface-to-volume ratio becomes smaller in larger spheres, FtsZ-FtsA density on the membrane might be increased for larger vesicles at the same protein expression level, as shown in our analysis (Supplementary Fig. 4e, 5h, i). Higher density of FtsZ-FtsA on the membrane would explain why significant deformations can be only observed in larger vesicles, suggesting that higher concentration of FtsZ and FtsA proteins on the membrane might be able to exert greater force, highlighting the importance of protein density on the membrane. Besides, size-dependent mechanical properties of vesicle

membrane such as surface tension and stiffness would favor higher deformation in larger vesicles⁴⁵⁻⁴⁷. Quantitative biophysical measurements, e.g., by micropipette aspiration and/or optical tweezers should be carried out in future studies to reveal the induced forces and clarify the key features driving vesicle deformation among a broad range of vesicle sizes. In addition, the lack of major deformations using the FtsZ-Venus-mts (Fig. 2b-e and Supplementary Fig. 3) remarked the influence of different membrane attachment, which could be a critical factor for the generation of greater forces on the membrane, as it can modulate the treadmilling behavior of FtsZ¹⁸⁻²⁰. Thus, the control of the protein density on the membrane together with different FtsZ attachment protein such as ZipA might be an interesting approach to improve the force generation by a FtsZ-ring and therefore deformation of vesicles.

Next, our experimental setup using minimal division proteins can serve as a platform to increase the complexity of the system adding more components such as the Zap proteins, which can enhance the bundling of FtsZ⁴⁸, the nucleoid occlusion system to reinforce the displacement of FtsZ from the lumen⁴⁹, or ZipA as a linker of the FtsZ protein to the membrane. The addition of complementary division components is an attractive approach to improve the system and achieve the reconstitution of a functional divisome *in vitro*. In this regard, ZipA can be a good candidate to improve the deformations by a FtsZ-ring as we discussed in the main text. Since ZipA contains a transmembrane region instead of a membrane binding domain as FtsA or MinD⁵⁰ and its insertion into membrane bilayer might be able to enhance the membrane bending as hypothesized previously⁵¹, the combination of FtsZ and ZipA might induce further deformations of membrane by FtsZ torsion and treadmilling. Hence, co-reconstitution of FtsZ, FtsA, and ZipA as a proto-ring together with Min proteins can potentially improve the current system

leading to a higher degree of membrane deformation.

Lastly, the study of different membrane properties and their impact in the formation of the FtsZ-ring formation and deformation of vesicles is an interesting approach to improve the system. For instance, crowding at the membrane is an interesting approach to enhance the polymerization dynamics of FtsZ, as it was previously shown by using bacterial cytoskeleton protein MreB⁵². Different PEG derivatives linked to the membrane⁵² can be a good candidate together with different lipid compositions to obtain further optimized membrane properties such as charge, rigidity, surface tension, diffusion, and phase-separation. Some of these properties have been already stated that affect the behavior of MinCDE and FtsZ³¹ and therefore, can potentially improve and modulate the membrane properties in order to achieve higher frequencies of ring formation, membrane deformability or even full scission of the membrane.

Supplementary Methods

Plasmid construction

The basic information for plasmid construction is given in methods in the main manuscript. However, again, plasmids were typically constructed using seamless cloning. DNA fragments were amplified with overlaps regions between adjacent fragments by PCR, and then PCR products were treated with DpnI and combined using GeneArt Seamless Cloning and Assembly Enzyme Mix. For deletion of sequences from plasmids, plasmids were constructed using blunt end cloning. A DNA fragment was amplified from the original plasmid, treated with DpnI, phosphorylated using T4 Phosphokinase, and then ligated with T4 DNA Ligase. All enzymes for cloning were purchased from Thermo Fisher Scientific (Waltham, MA, USA). Detailed methods of each plasmid are described below, and primers are listed in Supplementary Table 1.

pIVEX2.3d-sfGFP-His for purification of sfGFP was a kind gift from Dr. Lei Kai from the School of Life Sciences, Jiangsu Normal University, China. A DNA fragment for pCoofy backbone was amplified from pCoofy1 (Addgene plasmid # 43974) with a 509/685 primer set, then, *sfGFP* gene was amplified from pIVEX2.3d-sfGFP-His with a 1021/1022 primer set. These PCR products were assembled using seamless cloning.

pET28a-His-msfGFP-MinC, pET28a-His-mCherry-MinC, and pET28a-His-mScarlet-I-MinC were constructed by substituting the *eGFP* gene from pET28a-His-eGFP-MinC⁵³ by genes encoding respective fluorescent proteins. First, pET28a backbone was amplified from pET28a-His-eGFP-MinC with an 885/886 primer set. Then, *msfGFP* gene was amplified from pET28a-His-MinE (2-31)-msfGFP⁵⁴ with a 692/693 primer set. These PCR products were assembled using seamless cloning to construct pET28a-His-msfGFP-MinC. For pET28a-His-mCherry-MinC, pET28a backbone was amplified in the

same manner with an 899/900 primer set. Then, *mCherry* gene was amplified from pLVX_mCherry-C1 (Clontech, Mountain View, CA, USA) with a 641/227 primer set. These PCR products were assembled using seamless cloning. For pET28a-His-mScarlet-I-MinC, pET28a backbone was similarly amplified from pET28a-His-eGFP-MinC with a 1065/979 primer set. *mScarlet-I* gene sequence was optimized for the *E. coli* expression system and synthesized as a DNA cassette (Thermo Fisher Scientific). *mScarlet-I* DNA cassette was then amplified with a 1063/1064 primer set and assembled with a pET28a backbone using seamless cloning.

To construct pPT1-MinD.MinE plasmid, we first deleted the His-tag from pET28a-His-MinD.MinE⁵⁵ to obtain *minD-minE* operon sequence without any tag sequences. A part of pET28a-His-MinD.MinE was amplified by PCR with a KN230/KN256 primer set, and subsequently, the PCR product was conjugated using blunt end cloning. The resultant plasmid (pET28a-MinD.MinE) was further optimized for the cell-free expression system by substituting the lac operator region with a stem-loop sequence. Two DNA fragments were amplified from pET28a-MinD.MinE using 932/PG43 and 933/PG44 sets, respectively. Then, PCR products were assembled using seamless cloning. The resultant plasmid was named pPT1-MinD.MinE since the plasmid is not suitable for protein expression like a typical pET system because of the lack of the lac operator region.

pPT1-FtsAopt was constructed by cloning the *ftsA* gene into pPT1-MinD.MinE and following optimization of *ftsA* gene for cell-free expression system. pPT1 plasmid backbone was amplified from pPT1-MinD.MinE with a 934/510 primer set. Then, *ftsA* gene was amplified from pET28a-FtsA⁵⁶ with a 945/946 primer set, and those PCR products were assembled using seamless cloning. The resultant plasmid (pPT1-FtsA)

was further optimized to increase the AT-content in the first 30 DNA sequences (10 Amino acids) by introducing silent point mutations^{2,22,35}. Then, the point mutations (substitution of 7 nucleotides) were introduced in three repeats of mutagenesis. First, two fragments were amplified from pPT1-FtsA using 947/PG43 and 948/PG44 primer sets, respectively. These fragments were assembled using seamless cloning to construct the intermediate plasmid (pPT1-FtsA_3xMut). Then, the same procedure was repeated to introduce further mutations with 949/PG43 and 950/PG44 primer sets (obtained the intermediate plasmid, pPT1-FtsA_5xMut). Finally, the rest of the mutations were introduced using 951/PG43 and 952/PG44 primer sets to obtain pPT1-FtsAopt.

pET11b-FtsZ-Venus (conjugation of Venus in the C-terminus of full-length FtsZ) was obtained from pET11b-mts-FtsZ-Venus (Venus was referred as YFP in the previous manuscripts)^{18,57} by removing the mts region. A DNA fragment was amplified from pET11b-mts-FtsZ-Venus using a KN908/KN170 primer set and conjugated using blunt end cloning.

pET11b-FtsZ⁵⁸ was first optimized for cell-free expression similar to FtsA optimization, and then *Venus* gene was inserted between G55 and Q56 amino acid residue of FtsZ to obtain pET11b-FtsZopt-G55-Venus-Q56. Two DNA fragments were amplified from pET11b-FtsZ using SC46/960 and SC47/959 primer sets. These fragments were assembled using seamless cloning. The resultant plasmid (pET11b-FtsZopt) was linearized into two parts using 1051/SC46 and 1050/SC47 primer sets, respectively. Then, *Venus* gene fragment was obtained from pET11b-FtsZ-YFP-mts¹⁶ using a 1052/1053 primer set. These three DNA fragments were then assembled using seamless cloning.

pET28a-His-mScarlet-I-MinC^{G10D} mutant¹⁰ was constructed by substituting the Gly10

residue of *minC* gene by Asp from pET28a-His-mScarlet-I-MinC. Two DNA fragments with G10D mutation were amplified from pET28a-His-mScarlet-I-MinC with PG43/1173 and PG44/1174 primer sets and then these PCR products were assembled using seamless cloning to obtain pET28a-His-mScarlet-I-MinC^{G10D}.

Supplementary References

1. Zieske, K., Chwastek, G. & Schwille, P. Protein patterns and oscillations on lipid monolayers and in microdroplets. *Angew. Chemie Int. Ed.* **55**, 13455–13459 (2016).
2. Godino, E. et al. De novo synthesized Min proteins drive oscillatory liposome deformation and regulate FtsA-FtsZ cytoskeletal patterns. *Nat. Commun.* **10**, 4969 (2019).
3. Litschel, T., Ramm, B., Maas, R., Heymann, M. & Schwille, P. Beating vesicles: Encapsulated protein oscillations cause dynamic membrane deformations. *Angew. Chemie Int. Ed.* **57**, 16286–16290 (2018).
4. Kohyama, S., Fujiwara, K., Yoshinaga, N. & Doi, N. Conformational equilibrium of MinE regulates the allowable concentration ranges of a protein wave for cell division. *Nanoscale* **12**, 11960–11970 (2020).
5. Robles-Ramos, M. Á. et al. Assembly of bacterial cell division protein FtsZ into dynamic biomolecular condensates. *Biochim. Biophys. Acta - Mol. Cell Res.* **1868**, 118986 (2021).
6. Rivas, G., Fernández, J. A. & Minton, A. P. Direct observation of the enhancement of noncooperative protein self-assembly by macromolecular crowding: indefinite linear self-association of bacterial cell division protein FtsZ. *Proc. Natl. Acad. Sci. USA* **98**, 3150–3155 (2001).
7. González, J. M. et al. Essential cell division protein FtsZ assembles into one monomer-thick ribbons under conditions resembling the crowded intracellular environment. *J. Biol. Chem.* **278**, 37664–37671 (2003).
8. Groen, J. et al. Associative interactions in crowded solutions of biopolymers

- counteract depletion effects. *J. Am. Chem. Soc.* **137**, 13041–13048 (2015).
9. Martos, A. et al. FtsZ polymers tethered to the membrane by ZipA are susceptible to spatial regulation by Min waves. *Biophys. J.* **108**, 2371–2383 (2015).
 10. Zieske, K. & Schwille, P. Reconstitution of self-organizing protein gradients as spatial cues in cell-free systems. *eLife* **3**, e03949 (2014).
 11. Ramm, B. et al. The MinDE system is a generic spatial cue for membrane protein distribution in vitro. *Nat. Comm.* **9**, 3942 (2018).
 12. Raskin, D. M. & de Boer, P. A. J. Rapid pole-to-pole oscillation of a protein required for directing division to the middle of Escherichia coli. *Proc. Natl. Acad. Sci. USA* **96**, 4971–4976 (1999).
 13. Hu, Z. & Lutkenhaus, J. Topological regulation of cell division in Escherichia coli involves rapid pole to pole oscillation of the division inhibitor MinC under the control of MinD and MinE. *Mol. Microbiol.* **34**, 82–90 (1999).
 14. Kohyama, S., Yoshinaga, N., Yanagisawa, M., Fujiwara, K. & Doi, N. Cell-sized confinement controls generation and stability of a protein wave for spatiotemporal regulation in cells. *eLife* **8**, e44591 (2019).
 15. Schweizer, J. et al. Geometry sensing by self-organized protein patterns. *Proc. Natl. Acad. Sci. USA* **109**, 15283–15288 (2012).
 16. Osawa, M., Anderson, D. E. & Erickson, H. P. Reconstitution of contractile ftsZ rings in liposomes. *Science* **320**, 792–794 (2008).
 17. Martos, A. et al. Isolation, Characterization and Lipid-Binding Properties of the Recalcitrant FtsA Division Protein from Escherichia coli. *PLoS ONE* **7**, e39829 (2012).

18. Ramirez-Diaz, D. A. *et al.* Treadmilling analysis reveals new insights into dynamic FtsZ ring architecture. *PLOS Biol.* **16**, e2004845 (2018).
19. García-Soriano, D. A., Heermann, T., Raso, A., Rivas, G. & Schwille, P. The speed of FtsZ treadmilling is tightly regulated by membrane binding. *Sci. Rep.* **10**, 10447 (2020).
20. Ramirez-Diaz, D. A. *et al.* FtsZ induces membrane deformations via torsional stress upon GTP hydrolysis. *Nat. Comm.* **12**, 3310 (2021).
21. Osawa, M. & Erickson, H. P. Liposome division by a simple bacterial division machinery. *Proc. Natl. Acad. Sci. USA* **110**, 11000–11004 (2013).
22. Furusato, T. *et al.* De novo synthesis of basal bacterial cell division proteins FtsZ, FtsA, and ZipA inside giant vesicles. *ACS Synth. Biol.* **7**, 953–961 (2018).
23. Norred, S. E. *et al.* Macromolecular crowding induces spatial correlations that control gene expression bursting patterns. *ACS Synth. Biol.* **7**, 1251–1258 (2018).
24. Ge, X., Luo, D. & Xu, J. Cell-free protein expression under macromolecular crowding conditions. *PLoS One* **6**, e28707 (2011).
25. Takahashi, K., Sato, G., Doi, N. & Fujiwara, K. A relationship between ntp and cell extract concentration for cell-free protein expression. *Life* **11**, 237 (2021).
26. Yoshida, A., Kohyama, S., Fujiwara, K., Nishikawa, S. & Doi, N. Regulation of spatiotemporal patterning in artificial cells by a defined protein expression system. *Chem. Sci.* **10**, 11064–11072 (2019).
27. Ma, X., Ehrhardt, D. W. & Margolin, W. Colocalization of cell division proteins FtsZ and FtsA to cytoskeletal structures in living *Escherichia coli* cells by using green fluorescent protein. *Proc. Nat. Acad. Sci. USA* **93**, 12998–13003 (1996).

28. Osawa, M. & Erickson, H. P. Probing the domain structure of FtsZ by random truncation and insertion of GFP. *Microbiology* **151**, 4033–4043 (2005).
29. Buske, P. J. & Levin, P. A. A flexible C-terminal linker is required for proper FtsZ assembly in vitro and cytokinetic ring formation in vivo. *Mol. Microbiol.* **89**, 249–263 (2013).
30. Ortiz, C., Natale, P., Cueto, L. & Vicente, M. The keepers of the ring: Regulators of FtsZ assembly. *FEMS Microbiol. Rev.* **40**, 57–67 (2015).
31. Ramm, B., Heermann, T. & Schwille, P. The E. coli MinCDE system in the regulation of protein patterns and gradients. *Cell. Mol. Life Sci.* **76**, 4245–4273 (2019).
32. Rueda, S., Vicente, M. & Mingorance, J. Concentration and assembly of the division ring proteins FtsZ, FtsA, and ZipA during the Escherichia coli cell cycle. *J. Bacteriol.* **185**, 3344–3351 (2003).
33. Schmidt, A. et al. The quantitative and condition-dependent Escherichia coli proteome. *Nat. Biotechnol.* **34**, 104–110 (2016).
34. Moore, D. A., Whatley, Z. N., Joshi, C. P., Osawa, M. & Erickson, H. P. Probing for binding regions of the FtsZ protein surface through site-directed insertions: Discovery of fully functional FtsZ-fluorescent proteins. *J. Bacteriol.* **199**, e00553-16 (2017).
35. Godino, E. et al. Cell-free biogenesis of bacterial division proto-rings that can constrict liposomes. *Commun. Biol.* **3**, 539 (2020).
36. Ganzinger, K. A. et al. FtsZ reorganization facilitates deformation of giant vesicles in microfluidic traps. *Angew. Chemie Int. Ed.* **132**, 21556–21560 (2020).

37. Zhou, H.-X., Rivas, G. & Minton, A. P. Macromolecular crowding and confinement: biochemical, biophysical, and potential physiological consequences. *Annu. Rev. Biophys.* **37**, 375–397 (2008).
38. Rivas, G. & Minton, A., Influence of Nonspecific Interactions on Protein Associations: Implications for Biochemistry In Vivo. *Annu. Rev. Biochem.* **91**, 5.1–5.31 (2022).
39. Rivas, G., Fernández, J. A. & Minton, A. P. Direct observation of the enhancement of noncooperative protein self-assembly by macromolecular crowding: indefinite linear self-association of bacterial cell division protein FtsZ. *Proc. Natl. Acad. Sci. USA* **98**, 3150–3155 (2001).
40. Minton, A. P. The effect of volume occupancy upon the thermodynamic activity of proteins: some biochemical consequences. *Mol. Cell Biochem.* **55**, 119–140 (1983).
41. Winzor, D. J. & Wills, P. R. Molecular crowding effects of linear polymers in protein solutions. *Biophys. Chem.* **119**, 186–195 (2006).
42. Cabré, E. J. et al. Bacterial division proteins FtsZ and ZipA induce vesicle shrinkage and cell membrane invagination. *J. Biol. Chem.* **288**, 26625–26634 (2013).
43. Monterroso, B., Reija, B., Jiménez, M., Zorrilla, S. & Rivas, G. Charged Molecules Modulate the Volume Exclusion Effects Exerted by Crowders on FtsZ Polymerization. *PLoS ONE* **11**, e0149060 (2016).
44. Wu, F., Van Schie, B. G. C., Keymer, J. E. & Dekker, C. Symmetry and scale orient Min protein patterns in shaped bacterial sculptures. *Nat. Nanotechnol.* **10**, 719–726 (2015).

45. Lin, C. M., Li, C. S., Sheng, Y. J., Wu, D. T. & Tsao, H. K. Size-dependent properties of small unilamellar vesicles formed by model lipids. *Langmuir* **28**, 689–700 (2012).
46. Lipowsky, R. Remodeling of membrane shape and topology by curvature elasticity and membrane tension. *Adv. Biol.* **6**, 2101020 (2021).
47. Dimova, R. & Marques, C. *The Giant Vesicle Book*. (CRC Press, 2019).
48. Durand-Heredia, J., Rivkin, E., Fan, G., Morales, J. & Janakiraman, A. Identification of ZapD as a cell division factor that promotes the assembly of FtsZ in Escherichia coli. *J. Bacteriol.* **194**, 3189–3198 (2012).
49. Tonthat, N.K., Milam, S.L., Chinnam, N., Whitfill, T., Margolin, W. & Schumacher, M. A. SImA forms a higher-order structure on DNA that inhibits cytokinetic Z-ring formation over the nucleoid. *Proc. Natl. Acad. Sci. USA* **110**, 10586–10591 (2013).
50. Moy, F. J., Glasfeld, E., Mosyak, L. & Powers, R. Solution Structure of ZipA, a Crucial Component of Escherichia coli Cell Division. *Biochemistry* **39**, 9146–9156 (2000).
51. Derganc, J. & Čopič, A. Membrane bending by protein crowding is affected by protein lateral confinement. *Biochim. Biophys. Acta - Biomembr.* **1858**, 1152–1159 (2016).
52. Garenne, D., Libchaber, A. & Noireaux, V. Membrane molecular crowding enhances MreB polymerization to shape synthetic cells from spheres to rods. *Proc. Natl. Acad. Sci. USA* **117**, 1902-1909 (2020).
53. Loose, M., Fischer-Friedrich, E., Herold, C., Kruse, K. & Schwille, P. Min protein patterns emerge from rapid rebinding and membrane interaction of MinE. *Nat.*

- Struct. Mol. Biol.* **18**, 577–583 (2011).
54. Glock, P., Brauns, F., Halatek, J., Frey, E. & Schwille, P. Design of biochemical pattern forming systems from minimal motifs. *eLife* **8**, e48646 (2019).
55. Loose, M., Fischer-Friedrich, E., Ries, J., Kruse, K. & Schwille, P. Spatial regulators for bacterial cell division self-organize into surface waves in vitro. *Science* **320**, 789–792 (2008).
56. Geissler, B., Elraheb, D. & Margolin, W. A gain-of-function mutation in *ftsA* bypasses the requirement for the essential cell division gene *zipA* in *Escherichia coli*. *Proc. Natl. Acad. Sci. USA* **100**, 4197–4202 (2003).
57. Osawa, M. & Erickson, H. P. Inside-out Z rings - constriction with and without GTP hydrolysis. *Mol. Microbiol.* **81**, 571–579 (2011).
58. Bramhill, D. & Thompson, C. M. GTP-dependent polymerization of *Escherichia coli* FtsZ protein to form tubules. *Proc. Natl. Acad. Sci. USA* **91**, 5812–5817 (1994).

3.5 Publication P5

Crosslinking by ZapD drives the assembly of short, discontinuous FtsZ filaments into ring-like structures in solution

Summary:

This manuscript studies the role of FtsZ-associated proteins, ZapD, in stabilizing the FtsZ ring in bacteria. We observe the formation of ring-like structures in solution, assembled by short crosslinked FtsZ filaments stabilized by ZapD. We employed cryo-ET and biochemical analysis to reveal their 3D organization and shed light on the mechanism of crosslinking by ZapD. The findings provide a model for how FtsZ-associated proteins can stabilize the FtsZ filaments into discontinuous ring-like structures similar to those in bacteria.

Reprinted with permission from:

Merino-Salomón, A., Schneider, J., Babl, L., Krohn, J-H., Sobrinos-Sanguino, M., Schäfer, T., Luque-Ortega, J.R., Alfonso, C., Jiménez, M., Jasnin, M., Rivas, G., Schwille, P. (2023). Crosslinking by ZapD drives the assembly of short, discontinuous FtsZ filaments into ring-like structures in solution. *BioRxiv* 2023.01.12.523557 (*in process of submission*)

Source online: <https://doi.org/10.1101/2023.01.12.523557>

Crosslinking by ZapD drives the assembly of short, discontinuous FtsZ filaments into ring-like structures in solution

Adrián Merino-Salomón¹, Jonathan Schneider^{2,3}, Leon Babl¹, Jan-Hagen Krohn^{1,4}, Marta Sobrinos-Sanguino⁵, Tillman Schäfer⁶, Juan R. Luque-Ortega⁵, Carlos Alfonso⁷, Mercedes Jiménez⁷, Marion Jasnin^{3*}, German Rivas^{7*} & Petra Schwillé^{1*}.

¹- Department of Cellular and Molecular Biophysics, Max Planck Institute of Biochemistry, 82152 Martinsried, Germany.

²- Department of Molecular Structural Biology, Max Planck Institute of Biochemistry, 82152 Martinsried, Germany.

³- Helmholtz Pioneer Campus, Helmholtz Zentrum München, 85764 Neuherberg, Germany.

⁴- Exzellenzcluster ORIGINS, Boltzmannstr. 2, 85748 Garching, Germany.

⁵- Molecular Interactions Facility, Centro de Investigaciones Biológicas Margarita Salas, Consejo Superior de Investigaciones Científicas (CSIC), 28040 Madrid, Spain.

⁶- Cryo-EM facility, Max Planck Institute of Biochemistry, 82152 Martinsried, Germany.

⁷- Centro de Investigaciones Biológicas Margarita Salas, Consejo Superior de Investigaciones Científicas (CSIC), 28040 Madrid, Spain.

Correspondence: marion.jasnin@helmholtz-muenchen.de; rivas@cib.csic.es; schwillé@biochem.mpg.de

Abstract

In most bacteria, division depends on a cytoskeletal structure, the FtsZ ring, that functions as a scaffold to recruit additional proteins, with which it forms the machinery responsible for division, the divisome. The detailed architecture of the ring, in particular the mechanisms of assembly, stabilization, and disassembly, are still largely unknown. Here, we highlight the role of FtsZ-associated proteins (Zaps) that stabilize the FtsZ ring by crosslinking the filaments. Among Zap proteins, ZapD binds the C-terminal domain of FtsZ, which serves as a hub for its regulation. We demonstrate that ZapD crosslinks FtsZ filaments into ring-like structures formed by a discontinuous arrangement of short filaments. Using cryo-electron tomography combined with biochemical analysis, we reveal the three-dimensional organization of the ring-like structures and shed light on the mechanism of FtsZ filament crosslinking by ZapD. Together, our data provide a model of how FtsZ-associated proteins can stabilize FtsZ filaments into discontinuous ring-like structures reminiscent of that existing in the bacterial cell.

Introduction

Cell division is mediated in bacteria by a multiprotein complex whose components interact reversibly to form a division ring that drives cytokinesis, the divisome¹⁻⁵. The FtsZ protein, a structural homolog of eukaryotic tubulin with which it shares its GTPase and polymerization activities, is central to this process in most bacteria⁶⁻¹². FtsZ is the main component of the Z-ring, a structure formed at mid-cell during cell division, which provides a scaffold for recruiting other division proteins and is essential for constricting the membrane¹³⁻¹⁷. The initial pathway for ring formation is the GTP-dependent polymerization of FtsZ, which occurs through a conformational switch in the polymer allowing treadmilling of single-stranded filaments¹⁸⁻²⁵. In response to environmental conditions, the FtsZ filaments can further assemble into various structures such as bundles, sheets, toroids, or spirals^{21,22,26-37}.

The molecular components involved in cell division must be in the right place at the right time during the cell cycle. Several factors in this spatiotemporal regulation modulate FtsZ assembly. In *Escherichia coli*, FtsA and ZipA tether FtsZ to the membrane^{34,38–43} and, together with a set of FtsZ-associated proteins (Zaps), stabilize the ring^{44–51}. Conversely, negative modulators prevent FtsZ assembly at other sites, namely Min proteins at the polar regions^{52,53} and SlmA on the nucleoid^{54,55}. Most of these modulators interact with FtsZ through its carboxy-terminal end, which acts as a central hub that modulates division assembly^{56–58}.

To date, a high-resolution structure of the FtsZ ring (Z ring) is still missing. Most data support a discontinuous arrangement of FtsZ filaments distributed in patches along the equatorial circle, and held together by their lateral interactions and interactions with Zap proteins^{4,16,59–63}. Cross-linking of filaments by Zap proteins is critical to maintain the juxtaposed organization of filaments into a ring-like structure, which may also be relevant to the functionality of the divisome and to the mechanism of force generation in cytokinesis^{1,5,16,19,64–68}.

Zap proteins have overlapping functions in stabilizing the Z ring within dividing cells. Individually, they are dispensable for division, exhibiting less compacted Z rings in the absence of individual genes, while co-knock-out of two or more Zaps leads to cell elongation^{4,44–47,50,69}. The different Zap proteins share no sequence homology, and their structure and mechanism of FtsZ filament crosslinking differ^{46,49,70}. Zap proteins may also participate in the mechanisms of active removal of FtsZ from the septum at the final stage of constriction^{71,72} and in guiding the Z ring to the replication terminus region of the chromosome, through interaction with MatP to form the scaffolding anchor called Ter-linkage⁷³.

ZapD is the only Zap protein known to crosslink FtsZ by binding its C-terminal domain, suggesting a function as a key stabilizer of the Z ring superstructure^{45,70,74–78} (Fig. 1a). ZapD is a symmetrical dimer consisting of an α -helical domain and a β -strand domain containing a positively charged binding pocket required for crosslinking and bundling FtsZ filaments^{74,78}. ZapD binds to the C-terminal region of FtsZ through electrostatic interactions⁷⁸. ZapD crosslinks FtsZ filaments, promoting bundling and significantly reducing the GTPase activity of FtsZ⁴⁵. The mechanism underlying the bundling of FtsZ filaments is still unknown, although a model of how ZapD crosslinks adjacent FtsZ filaments has been proposed based on the structural analysis of ZapD-FtsZ interactions⁷⁴. In this model, the ZapD dimer connects two FtsZ filaments through the C-terminal domain, which organizes them in an antiparallel orientation (Fig. 1a). However, the experimental validation of this model is still pending. Characterizing how ZapD crosslinks FtsZ filaments can shed light on the molecular mechanism behind Z ring assembly.

Here, we used cryo-electron microscopy (cryo-EM) and cryo-electron tomography (cryo-ET) combined with biochemical and biophysical assays to study the structural organization of FtsZ polymers in the presence of ZapD. This integrated approach revealed that ZapD promotes the assembly of FtsZ filaments into toroidal polymers, which is consistent with the low resolution structure of the Z ring visualized *in vivo*^{16,79–81}. Our findings allowed us to propose a molecular mechanism that leads to toroid formation, providing valuable information for understanding the stabilization of the Z ring driven by crosslinking division proteins.

Results

ZapD dimer interacts with FtsZ-GDP oligomers

Before characterizing the interaction between FtsZ and ZapD, we first confirmed the robust dimeric state of ZapD through analytical ultracentrifugation (AUC) (Supplementary Fig. 1a (I) and b), in agreement with previous studies^{45,75,76,78}. On the other hand, unpolymerized FtsZ-GDP sedimented as two major species compatible with monomers and dimers, as well as a small amount of other oligomeric species of FtsZ⁸² (Supplementary Fig. 1a (II)).

Previous structural studies identified a direct interaction of ZapD through the C-terminal domain or central hub of FtsZ, finding charged residues involved in the interaction^{75,78}. To independently confirm these results, we studied the interaction between FtsZ-GDP and ZapD by AUC (Supplementary Fig. 1a (III)). We demonstrated the formation of FtsZ-ZapD complexes that corresponded to a stoichiometry of approximately 2 moles of ZapD per mole of FtsZ (Supplementary Fig. 1a (IV)). In addition, we also confirmed the interaction of both proteins by fluorescence anisotropy and fluorescence correlation spectroscopy (FCS) (Supplementary Fig. 2a and b). In these experiments, an increase in fluorescence anisotropy or diffusion time, respectively, suggests the formation of larger particles as a result of protein-protein interactions.

Thus, we confirmed the interaction between ZapD and unpolymerized FtsZ-GDP, which forms complexes in solution. The AUC results highlight the formation of specific species of FtsZ and ZapD at a molar ratio of approximately 1:2, consistent with the proposed interaction model⁷⁴.

ZapD interacts with FtsZ-GTP polymers promoting bundling

ZapD has been suggested to act as a crosslinker of FtsZ filaments promoting bundling in solution⁴⁵, although the molecular mechanism of how ZapD crosslinks filaments remains elusive. To decipher the biochemical features underlying the bundling process, we analyzed the formation of large FtsZ macrostructures following interaction with ZapD using light scattering at 350 nm. Neither FtsZ alone nor ZapD alone showed significant light scattering with or without GTP addition. However, ZapD promoted the formation of FtsZ macrostructures upon addition of GTP (Fig. 1b). Increasing concentrations of ZapD showed an increase of light scattering reaching its maximum at molar ratio of about 1:2 (FtsZ:ZapD) (Fig. 1b). In addition, the FtsZ macrostructures disassembled over time. Recurrent replenishment of GTP allowed partial recovery of the light scattering signal, suggesting rapid reassembly of the FtsZ bundles (Supplementary Fig. 3a).

Additionally, ionic strength and pH modulated the interaction of ZapD and FtsZ, also affecting its ability to crosslink FtsZ filaments (Supplementary Fig. 3b and c). The presence of ZapD prior to the addition of GTP did not significantly affect the crosslinking of the filaments (Supplementary Fig. 3d). Interestingly, increasing concentrations of FtsZ at a fixed ZapD concentration did not further promote bundle formation (Supplementary Fig. 3e). This suggests that a certain number of ZapD molecules per FtsZ filament might be required or optimal to crosslink them efficiently. ZapD also decreased the GTPase activity of FtsZ due to filament crosslinking, decreasing it to 30% and reaching 20% at equimolar or higher ZapD concentrations, respectively (Fig. 1c), in agreement with previous studies⁴⁵. Similarly, at higher ionic strength, the bundling effect of ZapD was limited (Supplementary Fig. 3b), favoring less bundle formation and decreased GTPase activity (Supplementary Fig. 4).

These results demonstrate that ZapD dimers can crosslink filaments into dynamic FtsZ bundles that disassemble over time. Lower pH and ionic strength favor bundle assembly, as predicted from the electrostatic nature of the interaction with ZapD^{75,78}. At the same time, the bundling effect of ZapD is strongly dependent on the protein ratio used. This highlights the role of the number of ZapD molecules per FtsZ filament in stabilizing the bundle structure, with an optimum at a molar ratio of about 1:1 or 1:2 (FtsZ:ZapD), following the same trend observed with FtsZ-GDP (Supplementary Fig. 1a (IV)).

ZapD promotes the formation of FtsZ toroids

Next, we used cryo-electron microscopy (cryo-EM) to reveal the structure and assembly mechanism of ZapD-mediated FtsZ bundles. Previous studies had visualized regular bundles by negative-stain transmission electron microscopy^{45,74,78}; cryo-EM allowed us to avoid any staining artifact. After the addition of GTP, we observed the formation of single and double FtsZ filaments in solution (Fig. 2a). In the presence of ZapD at equimolar or higher concentrations, FtsZ filaments assemble into bundles that form circular toroidal structures (Fig. 2b and c). These toroids have not been observed before for other protein interactions with FtsZ. Toroids coexist with other bundle types, but remain predominant (Fig. 2b, c and Supplementary Fig. 5a). A close-up view of the FtsZ toroid suggests a partially ordered arrangement of filaments in the toroidal structure (Fig. 2c).

Quantitative analysis of the toroidal structure showed a conserved organization, with an outer diameter in the range of the bacterial cell size (502 ± 55 nm) (Fig. 2d), a typical thickness of 127 ± 25 nm (Fig. 2e) and an average height of 93 ± 15 nm (Supplementary Fig. 5b). By measuring the shortest and longest axes, we determined that the circularity of the structure was 0.92 ± 0.1 and 0.85 ± 0.1 for the outer and inner diameter, respectively (Supplementary Fig. 5c). This conserved toroidal structure could arise from the intrinsic curvature of the FtsZ filaments stabilized by ZapD connections.

FtsZ bundle formation increases at higher concentrations of ZapD, showing a strong dependence on protein ratios (Supplementary Fig. 5a). At sub-equimolar concentrations, we could not observe FtsZ bundles, in agreement with previous studies^{45,75,78} and light scattering experiments (Fig. 1b, Supplementary Fig. 3). At molar ratios of 1:1 or 1:2 (FtsZ:ZapD), curved bundles and toroidal structures are abundant (Supplementary Fig. 5a), with some single and double FtsZ filaments (Supplementary Fig. 6). At even higher concentrations of ZapD (typically of 1:4 or 1:6 (FtsZ:ZapD)), we observed the formation of straight bundles with striated patterns between the FtsZ filaments (Supplementary Fig. 6), as well as the presence of some toroidal structures (Supplementary Figs. 5a and 6). Here, the high concentration of ZapD molecules may have increased the number of connections between filaments and ultimately promoted the formation of straight bundles. This indicates that the assembly of FtsZ-ZapD structures is a dynamic process that highly depends on the amount of connections established between filaments. Toroids and curved bundles always coexist, but the ratio shifts from toroids to straight bundles at high ZapD concentrations.

Our data demonstrate that ZapD dimers can crosslink adjacent FtsZ filaments, which self-assemble into bundles and toroidal structures. These toroids are remarkably regular in size that matches the bacterial diameter^{16,79,81,83}. This indicates that the inherent curvature of the FtsZ filaments is preserved within a range of ZapD connections⁶⁸.

The 3D structure of ZapD-mediated FtsZ toroids revealed by cryo-electron tomography

Visualization of FtsZ toroidal structures using cryo-EM suggested a regular arrangement of the FtsZ filaments within the toroid (Fig. 2c). We then used cryo-electron tomography (cryo-ET) to reveal their three-dimensional (3D) organization with greater precision. We first analyzed ZapD-mediated toroidal FtsZ structures at equimolar concentrations (Supplementary Fig. 7a).

Cryo-ET revealed the dense packing of the toroidal structures, with numerous densities connecting the filaments (Fig. 3a, Supplementary Figs. 7a and 8a). Zoomed-in views of the toroids showed a near parallel alignment of FtsZ filaments (Fig. 3b and Supplementary Fig. 8a). In addition, cross-sectional views of the toroids revealed an elongation of the filaments along the Z direction: FtsZ form rather small vertical sheets than filaments. A small elongation in Z is expected due to the missing wedge artefacts in cryo-ET; however, the observed elongation goes far beyond this effect and reveals an intrinsic property of FtsZ structures. FtsZ minisheets are either aligned or shifted in Z, while remaining fairly parallel to each other, with lateral connections between them (Fig. 3c left and Supplementary Fig. 8d).

We then extracted the isosurface of the toroids from the tomograms (Fig. 3c right, 3d, Supplementary Fig. 8b and Supplementary movie 1). This allowed us to visualize the 3D structure of the toroids (Fig 3e, Supplementary Fig. 8c, e and Supplementary Movie 1), consisting of parallel FtsZ minisheets connected by lateral connections, presumably mediated by ZapD (Fig 3e and Supplementary Fig. 8c and e).

To assess the role of ZapD in the formation of the observed lateral connections, we compared the isosurfaces of single and double filaments in the absence of ZapD (Supplementary Fig. 9a) with the individual filaments extracted from the toroids (Supplementary Fig. 9b). FtsZ filaments were similar regardless of the presence of ZapD. However, filaments extracted from toroids were decorated by additional densities (Supplementary Fig. 9b), which were not found in the absence of ZapD, suggesting that they correspond to ZapD proteins interacting with FtsZ filaments, as observed within the toroidal structure (Fig. 3e and Supplementary Fig. 8c and e).

ZapD plasticity is essential for toroid shape and stabilization

Next, we identified putative ZapD connections within the toroids (Fig. 4a; Supplementary Movie 2). Most connections showed a characteristic bi-spherical shape connecting filaments, reminiscent of ZapD dimers (Fig. 4 b-d). A large variability in the putative ZapD connections gives rise to the overall toroidal structure. We found lateral connections between two parallel FtsZ filaments (or minisheets) at the same toroid height (Fig 4. b). FtsZ filaments at different heights can connect diagonally through ZapD connections, forming a 3D mesh (Fig. 4c, d and Supplementary Movie 2). We also identified the presence of putative ZapD proteins decorating a single FtsZ filament, which can be used to connect other nearby filaments (Fig. 4b). In addition, more than one connection between two filaments occurs, allowing strong attachment between the filaments (Fig. 4d).

Visualization of the 3D filament organization showed that the toroid is formed by a discontinuous arrangement of short, laterally connected filaments (Supplementary Fig. 10a), forming a dense 3D mesh (Fig 4.a and supplementary Fig. 8e). Filament discontinuity does not correlate with a higher number of ZapD connections (Supplementary Fig. 10b), indicating that ZapD is able to crosslink filaments without causing filament breakage. ZapD can crosslink individual filaments laterally in all spatial orientations, resulting in a 3D toroidal structure of

curved filaments parallel to each other and connected across the height of the toroid. Therefore, the preferential curvature of the filaments is conserved by the lateral connections through ZapD at equimolar concentrations, essential for the formation of regular and bacterial-sized toroids⁶⁸.

3D imaging of ZapD-mediated FtsZ toroidal structures by cryo-ET provided crucial information about the 3D organization, connectivity and length of filaments inside the toroid. Our data revealed that toroids consist of a discontinuous arrangement of FtsZ filaments connected by ZapD dimers, resulting in a conserved toroidal structure that has never been observed before following the interaction between FtsZ and one of its natural partners *in vitro*.

A high density of ZapD connections promotes the formation of straight FtsZ bundles

Our cryo-ET results showed that ZapD dimers crosslink FtsZ filaments and establish multiple connections between the filaments in toroids, thereby enhancing their interaction (Fig. 4). Biochemical analyses as well as cryo-EM experiments indicate an important role of the FtsZ:ZapD ratio in the formation of toroidal structures or straight bundles (Supplementary Fig. 5a and Supplementary Fig. 6). We then explored how higher densities of ZapD lead to the formation of straight bundles using cryo-ET.

Using the same approach as for the toroids, we collected tomograms of the straight bundles and extracted their isosurfaces (Fig. 5a, Supplementary Fig. 7b and Supplementary Movie 3). The straight bundles are formed at high ZapD concentrations and consist of a highly organized stack of well aligned FtsZ filaments (Fig. 5b). Filaments are connected by multiple ZapD proteins, which straighten the structure of the inherently curved filament (Fig. 5c). Interestingly, ZapD does not crosslink FtsZ filaments laterally but from the top or the bottom of the filaments forming a row of ZapD proteins interacting with both filaments (Fig. 5d). The distance between ZapD proteins provided a mean value of 4.5 ± 0.5 nm (Supplementary Fig. 11b), which is consistent with the size of FtsZ²⁴. This suggests that all FtsZ proteins interact with the ZapD dimers that crosslink the filaments. On the other hand, the distance between two FtsZ filaments connected by multiple ZapD proteins was found to be larger than in the absence of ZapD (from 5.9 ± 0.8 nm to 7.6 ± 1.5 nm) (Supplementary Fig. 11a). This indicates that ZapD not only connects FtsZ filaments laterally but also stretches them, which could have important implications for the functionality of the FtsZ ring.

These results reveal the important role of the FtsZ:ZapD ratio and the number of connections between filaments in the crosslinking mechanism (Fig. 6). Saturating FtsZ filaments with ZapD proteins straighten their structure and arranges them into large straight bundles. This supports that an equimolar ratio of FtsZ and ZapD is optimal to maintain the preferential curvature of the FtsZ filaments and allow toroid assembly.

Dimerization of ZapD is essential to form FtsZ toroids

Our results suggest that ZapD dimers connect two FtsZ filaments, although the role of dimerization has not yet been experimentally established⁷⁴. We therefore investigated whether the dimerization of ZapD was essential to assemble straight bundles and toroidal structures. To test this, we produced a mutant of ZapD (“mZapD”) by substituting three amino acids (R20, R116 and H140) involved in its dimerization by Alanine, thus decreasing the stability of the dimerization interface (Supplementary Fig. 12a).

mZapD can interact with unpolymerized FtsZ-GDP as evidenced by fluorescence anisotropy and FCS (Supplementary Fig. 12b and c). mZapD is still able to promote FtsZ bundle formation but to a much lower extent than wild-type ZapD, as shown by light scattering (Supplementary Fig. 12d). We also visualized these bundles by cryo-EM and observed the formation of thinner bundles (Supplementary Fig. 13b and c). However, toroidal structures and straight bundles were absent in these samples even at high concentrations of mZapD (1:6 molar ratios of FtsZ and mZapD). This indicates that a stable dimerization interface is required to assemble ZapD-mediated structures (Supplementary Fig 13a).

These results demonstrated that dimerization of ZapD is essential to promote the assembly of toroidal structures and straight bundles, although it is not required to promote filament bundling.

Discussion

In this study, we demonstrate that ZapD proteins laterally crosslink FtsZ filaments, forming discontinuous multilayered toroidal structures of the bacterial size. Exploration of these structures using cryo-ET revealed their 3D organization, providing essential information on the molecular mechanism behind filament crosslinking into organized macrostructures. We also highlighted the importance of FtsZ:ZapD protein ratios and ZapD dimerization for FtsZ toroid assembly. This work expanded the current understanding of the FtsZ-ZapD interaction, providing new insights into the crosslinking of FtsZ filaments and the structure of a functional Z ring.

Specifically, we show the assembly of FtsZ filaments into toroidal structures by lateral crosslinking through ZapD. Preferential assembly of toroids in solution likely is a physiologically relevant process given their similarities in shape and size to the Z ring in the cell^{16,63,79,80,84,85}. Furthermore, these toroidal structures are an excellent example of what Erickson and coworkers have termed the "intermediate curved conformation" of FtsZ filaments, which appears to be widespread, as evidenced by many studies performed *in vitro* and *in vivo* (see Erickson and Osawa 2017⁶⁸ for more details). In qualitative agreement with our observations, single-stranded FtsZ filaments can form ring-like structures with a 100-200 nm diameter, as revealed by negative stain EM and AFM^{20,23–25,32,86–88}. FtsZ can also form lateral interactions among filaments in response to environmental conditions and assemble into macrostructures^{30,46,58,60,65}. Surprisingly, using negative stain TEM, Popp and coworkers also observed the formation of toroidal structures under non-physiological additives such as methylcellulose and polyvinyl alcohol (PVA)³⁷. The size of these toroids range from 100 – 500 nm diameter, similar to what we observed here (Fig. 2d and e). However, unlike the toroidal structures formed in the presence of ZapD, no evidence of disassembly upon GTP consumption has been described.

The formation of toroidal structures as a result of filament crosslinking in solution is a clear evidence of the robust preferential curvature of the FtsZ filaments favored by nature to form bacterial-sized ring-like structures^{16,68}. The presence of ZapD can help, shape and provide stability to the network, spacing the filaments and crosslinking them into a discontinuous toroid. These features can be further modulated by surface effects at the cell membrane, acting as a scaffold for protein self-organization, a process analyzed experimentally^{67,89–93}. In addition, FtsZ can also polymerize into ~1 μ m diameter ring-like vortices when bound to artificial membranes, either through ZipA⁹⁴, FtsA⁹⁵, or using a membrane-targeting variant of FtsZ⁹⁶.

Interestingly, ZapA proteins can crosslink FtsZ filaments into bundles on the membrane without affecting their treadmilling dynamics⁹⁷. This suggests that lateral interactions through Zap proteins can promote bundling without affecting significantly filament dynamics, consistent with their role inside the cell.

We also demonstrated that ZapD-mediated FtsZ toroids recapitulate many of the structural features of the FtsZ ring architecture *in vivo*. The current model of the Z ring based on super-resolution imaging and cryo-ET, defines a somewhat discontinuous and heterogeneous structure composed of randomly overlapping filaments^{63,79,84}. They are arranged in a belt-like macromolecular entity containing nodes with a higher density of dispersed filaments, with the FtsZ filaments confined to a toroidal zone of about 80–100 nm width and approximately 40–60 nm radial thickness, located 13-16 nm below the inner membrane^{63,69,79,81,84,85,98,99}. These dimensions are similar to the ones of the toroidal structures promoted by ZapD (Fig. 2d and e, Supplementary Fig. 5b).

The Z ring model also suggests that FtsZ filaments are weakly associated with each other via protein factors such as Zaps and weak FtsZ-FtsZ interactions, which may play a crucial role in their functionality^{4,16,59,60,102}. The similarities of the Z ring to the toroidal structures support the important role of FtsZ-associated proteins for filament crosslinking and the mechanism behind Z ring assembly. Structural characterization of the toroids using cryo-ET identified individual ZapD dimers crosslinking the filaments (Fig. 4). We also confirmed a large variability in the conformation of the connections between filaments. Because ZapD is a dimeric protein, it might be expected to act as a rigid linker; however, interaction with FtsZ via the central hub could provide additional spatial freedom to connect other filaments in various conformations, enabling different filament organizations and heterogeneity in the structure (Fig. 4 b-d). This suggests that these crosslinkers act as modulators within the ring structure, spacing the filaments and allowing them to slide^{61,63,66,89,93}. The ability of FtsZ to treadmill directionally^{95,96,103–105}, together with a discontinuous antiparallel organization of transiently crosslinked filaments, is hypothesized to underlie the functionality of the Z ring and force constriction^{65–68,106–108}. Thus, Zap proteins can ensure correct filament placement and stabilization, which is consistent with the toroidal structure assembled by ZapD.

We found a significant dependence of ZapD concentration in the crosslinking and assembly of FtsZ macrostructures. Saturation of ZapD proteins connecting FtsZ filaments promoted their assembly into straight bundles, which was never observed at lower ZapD concentrations (Fig. 5 and Supplementary Fig. 7b). This organization results from increased ZapD connections between FtsZ filaments (Fig. 5b-d). The presence of multiple lateral interactions between filaments can reduce the flexibility required to form the toroidal structure, forcing the filaments into a straight bundle conformation. Therefore, we can hypothesize that the assembly of functional FtsZ macrostructures occurs only within a specific range of lateral interactions. At the same time, an increase in these lateral connections would shift the interaction toward the assembly of non-functional, probably rigid and less dynamic straight bundles (Fig. 6). This, along with the large conformational variability found in ZapD connections, may indicate that ZapD can modulate the behavior of the entire structure based on a concentration-dependent mechanism and due to its high plasticity.

The assembly of FtsZ macrostructures promoted by ZapD may also open new horizons for the biochemical reconstitution of contractile division engines in cell-like test tubes^{109–111} in the framework of bottom-up synthetic biology^{112,113}. Our preliminary results show that crosslinking of filaments by ZapD promoted the formation of dynamic FtsZ bundles within lipid vesicles that disassembled over time (Supplementary Fig. 13 and 14).

To summarize, we demonstrate the assembly of FtsZ toroidal structures formed by a discontinuous arrangement of filaments stabilized by crosslinking with ZapD dimers, which are consistent with some of the structural features of the FtsZ ring observed *in vivo*. We also proposed a concentration-dependent molecular mechanism of filament crosslinking based on previous studies of the interaction and new insights gained from our results. Our *in vitro* study provides new information on the organization and stabilization of FtsZ filaments in a ring-like structure that can improve our understanding of the Z ring stabilization and thus the entire division process.

Methods

Protein purification: ZapD protein has been overproduced and purified following the procedure previously described in⁴⁵ with some modifications. The bacterial strain was an *E. coli* BL21 (DE3) transformed with pET28b-h10-smt3-ZapD fusion plasmid⁴⁵. The cells were sonicated for 6-8 cycles of 20 secs and centrifuged at 40,000 rpm in MLA 80 rotor (Beckman coulter) for 45 min. The protein was eluted by chromatography in 5-ml HisTrap (GE Healthcare) and digested with Smt3-specific protease Ulp1 (SUMO protease encoded in Rosetta pTB145), at 1:1 molar relation. Digestion proceeded for two dialysis of 1 hour at 4°C to avoid protein precipitation. ZapD and His-Smt3 were separated by chromatography in 5-ml HisTrap (GE Healthcare), then the protein was eluted in a 5-ml HiTrap Desalting column (Healtcare) to eliminate completely possible traces of free phosphates in the buffer. Final concentration of ZapD was determined by absorbance at 280 nm using an extinction coefficient (ϵ) of 25230 M⁻¹ cm⁻¹ and ZapD purity was checked by SDS-polyacrylamide gel electrophoresis. Protein fractions were frozen in buffer 50 mM KCL, 50 mM Tris-CL, 10 mM MgCl₂, 0.2 mM DTT and 2% glycerol. ZapD mutant (mZapD) was purified following the same procedure using the corresponding plasmid. *E. coli* FtsZ was overproduced and purified following the calcium precipitation method described previously⁸². Briefly, *E. coli* BL21 (DE3) pLysS cells were transformed with pET11b-FtsZ, grown in LB medium and selected with Ampicillin 100 µg/mL. After induction and growth, the pellet was resuspended in PEM buffer (50 mM PIPES-NaOH, pH 6.5, 5 mM MgCl₂, 1 mM EDTA) and disrupted using a tip sonicator for 3-4 cycles. The lysate was then separated by centrifugation for 30 min at 20,000 x g at 4 °C, and the supernatant was mixed with 1 mM GTP, 20 mM CaCl₂ and incubated at 30 °C for 15 min to induce FtsZ polymerization and bundling. Subsequently, the FtsZ bundles were pelleted by centrifugation for 15 min at 20,000 x g at 4 °C, and the pellet was resuspended in PEM buffer and centrifuged again for 15 min at 20,000 x g, 4 °C, collecting the supernatant. Precipitation and resuspension steps were repeated to improve the purification. The buffer was then exchanged using an Amicon Ultra-0.5 centrifugal filter unit 50 kDa (Merck KGaA). FtsZ purity was checked by SDS-polyacrylamide gel electrophoresis and concentration was determined by absorbance at 280 nm using an extinction coefficient (ϵ) of 14000 M⁻¹ cm⁻¹⁸². Protein solutions were aliquoted, frozen in liquid nitrogen, and stored at -80 °C until further use.

Plasmid Design and Molecular Cloning: To generate the ZapD mutant (mZapD), seamless cloning method was used according to the provider's protocol (ThermoFisher Scientific /Invitrogen GeneArt™ Seamless Cloning and Assembly Enzyme Mix (A14606)) using the plasmid pET28b-h10-smt3-ZapD and the primers listed in (Supplementary Table 1). All enzymes for cloning were from Thermo Fisher Scientific (Waltham, MA, USA). Briefly, DNA fragments were amplified with Phusion High-Fidelity DNA Polymerase and origo primers (Sigma–Aldrich, St. Louis, MO, USA). Then, PCR products were treated with DpnI and

combined using GeneArt Seamless Cloning and Assembly Enzyme Mix. The plasmid was propagated in *E. coli* OneShot TOP10 (Thermo Fisher Scientific) and purified using NucleoBond Xtra Midi kit (Macherey-Nagel GmbH, Duren, Germany). Directed site mutagenesis was made by substituting three amino acids in the ZapD sequence by Alanine (R20, R116, H140). The plasmid was then verified using Sanger Sequencing Service (Microsynth AG, Balgach, Switzerland).

Protein labelling: Covalent labelling of FtsZ with Alexa 488 the amino groups of N-terminal amino acid residue with Alexa Fluor 488 carboxylic acid succinimidyl ester dye following the procedure previously described²². ZapD and mZapD were labelled with ATTO-647N carboxylic acid succinimidyl ester dye in the amino group. Before the reaction, ZapD was dialyzed in 20 mM HEPES, 50 mM KCl, 5 mM MgCl₂, pH 7.5 and the probe was dissolved in Dimethylsulfoxide (DMSO). The reaction was allowed to proceed for 35-60 min at RT and stopped with 10 % Tris-HCl 1 M. The free dye was separated from labelled protein by a Hi-TRAP Desalting column (GE Healthcare). The final degree of labelling of FtsZ and ZapD was calculated from the molar absorption coefficients of the protein and the dye. It was around 0.5 moles of probe per mole of FtsZ and around 0.3/0.4 moles of dye per mole of ZapD.

Analytical ultracentrifugation; sedimentation velocity (SV) and sedimentation equilibrium (SE): Sedimentation velocity assays were performed to detect the homogeneity and association state of individual proteins and the stoichiometry of the formed protein-protein complexes. In brief, the experiments were carried out at 43-48 Krpm in an Optima XL-I analytical ultracentrifuge, equipped with UV-VIS absorbance and Raleigh interference detection systems. The sedimentation coefficient distributions were calculated by least-squares boundary modeling of sedimentation velocity data using the *c(s)* method¹¹⁴ as implemented in the SEDFIT program. The *s*-values of the present species were corrected to standard conditions (pure water at 20°C, and extrapolated to infinite dilution) to obtain the corresponding standard *s*-values (*s*_{20,w}) using the program SEDNTERP¹¹⁵. Multi-signal sedimentation velocity (MSSV) data were globally analyzed by SEDPHAT software¹¹⁶ using the “multi-wavelength discrete/continuous distribution analysis” model, to determine the spectral and diffusion deconvoluted sedimentation coefficient distributions, *ck(s)*, from which the stoichiometry of protein complexes can be derived¹¹⁷. Sedimentation equilibrium of ZapD was carried out to confirm the association state of the protein in the same experimental conditions and concentration range tested by sedimentation velocity (2-30 μM). Short columns (100 μL) SE experiments were carried out at 14000 and 10000 rpm. Weight-average buoyant molecular weights were obtained by fitting a single-species model to the experimental data using the HeteroAnalysis program¹¹⁸, once corrected for temperature and buffer composition with the program SEDNTERP¹¹⁵.

Light scattering assay: Light scattering of protein samples was collected by measuring the absorbance at 350 nm in a TECAN plate reader (Tecan Group Ltd., Mannedorf, Switzerland). All samples reached a final volume of 50 μL in a 364-Well Flat-Bottom Microplate (UV-Star, Greiner Bio-One GmbH) before measuring the absorbance. Different concentrations of FtsZ and ZapD were premixed in the well-plate and measured before addition of GTP to extract subsequently the individual blank values. Concentrations of FtsZ and ZapD varied from 0 to 80 μM and buffer conditions are specified in each graph and the caption of the figures ranging from 50 to 500 mM KCl, 6 to 8 pH, always supplemented with 50 mM Tris-Cl and 5 mM MgCl₂. Manual mixing was performed after addition of GTP and orbital oscillations for 5 sec in the TECAN were made prior to any measurement to avoid sedimentation of the samples. Time

measurements were taken as specified in each condition. Reported values are the average of 3-12 independent measurements \pm Standard deviation.

GTPase activity of FtsZ: GTPase activity of FtsZ was measured by quantification of the inorganic phosphate with a colorimetric assay (BIOMOL GREENÒ kit from ENZO life sciences) for two minutes. 5 μ M FtsZ was used in our standard buffer (5 mM MgCl₂, 50 mM Tris-HCl, 50 mM KCl, pH 7) or buffers at higher KCl concentrations (50-500 mM KCl) and polymerization was triggered by 1 mM GTP. ZapD was added at different concentrations and premixed with FtsZ before addition of GTP. 13 μ L fractions were added to a 96-Well Flat-Bottom Microplate (UV-Star, Greiner Bio-One GmbH) every 20 sec after addition of GTP and mixed with the Reaction buffer reaching 50 μ L and 100 μ L of BIOMOL GREEN reagent, to stop the reaction. After stopping the reaction, samples were incubated for 10 min at RT and the absorbance was measured at 620 nm in a Varioskan Flash plate reader (Thermo Fisher Scientific, MA, USA). Concentrations of inorganic Phosphate were calculated from a phosphate standard curve, while the GTPase activity reaction rate (V , mol P/mol FtsZ/ min) was determined from the slope of the linear part of phosphate accumulation curves.

Preparation of EM grids. Cryo-EM grids were plunge frozen with a Vitrobot Mk.IV (Thermo Fischer Scientific) using 3 μ L of the samples applied to previously glow discharged R 2/1 Holey Carbon Cu 200 mesh EM grids (Quantifoil). Samples were 10 μ M FtsZ with or without ZapD or mZapD at different concentrations specified in each case (0 – 60 μ M). Proteins were mixed in our working buffer containing 50 mM, 5 mM MgCl₂, 50 mM Tris-HCl, pH 7. Samples were incubated for 2 minutes after the addition of 1 mM GTP to trigger polymerization. The Vitrobot was set to 4° C, 100% humidity, blot time 3 s, blot force 3. Whatman no. 1 filter paper was used for blotting and liquid ethane kept at liquid nitrogen temperatures was used as a cryogen for vitrification.

Cryo-EM and cryo-ET. Cryo-EM data was acquired on two microscopes as follows. Cryo-EM micrographs were acquired within SerialEM¹⁹ on a Talos Arctica transmission electron microscope (Thermo Fisher Scientific) operated at 200 kV, equipped with a Falcon III (Thermo Fisher Scientific) direct electron detector operated in integrating mode. Images were recorded at 73,000x magnification (pixel size 1.997 Å) and 92,000x magnification (pixel size 1.612 Å) at -2.5 μ m to -5 μ m target defocus with an approximate total electron dose of 60 electrons / Å².

Cryo-EM micrographs and Cryo-ET tilt series were acquired within SerialEM on a G2 Titan Krios transmission electron microscope (Thermo Fisher Scientific) operated at 300 kV, equipped with a FEG, post-column energy filter (Gatan) and a K3 camera (Gatan) operated in electron counting mode. Micrographs were recorded at 42,000x magnification (pixel size 2.154 Å) at -5 μ m target defocus with an approximate total electron dose of 60 electrons / Å². Tilt series were recorded at 42,000x magnification (pixel size 2.154 Å) at -5 μ m target defocus with an approximate total electron dose of 100-140 electrons / Å². Acquisition was performed using a dose-symmetric tilt scheme, a tilt range of +/-60°, an angular increment of 2°.

Tomogram reconstruction: Tilt series preprocessing was performed using the TOMOMAN package (<https://github.com/williamnwan/TOMOMAN>). In brief, MotionCor2¹²⁰ was used to align individual frames, followed by cumulative dose-weighting using an exposure-dependent attenuation function, as described in¹²¹. Dose-weighted tilt series were aligned using IMOD¹²² either by employing gold fiducials (if available) or by patch-tracking, and binned tomograms (pixel size 8.616 Å) were generated using weighted back-projection. Stacks were split into odd

and even frames to generate half-set tomograms which were used for training and subsequent denoising in cryoCARE¹²³.

Denoised tomograms were directly employed for segmentation of the toroids, straight bundles and individual filaments by cropping an area of interest and displaying the volume as isosurface in USCF ChimeraX¹²⁴. To highlight connections between filaments, the respective parts were cropped from the volume using the Volume Eraser tool in USCF Chimera¹²⁵.

All micrographs and slices through tomograms were visualized using IMOD. Isosurface renderings of toroids, straight bundles and individual filaments were displayed using USCF ChimeraX and USCF Chimera.

Fluorescence anisotropy: Anisotropy measurements were performed using a TECAN plate reader (Tecan Group Ltd., Mannedorf, Switzerland). Excitation and emission wavelengths were 625 nm and 680 nm, respectively. ZapD or mZapD labelled with ATTO 647N were used as fluorescence tracer with a final concentration of 150 nM of ATTO-647N and supplemented with unlabeled ZapD reaching a concentration of 5 μ M. FtsZ was added at increasing concentrations to analyze their interaction. Binding affinities (apparent K_D) were determined by fitting the Hill equation to the normalized anisotropy data. Each condition was measured in three independent samples.

Fluorescence correlation spectroscopy (FCS): FCS measurements were performed using a PicoQuant MicroTime200 system equipped with an Olympus 60x, NA1.2 UPlanApo water immersion objective. A pulsed 636 nm diode laser was used to excite fluorescence of Atto647N-labelled ZapD, mZapD or free Atto647N carboxylate (for calibration). Three measurements of 60 s each were performed per sample at room temperature (21°C), and three samples per condition were measured. The repetition rate of the pulsed laser was 26.7 MHz, and the average power was 1 μ W at the objective back pupil. Fluorescence was collected through the same objective, spatially filtered through a 50 μ m diameter pinhole, and spectrally filtered through a 690/70 nm bandpass filter before being split by a neutral beam splitter onto two avalanche photodiodes (Excelitas SPCM-AQRH-14-TR). Photon count events were digitized using a PicoQuant TimeHarp 260 Nano TCSPC card. Time-correlated single photon counting information was used for monitoring data quality during measurements, but not in further analysis. As especially in samples with FtsZ ZapD, and GTP present simultaneously we occasionally saw large, bright particles that are difficult to treat in FCS analysis, data was subjected to a burst removal algorithm similar to Margineanu et al.¹²⁶ and only “non-burst” data was used in correlation analysis to obtain statistics representative of the large number of small oligomer particles, ignoring rare large ones. Cross-correlation functions of the two detectors were calculated and fitted with a standard model for three-dimensional diffusion in with rapid dye blinking:

$$G(\tau) = G_0 \left[\frac{1 - F_B + F_B e^{-\frac{\tau}{\tau_B}}}{1 - F_B} \right] \frac{1}{1 + \frac{\tau}{\tau_d}} \sqrt{\frac{1}{1 + \frac{\tau}{S^2 \tau_d}}}$$

With amplitude G_0 , diffusion time τ_d , point spread function aspect ratio S , and blinking parameters F_B and τ_B . Custom software was written in Python for burst removal, correlation, and fitting, based on ttrlib 0.0.19 (<https://github.com/Fluorescence-Tools/ttrlib>). The software is in ongoing development, and available upon request.

Fluorescence Microscopy: Images of lipid vesicles were recorded on a Zeiss LSM780 confocal laser scanning microscope using a Zeiss C-Apochromat x40/1.20 water-immersion objective (Carl Zeiss AG, Oberkochen, Germany). FtsZ-Alexa 488 was excited using a 488 nm argon laser, while ZapD-ATTO 647N and DOPE-ATTO 655 were excited by the 633 nm HeNe laser. All confocal images were processed using ImageJ.

Fluorescence recovery after photobleaching (FRAP): On lipid vesicles, a circular spot on the bundle was illuminated with full 488 laser power for 0.164 s (10 iterations on the Zen Black software (Carl Zeiss AG, Oberkochen, Germany)). The average fluorescence intensity was recorded every 5 second for 250 seconds and the mean intensity in a second area of the same dimensions was recorded in the same field of view to correct for the intensity drift. The fluorescence intensity was then corrected and normalized to facilitate its interpretation. The data represents 5 independent measurements and the standard deviation from different vesicles in 3 different samples.

Preparation of lipid vesicles: Lipid vesicles were prepared following the double emulsion principle^{109,127}. 1-palmitoyl-2-oleoyl-glycero-3-phosphocholine (POPC) and 1-palmitoyl-2-oleoyl-sn-glycero-3-phospho-(1'-rac-glycerol) (POPG) (Avanti Polar Lipids, Alabaster, AL, USA) were mixed and dissolved in chloroform at 25 g/L in a molecular ratio of 7:3. 100 μ L of the lipid mixture was dried by nitrogen gas stream and 10 μ L of decane (TCI Deutschland GmbH, Eschborn, Germany) was added to resuspend the lipids inside a N₂ globe box at low humidity. Subsequently, 1 mL of mineral oil (Carl Roth GmbH, Karlsruhe, Germany) was added and vortexed for 1 min to prepare a lipid-oil mixture. To form the lipid vesicles, a 96-well Flat-Bottom Microplate (Sensoplate, Greiner Bio-One GmbH, Kremsmuenster, Austria) was used for both, vesicle formation and visualization. The inner and outer solutions were prepared in working buffer at the same osmolarity, which was measured using an osmometer (Fiske Micro-Osmometer model120, Fiske Associates, Norwood, MA, USA). Sucrose and glucose 100 mM were added in outer and inner solutions respectively to create a density gradient. 100 μ L of the outer solution was added into a well in a 96 well-plate, and subsequently, 50 μ L of the lipid-oil mixture was layered on top of the outer solution. Emulsion solution containing the protein mixture was obtained from 2 μ L of the inner solution and 100 μ L of the lipid-oil mixture mixed in a 1.5 mL tube by tapping. Then, ~80 μ L of this emulsion solution was dripped on the multi-layered solution. Next, lipid vesicles were obtained by centrifugation for 10 min at 1500 rcf at room temperature and directly visualized under the confocal microscope. FtsZ (5 μ M) and ZapD (0 - 20 μ M) were added at different protein ratios and 1 mM GTP was added to trigger FtsZ polymerization in working buffer. To allow visualization of the membrane in confocal microscopy, 0.01% Mol of DOPE-ATTO 655 was added to the lipid mixture.

Image analysis: Electron microscopy images were processed and analyzed using IMOD and ImageJ. The dimensions of the toroidal structures, FtsZ bundles and distances between filaments were manually measured using ImageJ and IMOD. Distances were plotted as histograms using Origin (OriginPro, Version 2019b, OriginLab Corporation, Northampton, MA, USA.). For each toroid analyzed (n = 67) the inner and outer diameter were measured collecting the major and minor distance in each case. The circularity of the toroid was the result of the division between the minor diameter divided by major diameter for each toroid. The height of the FtsZ toroid was manually measured from the tomograms, collecting 4 measurements per toroid to assure a correct representation of the size (n = 17). For the distances between double filaments and straight bundles, they were also manually measured by using IMOD. Each measurement represents only one FtsZ double filament or one FtsZ-

ZapD double filament, however, the same bundle could be measured more than once as they are composed for multiple filaments. The measurements were collected from >3 independent samples. The distances between ZapDs connecting two FtsZ filaments were measured following the same methodology. The mean value and standard deviation of different datasets were calculated and added to the figures together with the n used for each case.

Acknowledgements

We thank Daniel Bollschweiler (MPIB cryo-EM facility) and Rafael Nuñez (CIB-CSIC imaging facility) for their help with the cryo-EM experiments. We also thank the MPIB core facility for assistance in protein purification, Michaela Schaper for plasmid cloning, Sigrid Bauer for lipid preparation and Noelia Roperro, Katharina Nakel and Kerstin Andersson for protein purification. We are also grateful to Miguel Robles-Ramos, Ana Raso, Hiromune Eto, Cristina Capitanio, Pedro Weickert, Kareem Al-Nahas, Yusuf Qutbuddin, Silvia Zorrilla, Henri Franquelim, Diego Ramirez and Daniela Garcia-Soriano for helpful discussions and fruitful input in this work. This project has been supported by the Max Planck-Bristol Centre for Minimal Biology (A.M.-S.) and the Deutsche Forschungsgemeinschaft (P. S.). J.S. and M. Jasnin are supported by the French Agence Nationale de la Recherche (ANR) and the Deutsche Forschungsgemeinschaft (DFG) call ANR-DFG 2020 NLE for the project no. JA-3038/2-1 (to M. Jasnin). J.-H.K. is funded by the Germany's Excellence Strategy – EXC-2094 – 390783311. This work was also supported by the Spanish Government through Grant PID2019-104544GB-I00/AEI/10.13039/501100011033 (M.Jimenez, C.A. and G.R.). M.S.-S. was supported by European Social Fund through Grant PTA2020-018219-I/AEI/10.13039/501100011033. J.R.L.-O and M S.-S. acknowledge support from the Molecular Interactions Facility at the CIB Margarita Salas-CSIC. A.M.-S and J.-H.K. are part of IMPRS-LS, J.-H.K. is also a CeNS Center for NanoScience associate.

Author contributions

A.M.-S., M. Jiménez and G.R. conceived the study. A.M.-S. purified and fluorescently labelled ZapD and FtsZ. M.S.-S. performed FtsZ GTPase assays. A.M.-S. and J.-H.K. designed, performed and analyzed FCS and fluorescence anisotropy experiments. A.M.-S. and M. Jiménez designed and performed light scattering assays. M. Jiménez, C.A. and J.R.L.-O. designed, performed and analyzed the AUC data. A.M.-S., J.S., T.S. and M. Jasnin designed, performed, and analyzed the cryo-EM and cryo-ET experiments. L.B. designed the plasmid and purified mZapD. A.M.-S. performed the encapsulation in lipid vesicles. A.M.-S. wrote the original draft. A.M.-S., L.B., M. Jiménez, M. Jasnin, G.R. and P.S. revised the manuscript and figures. All authors discussed the results and revised the manuscript

References

1. Levin, P. A. & Janakiraman, A. *Localization, Assembly, and Activation of the Escherichia coli Cell Division Machinery*. <https://journals.asm.org/journal/ecosalplus> (2021).
2. den Blaauwen, T., Hamoen, L. W. & Levin, P. A. The divisome at 25: the road ahead. *Curr. Opin. Microbiol.* **36**, 85–94 (2017).
3. Du, S. & Lutkenhaus, J. Assembly and Activation of the *Escherichia coli* Divisome. *Mol. Microbiol.* **105**, 177–187 (2017).

4. Du, S. & Lutkenhaus, J. At the Heart of Bacterial Cytokinesis: The Z Ring. *Trends in Microbiology* (2019) doi:10.1016/j.tim.2019.04.011.
5. Attaibi, M. & Den Blaauwen, T. An Updated Model of the Divisome: Regulation of the Septal Peptidoglycan Synthesis Machinery by the Divisome. (2022) doi:10.3390/ijms23073537.
6. Nogales, E., Downing, K. H., Amos, L. A. & Löwe, J. Tubulin and FtsZ form a distinct family of GTPases. *Nat. Struct. Biol.* 1998 56 **5**, 451–458 (1998).
7. Erickson, H. P. FtsZ, a prokaryotic homolog of tubulin? *Cell* **80**, 367–370 (1995).
8. Mukherjee, A., Dai, K. & Lutkenhaus, J. Escherichia coli cell division protein FtsZ is a guanine nucleotide binding protein. *Proc. Natl. Acad. Sci. U. S. A.* **90**, 1053–1057 (1993).
9. De Boer, P., Crossley, R. & Rothfield, L. The essential bacterial cell-division protein FtsZ is a GTPase. *Nat.* 1992 3596392 **359**, 254–256 (1992).
10. Escobar-Henriques, M. & Anton, F. Mechanistic perspective of mitochondrial fusion: Tubulation vs. fragmentation. *Biochimica et Biophysica Acta - Molecular Cell Research* (2013) doi:10.1016/j.bbamcr.2012.07.016.
11. RayChaudhuri, D. & Park, J. T. Escherichia coli cell-division gene ftsZ encodes a novel GTP-binding protein. *Nature* **359**, 251–254 (1992).
12. Bramhill, D. & Thompson, C. M. GTP-dependent polymerization of Escherichia coli FtsZ protein to form tubules. *Proc. Natl. Acad. Sci. U. S. A.* **91**, 5813 (1994).
13. Lutkenhaus, J. & Addinall, S. G. Bacterial cell division and the Z ring. *Annu. Rev. Biochem.* **66**, 93–116 (1997).
14. Addinall, S. G., Erfei, B. & Lutkenhaus, J. FtsZ ring formation in fts mutants. *J. Bacteriol.* **178**, 3877–3884 (1996).
15. Wang, M., Chao Fang, -, Ma, B., Luo, X. & Hou, Z. Regulation of cytokinesis: FtsZ and its accessory proteins. *Curr. Genet.* **66**, 43–49 (2020).
16. Mcquillen, R. & Xiao, J. Insights into the Structure, Function, and Dynamics of the Bacterial Cytokinetic FtsZ-Ring. (2020) doi:10.1146/annurev-biophys-121219.
17. Goehring, N. W., Gonzalez, M. D. & Beckwith, J. Premature targeting of cell division proteins to midcell reveals hierarchies of protein interactions involved in divisome assembly. *Mol. Microbiol.* **61**, 33–45 (2006).
18. Small, E. & Addinall, S. G. Dynamic FtsZ polymerization is sensitive to the GTP to GDP ratio and can be maintained at steady state using a GTP-regeneration system. *Microbiology* **149**, 2235–2242 (2003).
19. Söderström, B., Daniel, - & Daley, O. The bacterial divisome: more than a ring? *Curr Genet* **63**, 161–164 (2017).
20. Erickson, H. P., Taylor, D. W., Taylor, K. A. & Bramhill, D. Bacterial cell division protein FtsZ assembles into protofilament sheets and minirings, structural homologs of tubulin polymers. *Proc. Natl. Acad. Sci. U. S. A.* **93**, 519–523 (1996).
21. Lu, C., Reedy, M. & Erickson, H. P. Straight and curved conformations of FtsZ are regulated by GTP hydrolysis. *J. Bacteriol.* **182**, 164–170 (2000).
22. González, J. M. *et al.* Essential cell division protein FtsZ assembles into one monomer-thick ribbons under conditions resembling the crowded intracellular environment. *J. Biol. Chem.* **278**, 37664–37671 (2003).

23. Mingorance, J. *et al.* Visualization of single Escherichia coli FtsZ filament dynamics with atomic force microscopy. *J. Biol. Chem.* **280**, 20909–20914 (2005).
24. Huecas, S. *et al.* The interactions of cell division protein FtsZ with guanine nucleotides. *J. Biol. Chem.* **282**, 37515–37528 (2007).
25. Hamon, L. *et al.* Mica surface promotes the assembly of cytoskeletal proteins. *Langmuir* **25**, 3331–3335 (2009).
26. Milam, S. L., Osawa, M. & Erickson, H. P. Negative-Stain Electron Microscopy of Inside-Out FtsZ Rings Reconstituted on Artificial Membrane Tubules Show Ribbons of Protofilaments. *Biophys. J.* **103**, 59–68 (2012).
27. Housman, M., Milam, S. L., Moore, D. A., Osawa, M. & Erickson, H. P. FtsZ Protofilament Curvature Is the Opposite of Tubulin Rings. *Biochemistry* **55**, 6 (2016).
28. Romberg, L. & Levin, P. A. Assembly Dynamics of the Bacterial Cell Division Protein FtsZ: Poised at the Edge of Stability. *Annu. Rev. Microbiol.* **57**, 125 (2003).
29. Scheffers, D. J. & Driessen, A. J. M. The polymerization mechanism of the bacterial cell division protein FtsZ. *FEBS Lett.* **506**, 6–10 (2001).
30. Mukherjee, A. & Lutkenhaus, J. Analysis of FtsZ assembly by light scattering and determination of the role of divalent metal cations. *J. Bacteriol.* **181**, 823–832 (1999).
31. Osawa, M., Anderson, D. E. & Erickson, H. P. Supporting Online Material Reconstitution of Contractile FtsZ Rings in Liposomes. *Z. Hu, J. Lutkenhaus, Mol. Microbiol* **52**, 89 (1990).
32. Erickson, H. P. & Stoffer, D. Protofilaments and rings, two conformations of the tubulin family conserved from bacterial FtsZ to alpha/beta and gamma tubulin. *J. Cell Biol.* **135**, 5 (1996).
33. Löwe, J. & Amos, L. A. Tubulin-like protofilaments in Ca²⁺-induced FtsZ sheets. *EMBO J.* **18**, 2364–2371 (1999).
34. Hale, C. A., Rhee, A. C. & De Boer, P. A. J. ZipA-Induced Bundling of FtsZ Polymers Mediated by an Interaction between C-Terminal Domains. *J. Bacteriol.* **182**, 5153–5166 (2000).
35. Marrington, R., Small, E., Rodger, A., Dafforn, T. R. & Addinall, S. G. FtsZ fiber bundling is triggered by a conformational change in bound GTP. *J. Biol. Chem.* **279**, 48821–48829 (2004).
36. Huecas, S. *et al.* Energetics and Geometry of FtsZ Polymers: Nucleated Self-Assembly of Single Protofilaments. *Biophys. J.* **94**, 1796–1806 (2008).
37. Popp, D., Iwasa, M., Narita, A., Erickson, H. P. & Maéda, Y. FtsZ Condensates: An In Vitro Electron Microscopy Study. (2009) doi:10.1002/bip.21136.
38. Ma, X. & Margolin, W. Genetic and Functional Analyses of the Conserved C-Terminal Core Domain of Escherichia coli FtsZ. *J. Bacteriol.* **181**, 7531–7544 (1999).
39. Pichoff, S. & Lutkenhaus, J. Overview of cell shape: cytoskeletons shape bacterial cells. *Curr. Opin. Microbiol.* **10**, 601–605 (2007).
40. Hale, C. A. & De Boer, P. A. J. Direct Binding of FtsZ to ZipA, an Essential Component of the Septal Ring Structure That Mediates Cell Division in E. coli. *Cell* **88**, 175–185 (1997).
41. Zhan, L., Mukherjee, A. & Lutkenhaus, J. Recruitment of ZipA to the division site by interaction with FtsZ. *Mol. Microbiol.* **31**, 1853–1861 (1999).

42. Mosyak, L. *et al.* The bacterial cell-division protein ZipA and its interaction with an FtsZ fragment revealed by X-ray crystallography. *EMBO J.* **19**, 3179–3191 (2000).
43. Wang, X., Huang, J., Mukherjee, A., Cao, C. & Lutkenhaus, J. Analysis of the interaction of FtsZ with itself, GTP, and FtsA. *J. Bacteriol.* **179**, 5551–5559 (1997).
44. Buss, J. A., Peters, N. T., Xiao, J. & Bernhardt, T. G. ZapA and ZapB form an FtsZ-independent structure at midcell. *Mol. Microbiol.* **104**, 652–663 (2017).
45. Durand-Heredia, J., Rivkin, E., Fan, G., Morales, J. & Janakiraman, A. Identification of ZapD as a cell division factor that promotes the assembly of FtsZ in *Escherichia coli*. *J. Bacteriol.* **194**, 3189–3198 (2012).
46. Huang, K. H., Durand-Heredia, J. & Janakiraman, A. FtsZ ring stability: Of bundles, tubules, crosslinks, and curves. *J. Bacteriol.* **195**, 1859–1868 (2013).
47. Durand-Heredia, J. M., Yu, H. H., De Carlo, S., Lesser, C. F. & Janakiraman, A. Identification and characterization of ZapC, a stabilizer of the FtsZ ring in *Escherichia coli*. *J. Bacteriol.* **193**, 1405–1413 (2011).
48. Ebersbach, G., Galli, E., Møller-Jensen, J., Löwe, J. & Gerdes, K. Novel coiled-coil cell division factor ZapB stimulates Z ring assembly and cell division. *Mol. Microbiol.* **68**, 720–735 (2008).
49. Gueiros-Filho, F. J. & Losick, R. A widely conserved bacterial cell division protein that promotes assembly of the tubulin-like protein FtsZ. (2002) doi:10.1101/gad.1014102.
50. Hale, C. A. *et al.* Identification of *Escherichia coli* ZapC (YcbW) as a component of the division apparatus that binds and bundles FtsZ polymers. *J. Bacteriol.* **193**, 1393–1404 (2011).
51. Woldemeskel, S. A., McQuillen, R., Hessel, A. M., Xiao, J. & Goley, E. D. A conserved coiled-coil protein pair focuses the cytokinetic Z-ring in *Caulobacter crescentus*. *Mol. Microbiol.* **105**, 721–740 (2017).
52. Raskin, D. M. & de Boer, P. A. J. MinDE-Dependent Pole-to-Pole Oscillation of Division Inhibitor MinC in *Escherichia coli*. *J. Bacteriol.* (1999) doi:10.1128/jb.181.20.6419-6424.1999.
53. de Boer, P. A. J., Crossley, R. E. & Rothfield, L. I. A division inhibitor and a topological specificity factor coded for by the minicell locus determine proper placement of the division septum in *E. coli*. *Cell* **56**, 641–649 (1989).
54. Woldringh, C. L., Mulder, E., Huls, P. G. & Vischer, N. Toporegulation of bacterial division according to the nucleoid occlusion model. *Res. Microbiol.* **142**, 309–320 (1991).
55. Tonthat, N. K. *et al.* Molecular mechanism by which the nucleoid occlusion factor, SlmA, keeps cytokinesis in check. *EMBO J.* **30**, 154–164 (2011).
56. Ortiz, C., Natale, P., Cueto, L. & Vicente, M. The keepers of the ring: regulators of FtsZ assembly. *FEMS Microbiol. Rev.* **040**, 57–67 (2016).
57. Buske, P. J., Mittal, A., Pappu, R. V. & Levin, P. A. An intrinsically disordered linker plays a critical role in bacterial cell division. *Semin. Cell Dev. Biol.* **37**, 3–10 (2015).
58. Buske, P. J. & Levin, P. A. Extreme C terminus of bacterial cytoskeletal protein FtsZ plays fundamental role in assembly independent of modulatory proteins. *J. Biol. Chem.* **287**, 10945–10957 (2012).
59. Huecas, S. *et al.* Self-Organization of FtsZ Polymers in Solution Reveals Spacer Role of the Disordered C-Terminal Tail. *Biophys. J.* **113**, 1831–1844 (2017).

60. Sundararajan, K. & Goley, E. D. The intrinsically disordered C-terminal linker of FtsZ regulates protofilament dynamics and superstructure in vitro. *J. Biol. Chem.* **292**, 20509–20527 (2017).
61. Lan, G., Daniels, B. R., Dobrowsky, T. M., Wirtz, D. & Sun, S. X. Condensation of FtsZ filaments can drive bacterial cell division. *Proc. Natl. Acad. Sci. U. S. A.* **106**, 121–126 (2009).
62. Surovtsev, I. V., Morgan, J. J. & Lindahl, P. A. Kinetic Modeling of the Assembly, Dynamic Steady State, and Contraction of the FtsZ Ring in Prokaryotic Cytokinesis. *PLoS Comput. Biol.* **4**, e1000102 (2008).
63. Szwedziak, P., Wang, Q., Bharat, T. A. M., Tsim, M. & Löwe, J. Architecture of the ring formed by the tubulin homologue FtsZ in bacterial cell division. *Elife* **3**, e04601 (2014).
64. Coltharp, C. & Xiao, J. Beyond force generation: Why is a dynamic ring of FtsZ polymers essential for bacterial cytokinesis?; Beyond force generation: Why is a dynamic ring of FtsZ polymers essential for bacterial cytokinesis?
doi:10.1002/bies.201600179.
65. Erickson, H. P., Anderson, D. E. & Osawa, M. FtsZ in Bacterial Cytokinesis: Cytoskeleton and Force Generator All in One. *Microbiol. Mol. Biol. Rev.* **74**, 504–528 (2010).
66. Nguyen, L. T., Oikonomou, C. M. & Jensen, G. J. *Simulations of Proposed Mechanisms of FtsZ-Driven Cell Constriction*. <https://doi.org/10> (2021).
67. Mateos-Gil, P., Tarazona, P. & Elez, M. V. Bacterial cell division: modeling FtsZ assembly and force generation from single filament experimental data. *FEMS Microbiol. Rev.* **039**, 73–87 (2019).
68. Erickson, H. P. & Osawa, M. FtsZ Constriction Force-Curved Protofilaments Bending Membranes. *Subcell. Biochem.* **84**, (2017).
69. Buss, J. *et al.* In vivo organization of the FtsZ-ring by ZapA and ZapB revealed by quantitative super-resolution microscopy. *Mol. Microbiol.* **89**, 1099–1120 (2013).
70. Schumacher, M. A., Zeng, W., Huang, K. H., Tchorzewski, L. & Janakiraman, A. Structural and functional analyses reveal insights into the molecular properties of the Escherichia coli Z ring stabilizing protein, ZapC. *J. Biol. Chem.* **291**, 2485–2498 (2016).
71. Pazos, M., Natale, P., Margolin, W. & Vicente, M. Interactions among the early Escherichia coli divisome proteins revealed by bimolecular fluorescence complementation. *Environ. Microbiol.* **15**, 3282–3291 (2013).
72. Marteyn, B. S. *et al.* ZapE Is a Novel Cell Division Protein Interacting with FtsZ and Modulating the Z-Ring Dynamics. (2014) doi:10.1128/mBio.00022-14.
73. Bailey, M. W., Bisicchia, P., Warren, B. T., Sherratt, D. J. & Männik, J. Evidence for Divisome Localization Mechanisms Independent of the Min System and SlmA in Escherichia coli. *PLoS Genet.* **10**, e1004504 (2014).
74. Schumacher, M. A., Huang, K. H., Zeng, W. & Janakiraman, A. Structure of the z ring-associated protein, zapd, bound to the c-terminal domain of the tubulin-like protein, ftsz, suggests mechanism of z ring stabilization through ftsz cross-linking. *J. Biol. Chem.* **292**, 3740–3750 (2017).
75. Huang, K. H., Mychack, A., Tchorzewski, L. & Janakiraman, A. Characterization of the FtsZ C-Terminal variable (CTV) Region in Z-Ring assembly and interaction with the Z-Ring stabilizer ZapD in E. coli cytokinesis. *PLoS One* **11**, 1–24 (2016).

76. Choi, H., Min, K., Mikami, B., Yoon, H. & Lee, H. H. Structural and Biochemical Studies Reveal a Putative FtsZ Recognition Site on the Z-ring Stabilizer ZapD. **39**, 814–820 (2016).
77. Son, S. H. & Lee, H. H. Crystallization and preliminary X-ray crystallographic analysis of Z-ring-associated protein (ZapD) from *Escherichia coli*. *Acta Crystallogr. Sect. F Struct. Biol. Commun.* **71**, 194–198 (2015).
78. Roach, E. J. *et al.* Structure and Mutational Analyses of. **198**, 1683–1693 (2016).
79. Fu, G. *et al.* In Vivo Structure of the E. coli FtsZ-ring Revealed by Photoactivated Localization Microscopy (PALM). *PLoS One* **5**, e12680 (2010).
80. Li, Z., Trimble, M. J., Brun, Y. V. & Jensen, G. J. The structure of FtsZ filaments in vivo suggests a force-generating role in cell division. *EMBO J.* **26**, 4694–4708 (2007).
81. Lyu, Z., Coltharp, C., Yang, X. & Xiao, J. Influence of FtsZ GTPase activity and concentration on nanoscale Z-ring structure in vivo revealed by three-dimensional Superresolution imaging. *Biopolymers* **105**, 725–734 (2016).
82. Rivas, G. *et al.* Magnesium-induced linear self-association of the FtsZ bacterial cell division protein monomer. The primary steps for FtsZ assembly. *J. Biol. Chem.* (2000) doi:10.1074/jbc.275.16.11740.
83. Trueba, F. J. & Woldringh, C. L. Changes in cell diameter during the division cycle of *Escherichia coli*. *J. Bacteriol.* **142**, 869–878 (1980).
84. Rowlett, V. W. & Margolin, W. 3D-SIM Super-resolution of FtsZ and Its Membrane Tethers in *Escherichia coli* Cells. *Biophys. J.* **107**, L17–L20 (2014).
85. Coltharp, C., Buss, J., Plumer, T. M. & Xiao, J. Defining the rate-limiting processes of bacterial cytokinesis. *Proc. Natl. Acad. Sci. U. S. A.* **113**, E1044–E1053 (2016).
86. Chen, Y. & Erickson, H. P. Rapid in vitro assembly dynamics and subunit turnover of FtsZ demonstrated by fluorescence resonance energy transfer. *J. Biol. Chem.* **280**, 22549–22554 (2005).
87. González, J. M. *et al.* Cooperative behavior of *Escherichia coli* cell-division protein FtsZ assembly involves the preferential cyclization of long single-stranded fibrils. *Proc. Natl. Acad. Sci.* **102**, 1895–1900 (2005).
88. GonzálezGonz, P. *et al.* Torsion and curvature of FtsZ filaments †. (2014) doi:10.1039/c3sm52516c.
89. Paez, A., Tarazona, P., Mateos-Gil, P. & Vélez, M. Self-organization of curved living polymers : FtsZ protein filaments. *Soft Matter* **5**, 2625–2637 (2009).
90. Paez, A. *et al.* Simple modeling of FtsZ polymers on flat and curved surfaces: correlation with experimental in vitro observations. *PMC Biophys.* 2009 21 **2**, 1–16 (2009).
91. Márquez, I., Díaz-Haro, G. & Vélez, M. Surface Orientation and Binding Strength Modulate Shape of FtsZ on Lipid Surfaces. doi:10.3390/ijms20102545.
92. Vélez, M. How Does the Spatial Confinement of FtsZ to a Membrane Surface Affect Its Polymerization Properties and Function? *Front. Microbiol.* **13**, 757711 (2022).
93. Hörger, I., Velasco, E., Rivas, G., Vélez, M. & Tarazona, P. FtsZ Bacterial Cytoskeletal Polymers on Curved Surfaces: The Importance of Lateral Interactions. *Biophys. J.* **94**, L81–L83 (2008).
94. Krupka, M., Sobrinos-Sanguino, M., Jiménez, M., Rivas, G. & Margolin, W. *Escherichia coli* Zipa organizes FtsZ polymers into dynamic ring-like protofilament

- structures. *MBio* **9**, (2018).
95. Loose, M. & Mitchison, T. J. The bacterial cell division proteins FtsA and FtsZ self-organize into dynamic cytoskeletal patterns. *Nat. Cell Biol.* **16**, (2014).
 96. Ramirez-Diaz, D. A. *et al.* Treadmilling analysis reveals new insights into dynamic FtsZ ring architecture. *PLoS Biol.* **16**, (2018).
 97. Caldas, P. *et al.* Cooperative ordering of treadmilling filaments in cytoskeletal networks of FtsZ and its crosslinker ZapA. *Nat. Commun.* **2019 101** **10**, 1–13 (2019).
 98. Holden, S. J. *et al.* High throughput 3D super-resolution microscopy reveals *Caulobacter crescentus* in vivo Z-ring organization. *Proc. Natl. Acad. Sci. U. S. A.* **111**, 4566–4571 (2014).
 99. Szwedziak, P., Ghosal, D., Szwedziak, P. & Ghosal, D. FtsZ-ring Architecture and Its Control by MinCD. *Subcell. Biochem.* **84**, (2017).
 100. Yao, Q. *et al.* Short FtsZ filaments can drive asymmetric cell envelope constriction at the onset of bacterial cytokinesis. *EMBO J.* **36**, 1577–1589 (2017).
 101. Shtengel, G. *et al.* Interferometric fluorescent super-resolution microscopy resolves 3D cellular ultrastructure. *Proc. Natl. Acad. Sci. U. S. A.* **106**, 3125–3130 (2009).
 102. Haeusser, D. P., Rowlett, V. W. & Margolin, W. A mutation in *Escherichia coli* ftsZ bypasses the requirement for the essential division gene zipA and confers resistance to FtsZ assembly inhibitors by stabilizing protofilament bundling. *Mol. Microbiol.* **97**, 988–1005 (2015).
 103. Yang, X. *et al.* GTPase activity-coupled treadmilling of the bacterial tubulin FtsZ organizes septal cell wall synthesis. *Science (80-.).* **355**, 744–747 (2017).
 104. Bisson-Filho, A. W. *et al.* Treadmilling by FtsZ filaments drives peptidoglycan synthesis and bacterial cell division. *Science (80-.).* **355**, 739–743 (2017).
 105. Whitley, K. D. *et al.* FtsZ treadmilling is essential for Z-ring condensation and septal constriction initiation in *Bacillus subtilis* cell division. *Nat. Commun.* **12**, (2021).
 106. Erickson, H. P. Modeling the physics of FtsZ assembly and force generation. *Proc. Natl. Acad. Sci.* **106**, 9238–9243 (2009).
 107. Xiao, J. & Goley, E. D. Redefining the roles of the FtsZ-ring in bacterial cytokinesis. *Curr. Opin. Microbiol.* **34**, 90–96 (2016).
 108. Coltharp, C. & Xiao, J. Beyond force generation: Why is a dynamic ring of FtsZ polymers essential for bacterial cytokinesis? *BioEssays* **39**, 1–11 (2017).
 109. Kohyama, S., Merino-Salomón, A. & Schwille, P. In vitro assembly, positioning and contraction of a division ring in minimal cells. *Nat. Commun.* **13**, 6098 (2022).
 110. Ramirez-Diaz, D. A. *et al.* FtsZ induces membrane deformations via torsional stress upon GTP hydrolysis. *Nat. Commun.* **2021 121** **12**, 1–11 (2021).
 111. Godino, E. *et al.* Cell-free biogenesis of bacterial division proto-rings that can constrict liposomes. *Commun. Biol.* **2020 31** **3**, 1–11 (2020).
 112. Hirschi, S., Ward, T. R., Meier, W. P., Müller, D. J. & Fotiadis, D. Synthetic Biology: Bottom-Up Assembly of Molecular Systems. *Chem. Rev.* (2022)
doi:10.1021/ACS.CHEMREV.2C00339/ASSET/IMAGES/LARGE/CR2C00339_0015.JPEG.
 113. Jiang, W. *et al.* Artificial Cells: Past, Present and Future. *ACS Nano* **16**, 15705–15733 (2022).

114. Schuck, P. Size-distribution analysis of macromolecules by sedimentation velocity ultracentrifugation and lamm equation modeling. *Biophys. J.* **78**, 1606–1619 (2000).
115. Laue, T. M., Shah, B. D., Ridgeway, T. M. & Pelletier, S. L. *Analytical ultracentrifugation in biochemistry and polymer science. Analytical ultracentrifugation in biochemistry and polymer science* (Royal Society of Chemistry, 1992).
116. Schuck, P. On the analysis of protein self-association by sedimentation velocity analytical ultracentrifugation. *Anal. Biochem.* **320**, 104–124 (2003).
117. Balbo, A. *et al.* Studying multiprotein complexes by multisignal sedimentation velocity analytical ultracentrifugation. *Proc. Natl. Acad. Sci. U. S. A.* **102**, 81–86 (2005).
118. Cole, J. L. Analysis of Heterogeneous Interactions. *Methods Enzymol.* **384**, 212–232 (2004).
119. Mastronarde, D. N. Automated electron microscope tomography using robust prediction of specimen movements. *J. Struct. Biol.* **152**, 36–51 (2005).
120. Zheng, S. Q. *et al.* MotionCor2: anisotropic correction of beam-induced motion for improved cryo-electron microscopy. *Nat. Methods* **14**, 331–332 (2017).
121. Schur, F. K. M. *et al.* An atomic model of HIV-1 capsid-SP1 reveals structures regulating assembly and maturation. *Science* (80-.). **353**, 506–508 (2016).
122. Kremer, J. R., Mastronarde, D. N. & McIntosh, J. R. Computer Visualization of Three-Dimensional Image Data Using IMOD. *J. Struct. Biol.* **116**, 71–76 (1996).
123. Buchholz, T. O., Jordan, M., Pigino, G. & Jug, F. Cryo-CARE: Content-aware image restoration for cryo-transmission electron microscopy data. *Proc. - Int. Symp. Biomed. Imaging* **2019-April**, 502–506 (2019).
124. Goddard, T. D. *et al.* UCSF ChimeraX: Meeting modern challenges in visualization and analysis. *Protein Sci.* **27**, 14–25 (2018).
125. Pettersen, E. F. *et al.* UCSF Chimera—A visualization system for exploratory research and analysis. *J. Comput. Chem.* **25**, 1605–1612 (2004).
126. Margineanu, A. *et al.* Complexation of Lipofectamine and Cholesterol-Modified DNA Sequences Studied by Single-Molecule Fluorescence Techniques. (2007) doi:10.1021/bm700486q.
127. Pautot, S., Frisken, B. J. & Weitz, D. A. Production of unilamellar vesicles using an inverted emulsion. *Langmuir* **19**, 2870–2879 (2003).

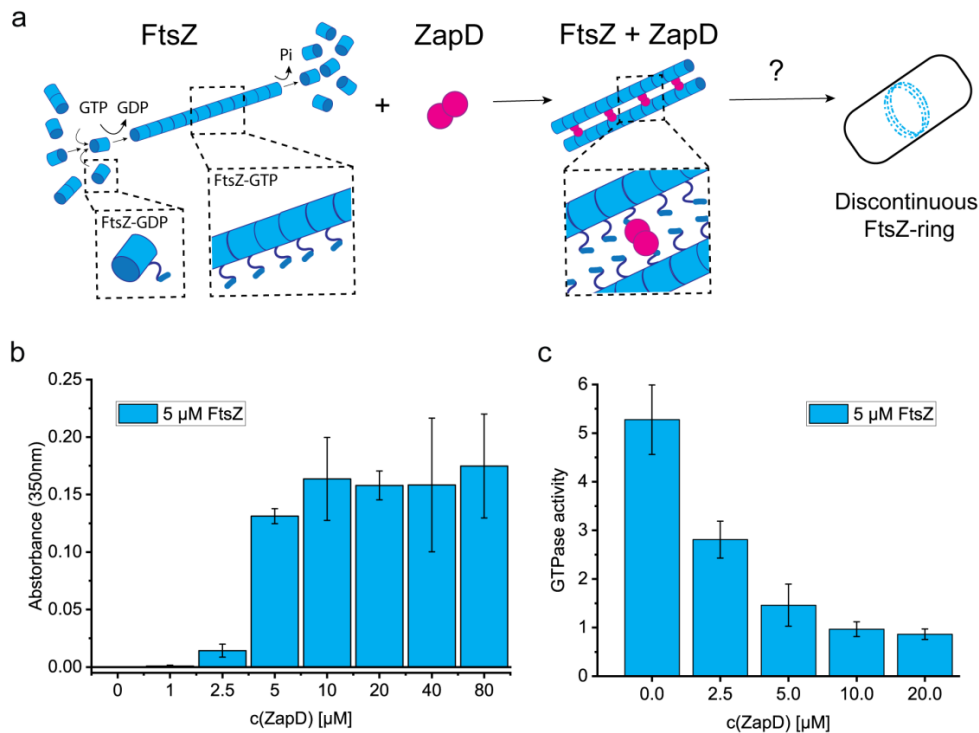


Figure 1. ZapD binds FtsZ and promotes filament bundling. **a** Scheme of the FtsZ protein and its interaction with ZapD. *E. coli* FtsZ (blue) forms monomers in solution that oligomerize depending on the buffer conditions. Upon GTP consumption, FtsZ homopolymerizes directionally, assembling single stranded filaments. ZapD is a robust dimer (magenta) that interacts directly with FtsZ, crosslinking filaments by promoting lateral interactions between them. Although the molecular mechanism is still unclear, the current hypothesis of interaction defines a dimer of ZapD crosslinking two FtsZ filaments through the C-terminal region of FtsZ. According to this model, the orientation of the FtsZ filaments is antiparallel, allowing the growth and treadmilling of the filaments in opposite directions. However, the mechanism of Z-ring assembly and crosslinking in the midcell is still unknown. **b** Light scattering assay measuring the absorbance at 350 nm of samples containing 5 μM FtsZ and increasing concentrations of ZapD. The light scattering of the sample was measured 5 minutes after the addition of 1 mM GTP at working buffer (50 mM KCl, 50 mM Tris-Cl, 5 mM MgCl₂ pH 7). FtsZ polymers do not scatter light at this wavelength; therefore, the signal at 350 nm corresponds to the presence of large FtsZ macrostructures and bundles. Blanks were measured before the addition of GTP and then subtracted from subsequent measurements. The mean value and SD of >3 independent replicates are plotted in the graph. **c** GTPase activity of FtsZ after addition of 1 mM GTP in presence of increasing concentrations of ZapD at working conditions (50 mM KCl, 50 mM Tris-Cl, 5 mM MgCl₂ pH 7). The mean value and SD plotted in the graph are the result of 3 independent replicates. The GTPase activity was measured as a result of the Pi released from GTP consumption. The units are Mol GTP consumed per Mol FtsZ per min.

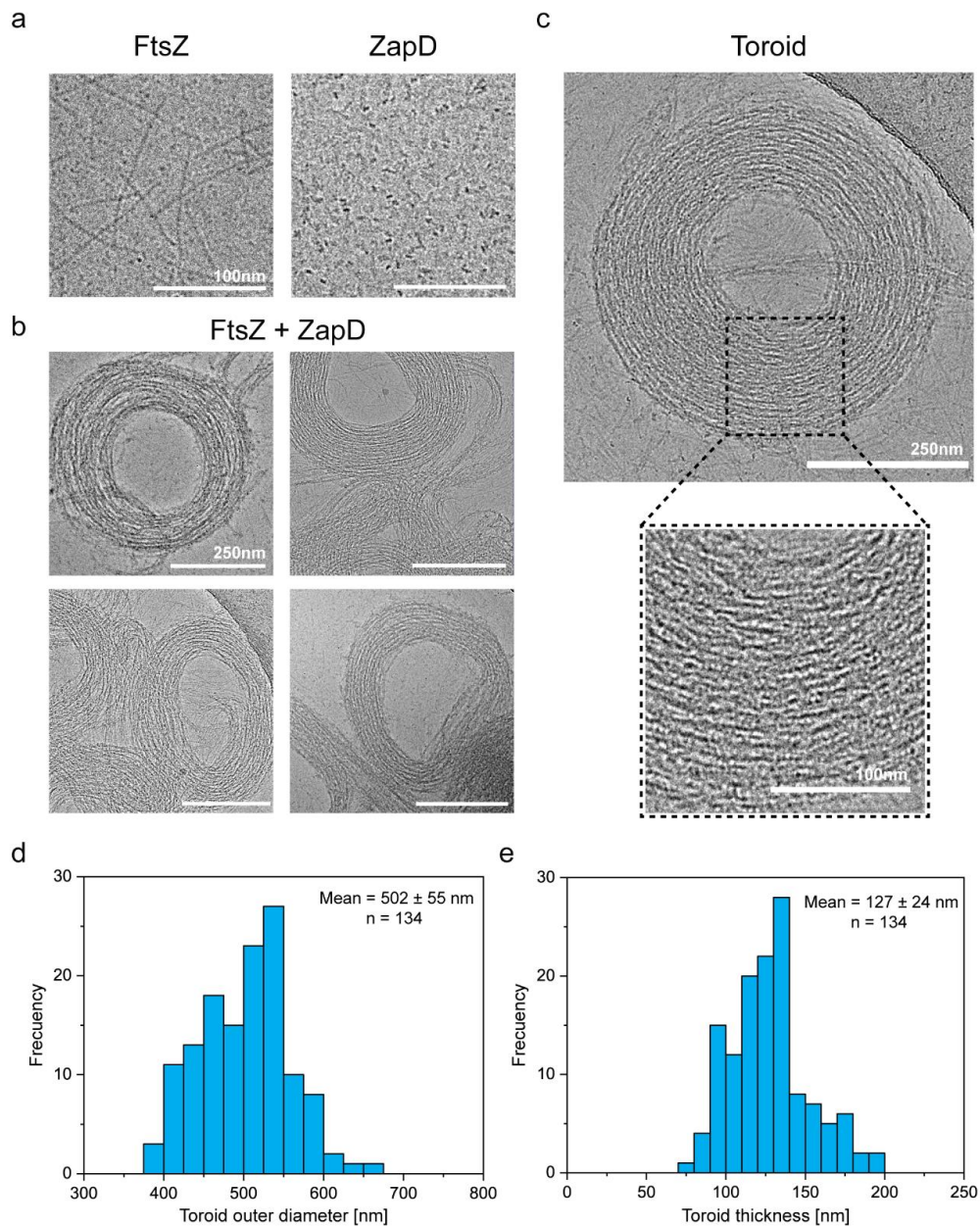


Figure 2. ZapD promotes the formation of FtsZ toroids. **a** Cryo-EM micrographs of FtsZ filaments (FtsZ-GTP form) (left) and ZapD protein (right) at 10 μ M under working conditions (50 mM KCl, 50 mM Tris-Cl, 5 mM MgCl₂ pH 7). Scale bars are 100 nm **b** Cryo-EM images of FtsZ (10 μ M) in the presence of equimolar concentrations of ZapD and 1 mM GTP in working conditions. Cryo-EM grids were plunge frozen 2 min after GTP addition to favor the assembly of FtsZ and ZapD structures. The proteins were mixed before the polymerization was triggered by GTP addition. Scale bars are 250 nm **c** Micrograph of an individual FtsZ toroid found under the same conditions as in **(b)**. Close-up view of an area within the toroid is framed by a dotted black line, revealing the large amount of FtsZ filaments that form its structure. **d** Distribution of the outer diameter of the FtsZ toroid. Each toroid was measured perpendicularly in the shortest and longest axis to ensure the reliability of the measurement. The mean value and standard deviation are shown in the graph. **e** Distribution of toroidal thickness. It was measured as the result of the difference between the outer and inner diameter of each toroid. The mean value and standard deviation are shown in the graph.

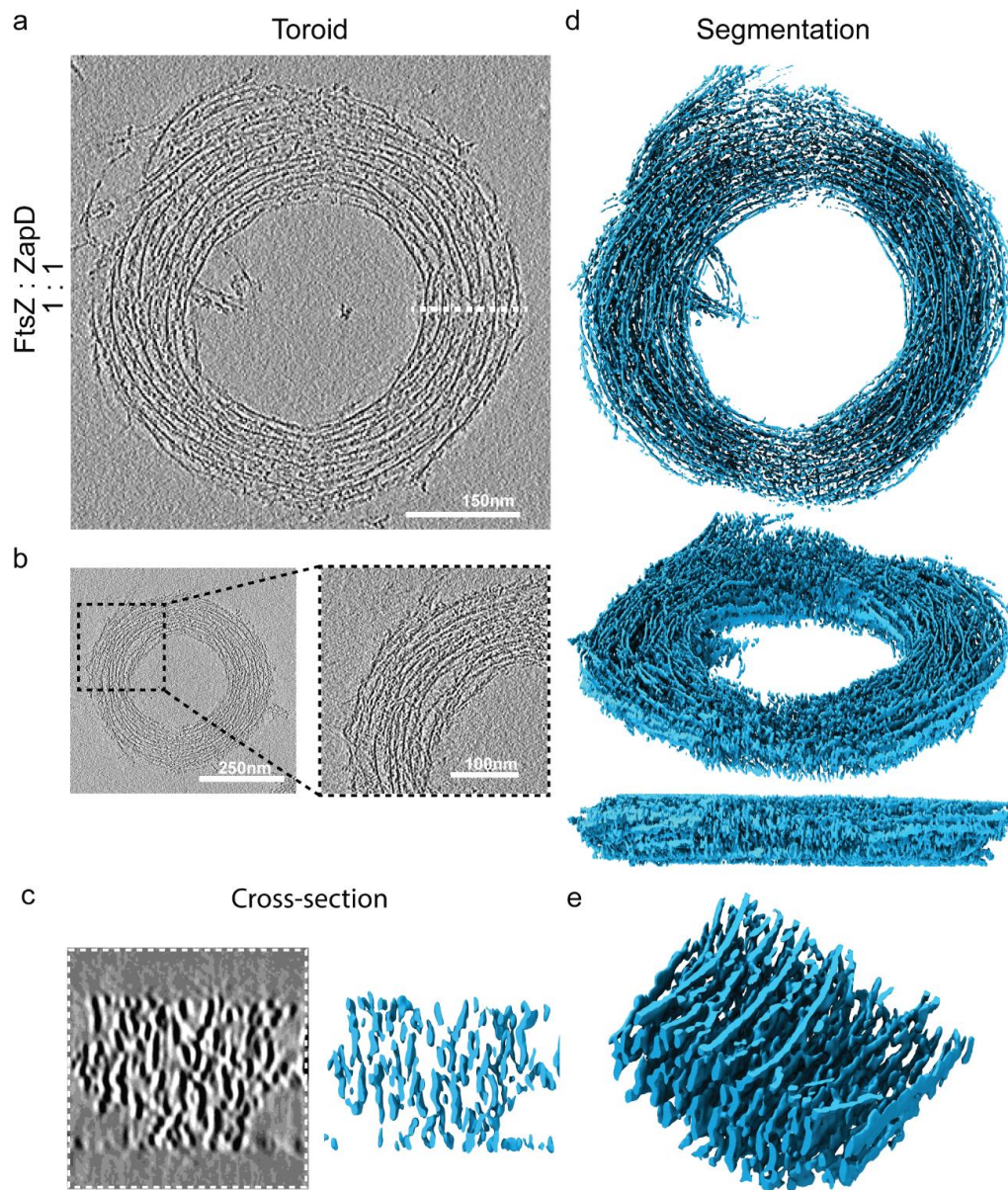


Figure 3. 3D structure of FtsZ toroids revealed by cryo-ET. **a** Representative micrograph of a FtsZ toroid resulting from the interaction of FtsZ with ZapD. The image is the average of five 6.4 nm thick tomographic slices (total thickness of 32 nm) of the reconstructed tomogram around the equatorial plane of a single FtsZ toroid. Scale bar is 150 nm. The concentrations of FtsZ and ZapD were 10 μ M and 1 mM of GTP was added to trigger polymerization under working conditions (50 mM KCl, 50 mM Tris-Cl, 5 mM MgCl₂ pH 7). **b** Cryo-ET image of a single FtsZ toroid. A close-up view of the toroidal structure (left) shows the alignment of FtsZ filaments forming the toroid. The image is the average of five tomographic slices of the reconstructed tomogram. 10 μ M FtsZ was used with either equimolar or double (20 μ M) concentration of ZapD in the presence of 1 mM GTP. No significant structural differences were observed in the toroidal structures among samples containing equimolar or double ZapD concentrations. **c** Cryo-ET image (left) shows the cross-section corresponding to the area located at the white dotted line in **(a)**. This image is the average of nine tomographic slices from the denoised tomogram. The isosurface of the cross-section (right) shows the alignment

and organization of the FtsZ filaments within the toroid. This suggests a regular distribution of filaments assembling the toroid. FtsZ filaments are represented in blue. **d** Isosurface of the FtsZ toroid shown in **(a)**. It was extracted from the reconstruction of the denoised tomographic volume and positioned in different views to facilitate its visualization: (top) front view, (middle) side view and (bottom) lateral view. **e** A close-up view of the segmented toroidal structure. It shows the complex internal organization of filaments assembling the toroid. It corresponds to a zone within the toroid shown in **(d)**.

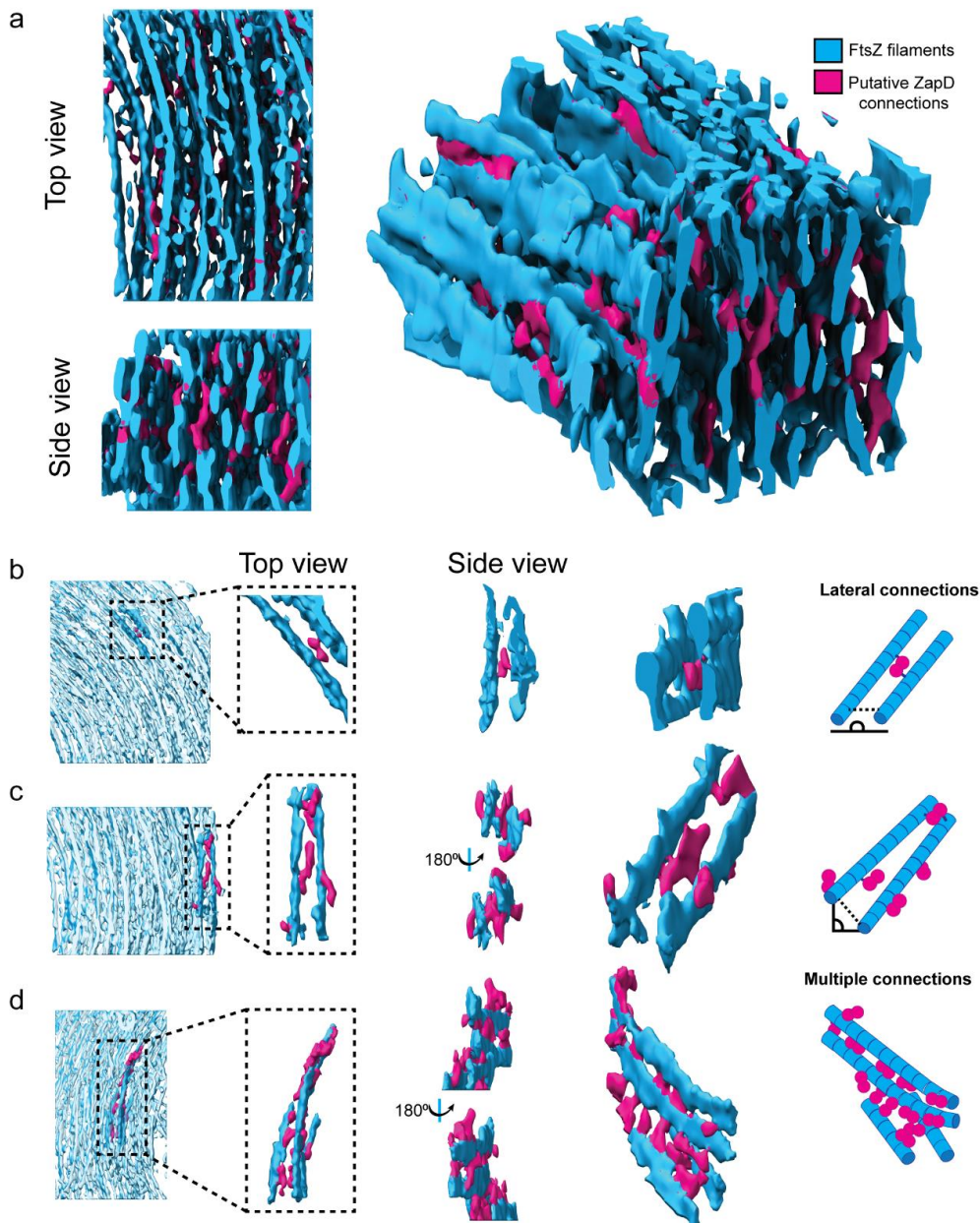


Figure 4. FtsZ filaments are connected by putative ZapD crosslinkers to assemble the toroidal structure. **a** Top (left, top), side (left, bottom) and lateral (right) views of the isosurface from an area within the toroidal structure shown in (Fig. 3a). The FtsZ filaments are colored blue, while filament connections or putative ZapD proteins are labelled magenta to facilitate interpretation of the results. Other putative ZapD proteins decorating the FtsZ filaments were not labelled in magenta because they were not forming any clear connection between the filaments. **b-d** Different examples of connections between filaments by putative ZapD proteins within the toroid. Filaments are labelled in blue and putative ZapD in magenta to facilitate their interpretation. From left to right, the localization of the analyzed area, a close-up view of the structure of interest, different views of the connections and a schematic to illustrate the interpretation of the data. The schematic (right) represents the localization of ZapD proteins (magenta) and FtsZ filaments (blue). **b** Lateral connection of two FtsZ filaments by a putative ZapD dimer. In this example, the attachment of each globular density or putative ZapD

monomer was bound to each filament, allowing for a lateral connection **c** Putative ZapD connections stabilizing two filaments by a lateral interaction. Additional ZapD decorations attached only to one of the filaments appear to be available for other connections. **d** Multiple ZapD proteins can connect to filaments and stabilize the interaction. First, the two upper filaments are connected to each other by lateral connections through several putative ZapD. The lower filament connects laterally with the two other filaments. In the upper part, additional decorations or putative ZapD proteins would be available to establish further connections forming a tridimensional mesh.

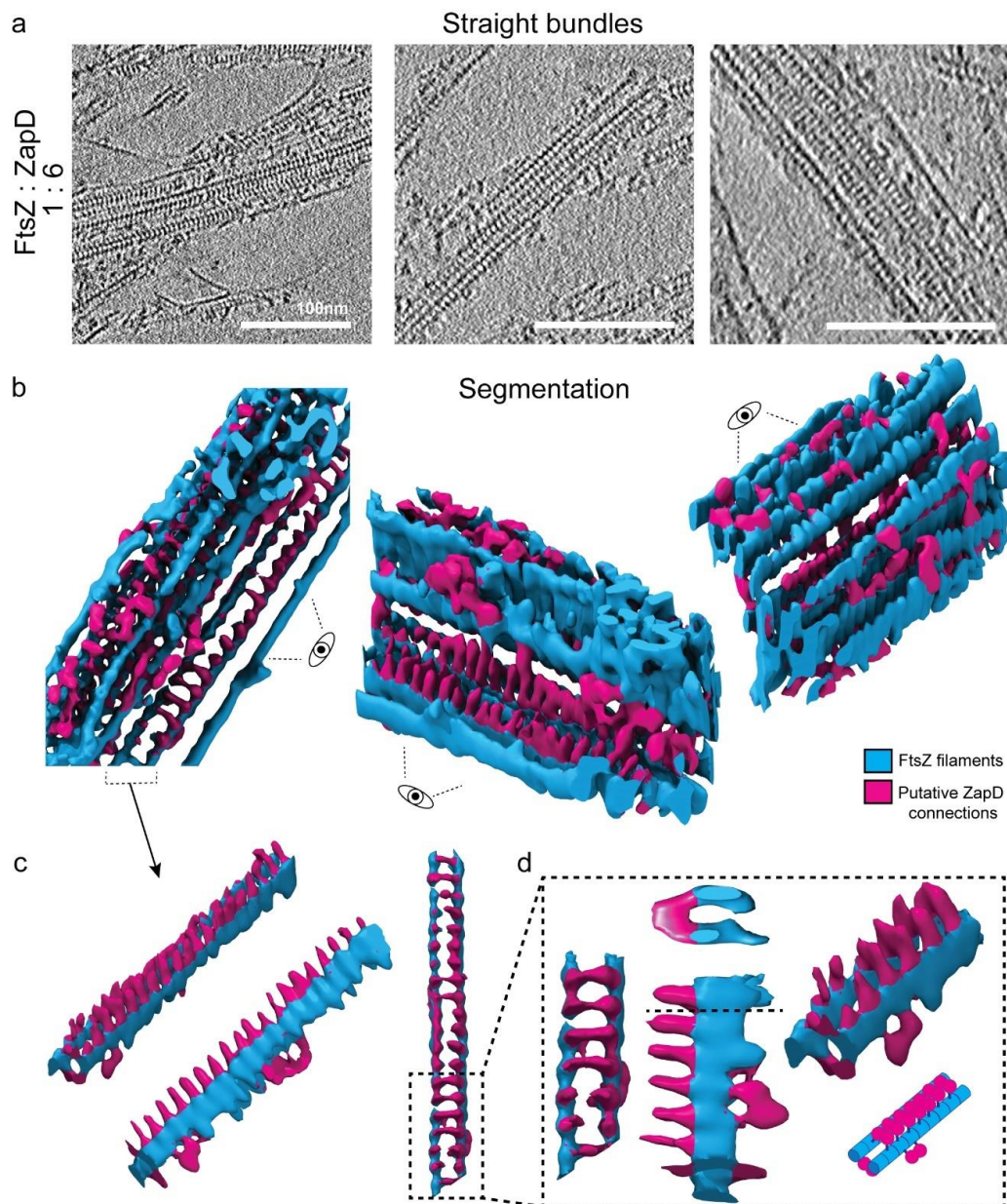


Figure 5. The presence of a high ZapD concentration promotes the formation of straight

FtsZ bundles. **a** Representative images of straight FtsZ bundles resulting from the interaction of FtsZ with high ZapD concentrations under working conditions (50 mM KCl, 50 mM Tris-Cl, 5 mM MgCl₂ pH 7). The concentrations of FtsZ and ZapD were 10 μ M and 60 μ M, respectively, and 1 mM of GTP was added to trigger polymerization. The straight bundles were only found at high ZapD concentrations. The image is the average of five 6.4 nm thick tomographic slices (total thickness of 32 nm) of the reconstructed tomogram. Scale bars are 100 nm. **b** Isosurface of the straight bundles from the denoised tomographic volume. FtsZ filaments are colored in blue and putative ZapD connections in magenta. Three different views (top (left) and side views (middle, right)) are shown. Straight bundles are organized in a regular organization. Multiple connections between filaments are found in a very regular manner; putative ZapD proteins align and stack to stabilize two FtsZ filaments by crosslinking them. In addition, lateral

connections were also found linking couple of stabilized filaments among them, ultimately assembling the straight bundle. **c** Different views of one of the isolated filaments from the straight bundle. A side view of the filaments (middle) shows a spike-like structure regularly located at the top of the FtsZ filaments, connecting them as observed in the top view (right). **d** Different close-up views of the filament structure shown in **(c)**. In the cross-section of the structure (middle, top), it is clearly visible that the ZapD proteins connect the two filaments, forming a bridge over them. A schematic of the suggested interaction (right, bottom) shows the location of putative ZapD dimer in this structure.

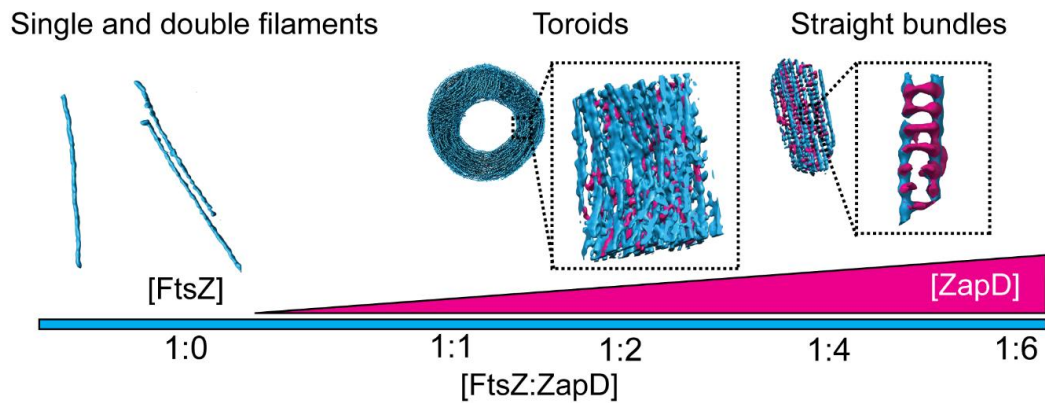


Figure 6. Proposed molecular mechanism of the bundling effect of ZapD on FtsZ filaments. Based on our experiments and in agreement with preliminary studies, we propose a molecular mechanism for the interaction between FtsZ and ZapD. FtsZ filaments are highly dynamic and they can interact laterally with each other, forming double filaments through weak lateral interactions. On the other hand, each ZapD dimer can bind to two FtsZ filaments, promoting the formation of lateral interactions between FtsZ filaments. At low concentrations of ZapD, only a few lateral connections are formed and thus no bundles can be assembled. However, at higher ZapD concentrations, reaching a protein ratio of FtsZ and ZapD of 1:1 or 1:2 (FtsZ:ZapD), more ZapD-mediated connections are established between FtsZ filaments and the formation of bundles and toroidal structures is favored. Toroidal structures are composed of a meshwork of short filaments, crosslinked laterally by ZapD dimers. A further increase in the concentration of ZapD (protein ratio of 1:4 or 1:6 (FtsZ:ZapD)) can also increase the number of connections on the FtsZ filaments, straighten up their structure and allowing the formation of straight bundles. This structure is formed only under high ZapD concentrations although coexists with scarce toroidal structures. The assembly of FtsZ macrostructures is dependent on the number of lateral connections through ZapD dimers and some intermediate states are expected between toroids and straight bundles.

Supplement to publication P5

Reprinted with permission from:

Merino-Salomón, A., Schneider, J., Babl, L., Krohn, J-H., Sobrinos-Sanguino, M., Schäfer, T., Luque-Ortega, J.R., Alfonso, C., Jiménez, M., Jasnin, M., Rivas, G., Schwille, P. (2023). Crosslinking by ZapD drives the assembly of short, discontinuous FtsZ filaments into ring-like structures in solution. *BioRxiv* 2023.01.12.523557 (*in process of submission*)

Source online: <https://doi.org/10.1101/2023.01.12.523557>

Supplementary Information

Crosslinking by ZapD drives the assembly of short, discontinuous FtsZ filaments into ring-like structures in solution

Adrián Merino-Salomón¹, Jonathan Schneider^{2,3}, Leon Babi¹, Jan-Hagen Krohn^{1,4}, Marta Sobrinos-Sanguino⁵, Tillman Schäfer⁶, Juan R. Luque-Ortega⁵, Carlos Alfonso⁷, Mercedes Jiménez⁷, Marion Jasnin^{3*}, German Rivas^{7*} & Petra Schwillle^{1*}.

- ¹- Department of Cellular and Molecular Biophysics, Max Planck Institute of Biochemistry, 82152 Martinsried, Germany.
- ²- Department of Molecular Structural Biology, Max Planck Institute of Biochemistry, 82152 Martinsried, Germany.
- ³- Helmholtz Pioneer Campus, Helmholtz Zentrum München, 85764 Neuherberg, Germany.
- ⁴- Exzellenzcluster ORIGINS, Boltzmannstr. 2, 85748 Garching, Germany.
- ⁵- Molecular Interactions Facility, Centro de Investigaciones Biológicas Margarita Salas, Consejo Superior de Investigaciones Científicas (CSIC), 28040 Madrid, Spain.
- ⁶- Cryo-EM facility, Max Planck Institute of Biochemistry, 82152 Martinsried, Germany.
- ⁷- Centro de Investigaciones Biológicas Margarita Salas, Consejo Superior de Investigaciones Científicas (CSIC), 28040 Madrid, Spain.

Correspondence: marion.jasnin@helmholtz-muenchen.de; rivas@cib.csic.es; schwillle@biochem.mpg.de

This file contains

- Legends to Supplementary Movies 1-3
- Supplementary Figures S1-S15
- Supplementary Table 1

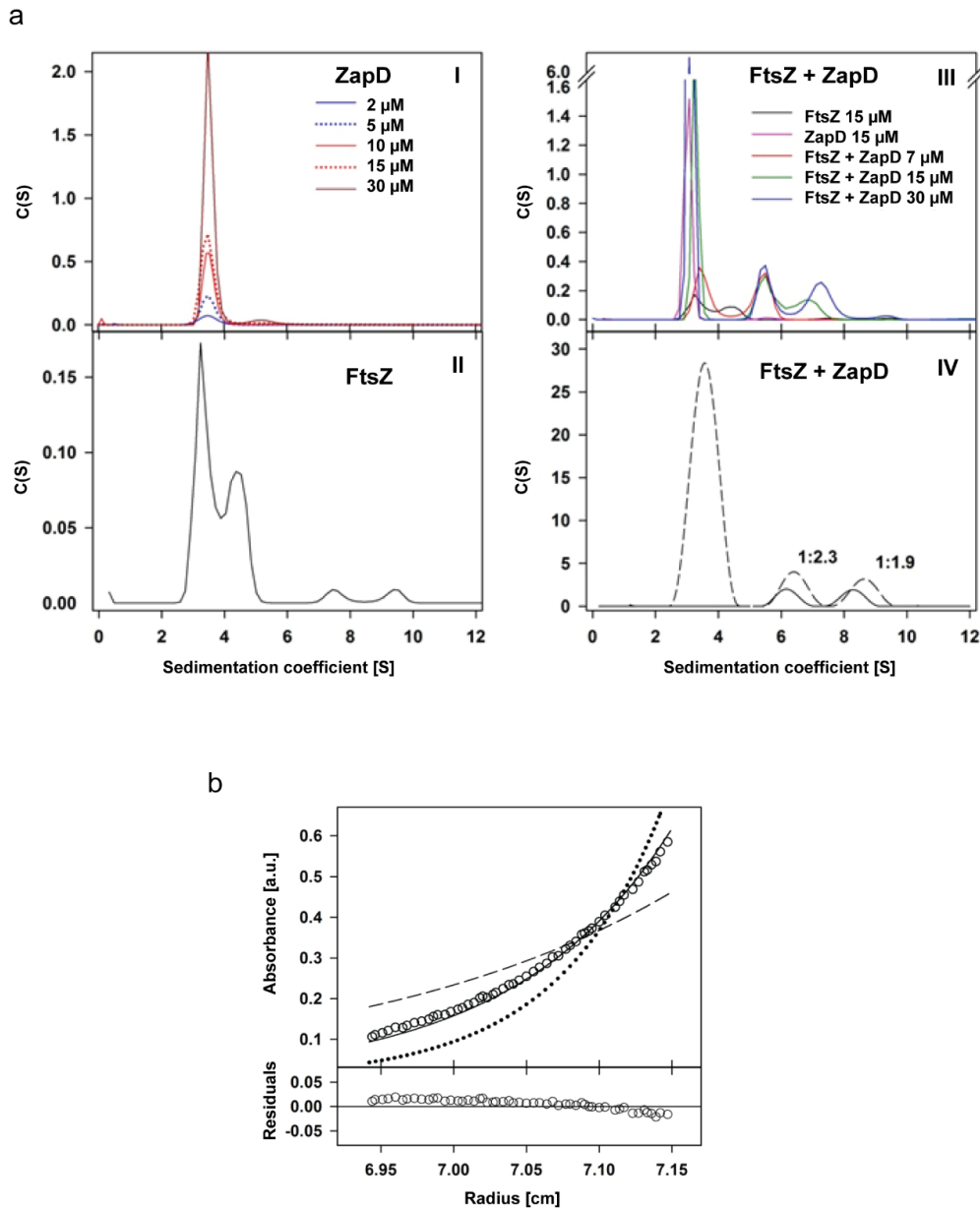
Legends to Supplementary Movies

Supplementary Movie 1. Tomogram of a FtsZ toroidal structure promoted by ZapD showed in Figure 3a followed by segmentation of the tomogram. FtsZ filaments are in blue. Successive rotations of the segmented volume allow to visualize the structure of the toroid in 3D.

Supplementary Movie 2. Isosurface from the toroid showed in Figure 2a. FtsZ filaments are shown in blue and putative ZapD connections in magenta. A close-up view and rotations of the segmented volume show the filament meshwork and the connections by ZapD in 3D.

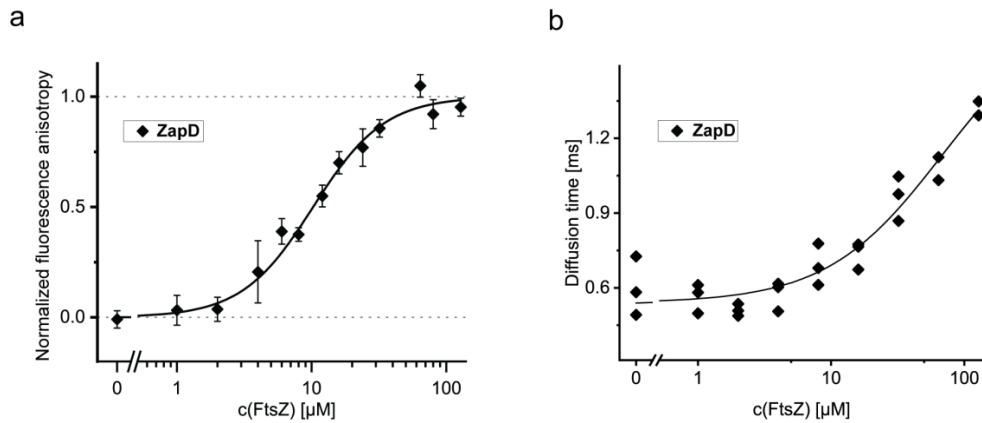
Supplementary Movie 3. Tomogram of a FtsZ straight bundle formed at high concentration of ZapD proteins showed in Figure 5b. Successive segmentation of the tomogram with FtsZ filaments labelled in blue and putative ZapD connections in magenta. Rotations, close-up views help the interpretation of the data and show the 3D structure of the straight bundle.

Supplementary Figures

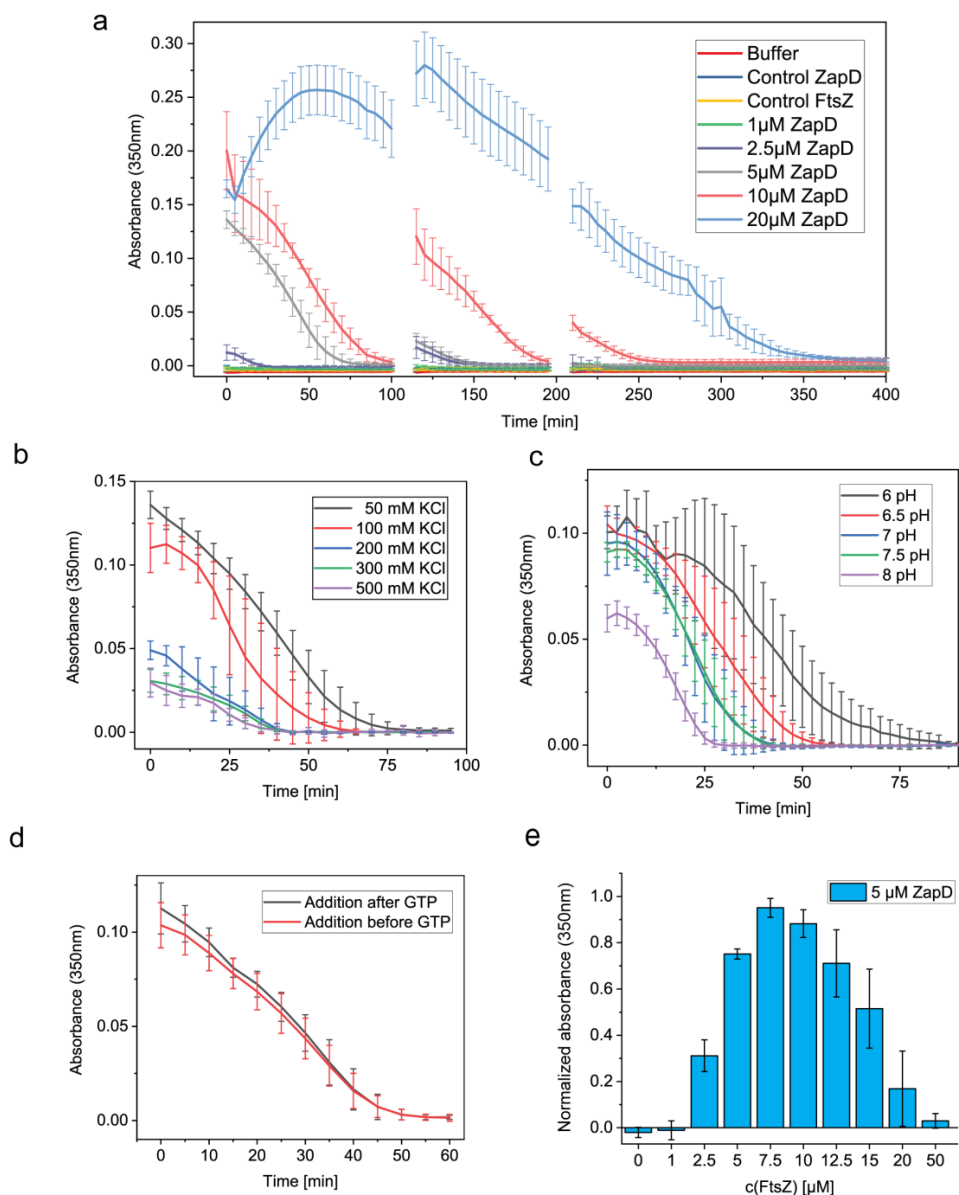


Supplementary Figure 1. Characterization of the ZapD dimer and ZapD-FtsZ-GDP interaction by Analytical ultracentrifugation (AUC). **a** Sedimentation coefficient distribution, $c(s)$, obtained by sedimentation velocity (SV) with (I) ZapD at different protein concentrations at working conditions (50 mM KCl, 50 mM Tris-Cl, 5 mM $MgCl_2$ pH 7). More than 95% of the sample sedimented as a single specie with an experimental sedimentation coefficient of 3.5 S once corrected to standard conditions ($s_{20, w}$: $3.6 S \pm 0.1$). It matched with the expected value for ZapD dimers. (II) Sedimentation coefficient distribution, $c(s)$, obtained by SV of FtsZ at 15 μM at working conditions (50 mM KCl, 50 mM Tris-Cl, 5 mM $MgCl_2$ pH 7). (III) Sedimentation coefficient distribution, $c(s)$, obtained by SV of 15 μM FtsZ and increasing concentrations of ZapD in physiological glutamate-acetate buffer. There is an axis break at 1.6

to highlight protein complexes. **(IV)** Represents the global multi-wavelength (280 and 250 nm) analysis of the sedimentation coefficient distribution for FtsZ-ZapD complexes obtained by SV and decomposition into component sedimentation coefficient distributions $c_k(s)$ for FtsZ (solid trace) and ZapD (dashed trace) using FtsZ:ZapD initial ratio of 1:4. Numbers over the peaks correspond to the FtsZ:ZapD molar stoichiometry observed for each complex. **b** Concentration gradient obtained by sedimentation equilibrium (SE) of ZapD at 10 μM . Experimental data (empty circles) are shown together with the best-fit analysis corresponding to ZapD dimer (solid line), monomer (dashed line) and trimer (dotted line). The lower plot represents the residuals of the fitting of the experimental data to the dimeric model. ZapD was shown as a stable dimer, showing a buoyant mass of 14,415 Da, corresponding to a molecular mass of 56200 ± 400 Da, considering the partial specific volume calculated from the ZapD amino acid sequence.



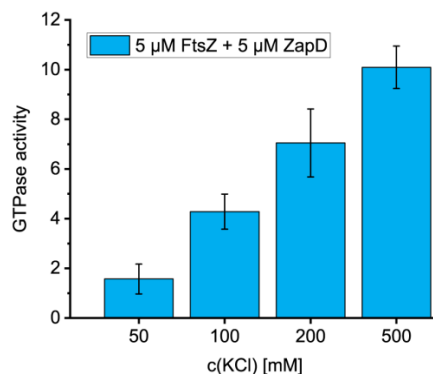
Supplementary Figure 2. Biochemical characterization of the ZapD-FtsZ-GDP interaction by FCS and fluorescence anisotropy. **a** Interaction curve of FtsZ-GDP and ZapD by fluorescence anisotropy. The fluorescence anisotropy measurement of 5 μM ZapD supplemented with 150 nM ZapD-ATTO 647N at increasing concentrations of FtsZ demonstrated a direct interaction between both proteins with an apparent K_d of 10.26 ± 1.07 (SE). Samples were in working conditions (50 mM KCl, 50 mM Tris-Cl, 5 mM MgCl_2 pH 7) and the error bars represent the standard deviation among 3 independent samples. **b** Fluorescence correlation microscopy (FCS) analysis of increasing concentrations of FtsZ-GDP with 5 μM of ZapD supplemented with 100 nM ZapD-ATTO 647N in working conditions. The FCS analysis demonstrated an increasing diffusion time of ZapD along with the FtsZ concentration as result of higher proportion of ZapD bound to FtsZ. The plotted line is only to guide the eye. Each condition was measured in three independent samples.



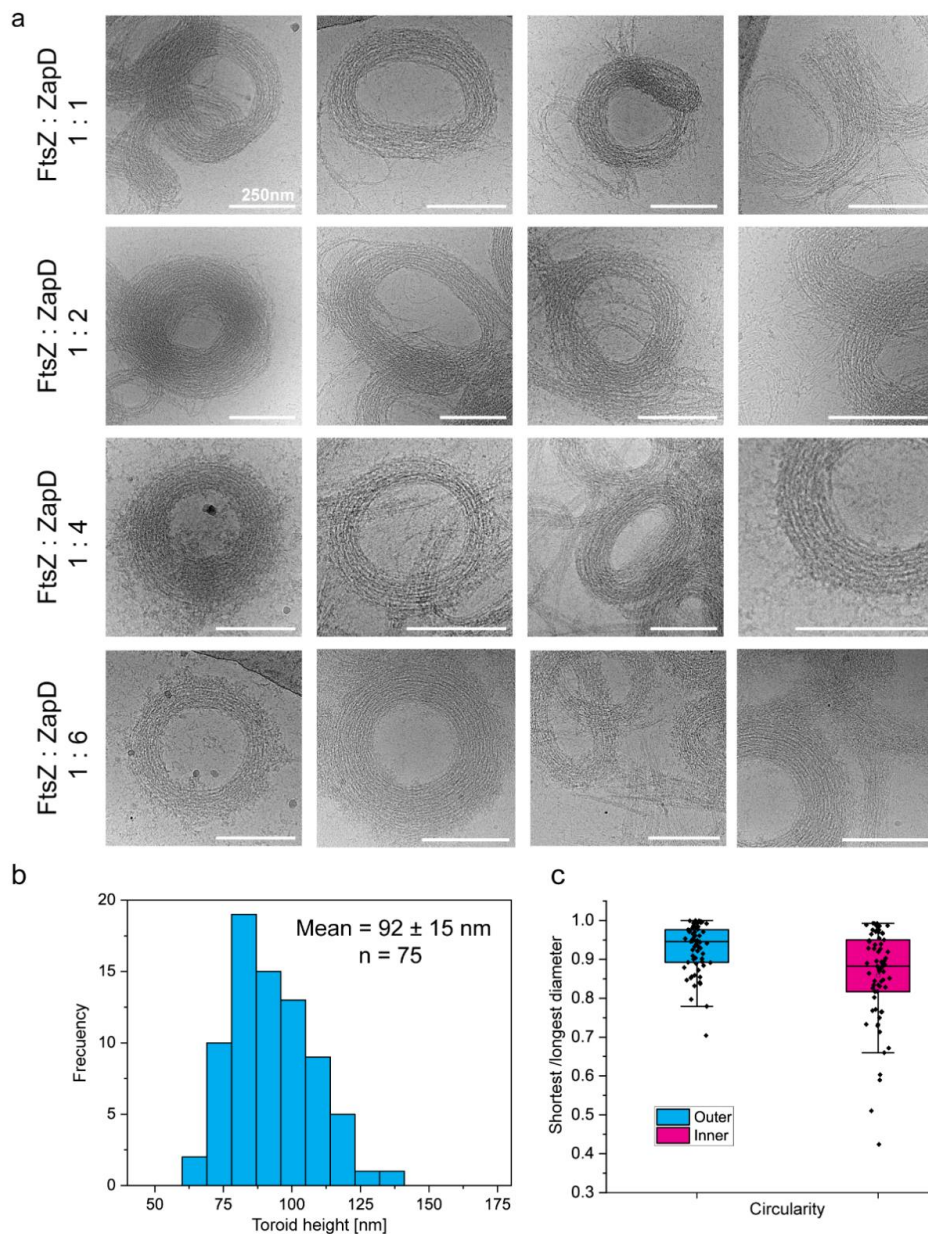
Supplementary Figure 3. Biochemical characterization of the ZapD and FtsZ bundles by light scattering.

The characterization of the FtsZ bundles resulting from the interaction with ZapD was made by measuring the light scattering of the samples at 350nm in a plate reader. The mean value and standard deviation are the result of 3-6 independent samples. The signal from the blanks was collected before polymerization of FtsZ and subtracted for further measurements. Control of ZapD and FtsZ polymers independently did not show any significant difference with the blank after GTP addition. The working buffer was used unless it is specified in the legend (50 mM KCl, 50 mM Tris-Cl, 5 mM MgCl₂ and pH 7). The absorbance was measured every 5 min for 100 min. **a** Measurement of light scattering over time of 5 μM FtsZ in the presence of ZapD at increasing concentrations. Both proteins were mixed prior to the addition of 1 mM GTP. A decay in the signal can be observed over time, highlighting the dynamic nature of the FtsZ bundles. After 100 min, extra 1 mM GTP was added and FtsZ bundles were reassembled, showing lower increase of the signal due to a higher concentration of GDP in the samples, likely sifting the reaction. The addition of 1 mM GTP was done twice

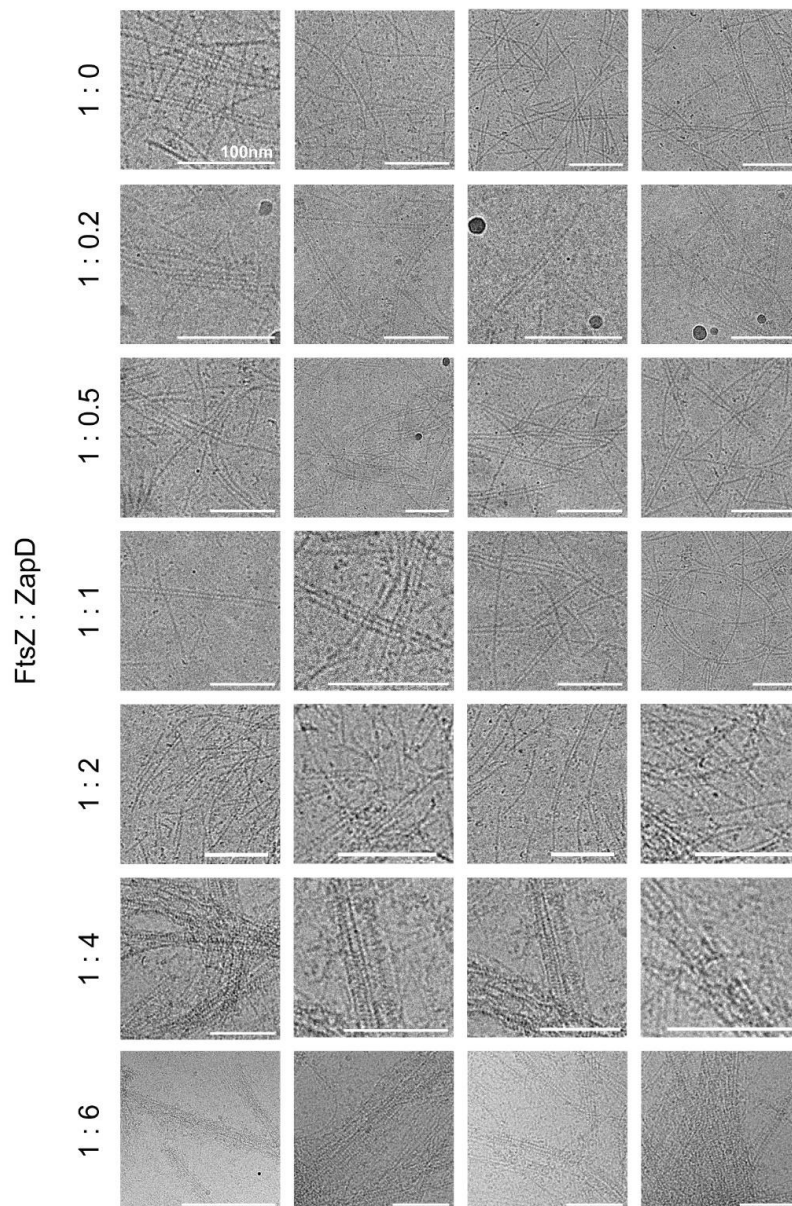
after 100 min. **b** Assembly of FtsZ bundles at different ionic strength conditions using KCl. The concentration of FtsZ and ZapD was 5 μ M for both proteins, adding 1 mM GTP in the working buffer supplemented with different concentrations of KCl (50-500 mM KCl). Higher ionic strength in the buffer reduced the amount or size of bundles formed in solution, as the FtsZ-ZapD interaction is decreased. **c** Effect of pH in the FtsZ bundling process. The protein concentration used was 5 μ M of ZapD and FtsZ with the addition of 1 mM GTP in the working buffer at different pH (6.5-8 pH). Lower pH enhanced the amount of FtsZ bundles promoted by ZapD, as lateral FtsZ-FtsZ interactions are promoted at lower pH. **d** Analysis of FtsZ bundling over time when ZapD was mixed with FtsZ prior or after the GTP addition and polymerization. The concentration of FtsZ and ZapD was 5 μ M and 1 mM GTP in working buffer. ZapD mixed with FtsZ before or after GTP addition did not show significant difference in the formation of FtsZ bundles. **e** FtsZ bundling at different concentration of FtsZ with 5 μ M ZapD and 1 mM GTP in working conditions. In this case, the signal from FtsZ bundles was normalized to facilitate the interpretation of the results. The signal plotted corresponds to 5 min after the addition of GTP. There was a clear decrease in the signal obtained at high concentration of FtsZ due to the low protein ratio ZapD/FtsZ.



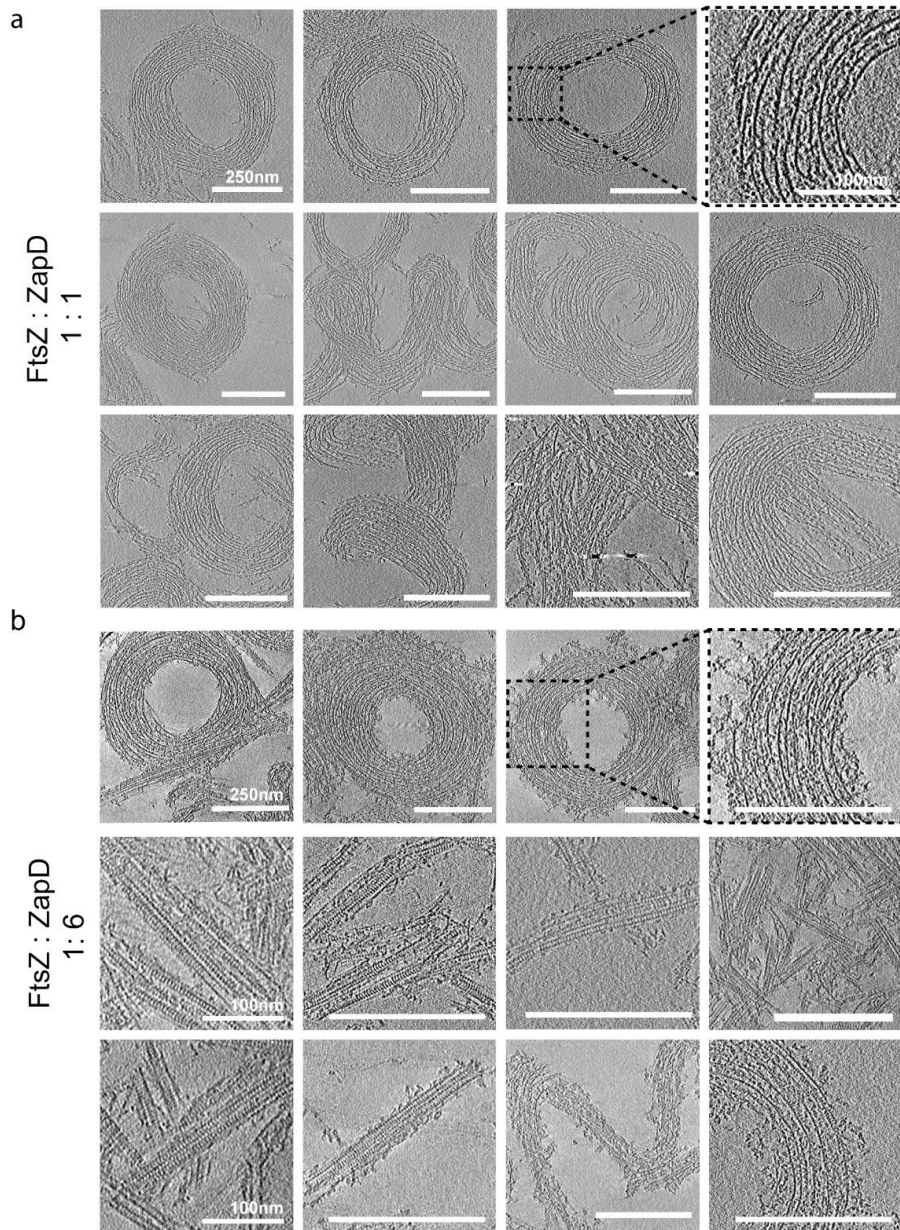
Supplementary Figure 4. Ionic strength in the buffer lowers the effect of ZapD over FtsZ GTPase activity. GTPase activity of FtsZ in the presence of equimolar concentration of ZapD (5 μ M) after addition of 1 mM GTP at different ionic strength conditions (50 – 500 mM KCl, 50 mM Tris-Cl, 5 mM MgCl₂ pH 7). The mean value and SD of the FtsZ GTPase activity correspond to 3 independent replicates. The GTPase activity was measured as result of the Pi released from GTP consumption. The units are Mol GTP consumed per Mol FtsZ per min.



Supplementary figure 5. FtsZ toroids and bundles formed at different protein ratios. **a** Cryo-EM images of FtsZ bundles and toroids promoted by interaction with ZapD at different protein ratios. From top to bottom, the protein ratios used were 1:1, 1:2, 1:4, 1:6 for FtsZ at 10 μ M and ZapD concentrations ranging from 10 to 60 μ M. Samples were plunge frozen two minutes after the addition of 1 mM GTP. In these samples, similar toroidal structures and bundles were observed regardless protein ratios, including spirals and curved bundles. Scale bars are 250 nm. **b** Distribution of the measured height of toroids from the tomographic volume. The cross-section of the toroids collected by tomography was used to measure the height of each toroid. Distance measurements were made from each toroid in the middle of the bundle at the four cardinal points to assure the reliability of the results. The mean value and SD are shown in the graph. **c** Circularity of FtsZ toroids. The shortest and largest distance of the outer and inner diameter were measured for each toroid from the cryo-EM images. The division between the shortest and longest diameter provided the circularity of the FtsZ toroids. The mean value and SD are shown in the graph. The circularity of the inner and outer diameter is significantly different (T-test $t(4.2)$, p -value <0.001).

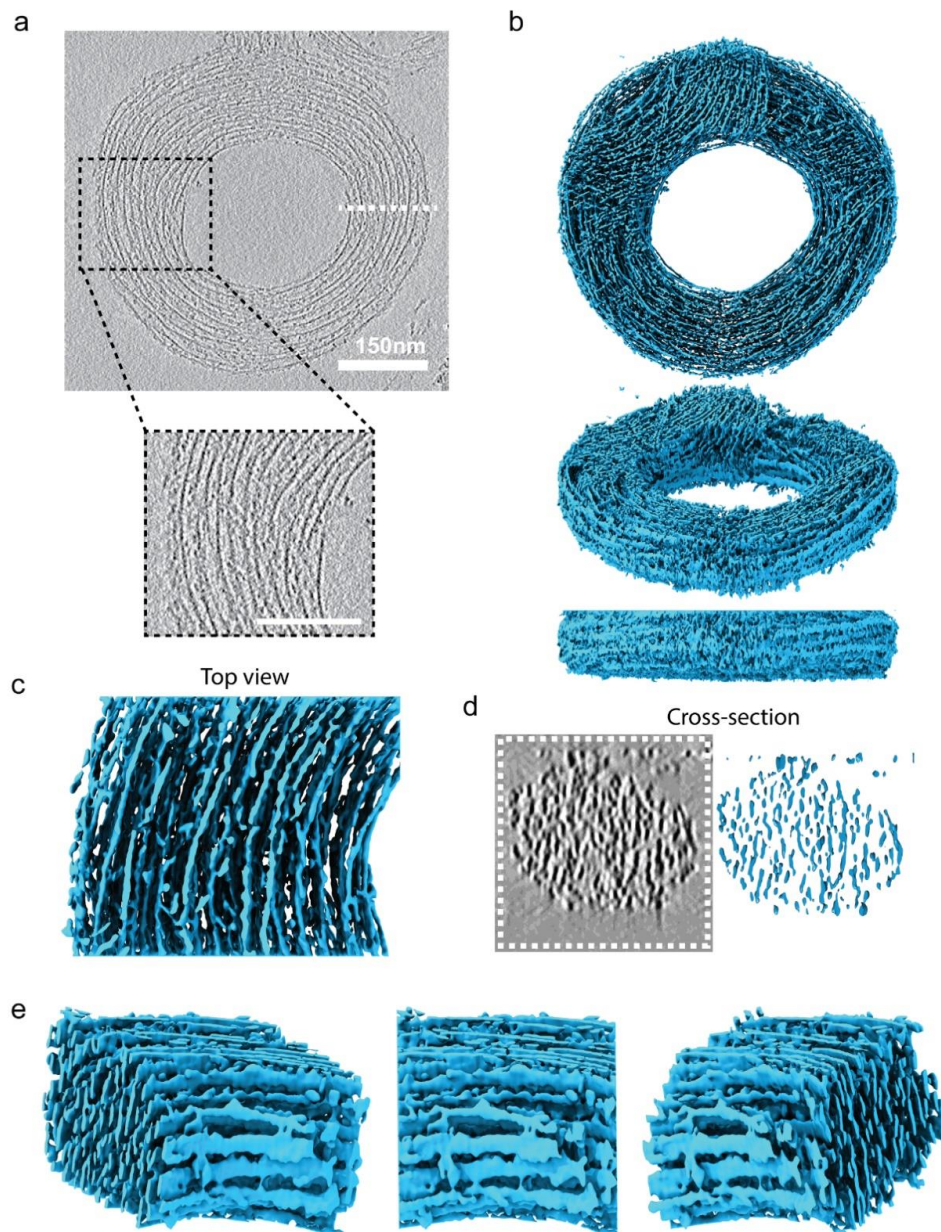


Supplementary figure 6. FtsZ single and double filaments found at different FtsZ and ZapD ratios. Cryo-EM images of single and double filaments found together with toroids and bundles in samples containing FtsZ and ZapD at different protein ratios. FtsZ concentration was 10 μM , while ZapD was present at increasing concentrations (from top to bottom 0, 2.5, 5, 10, 20, 40 and 60 μM), mixed prior addition of 1 mM GTP. In the cryo-EM samples, only single and double filaments were found as shown in samples from 1:0 to 1:1. In these filaments, we could not discard or confirm the presence of ZapD connecting the FtsZ filaments. They were not easily differentiated from double filaments formed in the absence of ZapD consequence of weak FtsZ-FtsZ lateral interactions. For the case of saturation of ZapD (1:4 or 1:6), double FtsZ filaments and straight bundles showing a characteristic striped pattern perpendicularly to the FtsZ filaments were found. Scale bars are 100 nm.

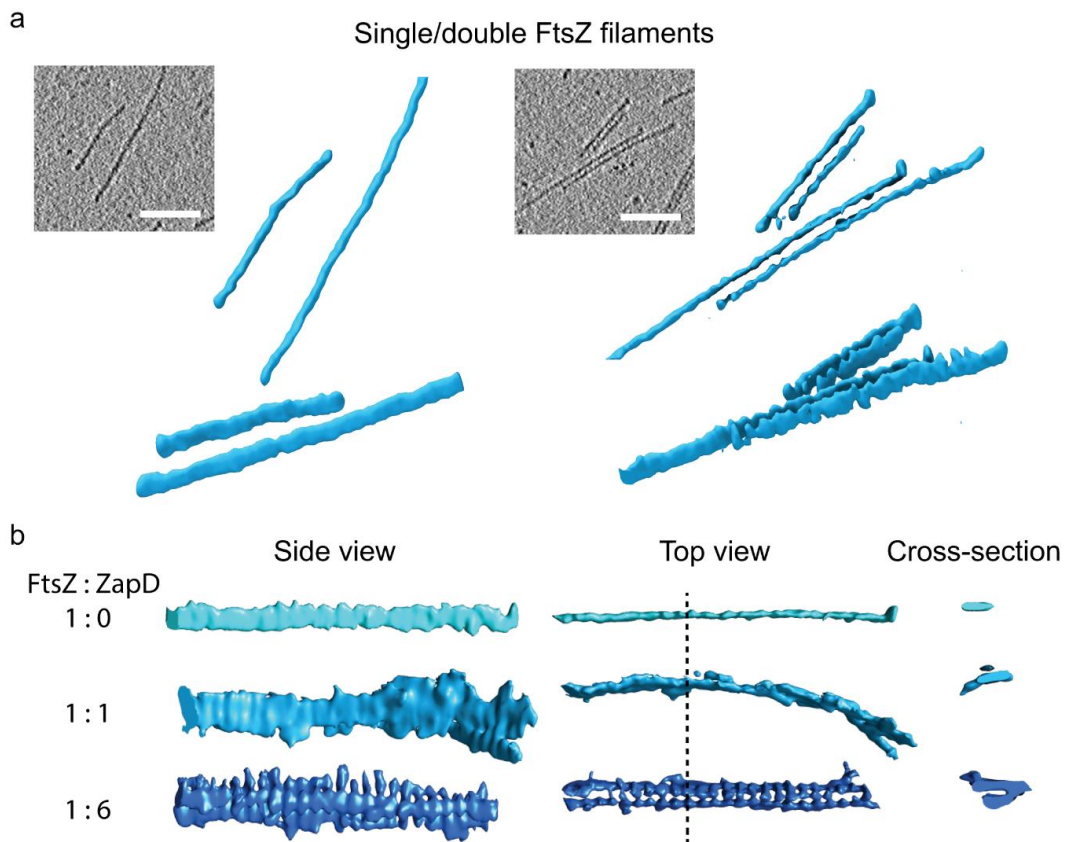


Supplementary figure 7. FtsZ structures found at low and high ZapD concentrations.

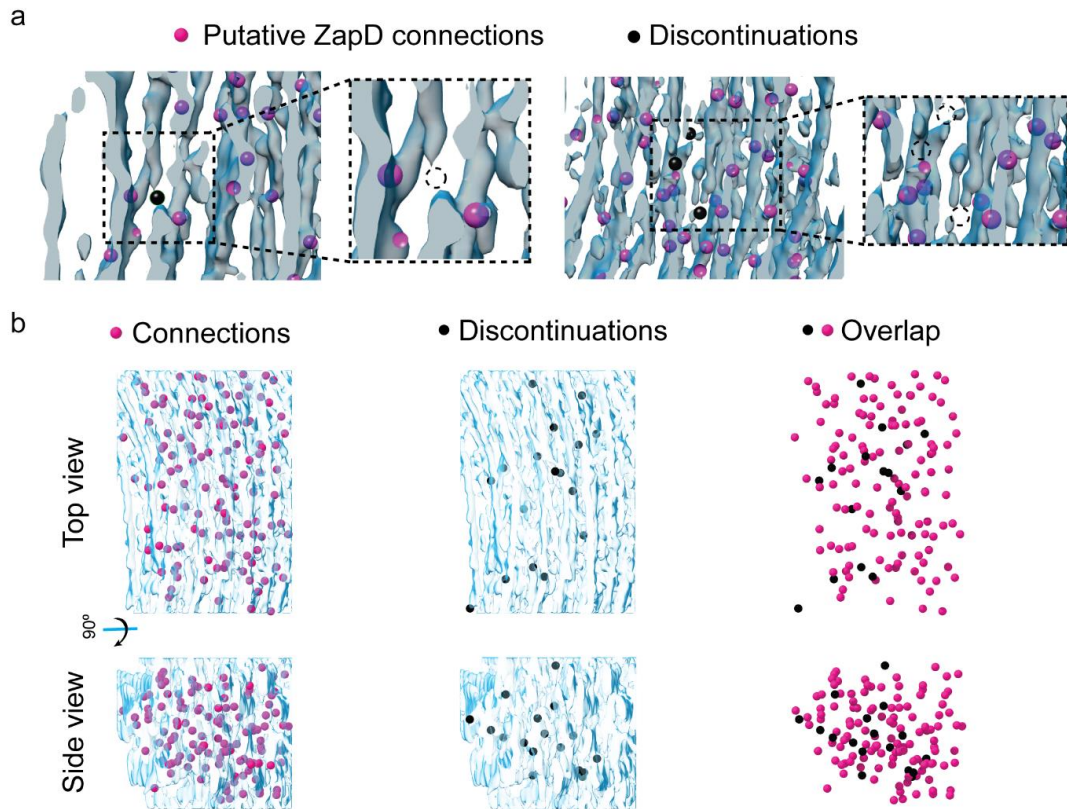
Representative micrographs of FtsZ structures and bundles promoted by ZapD at different protein ratios under working conditions. The images are an average of five slices from the reconstructed tomographic volume to enhance the signal to noise ratio of the image. Scale bars are 250 nm unless they are labelled with 100 nm. **a** Equimolar concentrations of FtsZ and ZapD (10 μ m) formed toroids and bundles after 1 mM GTP addition. Samples were plunge frozen 2 min after triggering polymerization. **b** High concentration of ZapD (60 μ m) promoted the formation of straight FtsZ bundles, although they coexisted with scarce amount of FtsZ toroids and double filaments showing striated patterns.



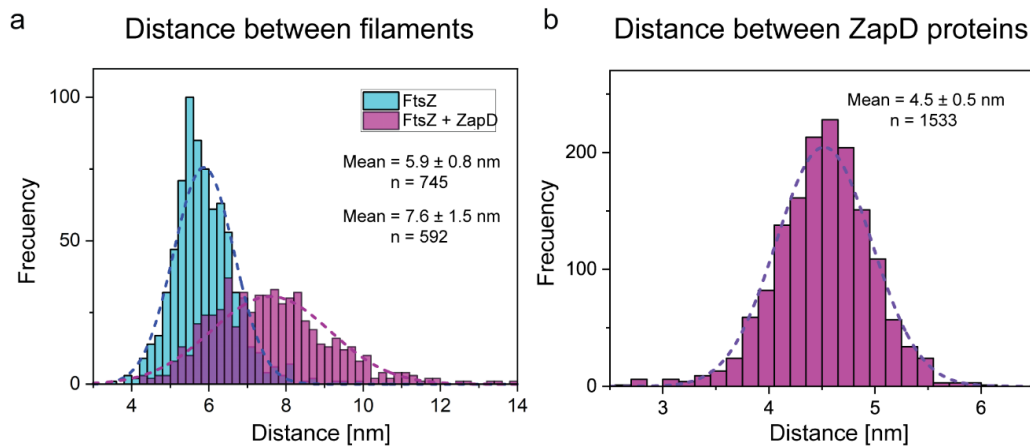
Supplementary Figure 8. Segmentation of a FtsZ toroid by using Cryo-ET. **a** Micrograph of a FtsZ toroidal structure from the reconstructed tomogram. FtsZ and ZapD were at equimolar concentrations (10 μM) mixed prior the addition of 1 mM GTP. The dotted white line represents the localization of the cross-section shown in **(e)**, while the black dotted square shows the area of a close-up view showed below the image. An average of five slices are shown. Scale bar of the zoomed area is 50 nm. **b** Segmentation of the toroid shown in **(a)**. The isosurface of the toroid was extracted from the denoised full tomographic volume and positioned in different views (top) front, (middle) side and (bottom) lateral views. The curved filaments observed at the upper part of the toroid corresponds to a bundle that was located at the top layer of the toroid. It was erased to facilitate the representation of the toroid. **c** Segmentation of the zoomed area shown in **(a)**. Top view of the isosurface from the toroidal structure. **d** Micrograph of the toroid cross-section (left) and its isosurface (right). The cross-section corresponds to the white dotted line shown in **(a)** and the micrograph is the average of five tomographic slices. **e** Different views of the isosurface of the toroidal structure. The represented meshwork of filaments corresponds to the image shown in **(c)** at different views.



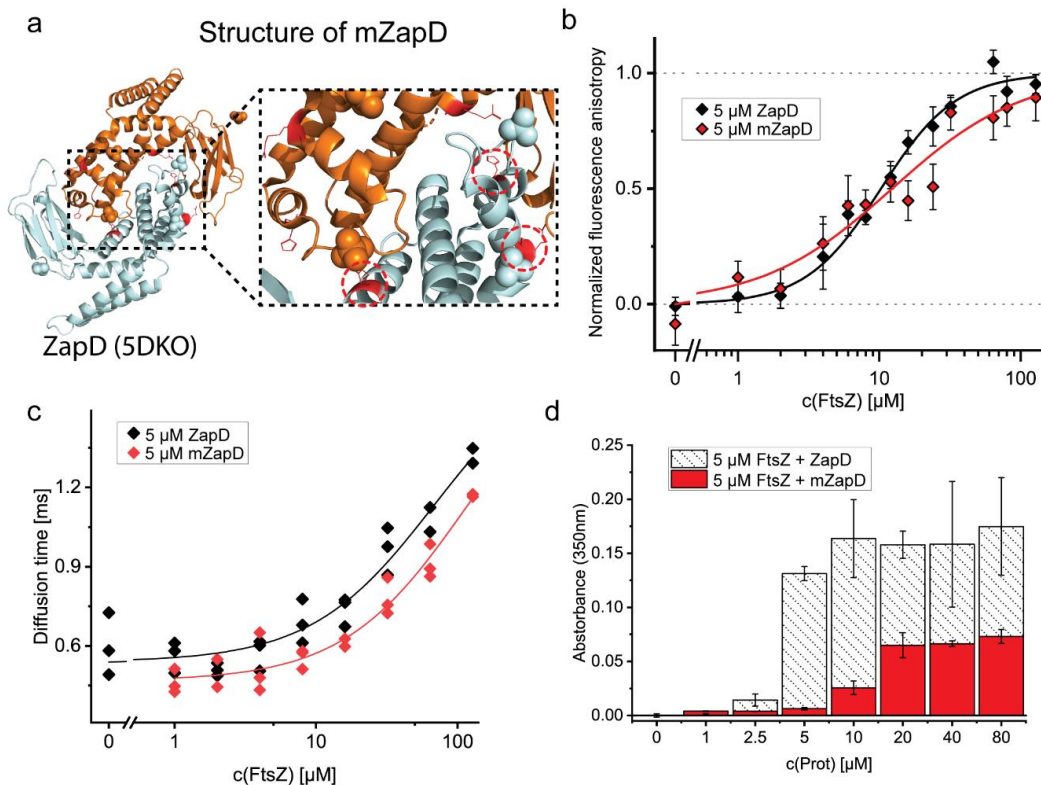
Supplementary figure 9. Segmentation of FtsZ filaments. **a** Isosurface of single and double FtsZ filaments in the absence of ZapD extracted from the denoised tomographic volume. FtsZ filaments from cryo-ET samples (10 μm) in presence of 2 mM GTP. The single and double filaments were extracted from the isosurface from the micrographs shown at the left side of each case. A top and lateral view of the segmented filaments are shown. Scale bars represent 50 nm. **b** Comparison of isolated FtsZ filaments from the following samples: (top) absence of ZapD, (Middle) a toroidal structure at equimolar concentrations of FtsZ and ZapD (10 μm) and (Bottom) a straight bundle at high concentration of ZapD (60 μm). The protein ratios in each case are shown at the left side of each example. Side and top views of the three segmented filaments are shown in left and center columns, while a cross-section of the filaments is shown at the right column. The cross-section corresponds to the dotted line shown at the side top view. Different blue tones differentiate the three analyzed conditions. The presence of extra densities decorating the FtsZ filaments are present in these structures, strongly suggesting that they are ZapD proteins decorating and connecting filaments.



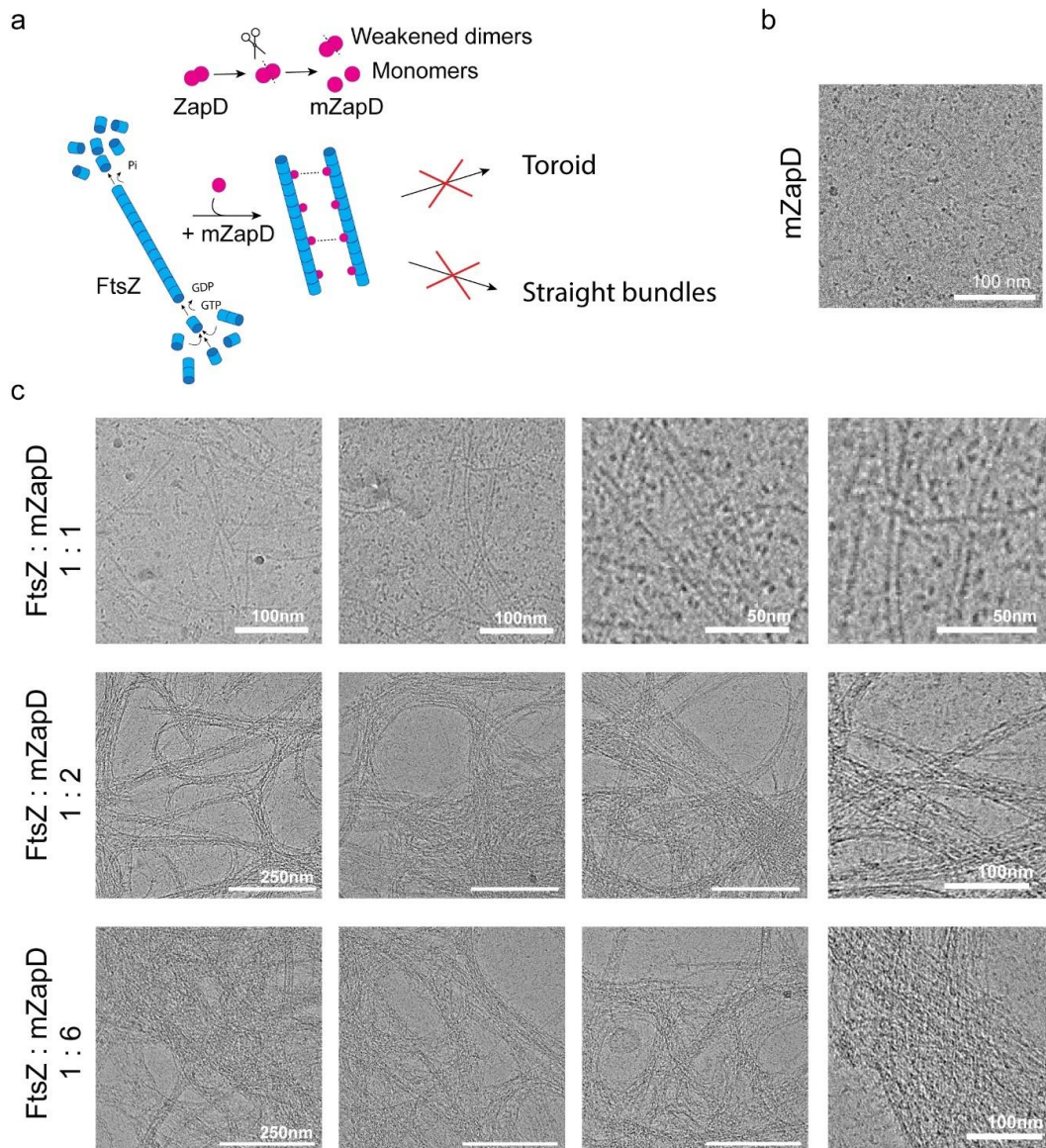
Supplementary figure 10. The FtsZ toroid is formed by a ZapD-linked discontinuous filaments. **a** Image of the isosurface from the meshwork of filaments shown in (Fig. 4a). A black marker (sphere) is positioned in every discontinuation or finalization of FtsZ filaments (blue) within the toroid. Magenta markers were located at every clear connection between FtsZ filaments in order to analyze their presence in areas near discontinuations. A closer view of the image framed by a dotted black line shows the finalization and discontinuation of some FtsZ filaments. The black marker was substituted by a dotted circle to demonstrate the absence of filaments in the area. The images at the left and right side are just different areas of the same mesh of filaments within the toroid. **b** Images on the left and center represent the spatial three-dimensional localization of discontinuations (black) and connections (magenta) of FtsZ filaments in the analyzed area of the toroid shown in (Fig. 4a) (blue filaments). A top and side view of the structure show the localization of the discontinuation and connections. The overlap of the two (right) does not show a significant colocalization or correlation among them.



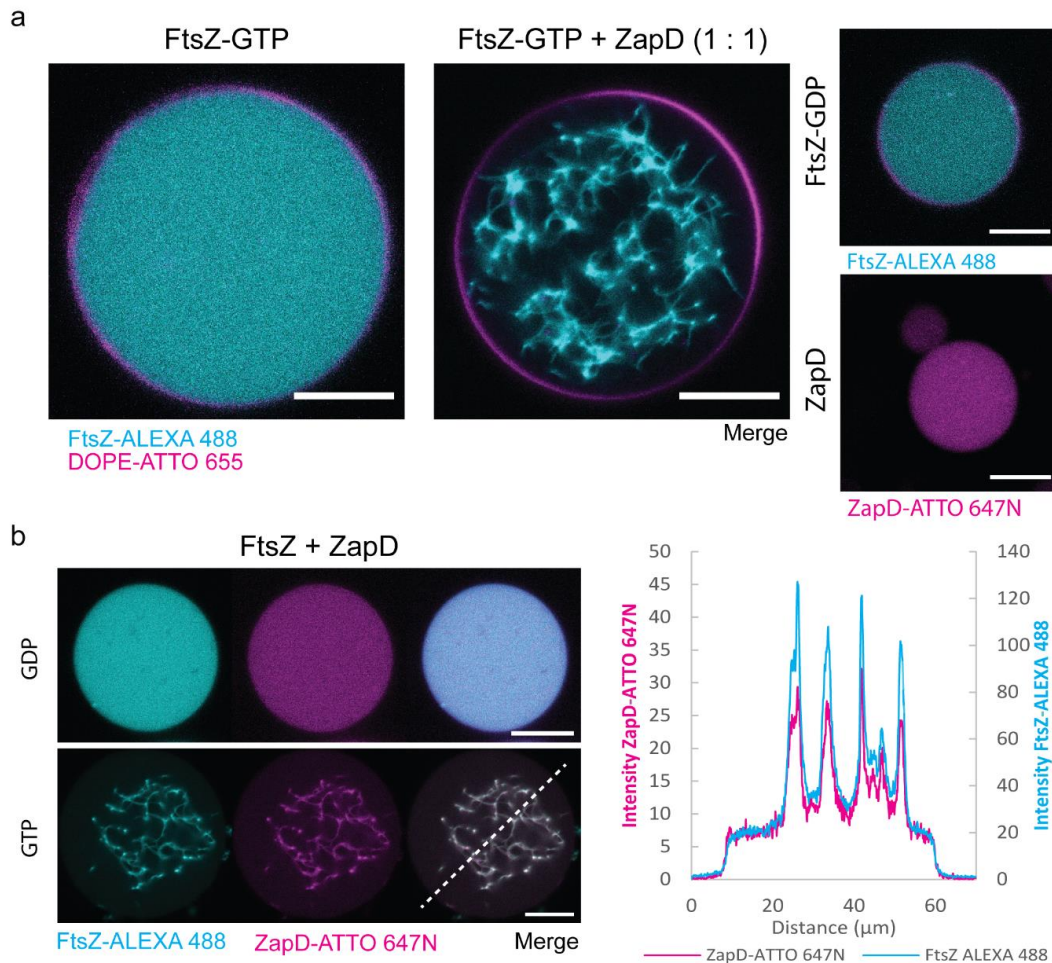
Supplementary figure 11. Distance between FtsZ filaments and ZapD-connected filaments. **a** Distribution of the distance between two FtsZ filaments in the absence (blue) or presence (magenta) of ZapD at high concentration (FtsZ:ZapD 1:6). The distance between filaments were measured from the cryo-EM and cryo-ET images and plotted in the graph as a distribution of distances. Both conditions fitted a normal distribution and images from >3 independent samples were used to measure the distance between filaments. The mean value and SD are shown in the graph for each condition. The data sets were significantly different as determined by a T-test with a $t(25)$, p -value <0.001 . The presence of ZapD crosslinking filaments enhances the distance among them in comparison with weak FtsZ-FtsZ interactions. **b** Distribution of the distance between two ZapD proteins in a straight bundle under saturation of ZapD. The distance between two ZapD proteins was measured from tomographic images obtained in samples containing FtsZ (10 μ M) in the presence of ZapD at high concentration (60 μ M) in presence of GTP. The distribution obtained fitted a normal distribution. The mean value and SD are shown in the graph. The regular distance found between ZapD proteins connecting filaments could indicate the presence of one ZapD dimer per FtsZ monomer forming the filament.



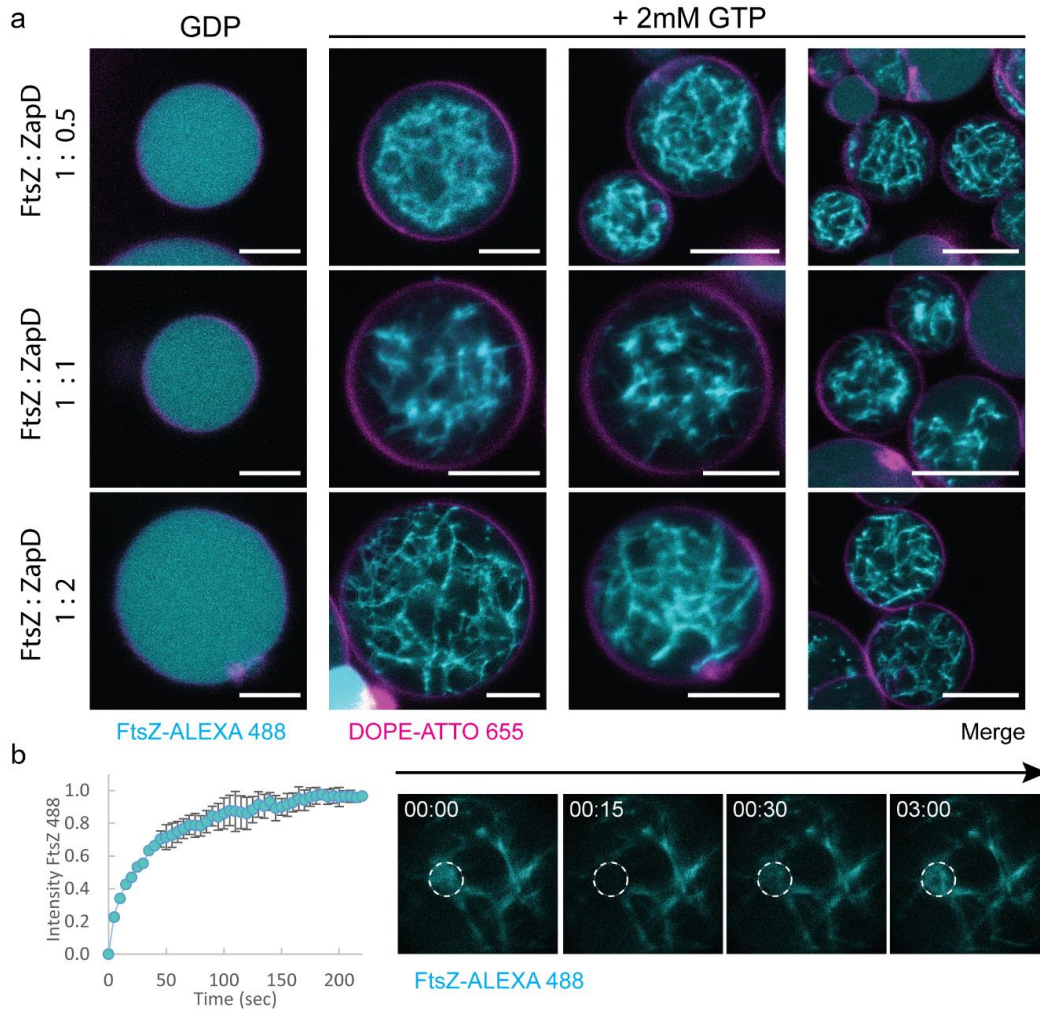
Supplementary figure 12. mZapD binds FtsZ-GDP and can promote bundling of FtsZ filaments. **a** Scheme of the structure of the weakened dimerization ZapD mutant (mZapD). The structure shown corresponds to the ZapD wt dimer (5DKO), highlighting the mutations made in red color. We mutated three amino acids involved in the dimerization of ZapD (R20, R116 and H140) by Alanine substitution, destabilizing and weakening the dimerization of the protein. A closer view of the dimerization site shows the mutations performed in the structure of one of the monomers (red dotted lines). **b** Molecular interaction between FtsZ-GDP and ZapD or ZapD mutant (mZapD) measured by fluorescence anisotropy and compared with the results shown in Supplementary Fig. 2a for ZapD and FtsZ-GDP. 5 μM of mZapD was supplemented with 150 nM of mZapD-ATTO 647N and FtsZ at increasing concentrations. mZapD (red) also binds FtsZ-GDP with an apparent K_d of 12.42 ± 5.45 (SE). The x-axis is represented in log units. The mean value and standard deviation are the result of 3 independent samples. **c** Fluorescence correlation spectroscopy (FCS) analysis of increasing concentrations of FtsZ-GDP with 5 μM of ZapD or mZapD supplemented with 100 nM ZapD or mZapD chemically labelled with ATTO 647N. The plot corresponding to ZapD was the same as shown in Supplementary Fig. 2b and it is included here to facilitate the interpretation of the results. The x-axis is represented in log units. The diffusion curve demonstrated an increasing diffusion time of mZapD along with the FtsZ concentration which supports a direct interaction of this protein with FtsZ-GDP. The plotted line is only to guide the eye. Each condition was measured in three independent samples. **d** Light scattering signal of FtsZ and ZapD by measuring absorbance at 350 nm after 5 min of GTP addition. The concentration used was 5 μM FtsZ at increasing concentrations of ZapD (0 - 80 μM) and 1 mM GTP in working buffer. The data represents the main value and standard deviation of >3 independent samples. The signal showed for ZapD is the same shown in Fig. 1b and it is included here to help the interpretation.



Supplementary figure 13. mZapD can bundle FtsZ without promoting toroids. **a** Proposed schematic of the interaction mechanism of FtsZ-GTP and mZapD protein. The mZapD protein is mutated in the dimerization site to weaken the dimerization and favor the monomerization of the protein. Thus, interaction of dynamic FtsZ filaments with mZapD monomers is weakened and the stabilization of toroidal structures or straight bundles is not possible, while dynamic bundles can still be formed. **b** Cryo-EM image of 10 μ M mZapD. mZapD is homogeneously distributed and it did not aggregate in our working conditions. Scale bar is 100 nm. **c** Representative cryo-EM images of FtsZ and mZapD at increasing concentrations of mZapD and 1 mM GTP under working conditions. At equimolar concentrations of FtsZ and ZapD (10 μ M) we could not find any FtsZ bundle and only single and double FtsZ filaments could be observed (top). At higher concentrations of mZapD (20 and 60 μ M, middle and bottom row, respectively), FtsZ bundles were formed despite no toroids or straight bundles were observed in these samples. The lack of these structures suggested that a stable dimer is required to form them. Scale bars are 250 nm unless 100 nm or 50 nm labels are shown.



Supplementary figure 14. FtsZ and ZapD form bundles inside artificial cell models. a Representative confocal image of co-reconstituted FtsZ and ZapD inside lipid vesicles as artificial cell models. FtsZ was encapsulated at 10 μM and supplemented with 1 μM FtsZ-Alexa 488 (cyan) in working buffer while lipid vesicles formed by POPC:POPG (80: 20) were fluorescently labelled adding DOPE-ATTO 655 (magenta) to allow their visualization. FtsZ in presence of 2 mM GTP was distributed homogeneously in the lumen of the vesicle (left) while co-reconstitution with equimolar concentration of ZapD (10 μM) and 2 mM GTP promoted the assembly of dynamic FtsZ bundles (middle). Formation of bundles was only possible inside lipid vesicles after the supplementation with macromolecular crowders. The assembly of FtsZ bundles crosslinked with ZapD inside lipid vesicles is a major advance towards the *in vitro* reconstitution of the division system, facilitating the study of a more physiologically relevant bundles. On the other hand, FtsZ-GDP was homogeneously distributed in the lumen of the vesicle and no significant differences were observed after polymerization, when FtsZ was encapsulated in the presence of 2 mM GTP (top, right). 10 μM ZapD supplemented with 0.5 μM ZapD-Alexa 647N (magenta) was also encapsulated in lipid vesicles and homogeneously located in the lumen (bottom, right). **B** Co-reconstitution of both proteins at equimolar concentrations (10 μM) in the absence (Top) or presence (bottom) of 2 mM GTP at working conditions. In this case, ZapD promoted the formation of large FtsZ bundles that disassembled over time. As represented in the graph on the right, the fluorescence intensity of a line drawn across the vesicle in the equatorial plane showed the colocalization of ZapD with FtsZ promoting the assembly of bundles by direct interaction and demonstrating the crosslinking of ZapD. Scale bars represent 10 μm



Supplementary figure 15. Formation of bundles at different FtsZ and ZapD ratios inside artificial cells. **A** Representative confocal images of the co-reconstitution of FtsZ and ZapD proteins inside lipid vesicles at different protein ratios (From top to bottom 1:2, 1:1, 2:1 FtsZ:ZapD) in the absence or presence of 2 mM GTP in the left or middle and right, respectively. FtsZ was encapsulated at 10 μ M and supplemented with 1 μ M FtsZ-Alexa 488 (cyan) in working buffer, while unlabeled ZapD was encapsulated at (5, 10, 20 μ M). Lipid vesicles formed mixing POPC:POPG (80: 20) were fluorescently labelled adding DOPE-ATTO 655 (magenta) (0.05%) to allow their visualization. The shape and phenotype of FtsZ bundles inside vesicles were not significantly different among different protein ratios, although the number of vesicles containing FtsZ bundles increased at higher ZapD concentrations. Scale bars are 5 μ m. All confocal images were collected from >3 independent experiments. **C** Fluorescence recovery after photobleaching (FRAP) of the FtsZ bundles inside lipid vesicles. The mean intensity of a circular area drawn in the FtsZ bundles was measured before and after the photobleaching, normalized and plotted in the graph. The mean intensity and standard deviation shown in the graph correspond to 6 independent replicates in different vesicles containing equimolar concentrations (10 μ M) of FtsZ and ZapD in presence of 2 mM GTP. On the left, confocal images of one of the analyzed samples during the bleaching process.

Supplementary Table 1 List of primers.

Name	Sequence (5' to 3')
ZapD-R20A	GAAAAAATGCGTACATGGCTG GCT ATTGAGTTTT
ZapD-R116A	GGCAATTTCTGCGTGAAGAT GCT TTTGATTGCTC
ZapD-H240A	CTTTGATTTACCTACATTG GCT ATTTGGCTGC

Discussion and perspectives

This thesis contributes to the understanding of the molecular dynamics of FtsZ from a bottom-up perspective, providing new insights into its role in cell division and cytokinesis. The findings of the presented papers not only focus on the molecular mechanism of FtsZ from various perspectives but also improves the *in vitro* reconstitution of minimal division components, bringing us closer to a complete bottom-up construction of a synthetic cell.

Briefly, we initially demonstrated a tension-dependent reorganization of FtsZ filaments on the membrane by trapping and deforming GUVs in a microfluidic device (P2). Furthermore, we uncovered the biophysical mechanism behind the generation of membrane constriction by FtsZ filaments, which is a GTP-driven torsional stress, providing important insights into our understanding of FtsZ's role in the cell (P3). Additionally, we examined the spatiotemporal localization of FtsZ and MinCDE by co-reconstituting them inside GUVs using purified proteins and cell-free expression. This led to the assembly of FtsZ-rings positioned in the equatorial plane of spherical GUVs by the MinCDE oscillatory system, and the discovery of a positive feedback between FtsZ and MinCDE in the positioning of the ring and the emergence of oscillatory waves (P4). Lastly, we characterized the interaction of FtsZ and ZapD, revealing the formation of bacterial-sized toroidal structures through filament crosslinking in solution. The characterization of these toroids using cryo-ET provided a novel understanding of the architecture, assembly, and stabilization of the FtsZ-ring. After a brief introduction of the findings, I proceed to revisit all the results presented in this dissertation to discuss them in the context of the original objectives, highlighting the principal conclusions and advances achieved over the course of this PhD study.

Publication P2.

Effects of the geometry of the compartment and membrane tension

In collaboration with Dr. Kristina Ganzinger, we developed a microfluidic device for the mechanical manipulation of giant unilamellar vesicles (P2). This device allows the trapping and reversible deformation of spherical GUVs into a bacterial rod-shape without compromising their free-standing membranes, enabling the analysis of the effect of the compartment geometry, curvature and membrane tension on processes reconstituted in and on vesicle-based minimal cells.

Other platforms to deform free-standing lipidic systems were developed using similar strategies, such as deforming small lipid droplets in microfluidic channels [168], printing BSA structures of various shapes to hold and squeeze GUVs [416], or micropatterning the surface and attaching GUVs [417]. Our microfluidic device is based on a previous design optimized to catch GUVs and facilitate their visualization without further deformation [418, 419]. In our design, we adapted and added extra features such as wider structures and longer funnels to promote the elongation of GUVs. Thus, we achieve controllable and reversible deformation by squeezing or releasing GUVs from the trap, maintaining high capture efficiency at various GUV sizes.

We successfully applied our microfluidics device to deepen our understanding of the behavior and functionality of FtsZ inside cellular models. Reconstituted membrane-bound FtsZ (FtsZ-YFP-mts) formed filaments and aligned along the shortest axis of rod-shaped GUVs, consistent with previous findings on SLBs [284] and their biological role. Additionally, reversible vesicle deformation required deflation of the GUVs, decreasing the membrane tension due to osmotic imbalance and, leading to a reorganization of FtsZ from filaments into cone-like structures on the membrane. These structures were only present on deflated membranes, stabilizing protrusions and promoting subsequent GUV deformations by serving as a membrane reservoir.

These results showed two new and interesting features of FtsZ: (1) its ability to adapt and reorganize into different structures based on the geometry and surface tension of the lipid membrane and (2) its ability to stabilize the excess of the membrane through deformation. We found that high membrane tension hinders the formation of FtsZ cone-like structures, as previously observed on planar surfaces [292, 55, 287] and in P3. Previous studies stated that spatial constraints imposed by planar surfaces impact other properties of FtsZ, affecting its functionality [294, 298]. In contrast, soft membranes offer less mechanical resistance, allowing the formation of cone-like or ring-like structures that can deform the membrane

and stabilize protrusions [158, 159]. Therefore, the use of GUVs as membrane platforms in the study of FtsZ structures avoid restrictions on filament assembly and allow for a wider range of structures to be formed, showing an advantage for the study of the structure, intrinsic curvature, and persistence length of the filaments. The combination of GUVs with other division proteins can uncover previously unseen features of FtsZ-ring assembly and functionality due to the lack of spatial constraints imposed by planar surfaces.

Overall, controllable deformation of GUVs represents a significant advance with respect to microfluidic devices previously created and a step towards bottom-up reconstitution of protein systems, adding an extra layer of complexity. Our microfluidic system allows the stable visualization of spatiotemporal processes inside rod-shape GUVs, making it desirable for reconstituting geometry or curvature-dependent biological systems [420], such as the oscillatory MinCDE, actin, MreB, developmental factors or membrane proteins. This microfluidic platform presents a new approach for testing the functionality of reconstituted cellular systems from a bottom-up perspective using GUVs. Future developments of this device may include a microfluidic-based system to generate GUVs with a tight range of sizes before trapping, making it more useful for studying reconstituted systems. Double emulsion methods to generate GUVs in microfluidic devices can also be coupled to a trapping system, as previously demonstrated [421, 422].

Publication P3.

The mechanism underlying FtsZ's force constriction

Next, and closely related to P2, I collaborated with Dr. Diego Ramirez on a project whose main goal was to address the highly debated role of the FtsZ system in the force generation process during cytokinesis (P3).

It is widely accepted that FtsZ assembles a minimal ring at the midcell, serving as a scaffold for the rest of the division components. However, its exact role in leading the division process or participating in cytokinesis is not yet clear. While several models have been proposed in recent years [232, 405, 298, 395, 233], the experimental characterization of the force exerted by FtsZ is a challenging task due to technical limitations and the large number of components involved in division [423, 185, 186]. FtsZ has been described to exert forces on lipid membranes, as previously shown by the group of Rivas using siZipA-FtsZ [325], and Danelon's group using FtsA-FtsZ [157] inside GUVs. Likewise, by reconstituting the FtsZ-YFP-mts mutant inside or outside of soft GUVs, we also observed the formation of outward or inward conical deformations, respectively. This suggests that drilling forces are acting against the membrane, in line with previous findings in P2 and Osawa et al.[158, 159]. The intrinsic curvature of FtsZ filaments arises from a twist in

their structure [276, 277], and the helical nature of these filaments has previously been demonstrated [284, 333]. On flat surfaces, FtsZ self-assembles into treadmilling vortices with a conserved direction [55, 287]. However, we have shown that in conical surfaces, the treadmilling becomes bidirectional, as confirmed *in vivo* [288, 246]. The geometry of FtsZ and its bidirectional treadmilling behavior can induce forces against deformable membranes and impose torsional stress in tubular geometries. Despite these findings, the relationship between the structure of FtsZ, its treadmilling, and force generation is still not fully understood.

Therefore, to gain a deeper understanding of the mechanics of FtsZ-dependent membrane deformations and constriction, we have developed an *in vitro* system using lipid tubes pulled by optical tweezers from FtsZ-decorated GUVs. Through the use of this experimental platform, we demonstrated that FtsZ can cause helical deformations in lipid tubes, which are further compressed by the protein's GTPase activity and likely through bidirectional treadmilling of the FtsZ filaments. We hypothesize that FtsZ's GTPase activity drives the extra force required to constrict the helix's pitch through torsional stress imposed by the intrinsic structure of the FtsZ filaments, which form ring-like structures. Our results also suggest that membrane tension and the nature of FtsZ's membrane attachment can play a role in the forces exerted. This was evident as super-coiled deformations of the lipid tubes were observed when siZipA was used instead of the FtsZ-YFP-*mts* mutant to bind FtsZ to the membrane. Additionally, the strong dependency of membrane attachment on the velocity of the treadmilling has been noted [329]. Future studies could be conducted using our optical tweezers-based experimental setup to further analyze this phenomenon.

Our *in vitro* setup let us quantify the directional forces exerted by FtsZ, which were found to be within the pN range, strong enough to deform and constrict soft lipid tubes, deflated GUVs, and even wall-less *E. coli* cells. Interestingly, we estimated that FtsZ can generate a force of approximately 1 pN per unit of FtsZ-ring. However, it has been calculated that around 8 pN of force is needed to constrict *E. coli* [424], while more than 15 pN is required to deform erythrocytes [425]. Although the force generated by FtsZ might not be enough for the entire process of bacterial cytokinesis, membrane budding was observed in both deflated GUVs and wall-less *E. coli* cells. The GTP-driven treadmilling of FtsZ inside cells has been found to be essential for correct placement and coordination during the initiation of septal constriction [392, 306] and PG synthesis [288, 246, 398], leading to the formation of abnormal septums in cells containing GTPase defective FtsZ. This suggests that treadmilling could coordinate and drive the process of cytokinesis by also applying force to the membrane. The new lipids synthesized during the division process might reduce the membrane tension, leading to an excess of the membrane at mid-cell [405, 217]. This may lower the force required to deform the membrane, allowing FtsZ to generate constriction and deform the membrane. This hypothesis is in line with the

reversible tension-dependent reorganization of FtsZ on the membrane described in P2, which could also trigger further events during the division process, including coordination with the late components of division, force generation, and ultimately cytokinesis.

Several mechanisms of membrane constriction have been hypothesized which can be grouped into three categories [232, 233]. These are (i) the FtsZ condensation model, with FtsZ-ring as the main force generator [411, 306], (ii) the bending model, in which FtsZ only constricts to trigger PG synthesis [424, 389], and (iii) the concerted constriction model, in which both machineries work together, with FtsZ pulling and the PG machinery pushing the membrane [408, 410]. Although a consensus has not yet been reached, all of these models involve some force exerted by FtsZ, either as the main force generator, trigger or driver of the process [236, 395, 426]. However, the large number of essential components involved in division and the low range of forces exerted by FtsZ make it difficult to isolate the role of FtsZ and understand its mechanism of function *in vivo*. Thus, our study helps to reveal the role of FtsZ, where the torsional stress driven by GTPase activity is compatible with the proposed mechanisms of force constriction, expanding the knowledge of the system. Future investigations could focus on the precise coordination of the FtsZ-ring, treadmilling of filaments, and PG synthesis machinery, revealing the forces involved in the process and the mechanism of function of participating proteins.

Publication P4.

First steps for the *in vitro* reconstitution of a minimal division system

Building upon the observations published in P2 and P3 that showed FtsZ's ability to deform free-standing membranes and exhibit reversible filament reorganization, we decided to study FtsZ's interaction with other division partners in cell-like environments. To this end, I collaborated with Dr. Shunshi Kohyama to develop a minimal division machinery using a bottom-up approach. We succeeded in coordinating MinCDE and FtsA-FtsZ proteins within cell-like systems, resulting in a minimal division machinery capable of self-assembling in the equatorial plane and constricting GUVs (P4).

The reconstitution of a macromolecular machinery *in vitro* is a complex challenge that requires precise control over all factors involved in order to optimize their performance and fulfil their function. Regarding the division of a synthetic cell, it involves the spatiotemporal localization of a division machinery that ultimately leads to the constriction and fission of the reaction compartment. In our study (P4), we successfully self-assembled a minimal bacterial division ring inside GUVs through two approaches: (1) using purified components,

combining a FtsZ-*mts* variant and the MinCDE system, and (2) expressing the full FtsA-FtsZ and MinCDE proteins using the PURE cell-free expression system. This led to the formation of FtsZ-ring structures in the equatorial plane of the spherical GUVs, guided by MinCDE pole-to-pole wave oscillations, and partially constricted the lipid container, resembling the physiological function of the division machinery.

Previous studies have succeeded in independently encapsulating the MinDE system inside GUVs using either purified proteins [364] or a cell-free expression system [151, 152], resulting in the emergence of oscillatory waves. For the FtsZ protein, the FtsZ-YFP-*mts* mutant [291] or FtsZ-ZipA [325] was reconstituted inside GUVs using purified proteins, causing the GUVs to deform. On the other hand, the expression of FtsA, ZipA, and FtsZ inside GUVs [150] or expression of FtsA with added purified FtsZ [157] led to the formation of filaments and membrane necks. However, coordination between the Min and FtsZ systems has only been possible in open membrane platforms, with FtsZ displacement caused by Min oscillations [151, 302, 303, 367]. In our study, we achieved the co-reconstitution of both systems inside cell-like compartments, using GUVs (P4). Additionally, the use of purified proteins and the cell-free expression system enabled the assembly of the FtsZ-ring inside GUVs from complementary perspectives.

Concretely, the reconstitution of purified protein systems offers higher control over each component, allowing for deeper characterization and optimization of critical factors in their functionality [33, 34]. Our use of purified components revealed new insights into the functional relationship between FtsZ and Min proteins in the assembly of the FtsZ-ring. For example, buffer conditions are critical to the functionality of FtsZ and MinCDE systems inside GUVs [335, 427], as well as protein concentrations and ratios that characterize MinCDE self-organization and wave-mode [362, 428], and the impact of macromolecular crowding [156, 76, 366, 302, 429, 430].

The addition of macromolecular crowders to mimic cellular environments *in vitro* is a growing trend in bottom-up reconstitution research. Volume exclusion effects enhance FtsZ self-association into large bundles of polymers, as previously analyzed in solution and planar membranes [76, 302, 429, 431, 432]. Macromolecular crowders such as ficoll or dextran have been used to facilitate the visualization of FtsZ assemblies by confocal microscopy, resulting in a bundling effect. Using GUVs, we found the minimum amount of crowders required to promote the assembly of bundles on the membrane, in agreement with previous studies [325, 432]. In the case of MinCDE, the presence of macromolecular crowders slows down the velocity and reduces the wavelength of oscillatory waves, limiting the exchange of Min proteins from the membrane to the solution [302, 430]. Experiments using lipid droplets also demonstrated enhanced wave emergence with BSA crowding [366]. In GUVs, macromolecular crowding did not have a clear impact on wave emergence in the

absence of FtsZ. However, high concentrations of crowders can affect membrane properties [75], reducing vesicle yield and cell-free expression of proteins [433]. Therefore crowding conditions must be optimized for each specific system.

Importantly, crowding might increase the protein localization to the interface between solution and membrane [61, 434]. This phenomenon is seen demonstrated in our experiments using GUVs, where a higher fraction of proteins bind to the membrane, improving its role as a nucleator and likely increasing protein-protein interactions. For example, crowding enhances the displacement of FtsZ by Min waves [302] in agreement with our results. Conversely, in the absence of crowders, no macrostructures of FtsZ can be observed on the membrane, and thus no ring formation can occur. Therefore, macromolecular crowding is a crucial factor for the assembly of a minimal division machinery in our experimental conditions, as bundle formation is necessary to form the ring.

Another key finding from the P4 study is the positive feedback between the MinCDE system and the FtsZ-ring structure. Our research showed that the FtsZ-ring is assembled and positioned in the equatorial plane of the GUV through pole-to-pole oscillatory waves, which are further stabilized by the presence of the ring, leading to mutual enhancement. This mechanism has potential biological implications, providing insight into the tight spatiotemporal control of FtsZ-ring assembly and positioning *in vivo*. This phenomenon is likely related to the geometrical effects reported in previous studies on both the FtsZ and MinCDE systems [284, 430, 340, 367]. Our findings in P2 showed the alignment of FtsZ to the shortest axis of the reaction container, while Min proteins can sense the geometry of the accessible membrane area and reorganize wave patterns aligning to the longer axis [340, 435]. Thus, the presence of large FtsZ bundles and partial constriction of GUVs at the equatorial plane can stabilize the pole-to-pole oscillations, defining certain polarity.

On the other hand, our findings confirmed that MinC is not essential for the positioning of the FtsZ-rings, although its presence enhances the displacement of FtsZ and the formation of rings. This is related to the recently found function of Min proteins, which defines the indirect directional displacement of membrane-bound molecules through a friction-driven mechanism called diffusiophoresis [303, 341]. This behavior stems from the Min reaction-diffusion mechanism and the cooperative attachment-detachment of MinD on the membrane [345, 344]. This was demonstrated on supported lipid bilayers (SLBs), as MinDE-mediated displacement of FtsZ was confirmed, but was improved by the presence of MinC [368, 303]. Our observations further characterize this molecular mechanism by showing that Min wave dynamics can be impacted by the presence of molecules as physical barriers on the membrane. In this case, thick FtsZ bundles can be pushed by Min waves at the time-averaged minima in the equatorial plane. At the same time, the bundles themselves occupy space on the membrane, dividing the membrane surface of GUVs into two distinct

regions and limiting the available area for Min proteins. Given this "separator" effect, Min waves may not be able to access the necessary consecutive membrane area to form other wave modes, such as travelling waves, leading to a preference for pole-to-pole oscillatory waves. This can enhance the positioning of FtsZ at the equatorial plane of the GUV, creating positive feedback that stabilizes both. Although these results are only the first demonstration of this phenomenon, further experiments and theoretical studies are needed to fully understand the positive feedback mechanism.

Furthermore, by utilizing a PURE cell-free expression system within GUVs, we were able to express and coordinate five functional proteins (MinCDE, FtsA, and FtsZ) which self-organized into a minimal division ring. The reconstitution of the MinCDE and FtsA-FtsZ "de novo" synthesized proteins is a significant advancement in the *in vitro* reconstitution of a minimal division machinery in cell-like systems. Cell-free expression systems help to overcome the limitations of purified systems, which often struggle with purifying components such as membrane proteins or enzymes. The PURE cell-free expression, on the other hand, provides the advantage of constructing complex biological systems within synthetic cells through the expression of proteins "in situ", enabling for reconstitution of a "life-like" synthetic cell [142, 144]. However, this strategy entails a higher degree of complexity and technical challenges, making it difficult to adjust parameters and optimize conditions such as salt, pH, lipid composition, macromolecular crowding, and protein concentrations [433, 144]. Despite these challenges, our demonstration shows that it is possible to reconstitute complex machinery *in vitro* using cell-free expression systems, providing exciting new opportunities for future research.

Interestingly, the results in P4 indicate that FtsZ-rings can generate constriction in the equatorial plane of GUVs. Notably, only FtsZ-rings formed through cell-free expression were able to generate enough force to deform GUVs at isosmotic conditions, while no deformations were observed in the purified protein system using the FtsZ-*mts* variant. A higher protein density of FtsA-FtsZ molecules attached to the membrane in the cell-free expression system, compared to the fixed concentration in the purified components could generate higher forces on the membrane. Moreover, differential attachment of FtsZ through FtsA, rather than direct binding of the FtsZ-*mts* variant, may also explain the deformations observed inside GUVs. The PURE cell-free system also requires a specific buffer and additional components that could have an effect on FtsZ's behavior. A good example of this is the high concentration of Mg^{2+} present in the PURE buffer, which is known to have an effect on FtsZ dynamics, as well as other charged molecules [281, 429, 431]. These differences highlight the role of external factors, either by direct interaction (protein-protein or membrane-protein) or indirect (buffer conditions) on the molecular dynamics of FtsZ on the membrane. In future experiments, the implementation of other division components or a decrease in surface tension, such as through SUV fusion and osmotic unbalance (P2),

might significantly enhance constriction and even lead to fission and full division of the compartment.

Publication P5.

Stabilization and crosslinking of FtsZ filaments

Finally, we studied the stabilization process of the FtsZ-ring and crosslinking of filaments to try to further describe the molecular mechanism behind the process and to progress in the understanding of FtsZ-ring assembly and structure. Our focus was on the interaction between FtsZ and ZapD, a stabilizer of the FtsZ-ring within cells. Our findings showed that ZapD can crosslink FtsZ filaments into regular toroidal structures in solution, which aligns with some of the features of the FtsZ-ring observed in bacteria.

The stabilization and condensation of the FtsZ-ring are crucial for correct cellular division [387, 268, 194]. This process is thought to be carried out by the crosslinking of filaments through the Zap proteins, however, the molecular details of this interaction and the structure of the ring are not yet well understood. By investigating the interaction between ZapD and FtsZ in solution, we gained insight into the organization of the FtsZ-ring and the process of filament crosslinking.

It has been previously stated that ZapD crosslinks FtsZ filaments through a transient and reversible interaction at the central hub of FtsZ [257, 380, 381]. By employing biochemical studies, we characterized the crosslinking of filaments and defined the crucial role of ZapD dimerization, supporting their current model of interaction [381]. Interestingly, ZapD promotes the stabilization of short FtsZ filaments into a toroidal structure (around 500 nm in diameter) which is in the range of a bacterial cell. Characterization of these 3D structures using cryo-EM and cryo-ET revealed that they are assembled into a multilayered array of discontinuous short filaments stabilized by crosslinking. These structures are similar to some models of the FtsZ-ring *in vivo* [397, 391, 186], suggesting that FtsZ has an intrinsic preference to form toroidal structures, even in solution and outside of cellular environments. Therefore, studying the toroidal structure can provide new information about the assembly and functional stability of the FtsZ-ring during division.

Indeed, the role of crosslinking proteins in the functionality of the FtsZ-ring is one of the biggest questions that remains unanswered. Although FtsZ filaments can self-assemble into bundles by electrostatic lateral interaction between filaments *in vitro*, the presence of these bundles *in vivo* and their biological function are uncertain [387]. The mechanistic implications of a FtsZ macrostructure crosslinked by protein factors compared to a bundle assembled by FtsZ lateral interactions are still unclear. It is thought that the space gener-

ated by crosslinkers plays an important role in the functionality of the FtsZ-ring, although the central hub of FtsZ can also function as a spacer [263, 268, 285]. Zap proteins may maintain a regular organization of the filaments, as observed *in vivo* [389, 333], likely by allowing them to slide and distribute the effects of FtsZ uniformly around the cell by treadmilling in both directions [288, 246], even exerting forces by torsion (P3). Additionally, Zap proteins can control the flexibility of filaments and their local density on the membrane, which can affect the behavior of FtsZ, as seen on SLBs [436].

Our study of the toroidal structures showed that ZapD can align the FtsZ filaments and generate space between them in an organized manner, while also controlling the structure of the FtsZ assemblies. The saturation of ZapD crosslinkers increases the connections between filaments, stiffening the structures from dynamic curved bundles and toroids into rigid straight bundles. This demonstrates that ZapD can modulate the structure of FtsZ via the crosslinking of filaments, which can also affect the behavior of FtsZ. This structural modulation suggests a functional implication of Zap proteins not only as stabilizers of the ring but also as modulators of the FtsZ-ring's behavior.

Additionally, the toroidal structure promoted by ZapD is compatible with an antiparallel distribution of filaments. In P3, we showed that FtsZ filaments can treadmill in both directions on cone-like surfaces or tubular membranes, replicating their natural behavior. However, stabilization by protein crosslinkers can potentially increase torsional stress and thus the force exerted on the membrane. This stabilization can also help in the aligning of FtsZ on the membrane, resulting in an antiparallel arrangement of short filaments connected laterally by Zap proteins, affecting their flexibility and local density [301, 436, 157]. This antiparallel filament arrangement has been considered a mechanism of force generation [387, 405, 395, 233]. The toroidal internal architecture supports this idea, although our observations are limited to assemblies in solution. The effects of filament crosslinking on FtsZ molecular dynamics and force generation are still unclear, and further research is needed to clarify the molecular details. Nevertheless, our results provide valuable insights into the FtsZ-structure and filament stabilization by crosslinking.

Last perspectives and conclusions.

To conclude, it is noteworthy to compare the different FtsZ structures assembled in each of the experiments presented in this dissertation, as they have significant implications then again diverse conditions and circumstances. The FtsZ-rings assembled on the membrane in P2 and P3, or the toroidal structures in solution shown in P5, could be considered more representative of a physiological state as they match the size of bacteria. However, the minimal division ring assembled inside GUVs in P4 is around ten times larger, which is more interesting from a synthetic biology viewpoint, as it allows a better visualization by fluorescent microscopy. The assembly of these larger FtsZ-rings made of FtsZ bundles was found to increase the force exerted on the membrane, leading to GUV constriction, while bacterial-sized vortices only created conical protrusions and deformed lipid tubes, generating forces in the pN range (P3). The mechanistic and structural differences between bacterial-sized or larger FtsZ-rings are still not clear, but they suggest that lateral associations of FtsZ filaments into bundles can result in higher forces on the membrane. These forces can be further increased by lateral associations mediated by protein crosslinking, although these effects are yet to be studied. Thus, the assembly of toroidal structures promoted by ZapD (P5), and their reconstitution on membranes could demonstrate the role of filament stabilization in the generation of forces. Differences among the molecular mechanisms behind the force generation from individual filaments (P2 and P3), FtsZ bundles (P4), or crosslinked filaments (P5) are not well understood, and their study represents an exciting opportunity to reveal the biological implications of filament stabilization and the basis of force constriction.

For this reason, and arising from the high plasticity and adaptability of FtsZ to different environments, it is interesting to study the various FtsZ structures in similar 3D platforms. This thesis presents evidence that FtsZ can reorganize in response to the biophysical properties of the membrane, from FtsZ vortices or FtsZ rings made of single filaments (as described in P2 and P3) and on flat surfaces to the assembly of larger ring structures made of bundles in crowded conditions (as shown in P4) or toroidal structures in solution induced by crosslinking (as seen in P5). Different attachments to the membrane (either independently using FtsZ-YFP-*mts*, or through FtsA or ZipA), along with the addition of division components like crosslinkers (ZapD) or crowding agents, adds an extra degree of complexity to the system with great potential to alter FtsZ's dynamics. As previously shown, ZipA-bound FtsZ can likely exert higher forces in pulled tubes than FtsZ-*mts* (P3) and FtsZ bundles attached through FtsA could also deform the vesicles in (P4). Characterizing the assembly and force exerted by these different structures, in conjunction with Zap proteins such as ZapD (P5), could aid in advancing our understanding of the intrinsic plasticity of FtsZ and its role inside the cell and the mechanisms for membrane constric-

tion. Our studies have only just begun to shed light on the assembly and constriction forces of FtsZ, not only in cells but also in synthetic systems.

Several valuable insights can be extracted from the combined work in regards to the bottom-up reconstitution of a functional FtsZ-based cell division machinery. Largely, it seems clear that FtsZ-based systems offer a wide range of options to undergo localized constriction of the GUV, although the use of other division components or external agents is required to efficiently drive the division of artificial cells. The findings advocate towards elegant strategies to engineer the ring by combining FtsZ with various membrane attachment factors and crosslinkers (such as ZapD or other Zap proteins) to potentially exert stronger force on the membrane and constrict the GUV. Adding MinCDE proteins and other cellular-mimicking components, such as nucleoid mimics, crowders, and LLPS systems can enhance the spatiotemporal localization of the contractile ring. The use of microfluidic approaches to deform GUVs into bacterial rod-shape can also improve the alignment of the FtsZ ring and oscillatory waves, as well as the use of differential lipid composition or vesicle types [105] to lower the membrane tension and facilitate deformation of the compartment. All these promising new avenues should be considered in the road map towards the creation of controllable minimal division machinery, bringing us closer to the goal of constructing a minimal synthetic cell. A monumental step that will unleash numerous capabilities offers new opportunities for designing biosynthesis pathways, drug delivery, smart sensing-reporting systems, tissue formation, and even symbiotic relationships with living cells.

Bibliography

- [1] S. A. Benner and A. M. Sismour, “Synthetic biology,” *Nature Reviews Genetics* 2005 6:7, vol. 6, pp. 533–543, jul 2005.
- [2] S. Hirschi, T. R. Ward, W. P. Meier, D. J. Müller, and D. Fotiadis, “Synthetic Biology: Bottom-Up Assembly of Molecular Systems,” *Chemical Reviews*, sep 2022.
- [3] F. Meng and T. Ellis, “The second decade of synthetic biology: 2010–2020,” *Nature Communications* 2020 11:1, vol. 11, pp. 1–4, oct 2020.
- [4] K. A. Ganzinger, C. Bonfio, and A. P. Liu, “Editorial: From reconstituting minimal cell-cell signaling systems to bioinspired synthetic communication networks,” *Frontiers in Molecular Biosciences*, vol. 9, p. 823, aug 2022.
- [5] W. Jiang, Z. Wu, Z. Gao, M. Wan, M. Zhou, C. Mao, and J. Shen, “Artificial Cells: Past, Present and Future,” *ACS Nano*, vol. 16, pp. 15705–15733, oct 2022.
- [6] S. Ausländer, D. Ausländer, and M. Fussenegger, “Synthetic Biology—The Synthesis of Biology,” *Angewandte Chemie International Edition*, vol. 56, pp. 6396–6419, jun 2017.
- [7] C. Ho and L. Morsut, “Novel synthetic biology approaches for developmental systems,” *Stem cell reports*, vol. 16, pp. 1051–1064, may 2021.
- [8] H. Jia and P. Schwillle, “Bottom-up synthetic biology: reconstitution in space and time,” *Current Opinion in Biotechnology*, vol. 60, pp. 179–187, dec 2019.
- [9] J. Santos-Moreno and Y. Schaerli, “Using Synthetic Biology to Engineer Spatial Patterns,” *Advanced biosystems*, vol. 3, apr 2019.
- [10] P. Supramaniam, O. Ces, and A. Salehi-Reyhani, “Microfluidics for Artificial Life: Techniques for Bottom-Up Synthetic Biology,” *Micromachines*, vol. 10, may 2019.
- [11] C. Xu, S. Hu, and X. Chen, “Artificial cells: from basic science to applications,” *Materials Today*, vol. 19, pp. 516–532, nov 2016.
- [12] H. Chi, X. Wang, Y. Shao, Y. Qin, Z. Deng, L. Wang, and S. Chen, “Engineering and modification of microbial chassis for systems and synthetic biology,” *Synthetic and Systems Biotechnology*, vol. 4, pp. 25–33, mar 2019.
- [13] J. N. Leonard, B. R. Fritz, L. E. Timmerman, N. M. Daringer, and M. C. Jewett, “Biology by design: from top to bottom and back,” *Journal of biomedicine biotechnology*, vol. 2010, 2010.

- [14] J. A. Doudna and E. Charpentier, “The new frontier of genome engineering with CRISPR-Cas9,” *Science*, vol. 346, nov 2014.
- [15] S. H. Jeong, H. J. Lee, and S. J. Lee, “Recent Advances in CRISPR-Cas Technologies for Synthetic Biology,” *Journal of microbiology (Seoul, Korea)*, feb 2023.
- [16] R. Kelwick, J. T. MacDonald, A. J. Webb, and P. Freemont, “Developments in the tools and methodologies of synthetic biology,” *Frontiers in Bioengineering and Biotechnology*, vol. 2, no. NOV, 2014.
- [17] D. G. Gibson, G. A. Benders, C. Andrews-Pfannkoch, E. A. Denisova, H. Baden-Tillson, J. Zaveri, T. B. Stockwell, A. Brownley, D. W. Thomas, M. A. Algire, C. Merryman, L. Young, V. N. Noskov, J. I. Glass, J. C. Venter, C. A. Hutchison, and H. O. Smith, “Complete chemical synthesis, assembly, and cloning of a *Mycoplasma genitalium* genome,” *Science*, vol. 319, pp. 1215–1220, feb 2008.
- [18] D. G. Gibson, J. I. Glass, C. Lartigue, V. N. Noskov, R. Y. Chuang, M. A. Algire, G. A. Benders, M. G. Montague, L. Ma, M. M. Moodie, C. Merryman, S. Vashee, R. Krishnakumar, N. Assad-Garcia, C. Andrews-Pfannkoch, E. A. Denisova, L. Young, Z. N. Qi, T. H. Segall-Shapiro, C. H. Calvey, P. P. Parmar, C. A. Hutchison, H. O. Smith, and J. C. Venter, “Creation of a bacterial cell controlled by a chemically synthesized genome,” *Science*, vol. 329, pp. 52–56, jul 2010.
- [19] C. Lartigue, J. I. Glass, N. Alperovich, R. Pieper, P. P. Parmar, C. A. Hutchison, H. O. Smith, and J. C. Venter, “Genome transplantation in bacteria: Changing one species to another,” *Science*, vol. 317, pp. 632–638, aug 2007.
- [20] M. Breuer, T. M. Earnest, C. Merryman, K. S. Wise, L. Sun, M. R. Lynott, C. A. Hutchison, H. O. Smith, J. D. Lapek, D. J. Gonzalez, V. de Crécy-Lagard, D. Haas, A. D. Hanson, P. Labhsetwar, J. I. Glass, Z. Luthey-Schulten, V. rie de Cré cy Lagard, D. Haas, A. D. Hanson, P. Labhsetwar, J. I. Glass, and Z. Luthey-Schulten, “Essential metabolism for a minimal cell,” *eLife*, vol. 8, pp. 1–75, 2019.
- [21] C. A. Hutchison, R. Y. Chuang, V. N. Noskov, N. Assad-Garcia, T. J. Deerinck, M. H. Ellisman, J. Gill, K. Kannan, B. J. Karas, L. Ma, J. F. Pelletier, Z. Q. Qi, R. A. Richter, E. A. Strychalski, L. Sun, Y. Suzuki, B. Tsvetanova, K. S. Wise, H. O. Smith, J. I. Glass, C. Merryman, D. G. Gibson, and J. C. Venter, “Design and synthesis of a minimal bacterial genome,” *Science*, vol. 351, mar 2016.
- [22] J. F. Pelletier, J. I. Glass, and E. A. Strychalski, “Cellular mechanics during division of a genomically minimal cell,” *Trends in Cell Biology*, vol. 32, pp. 900–907, nov 2022.
- [23] G. Wu, Q. Yan, J. A. Jones, Y. J. Tang, S. S. Fong, and M. A. Koffas, “Metabolic Burden: Cornerstones in Synthetic Biology and Metabolic Engineering Applications,” *Trends in Biotechnology*, vol. 34, pp. 652–664, aug 2016.
- [24] N. Gurdo, D. C. Volke, D. McCloskey, and P. I. Nikel, “Automating the design-build-test-learn cycle towards next-generation bacterial cell factories,” *New Biotechnology*,

feb 2023.

- [25] K. A. Ganzinger and P. Schwille, “More from less – Bottom-up reconstitution of cell biology,” *Journal of Cell Science*, vol. 132, feb 2019.
- [26] D. M. Miller, J. M. Gulbis, P. Stano, and F. Mavelli, “Engineering protocells: prospects for self-assembly and nanoscale production-lines,” *mdpi.com*, vol. 5, pp. 1019–1053, mar 2015.
- [27] C. Guindani, L. C. da Silva, S. Cao, T. Ivanov, and K. Landfester, “Synthetic Cells: From Simple Bio-Inspired Modules to Sophisticated Integrated Systems,” *Angewandte Chemie International Edition*, vol. 61, p. e202110855, apr 2022.
- [28] K. Göpfrich, I. Platzman, and J. P. Spatz, “Mastering Complexity: Towards Bottom-up Construction of Multifunctional Eukaryotic Synthetic Cells,” *Trends in Biotechnology*, vol. 36, pp. 938–951, sep 2018.
- [29] Y. H. M. Chan and S. G. Boxer, “Model membrane systems and their applications,” *Current Opinion in Chemical Biology*, vol. 11, pp. 581–587, dec 2007.
- [30] N. J. Gaut and K. P. Adamala, “Reconstituting Natural Cell Elements in Synthetic Cells,” *Advanced Biology*, vol. 5, mar 2021.
- [31] Y. Lu, “Cell-free synthetic biology: Engineering in an open world,” *Synthetic and Systems Biotechnology*, vol. 2, pp. 23–27, mar 2017.
- [32] F. Lussier, O. Staufer, I. Platzman, and J. P. Spatz, “Can Bottom-Up Synthetic Biology Generate Advanced Drug-Delivery Systems?,” *Trends in Biotechnology*, vol. 39, pp. 445–459, may 2021.
- [33] M. Dasso, “In Vitro Reconstitution,” *Current Protocols in Cell Biology*, vol. 36, pp. 11.0.1–11.0.4, sep 2007.
- [34] A. P. Liu and D. A. Fletcher, “Biology under construction: in vitro reconstitution of cellular function,” *Nature Reviews Molecular Cell Biology 2009 10:9*, vol. 10, pp. 644–650, aug 2009.
- [35] A. J. García-Sáez, S. Chiantia, and P. Schwille, “Effect of line tension on the lateral organization of lipid membranes,” *Journal of Biological Chemistry*, vol. 282, pp. 33537–33544, nov 2007.
- [36] J. T. Groves, “Bending Mechanics and Molecular Organization in Biological Membranes,” *Annual Review of Physical Chemistry.*, vol. 58, pp. 697–717, apr 2007.
- [37] R. Skrzypek, S. Iqbal, and R. Callaghan, “Methods of reconstitution to investigate membrane protein function,” *Methods*, vol. 147, pp. 126–141, sep 2018.
- [38] W. L. Liu, M. Z. Zou, S. Y. Qin, Y. J. Cheng, Y. H. Ma, Y. X. Sun, and X. Z. Zhang, “Recent Advances of Cell Membrane-Coated Nanomaterials for Biomedical Applications,” *Advanced Functional Materials*, vol. 30, p. 2003559, sep 2020.
- [39] S. Tang, Z. Davoudi, G. Wang, Z. Xu, T. Rehman, A. Prominski, B. Tian, K. M. Bratlie, H. Peng, and Q. Wang, “Soft materials as biological and artificial membranes,” *Chemical Society reviews*, vol. 50, pp. 12679–12701, nov 2021.
- [40] B. György, M. E. Hung, X. O. Breakefield, and J. N. Leonard, “Therapeutic Ap-

- plications of Extracellular Vesicles: Clinical Promise and Open Questions,” *Annual Review of Pharmacology and Toxicology.*, vol. 55, pp. 439–464, jan 2015.
- [41] M. S. Almén, K. J. Nordström, R. Fredriksson, and H. B. Schiöth, “Mapping the human membrane proteome: A majority of the human membrane proteins can be classified according to function and evolutionary origin,” *BMC Biology*, vol. 7, p. 50, aug 2009.
- [42] B. Alberts, D. Bray, K. Hopkins, A. Johnson, J. Lewis, M. Raff, K. Roberts, and P. Walter, “Essential Cell Biology Fourth Edition,” *Garland Science*, p. 728, 2014.
- [43] T. Bhatia, “Micromechanics of Biomembranes,” *Journal of Membrane Biology*, vol. 255, pp. 637–649, dec 2022.
- [44] T. Litschel and P. Schwille, “Protein Reconstitution Inside Giant Unilamellar Vesicles,” *Annual review of biophysics*, vol. 50, pp. 525–548, may 2021.
- [45] H. Keller, R. Worch, and P. Schwille, “Model membrane systems,” *Methods in Molecular Biology*, vol. 1008, pp. 417–438, 2013.
- [46] T. J. Lagny and P. Bassereau, “Bioinspired membrane-based systems for a physical approach of cell organization and dynamics: usefulness and limitations,” *Interface Focus*, vol. 5, may 2015.
- [47] H. H. Shen, T. Lithgow, and L. L. Martin, “Reconstitution of Membrane Proteins into Model Membranes: Seeking Better Ways to Retain Protein Activities,” *International Journal of Molecular Sciences 2013, Vol. 14, Pages 1589-1607*, vol. 14, pp. 1589–1607, jan 2013.
- [48] S. Arumugam, G. Chwastek, and P. Schwille, “Protein–membrane interactions: the virtue of minimal systems in systems biology,” *Wiley Interdisciplinary Reviews: Systems Biology and Medicine*, vol. 3, pp. 269–280, may 2011.
- [49] A. J. García-Sáez and P. Schwille, “Surface analysis of membrane dynamics,” *Biochimica et Biophysica Acta (BBA) - Biomembranes*, vol. 1798, pp. 766–776, apr 2010.
- [50] V. M. Hernández-Rocamora, C. García-Montañés, G. Rivas, and O. Llorca, “Reconstitution of the Escherichia coli cell division ZipA–FtsZ complexes in nanodiscs as revealed by electron microscopy,” *Journal of Structural Biology*, vol. 180, pp. 531–538, dec 2012.
- [51] A. Nath, A. J. Trexler, P. Koo, A. D. Miranker, W. M. Atkins, and E. Rhoades, “Single-Molecule Fluorescence Spectroscopy Using Phospholipid Bilayer Nanodiscs,” *Methods in Enzymology*, vol. 472, pp. 89–117, jan 2010.
- [52] T. K. Ritchie, Y. V. Grinkova, T. H. Bayburt, I. G. Denisov, J. K. Zolnericiks, W. M. Atkins, and S. G. Sligar, “Reconstitution of Membrane Proteins in Phospholipid Bilayer Nanodiscs,” *Methods in Enzymology*, vol. 464, pp. 211–231, jan 2009.
- [53] A. Martos, M. Jiménez, G. Rivas, and P. Schwille, “Towards a bottom-up reconstitution of bacterial cell division,” *Trends in Cell Biology*, vol. 22, pp. 634–643, dec

- 2012.
- [54] L. Baldauf, L. Van Buren, F. Fanalista, and G. H. Koenderink, “Actomyosin-Driven Division of a Synthetic Cell,” *ACS synthetic biology*, vol. 11, pp. 3120–3133, oct 2022.
 - [55] M. Loose and T. J. Mitchison, “The bacterial cell division proteins FtsA and FtsZ self-organize into dynamic cytoskeletal patterns,” *Nature Cell Biology*, vol. 16, no. 1, 2014.
 - [56] A. A. André and E. Spruijt, “Liquid–Liquid Phase Separation in Crowded Environments,” *International Journal of Molecular Sciences 2020, Vol. 21, Page 5908*, vol. 21, p. 5908, aug 2020.
 - [57] Y. Zhu, X. Guo, J. Liu, F. Li, and D. Yang, “Emerging Advances of Cell-Free Systems toward Artificial Cells,” *Small Methods*, vol. 4, p. 2000406, oct 2020.
 - [58] A. P. Minton, “How can biochemical reactions within cells differ from those in test tubes?,” *Journal of cell science*, vol. 119, pp. 2863–2869, jul 2006.
 - [59] I. M. Kuznetsova, K. K. Turoverov, and V. N. Uversky, “What macromolecular crowding can do to a protein,” dec 2014.
 - [60] I. M. Kuznetsova, B. Y. Zaslavsky, L. Breydo, K. K. Turoverov, and V. N. Uversky, “Beyond the excluded volume effects: Mechanistic complexity of the crowded milieu,” 2015.
 - [61] G. Rivas and A. Minton, “Annual Review of Biochemistry Influence of Nonspecific Interactions on Protein Associations: Implications for Biochemistry In Vivo,” *Annual Review of Biochemistry*, 2022.
 - [62] Q. Ma, Y. Song, W. Sun, J. Cao, H. Yuan, X. Wang, Y. Sun, and H. C. Shum, “Cell-Inspired All-Aqueous Microfluidics: From Intracellular Liquid–Liquid Phase Separation toward Advanced Biomaterials,” *Advanced Science*, vol. 7, p. 1903359, apr 2020.
 - [63] S. Alberti, A. Gladfelter, and T. Mittag, “Considerations and Challenges in Studying Liquid-Liquid Phase Separation and Biomolecular Condensates,” *Cell*, vol. 176, pp. 419–434, jan 2019.
 - [64] S. Deshpande and C. Dekker, “Studying phase separation in confinement,” *Current Opinion in Colloid Interface Science*, vol. 52, p. 101419, apr 2021.
 - [65] A. A. Hyman, C. A. Weber, and F. Jülicher, “Liquid-Liquid Phase Separation in Biology,” *Annual Review of Cell and Developmental Biology.*, vol. 30, pp. 39–58, oct 2014.
 - [66] Y. Shin and C. P. Brangwynne, “Liquid phase condensation in cell physiology and disease,” *Science*, vol. 357, sep 2017.
 - [67] S. Smith, C. Cianci, and R. Grima, “Macromolecular crowding directs the motion of small molecules inside cells,” *Journal of The Royal Society Interface*, vol. 14, jun 2017.
 - [68] C. Tan, S. Saurabh, M. P. Bruchez, R. Schwartz, and P. Leduc, “Molecular crowding shapes gene expression in synthetic cellular nanosystems,” *Nature Nanotechnology*

- 2013 8:8, vol. 8, pp. 602–608, jul 2013.
- [69] R. J. Ellis, “Macromolecular crowding: Obvious but underappreciated,” *Trends in Biochemical Sciences*, vol. 26, no. 10, pp. 597–604, 2001.
- [70] J. Van Den Berg, A. J. Boersma, and B. Poolman, “Microorganisms maintain crowding homeostasis,” *Nature Reviews Microbiology* 2017 15:5, vol. 15, pp. 309–318, mar 2017.
- [71] G. Chauhan, S. E. Norred, R. M. Dabbs, P. M. Caveney, J. K. George, C. P. Collier, M. L. Simpson, and S. M. Abel, “Crowding-Induced Spatial Organization of Gene Expression in Cell-Sized Vesicles,” *ACS Synthetic Biology*, pp. 3733–3742, nov 2022.
- [72] P. Chien and L. M. Gierasch, “Challenges and dreams: Physics of weak interactions essential to life,” *Molecular Biology of the Cell*, vol. 25, pp. 3474–3477, nov 2014.
- [73] D. Gnutt and S. Ebbinghaus, “The macromolecular crowding effect - From in vitro into the cell,” *Biological Chemistry*, vol. 397, pp. 37–44, jan 2016.
- [74] G. Rivas and A. P. Minton, “Macromolecular Crowding In Vitro, In Vivo, and In Between,” *Trends in Biochemical Sciences*, vol. 41, pp. 970–981, nov 2016.
- [75] M. Löwe, M. Kalacheva, A. J. Boersma, and A. Kedrov, “The more the merrier: effects of macromolecular crowding on the structure and dynamics of biological membranes,” *The FEBS Journal*, vol. 287, pp. 5039–5067, dec 2020.
- [76] J. M. González, M. Jiménez, M. Vélez, J. Mingorance, J. M. Andreu, M. Vicente, and G. Rivas, “Essential cell division protein FtsZ assembles into one monomer-thick ribbons under conditions resembling the crowded intracellular environment,” *Journal of Biological Chemistry*, vol. 278, pp. 37664–37671, sep 2003.
- [77] M. Á. Robles-Ramos, S. Zorrilla, C. Alfonso, W. Margolin, G. Rivas, and B. Monterroso, “Assembly of bacterial cell division protein FtsZ into dynamic biomolecular condensates,” *Biochimica et Biophysica Acta (BBA) - Molecular Cell Research*, vol. 1868, p. 118986, apr 2021.
- [78] C. Tanford, “The hydrophobic effect and the organization of living matter,” *Science*, vol. 200, no. 4345, pp. 1012–1018, 1978.
- [79] E. Rideau, R. Dimova, P. Schwille, F. R. Wurm, and K. Landfester, “Liposomes and polymersomes: a comparative review towards cell mimicking,” *Chemical Society reviews*, vol. 47, pp. 8572–8610, nov 2018.
- [80] R. V. Solé, “Evolution and self-assembly of protocells,” *The International Journal of Biochemistry Cell Biology*, vol. 41, pp. 274–284, feb 2009.
- [81] J. L. Rigaud and D. Lévy, “Reconstitution of Membrane Proteins into Liposomes,” *Methods in Enzymology*, vol. 372, pp. 65–86, jan 2003.
- [82] R. Dimova, “Giant Vesicles and Their Use in Assays for Assessing Membrane Phase State, Curvature, Mechanics, and Electrical Properties,” *Annual Review of Biophysics. Vol. 48:93-119*, vol. 48, pp. 93–119, may 2019.
- [83] I. L. Jørgensen, G. C. Kemmer, and T. G. Pomorski, “Membrane protein reconstitution into giant unilamellar vesicles: a review on current techniques,” mar 2017.

- [84] N. Kahya, “Protein-protein and protein-lipid interactions in domain-assembly: lessons from giant unilamellar vesicles,” *Biochimica et biophysica acta*, vol. 1798, pp. 1392–1398, jul 2010.
- [85] P. Walde, K. Cosentino, H. Engel, and P. Stano, “Giant Vesicles: Preparations and Applications,” *ChemBioChem*, vol. 11, pp. 848–865, may 2010.
- [86] R. Dimova and C. Marques, *The giant vesicle book*. 2019.
- [87] E. Gulezian, C. Crivello, J. Bednenko, C. Zafra, Y. Zhang, P. Colussi, and S. Husain, “Membrane protein production and formulation for drug discovery,” *Trends in Pharmacological Sciences*, vol. 42, pp. 657–674, aug 2021.
- [88] L. Heuberger, M. Korphidou, O. M. Eggenberger, M. Kyropoulou, and C. G. Palivan, “Current Perspectives on Synthetic Compartments for Biomedical Applications,” *International journal of molecular sciences*, vol. 23, p. 5718, may 2022.
- [89] C. H. Lo, J. Zeng, H. Lo, and L. K. Chian, “Application of polymersomes in membrane protein study and drug discovery: Progress, strategies, and perspectives,” *Bioengineering Translational Medicine*, vol. 8, p. e10350, jan 2023.
- [90] M. Scalise, L. Pochini, N. Giangregorio, A. Tonazzi, and C. Indiveri, “Proteoliposomes as Tool for Assaying Membrane Transporter Functions and Interactions with Xenobiotics,” *Pharmaceutics 2013, Vol. 5, Pages 472-497*, vol. 5, pp. 472–497, sep 2013.
- [91] A. Akbarzadeh, R. Rezaei-Sadabady, S. Davaran, S. W. Joo, N. Zarghami, Y. Hanifehpour, M. Samiei, M. Kouhi, and K. Nejati-Koshki, “Liposome: classification, preparation, and applications.,” *Nanoscale Research Letters*, vol. 8, pp. 102–102, feb 2013.
- [92] M. Dua, A. Singh, N. Sethunathan, and A. Johri, “Biotechnology and bioremediation: Successes and limitations,” *Applied Microbiology and Biotechnology*, vol. 59, no. 2-3, pp. 143–152, 2002.
- [93] M. S. Gebre, L. A. Brito, L. H. Tostanoski, D. K. Edwards, A. Carfi, and D. H. Barouch, “Novel approaches for vaccine development,” *Cell*, vol. 184, pp. 1589–1603, mar 2021.
- [94] A. Jesorka and O. Orwar, “Liposomes: Technologies and Analytical Applications,” *Annual Review of Analytical Chemistry. Vol. 1:801-832*, vol. 1, pp. 801–832, jun 2008.
- [95] U. Kauscher, M. N. Holme, M. Björnmalm, and M. M. Stevens, “Physical stimuli-responsive vesicles in drug delivery: Beyond liposomes and polymersomes,” *Advanced Drug Delivery Reviews*, vol. 138, pp. 259–275, jan 2019.
- [96] R. Tenchov, R. Bird, A. E. Curtze, and Q. Zhou, “Lipid Nanoparticles from Liposomes to mRNA Vaccine Delivery, a Landscape of Research Diversity and Advancement,” *ACS Nano*, vol. 15, pp. 16982–17015, nov 2021.
- [97] Y. Lu, G. Allegri, and J. Huskens, “Vesicle-based artificial cells: materials, construction methods and applications,” *Materials Horizons*, vol. 9, pp. 892–907, mar

- 2022.
- [98] J. Li, X. Wang, T. Zhang, C. Wang, Z. Huang, X. Luo, and Y. Deng, "A review on phospholipids and their main applications in drug delivery systems," *Asian Journal of Pharmaceutical Sciences*, vol. 10, pp. 81–98, apr 2015.
- [99] J. Steinkühler, E. Sezgin, I. Urbančič, C. Eggeling, and R. Dimova, "Mechanical properties of plasma membrane vesicles correlate with lipid order, viscosity and cell density," *Communications Biology* 2019 2:1, vol. 2, pp. 1–8, sep 2019.
- [100] A. Mecke, C. Dittrich, and W. Meier, "Biomimetic membranes designed from amphiphilic block copolymers," *Soft Matter*, vol. 2, pp. 751–759, aug 2006.
- [101] X. Huang, M. Li, and S. Mann, "Membrane-mediated cascade reactions by enzyme-polymer proteinosomes," *Chemical Communications*, vol. 50, pp. 6278–6280, may 2014.
- [102] V. Percec, D. A. Wilson, P. Leowanawat, C. J. Wilson, A. D. Hughes, M. S. Kaucher, D. A. Hammer, D. H. Levine, A. J. Kim, F. S. Bates, K. P. Davis, T. P. Lodge, M. L. Klein, R. H. Devane, E. Aqad, B. M. Rosen, A. O. Argintaru, M. J. Sienkowska, K. Rissanen, S. Nummelin, and J. Ropponen, "Self-assembly of Janus dendrimers into uniform dendrimersomes and other complex architectures," *Science (New York, N.Y.)*, vol. 328, pp. 1009–1014, may 2010.
- [103] M. Sutter, D. Boehringer, S. Gutmann, S. Günther, D. Prangishvili, M. J. Loessner, K. O. Stetter, E. Weber-Ban, and N. Ban, "Structural basis of enzyme encapsulation into a bacterial nanocompartment," *Nature structural molecular biology*, vol. 15, pp. 939–947, sep 2008.
- [104] C. Martino, S.-H. Kim, L. Horsfall, A. Abbaspourrad, S. J. Rosser, J. Cooper, and D. A. Weitz, "Protein Expression, Aggregation, and Triggered Release from Polymersomes as Artificial Cell-like Structures," *Angewandte Chemie*, vol. 124, pp. 6522–6526, jun 2012.
- [105] A. M. Wagner, H. Eto, A. Joseph, S. Kohyama, T. Haraszti, R. A. Zamora, M. Vorobii, M. I. Giannotti, P. Schwille, C. Rodriguez-Emmenegger, A. M. Wagner, A. Joseph, T. Haraszti, M. Vorobii, C. Rodriguez-Emmenegger, H. Eto, S. Kohyama, and P. Schwille, "Dendrimersome Synthetic Cells Harbor Cell Division Machinery of Bacteria," *Advanced Materials*, vol. 34, p. 2202364, jul 2022.
- [106] H. A. Faizi, A. Tsui, R. Dimova, and P. M. Vlahovska, "Bending Rigidity, Capacitance, and Shear Viscosity of Giant Vesicle Membranes Prepared by Spontaneous Swelling, Electroformation, Gel-Assisted, and Phase Transfer Methods: A Comparative Study," *Langmuir : the ACS journal of surfaces and colloids*, vol. 38, pp. 10548–10557, aug 2022.
- [107] J. P. Reeves and R. M. Dowben, "Formation and properties of thin-walled phospholipid vesicles," *Journal of Cellular Physiology*, vol. 73, pp. 49–60, feb 1969.
- [108] K. I. Akashi, H. Miyata, H. Itoh, and K. Kinoshita, "Preparation of giant liposomes

- in physiological conditions and their characterization under an optical microscope,” *Biophysical Journal*, vol. 71, pp. 3242–3250, dec 1996.
- [109] B. Chaize, J. P. Colletier, M. Winterhalter, and D. Fournier, “Encapsulation of Enzymes in Liposomes: High Encapsulation Efficiency and Control of Substrate Permeability,” *Artificial Cells, Blood Substitutes, and Biotechnology*, 32:1, 67-75, vol. 32, no. 1, pp. 67–75, 2009.
- [110] M. I. Angelova and D. S. Dimitrov, “Liposome electroformation,” *Faraday Discussions of the Chemical Society*, vol. 81, pp. 303–311, jan 1986.
- [111] K. S. Horgan, D. J. Estes, R. Capone, and M. Mayer, “Films of agarose enable rapid formation of giant liposomes in solutions of physiologic ionic strength,” *Journal of the American Chemical Society*, vol. 131, pp. 1810–1819, feb 2009.
- [112] A. Weinberger, F. C. Tsai, G. H. Koenderink, T. F. Schmidt, R. Itri, W. Meier, T. Schmatko, A. Schröder, and C. Marques, “Gel-Assisted Formation of Giant Unilamellar Vesicles,” *Biophysical Journal*, vol. 105, pp. 154–164, jul 2013.
- [113] L. R. Montes, A. Alonso, F. M. Goñi, and L. A. Bagatolli, “Giant Unilamellar Vesicles Electroformed from Native Membranes and Organic Lipid Mixtures under Physiological Conditions,” *Biophysical Journal*, vol. 93, pp. 3548–3554, nov 2007.
- [114] T. Pott, H. Bouvrais, and P. Méléard, “Giant unilamellar vesicle formation under physiologically relevant conditions,” *Chemistry and Physics of Lipids*, vol. 154, pp. 115–119, aug 2008.
- [115] P. M. Shaklee, S. Semrau, M. Malkus, S. Kubick, M. Dogterom, and T. Schmidt, “Protein Incorporation in Giant Lipid Vesicles under Physiological Conditions,” *ChemBioChem*, vol. 11, pp. 175–179, jan 2010.
- [116] J. Steinkühler, P. De Tillieux, R. L. Knorr, R. Lipowsky, and R. Dimova, “Charged giant unilamellar vesicles prepared by electroformation exhibit nanotubes and transbilayer lipid asymmetry,” *Scientific Reports*, vol. 8, dec 2018.
- [117] S. Pautot, B. J. Frisken, and D. A. Weitz, “Production of unilamellar vesicles using an inverted emulsion,” *Langmuir*, vol. 19, pp. 2870–2879, apr 2003.
- [118] S. Chen, Z. G. Sun, and M. P. Murrell, “In Vitro Reconstitution of the Actin Cytoskeleton Inside Giant Unilamellar Vesicles,” *Journal of visualized experiments : JoVE*, aug 2022.
- [119] M. Tsugane and H. Suzuki, “Reverse Transcription Polymerase Chain Reaction in Giant Unilamellar Vesicles,” *Scientific Reports 2018 8:1*, vol. 8, pp. 1–11, jun 2018.
- [120] F. C. Tsai, B. Stuhmann, and G. H. Koenderink, “Encapsulation of active cytoskeletal protein networks in cell-sized liposomes,” *Langmuir*, vol. 27, pp. 10061–10071, aug 2011.
- [121] S. Matosevic and B. M. Paegel, “Layer-by-layer cell membrane assembly,” *Nature Chemistry 2013 5:11*, vol. 5, pp. 958–963, sep 2013.
- [122] K. Nishimura, H. Suzuki, T. Toyota, and T. Yomo, “Size control of giant unilamellar vesicles prepared from inverted emulsion droplets,” *Journal of Colloid and Interface*

- Science*, vol. 376, pp. 119–125, jun 2012.
- [123] F. C. Keber, E. Loiseau, T. Sanchez, S. J. DeCamp, L. Giomi, M. J. Bowick, M. C. Marchetti, Z. Dogic, and A. R. Bausch, “Topology and dynamics of active nematic vesicles,” *Science*, vol. 345, pp. 1135–1139, sep 2014.
- [124] L. Van De Cauter, F. Fanalista, L. Van Buren, N. De Franceschi, E. Godino, S. Bouw, C. Danelon, C. Dekker, G. H. Koenderink, and K. A. Ganzinger, “Optimized cDICE for Efficient Reconstitution of Biological Systems in Giant Unilamellar Vesicles,” *ACS Synthetic Biology*, vol. 10, pp. 1690–1702, jul 2021.
- [125] Manouk Abkarian, Etienne Loiseau, and Gladys Massiera, “Continuous droplet interface crossing encapsulation (cDICE) for high throughput monodisperse vesicle design,” *Soft Matter*, vol. 7, pp. 4610–4614, may 2011.
- [126] K. Göpfrich, B. Haller, O. Staufer, Y. Dreher, U. Mersdorf, I. Platzman, and J. P. Spatz, “One-Pot Assembly of Complex Giant Unilamellar Vesicle-Based Synthetic Cells,” *ACS Synthetic Biology*, vol. 8, pp. 937–947, may 2019.
- [127] Y. Ai, R. Xie, J. Xiong, and Q. Liang, “Microfluidics for Biosynthesizing: from Droplets and Vesicles to Artificial Cells,” *Small*, vol. 16, p. 1903940, mar 2020.
- [128] C. Martino and A. J. DeMello, “Droplet-based microfluidics for artificial cell generation: a brief review,” *Interface Focus*, vol. 6, aug 2016.
- [129] A. Napoli, M. Valentini, N. Tirelli, M. Müller, and J. A. Hubbell, “Oxidation-responsive polymeric vesicles,” *Nature Materials 2004 3:3*, vol. 3, pp. 183–189, feb 2004.
- [130] T. Robinson, “Microfluidic Handling and Analysis of Giant Vesicles for Use as Artificial Cells: A Review,” *Advanced Biosystems*, vol. 3, jun 2019.
- [131] A. M. Ganan-Calvo, R. Gonzalez-Prieto, P. Riesco-Chueca, M. A. Herrada, and M. Flores-Mosquera, “Focusing capillary jets close to the continuum limit,” *Nature Physics 2007 3:10*, vol. 3, pp. 737–742, sep 2007.
- [132] K. Kamiya, “Development of artificial cell models using microfluidic technology and synthetic biology,” may 2020.
- [133] A. Moga, N. Yandrapalli, R. Dimova, and T. Robinson, “Optimization of the Inverted Emulsion Method for High-Yield Production of Biomimetic Giant Unilamellar Vesicles,” *ChemBioChem*, vol. 20, pp. 2674–2682, oct 2019.
- [134] M. Weiss, J. P. Frohnmayer, L. T. Benk, B. Haller, J. W. Janiesch, T. Heitkamp, M. Börsch, R. B. Lira, R. Dimova, R. Lipowsky, E. Bodenschatz, J. C. Baret, T. Vidakovic-Koch, K. Sundmacher, I. Platzman, and J. P. Spatz, “Sequential bottom-up assembly of mechanically stabilized synthetic cells by microfluidics,” *Nature Materials 2017 17:1*, vol. 17, pp. 89–96, oct 2017.
- [135] N. N. Deng, M. Yelleswarapu, L. Zheng, and W. T. Huck, “Microfluidic assembly of monodisperse vesosomes as artificial cell models,” *Journal of the American Chemical Society*, vol. 139, pp. 587–590, jan 2017.
- [136] C. Wang, J. Yang, and Y. Lu, “Modularize and Unite: Toward Creating a Functional

- Artificial Cell,” *Frontiers in Molecular Biosciences*, vol. 8, p. 1203, nov 2021.
- [137] D. Hürtgen, J. Mascarenhas, M. Heymann, S. M. Murray, P. Schwille, and V. Sourjik, “Reconstitution and Coupling of DNA Replication and Segregation in a Biomimetic System,” *ChemBioChem*, vol. 20, pp. 2633–2642, oct 2019.
- [138] L. Olivi, M. Berger, R. N. Creyghton, N. De Franceschi, C. Dekker, B. M. Mulder, N. J. Claassens, P. R. ten Wolde, and J. van der Oost, “Towards a synthetic cell cycle,” *Nature Communications 2021 12:1*, vol. 12, pp. 1–11, jul 2021.
- [139] S. Kretschmer, K. A. Ganzinger, H. G. Franquelim, and P. Schwille, “Synthetic cell division via membrane-transforming molecular assemblies,” *BMC Biology 2019 17:1*, vol. 17, pp. 1–10, may 2019.
- [140] C. E. Hodgman and M. C. Jewett, “Cell-free synthetic biology: Thinking outside the cell,” *Metabolic Engineering*, vol. 14, pp. 261–269, may 2012.
- [141] P. Stano, “Gene Expression Inside Liposomes: From Early Studies to Current Protocols,” *Chemistry – A European Journal*, vol. 25, pp. 7798–7814, jun 2019.
- [142] L. Kai and P. Schwille, “Cell-Free Protein Synthesis and Its Perspectives for Assembling Cells from the Bottom-Up,” *Advanced Biosystems*, vol. 3, jun 2019.
- [143] K. Yue, Y. Zhu, and L. Kai, “Cell-Free Protein Synthesis: Chassis toward the Minimal Cell,” *Cells 2019, Vol. 8, Page 315*, vol. 8, p. 315, apr 2019.
- [144] N. Laohakunakorn, L. Grasmann, B. Lavickova, G. Michielin, A. Shahein, Z. Swank, and S. J. Maerkl, “Bottom-Up Construction of Complex Biomolecular Systems With Cell-Free Synthetic Biology,” *Frontiers in bioengineering and biotechnology*, vol. 8, mar 2020.
- [145] J. Garamella, D. Garenne, and V. Noireaux, “TXTL-based approach to synthetic cells,” *Methods in Enzymology*, vol. 617, pp. 217–239, jan 2019.
- [146] H. Jia, M. Heymann, F. Bernhard, P. Schwille, and L. Kai, “Cell-free protein synthesis in micro compartments: building a minimal cell from biobricks,” *New Biotechnology*, vol. 39, pp. 199–205, oct 2017.
- [147] P. Van Nies, I. Westerlaken, D. Blanken, M. Salas, M. Mencía, and C. Danelon, “Self-replication of DNA by its encoded proteins in liposome-based synthetic cells,” *Nature Communications 2018 9:1*, vol. 9, pp. 1–12, apr 2018.
- [148] S. Berhanu, T. Ueda, and Y. Kuruma, “Artificial photosynthetic cell producing energy for protein synthesis,” *Nature Communications 2019 10:1*, vol. 10, pp. 1–10, mar 2019.
- [149] D. Blanken, D. Foschepoth, A. C. Serrão, and C. Danelon, “Genetically controlled membrane synthesis in liposomes,” *Nature Communications 2020 11:1*, vol. 11, pp. 1–13, aug 2020.
- [150] T. Furusato, F. Horie, H. T. Matsubayashi, K. Amikura, Y. Kuruma, and T. Ueda, “De Novo Synthesis of Basal Bacterial Cell Division Proteins FtsZ, FtsA, and ZipA Inside Giant Vesicles,” *ACS synthetic biology*, vol. 7, pp. 953–961, apr 2018.
- [151] E. Godino, J. N. López, D. Foschepoth, C. Cleij, A. Doerr, C. F. Castellà, and

- C. Danelon, “De novo synthesized Min proteins drive oscillatory liposome deformation and regulate FtsA-FtsZ cytoskeletal patterns,” *Nature Communications*, vol. 10, dec 2019.
- [152] A. Yoshida, S. Kohyama, K. Fujiwara, S. Nishikawa, and N. Doi, “Regulation of spatiotemporal patterning in artificial cells by a defined protein expression system,” *Chemical Science*, vol. 10, pp. 11064–11072, dec 2019.
- [153] Y. Kuruma and T. Ueda, “The PURE system for the cell-free synthesis of membrane proteins,” *Nature Protocols 2015 10:9*, vol. 10, pp. 1328–1344, aug 2015.
- [154] Y. Shimizu, A. Inoue, Y. Tomari, T. Suzuki, T. Yokogawa, K. Nishikawa, and T. Ueda, “Cell-free translation reconstituted with purified components,” *Nature Biotechnology 2001 19:8*, vol. 19, pp. 751–755, aug 2001.
- [155] D. Hürtgen, S. M. Murray, J. Mascarenhas, V. Sourjik, D. Hürtgen, S. M. Murray, J. Mascarenhas, and V. Sourjik, “DNA Segregation in Natural and Synthetic Minimal Systems,” *Advanced Biosystems*, vol. 3, p. 1800316, jun 2019.
- [156] Y. Caspi and C. Dekker, “Mapping out Min protein patterns in fully confined fluidic chambers,” *eLife*, vol. 5, nov 2016.
- [157] E. Godino, J. N. López, I. Zarguit, A. Doerr, M. Jimenez, G. Rivas, and C. Danelon, “Cell-free biogenesis of bacterial division proto-rings that can constrict liposomes,” *Communications Biology 2020 3:1*, vol. 3, pp. 1–11, sep 2020.
- [158] M. Osawa, D. E. Anderson, and H. P. Erickson, “Curved FtsZ protofilaments generate bending forces on liposome membranes,” *The EMBO Journal*, vol. 28, pp. 3476–3484, nov 2009.
- [159] M. Osawa and H. P. Erickson, “Inside-out Z rings - constriction with and without GTP hydrolysis,” *Molecular Microbiology*, vol. 81, pp. 571–579, jul 2011.
- [160] E. Loiseau, J. A. Schneider, F. C. Keber, C. Pelzl, G. Massiera, G. Salbreux, and A. R. Bausch, “Shape remodeling and blebbing of active cytoskeletal vesicles,” *Science Advances*, vol. 2, apr 2016.
- [161] T. D. Pollard and B. O’Shaughnessy, “Molecular Mechanism of Cytokinesis,” *Annual Review of Biochemistry*, vol. 88, pp. 661–689, jun 2019.
- [162] B. E. Mierzwa, N. Chiaruttini, L. Redondo-Morata, J. Moser Von Filseck, J. König, J. Larios, I. Poser, T. Müller-Reichert, S. Scheuring, A. Roux, and D. W. Gerlich, “Dynamic subunit turnover in ESCRT-III assemblies is regulated by Vps4 to mediate membrane remodelling during cytokinesis,” *Nature Cell Biology 2017 19:7*, vol. 19, pp. 787–798, jun 2017.
- [163] J. Schöneberg, M. R. Pavlin, S. Yan, M. Righini, I. H. Lee, L. A. Carlson, A. H. Bahrami, D. H. Goldman, X. Ren, G. Hummer, C. Bustamante, and J. H. Hurley, “ATP-dependent force generation and membrane scission by ESCRT-III and Vps4,” *Science*, vol. 362, pp. 1423–1428, dec 2018.
- [164] K. Nordstrom and S. J. Austin, “Mechanisms that contribute to the stable segrega-

- tion of plasmids,” *Annual review of genetics*, vol. 23, pp. 37–69, 1989.
- [165] S. Jun and B. Mulder, “Entropy-driven spatial organization of highly confined polymers: Lessons for the bacterial chromosome,” *Proceedings of the National Academy of Sciences of the United States of America*, vol. 103, pp. 12388–12393, aug 2006.
- [166] S. Deshpande, W. K. Spoelstra, M. Van Doorn, J. Kerssemakers, and C. Dekker, “Mechanical Division of Cell-Sized Liposomes,” *ACS Nano*, vol. 12, pp. 2560–2568, mar 2018.
- [167] N. D. Franceschi, W. Pezeshkian, A. Fragasso, B. M. H. Bruininks, S. Tsai, S. J. Marrink, C. Dekker, N. De Franceschi, W. Pezeshkian, A. Fragasso, B. M. H. Bruininks, S. Tsai, S. J. Marrink, and C. Dekker, “Synthetic Membrane Shaper for Controlled Liposome Deformation,” *ACS Nano*, vol. 17, pp. 966–978, nov 2022.
- [168] F. Fanalista, A. Birnie, R. Maan, F. Burla, K. Charles, G. Pawlik, S. Deshpande, G. H. Koenderink, M. Dogterom, and C. Dekker, “Shape and Size Control of Artificial Cells for Bottom-Up Biology,” *ACS Nano*, vol. 13, pp. 5439–5450, may 2019.
- [169] R. Wick, P. Walde, and P. L. Luisi, “Light Microscopic Investigations of the Autocatalytic Self-Reproduction of Giant Vesicles,” *Journal of the American Chemical Society*, vol. 117, no. 4, pp. 1435–1436, 1995.
- [170] R. J. Brea, C. M. Cole, and N. K. Devaraj, “In Situ Vesicle Formation by Native Chemical Ligation,” *Angewandte Chemie*, vol. 126, pp. 14326–14329, dec 2014.
- [171] M. D. Hardy, J. Yang, J. Selimkhanov, C. M. Cole, L. S. Tsimring, N. K. Devaraj, and J. W. Szostak, “Self-reproducing catalyst drives repeated phospholipid synthesis and membrane growth,” *Proceedings of the National Academy of Sciences of the United States of America*, vol. 112, pp. 8187–8192, jul 2015.
- [172] M. Exterkate, A. Caforio, M. C. Stuart, and A. J. Driessen, “Growing Membranes in Vitro by Continuous Phospholipid Biosynthesis from Free Fatty Acids,” *ACS Synthetic Biology*, vol. 7, pp. 153–165, jan 2018.
- [173] A. Scott, M. J. Noga, P. De Graaf, I. Westerlaken, E. Yildirim, and C. Danelon, “Cell-Free Phospholipid Biosynthesis by Gene-Encoded Enzymes Reconstituted in Liposomes,” *PLOS ONE*, vol. 11, p. e0163058, oct 2016.
- [174] M. Hoppert and F. Mayer, “Principles of macromolecular organization and cell function in bacteria and archaea,” *Cell Biochemistry and Biophysics 1999 31:3*, vol. 31, no. 3, pp. 247–284, 1999.
- [175] A. Meunier, F. Cornet, and M. Campos, “Bacterial cell proliferation: from molecules to cells,” *FEMS Microbiology Reviews*, vol. 45, pp. 1–21, jan 2021.
- [176] J. G. Carlton, H. Jones, and U. S. Eggert, “Membrane and organelle dynamics during cell division,” *Nature Reviews Molecular Cell Biology 2020 21:3*, vol. 21, pp. 151–166, feb 2020.
- [177] S. Du and J. Lutkenhaus, “Assembly and activation of the Escherichia coli divisome,” *Molecular Microbiology*, vol. 105, pp. 177–187, jul 2017.
- [178] C. R. Mahone and E. D. Goley, “Bacterial cell division at a glance,” 2020.

- [179] W. Margolin, "FtsZ and the division of prokaryotic cells and organelles," *Nature Reviews Molecular Cell Biology* 2005 6:11, vol. 6, pp. 862–871, oct 2005.
- [180] L. Romberg and P. A. Levin, "Assembly Dynamics of the Bacterial Cell Division Protein FtsZ: Poised at the Edge of Stability," *Annual review of microbiology*, vol. 57, p. 125, 2003.
- [181] N. Buddelmeijer and J. Beckwith, "Assembly of cell division proteins at the E. coli cell center," *Current Opinion in Microbiology*, vol. 5, no. 6, pp. 553–557, 2002.
- [182] N. W. Goehring and J. Beckwith, "Diverse Paths to Midcell: Assembly of the Bacterial Cell Division Machinery," *Current Biology*, vol. 15, pp. R514–R526, jul 2005.
- [183] A. I. Rico, M. Krupka, and M. Vicente, "In the beginning, escherichia coli assembled the proto-ring: An initial phase of division," *Journal of Biological Chemistry*, vol. 288, no. 29, pp. 20830–20836, 2013.
- [184] M. Attaibi and T. Den Blaauwen, "An Updated Model of the Divisome: Regulation of the Septal Peptidoglycan Synthesis Machinery by the Divisome," *International journal of molecular sciences*, 2022.
- [185] P. A. Levin and A. Janakiraman, "Localization, Assembly, and Activation of the Escherichia coli Cell Division Machinery," *EcoSal Plus*, vol. 9, no. 2, 2021.
- [186] R. McQuillen and J. Xiao, "Insights into the Structure, Function, and Dynamics of the Bacterial Cytokinetic FtsZ-Ring," *Annual Review of Biophysics*, vol. 49, pp. 309–341, may 2020.
- [187] D. Bramhill, "Bacterial cell division," *Annual Review of Cell and Developmental Biology*, vol. 13, pp. 395–424, 1997.
- [188] D. P. Haeusser and W. Margolin, "Splitsville: structural and functional insights into the dynamic bacterial Z ring," *Nature Reviews Microbiology*, vol. 14, pp. 305–319, may 2016.
- [189] E. Bi and J. Lutkenhaus, "FtsZ ring structure associated with division in Escherichia coli," *Nature*, vol. 354, pp. 161–164, nov 1991.
- [190] X. Ma and W. Margolin, "Genetic and Functional Analyses of the Conserved C-Terminal Core Domain of Escherichia coli FtsZ," *Journal of Bacteriology*, vol. 181, pp. 7531–7544, dec 1999.
- [191] X. Ma, D. W. Ehrhardt, and W. Margolin, "Colocalization of cell division proteins FtsZ and FtsA to cytoskeletal structures in living Escherichia coli cells by using green fluorescent protein," *Proceedings of the National Academy of Sciences of the United States of America*, vol. 93, pp. 12998–13003, nov 1996.
- [192] Y. Chen, K. Bjornson, S. D. Redick, and H. P. Erickson, "A Rapid Fluorescence Assay for FtsZ Assembly Indicates Cooperative Assembly with a Dimer Nucleus," *Biophysical Journal*, vol. 88, pp. 505–514, jan 2005.
- [193] K.-H. H. Huang, J. Durand-Heredia, and A. Janakiraman, "FtsZ ring stability: Of bundles, tubules, crosslinks, and curves," *Journal of Bacteriology*, vol. 195, pp. 1859–1868, may 2013.

- [194] C. Ortiz, P. Natale, L. Cueto, and M. Vicente, “The keepers of the ring: Regulators of FtsZ assembly,” *FEMS Microbiology Reviews*, vol. 40, no. 1, pp. 57–67, 2015.
- [195] J. Lutkenhaus, “Assembly dynamics of the bacterial minCDE system and spatial regulation of the z ring,” *Annual Review of Biochemistry*, vol. 76, pp. 539–562, 2007.
- [196] J. Männik and M. W. Bailey, “Spatial coordination between chromosomes and cell division proteins in *Escherichia coli*,” *Frontiers in Microbiology*, vol. 6, p. 306, apr 2015.
- [197] L. G. Monahan, A. T. Liew, A. L. Bottomley, and E. J. Harry, “Division site positioning in bacteria: One size does not fit all,” *Frontiers in Microbiology*, vol. 5, p. 19, feb 2014.
- [198] S. Arumugam, Z. Petrášek, and P. Schwille, “MinCDE exploits the dynamic nature of FtsZ filaments for its spatial regulation,” *Proceedings of the National Academy of Sciences of the United States of America*, vol. 111, pp. E1192–E1200, apr 2014.
- [199] H. Meinhardt and P. A. De Boer, “Pattern formation in *Escherichia coli*: A model for the pole-to-pole oscillations of Min proteins and the localization of the division site,” *Proceedings of the National Academy of Sciences of the United States of America*, vol. 98, pp. 14202–14207, dec 2001.
- [200] K. T. Park, A. Dajkovic, M. Wissel, S. Du, and J. Lutkenhaus, “MinC and FtsZ mutant analysis provides insight into MinC/ MinD-mediated Z ring disassembly,” *Journal of Biological Chemistry*, vol. 293, pp. 5834–5846, apr 2018.
- [201] H. Cho, H. R. McManus, S. L. Dove, and T. G. Bernhardt, “Nucleoid occlusion factor SlmA is a DNA-activated FtsZ polymerization antagonist,” *Proceedings of the National Academy of Sciences of the United States of America*, vol. 108, pp. 3773–3778, mar 2011.
- [202] H. Cho and T. G. Bernhardt, “Identification of the SlmA Active Site Responsible for Blocking Bacterial Cytokinetic Ring Assembly over the Chromosome,” *PLOS Genetics*, vol. 9, p. e1003304, feb 2013.
- [203] T. G. Bernhardt and P. A. De Boer, “SlmA, a Nucleoid-Associated, FtsZ Binding Protein Required for Blocking Septal Ring Assembly over Chromosomes in *E. coli*,” *Molecular Cell*, vol. 18, pp. 555–564, may 2005.
- [204] N. K. Tonthat, S. T. Arold, B. F. Pickering, M. W. Van Dyke, S. Liang, Y. Lu, T. K. Beuria, W. Margolin, and M. A. Schumacher, “Molecular mechanism by which the nucleoid occlusion factor, SlmA, keeps cytokinesis in check,” *The EMBO Journal*, vol. 30, pp. 154–164, jan 2011.
- [205] M. W. Bailey, P. Bisicchia, B. T. Warren, D. J. Sherratt, and J. Männik, “Evidence for Divisome Localization Mechanisms Independent of the Min System and SlmA in *Escherichia coli*,” *PLOS Genetics*, vol. 10, p. e1004504, aug 2014.
- [206] T. den Blaauwen, L. W. Hamoen, and P. A. Levin, “The divisome at 25: the road ahead,” *Current Opinion in Microbiology*, vol. 36, pp. 85–94, apr 2017.

- [207] J. Buss, C. Coltharp, T. Huang, C. Pohlmeier, S. C. Wang, C. Hatem, and J. Xiao, “In vivo organization of the FtsZ-ring by ZapA and ZapB revealed by quantitative super-resolution microscopy,” *Molecular Microbiology*, vol. 89, pp. 1099–1120, sep 2013.
- [208] D. E. Castillo, D. Yang, G. Siopsis, J. Männik, and J. Männik, “The role of MatP, ZapA and ZapB in chromosomal organization and dynamics in *Escherichia coli*,” *Nucleic Acids Research*, vol. 44, pp. 1216–1226, feb 2015.
- [209] O. Espéli, R. Borne, P. Dupaigne, A. Thiel, E. Gigant, R. Mercier, and F. Boccard, “A MatP–divisome interaction coordinates chromosome segregation with cell division in *E. coli*,” *EMBO Journal*, vol. 31, pp. 3198–3211, jul 2012.
- [210] K. J. Begg, S. J. Dewar, and W. D. Donachie, “A new *Escherichia coli* cell division gene, *ftsK*,” *Journal of Bacteriology*, vol. 177, no. 21, pp. 6211–6222, 1995.
- [211] N. L. Jean, T. J. Rutherford, and J. Löwe, “FtsK in motion reveals its mechanism for double-stranded DNA translocation,” *Proceedings of the National Academy of Sciences of the United States of America*, vol. 117, pp. 14202–14208, jun 2020.
- [212] M. Wang, . Chao Fang, B. Ma, X. Luo, and Z. Hou, “Regulation of cytokinesis: FtsZ and its accessory proteins,” *Current Genetics*, vol. 66, pp. 43–49, 2020.
- [213] M. Petiti, B. Serrano, L. Faure, R. Lloubes, T. Mignot, and D. Duché, “Tol Energy-Driven Localization of Pal and Anchoring to the Peptidoglycan Promote Outer-Membrane Constriction,” *Journal of molecular biology*, vol. 431, pp. 3275–3288, aug 2019.
- [214] M. N. Webby, D. P. Williams-Jones, C. Press, and C. Kleanthous, “No Title,” *Frontiers in microbiology*, vol. 13, p. 852176, mar 2022.
- [215] J. M. Monteiro, A. R. Pereira, N. T. Reichmann, B. M. Saraiva, P. B. Fernandes, H. Veiga, A. C. Tavares, M. Santos, M. T. Ferreira, V. Macário, M. S. Van-Nieuwenhze, S. R. Filipe, and M. G. Pinho, “Peptidoglycan synthesis drives an FtsZ-treadmilling-independent step of cytokinesis,” *Nature 2018 554:7693*, vol. 554, pp. 528–532, feb 2018.
- [216] N. Nanninga, “Morphogenesis of *Escherichia coli*,” *Microbiology and molecular biology reviews : MMBR*, vol. 62, pp. 110–129, mar 1998.
- [217] A. Zaritsky, D. Haeusser, M. Feingold, M. Osawa, and H. P. Erickson, “Turgor Pressure and Possible Constriction Mechanisms in Bacterial Division,” *Frontiers in Microbiology*, 2018.
- [218] P. D. Rohs and T. G. Bernhardt, “Growth and Division of the Peptidoglycan Matrix,” *Annual Review of Microbiology*, vol. 75, pp. 315–336, oct 2021.
- [219] B. Söderström, H. Chan, and D. O. Daley, “Super-resolution images of peptidoglycan remodelling enzymes at the division site of *Escherichia coli*,” *Current Genetics*, vol. 65, pp. 99–101, feb 2019.
- [220] A. Boes, S. Olatunji, E. Breukink, and M. Terrak, “Regulation of the peptidoglycan

- polymerase activity of PBP1b by antagonist actions of the core divisome proteins FtsBLQ and FtsN,” *mBio*, vol. 10, jan 2019.
- [221] S. G. Condon, D. A. Mahbuba, C. R. Armstrong, G. Diaz-Vazquez, S. J. Craven, L. M. LaPointe, A. S. Khadria, R. Chadda, J. A. Crooks, N. Rangarajan, D. B. Weibel, A. A. Hoskins, J. L. Robertson, Q. Cui, and A. Senes, “The FtsLB sub-complex of the bacterial divisome is a tetramer with an uninterrupted FtsL helix linking the transmembrane and periplasmic regions,” *Journal of Biological Chemistry*, vol. 293, pp. 1623–1641, feb 2018.
- [222] D. Kureisaite-Ciziene, A. Varadajan, S. H. McLaughlin, M. Glas, A. M. Silva, R. Luirink, C. Mueller, T. D. Blaauwen, T. N. Grossmann, J. Luirink, and J. Löwe, “Structural analysis of the interaction between the bacterial cell division proteins FTSQ and FTSB,” *mBio*, vol. 9, sep 2018.
- [223] F. Villanelo, A. Ordenes, J. Brunet, R. Lagos, and O. Monasterio, “A model for the Escherichia coli FtsB/FtsL/FtsQ cell division complex,” *BMC Structural Biology*, vol. 11, pp. 1–15, jun 2011.
- [224] M. A. Gerding, B. Liu, F. O. Bendezú, C. A. Hale, T. G. Bernhardt, and P. A. De Boer, “Self-enhanced accumulation of FtsN at division sites and roles for other proteins with a SPOR domain (DamX, DedD, and RlpA) in Escherichia coli cell constriction,” *Journal of Bacteriology*, vol. 191, pp. 7383–7401, dec 2009.
- [225] B. Shen and J. Lutkenhaus, “The conserved C-terminal tail of FtsZ is required for the septal localization and division inhibitory activity of MinCC/MinD,” *Molecular Microbiology*, vol. 72, pp. 410–424, apr 2009.
- [226] B. Liu, L. Persons, L. Lee, and P. A. de Boer, “Roles for both FtsA and the FtsBLQ subcomplex in FtsN-stimulated cell constriction in Escherichia coli,” *Molecular Microbiology*, vol. 95, pp. 945–970, mar 2015.
- [227] S. Pichoff, S. Du, and J. Lutkenhaus, “Disruption of divisome assembly rescued by FtsN–FtsA interaction in Escherichia coli,” *Proceedings of the National Academy of Sciences of the United States of America*, vol. 115, pp. E6855–E6862, jul 2018.
- [228] D. S. Weiss, “Last but not least: new insights into how FtsN triggers constriction during Escherichiacoli cell division,” *Molecular Microbiology*, vol. 95, pp. 903–909, mar 2015.
- [229] A. Dubey and R. Priyadarshini, “Amidase activity is essential for medial localization of AmiC in Caulobacter crescentus,” *Current Genetics*, vol. 64, pp. 661–675, jun 2018.
- [230] G. Ercoli, C. Tani, A. Pezzicoli, I. Vacca, M. Martinelli, S. Pecetta, R. Petracca, R. Rappuoli, M. Pizza, N. Norais, M. Soriani, and B. Aricò, “Lytm proteins play a crucial role in cell separation, outer membrane composition, and pathogenesis in nontypeable Haemophilus influenzae,” *mBio*, vol. 6, no. 2, 2015.
- [231] B. E. Rued, M. Alcorlo, K. A. Edmonds, S. Martínez-Caballero, D. Straume, Y. Fu, K. E. Bruce, H. Wu, L. S. Håvarstein, J. A. Hermoso, M. E. Winkler, and D. P.

- Giedroc, "Structure of the large extracellular loop of FtsX and its interaction with the essential peptidoglycan hydrolase PcsB in streptococcus pneumoniae," *mBio*, vol. 10, jan 2019.
- [232] C. Coltharp and J. Xiao, "Beyond force generation: Why is a dynamic ring of FtsZ polymers essential for bacterial cytokinesis?," *BioEssays*, vol. 39, pp. 1–11, jan 2017.
- [233] N. Yadu, A. Namboothiri, and S. Arumugam, "FtsZ: The Force Awakens," *Journal of the Indian Institute of Science*, vol. 101, pp. 31–38, jan 2021.
- [234] B. Söderström, K. Mirzadeh, S. Toddo, G. von Heijne, U. Skoglund, and D. O. Daley, "Coordinated disassembly of the divisome complex in Escherichia coli," *Molecular Microbiology*, vol. 101, pp. 425–438, aug 2016.
- [235] B. Söderström, K. Skoog, H. Blom, D. S. Weiss, G. von Heijne, and D. O. Daley, "Disassembly of the divisome in Escherichia coli: Evidence that FtsZ dissociates before compartmentalization," *Molecular Microbiology*, vol. 92, pp. 1–9, apr 2014.
- [236] L. C. Goodman and H. P. Erickson, "FtsZ at mid-cell is essential in Escherichia coli until the late stage of constriction," *Microbiology (United Kingdom)*, vol. 168, no. 6, 2022.
- [237] K. Skoog, B. Söderström, J. Widengren, G. Von Heijne, and D. O. Daley, "Sequential closure of the cytoplasm and then the periplasm during cell division in Escherichia coli," *Journal of Bacteriology*, vol. 194, pp. 584–586, feb 2012.
- [238] J. M. Barrows and E. D. Goley, "FtsZ dynamics in bacterial division: what, how, and why?," *Current Opinion in Cell Biology*, vol. 68, pp. 163–172, feb 2021.
- [239] P. De Boer, R. Crossley, and L. Rothfield, "The essential bacterial cell-division protein FtsZ is a GTPase," *Nature 1992 359:6392*, vol. 359, no. 6392, pp. 254–256, 1992.
- [240] R. R. Battaje, R. Piyush, V. Pratap, and D. Panda, "Models Vs pathogens: How conserved is the FtsZ in bacteria?," *Bioscience reports*, vol. 43, no. 2, 2023.
- [241] K. A. Hurley, T. M. Santos, G. M. Nepomuceno, V. Huynh, J. T. Shaw, and D. B. Weibel, "Targeting the Bacterial Division Protein FtsZ," *Journal of Medicinal Chemistry*, vol. 59, pp. 6975–6998, aug 2016.
- [242] J. Löwe and L. A. Amos, "Crystal structure of the bacterial cell-division protein FtsZ," *Nature 1998 391:6663*, vol. 391, pp. 203–206, jan 1998.
- [243] E. Nogales, K. H. Downing, L. A. Amos, and J. Löwe, "Tubulin and FtsZ form a distinct family of GTPases," *Nature Structural Biology 1998 5:6*, vol. 5, pp. 451–458, jun 1998.
- [244] C. Santana-Molina, D. del Saz-Navarro, and D. P. Devos, "Early origin and evolution of the FtsZ/tubulin protein family," *Frontiers in Microbiology*, vol. 13, p. 5275, jan 2023.
- [245] A. Mukherjee, K. Dai, and J. Lutkenhaus, "Escherichia coli cell division protein FtsZ is a guanine nucleotide binding protein," *Proceedings of the National Academy of Sciences of the United States of America*, vol. 90, no. 3, pp. 1053–1057, 1993.

- [246] X. Yang, Z. Lyu, A. Miguel, R. McQuillen, K. C. Huang, and J. Xiao, “GTPase activity-coupled treadmilling of the bacterial tubulin FtsZ organizes septal cell wall synthesis,” *Science*, vol. 355, pp. 744–747, feb 2017.
- [247] H. P. Erickson, D. W. Taylor, K. A. Taylor, and D. Bramhill, “Bacterial cell division protein FtsZ assembles into protofilament sheets and minirings, structural homologs of tubulin polymers.,” *Proceedings of the National Academy of Sciences*, vol. 93, pp. 519–523, jan 1996.
- [248] J. M. González, M. Vélez, M. Jiménez, C. Alfonso, P. Schuck, J. Mingorance, M. Vicente, A. P. Minton, and G. Rivas, “Cooperative behavior of Escherichia coli cell-division protein FtsZ assembly involves the preferential cyclization of long single-stranded fibrils,” *Proceedings of the National Academy of Sciences*, vol. 102, pp. 1895–1900, feb 2005.
- [249] J. Mingorance, M. Tadros, M. Vicente, J. M. González, G. Rivas, and M. Vélez, “Visualization of single Escherichia coli FtsZ filament dynamics with atomic force microscopy,” *Journal of Biological Chemistry*, vol. 280, pp. 20909–20914, may 2005.
- [250] A. K. Leung, E. Lucile White, L. J. Ross, R. C. Reynolds, J. A. Devito, and D. W. Borhani, “Structure of Mycobacterium tuberculosis FtsZ Reveals Unexpected, G Protein-like Conformational Switches,” *Journal of Molecular Biology*, vol. 342, pp. 953–970, sep 2004.
- [251] Y. Li, J. Hsin, L. Zhao, Y. Cheng, W. Shang, K. C. Huang, H. W. Wang, and S. Ye, “FtsZ protofilaments use a hinge-opening mechanism for constrictive force generation,” *Science*, vol. 341, pp. 392–395, jul 2013.
- [252] T. Matsui, X. Han, J. Yu, M. Yao, and I. Tanaka, “Structural change in FtsZ induced by Intermolecular interactions between Bound GTP and the T7 Loop,” *Journal of Biological Chemistry*, vol. 289, pp. 3501–3509, feb 2014.
- [253] M. A. Oliva, S. C. Cordell, and J. Löwe, “Structural insights into FtsZ protofilament formation,” *Nature Structural Molecular Biology* 2004 11:12, vol. 11, pp. 1243–1250, nov 2004.
- [254] M. A. Oliva, D. Trambaiolo, and J. Löwe, “Structural Insights into the Conformational Variability of FtsZ,” *Journal of Molecular Biology*, vol. 373, pp. 1229–1242, nov 2007.
- [255] P. J. Buske and P. A. Levin, “Extreme C terminus of bacterial cytoskeletal protein FtsZ plays fundamental role in assembly independent of modulatory proteins,” *Journal of Biological Chemistry*, vol. 287, pp. 10945–10957, mar 2012.
- [256] S. Du, K. Park, J. L. M. Microbiology, and undefined 2015, “Oligomerization of FtsZ converts the FtsZ tail motif (conserved carboxy-terminal peptide) into a multivalent ligand with high avidity for partners ZipA and SlmA,” *Wiley Online Library*, vol. 95, pp. 173–188, jan 2014.
- [257] J. Durand-Heredia, E. Rivkin, G. Fan, J. Morales, and A. Janakiraman, “Identi-

- fication of ZapD as a cell division factor that promotes the assembly of FtsZ in *Escherichia coli*,” *Journal of Bacteriology*, vol. 194, pp. 3189–3198, jun 2012.
- [258] Z. Hu, A. Mukherjee, S. Pichoff, and J. Lutkenhaus, “The MinC component of the division site selection system in *Escherichia coli* interacts with FtsZ to prevent polymerization,” *Proceedings of the National Academy of Sciences*, vol. 96, pp. 14819–14824, dec 1999.
- [259] L. Mosyak, Y. Zhang, E. Glasfeld, S. Haney, M. Stahl, J. Seehra, and W. S. Somers, “The bacterial cell-division protein ZipA and its interaction with an FtsZ fragment revealed by X-ray crystallography,” *EMBO Journal*, vol. 19, pp. 3179–3191, jul 2000.
- [260] P. Szwedziak, Q. Wang, S. M. Freund, and J. Löwe, “FtsA forms actin-like protofilaments,” *EMBO Journal*, vol. 31, pp. 2249–2260, may 2012.
- [261] P. Szwedziak and D. Ghosal, “FtsZ-ring architecture and its control by MinCD,” *Sub-Cellular Biochemistry*, vol. 84, pp. 213–244, 2017.
- [262] P. J. Buske, A. Mittal, R. V. Pappu, and P. A. Levin, “An intrinsically disordered linker plays a critical role in bacterial cell division,” *Seminars in cell developmental biology*, vol. 37, pp. 3–10, jan 2015.
- [263] P. J. Buske and P. A. Levin, “A flexible C-terminal linker is required for proper FtsZ assembly in vitro and cytokinetic ring formation in vivo,” *Molecular Microbiology*, vol. 89, pp. 249–263, jul 2013.
- [264] M. C. Cohan, A. M. Eddelbuettel, P. A. Levin, and R. V. Pappu, “Dissecting the Functional Contributions of the Intrinsically Disordered C-terminal Tail of *Bacillus subtilis* FtsZ,” *Journal of Molecular Biology*, vol. 432, pp. 3205–3221, may 2020.
- [265] T. Ohashi, C. A. Hale, P. A. De Boer, and H. P. Erickson, “Structural evidence that the P/Q domain of ZipA is an unstructured, flexible tether between the membrane and the C-terminal FtsZ-binding domain,” *Journal of Bacteriology*, vol. 184, no. 15, pp. 4313–4315, 2002.
- [266] K. Sundararajan, A. Vecchiarelli, K. Mizuuchi, and E. D. Goley, “Species- and C-terminal linker-dependent variations in the dynamic behavior of FtsZ on membranes in vitro,” *Molecular Microbiology*, vol. 110, pp. 47–63, oct 2018.
- [267] K. Sundararajan and E. D. Goley, “The intrinsically disordered C-terminal linker of FtsZ regulates protofilament dynamics and superstructure in vitro,” *Journal of Biological Chemistry*, vol. 292, pp. 20509–20527, dec 2017.
- [268] F. Guan, J. J. J. Yu, Y. Liu, Y. Li, X. H. Feng, K. C. Huang, Z. Chang, and S. Ye, “Lateral interactions between protofilaments of the bacterial tubulin homolog FtsZ are essential for cell division,” *eLife*, vol. 7, jun 2018.
- [269] Y. Chen and H. P. Erickson, “FtsZ filament dynamics at steady state: Subunit exchange with and without nucleotide hydrolysis,” *Biochemistry*, vol. 48, pp. 6664–6673, jul 2009.
- [270] J. Stricker, P. Maddox, E. D. Salmon, and H. P. Erickson, “Rapid assembly dynamics

- of the *Escherichia coli* FtsZ-ring demonstrated by fluorescence recovery after photo-bleaching,” *Proceedings of the National Academy of Sciences*, vol. 99, pp. 3171–3175, mar 2002.
- [271] J. Fujita, R. Harada, Y. Maeda, Y. Saito, E. Mizohata, T. Inoue, Y. Shigeta, and H. Matsumura, “Identification of the key interactions in structural transition pathway of FtsZ from *Staphylococcus aureus*,” *Journal of Structural Biology*, vol. 198, pp. 65–73, may 2017.
- [272] A. J. Martín-Galiano, R. M. Buey, M. Cabezas, and J. M. Andreu, “Mapping flexibility and the assembly switch of cell division protein FtsZ by computational and mutational approaches,” *Journal of Biological Chemistry*, vol. 285, pp. 22554–22565, jul 2010.
- [273] T. Matsui, J. Yamane, N. Mogi, H. Yamaguchi, H. Takemoto, M. Yao, and I. Tanaka, “Structural reorganization of the bacterial cell-division protein FtsZ from *Staphylococcus aureus*,” *Acta Crystallographica Section D: Biological Crystallography*, vol. 68, pp. 1175–1188, sep 2012.
- [274] J. M. Wagstaff, M. Tsim, M. A. Oliva, A. García-Sánchez, D. Kureisaite-Ciziene, J. M. Andreu, and J. Löwe, “A polymerization-associated structural switch in ftsz that enables treadmilling of model filaments,” *mBio*, vol. 8, may 2017.
- [275] M. A. Schumacher, T. Ohashi, L. Corbin, and H. P. Erickson, “High-resolution crystal structures of *Escherichia coli* FtsZ bound to GDP and GTP,” *urn:issn:2053-230X*, vol. 76, pp. 94–102, feb 2020.
- [276] P. GonzálezGonz, G. de Prado Salas, F. MartínMartín-GarcíaGarcía, B. JesúsJes, J. Mendieta, A. Alonso, M. Encinar, and P. Tarazona, “Torsion and curvature of FtsZ filaments †,” *Soft Matter*, 2014.
- [277] J. Hsin, A. Gopinathan, and K. C. Huang, “Nucleotide-dependent conformations of FtsZ dimers and force generation observed through molecular dynamics simulations,” *Proceedings of the National Academy of Sciences of the United States of America*, vol. 109, pp. 9432–9437, jun 2012.
- [278] D. Lv, J. Li, and S. Ye, “The Assembly Switch Mechanism of FtsZ Filament Revealed by All-Atom Molecular Dynamics Simulations and Coarse-Grained Models,” *Frontiers in Microbiology*, vol. 12, p. 667, mar 2021.
- [279] M. Osawa, H. P. Erickson Correspondence, H. P. Erickson, and H. Erickson@cellbio, “Probing the domain structure of FtsZ by random truncation and insertion of GFP,” *microbiologyresearch.org*, vol. 151, pp. 4033–4043, dec 2005.
- [280] S. D. Redick, J. Stricker, G. Briscoe, and H. P. Erickson, “Mutants of FtsZ targeting the protofilament interface: Effects on cell division and GTPase activity,” *Journal of Bacteriology*, vol. 187, pp. 2727–2736, apr 2005.
- [281] R. Ahijado-Guzmán, C. Alfonso, B. Reija, E. Salvarelli, J. Mingorance, S. Zorrilla, B. Monterroso, and G. Rivas, “Control by potassium of the size distribution of es-

- cherichia coli FtsZ polymers is independent of GTPase activity,” *Journal of Biological Chemistry*, vol. 288, no. 38, pp. 27358–27365, 2013.
- [282] D. J. Scheffers and A. J. Driessen, “The polymerization mechanism of the bacterial cell division protein FtsZ,” *FEBS Letters*, vol. 506, pp. 6–10, sep 2001.
- [283] G. Rivas, J. a. Fernández, and a. P. Minton, “Direct observation of the enhancement of noncooperative protein self-assembly by macromolecular crowding: indefinite linear self-association of bacterial cell division protein FtsZ.,” *Proceedings of the National Academy of Sciences of the United States of America*, vol. 98, pp. 3150–3155, 2001.
- [284] S. Arumugam, G. Chwastek, E. Fischer-Friedrich, C. Ehrig, I. Mönch, P. Schwille, I. Mönch, and P. Schwille, “Synthetic Biology Surface Topology Engineering of Membranes for the Mechanical Investigation of the Tubulin Homologue FtsZ**,” *Angewandte Chemie*, vol. 124, pp. 12028–12032, nov 2012.
- [285] S. Huecas, E. Ramírez-Aportela, A. Vergoñós, R. Núñez-Ramírez, O. Llorca, J. F. Díaz, D. Juan-Rodríguez, M. A. Oliva, P. Castellen, and J. M. Andreu, “Self-Organization of FtsZ Polymers in Solution Reveals Spacer Role of the Disordered C-Terminal Tail,” *Biophysical Journal*, vol. 113, pp. 1831–1844, oct 2017.
- [286] D. Popp, M. Iwasa, A. Narita, H. P. Erickson, and Y. Maéda, “FtsZ Condensates: An In Vitro Electron Microscopy Study,” *Biopolymers*, vol. 91, no. 5, pp. 340–350, 2009.
- [287] D. A. Ramirez-Diaz, D. A. García-Soriano, A. Raso, J. Mücksch, M. Feingold, G. Rivas, and P. Schwille, “Treadmilling analysis reveals new insights into dynamic FtsZ ring architecture,” *PLOS Biology*, vol. 16, p. e2004845, may 2018.
- [288] A. W. Bisson-Filho, Y. P. Hsu, G. R. Squyres, E. Kuru, F. Wu, C. Jukes, Y. Sun, C. Dekker, S. Holden, M. S. VanNieuwenhze, Y. V. Brun, and E. C. Garner, “Treadmilling by FtsZ filaments drives peptidoglycan synthesis and bacterial cell division,” *Science*, vol. 355, pp. 739–743, feb 2017.
- [289] S. G. Addinall and J. Lutkenhaus, “FtsA is localized to the septum in an FtsZ-dependent manner,” *Journal of Bacteriology*, vol. 178, no. 24, pp. 7167–7172, 1996.
- [290] C. A. Hale and P. A. J. De Boer, “Direct binding of FtsZ to ZipA, an essential component of the septal ring structure that mediates cell division in *E. coli*,” *Cell*, vol. 88, pp. 175–185, jan 1997.
- [291] M. Osawa, D. E. Anderson, and H. P. Erickson, “Reconstitution of contractile FtsZ rings in liposomes,” *Science*, vol. 320, pp. 792–794, may 2008.
- [292] M. Krupka, M. Sobrinos-Sanguino, M. Jiménez, G. Rivas, and W. Margolin, “*Escherichia coli* ZipA organizes FtsZ polymers into dynamic ring-like protofilament structures,” *mBio*, vol. 9, may 2018.
- [293] P. Mateos-Gil, A. Tsortos, M. Veandlez, and E. Gizeli, “Monitoring structural changes in intrinsically disordered proteins using QCM-D: application to the bac-

- terial cell division protein ZipA,” *Chemical Communications*, vol. 52, pp. 6541–6544, may 2016.
- [294] C. C. Boutte, R. Srinivasan, P. Sass, and M. Vélez, “How Does the Spatial Confinement of FtsZ to a Membrane Surface Affect Its Polymerization Properties and Function?,” *Frontiers in microbiology*, vol. 13, p. 757711, may 2022.
- [295] M. Encinar, A. V. Kralicek, A. Martos, M. Krupka, S. Cid, A. Alonso, A. I. Rico, M. Jiménez, and M. Vélez, “Polymorphism of FtsZ filaments on lipid surfaces: Role of monomer orientation,” *Langmuir*, vol. 29, pp. 9436–9446, jul 2013.
- [296] P. Mateos-Gil, A. Paez, I. Hörger, G. Rivas, M. Vicente, P. Tarazona, and M. Vélez, “Depolymerization dynamics of individual filaments of bacterial cytoskeletal protein FtsZ,” *Proceedings of the National Academy of Sciences of the United States of America*, vol. 109, pp. 8133–8138, may 2012.
- [297] I. Márquez, G. Díaz-Haro, and M. Vélez, “Surface Orientation and Binding Strength Modulate Shape of FtsZ on Lipid Surfaces,” *International Journal of Molecular Sciences 2019, Vol. 20, Page 2545*, vol. 20, p. 2545, may 2019.
- [298] P. Mateos-Gil, P. Tarazona, M. V. Elez, and M. Vélez, “Bacterial cell division: modeling FtsZ assembly and force generation from single filament experimental data,” *FEMS Microbiology Reviews*, vol. 039, pp. 73–87, jan 2019.
- [299] A. Paez, P. Tarazona, P. Mateos-Gil, and M. Vélez, “Self-organization of curved living polymers : FtsZ protein filaments,” *Soft Matter*, vol. 5, pp. 2625–2637, jun 2009.
- [300] A. Paez, P. Mateos-Gil, I. Hörger, J. Mingorance, G. Rivas, M. Vicente, M. Vélez, and P. Tarazona, “Simple modeling of FtsZ polymers on flat and curved surfaces: correlation with experimental in vitro observations,” *PMC Biophysics 2009 2:1*, vol. 2, pp. 1–16, oct 2009.
- [301] P. Caldas, M. López-Peigrín, D. J. G. Pearce, N. Burak Budanur, J. Brugués, M. Loose, N. B. Budanur, J. Brugués, and M. Loose, “Cooperative ordering of treadmill filaments in cytoskeletal networks of FtsZ and its crosslinker ZapA,” *Nature Communications 2019 10:1*, vol. 10, pp. 1–13, dec 2019.
- [302] A. Martos, A. Raso, M. Jiménez, Z. Petrášek, G. Rivas, and P. Schwille, “FtsZ polymers tethered to the membrane by ZipA are susceptible to spatial regulation by min waves,” *Biophysical Journal*, vol. 108, pp. 2371–2383, may 2015.
- [303] B. Ramm, P. Glock, J. Mücksch, P. Blumhardt, D. A. García-Soriano, M. Heymann, and P. Schwille, “The MinDE system is a generic spatial cue for membrane protein distribution in vitro,” *Nature Communications*, 2018.
- [304] E. J. Cabré, B. Monterroso, C. Alfonso, A. Sánchez-Gorostiaga, B. Reija, M. Jiménez, M. Vicente, S. Zorrilla, and G. Rivas, “The nucleoid occlusion SlmA protein accelerates the disassembly of the FtsZ protein polymers without affecting their GTPase activity,” *PLoS ONE*, vol. 10, may 2015.

- [305] A. J. Perez, Y. Cesbron, S. L. Shaw, J. B. Villicana, H. C. T. Tsui, M. J. Boersma, Z. A. Ye, Y. Tovpeko, C. Dekker, S. Holden, and M. E. Winkler, “Movement dynamics of divisome proteins and PBP2x: FtsW in cells of *Streptococcus pneumoniae*,” *Proceedings of the National Academy of Sciences of the United States of America*, vol. 116, pp. 3211–3220, feb 2019.
- [306] K. D. Whitley, C. Jukes, N. Tregidgo, E. Karinou, P. Almada, Y. Cesbron, R. Henriques, C. Dekker, and S. Holden, “FtsZ treadmilling is essential for Z-ring condensation and septal constriction initiation in *Bacillus subtilis* cell division,” *Nature Communications*, vol. 12, no. 1, pp. 1–13, 2021.
- [307] L. C. Corbin and H. P. Erickson, “A Unified Model for Treadmilling and Nucleation of Single-Stranded FtsZ Protofilaments,” *Biophysical Journal*, vol. 119, pp. 792–805, aug 2020.
- [308] M. Osawa and H. P. Erickson, “Liposome division by a simple bacterial division machinery,” *Proceedings of the National Academy of Sciences*, vol. 110, no. 27, 2013.
- [309] S. Pichoff and J. Lutkenhaus, “Tethering the Z ring to the membrane through a conserved membrane targeting sequence in FtsA,” *Molecular Microbiology*, vol. 55, pp. 1722–1734, mar 2005.
- [310] S. Pichoff and J. Lutkenhaus, “Unique and overlapping roles for ZipA and FtsA in septal ring assembly in *Escherichia coli*,” *The EMBO Journal*, vol. 21, pp. 685–693, feb 2002.
- [311] M. Krupka, V. W. Rowlett, D. Morado, H. Vitrac, K. Schoenemann, J. Liu, and W. Margolin, “*Escherichia coli* FtsA forms lipid-bound minirings that antagonize lateral interactions between FtsZ protofilaments,” *Nature Communications 2017 8:1*, vol. 8, pp. 1–12, jul 2017.
- [312] T. Nierhaus, S. H. McLaughlin, F. Bürmann, D. Kureisaite-Ciziene, S. L. Maslen, J. M. Skehel, C. W. Yu, S. M. Freund, L. F. Funke, J. W. Chin, and J. Löwe, “Bacterial divisome protein FtsA forms curved antiparallel double filaments when binding to FtsN,” *Nature Microbiology 2022 7:10*, vol. 7, pp. 1686–1701, sep 2022.
- [313] J. Conti, M. G. Viola, and J. L. Camberg, “FtsA reshapes membrane architecture and remodels the Z-ring in *Escherichia coli*,” *Molecular microbiology*, vol. 107, pp. 558–576, feb 2018.
- [314] B. Geissler, D. Elraheb, and W. Margolin, “A gain-of-function mutation in ftsA bypasses the requirement for the essential cell division gene zipA in *Escherichia coli*,” *Proceedings of the National Academy of Sciences of the United States of America*, vol. 100, pp. 4197–4202, apr 2003.
- [315] K. K. Busiek, J. M. Eraso, Y. Wang, and W. Margolin, “The Early Divisome Protein FtsA Interacts Directly through Its 1c: Subdomain with the Cytoplasmic Domain of the Late Divisome: Protein FtsN,” *Journal of Bacteriology*, vol. 194, pp. 1989–2000, apr 2012.

- [316] P. Radler, N. Baranova, P. Caldas, C. Sommer, M. López-Peigrín, D. Michalik, and M. Loose, “In vitro reconstitution of Escherichia coli divisome activation,” *Nature Communications* 2022 13:1, vol. 13, pp. 1–15, may 2022.
- [317] K. T. Park, S. Pichoff, S. Du, and J. Lutkenhaus, “FtsA acts through FtsW to promote cell wall synthesis during cell division in Escherichia coli,” *Proceedings of the National Academy of Sciences of the United States of America*, vol. 118, aug 2021.
- [318] N. Baranova, P. Radler, V. M. Hernández-Rocamora, C. Alfonso, M. López-Peigrín, G. Rivas, W. Vollmer, and M. Loose, “Diffusion and capture permits dynamic coupling between treadmilling FtsZ filaments and cell division proteins,” 2020.
- [319] T. A. Cameron, D. E. Vega, C. Yu, H. Xiao, and W. Margolin, “ZipA Uses a Two-Pronged FtsZ-Binding Mechanism Necessary for Cell Division,” *mBio*, vol. 12, dec 2021.
- [320] S. Rueda, M. Vicente, and J. Mingorance, “Concentration and assembly of the division ring proteins FtsZ, FtsA, and ZipA during the Escherichia coli cell cycle,” *Journal of Bacteriology*, vol. 185, pp. 3344–3351, jun 2003.
- [321] M. Pazos, P. Natale, W. Margolin, and M. Vicente, “Interactions among the early Escherichia coli divisome proteins revealed by bimolecular fluorescence complementation,” *Environmental Microbiology*, vol. 15, pp. 3282–3291, dec 2013.
- [322] D. E. Vega and W. Margolin, “Direct interaction between the two Z ring membrane anchors FtsA and ZipA,” *Journal of Bacteriology*, vol. 201, feb 2019.
- [323] S. Pichoff, B. Shen, B. Sullivan, and J. Lutkenhaus, “FtsA mutants impaired for self-interaction bypass ZipA suggesting a model in which FtsA’s self-interaction competes with its ability to recruit downstream division proteins,” *Molecular Microbiology*, vol. 83, pp. 151–167, jan 2012.
- [324] K. M. Schoenemann, M. Krupka, V. W. Rowlett, S. L. Distelhorst, B. Hu, and W. Margolin, “Gain-of-function variants of FtsA form diverse oligomeric structures on lipids and enhance FtsZ protofilament bundling,” *Molecular Microbiology*, vol. 109, pp. 676–693, sep 2018.
- [325] E. J. Cabré, A. Sánchez-Gorostiaga, P. Carrara, N. Roperro, M. Casanova, P. Palacios, P. Stano, M. Jiménez, G. Rivas, and M. Vicente, “Bacterial division proteins FtsZ and ZipA induce vesicle shrinkage and cell membrane invagination,” *The Journal of biological chemistry*, vol. 288, pp. 26625–26634, sep 2013.
- [326] A. Martos, C. Alfonso, P. López-Navajas, R. Ahijado-Guzmán, J. Mingorance, A. P. Minton, and G. Rivas, “Characterization of self-association and heteroassociation of bacterial cell division proteins FtsZ and ZipA in solution by composition gradient-static light scattering,” *Biochemistry*, vol. 49, pp. 10780–10787, dec 2010.
- [327] L. D. Renner and D. B. Weibel, “MinD and MinE interact with anionic phospholipids and regulate division plane formation in Escherichia coli,” *Journal of Biological*

- Chemistry*, vol. 287, pp. 38835–38844, nov 2012.
- [328] D. E. Anderson, F. J. Gueiros-Filho, and H. P. Erickson, “Assembly dynamics of FtsZ rings in *Bacillus subtilis* and *Escherichia coli* and effects of FtsZ-regulating proteins,” *Journal of Bacteriology*, vol. 186, pp. 5775–5781, sep 2004.
- [329] D. A. García-Soriano, T. Heermann, A. Raso, G. Rivas, and P. Schwille, “The speed of FtsZ treadmilling is tightly regulated by membrane binding,” *Scientific Reports* 2020 10:1, vol. 10, pp. 1–9, jun 2020.
- [330] H. Jia, L. Kai, M. Heymann, D. A. García-Soriano, T. Härtel, and P. Schwille, “Light-Induced Printing of Protein Structures on Membranes in Vitro,” *Nano Letters*, vol. 18, pp. 7133–7140, nov 2018.
- [331] H. Sun, H. Jia, D. A. Ramirez-Diaz, N. Budisa, and P. Schwille, “Fine-Tuning Protein Self-Organization by Orthogonal Chemo-Optogenetic Tools,” *Angewandte Chemie*, vol. 133, pp. 4551–4556, feb 2021.
- [332] H. Sun, H. Jia, O. Kendall, J. Dragelj, V. Kubyshkin, T. Baumann, M. A. Mroginski, P. Schwille, and N. Budisa, “Halogenation of tyrosine perturbs large-scale protein self-organization,” *Nature Communications* 2022 13:1, vol. 13, pp. 1–13, aug 2022.
- [333] P. Szwedziak, Q. Wang, T. A. M. Bharat, M. Tsim, and J. Löwe, “Architecture of the ring formed by the tubulin homologue FtsZ in bacterial cell division,” *eLife*, vol. 3, p. e04601, 2014.
- [334] S. L. Milam, M. Osawa, and H. P. Erickson, “Negative-Stain Electron Microscopy of Inside-Out FtsZ Rings Reconstituted on Artificial Membrane Tubules Show Ribbons of Protofilaments,” *Biophysical Journal*, vol. 103, pp. 59–68, jul 2012.
- [335] B. Ramm, T. Heermann, and P. Schwille, “The *E. coli* MinCDE system in the regulation of protein patterns and gradients,” *Cellular and Molecular Life Sciences*, vol. 76, pp. 4245–4273, 2019.
- [336] Z. Hu and J. Lutkenhaus, “Topological regulation of cell division in *Escherichia coli* involves rapid pole to pole oscillation of the division inhibitor MinC under the control of MinD and MinE,” *Molecular Microbiology*, vol. 34, pp. 82–90, oct 1999.
- [337] J. Halatek, F. Brauns, and E. Frey, “Self-organization principles of intracellular pattern formation,” *Philosophical Transactions of the Royal Society B: Biological Sciences*, vol. 373, no. 1747, 2018.
- [338] L. Wettmann and K. Kruse, “The min-protein oscillations in *Escherichia coli*: An example of self-organized cellular protein waves,” 2018.
- [339] H. C. Lim, I. V. Surovtsev, B. G. Beltran, F. Huang, J. Bewersdorf, and C. Jacobs-Wagner, “Evidence for a DNA-relay mechanism in ParABS-mediated chromosome segregation,” *eLife*, 2014.
- [340] F. Wu, B. G. Van Schie, J. E. Keymer, and C. Dekker, “Symmetry and scale orient Min protein patterns in shaped bacterial sculptures,” *Nature Nanotechnology*, 2015.
- [341] B. Ramm, A. Goychuk, A. Khmelinskaia, P. Blumhardt, H. Eto, K. A. Ganzinger, E. Frey, and P. Schwille, “A diffusiphoretic mechanism for ATP-driven transport

- without motor proteins,” *Nature Physics* 2021 17:7, vol. 17, pp. 850–858, apr 2021.
- [342] L. L. Lackner, D. M. Raskin, and P. A. De Boer, “ATP-dependent interactions between *Escherichia coli* Min proteins and the phospholipid membrane in vitro,” *Journal of Bacteriology*, 2003.
- [343] E. Mileykovskaya, I. Fishov, X. Fu, B. D. Corbin, W. Margolin, and W. Dowhan, “Effects of phospholipid composition on MinD-membrane interactions in vitro and in vivo,” *Journal of Biological Chemistry*, 2003.
- [344] A. Miyagi, B. Ramm, P. Schwille, and S. Scheuring, “High-Speed Atomic Force Microscopy Reveals the Inner Workings of the MinDE Protein Oscillator,” *Nano Letters*, 2018.
- [345] T. Heermann, B. Ramm, S. Glaser, and P. Schwille, “Local Self-Enhancement of MinD Membrane Binding in Min Protein Pattern Formation,” *Journal of Molecular Biology*, 2020.
- [346] M. Loose, E. Fischer-Friedrich, C. Herold, K. Kruse, and P. Schwille, “Min protein patterns emerge from rapid rebinding and membrane interaction of MinE,” *Nature Structural and Molecular Biology*, 2011.
- [347] S. Pichoff, B. Vollrath, C. Touriol, and J. Ouché, “Deletion analysis of gene *minE* which encodes the topological specificity factor of cell division in *Escherichia coli*,” *Molecular Microbiology*, vol. 18, no. 2, pp. 321–329, 1995.
- [348] C. R. Zhao, P. A. De Boer, and L. I. Rothfield, “Proper placement of the *Escherichia coli* division site requires two functions that are associated with different domains of the MinE protein,” *Proceedings of the National Academy of Sciences*, vol. 92, pp. 4313–4317, may 1995.
- [349] C. W. Hsieh, T. Y. Lin, H. M. Lai, C. C. Lin, T. S. Hsieh, and Y. L. Shih, “Direct MinE-membrane interaction contributes to the proper localization of MinDE in *E. coli*,” *Molecular Microbiology*, vol. 75, pp. 499–512, jan 2010.
- [350] Y. L. Shih, K. F. Huang, H. M. Lai, J. H. Liao, C. S. Lee, C. M. Chang, H. M. Mak, C. W. Hsieh, and C. C. Lin, “The N-terminal Amphipathic Helix of the topological specificity factor *minE* is associated with shaping membrane curvature,” *PLoS ONE*, vol. 6, no. 6, 2011.
- [351] K. T. Park, W. Wu, S. Lovell, and J. Lutkenhaus, “Mechanism of the asymmetric activation of the MinD ATPase by MinE,” *Molecular Microbiology*, 2012.
- [352] K. T. Park, W. Wu, K. P. Battaile, S. Lovell, T. Holyoak, and J. Lutkenhaus, “The min oscillator uses MinD-dependent conformational changes in MinE to spatially regulate cytokinesis,” *Cell*, vol. 146, pp. 396–407, aug 2011.
- [353] S. C. Cordell, R. E. Anderson, and J. Löwe, “Crystal structure of the bacterial cell division inhibitor MinC,” *EMBO Journal*, vol. 20, pp. 2454–2461, may 2001.
- [354] Z. Hu and J. Lutkenhaus, “Analysis of MinC reveals two independent domains involved in interaction with MinD and FtsZ,” *Journal of Bacteriology*, vol. 182,

- pp. 3965–3971, jul 2000.
- [355] L. Ma, G. King, L. R. M. Microbiology, and undefined 2004, “Positioning of the MinE binding site on the MinD surface suggests a plausible mechanism for activation of the Escherichia coli MinD ATPase during division site,” *Wiley Online Library*, vol. 54, pp. 99–108, oct 2004.
- [356] J. E. Walker, M. Saraste, M. J. Runswick, and N. J. Gay, “Distantly related sequences in the alpha- and beta-subunits of ATP synthase, myosin, kinases and other ATP-requiring enzymes and a common nucleotide binding fold.,” *The EMBO journal*, vol. 1, no. 8, pp. 945–951, 1982.
- [357] S. Yang, Q. Shen, S. Wang, C. Song, Z. Lei, S. Han, X. Zhang, J. Zheng, and Z. Jia, “Characterization of C-terminal structure of MinC and its implication in evolution of bacterial cell division,” *Scientific Reports*, vol. 7, dec 2017.
- [358] Z. Hu, C. Saez, and J. Lutkenhaus, “Recruitment of MinC, an inhibitor of Z-ring formation, to the membrane in Escherichia coli: Role of minD and minE,” *Journal of Bacteriology*, vol. 185, pp. 196–203, jan 2003.
- [359] V. M. Hernández-Rocamora, C. García-Montañés, B. Reija, B. Monterroso, W. Margolin, C. Alfonso, S. Zorrilla, and G. Rivas, “MinC protein shortens FtsZ protofilaments by preferentially interacting with GDP-bound subunits,” *Journal of Biological Chemistry*, vol. 288, pp. 24625–24635, aug 2013.
- [360] B. Shen, J. L. M. Microbiology, and undefined 2010, “Examination of the interaction between FtsZ and MinCN in E. coli suggests how MinC disrupts Z rings,” *Wiley Online Library*, vol. 75, no. 5, pp. 1285–1298, 2010.
- [361] D. M. Raskin and P. A. J. de Boer, “MinDE-Dependent Pole-to-Pole Oscillation of Division Inhibitor MinC in Escherichia coli,” *Journal of Bacteriology*, 1999.
- [362] P. Glock, B. Ramm, T. Heermann, S. Kretschmer, J. Schweizer, J. Mücksch, G. Alagöz, and P. Schwille, “Stationary Patterns in a Two-Protein Reaction-Diffusion System,” *ACS Synthetic Biology*, 2019.
- [363] M. Loose, E. Fischer-Friedrich, J. Ries, K. Kruse, and P. Schwille, “Spatial regulators for bacterial cell division self-organize into surface waves in vitro,” *Science*, 2008.
- [364] T. Litschel, B. Ramm, R. Maas, M. Heymann, and P. Schwille, “Beating Vesicles: Encapsulated Protein Oscillations Cause Dynamic Membrane Deformations,” *Angewandte Chemie - International Edition*, 2018.
- [365] S. Kohyama, K. Fujiwara, N. Yoshinaga, and N. Doi, “Conformational equilibrium of MinE regulates the allowable concentration ranges of a protein wave for cell division,” *Nanoscale*, 2020.
- [366] S. Kohyama, N. Yoshinaga, M. Yanagisawa, K. Fujiwara, and N. Doi, “Cell-sized confinement controls generation and stability of a protein wave for spatiotemporal regulation in cells,” *eLife*, vol. 8, no. 44591, 2019.
- [367] K. Zieske and P. Schwille, “Reconstitution of self-organizing protein gradients as

- spatial cues in cell-free systems,” *eLife*, vol. 3, pp. 1–19, 2014.
- [368] E. Godino, A. Doerr, and C. Danelon, “Min waves without MinC can pattern FtsA-anchored FtsZ filaments on model membranes,” *Communications biology*, vol. 5, dec 2022.
- [369] G. R. Squyres, M. J. olmes, M. J. olmes, S. R. Barger, B. R. Pennycook, J. Ryan, V. T. Yan, and E. C. Garner, “Single-molecule imaging reveals that Z-ring condensation is essential for cell division in *Bacillus subtilis*,” *Nature Microbiology*, vol. 6, no. 5, pp. 553–562, 2021.
- [370] M. G. Viola, C. J. Labreck, J. Conti, and J. L. Camberg, “Proteolysis-dependent remodeling of the tubulin homolog FtsZ at the division septum in *Escherichia coli*,” *PLoS ONE*, vol. 12, jan 2017.
- [371] S. Wang and N. S. Wingreen, “Cell Shape Can Mediate the Spatial Organization of the Bacterial Cytoskeleton,” *Biophysical Journal*, vol. 104, p. 642a, jan 2013.
- [372] J. Buss, C. Coltharp, G. Shtengel, X. Yang, H. Hess, and J. Xiao, “A Multi-layered Protein Network Stabilizes the *Escherichia coli* FtsZ-ring and Modulates Constriction Dynamics,” *PLoS Genetics*, vol. 11, apr 2015.
- [373] J. M. Durand-Heredia, H. H. Yu, S. De Carlo, C. F. Lesser, and A. Janakiraman, “Identification and characterization of ZapC, a stabilizer of the FtsZ ring in *Escherichia coli*,” *Journal of Bacteriology*, vol. 193, pp. 1405–1413, mar 2011.
- [374] C. A. Hale, D. Shiomi, B. Liu, T. G. Bernhardt, W. Margolin, H. Niki, and P. A. J. De Boer, “Identification of *Escherichia coli* ZapC (YcbW) as a component of the division apparatus that binds and bundles FtsZ polymers,” *Journal of Bacteriology*, vol. 193, pp. 1393–1404, mar 2011.
- [375] G. Ebersbach, E. Galli, J. Møller-Jensen, J. Löwe, and K. Gerdes, “Novel coiled-coil cell division factor ZapB stimulates Z ring assembly and cell division,” *Molecular Microbiology*, vol. 68, pp. 720–735, may 2008.
- [376] F. J. Gueiros-Filho and R. Losick, “A widely conserved bacterial cell division protein that promotes assembly of the tubulin-like protein FtsZ,” *Genes Development*, vol. 16, pp. 2544–2556, oct 2002.
- [377] H. H. Low, M. C. Moncrieffe, and J. Löwe, “The crystal structure of ZapA and its modulation of FtsZ polymerisation,” *Journal of Molecular Biology*, vol. 341, pp. 839–852, aug 2004.
- [378] T. Mohammadi, G. E. J. Ploeger, J. Verheul, A. D. Comvalius, A. Martos, C. Alfonso, J. Van Marle, G. Rivas, T. Den Blaauwen, . Germ, A. Rivas, and T. Den Blaauwen, “The GTPase activity of *Escherichia coli* FtsZ determines the magnitude of the FtsZ polymer bundling by ZapA in vitro,” *Biochemistry*, vol. 48, pp. 11056–11066, nov 2009.
- [379] M. A. Schumacher, W. Zeng, K. H. Huang, L. Tchorzewski, and A. Janakiraman, “Structural and functional analyses reveal insights into the molecular properties of

- the Escherichia coli Z ring stabilizing protein, ZapC,” *Journal of Biological Chemistry*, vol. 291, pp. 2485–2498, jan 2016.
- [380] E. J. Roach, C. Wroblewski, L. Seidel, A. M. Berezuk, D. Brewer, M. S. Kimber, and C. M. Khursigara, “Structure and mutational analyses of Escherichia coli ZapD reveal charged residues involved in FtsZ filament bundling,” *Journal of Bacteriology*, vol. 198, pp. 1683–1693, jun 2016.
- [381] M. A. Schumacher, K. H. Huang, W. Zeng, and A. Janakiraman, “Structure of the z ring-associated protein, zapd, bound to the c-terminal domain of the tubulin-like protein, ftsz, suggests mechanism of z ring stabilization through ftsz cross-linking,” *Journal of Biological Chemistry*, vol. 292, pp. 3740–3750, mar 2017.
- [382] J. A. Buss, N. T. Peters, J. Xiao, and T. G. Bernhardt, “ZapA and ZapB form an FtsZ-independent structure at midcell,” *Molecular Microbiology*, vol. 00, pp. 652–663, may 2017.
- [383] R. Mercier, M. A. Petit, S. Schbath, S. Robin, M. El Karoui, F. Boccard, and O. Espéli, “The MatP/matS Site-Specific System Organizes the Terminus Region of the E. coli Chromosome into a Macrodomain,” *Cell*, vol. 135, pp. 475–485, oct 2008.
- [384] H. P. Erickson, D. E. Anderson, and M. Osawa, “FtsZ in Bacterial Cytokinesis: Cytoskeleton and Force Generator All in One,” *Microbiology and Molecular Biology Reviews*, vol. 74, no. 4, pp. 504–528, 2010.
- [385] A. Mukherjee and J. Lutkenhaus, “Analysis of FtsZ assembly by light scattering and determination of the role of divalent metal cations,” *Journal of bacteriology*, vol. 181, no. 3, pp. 823–832, 1999.
- [386] K. A. Gardner, D. A. Moore, and H. P. Erickson, “The C-terminal linker of Escherichia coli FtsZ functions as an intrinsically disordered peptide,” *Molecular Microbiology*, vol. 89, pp. 264–275, jul 2013.
- [387] S. Du and J. Lutkenhaus, “At the Heart of Bacterial Cytokinesis: The Z Ring,” *Trends in Microbiology*, vol. 27, pp. 781–791, sep 2019.
- [388] C.-M. Koppelman, Mirjam, E. G. Aarsman, J. Postmus, E. Pas, A. O. Muijsers, D.-J. Scheffers, N. Nanninga, and T. Den Blaauwen, “R174 of Escherichia coli FtsZ is involved in membrane interaction and protofilament bundling, and is essential for cell division,” *Wiley Online Library*, vol. 51, pp. 645–657, feb 2004.
- [389] Z. Li, M. J. Trimble, Y. V. Brun, and G. J. Jensen, “The structure of FtsZ filaments in vivo suggests a force-generating role in cell division,” *EMBO Journal*, vol. 26, pp. 4694–4708, nov 2007.
- [390] G. Fu, T. Huang, J. Buss, C. Coltharp, Z. Hensel, and J. Xiao, “In Vivo Structure of the E. coli FtsZ-ring Revealed by Photoactivated Localization Microscopy (PALM),” *PLOS ONE*, vol. 5, no. 9, p. e12680, 2010.
- [391] Z. Lyu, C. Coltharp, X. Yang, and J. Xiao, “Influence of FtsZ GTPase activity and concentration on nanoscale Z-ring structure in vivo revealed by three-dimensional

- Superresolution imaging,” *Biopolymers*, vol. 105, pp. 725–734, oct 2016.
- [392] S. G. Addinall, B. Erfei, and J. Lutkenhaus, “FtsZ ring formation in fts mutants,” *Journal of Bacteriology*, vol. 178, no. 13, pp. 3877–3884, 1996.
- [393] S. G. Addinall and J. Lutkenhaus, “FtsZ-spirals and -arcs determine the shape of the invaginating septa in some mutants of *Escherichia coli*,” *Molecular Microbiology*, vol. 22, pp. 231–237, oct 1996.
- [394] V. W. Rowlett and W. Margolin, “3D-SIM Super-resolution of FtsZ and Its Membrane Tethers in *Escherichia coli* Cells,” *Biophysical Journal*, vol. 107, pp. L17–L20, oct 2014.
- [395] L. T. Nguyen, C. M. Oikonomou, and G. J. Jensen, “Simulations of Proposed Mechanisms of FtsZ-Driven Cell Constriction,” *Journal of Bacteriology*, vol. 203, 2021.
- [396] C. Coltharp, J. Buss, T. M. Plumer, and J. Xiao, “Defining the rate-limiting processes of bacterial cytokinesis,” *Proceedings of the National Academy of Sciences of the United States of America*, vol. 113, pp. E1044–E1053, feb 2016.
- [397] S. J. Holden, T. Pengo, K. L. Meibom, C. F. Fernandez, J. Collier, and S. Manley, “High throughput 3D super-resolution microscopy reveals *Caulobacter crescentus* in vivo Z-ring organization,” *Proceedings of the National Academy of Sciences of the United States of America*, vol. 111, pp. 4566–4571, mar 2014.
- [398] J. W. McCausland, X. Yang, G. R. Squyres, Z. Lyu, K. E. Bruce, M. M. Lamanna, B. Söderström, E. C. Garner, M. E. Winkler, J. Xiao, J. Liu, B. So, E. C. Garner, M. E. Winkler, J. Xiao, J. Liu, B. Söderström, E. C. Garner, M. E. Winkler, J. Xiao, and J. Liu, “Treadmilling FtsZ polymers drive the directional movement of sPG-synthesis enzymes via a Brownian ratchet mechanism,” *Nature Communications*, vol. 12, dec 2021.
- [399] H. A. Arjes, B. Lai, E. Emelue, A. Steinbach, and P. A. Levin, “Mutations in the bacterial cell division protein FtsZ highlight the role of GTP binding and longitudinal subunit interactions in assembly and function,” *BMC Microbiology*, vol. 15, no. 1, 2015.
- [400] A. Mukherjee, C. Saez, and J. Lutkenhaus, “Assembly of an FtsZ mutant deficient in GTPase activity has implications for FtsZ assembly and the role of the Z ring in cell division,” *Journal of Bacteriology*, vol. 183, pp. 7190–7197, dec 2001.
- [401] D. RayChaudhuri and J. T. Park, “*Escherichia coli* cell-division gene ftsZ encodes a novel GTP-binding protein,” *Nature*, vol. 359, no. 6392, pp. 251–254, 1992.
- [402] E. Bi and J. Lutkenhaus, “Cell division inhibitors Sula and MinCD prevent formation of the FtsZ ring,” *Journal of Bacteriology*, vol. 175, no. 4, pp. 1118–1125, 1993.
- [403] J. Xiao and E. D. Goley, “Redefining the roles of the FtsZ-ring in bacterial cytokinesis,” *Current Opinion in Microbiology*, vol. 34, pp. 90–96, dec 2016.
- [404] S. Holden, “Probing the mechanistic principles of bacterial cell division with super-resolution microscopy,” *Current Opinion in Microbiology*, vol. 43, pp. 84–91, jun

- 2018.
- [405] H. P. Erickson and M. Osawa, “FtsZ Constriction Force-Curved Protofilaments Bending Membranes,” *Subcellular Biochemistry*, vol. 84, 2017.
 - [406] C. Lu, M. Reedy, and H. P. Erickson, “Straight and curved conformations of FtsZ are regulated by GTP hydrolysis,” *Journal of Bacteriology*, vol. 182, no. 1, pp. 164–170, 2000.
 - [407] L. Romberg, M. Simon, and H. P. Erickson, “Polymerization of FtsZ, a Bacterial Homolog of Tubulin,” *Journal of Biological Chemistry*, vol. 276, pp. 11743–11753, apr 2001.
 - [408] B. Ghosh and A. Sain, “Origin of contractile force during cell division of bacteria,” *Physical Review Letters*, vol. 101, p. 178101, oct 2008.
 - [409] I. Hörger, E. Velasco, G. Rivas, M. Vélez, and P. Tarazona, “FtsZ Bacterial Cytoskeletal Polymers on Curved Surfaces: The Importance of Lateral Interactions,” *Biophysical Journal*, vol. 94, pp. L81–L83, jun 2008.
 - [410] I. V. Surovtsev, J. J. Morgan, and P. A. Lindahl, “Kinetic Modeling of the Assembly, Dynamic Steady State, and Contraction of the FtsZ Ring in Prokaryotic Cytokinesis,” *PLOS Computational Biology*, vol. 4, no. 7, p. e1000102, 2008.
 - [411] G. Lan, B. R. Daniels, T. M. Dobrowsky, D. Wirtz, and S. X. Sun, “Condensation of FtsZ filaments can drive bacterial cell division,” *Proceedings of the National Academy of Sciences of the United States of America*, vol. 106, pp. 121–126, jan 2009.
 - [412] D. J. Turner, I. Portman, T. R. Dafforn, A. Rodger, D. I. Roper, C. J. Smith, and M. S. Turner, “The mechanics of FtsZ fibers,” *Biophysical Journal*, vol. 102, pp. 731–738, feb 2012.
 - [413] Q. Yao, A. I. Jewett, Y.-W. Chang, C. M. Oikonomou, M. Beeby, C. V. Iancu, A. Briegel, D. Ghosal, and G. J. Jensen, “Short FtsZ filaments can drive asymmetric cell envelope constriction at the onset of bacterial cytokinesis,” *The EMBO Journal*, vol. 36, pp. 1577–1589, jun 2017.
 - [414] C. Lu and H. P. Erickson, “The straight and curved conformation of FtsZ protofilaments-evidence for rapid exchange of GTP into the curved protofilament,” *Cell Structure and Function*, vol. 24, no. 5, pp. 285–290, 1999.
 - [415] T. Lappchen, V. A. Pinas, A. F. Hartog, G. J. Koomen, C. Schaffner-Barbero, J. M. Andreu, D. Trambaiolo, J. Löwe, A. Juhem, A. V. Popov, and T. den Blaauwen, “Probing FtsZ and Tubulin with C8-Substituted GTP Analogs Reveals Differences in Their Nucleotide Binding Sites,” *Chemistry Biology*, vol. 15, pp. 189–199, feb 2008.
 - [416] H. Jia, T. Litschel, M. Heymann, H. Eto, H. G. Franquelim, and P. Schwill, “Shaping Giant Membrane Vesicles in 3D-Printed Protein Hydrogel Cages,” *Small*, vol. 16, jul 2020.
 - [417] A. Fink, C. R. Doll, A. Yagüe Relimpio, Y. Dreher, J. P. Spatz, K. Göpfrich, and E. A.

- Cavalcanti-Adam, “Extracellular Cues Govern Shape and Cytoskeletal Organization in Giant Unilamellar Lipid Vesicles,” *ACS Synthetic Biology*, 2022.
- [418] T. Robinson, P. Kuhn, K. Eyer, and P. S. Dittrich, “Microfluidic trapping of giant unilamellar vesicles to study transport through a membrane pore,” *Biomicrofluidics*, vol. 7, p. 044105, jul 2013.
- [419] Q. Wang, M. Taschner, K. A. Ganzinger, C. Kelley, A. Villasenor, M. Heymann, P. Schwille, E. Lorentzen, and N. Mizuno, “Membrane association and remodeling by intraflagellar transport protein IFT172,” *Nature Communications* 2018 9:1, vol. 9, pp. 1–13, nov 2018.
- [420] B. Schamberger, R. Ziege, K. Anselme, M. Ben Amar, M. Bykowski, A. P. G Castro, A. Cipitria, R. A. Coles, R. Dimova, M. Eder, S. Ehrig, L. M. Escudero, M. E. Evans, P. R. Fernandes, P. Fratzl, L. Geris, N. Gierlinger, E. Hannezo, A. Iglić, J. J. K Kirkensgaard, P. Kollmannsberger, Ł. Kowalewska, N. A. Kurniawan, I. Papanтониou, L. Pieuchot, T. H. V Pires, L. D. Renner, A. O. Sageman-Furnas, G. E. Schröder-Turk, A. Sengupta, V. R. Sharma, A. Tagua, C. Tomba, X. Trepap, S. L. Waters, E. F. Yeo, A. Roschger, C. M. Bidan, J. W. C Dunlop, B. Schamberger, V. R. Sharma, A. Roschger, and J. W. C Dunlop, “Curvature in Biological Systems: Its Quantification, Emergence, and Implications across the Scales,” *Advanced Materials*, p. 2206110, dec 2022.
- [421] K. Al Nahas, J. Cama, M. Schaich, K. Hammond, S. Deshpande, C. Dekker, M. G. Ryadnov, and U. F. Keyser, “A microfluidic platform for the characterisation of membrane active antimicrobials,” *Lab on a Chip*, vol. 19, pp. 837–844, feb 2019.
- [422] N. Yandrapalli, T. Seemann, and T. Robinson, “On-Chip Inverted Emulsion Method for Fast Giant Vesicle Production, Handling, and Analysis,” *Micromachines* 2020, Vol. 11, Page 285, vol. 11, p. 285, mar 2020.
- [423] S. Du and J. Lutkenhaus, “Assembly and Activation of the μ Escherichia coli/ μ Divisome,” *Molecular Microbiology*, vol. 105, no. May, pp. 177–187, 2017.
- [424] G. Lan, C. W. Wolgemuth, and S. X. Sun, “Z-ring force and cell shape during division in rod-like bacteria,” *Proceedings of the National Academy of Sciences of the United States of America*, vol. 104, pp. 16110–16115, oct 2007.
- [425] S. Hénon, G. Lenormand, A. Richert, F. Gallet, S. Hé, G. Lenormand, A. Richert, and F. Ois Gallet, “A New Determination of the Shear Modulus of the Human Erythrocyte Membrane Using Optical Tweezers,” *Biophysical Journal*, vol. 76, pp. 1145–1151, feb 1999.
- [426] K. M. Schoenemann and W. Margolin, “Bacterial Division: FtsZ Treadmills to Build a Beautiful Wall,” *Current Biology*, vol. 27, pp. R301–R303, apr 2017.
- [427] A. G. Vecchiarelli, M. Li, M. Mizuuchi, and K. Mizuuchi, “Differential affinities of MinD and MinE to anionic phospholipid influence Min patterning dynamics in vitro,” *Molecular Microbiology*, vol. 93, pp. 453–463, aug 2014.

- [428] S. Kretschmer, K. Zieske, and P. Schwille, “Large-scale modulation of reconstituted Min protein patterns and gradients by defined mutations in MinE’s membrane targeting sequence,” *PLoS ONE*, vol. 12, p. e0179582, jun 2017.
- [429] B. Monterroso, B. Reija, M. Jiménez, S. Zorrilla, and G. Rivas, “Charged Molecules Modulate the Volume Exclusion Effects Exerted by Crowders on FtsZ Polymerization,” *PLoS ONE*, 2016.
- [430] J. Schweizer, M. Loose, M. Bonny, K. Kruse, I. Monch, and P. Schwille, “Geometry sensing by self-organized protein patterns,” *Proceedings of the National Academy of Sciences of the United States of America*, vol. 109, pp. 15283–15288, sep 2012.
- [431] G. Rivas, A. López, J. Mingorance, M. J. Ferrándiz, S. Zorrilla, A. P. Minton, M. Vicente, and J. M. Andreu, “Magnesium-induced linear self-association of the FtsZ bacterial cell division protein monomer. The primary steps for FtsZ assembly,” *Journal of Biological Chemistry*, 2000.
- [432] S. Zorrilla, M. A. Hink, A. J. Visser, and M. P. Lillo, “Translational and rotational motions of proteins in a protein crowded environment,” *Biophysical Chemistry*, vol. 125, pp. 298–305, feb 2007.
- [433] X. Ge, D. Luo, and J. Xu, “Cell-Free Protein Expression under Macromolecular Crowding Conditions,” *PLoS ONE*, vol. 6, p. e28707, dec 2011.
- [434] H. X. Zhou, G. Rivas, and A. P. Minton, “Macromolecular Crowding and Confinement: Biochemical, Biophysical, and Potential Physiological Consequences*,” *Annual review of biophysics*, vol. 37, pp. 375–397, may 2008.
- [435] K. Zieske and P. Schwille, “Reconstituting geometry-modulated protein patterns in membrane compartments,” *Methods in Cell Biology*, 2015.
- [436] Z. Dunajova, B. Prats Mateu, P. Radler, K. Lim, P. Velicky, J. G. Danzl, R. W. Wong, J. Elgeti, E. H. 1, and M. Loose, “Chiral and nematic phases of flexible active filaments,” *bioRxiv*, p. 2022.12.15.520425, dec 2022.

List of abbreviations

ADP Adenosine diphosphate.

AFM Atomic force microscopy.

ATP Adenosine triphosphate.

AUC Analytical Ultracentrifugation.

BSA Bovine serum albumin.

cDICE Continuous droplet interface crossing encapsulation.

cryo-EM Cryo-electron microscopy.

cryo-ET Cryo-electron tomography.

CTL C-terminal linker.

CTT C-terminal tail.

CTV C-terminal variable region.

DNA Deoxyribonucleic acid.

E. coli Escherichia coli.

ESCRT Endosomal sorting complexes for transport.

GDP Guanosine diphosphate.

GTP Guanosine triphosphate.

GUV Giant unilamellar vesicles.

IM Inner membrane.

ITO Indium Tin Oxide.

LLPS Liquid-liquid phase separation.

LUV Large unilamellar vesicles.

M. jannaschii Methanococcus jannaschii.

mts Membrane targeting sequence.

NO Nucleoid Occlusion.

NTP N-terminal peptide.

OM Outer membrane.

PALM Photoactivated localization microscopy.
PDMS Poly-(dimethyl)-siloxane.
PEG Polyethylene glycol.
PG Peptidoglycan.
pN Piconewton.
PURE Protein synthesis using recombinant elements.

SBS Chromosomal DNA containing the SlmA binding site.
SEM Scanning electron microscopy.
siZipA His-tagged soluble variant of ZipA.
SLB Supported lipid bilayers.
SUV Small unilamellar vesicles.

TEM Transmission-electron microscopy.
Ter Terminal region of bacterial nucleoid.
TIRFM Total internal reflection fluorescence microscopy.
tRNA Transfer ribonucleic acid.

YFP Yellow fluorescent protein.

Acknowledgements

What a journey! It feels like it just passed me by, but it has been almost five years since the first day I visited the lab for an internship. I would like to send my most heartfelt gratitude to everyone who has helped me along this journey. All the people with whom I have had the pleasure of meeting along the way have contributed to this work and have shaped who I am today, both scientifically and personally. I feel really grateful to have met you all during my PhD.

First of all, I would like to thank Petra Schulle for giving me the opportunity to be part of her lab and for all the trust and freedom given to me to develop the research the way I wanted. I feel really lucky to have been part of this group. Thank you for this fruitful time.

My thanks to all my collaborators and co-authors, who have taught me how to approach scientific problems and have had a real impact on my research. Kristina Ganzinger, for being a fantastic collaborator, guiding me from a distance in what turned out to be my first paper. Diego Ramirez, for supporting me at the beginning of the thesis and introducing me deeper into the world of FtsZ. Leon Babl, for being the person I have spent the longest time in the lab and who has always been there to give me advice and support in everything I have needed. Shunshi Kohyama, for literally putting my PhD back on track, always willing to help me and guide my research with new ideas and projects. Marion and Jonathan, for helping me improve my last project with good ideas and nice cryo-EM data.

I would like to especially thank Germán Rivas for being one of the most important pillars of my PhD. I would not be here if it were not for your help, constant support, and guidance over the years, providing scientific and personal advice when I needed it. Thank you for introducing me to the field of synthetic biology and encouraging me to come to Munich. I will be eternally grateful. I also want to thank all the people with whom I shared time in the Rivas' lab during my master's thesis, who have continued to support and help me from a distance. Mercedes, Carlos, Luque, Silvia, Noe, and Ana, many thanks to all for creating such a friendly environment in the lab during my time there. I wouldn't have pursued

a PhD without that experience. A special mention goes to Marta and Michel, who have always been helpful in answering my scientific questions and meeting with me every time I returned to Spain.

Many thanks to Leon, Shunshi, Miguel, Germán and Kareem for helping me to write the thesis and for your insightful comments.

I would like to thank all my past and present colleagues who have become my advisers but also my friends. Daniela, thank you for being a good support and friend over the years. It was always a pleasure to have coffee with you and catch up. Thomas Litschel, thank you for providing me with great scientific ideas and discussions. Henri Franquelim, thank you for always having the right answer to every question and being so helpful. Hiro, thank you for all your support over the years, always willing to give me advice and spend some time talking over a coffee break. A special mention to my old "silent" office mates: Bea and Tamara, thank you for teaching me everything about the Min system but also for your good advice. Johannes, thank you for bringing such a good mood to the lab. Meifang, for being a great office mate. Laura, thank you for our talks and for introducing me to cryo-EM. Thanks to Katharina, Michaela, Kerstin, and Sigrid for making my life much easier in the lab. Frank, thank you for always being willing to help and implement new technologies in my projects. Silke, thank you for your invaluable administrative support. Jan, thank you for your help with any technical problem I might encounter. Maria, thank you for being my Spanish relief and for chatting with me about anything that happens in our daily lives.

Many thanks to all the people who have contributed to create such a great and inspiring environment in our lab: Nishu, Bela, Viktoriia, Anastasija, Benni, Gereon and Ana. Special thanks to Henry, Kareem, Yusuf, and Sveto for being great friends and making my time in the lab so enjoyable over the last year. Henry, thank you for your "all right" every day and for all the great and fun times outside the lab. Svetozar, thank you for being my Serbian brother and someone with whom I identify in many aspects. Kareem, thank you for your advice and insightful comments on my work. Yusuf, thank you for always being there for a coffee break and a nice chat and for your constant support every time I needed it. It has been really great to spend time with you all.

I want to thank all of you for creating a spectacular and inspiring environment in which it is a pleasure to work every day, regardless of the success or failure of the experiments, and in which it would have been much more boring to do a PhD. Many of the people I had the pleasure of working with have become good friends of mine. I am sad to see this time go by, but I am sure I will remain in contact with many of you.

I am also grateful to have been an IMPRS-LS student. IMPRS allowed me not only to

learn a lot through courses and seminars but also taught me how to steer my career and rethink my priorities in life. Most importantly, IMPRS has given me the opportunity to meet great people whom I consider good friends. I want to thank Karl, Dennis, Georg, Julian, Beth, Sophie, Kata, Anja, and Philip for all the fun times outside the lab. I would also like to give special thanks to Cristina Capitanio for being a great friend along the journey and for all the support given to cope with the PhD life. It has been great meeting all of you.

Many thanks to my friends from the MPI, Natalia and Favio, for the fun coffee and lunch breaks. Many thanks to Araceli for being one of my first friends in Munich and for cheering me up with your positivity and good mood. I would also like to thank my friends from University: Caye, Zoe, José, Miguel, Pablo, and Diego, for being great friends and for all the fun times and long discussions about life. You have always been there to meet me whenever we had the chance to be in Madrid at the same time.

I need to express my sincere gratitude to Pedro Weickert for being the person with whom I have spent the most time throughout my PhD. Thanks to you, I have been able to get through the ups and downs of my PhD, sharing evenings and weekends disconnecting from science. If there is one thing I take away from this whole journey, it is having made friends with you.

I would like to thank all of my friends and family who have supported me throughout my life and looked after me from a distance during this journey. Many thanks to all of my friends in Fuenlabrada - Carlos, Vurro, Rubén, Tego, and Raul. I feel very lucky to have such a great group of friends. I am eternally grateful to my parents, María del Carmen and Jesús, and my sister, Iris. I would not be here without your unconditional support and love. I feel blessed to have such an amazing family. And last but not least, my special person, Esther. I can't even imagine where I would be if it weren't for you. I know it hasn't been easy, and the distance was really hard to bear, but your unwavering support has been a constant source of strength for me. You have been there for me in every aspect of my life, and I could not have achieved all of this without you. Thank you for everything.

Curriculum Vitae

Scientific Education

Max Planck Institute of Biochemistry Martinsried, Germany

PhD student in Biology at Ludwig-Maximilians-University Munich, (2019-present)

Research group: Cellular and Molecular Biophysics

Mentor: Prof. Dr. Petra Schwille

Topic: Bottom-up reconstitution of a functional FtsZ-based cell division machinery

Biological Research Center (CIB-CSIC), Madrid, Spain

Master's degree in Cellular and Molecular Biology (2016-2018)

Menéndez Pelayo University

Research group: Systems Biochemistry of Bacterial Division

Supervisor: Prof. Dr. Germán Rivas

Thesis: Biochemical Analysis of the Essential Cell Division FtsZ Protein: Control by ZapD and Co-reconstitution with Ribosomes

Complutense University, Madrid, Spain

Bachelor's degree in Biology (2012-2016)

